

Wrocław University of Science and Technology
Faculty of Environmental Engineering

**Space-time analysis and modelling
of urban precipitation field**

Przestrzenno-czasowa analiza i modelowanie miejskiego pola opadowego

PhD thesis by
Katarzyna Siekanowicz

Dissertation supervisor:
Prof. Paweł Licznar
Wrocław University
of Science and Technology
Poland

Auxiliary supervisor:
Prof. Roberto Deidda
University of Cagliari
Italy

Wrocław, 2019

Acknowledgements

This dissertation is part of the project (2011/03/B/ST10/06338): “Spatio-temporal analysis and modelling of urban precipitation field”, financed by the Polish National Science Centre (NCN).

The author wishes to thank the Municipal Water Supply and Sewerage Company in Warsaw (MPWiK w m.st. Warszawie SA) and the Institute of Meteorology and Water Management – National Research Institute (Instytut Meteorologii i Gospodarki Wodnej – Państwowy Instytut Badawczy) for providing access to gauge and radar data.

Table of Contents

Abstract.....	5
Streszczenie.....	8
1. Introduction	11
2. Research goal	14
3. Radar measurements of precipitation structures	16
3.1. Space and time variability of precipitations	16
3.2. Radar measurements of precipitation.....	21
3.2.1. Radar measurement principle	21
3.2.2. Radar application to rainfall measurements.....	22
3.2.3. Temporal and spatial resolution of weather radar data	26
3.2.4. Z-R relationship.....	29
3.2.5. Sources of uncertainty and data quality in radar rainfall measurements	33
3.2.6. POLRAD system and selected radar products description	37
3.2.7. Weather radar data applications in urban hydrology	41
3.2.8. Weather radar data downscaling.....	44
4. Study area and data sources	45
4.1. Study area.....	45
4.1.1. Warsaw land use and development	45
4.1.2. Warsaw climate conditions	50
5. Local Z-R relationship for Warsaw.....	53
5.1. Local Z-R relationship study	53
5.2. Metodology	53
5.3. Results and discussion.....	55
5.4. Conclusions	62
6. Comparison between rain gauge and radar data for Warsaw	64
6.1. Rain gauge vs. radar data for urban hydrology applications	64
6.2. Metodology	64
6.3. Results and discussion.....	65
6.4. Conclusions	70
7. Multifractal analysis and modelling of Warsaw precipitation field	72
7.1. Space-Time Rainfall (STRAIN) model	74
7.2. Taylor hypothesis verification and advection velocity estimation.....	77
7.3. Moving window algorithm and rainfall events selection	83
7.4. Results and discussion.....	86

7.4.1. Multifractal analysis of Warsaw precipitation field.....	87
7.4.2. Multifractal modelling of precipitation field	98
7.5. Conclusions	108
8. Summary and final conclusions.....	109
References	112
List of web pages.....	120
List of appendices	120
List of figures and tables	121
Figures.....	121
Tables.....	124
List of symbols and abbreviations	125
List of symbols.....	125
List of abbreviations.....	126

Abstract

Urban areas, because of their high imperviousness and dense, valuable land use, are prone to flash floods caused by extreme rainfall events. Due to the urbanization process intensification and climate change, knowledge about precipitation fields over urban areas is crucial for the safety and resilience of their drainage systems.

Moreover, atmospheric precipitation is a variable process in space and time, hence, the recommended resolution of monitoring it over urban fields is single minutes in time and one kilometre or less in space. Today, urban hydrologists still face the problem of such quality rainfall data access as most design and modelling of urban drainage systems is performed based on rainfall models or rainfall series originating from a single gauge. Despite precipitation variability and intermittency among wide temporal and spatial scales, no adjustment is introduced to cope with the spatial rainfall variability even in the case of hydrodynamic modelling of large-scale urban drainage systems. In the future this could be ameliorated with the spread of weather radar precipitation fields monitoring coupled with dense gauge network, and with the introduction of more advanced spatio-temporal rainfall models.

In this dissertation, analysis and modelling of urban precipitation field over Warsaw are conducted. The study area focuses on Warsaw city and its surroundings, i.e. the most populated and highly impervious city in Poland, equipped with the most advanced rainfall monitoring network in the country.

The main goal of the study is to deliver a framework of analysis and modelling for precipitation structures in space and time with the resolution required in urban hydrology in Poland. To meet these requirements the STRAIN (Space-Time Rainfall) model, originally proposed by Deidda in 2000 is adapted to local conditions, is used. This model based on multifractal formalism and has a 3D multiplicative cascade structure. To verify the model applicability, i.e. to appraise multifractality of spatio-temporal structures of local precipitation fields, to derive model parameters, and to test its further performance in synthetic rainfall fields generation, the data from C-band weather radar from POLRAD was used. This radar network is managed by the Institute of Meteorology and Water Management – National Research Institute (Instytut Meteorologii i Gospodarki Wodnej – Państwowy Instytut Badawczy). The native resolution of POLRAD radar data is 1 km in space and 10 min in time.

The history of weather radar observations precipitation structures in Poland is relatively short. Thus, only complete and accessible for author precipitation fields scans covering summer months rainfall observations from 5 years are analysed.

Preliminary studies were conducted to verify radar data calibration and to test radar data quality against on ground rainfall measurements. Laser disdrometer recordings of Drop Size Distributions (DSD) from Warsaw were used to develop local radar reflectivity vs. rain rate Z - R relationships. In addition, already calibrated radar rain rate series were compared with the rain rate series recorded by 25 electronic gauges of the rainfall monitoring network, managed by the Water Supply and Sewerage Company in Warsaw (MPWiK w m.st. Warszawie S A).

The calibrated and verified radar scans are used to estimate the overall advection velocity U for selected rainfall events. For a central part of Poland conditions this advection velocity value, allowing for further assumption of the self-similarity of the precipitation structures in space and time, is estimated to be equal ca. $48 \text{ km}\cdot\text{h}^{-1}$.

A detailed analysis of multifractal scaling properties of spatio-temporal rainfall structures was then performed. The empirical multifractal scaling functions $K(q)$ are derived for each of 115 analysed rainfall events. Theoretical models are fitted to empirical $K(q)$ functions and their c and β parameters are calculated. Finally, the three-dimensional (3D) random cascade based on locally derived parameters of log-Poisson distribution (c and β), was used for generating synthetical precipitation fields. The statistical properties of synthetically generated rainfall structures were compared with the statistics observed in natural rainfall structures.

It was confirmed that 3D random cascade is an adequate tool for precipitation structures simultaneous downscaling in space and time. Moreover, the obtained model resolution in the end of cascade process meets urban hydrology requirements. The adjustment of STRAIN can be refined by three parameters: the overall advection velocity U , and the log-Poisson distribution parameters c and β .

The obtained values of parameters of log-Poisson distribution for analysed rainfall structures are highly diversified. Unlike in the original paper by Deidda (2000), the functional relationship between parameters c and β and mean the rain rate is not observed.

Moreover, the statistical properties of synthetic rainfall structures generated using dressed multifractal cascade process show to be closer to the properties of precipitation

fields observed in nature. Further model improvements could be achieved by performing extended fine-grained process for additional cascade levels and dressing final rainfall fields to those required in urban hydrology space and time resolutions.

Key words: weather radar, precipitation field, urban hydrology, downscaling, 3-D random cascade

Streszczenie

Obszary zurbanizowane, z uwagi na ich wysoki stopień uszczelnienia i cenne zagospodarowanie są podatne na zjawiska podtopień i powodzi związanych z intensywnymi opadami deszczu. Z uwagi na zintensyfikowane zjawisko urbanizacji i zmiany klimatyczne, wiedza o miejskich polach opadowych jest kluczowa dla bezpieczeństwa i odporności systemów odwodnienia miast.

Ponadto, opad atmosferyczny to zjawisko wykazujące dużą zmienność w czasie i przestrzeni, stąd zalecana rozdzielczość pomiarów na potrzeby monitoringu pól opadowych powinna być rzędu pojedynczych minut w czasie i kilometra, bądź mniej, w przestrzeni. Hydrolodzy miejscy stają przed problemem dostępu do danych o opadach w takiej rozdzielczości. Obecnie, większość procesów projektowych i modelowania systemów odwodnień nadal jest prowadzona w oparciu o model opadowy bądź rejestracje opadów, pochodzące z pojedynczego deszczomierza. Pomimo zmienności i nieciągłości opadów w szerokim spektrum skal w czasie i przestrzeni, zazwyczaj nie wprowadza się korekty z uwagi na przestrzenną zmienność opadów, nawet w przypadku modelowania hydrodynamicznego systemów odwodnień dużych miast. W przyszłości postęp w tym zakresie może nastąpić dzięki wprowadzeniu na szeroką skalę monitoringu pól opadowych zarówno z użyciem radarów meteorologicznych jak i pomiarów z sieci deszczomierzowych o dużym zagęszczeniu, a także poprzez wprowadzenie bardziej zaawansowanych czasowo-przestrzennych modeli opadowych.

W tej pracy przeprowadzono analizę i modelowanie miejskiego pola opadowego nad Warszawą. Obszar opracowania obejmuje Warszawę i jej okolicę, tj. najbardziej zaludnione miasto w Polsce, o bardzo wysokim stopniu uszczelnienia i o jednej z najlepiej rozwiniętych sieci pomiarów opadów w kraju.

Głównym celem pracy było wypracowanie warsztatu analizy i modelowania struktur opadowych w rozdzielczości czasowej i przestrzennej wymaganej do stosowania w hydrologii miejskiej w Polsce. W tym celu dokonano adaptacji do lokalnych warunków modelu STRAIN (Space-Time Rainfall), który został opracowany przez Deidde w 2000 r. Model ten, opiera się o formalizm multifraktalny i ma strukturę trójwymiarowej kaskady losowej. W celu weryfikacji możliwości zastosowania modelu, tj. oceny multifraktalności lokalnych struktur opadowych, doboru parametrów modelu i sprawdzenia możliwości generowania z jego użyciem syntetycznych struktur opadowych, użyto danych pochodzących z radarów meteorologicznych, pracujących

w paśmie C i należących do systemu POLRAD. Ta sieć radarów jest zarządzana przez Instytut Meteorologii i Gospodarki Wodnej – Państwowy Instytut Badawczy. Natywna rozdzielczość danych z radarów systemu POLRAD wynosi 1 km w przestrzeni i 10 min w czasie.

Okres prowadzenia obserwacji struktur opadowych z użyciem radarów meteorologicznych w Polsce jest relatywnie krótki. Z tego względu przeanalizowano kompletne i dostępne dla autorki skany radarowe pól opadowych z okresu 5 lat obserwacji w miesiącach letnich.

Jako badania wstępne wykonano weryfikację kalibracji danych radarowych oraz przeprowadzono sprawdzenie ich zgodności z pomiarami deszczomierzowymi. Do opracowania lokalnej zależności funkcyjnej $Z-R$ dla Warszawy, łączącej odbiciowość radarową Z z intensywnością opadu R , użyto rejestracji rozkładu wielkości hydrometeorów (DSD) przeprowadzonej z użyciem disdrometru laserowego. Ponadto, już skalibrowane serie rejestracji intensywności opadów, pochodzące z radaru meteorologicznego porównano z tymi, zarejestrowanymi przy użyciu sieci 25 deszczomierzy, zarządzanej przez MPWiK w m.st. Warszawie S A.

Skalibrowane i zweryfikowane skany radarowe zostały użyte do oszacowania wielkości uogólnionej prędkości adwekcji U dla wybranych zdarzeń opadowych. Dla warunków centralnej części Polski ta prędkość, która pozwala w kolejnych krokach na wprowadzenie założenia o samopodobieństwie struktur opadowych w czasie i przestrzeni, wynosi ok. $48 \text{ km} \cdot \text{h}^{-1}$.

Następnie przeprowadzono szczegółową analizę właściwości multifraktalnych czasowo-przestrzennych struktur opadowych. Dla każdego ze 115 wybranych zdarzeń opadowych wyznaczono empiryczną multifraktalną funkcję skalowania momentów $K(q)$. Do empirycznych funkcji $K(q)$ dopasowano modele teoretyczne oraz obliczono ich parametry c i β . Ostatecznie użyto trójwymiarowej kaskady losowej stworzonej w oparciu o parametry rozkładu log-Poissona (c i β) wyznaczone dla warunków lokalnych do generowania sztucznych pól opasowych. Następnie porównano ich właściwości statystyczne z tymi, które charakteryzują struktury opadowe zaobserwowane w naturze.

Potwierdzono możliwość użycia trójwymiarowej kaskady losowej jest właściwej metody do prowadzenia downscalingu struktur opadowych z jednoczesnym uwzględnieniem wymiaru czas i przestrzeni. Ponadto, otrzymana końcowo w procesie kaskadowym

rozdzielczość modelu pozwala na stosowanie go na potrzeby hydrologii miejskiej. Na dopasowanie modelu STRAIN mają wpływ trzy parametry: uogólniona prędkość adwekcji oraz parametry rozkładu log-Poissona c i β .

Uzyskane wielkości parametrów rozkładu log-Poissona dla analizowanych struktur opadowych były wysoce zróżnicowane. W przeciwieństwie do wyników uzyskanych przez Deiddę (2000) istnienie zależności parametrów c i β od średniej intensywności opadu nie zostało potwierdzone.

Ponadto, właściwości statystyczne syntetycznych struktur opadowych wygenerowanych w procesie multifraktalnej kaskady ubranej są bliższe właściwościom pól opadowych obserwowanych w naturze. Dalsze udoskonalenie modelu może być uzyskane poprzez wprowadzenie procesu drobnoziarnistego dla dodatkowych poziomów kaskady i ubierania pól opadowych do rozdzielczości czasowych i przestrzennych pożądanych w hydrologii miejskiej.

Słowa kluczowe: radar meteorologiczny, pole opadowe, hydrologia miejska, downscaling, trójwymiarowa kaskada losowa

To mitigate the influence of extreme rainfall events on urban structures, design, hydrodynamic modelling, maintenance, and management of stormwater systems based on reliable information about rainfall is needed. Also, because of the development of real time control (RTC) of urban drainage systems, of which the main goal is urban flooding and combined sewerage overflows limitation, the discharge controlling and the efficiency improvement of whole drainage system including wastewater treatment plants, the demand for quantitative precipitation estimates, and information about its space and time distribution has increased (Schütze et al., 2004).

Because of spatial and temporal variability, rainfall events are challenging to measure (Krajewski et al., 2003). Among the different types of rainfall measurement techniques, weather radar achieves the highest spatial and temporal resolution of sampling, which is needed in hydrological applications. The weather radar uses remote sensing technology that estimates rainfall based on the reflectivity of precipitation measurements at a given altitude. Moreover, weather radar can provide high resolution data over a large area dependent on its range (Einfalt et al., 2004; Thorndahl et al., 2017).

Although a rain gauge network may provide more accurate estimates in single locations, the spatial continuity of measurements is not preserved (Goudenhoofd and Delobbe, 2009). Einfalt et al. (2004) pointed on the complementarity of both measurements technique – their concurrent usage improves rainfall estimations and is essential for hydrological applications.

However, the radar scanning strategy adequate to providing meteorological services, may not be sufficient for urban hydrology purposes (Nielsen et al., 2014). Several sources of uncertainties may affect radar data quality (e.g., Wilson and Brandes, 1979; Ciach et al., 2007, Szturc et al., 2008a; Villarini and Krajewski, 2010), i.e. miscalibration, non-meteorological echoes, or range effect.

To analyse and model urban precipitation field the minimum time resolution of single minutes (1–5 min) and spatial resolution of minimum 1 km² is required (Schilling 1991). Fabry et al. (1994) suggested an even finer spatial resolution (i.e. 100–500m) for the same time resolution (1–5 min). The space-time resolution requirements may differ according to the specific application (Einfalt et al., 2004). Ochoa-Rodriguez et al. (2015a) conducted a detailed sewer system simulation for those finer spatial–temporal resolutions suggested by Fabry et al. (1994) and considered them as essential for hydraulic modelling of urban catchments. To meet the requirements of spatial and

temporal rainfall data resolution for urban hydrology applications, X-band radars may be used or the conversion of C-band radar data must be carried out.

For urban hydrology applications, not only measurements of precipitation fields are needed, but also advanced rainfall modelling techniques. To study or simulate extremely variable fields over wide range of scales, a multifractal framework is used. Multifractals have become a rather typical tool for analysing and modelling variability in geophysics and hydrology, including rainfalls (Gires et al., 2012). Basically, multifractals are space or space-time fields that have structures at all scales (Schertzer and Lovejoy, 2011).

The assumption of self-similarity of the precipitation both in time and space domains allows to introduce downscaling models based on multifractal framework. There have been successful attempts to construct such models performed, e.g. Ferraris et al. (2003) and Kang and Ramirez (2010). However, their methods are not universal: in various areas different precipitation mechanisms dominate due to different surface conditions, large-scale climatology, and local variability. Hence, multifractal downscaling models need local verifications and refinements (e.g. Ebtehaj and Foufoula-Georgiou, 2010).

The weather radar data and multifractal framework are used for the first time in Poland for this study to conduct analysis and modelling of precipitation fields simultaneously in the time and space domain at high resolutions suitable for the current needs of urban hydrology.

2. Research goal

The main goal of this dissertation is to conduct a space-time analysis and modelling of urban precipitation field based on selected weather radar sequences.

The research bases mainly on a 10-minute resolution data originating from the Polish C-band radar system (POLRAD). Precisely, maximum rainfall events recorded during the summer months over a 5- year long radar observation period are selected for further multifractal studies, model parameters retrieval, and performance testing. Due to the model assumptions and its structure, the area of interest significantly extends the city limits. However, the model domain is centred over the capital city of Poland, Warsaw. This city area is used as a specific small-scale test site because of its deployed advanced ground rainfall monitoring network.

The selected precipitation fields obtained from weather radar sequences are the subject of space-time multifractal analyses based on a three-dimensional (3-D) cascade. To investigate spatial and temporal properties of the precipitation field, multifractal analysis is carried out using the STRAIN model by Deidda (2000), based on log-Poisson distribution.

Two parameters of log-Poisson distribution are estimated for all selected rainfall events to characterize the statistical properties of multifractal processes, and to further generate synthetic rainfall events. Finally, statistical properties of the synthetically generated data are investigated and compared with those derived from the original radar sequences.

This dissertation is aimed to verify the following hypothesis:

- I A precipitation field structure is varied in both, space and time, in a wide range of scales, especially, for a case study of the large city.
- II A precipitation field has a multifractal character. It is possible to analyse and model its space and time variability using multifractal formalism.
- III Multifractal generator allows to create a synthetic time series of precipitation fields that are statistically close to natural ones.
- IV Downscaling provides space-time resolution of precipitation fields that meets urban hydrology requirements.

Moreover, an additional study aim is to verify if standard radar data calibration procedures implemented in the POLRAD system delivers radar products of quality desired for local urban hydrology in Warsaw applications. Thus, a local functional relationship between rain rate and radar reflectivity (Z-R relationship), based on disdrometer data is derived. In addition, comparison between precipitation time series recorded on rain-gauges network and originating from corresponding cells of radar scan sequences is performed.

3. Radar measurements of precipitation structures

3.1. Space and time variability of precipitations

Reliable precipitation data is crucial for urban hydrology because rainfalls are the driving force of runoff formation in the urban environment (Berne et al, 2004). Rainfall phenomena are variable over a wide range of scales resulting in significant uncertainties for hydrological modelling. To meet the requirements for rainfall data resolution for urban hydrology (Schilling, 1991; Fabry et al., 1994) – single minutes in time and less than one kilometre in space – radar technology and/or downscaling methods are introduced.

The variability of sizes and durations of precipitation structures is presented in table 3.1 below. The fields range from several to even several hundred square kilometres, while the duration ranges from several dozen minutes to several hours. Both space and time dimensions depend mostly on the meteorological origin of the rainfall event.

Table 3.1 Characteristics of some important precipitation systems (Einfalt et al., 1998)

<i>Name</i>	<i>Size</i>	<i>Life time</i>	<i>Shape</i>	<i>Meteorological origin</i>
single cell	several km ²	several dozen minutes	symmetrical	convection
super cell	several dozen km ²	one hour or more	symmetrical	convection with wind shear
multicellular thunderstorm	several dozens to several hundred km ²	several hours	symmetrical	convection with wind shear
squall line	several dozens to several hundred km ²	several hours	oriented	convection with wind shear
narrow rain band	several km x several hundred km	several hours	elongated	warm belt with an anabatic band hundred km cold front
wide rain band	several dozen km x several hundred km	several hours	elongated	warm belt of a perturbation

The features of the precipitation structure influencing space and time variability are as follows (Einfalt et al., 1998):

- travelling speed;
- size;
- mean intensity;
- inside convective activity.

Discrete point rainfall measurements (e.g. using rain gauge) show their variability in time and high dynamics, which are visible regardless of the temporal resolution. The rainfall intensity fluctuations are substantial and noticeable even at a time scale of single seconds. Hence, the time step of measurements should be defined consciously, knowing that with the increase of time steps the dynamic nature of precipitation is smoothed out. According to Einfalt et al. (1998), the aggregation from one to five-minutes of rain rates may result in a decrease of their maximum value by a factor of 80%.

This study focusses on the urban precipitation field, hence the micro- local and mesoscale categories of scales of urban climate according to Oke (2006a), will be used. However, the diversity of urban climates should be underlined. Every city has its unique conditions like geographical location, setting, architecture and cultural background (Oke, 2006b). All this makes the local climate investigation, including precipitation field studies, essential for the description of the urban water cycle.

Microscale is related to the scale of individual objects in the city, e.g. buildings, roads, streets, trees, gardens, etc. – whose dimensions range from less than one to several hundreds of metres. Even small objects in urban space can have an impact on airflow due to surface and air temperatures variations (even several degrees in very short distances). In general, the climate data gathered on urban weather stations in the microscale may also be used to evaluate climate trends at even larger scales. However, these urban stations should not be prone to microclimate influences, which is difficult to fulfil.

The local scale, considered the “standard” scale to monitor urban climate, includes features whose dimensions range from one to several kilometres. Thus, in this scale, landscape features such as topography are included but microscale effects are omitted. In urban areas this translates to averaging of the climate of urban units/districts with similar types of urban development (including land cover, proportion between built and non-built areas, size of the buildings, activity).

The mesoscale is the scale of the entire city, typically tens of kilometres in extent. A single weather station is not representative for such an extensive scale. Weather parameters, including precipitation depths, recorded by instruments installed on some arbitrarily chosen single locations of the city should not be considered as representative for the whole urban area. However, historically, single gauge records were used for the development of IDF/DDF (intensity-duration-frequency/depth-duration-frequency) curves or even used as inputs to hydrodynamic models of whole city drainage systems.

In figure 3.1 the spatial scales of urban climate analysis and vertical layers found in urban areas (i.e. planetary boundary layer (PBL), urban boundary layer (uBl), urban canopy layer (ucl), and rural boundary layer (rBl)) are presented. In figure 3.2, time and space scales involved in some exemplary urban climate phenomena creation are displayed. This diagram shows air circulation related phenomena, and thus has a lot in common with turbulence scales in the urban environment. Further, it has a direct relation to the local precipitation process as rainfall in general is considered to be a visible trace of turbulence in atmosphere.

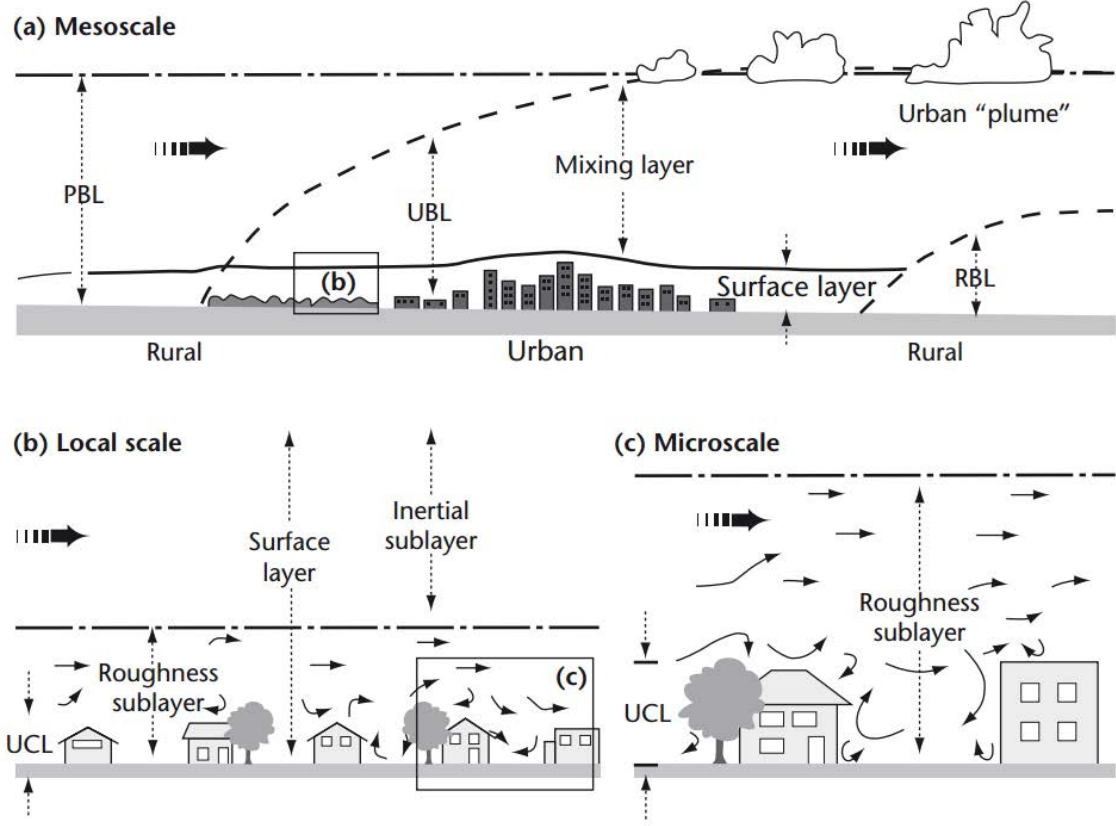


Figure 3.1 Spatial scales of urban climate analysis schematic of climatic scales and vertical layers found in urban areas. Reprinted from World Meteorological Organization, 2012

To gain an appreciation of the spatial variability and intermittency of rainfall, the remote sensing technology, such as by radar or satellite, should be used. Rain gauges, due to discrete point measurements, are not sufficient enough to provide spatial coverage of rainfall data comparable to weather radar quality; even when operating in synchronized networks. In fact, rain gauge networks can only be used to recognize an approximate spatial rainfall variability (Einfalt et al., 1998).

At the same time weather radar resolution of measurements in space and time is strongly limited by radar antenna operating principles and the velocity of recorded echoes post-processing. Often, radar resolution in space is higher than in time, especially if the comparison is made for convective velocity of storms and the velocity of precipitation structures is higher than $0.8\text{m}\cdot\text{s}^{-1}$. In such circumstances, the achievable spatial radar resolution of 500m does not correspond to the standard 10 min resolution in time (Nielsen et al., 2014). Further discussion of this topic, as well as detailed description of radar rainfall measurements and their applications for urban hydrology is presented in next chapter 3.2.

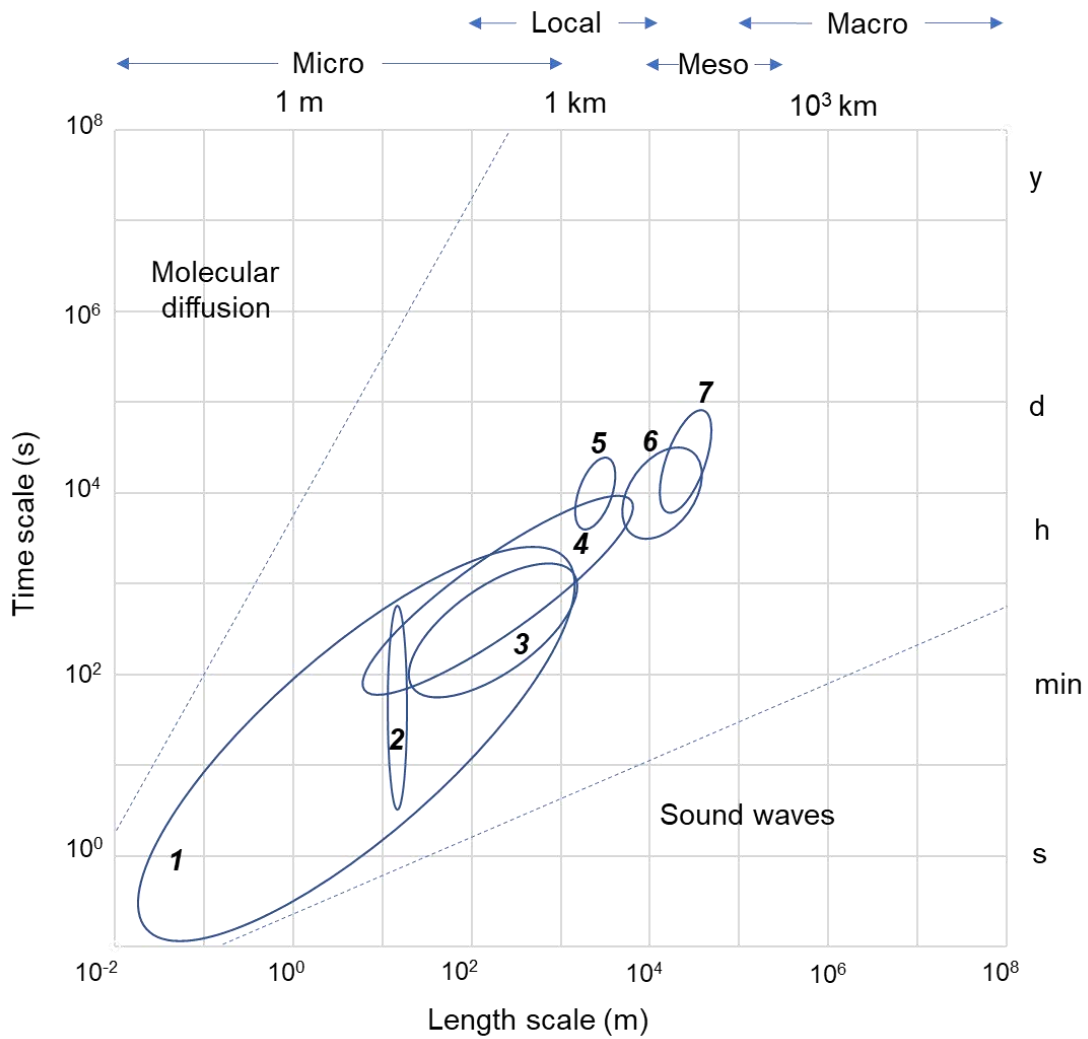


Figure 3.2 Time and space scales involved in urban climate phenomena.

Examples of some motion phenomena: 1 – mechanical eddies shed by obstacles; 2 – cross-canyon vortex; 3 – individual building wake; 4 – chimney stack plume; 5 – urban park breeze circulation; 6 – urban-rural breeze system; 7 – uplift in city ‘plume’ (based on: Oke, 2006b)

3.2. Radar measurements of precipitation

3.2.1. Radar measurement principle

Radar — an English acronym, derived from RAdio Detection And Ranging — was first used as a code by the U.S. Navy in 1940 during World War II. Radar is a remote sensing technique using electromagnetic (EM) waves that allow detection of the location and distance of a target by its reflection. Information about the target is derived from the correlation of the received and transmitted signals. Possible information that can be obtained by radar signal correlation is listed in Table 3.2.

Table 3.2 The derivation of target data based on received and transmitted signals correlation (Eaves, 1987)

<i>Target Information</i>	<i>Derived by Correlating:</i>		
	<i>Received Signal</i>		<i>Transmitted Signal</i>
Size (radar cross section)	Strength	with	Power
Range	Time delay	with	Time reference
Angular coordinates	Antenna beam position	with	Antenna beam reference
Radial velocity (Doppler)	Radio frequency	with	Frequency reference
Scattering signature	Polarization scattering matrix (PSM)	with	EM wave reference
Identification	Measured PSM with stored signature	for	EM wave reference

There are four basic elements in any functional radar (Eaves, 1987):

- a transmitter – which generates a desired radio frequency (RF) waveform at required power level,
- an antenna – which transmits and receives RF energy into the propagation medium,
- a receiver – which collects target signals, amplifies them, and translates the information to the baseband,
- an indicator – which delivers target information to the user.

The major elements of radar system are illustrated in fig. 3.3.

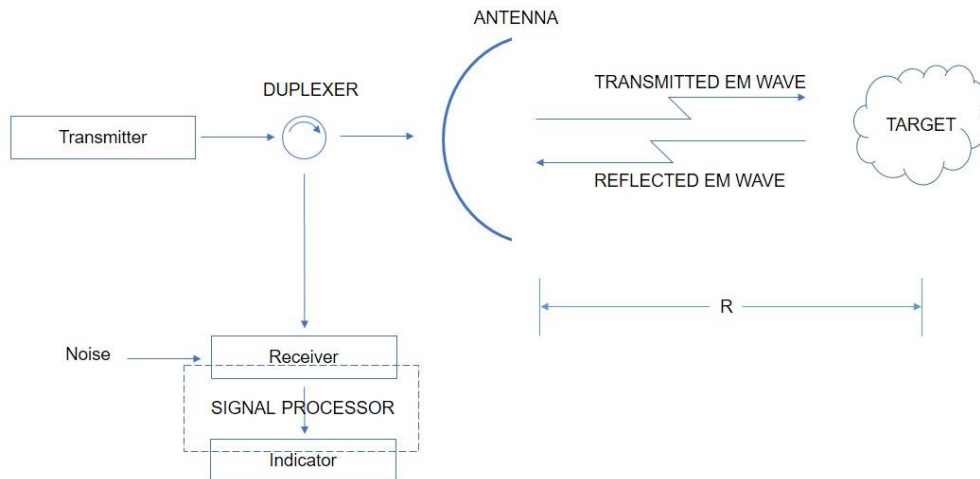


Figure 3.3 Radar basic system elements (based on: Eaves, 1987)

3.2.2. Radar application to rainfall measurements

Radar was introduced primarily for military usage, but its ability to detect precipitation was discovered almost immediately. Rain and snow cause radar interference and just like obscure objects, e.g. airplanes or ships. During World War II the investigation of the scattering properties of precipitation was conducted i.a. by the Canadian Army Operational Research Group—Stormy Weather Group—in Ottawa led by J. S. Marshall (Douglas, 1990). Their studies on unwanted interference initiated a new way of observing the atmosphere.

Since the first weather radar was introduced in the 1950s (Douglas, 1990), the improvement in radar engineering, signal processing, and meteorology has influenced the accuracy, resolution, and number of products (Kumjian, 2018).

The main advantage of radars used for rainfall estimations is their capability to provide spatial distributed information about precipitation (Thorndhal et al., 2017). The radar method of rainfall measuring enables the monitoring of space and time variability in the precipitation field in real time.

The EM waves emitted from weather radar spread through the atmosphere and can interact with cloud and hydrometeors, but also with other objects (e.g. non-meteorological particles, planes, biota and on-ground targets). Some of the radar signals may be absorbed, but some may be also scattered back (*backscattering*) by objects that caused the wave's power loss during propagation—called *attenuation* (Kumjian, 2018).

The weather radar equation is as follows (Brock and Richardson, 2001):

$$P_r = \frac{\pi^3 P_t g^2 S^2 c \omega \theta_1^2 |K_w|^2 Z}{2^{10} (\ln 2) l^2 \lambda^2} \quad (3.1)$$

P_r – received power in W,

P_t – transmitted power in W (about 750 kW),

S – signal loss factor due to absorption along the path,

c – speed of light, $3 \cdot 10^8$ m s⁻¹,

ω – pulse width in s (e.g., 1,57 or 4,5 μs)

θ_1 – antenna beam width in radians (e.g., 1° = 0,01745 radians),

l – range to target in m (up to 450 km),

λ – wave length in m (form several mm to 10 cm),

Z – effective reflectivity factor,

$|K_w|^2$ – parameter associated with the complex index of refraction of the scatter (0.93 for water droplets and 0.19 for ice particles)

The radar measurements of hydrometeors based on effective reflectivity factor (Z), which depends on their diameter (D) – equation 3.2 (Brock and Richardson, 2001). However, in the atmosphere, hydrometeors are not single, but are found in enormous populations. If the radar signal intercepts such a population of particles, it is scattered by many of them simultaneously. The radar probes the atmosphere in sampling volumes, which are the sections of the atmosphere at a given moment. The total sum of backscattered signals from each particle in cross sections per unit volume is called the *radar reflectivity* (Kumjian, 2018). Finally, the rain rate (R) can be estimated based on droplet sizes as is defined in equation 3.3 (Brock and Richardson, 2001).

$$Z = \sum_{i=1}^N D_i^6 = \int_0^{\infty} N(D) D^6 dD \quad (3.2)$$

$$R = \frac{\pi}{6} \int_0^{\infty} N(D) D^3 V_t(D) dD \quad (3.3)$$

where for a unit volume of 1 m³:

Z – radar reflectivity, mm⁶·m⁻³,

D – diameter of the particle, mm,

R – rain rate, mm·h⁻¹,

N – number of particles,

V_t – drop terminal fall velocity, m·s⁻¹.

Rain drop terminal fall velocity (V_t) can be estimated with a satisfying accuracy on the basis of single drops equivalent to the diameter using equation 3.4 (Brock and Richardson, 2001):

$$V_t(D) = 9.65 - 10.3 e^{-600D} \quad (3.4)$$

The relationship between radar reflectivity (Z) and rain rate (R) is formulated by an empirical, power-type formula and is discussed in more detail in chapter 3.2.4.

Traditional weather radars can be grouped into precipitation radars (S-X bands) and cloud radars (Ku-W). Recently, G-band radars also have been proposed for cloud studies (Kumjian, 2018). The nominal frequency bands and wavelengths for each type of weather radar are listed in table 3.3.

The X-band radars, because of their antenna size, may be mobile, and are often used to investigate dynamic phenomena such as tornadoes and severe convective storms (e.g., French et al., 2015; Pazmany et al., 2013; Wurman and Kosiba, 2013). Higher-frequency cloud radars are mainly used in scientific research (e.g., Kalesse et al., 2013; Kneifel et al., 2015) and spaceborne applications (e.g., Heymsfield et al., 2013).

Table 3.3 Naming conventions for different frequency bands and wavelengths (Kumjian, 2018)

<i>Naming convention</i>	<i>Nominal frequency</i>	<i>Nominal wavelength</i>
S	2–4 GHz	15–8 cm
C	4–8 GHz	8–4 cm
X	8–12 GHz	4–2,5 cm
Ku	12–18 GHz	2,5–1,7 cm
K	18–27 GHz	1,7–1,2 cm
Ka	27–40 GHz	1,2–0,75 cm
W	75–110 GHz	4–2,73 mm
G	110–300 GHz	2,73–0,1 mm

In the research part of this dissertation, data obtained from C-band radar is used. C-band and S-band radars belong to the most globally spread weather radar types (Einfalt et al., 2004). For example, the European network of C-band and S-band radars covers almost the entire continent. (Einfalt et al., 2004). Similarly, a network NEXRAD of 159

high-resolution S-band Doppler weather radars operated by the National Weather Service (NWS) covers all the continental U.S. territory (Cunha et al., 2013).

In general, radar measurements are used for the following meteorological applications (World Meteorological Organization, 2012):

- detection, tracking and warning of severe weather, including thunderstorms, hail and strong winds;
- observation of synoptic and mesoscale weather systems;
- estimation of precipitation.

Meteorological radar generally does not detect rain-free clouds (Ci, Cs, Cc, St, As, Ac, Cu hum, Cu med, Cu cong). In such case, the detection range is nearly equal to zero and the probability of rain-free clouds detection is very low, even within a short distance from the radar probe. In table 3.4 an approximate probability of meteorological objects detection by radar in three different distance ranges (< 100 km, 100 – 150 km and 150 – 200 km) is provided.

Table 3.4 An approximate probabilities of meteorological objects detection by radar (Moszkowicz and Tuszyńska, 2006)

<i>Object</i>	<i>Distance range</i>		
	<i>< 100 km</i>	<i>100 – 150 km</i>	<i>150 – 200 km</i>
Altostratus without rainfall	20	-	-
Drizzle, snow grains, ice snow	5	-	-
Heavy snow	60	30	-
Heavy rain and snow mixed	70	40	10
Heavy rain	90	70	30
Light snow	60	30	-
Light rain and snow mixed	70	40	10
Light rain	90	80	50
Light rain with storm	100	95	75
Hail	100	100	100

3.2.3. Temporal and spatial resolution of weather radar data

Weather radar data temporal resolution is provided by a scanning strategy of radar. The total time to obtain a full azimuthal volume scan depends on the rotational speed and number of scanning elevations (Thorndahl et al., 2017).

According to the summary in table 3.5 operational weather S-, C-, and X-band radars work with the temporal resolution of 5–15 min. However, temporal resolution of radars that are used for research purposes – dedicated for a higher resolution precipitation monitoring for a specified area and specific elevation – may provide a finer, up to 15s resolution (van de Beek et al., 2010, Mishra et al., 2016).

The most significant advantage of meteorological radars over other precipitation measurement methods is their capability to provide the information of spatial rainfall distribution. The spatial radar resolution depends on radial and azimuth resolution (Thorndahl et al., 2017).

The radial resolution (or range resolution) is strictly connected with pulse length, and is equal to half of it (Battan, 1973). The storage data limitations result in subdivision radar scanlines into a fixed number of bins. The number of range bins is related with the ratio of the maximum unambiguous range and half of the pulse length (radial resolution). Radars operated in X-band have a shorter range than C- and S-bands, but a finer resolution (hundreds of meters – see table 3.5). The radial resolution ranges from 3 to 1000m (e. g. Leijnse et al., 2010; Mishra et al., 2016).

The azimuthal resolution (angular) horizontal resolution is defined by the size and construction of the antenna and is related to beam width. Parabolic dish antenna, which is commonly used in operational radars allows to obtain a 1° azimuthal resolution (Thorndahl et al., 2017) – in this case, a distance of 100 km the width of the beam is equal to ca. 1750 m.

In figure 3.4, radar reflectivity in four different spatial resolution obtained from dual-polarimetric X-band radars (100, 500, 1000 and 2000 m) are shown. The data cover the area (ca. 12 km × 12 km) over the city of Aalborg, Denmark. The illustration shows the significance of higher spatial resolution data to observe the spatial variability of precipitation over an urban area.

The spatial range and typical time and spatial resolution of weather radar measurements are listed in table 3.5 below. The spatial and temporal resolution of X-

band radars is usually finer than C- and S-band because X-band radars operate using smaller antenna to obtain the same angular resolution. However, C- and S- band radar may achieve a “super resolution” (e.g. Ochoa Rodriguez et al., 2015b).

Table 3.5 Typical operating resolutions and maximum ranges for different types of weather radars used in hydrological applications (Thorndahl et al, 2017)

	X-band	C-band	S-band
Spatial resolution	100-1000 m	250-2000 m	1000-4000 m
Temporal resolution	1-5 min	5-10 min	10-15 min
Maximum quantitative range	30-60 km	100-130 km	100-200 km

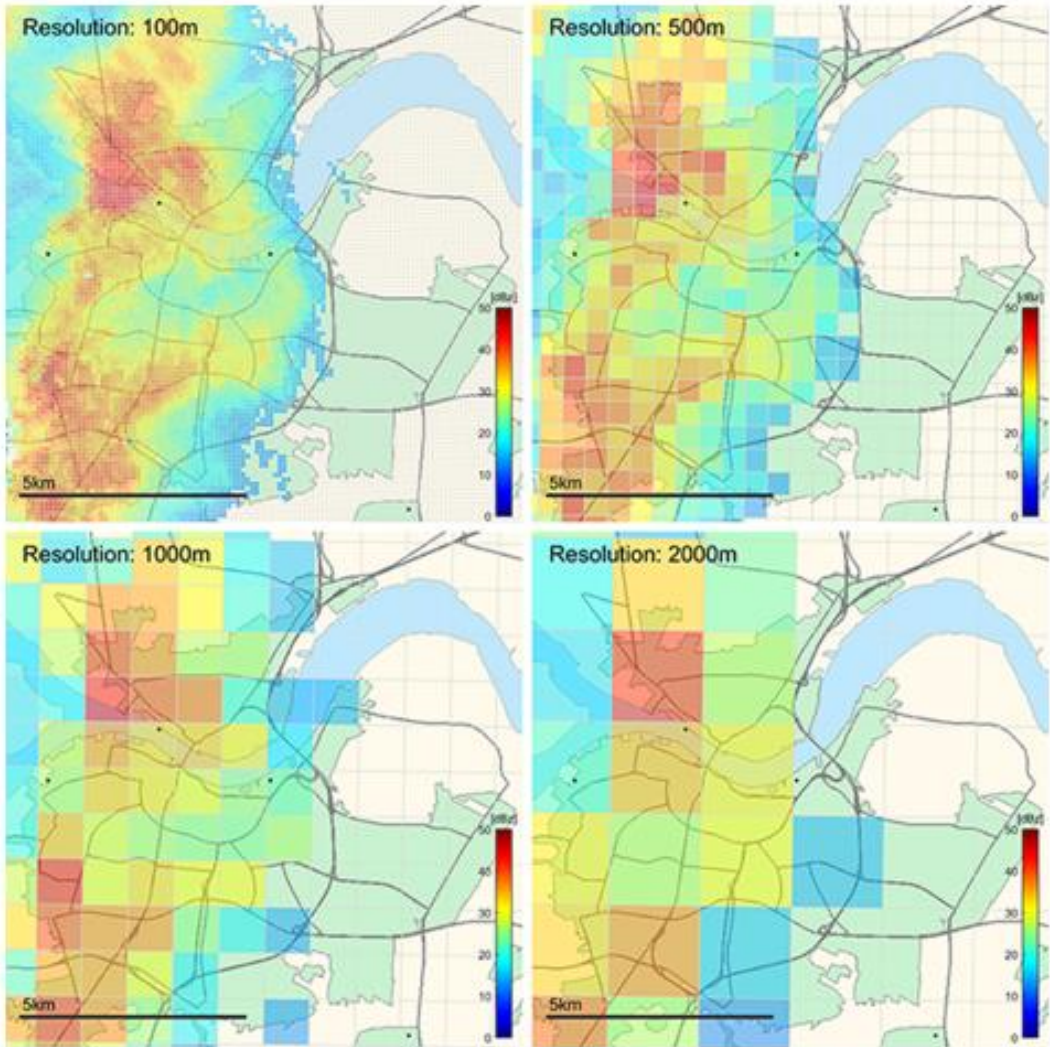


Figure 3.4 Example of radar reflectivity at four different Cartesian spatial resolutions over Aalborg, Denmark. Reproduced from Thorndahl et al., 2017

The impact of radar data resolution in space and time for hydrological modelling is difficult to define because numerous case studies differ by initial conditions (i.e. catchment size, its imperviousness, slopes, model scale), model outputs (i.e. water levels, peak flows, discharges). However, according to Thorndahl et al. (2017), three statements about the requirements for spatial and temporal resolution of radar inputs data for runoff response models can be determined, i.e.:

- *the demand for high resolution of weather radar data in space and time decreases for more vast catchment cases.* The minimum recommended spatial and temporal resolutions for defined catchment sizes are collected in table 3.6;

Table 3.6 Recommended spatial and temporal resolution for weather radar data for defined catchment sizes

Size of the catchment	Recommended temporal resolution	Recommended spatial resolution	Source:
1 ha	1 min	100 m	Ochoa-Rodriguez et al., 2015a
10 ha	1 min	2 km	Berne et al., 2004
100 ha	3 min	3 km	
1000 ha	6 min	4 km	

- *the resolution requirements for radar data depend on catchment characteristics and modelled runoff response.* For instance, higher resolution is required for peak-runoff simulation upstream in urban catchment. The resolution may be reduced for total catchment runoff evaluation purposes;
- *the characteristic of storm structure (e.g. size, movement, lifespan, intensity, etc.) are important in selection of space-time resolution of radar data.* The velocity of the precipitation field influences adequate spatial and temporal resolution distribution of rainfall for urban hydrology applications. Higher resolution is required for higher-intensity convective thunderstorms (in narrow spatial extent) in comparison to stratiform long-duration storms.

According to Berne et al. (2004) the optimal relation between spatial (s) and temporal (t) resolution of weather radar data for hydrological modelling purposes for Mediterranean conditions is $s=1.5t^{0.5}$, and according to van de Beek et al. (2012) it is $s=5t^{0.3}$ for summer conditions in the Netherlands.

3.2.4. Z-R relationship

The relationship between radar reflectivity, Z ($\text{mm}^6 \text{m}^{-3}$), and rain rate, R (mm h^{-1}), has been examined for over 70 years. The conversion from radar reflectivity Z into rain rate R depends on the drop size distribution (DSD) of the investigated precipitation (Thorndahl et al., 2017). The Z - R relationship formulation is crucial for calibration of weather radar and is a source of possible uncertainties in radar measurements of precipitation (Wilson and Brandes, 1979, Villarini and Krajewski 2010; Sassi et al., 2014).

The Z - R relationship is empirical and has a structure of two-parameter power-law (eq. 3.5):

$$Z = A \cdot R^b \quad (3.5)$$

where:

Z – radar reflectivity, $\text{mm}^6 \text{m}^{-3}$

R – rainfall intensity, mm h^{-1}

A, b – parameters.

The A and b parameters are related to the climate of a geographic area, season, and precipitation type (e.g. stratiform or convective) (Uijlenhoet, 2001). However, even for similar storm characteristics in the same location, Z - R relationships may vary (Wilson and Brandes, 1979). When the intensity of convective rainfall increases, usually, the parameter A value increases and b decreases (Wilson and Brandes, 1979).

A commonly used formula between radar reflectivity and rain rate based on the empirical study of Marshall and Palmer (1948) is formulated as: $Z = 200 \cdot R^{1.6}$ (Wilson and Brandes, 1979; Lee and Zawadzki, 2005).

However, the diversification of the reported parameter value of Z - R relationship is wide. Stout and Mueller (1968) divided the methods of relationships between radar reflectivity and rain rate formulation into two groups: first, direct ones that base simultaneous measurements of radar backscatter cross section and rainfall rate registered by on ground gauges, and the second, using measurements of drop size spectra. In tables 3.7 and 3.8 the Z - R relationship parameters obtained by both methods, reviewed by Stout and Mueller (1968) are listed.

Table 3.7 Radar reflectivity, rainfall rate relationship from direct measurement (Stout and Mueller, 1968)

Investigator	Geographical location	Range of applicability*	$Z = A R^b$		Accuracy estimate, standard deviation, dB	Comments
			A	b		
Doherty (1963)	Ottawa, Canada	TRW	70	1.42	2.5	
		not TRW	38.4	1.63	1.7	
		R<10	18.6	2.37	1.6	
		R<20	25.9	2.02	1.7	
		R<40	33.9	1.79	1.9	
		R<60	38.2	1.69	2.0	
Berjuljew et al. (1966)	Valday, USSR		340	1.5		The exponent is assumed equal to 1.5 and the coefficient determined from 2 years of rainfall.
Wilson (1963)	Norman, Okla.	TRW	45	1.43		Extreme low coefficient
		TRW	241	1.45		Extreme high coefficient
		TRW	183	1.18		Extreme low exponent
		TRW	141	1.72		Extreme high exponent
Aoyagi (1964)	Tokyo		100	1.4		For diffuse echoes

*TRW - thunderstorm; R – rain rate in mm hr⁻¹.

Table 3.8 Radar reflectivity, rainfall rate relationship from drop size spectra (Stout and Mueller, 1968)

Investigator	$Z = A R^b$		Standard error of estimate of $\log R$	Comments
	A	b		
Marshall et al. (1947)	220	1.6		Canada, widely accepted and used
Blanchard (1953)	31	1.71		Orographic Hawaiian rain at cloud base
	16.6	1.55		Orographic Hawaiian rain within the cloud
Fujiwara (1967)	80	1.38		Orographic Hawaiian rain
Hardy (1962)	312	1.36		Arizona and Michigan rain with rates greater than $5 \text{ mm} \cdot \text{hr}^{-1}$
Imai (1960) [Japan]	700	1.6		One day of probably warm rain
	300	1.6		One day continuous rain
	200	1.5		Air mass showers
	80	1.5		Pre-warm front rain
Diem (1966)	184	1.28		Overall average of different locations
	278	1.30		Entebbe, Uganda (tropical)
	240	1.30		Lwiro, Congo (tropical)
	176	1.18		Palma
	151	1.36		Barza, Italy
	179	1.25		Karlsruhe, Germany, spring
	227	1.31		Karlsruhe, Germany, summer
	178	1.25		Karlsruhe, Germany, fall
	150	1.23		Karlsruhe, Germany, winter
	137	1.36		Axel Heiberg Land
Foote (1966)	520	1.81		Tuscon, Arizona
Dumoulin and Gogolombles (1966)	730	1.55		France, highest coefficient
	255	1.45		Lowest coefficient
	426	1.5		Average of all observations, 0.95 correlation coefficient
	286	1.43	0.198	Florida

Mueller and Sims (1966)	221	1.32	0.170	Marshall Islands
	301	1.64	0.136	Oregon
	311	1.44	0.147	Indonesia
	267	1.54	0.142	Alaska
	230	1.40	0.171	North Carolina
	372	1.47	0.153	Illinois
	593	1.61	0.175	Arizona
	256	1.41	0.163	New Jersey

Figure 3.5 visualizes the A and b parameters variety prepared by Uijlenhoet (2001), based on Battan's (1973) review of the 69 power-law relationship and one linear formulated by List (1988) for tropical rain.

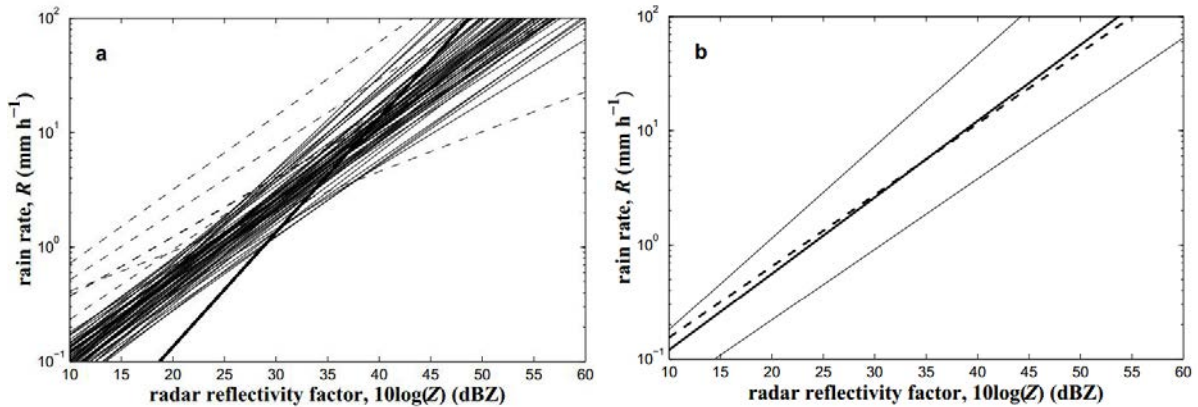


Figure 3.5 (a) The 69 power law Z - R relationships $Z = AR^b$ quoted by Battan (1973), including 5 deviating relationships (dashed lines): 4 which have prefactors A smaller than 100 and 1 of which has a high exponent b (2.87). The bold line indicates the linear relationship $Z = 742R$ (List, 1988). (b) the mean of Battan's relationships, $Z = 238R^{1.50}$ (bold solid line), the reference relationship $Z = 200R^{1.6}$ (bold dashed line) and the envelope of 64 (the thin solid lines in (a)) of Battan's 69 Z - R relationships (thin solid lines). Reproduced from Uijlenhoet, 2001

3.2.5. Sources of uncertainty and data quality in radar rainfall measurements

Rainfall measurements through radar are associated with large uncertainties, whose sources are miscellaneous (Villarini and Krajewski, 2010). These uncertainties should be propagated through the models that use radar data as an input (e.g. hydrologic model of catchment) or as initial conditions (e.g. weather forecast models) to interpret the results (Villarini and Krajewski, 2010).

The standard for precipitation measurement by radar were introduced by VDI (Verein Deutscher Ingenieure) in 2014 (VDI, 2014) and ISO (International Organization for Standardization) in 2017 (International Organization for Standardisation, 2017).

According to Villarini and Krajewski (2010), errors associated with radar rainfall estimation may be divided into nine main categories:

- radar miscalibration;
- radar signal attenuation by rain;
- ground clutter and anomalous propagation;
- beam blockage;
- variability of the Z – R relation;
- range effects;
- vertical variability of the precipitation system;
- vertical air motion and precipitation drift;
- temporal sampling errors.

An additional factor that may impact radar precipitation measurements is associated with the transformation of the grid (polar into Cartesian), transmitted power variability, wireless internet devices interference on weather radars, and non-uniform beam filling (Villarini and Krajewski, 2010).

To characterize and quantify radar data quality, a quality index (QI) has been introduced. The scale of the QI is not standardized and is specific for different radar networks. In table 3.9, QI , operational schemes, used by several European national meteorological services are given. The QI values are not Boolean type data, but in the range from 0 (bad quality) to 1, or alternatively, to 100 or to 255 (excellent quality). An assessment of data quality requires an independent measurement of precipitation, as a reference. It may be a compilation of data from satellite, ground stations, and lightning detection systems, etc. Nevertheless, the only direct method of precipitation measurements is provided by rain gauges, although only discretely at point. (Einfalt et al., 2010)

Table 3.9 Quality index schemes operationally used in European national meteorological services for surface precipitation fields (Einfalt et al., 2010)

<i>National meteorological service</i>	<i>Number of quality factors</i>	<i>Final QI formula</i>	<i>Range of QI</i>	<i>Used for rates</i>	<i>Used for accums.</i>	<i>Used for nowcasts</i>	<i>Reference</i>
DWD (Germany)	7	Additive	Errors encoded	Yes	No	No	Helmert et al., 2012
IMGW (Poland)	5 for QPE rate + 2 for QPE accums. + 4 for nowcasts	Additive	0-1	Yes	Yes	Yes	Szturc et al., 2008b
Météo France (France)	4	Multiplicative	0-100	Yes	Yes	No	Tabary et al., 2007
ARPA-SIM (Italy: Emilia Romagna region)	7	Multiplicative	0-100	Yes	No	No	Fornasiero et al., 2005
Met Office (UK)	1	-	0-255	Yes	No	No	Harrison, 2007
SMHI (Sweden)	1	-	0-1	No	Yes	No	Michelson, 2006
MeteoSwiss (Switzerland)	1	-	0-255	Yes	No	No	Harrison, 2007
FMI (Finland)	1	-	0-255	Yes	No	No	Peura et al., 2006

Szturc et al. (2008a) analysed the main radar errors in local Polish conditions; specifically, their magnitude, frequency, range, and an exemplary quality parameters related to them (see: table 3.10). Those quality parameters are described below.

Table 3.10 Magnitude, frequency and range of rain radar errors (Szturc et al., 2008a)

<i>Error</i>	<i>Quality parameter</i>	<i>Magnitude</i>	<i>Frequency</i>	<i>Range</i>
Hardware problems, miscalibration, pointing error, etc	-	medium – big	continuous	continuous
Earth curvature	DR, MH	medium	continuous	continuous
Vertical profile of reflectivity variability	DR, MH	medium	seasonal	continuous
Spatial resolution	DR, MH	small	continuous	continuous
Beam blocking, shielding	MH	big	continuous	local
Total beam overshooting	MH	small – big	seasonal	local
Ground clutter	DEM	small – big	continuous	local
AP clutter, propagation changes	-	small – medium	seasonal	local
Interfering emitters, jamming	-	small – medium	occasional	local
Attenuation by precipitation	DR	small	continuous	continuous
Attenuation by wet/icy radome	-	small	seasonal	local
Hail, water phase, Z - R relationship	SV	small	seasonal	continuous
Orographic enhancement	DEM	small – medium	continuous	local
Overhanging precipitation	-	medium	seasonal	local
Temporal resolution	NP, TV	medium	continuous	continuous

The first group of radar data quality parameters listed in tab. 3.10 is related with topography. Parameters forming this specific group are:

- *DR* - distance from radar site. With increasing distance, radar beams expand and the vertical distance from radar beam to the ground also increases due to the curvature of the surface of the Earth;
- *DEM* - spatial patterns of altitude represented by digital elevation model. The errors may originate from ground clutters, radar beam blocking, and shielding;

- *MH* - height of the lowest scan. The *MH* parameter is a combination of DR and DEM. This height is the lowest point of vertical profile visible by any radar beam and not covered by terrain obstacles between a radar site and an analysed location.

The second group of quality parameters is more specific and related to the study methodology of Szturc et al. (2008a). *SV* is a spatial variability calculated for every pixel larger than a native radar pixel size (e.g. 3×3 or 5×5 pixels). *TV* is a temporal variability determined for each pixel in an n-hour moving time-window. *NP* is the number of rain rate products included in a particular hourly accumulation (from 0 to 7 maps).

3.2.6. POLRAD system and selected radar products description

The Polish radar system (POLRAD) consists of eight C-band (ca. 5.6 GHz) Doppler weather radars managed by the Institute of Meteorology and Water Management – National Research Institute (Instytut Meteorologii i Gospodarki Wodnej – Państwowy Instytut Badawczy). All these radars were manufactured by Selex ES GmbH. Three of them are dual-polarization (Moszkowicz and Tuszyńska, 2006; Szturc, personal communication). Table 3.11 lists the location and properties of POLRAD radars.

Table 3.11 List of POLRAD radars (Szturc, personal communication)

<i>Location</i>	<i>Coordinates</i>	<i>Type</i>	<i>Polarization</i>
Gdańsk	54.3843 N, 18.4563 E	Selex Meteor 1500C	single
Świdwin	53.7903 N, 15.8311 E	Selex Meteor 500C	single
Poznań	52.4133 N, 16.7971 E	Selex Meteor 500C	single
Legionowo	52.4052 N, 20.9609 E	Selex Meteor 1500C	single
Ramża	50.1517 N, 18.7267 E	Selex Meteor 1600C	dual
Pastewnik	50.8920 N, 16.0395 E	Selex Meteor 1600C	dual
Brzuchania	50.3942 N, 20.0797 E	Selex Meteor 500C	single
Rzeszów	50.1141 N, 22.0370 E	Selex Meteor 500C	dual

In figure 3.6 POLRAD network radar locations and their operational ranges of 100 km and 200 km, respectively, are presented. The observation range of radar should not be confused with the actual detection range. In POLRAD network two ranges of measurement are applied, 250 km and 125 km, for observations of reflectivity and Doppler wind measurements. The data is presented in a range, respectively, of 200 km and 100 km (figure 3.6), but the real range of observation may be shorter. For instance, in winter, for low and low-dispersed clouds the distance of detection may be equal to 120 km. If so, the characteristic “ring” pattern is displayed. (Moszkowicz and Tuszyńska, 2006). The radar scan strategy parameters of POLRAD network are listed in table 3.12.

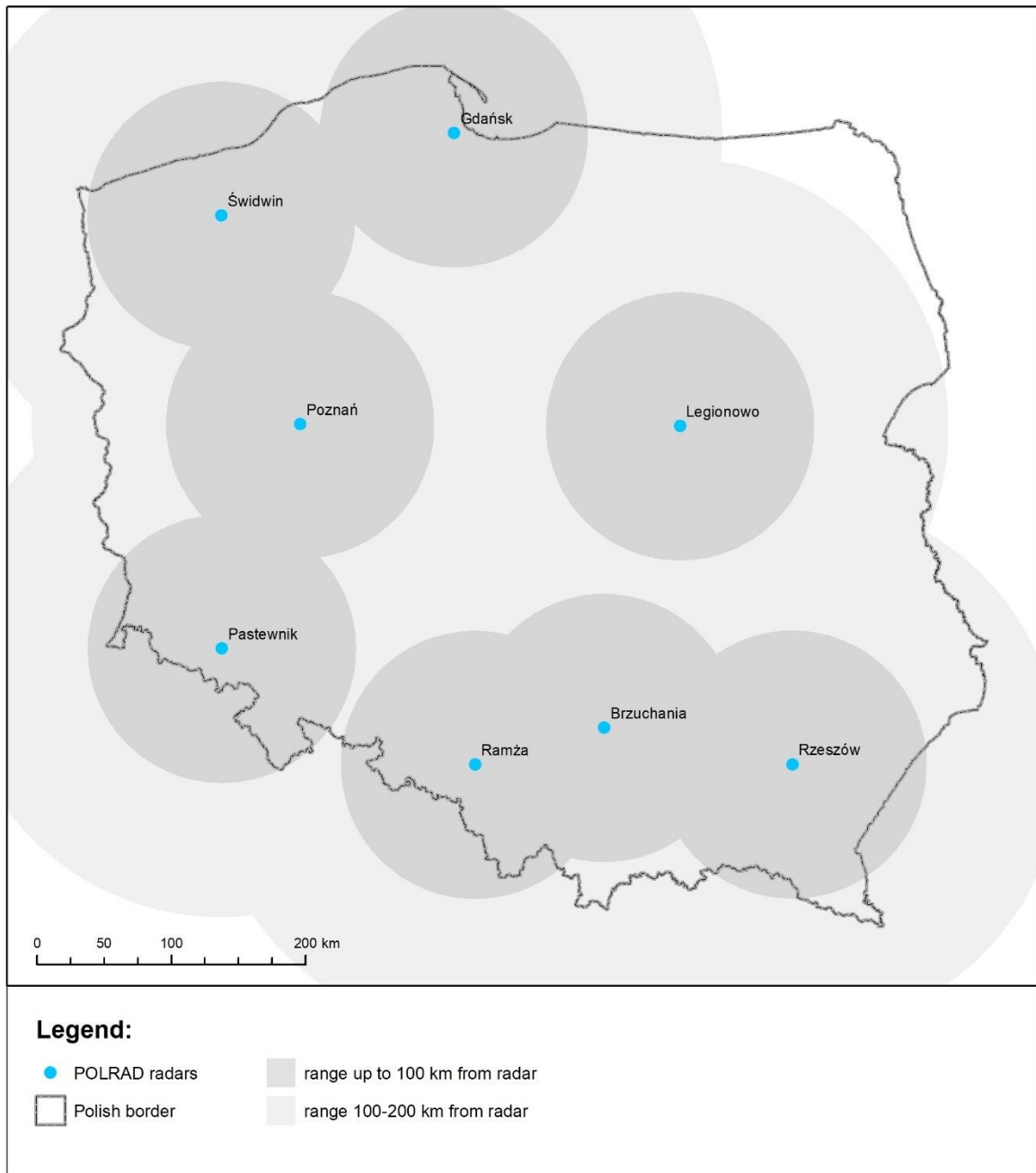


Figure 3.6 POLRAD radar network in Poland

Table 3.12 Scan parameters used in the POLRAD weather radar network (Ośródka and Szturc, 2015)

<i>Parameter</i>	<i>Value</i>
Radar beam width	1°
Number of azimuths	360
Maximum range from radar site	250 km
Distance between sampling along radar beam	1 km
Number of elevations	10
Elevation angles (°)	0.5, 1.4, 2.4, 3.4, 5.3, 7.7, 10.6, 14.1, 18.5, 23.8

The selected radar products operationally accessible from POLRAD could be divided into subsets as follows: standard products, hydrological products, wind products, and forecasting & phenomena detection products. These products are listed below (Tuszyńska, 2011):

- standard products:
 - PPI(dBZ) (Plan Position Indicator) - conical section - the distribution of reflectivity along the specified elevation,
 - PCAPPI(dBZ) (Pseudo Constant Altitude PPI) - horizontal section - the distribution of reflectivity at a certain height,
 - LMR (Layer Mean Reflectivity) - average reflectivity in a given layer,
 - RHI (dBZ) (Range Height Indicator radial reflectivity) - vertical cross-section on a given azimuth of radar reflectivity;
- hydrological products:
 - SRI (dBR) (Surface Rainfall Intensity) - the intensity of precipitation at a certain height,
 - PAC(dBA) (Precipitation Accumulation) - sum of precipitation in: 1 hour, 6 hours, 1 day;
- wind products:
 - VVP (Volume Velocity Processing) - vertical wind profile,
 - HWIND (Horizontal Wind Technique) - distribution of horizontal wind at a certain height;
- forecasting & phenomena detection products
 - SWI (Severe Weather Indicator) - indicator of severe weather phenomena,
 - CTR (Cell Centroid Tracking) - storm cell tracking.

The product used in further analysis (see: chapters 6 and 7) is PAC (Precipitation Accumulation), which is a sum of precipitation—in this case, 10 min. PAC is based on SRI (Surface Rainfall Intensity) products generated for a precipitation field of 1 km above the ground. SRI is a discrete estimation of instantaneous rainfall intensity for the following laps of radar. The calculation of SRI is conducted usually at a standard 10 min intervals. It is based on PCAPPI radar reflectivity values conversion into rain rate for certain elevation above the ground (usually for standard elevation of 1km above the ground). Hence, SRI product range for real elevation of 1 km above the ground is ca. 75 km, whereas for more distant locations the data from higher radar scan elevations has to be used as shown in figure 3.7.

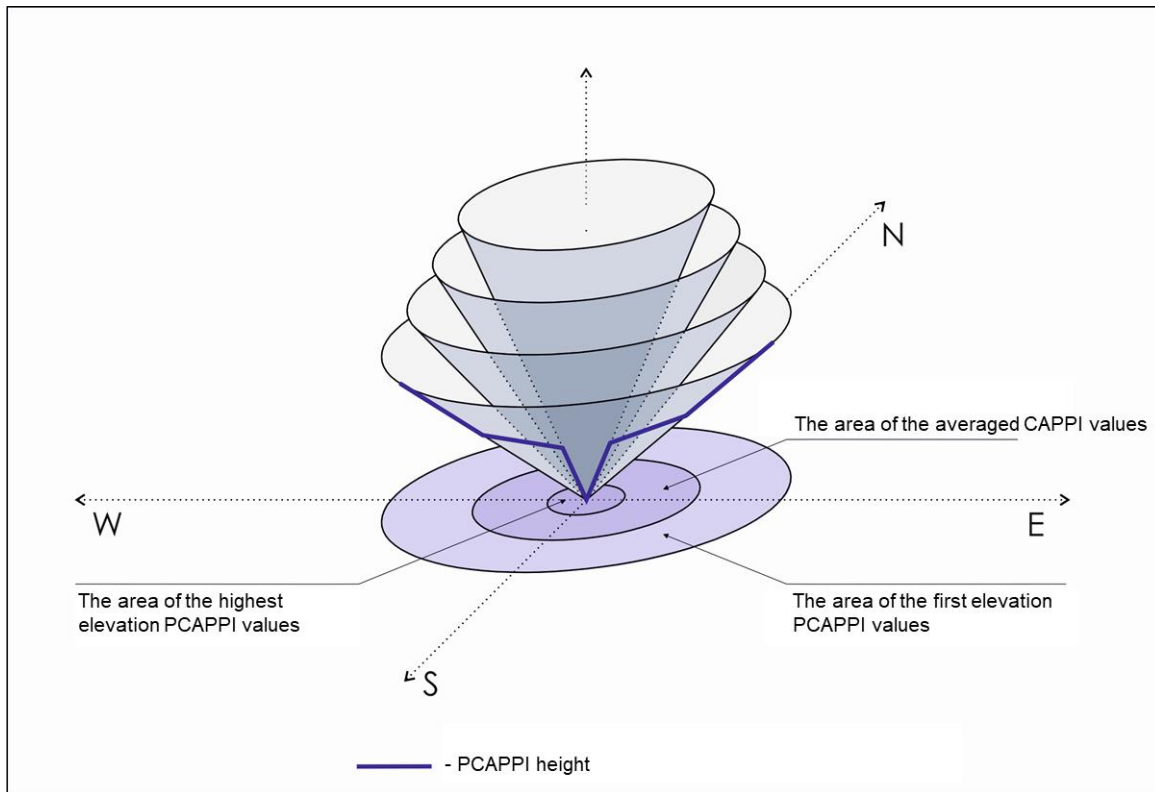


Figure 3.7 Geometry of CAPPI and PCAPPI products (based on: Tuszyńska, 2011)

Finally, to accumulate the precipitation between two following SRI measurements and to estimate the PAC value for 10 min intervals, the space-time interpolation based on direction and value of advection is performed through the RAINBOW computer processing system delivered as part of POLRAD (Moszkowicz and Tuszyńska, 2006). The timestamp for PAC products is the end of the accumulation period (e.g. based on two SRI scans: from 00:00 and 00:10, calculated PAC value has 00:10 timestamp).

3.2.7. Weather radar data applications in urban hydrology

Weather radar applications for urban hydrology may be divided into two offline and online groups (Einfalt et al., 2004).

According to Schilling (1991) and Einfalt et al. (2004), precipitation information suitable for operation and design of urban drainage systems should feature:

- at least 20 years of recordings without data gaps,
- a volumetric accuracy of less than 3 %,
- a spatio-temporal resolution of 1 km² and 1 min, respectively.

The radar precipitation data can meet these requirements.

The wide and current review of weather radar applications for urban hydrology was presented by Thorndhal et al. (2017). In table 3.13, the list of meteorological radar data applications in urban hydrology is presented.

Table 3.13 Application fields for radar rainfall in urban hydrology (Thorndhal et al., 2017)

<i>Offline applications</i>	<i>Online applications</i>
General statistical and hydrometeorological characterization of precipitation at urban scale: <ul style="list-style-type: none"> – present climate, – extremes, – future climate. 	Nowcasting and operational warning: <ul style="list-style-type: none"> – severe rainfall warning – flow/flood warning based on online hydrological models
Re-analysis of damaging extreme events: <ul style="list-style-type: none"> – insurance claims, – hydrological re-analysis of flood events, – distributed hydrological modelling for flood risk assessment. 	Operational real-time control of hydrological systems: <ul style="list-style-type: none"> – nowcasting, – real-time hydrological models with data assimilation, – scenario/ensemble modelling for online evaluation of control strategies.
Urban water management <ul style="list-style-type: none"> – design of basins and pipes, – resilience and livability measures. 	

First mentioned in table 3.13, the offline application field of weather radar data is a statistical and hydrometeorological characterization of rainfall. Although a minimum period of observation for urban catchment is 20 years (Schilling, 1991; Einfalt et al., 2004, Thorndhal et al., 2017), some characteristics were developed using mid-long C-band radar observations to quantify precipitation, e.g. for regions in:

- Netherlands – 10 years of observations, (Overeem et al. 2009a),

- USA, North Carolina – 10 years of observations (Wright et al., 2014)
- UK – 9 years of observations (Kendon et al., 2014),
- Denmark – 10 years of observations (Thorndhal et al., 2014),
- Sweden – 6 years of observations (Berg et al., 2015),
- Belgium – 10 years of observations (Goudenhoofdt and Delobbe, 2016).

The main advantages of radar data application for quantitative precipitation estimates are their spatial and temporal resolution and their spatial range. On the other hand, the time series of precipitation radar observations are about 10 years, so the precipitation models derived from this data are applicable for design rainfalls estimation characterised by probability levels not exceeding 10%.

Precipitation data derived from radar are anticipated to provide better estimates of rainfall values for regional climate models than those from point rain gauge measurements (Thorndhal et al., 2017).

Weather radar data are also used for extreme (maximum) precipitation values analysis (e.g. Allen and DeGaetano, 2005; Overeem et al., 2010). Radar data can be used for production of IDF (intensity-duration-frequency) and DDF (depth-duration-frequency) curves (Overeem et al., 2009b; Marra and Morin, 2015; Paixao, et al., 2015), even in subpixel scales and for very local, extreme rainfall value estimates (Peleg et al., 2018).

Rainfall radar data can be used for a re-analysis of extreme events of specific catchments, including the rainfall type identification, rainfall spatial distribution and their changes in time. Very accurate re-analysis of historical rainfall events using radar data were conducted, for example in North Rhine–Westphalia (Jessen et al., 2005), the Dead Run drainage basin in Baltimore County, Maryland (Smith et al., 2007), Milwaukee metropolitan region (Yang et al., 2013), and the Copenhagen region, Denmark (Thorndahl et al., 2014).

These analyses can also be used for identification of rainfall causing sewer overflows, and the recognition of the areas affected by extreme rainfall events for insurance claim procedures (Einfalt et al., 2004).

Weather radar measurements, because of their property to represent the rainfall variability over a large area are a valuable data source for urban water management. The radar data may be used as an input for hydraulic/hydrological modelling. Urban drainage modelling requires high spatial and temporal resolution rainfall measurements, which nowadays are possible to be obtained only through radar

techniques. The case studies of using downscaled C-band radar data for urban catchment modelling are described i.a. by Gires (Gires et al., 2012; Gires et al., 2013; Gires et al., 2015). The usage of X-band radar data, because of their hectometric and single-minute resolution, for urban modelling purpose is even more desirable (Borup et al., 2009, Alves de Souza, 2018).

The online application of weather radar includes nowcasting and operational warnings, which are particularly important in the case of extreme rainfall events. Numerical weather-model resolution is not fine enough for many of urban hydrology applications. Moreover, spatial shifts of predicted location of rain cells (even for tens of kilometres or more) may occur (Thorndhal et al., 2017). In urban drainage and hydrological systems, the knowledge of heavy rainfall and cloudburst localisation is crucial for the prediction of drainage system response. Hence, for short-time forecasts, the solution is to use radar nowcasts to improve initial conditions of numerical weather prediction models (e.g. Stephan et al., 2008; Dixon et al., 2009). However, the operational systems with radar data assimilation are still rare (Thorndhal et al., 2017).

The operational warning systems based on weather radar data are used for specific locations, usually as a part of flood warning and emergency planning systems. The warning is related with the radar precipitation estimates exceedance (over a given threshold) or alternatively, the hydrological warning is issued by an online hydrological model or supplied online by radar data inputs. However, the online flood warning models are still computationally demanding to run in real time (Thorndhal et al., 2017).

Weather radar data may be also applied in real-time control (RTC) for urban drainage systems. Most often, it is not the sole precipitation input and operational RTC systems usually combine the information from traditional rain gauges network with radar data (Campisano et al, 2013; U.S. Environmental Protection Agency, 2018). Radar in RTC systems is also a source of weather forecasts in e.g. Vienna (Fuchs and Beeneken, 2005) and Quebec (Pleau et al., 2010).

3.2.8. Weather radar data downscaling

The downscaling technique is used in several scientific fields, especially in meteorology, climatology, and remote sensing to obtain finer resolution information from lower resolution variables, i.e. “sensibly projecting the large-scale information on the regional scale”(von Storch et al., 1993). This method is also implemented for rainfall estimates investigation and allows to reproduce the natural variability of the precipitation field based on rain gauges time series (e.g. Rupp et al., 2012, Licznar et al., 2015) or based on weather radar sequences (e.g. Deidda, 2000, Deidda et. al, 2004). The downscaling allows to recognize the probable peak values of rainfall in space and time that are crucial for urban hydrology systems.

The downscaling of weather radar data is based on statistical properties of precipitation structures. The rainfall field statistical properties exhibit a high level of intermittency and long-range correlation (Menabde et al., 1997a).

Ferraris et al. (2003) divided disaggregation models into three groups: (multi)fractal cascades, nonlinearly filtered autoregressive processes, and point processes based on the random positioning of a given number of rainfall cells. In this paper the first approach is used (see: chapter 7).

The multifractal framework uses the assumption of self-similarity of precipitation structures. However, the statistical properties of the precipitation fields depend on specific localisation conditions and large scale mechanisms. Hence, downscaling models based on multifractal approach need to be adjusted to local conditions (e.g. Harris et al., 1996; Ebtehaj and Foufoula-Georgiou, 2010).

The multifractal cascades allow to obtain a finer resolution of precipitation data that are required in urban hydrology (see: chapter 3.1). An exemplary case study of multifractal cascades implementation for rainfall downscaling for urban catchments based on weather radar data for one of the largest European cities was described by Gires et al. (2012, 2013, 2015). The final data resolution (after downscaling) was described for the cases of: Cranbrook (London) catchment (Gires at al., 2012) and North-East Paris catchment (Gires at al., 2013) is 111m x 111m x 1.25 min. In the study of Gires et al. (2015) the final resolution was even finer—12.3 m in space and 18.75 s for the North-East Paris catchment.

4. Study area and data sources

4.1. Study area

This study was conducted for the precipitation field of Warsaw and its surroundings. Warsaw is the capital city of Poland, with 1.7646 million inhabitants on 517.2 km² (Kozłowska 2018). Due to high development and urbanisation of this region, urban hydrology issues are critical for its safety and resilience. Thereby, analysis and modelling of the Warsaw precipitation field were considered as relevant not only from a scientific point of view, but also due to the possibility of engineering applications in the field of urban hydrology in Poland.

Another reason for the selection of Warsaw as the study area was an accessibility to precipitation data resources. The precipitation data used in this study were gathered from three sources: C-band radar scans, rain gauges, and disdrometer. All the precipitation datasets are outlined in chapter 4.2.

4.1.1. Warsaw land use and development

The intensive changes in land cover in Warsaw are visible in figure 4.1. According to the data obtained from the Urban Atlas – based on very high resolution (VHR) satellite imagery classification and visual interpretation (<https://land.copernicus.eu/local/urban-atlas>) – between 2006 and 2012, the area of impermeable surfaces (including: continuous and discontinuous urban fabric; industrial, commercial, public, military and private units; transportation facilities, i.e.: fast transit roads and other roads, railways and associated land and construction sites) increased by ca. 11.5 km² (more than 2 % of total city area).

More detailed maps of impervious and pervious city surface coverage are shown in figures 4.2 and 4.3, respectively. Over half (50.8 %) of the total city area is covered by impermeable surfaces (mentioned above and airports). According to the European Environment Agency, in 2012 Warsaw had the highest imperviousness density index in Poland and one of the highest in Europe (see figure 4.4). Due to the time demanding satellite data processing, a more recent comparison based on Urban Atlas is not available.

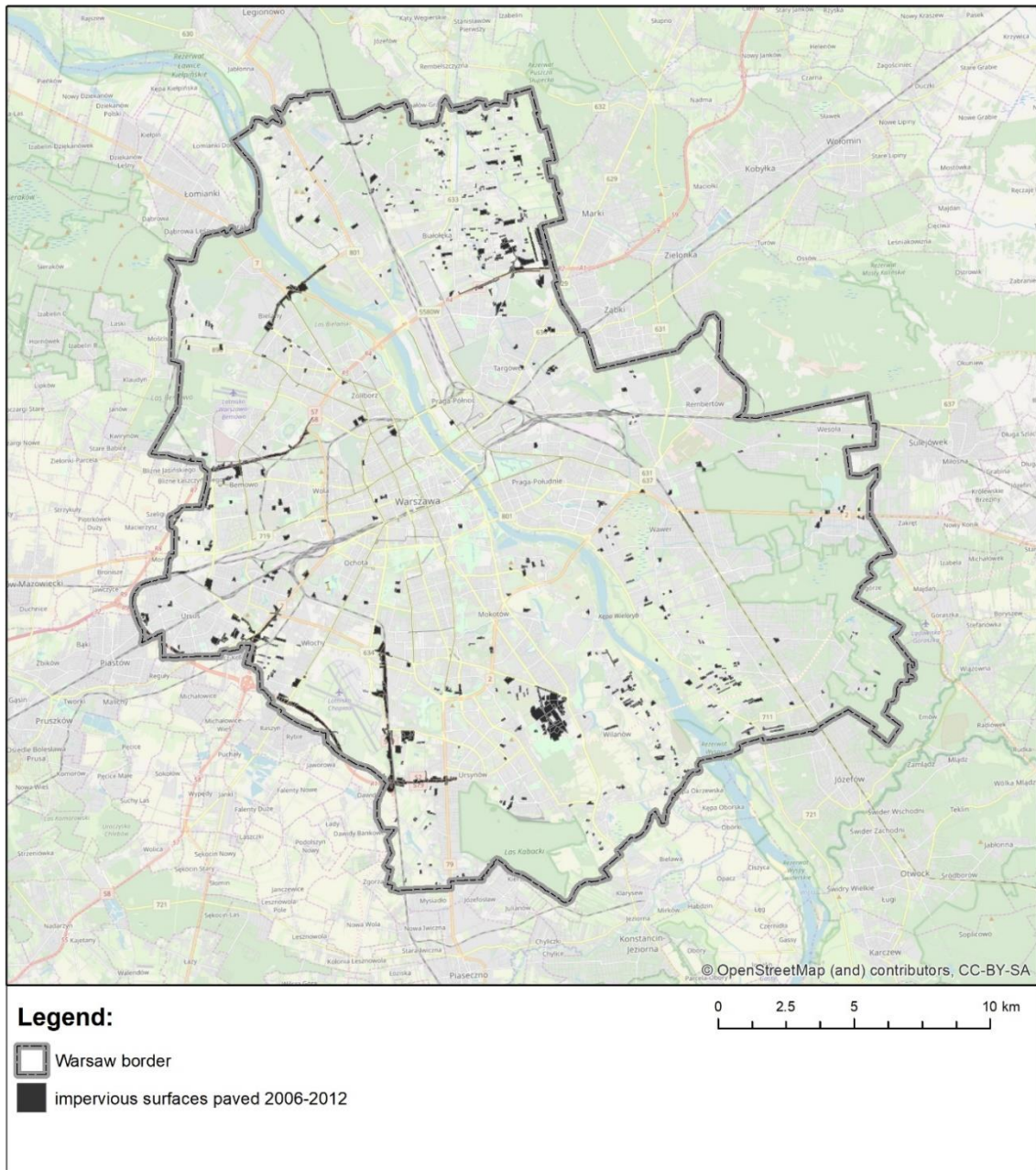


Figure 4.1 Changes in land cover - impervious surfaces paved between 2006-2012 in Warsaw (based on data from: Urban Atlas. Change 2006-2012, <https://land.copernicus.eu/local/urban-atlas>)

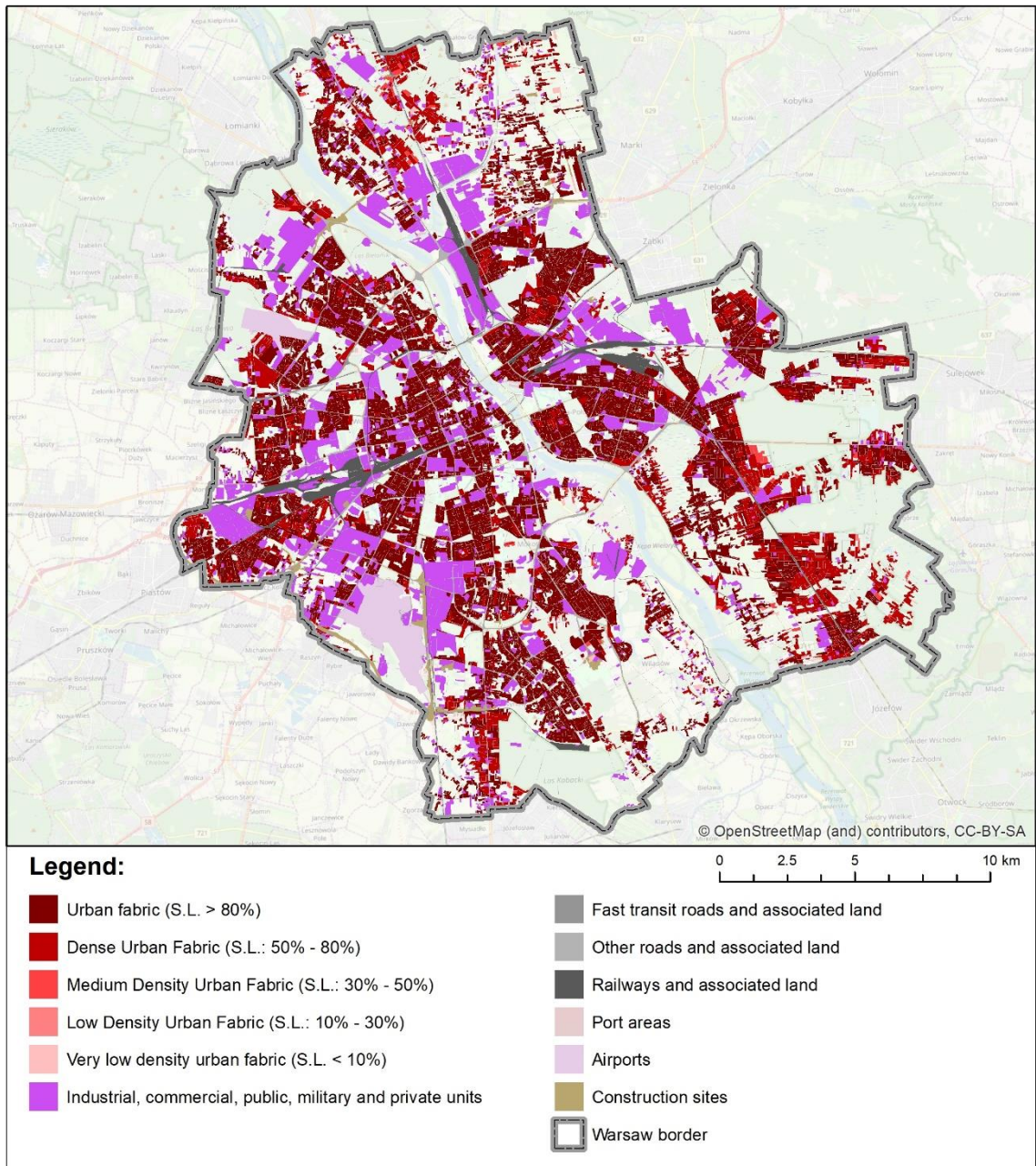


Figure 4.2 Impervious surfaces in Warsaw in 2012 (based on data from: Urban Atlas: <https://land.copernicus.eu/local/urban-atlas>)

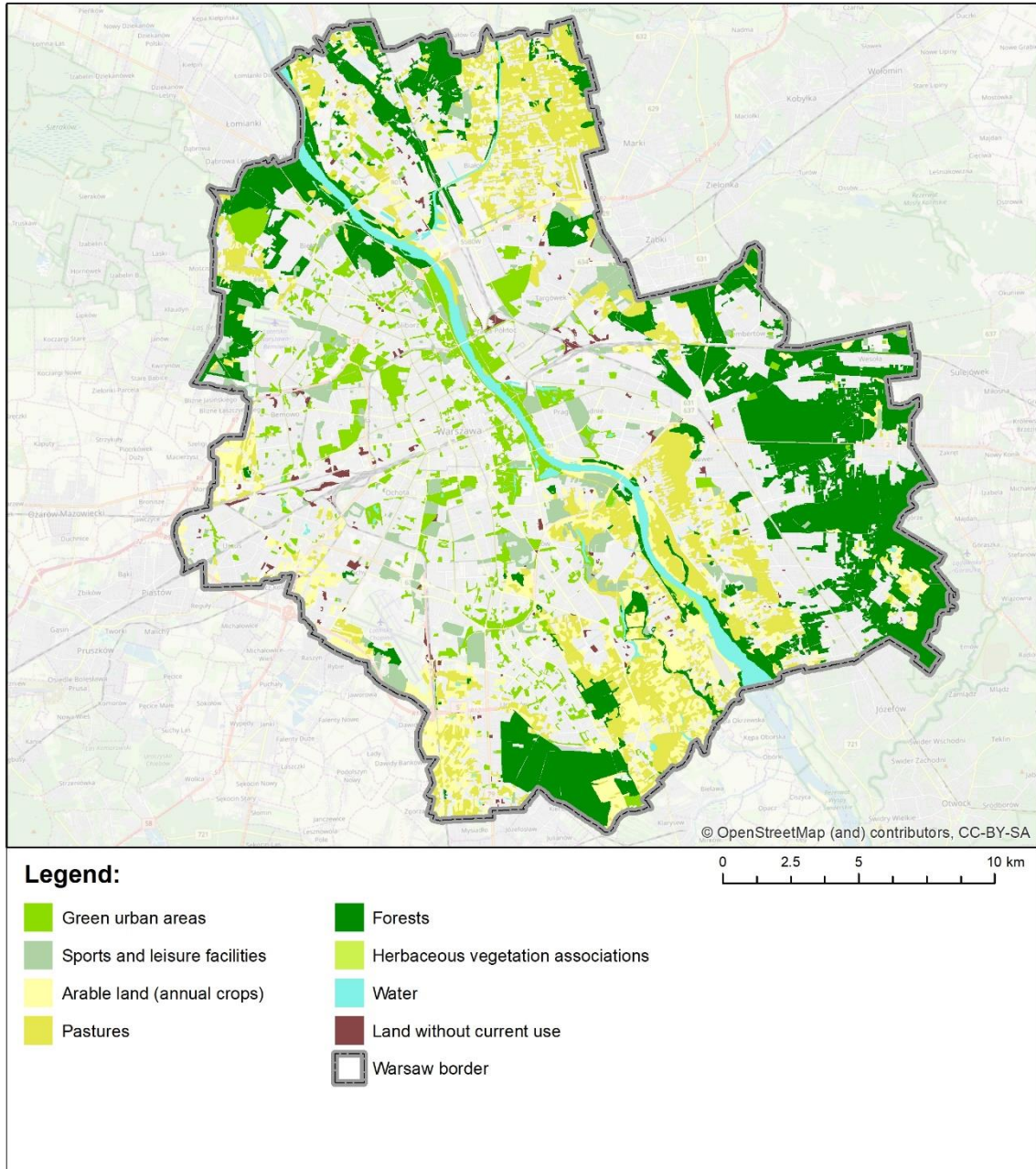


Figure 4.3 Pervious surfaces in Warsaw in 2012 (based on data from: Urban Atlas: <https://land.copernicus.eu/local/urban-atlas>)

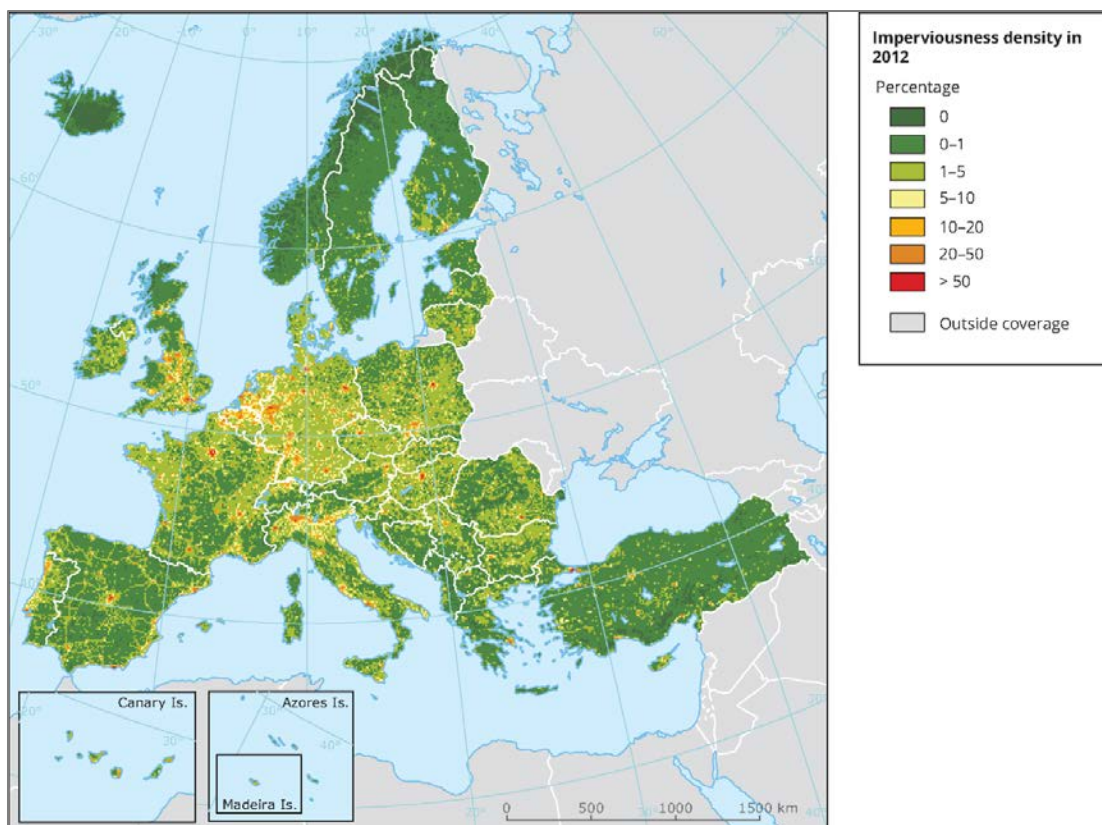


Figure 4.4 Imperviousness density in 2012 aggregated to 10 km grid (source: European Environment Agency <https://www.eea.europa.eu/data-and-maps/figures/map-showing-based-on-a-1#tab-based-on-data>)

Based on geodesic area inventories of the city with reference to land use categories published in the Statistical Yearbook of Warsaw (Kozłowska 2014, 2015, 2018)), one may conclude that the urbanization process was evidently dynamic between 2012-2017. The built-up and urbanized areas and percent of total area covered by impervious surfaces are presented year by year for the above-mentioned period for Warsaw in table 4.1. Between 2012 and 2017 the percent of total built-up and urbanized areas increased by additional 1.6%.

Table 4.1 Built-up and urbanized areas in Warsaw in 2012-2017 based on Statistical Yearbook of Warsaw (Kozłowska 2014, 2015, 2018)

Year	2012	2013	2014	2015	2016	2017
built-up and urbanized areas, ha	28 220	28 368	28 646	28 765	28 929	29 063
percent of total area of Warsaw covered by built-up and urbanized areas	54.56%	54.84%	55.38%	55.61%	55.93%	56.19%

The discrepancies in total area of impervious surfaces according to the Urban Atlas and Statistical Yearbooks of Warsaw results from different surface classification methodologies. The more detailed data about the growth of urbanized areas between 2012-2017, with categorization by type, is shown below in figure 4.5. The systematic growth of residential and transport areas year by year is clearly visible, with a simultaneous decrease of industrial areas.

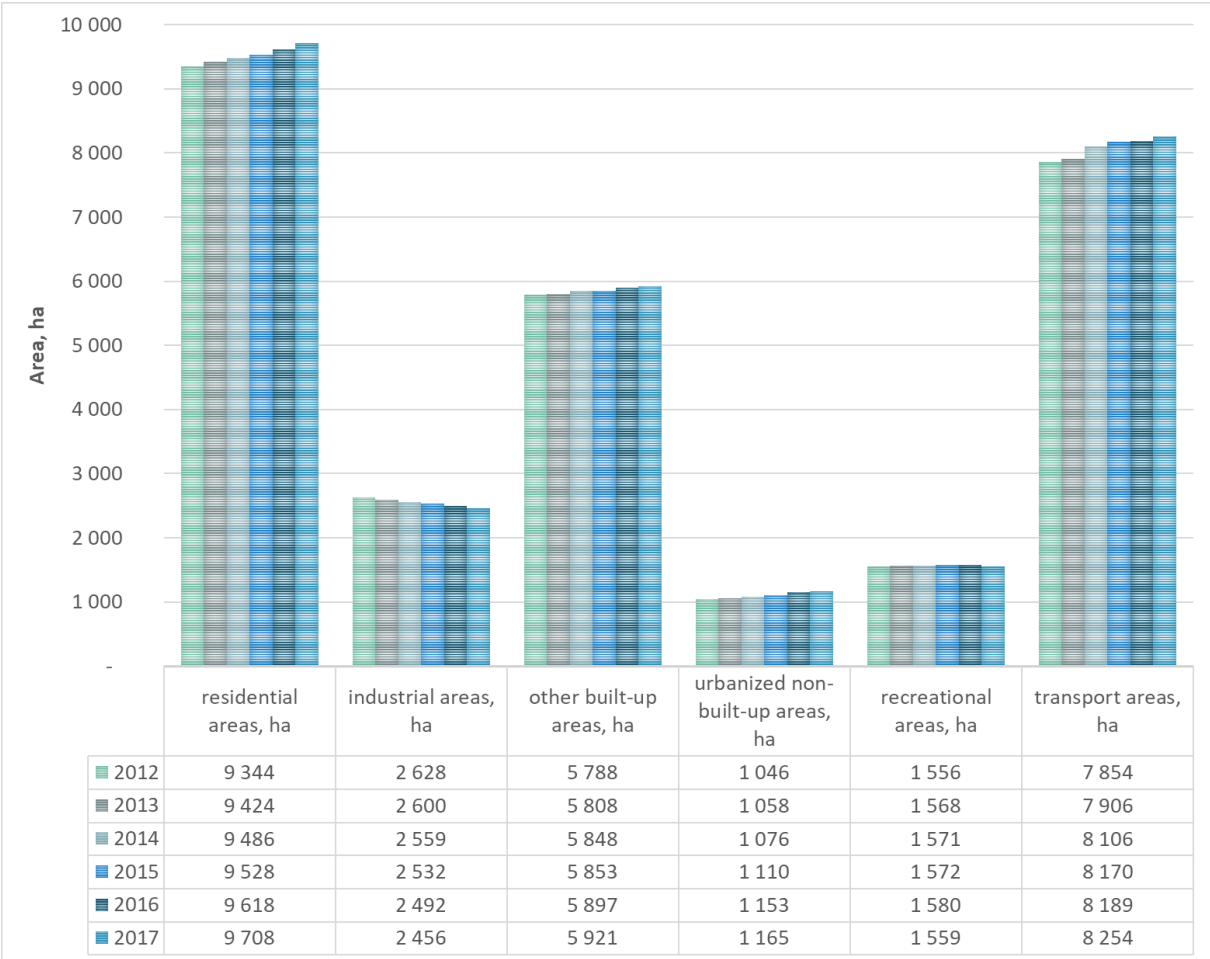


Figure 4.5 Built-up and urbanized areas in Warsaw by types between 2012-2017 based on Statistical Yearbook of Warsaw (Kozłowska 2014, 2015, 2018)

In general, due to the increase of impervious surface areas, the surface run-off becomes more and more intense, hence, the resilient design and management of urban drainage system based on reliable precipitation data is required.

4.1.2. Warsaw climate conditions

Warsaw’s lowland climate region, named middle-Mazovian (Pol. Śródkowomazowiecki) (Woś, 1993), results in a mixture of continental and oceanic (Atlantic) air that causes a high variability of weather conditions during the year for this region (Pawlak et al.,

2006). However, Warsaw's climate differs from the climatic conditions prevailing in the surrounding areas. The differences are revealed in parameters such as: air temperature, precipitation, and air humidity. In Warsaw city we can observe the phenomenon of an "urban heat island". It occurs in the central districts of Warsaw, where the density of impervious surfaces is the highest. Warsaw's heat island is a result of changes in radiation balance, different thermal conductivity, and a different thermal capacity of urban and extra-urban surfaces. Higher emissions of heat and air pollution also add to this phenomenon (Pawlak et al., 2006).

The average annual air temperature in Warsaw is 8.2°C. The coldest month is January with an average temperature of -2.0°C, and the warmest, July, with an average temperature 18.0 °C. (Pawlak et al., 2006).

According to the main ecophysiology document for Warsaw (Pawlak et al., 2006) an average annual rainfall in Warsaw ranges from about 500 mm to 600+ mm and the amount is significantly higher in comparison with the annual sum of precipitation for the Mazovian Plain (under 500 mm). The influence of city structures on air mass motion and condensation of water vapour results in higher sums of precipitation in Warsaw than in its surroundings (Pawlak et al., 2006). Detailed data of the annual sum of precipitation, according Statistical Yearbook of the Republic of Poland (Dmochowska 2015; Rozkurt 2016, 2017, 2018), are presented in table 4.2.

Table 4.2 Total annual precipitation in Warsaw, in mm (Dmochowska 2015; Rozkurt 2016, 2017, 2018)

	<i>Period of years:</i>		<i>Year</i>		
	<i>1971-2000*</i>	<i>2001-2010*</i>	<i>2015</i>	<i>2016</i>	<i>2017</i>
Total annual precipitation	519	571	404	593	705

* - data for multi—year periods present annual averages from these periods

Monthly precipitation is highest during the summer half-year, especially from June till September. This is observed for multi—year periods, as well as for recent years (2015-2017). Detailed monthly sums of precipitation are reported in table 4.3 and for every analysed period the maximum monthly sum is bolded.

The spatial variability of the precipitation field based on multi—year periods is presented in figures 3.4a and 3.4b. The mean annual sum of precipitation for 1981-2014 is presented in figure 4.6a. The spatial distribution of the annual sum of rainfall for

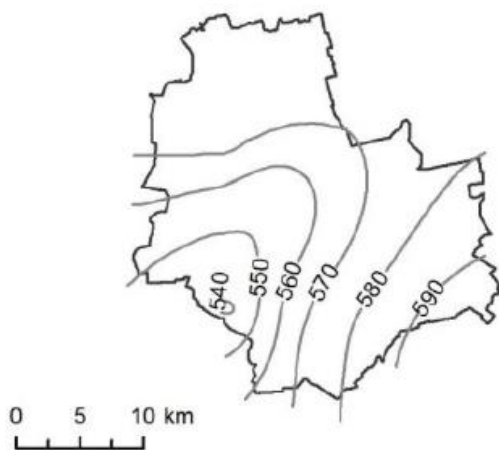
more recent years (2008-2014) is presented in figure 4.6b. The map (figure 4.6b) is a result of interpolation data registered from 2008 to 2014 on 32 rain gauges (belonging to MPWiK S A, IGiPZ PAN, IMGW, University of Warsaw and SGGW). The mean annual sum of precipitation between 2008-2014 was clearly higher than in the period 1981-2014. However, the distribution of rainfall was similar in some respects, e.g. the higher sum of precipitation occurred in the south-eastern part of the city.

Table 4.3 Monthly precipitation in Warsaw, in mm (Dmochowska 2015; Rozkurt 2016, 2017, 2018)

Years	Monthly precipitation in mm:											
	I	II	III	IV	V	VI	VII	VIII	IX	X	XI	XII
1971-2000*	22	22	28	35	51	71	73	59	49	38	36	34
2001-2010*	36	34	30	31	56	64	82	81	46	37	43	32
2015	39	6	30	35	39	19	59	8	58	40	53	17
2016	21	67	33	31	28	56	71	61	11	110	41	63
2017	19	39	39	48	49	86	90	48	127	83	45	33

* - data for multi—year periods include monthly averages from these periods.

a.



b.

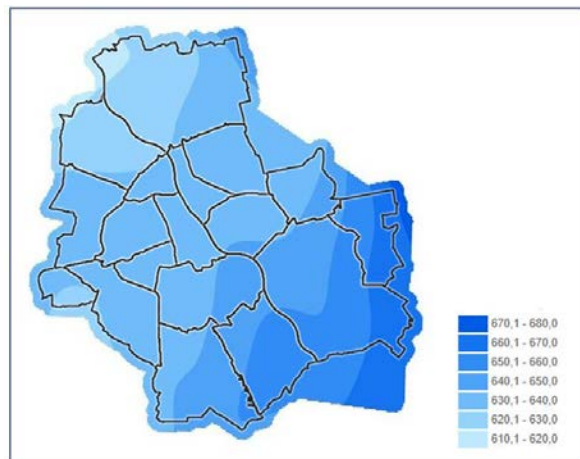


Figure 4.6 Mean annual sum of precipitation for (a) 1981-2014 (source: <http://adaptcity.pl/opady-roczne/>); (b) 2008-2014 (source: <http://mapa.um.warszawa.pl/mapaApp1/mapa>) in Warsaw

5. Local Z-R relationship for Warsaw

5.1. Local Z-R relationship study

The Z - R relationship between radar reflectivity Z and rain rate R was investigated for the local conditions of Warsaw, Poland. The aim of this part of the research was to determine the empirical coefficients for Marshall-Palmer Z - R power-type relationships and thus to verify the correctness of the Z - R function operationally used in POLRAD.

The overview from the literature on Z - R relationships derived for different locations worldwide was presented in chapter 3.2.4. The proper Z - R relationship formulation accounting for local specific of precipitation process was essential for weather radar data calibration and their application in urban hydrology. However, rain rate calculations in most operational radars based on a simple relationship, such as $Z=200\cdot R^{1.6}$ or $Z=300\cdot R^{1.5}$ (Lee and Zawadzki, 2005). Also, the first standard function $Z=200\cdot R^{1.6}$ is used implicitly in POLRAD. Radar reflectivity Z and rain rate R are strictly related to drop size distribution (DSD).

Both these precipitation parameters are statistical moments of DSD of the order of 3 and 6 respectively, as it is defined by equations 3.2 and 3.3. At the same time, the variability of drop size distributions determines the radar precipitation measurements precision (Lee and Zawadzki, 2005). Considering the wide-range of radar reflectivity values, the original units from equation 3.2 – i.e. $\text{mm}^6\cdot\text{m}^{-3}$ are not used. Preferred is the logarithmic scale of decibels, defined as follows:

$$Z_{dBZ} = 10 \log_{10} Z_{\text{mm}^6\text{m}^{-3}}. \quad (5.1)$$

5.2. Metodology

As mentioned in chapter 4.2.1, the DSDs were recorded by disdrometer from 13.12.2012 to 30.11.2014 in native 10 second resolution (5 411 325 observations, 2 489 783 in winter half years (from 1st November to 30th April) and 2 921 542 in summer half years (from 1st May to 31st October)). An exemplary visualization of the rain rate time series R and radar reflectivity Z calculated based on recorded DSDs for the calendar year of 2013 are presented in figure 5.1.

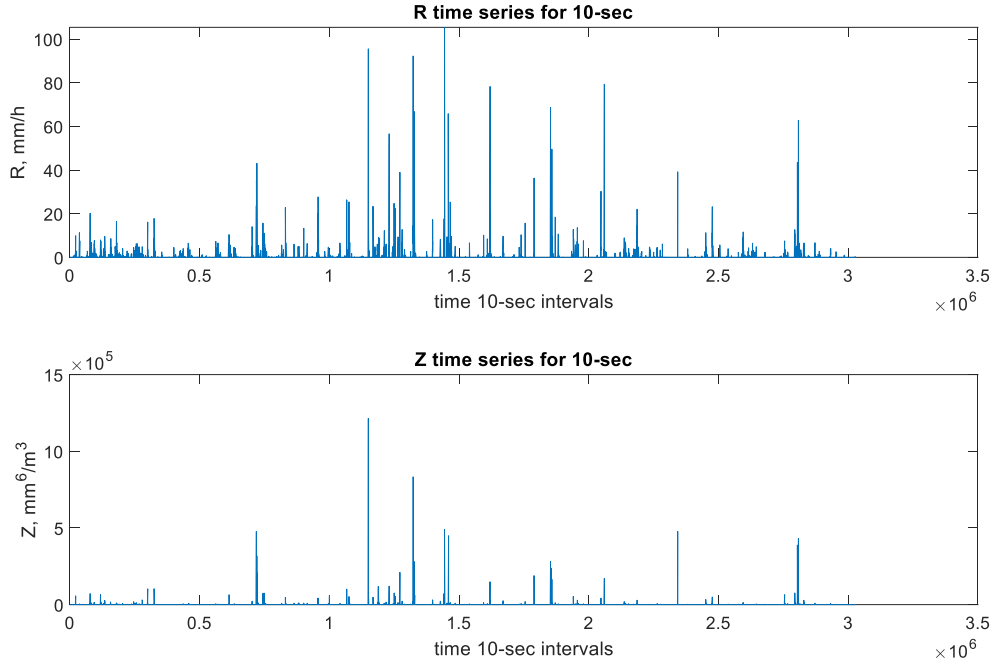


Figure 5.1 Time series of reflectivity Z (lower panel) and rain rate R (upper panel) registered by disdrometer OTT in Warsaw Parsivel² for year 2013

The relationship between radar reflectivity Z and rain rate R is analysed by four-time resolutions of: 10 s, 1 min, 5 min and 10 min. The first one is a native resolution of disdrometer and the last one – corresponds to the weather radar data resolution from POLRAD.

The Z - R relationship is modelled using a power-type function (eq. 5.2), originally postulated by Marshall, Langille and Palmer in 1947 (Marshall et al., 1947)

$$Z = A \cdot R^b. \quad (5.2)$$

An estimate of A and b parameters in eq. 5.3 is performed at logarithmic scales of Z and R , after function (5.2) conversion to linear equation:

$$\log_{10} Z = b(\log_{10} R) + \log_{10} A. \quad (5.3)$$

Use of the above described conversion into logarithmic scales is convenient because the observational sets of Z and R values do not have uniform distributions but are clearly dominated by small or moderate values.

5.3. Results and discussion

In figure 5.2 the results of Z-R linear function fitting (according to eq. 5.3) are presented. The deviation from the expected linear type relationship is observed only for very low rainfall intensities. These low rainfall intensities might not be properly recorded due to disdrometer measurement limitations. The accuracy of measurements declared by the manufacturer is $0.001 \text{ mm}\cdot\text{h}^{-1}$. Nevertheless, after investigation of rainfall intensity values recorded at the original 10-second resolution, the minimal value is assumed to be one order of magnitude higher, i.e. $R_{min}=0.01 \text{ mm}\cdot\text{h}^{-1}$. Hence, the cut-off value of rainfall intensities for parameter estimation of linear function (eq. 5.5) for this original time resolution is $\log_{10}R_{min}=-2$. Consequently, the minimum rainfall intensity R_{min} values for the other derivated and sparse resolutions are estimated as for averaged magnitudes, as follows:

$$R_{min} = \frac{0,01 \cdot \sqrt{m}}{m}, \quad (5.4)$$

where m is the number of average 10-second intervals.

The R_{min} and $\log_{10}R_{min}$ values are given in table 5.1. Maximum values of rainfall intensities, R_{max} , as well as radar reflectivity, Z_{max} , are presented for all four analysed time resolutions.

With the increase of time resolution, reduction of maximum values of rain rate R and radar reflectivity Z is observed. Moving from 10-second to 10-minute resolution, the maximum value of rain rate R reduces up to 50 percent and the maximum value of radar reflectivity Z decreases by one order of magnitude.

After cutting off the smallest values of rainfall intensities R (less than R_{min} values collated in tab. 5.1), the linear models are fitted. Their parameters are presented in table 5.2.

Table 5.1 Values characterizing disdrometer observational sets for analysed temporal resolutions

<i>Time resolution</i>	<i>m</i>	<i>R_{min}</i> <i>mm · h⁻¹</i>	<i>log₁₀R_{min}</i> <i>log₁₀(mm · h⁻¹)</i>	<i>R_{max}</i> <i>mm · h⁻¹</i>	<i>Z_{max}</i> <i>mm⁶ · m⁻³</i>
10-sec	1	0.010	-2.0000	141.0220	1.2142·10 ⁶
1-min	6	0.004	-2.3891	98.4818	3.6196·10 ⁵
5-min	30	0.002	-2.7386	63.1789	1.6522·10 ⁵
10-min	60	0.001	-2.8891	55.5229	1.0790·10 ⁵

Z-R relationships and derived models are shown in figures 5.2-5.5. The number of nonzero *Z-R* pairs at the highest time resolution (10-second) is 385 921 and even after aggregation to 10-minutes is still high and equal to 10 353. Good fits of the models (eq. 5.3) are confirmed not only by the narrow shape of confidence intervals, but also by the high values of coefficients of determination R^2 (higher than 0.9) and relatively low values of root-mean-square error (*RMSE*) – exceeding value of 0.3 only for 5- and 10-minute resolution (table 5.2).

The colour ramps placed on the right side of the figures 5.2-5.5 are used to symbolize density of *Z-R* pairs. For every point, the number of neighbours is calculated in 2x2-unit square.

Table 5.2 Values characterizing fitted models and parameters of *Z-R* relations

<i>Time resolution</i>	<i>n</i>	R^2	<i>RMSE</i> <i>log₁₀ (mm⁶ · m⁻³)</i>	<i>A</i>	<i>b</i>
10-sec	385 921	0.9035	0.2514	163.154 (162.799, 163.509)	1.530 (1.529, 1.532)
1-min	78 245	0.9079	0.2797	178.165 (177.143, 179.194)	1.354 (1.351, 1.357)
5-min	18 675	0.9135	0.3063	184.178 (181.698, 186.693)	1.232 (1.227, 1.238)
10-min	10 353	0.9154	0.3184	188.817 (185.179, 192.525)	1.192 (1.185, 1.199)

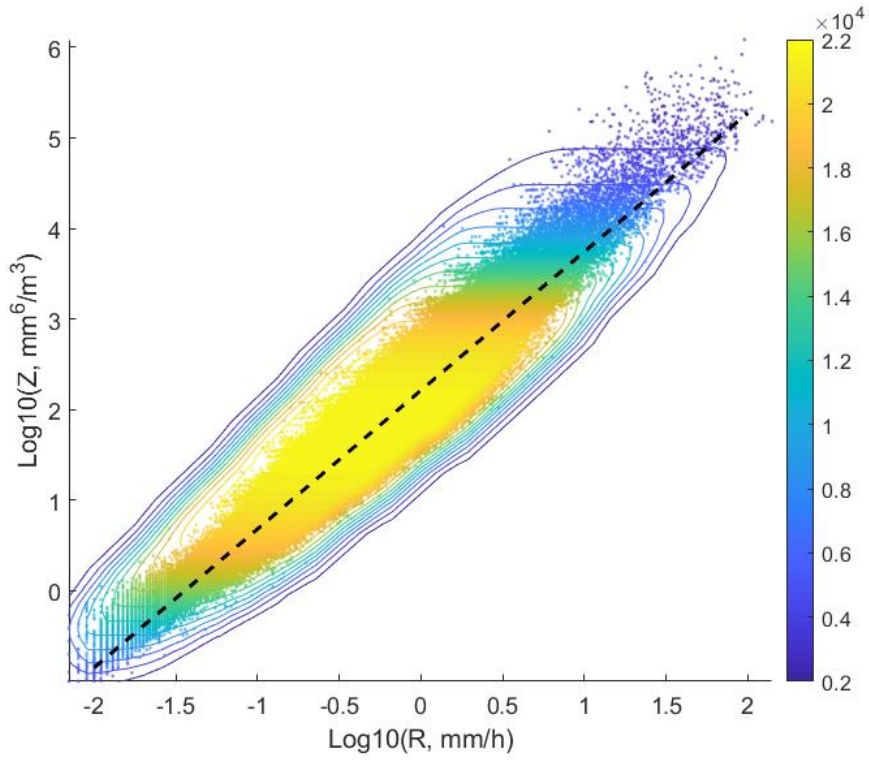


Figure 5.2 Z-R functional relationships for Warsaw, developed based on laser disdrometer records in temporal resolution of 10 seconds

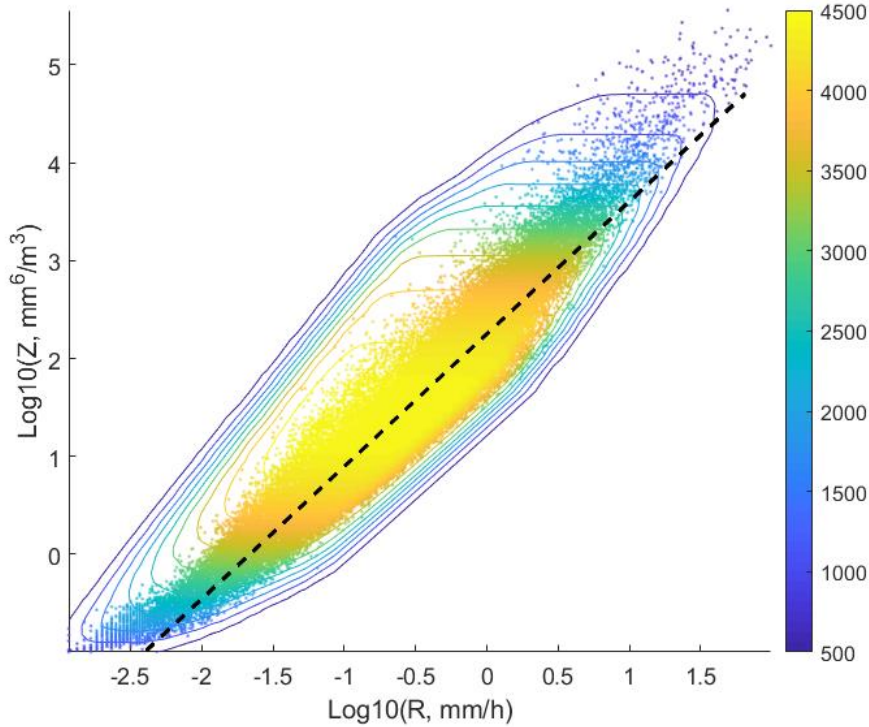


Figure 5.3 Z-R functional relationships for Warsaw, developed based on laser disdrometer records in temporal resolution of 1 minute

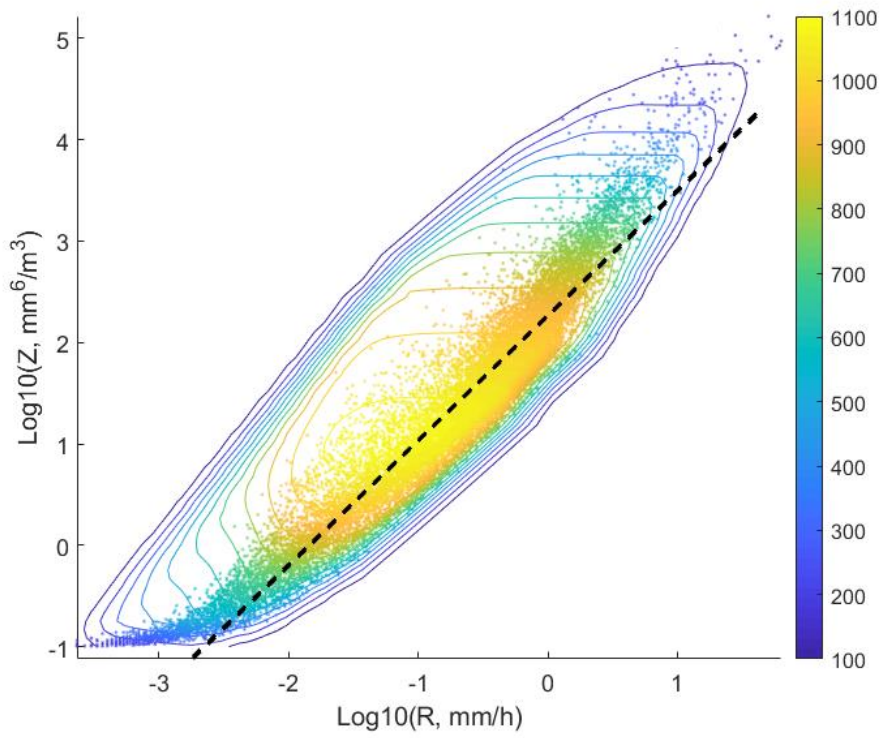


Figure 5.4 Z-R functional relationships for Warsaw, developed based on laser disdrometer records in temporal resolution of 5 minutes

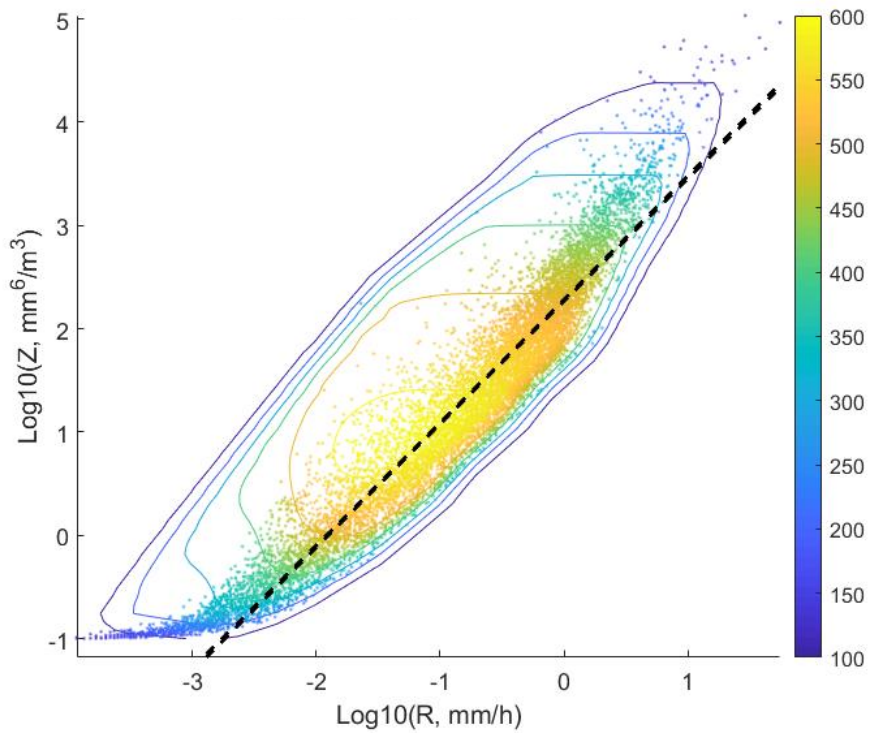


Figure 5.5 Z-R functional relationships for Warsaw, developed based on laser disdrometer records in temporal resolution of 10 minutes

Following, the seasonality of the Z - R relationship is analysed for the summer half-year (from May 1 to October 30) and the winter half-year (the remaining months). In figure 5.6 and 5.7 the results of Z - R linear functions fitting (according to eq. 5.3) are presented, for the summer and winter half-year respectively. Finally, derived A and b parameters with their confidence bounds are listed in table 5.3.

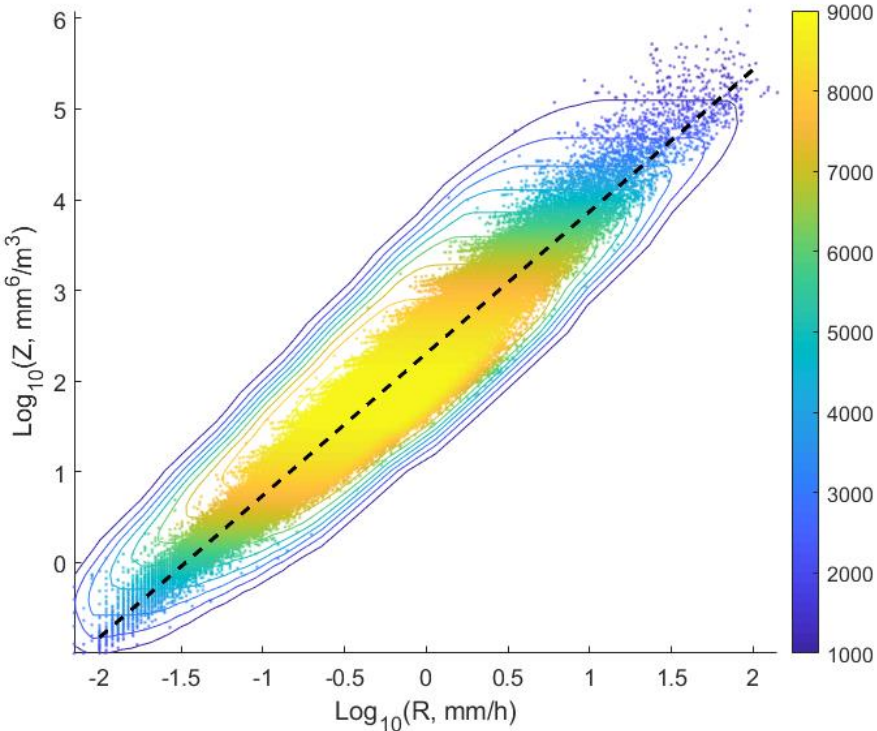


Figure 5.6 Z - R functional relationships for Warsaw for summertime period based on Parsivel² records.

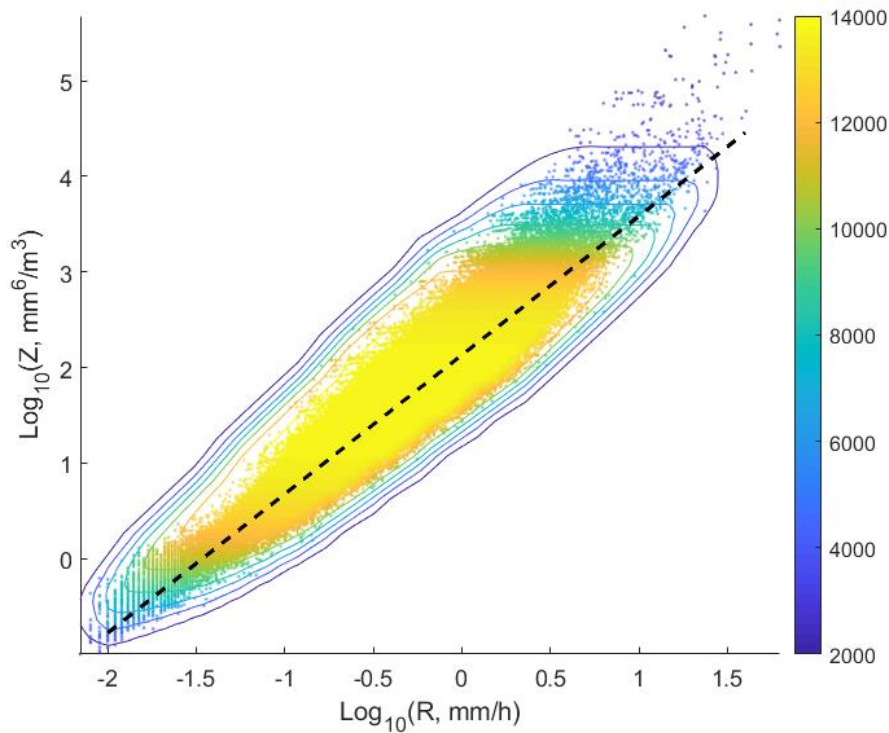


Figure 5.7 Z-R functional relationships for Warsaw for wintertime period based on Parsivel² records.

Table 5.3 Values characterizing fitted models and parameters of Z-R relations for summer and winter half year

Season	N	R^2	$RMSE$ \log_{10} ($mm^6 m^{-3}$)	A	b
Summer half-year	153 408	0.9411	0.2338	201.727 (201.134, 202.322)	1.565 (1.563, 1.567)
Winter half-year	232 513	0.8639	0.2448	134.841 (134.434, 135.250)	1.454 (1.451, 1.456)

The analysis of the results should begin with the statement that A and b parameters for Z - R relationship determined in native time resolution (10-second) for the whole observational period were close to the most commonly used and, originally introduced by Marshall, Langille and Palmer in 1947 (Marshall et al., 1947), values of $A=190$ and $b=1.72$ for rain. The discrepancies most likely result from the diversity of precipitation types observed during the observational period, when not only the rain, but also drizzle, snow, graupel or hail precipitation were recorded.

Moreover, the systematic change of Z - R relationship parameters values with the decrease of temporal resolution is observed. The A parameter values increase from ca. 163 to 189 with the shift from 10-second resolution up to 10-minute resolution

respectively. Simultaneously, the b parameter value decrease is even more evident, i.e. from ca. 1.53 to 1.19.

Unfortunately, despite the numerous attempts of studies of this subject through microphysics of the atmosphere, the interpretation of the observed changes of A and b parameter values is not apparent.

For instance, Dotzek and Beheng (2001) assumed—taking into consideration different hydrometeors distributions and for varying velocities of the particles—that the exponent b (eq. 5.2) can vary from $b = 7/4$ to $b = 7/5$ or even to $b = 1$. The authors considered $b = 7/4$ for uncommon situations –particles whose temporal velocity is constant and irrespective from their diameter. The value of $b = 7/5$ is adequate for the case when linear relationship between hydrometeors diameters and their velocities occur. Also, well-known cases of rainfall events dominated by hydrometeors, whose velocities are dependent on the square root of their diameters were investigated. For these conditions $b=1.55\pm 0.05$ and corresponds to the b parameter value for Warsaw and the 10-second time resolution.

Villarini and Krajewski (2010) noticed that lower values of A parameters were observed for frontal rainfall events and these values increased with convective processes, while b parameters showed the opposite direction of value changes (was lower for convection events and higher for frontal ones).

Steiner et al. (2004) attempted to make microphysical interpretation of $Z-R$ relationships. Their conclusions pointed on significant uncertainties (15 ÷ 20 percent) in mass-weighted mean drop size estimations based on $Z-R$ relationship. The authors also noticed, that for longer observation periods, a mix of different types of precipitation occurred. This statement is also important for the interpretation of the results obtained for Warsaw conditions in sparser time resolutions. In these, the averaging of $Z-R$ relationship parameters for different precipitation types is inevitable. Thus, derived $Z-R$ relationships do not reveal microphysical information at these time scales.

The b parameter values obtained for summer and winter half years are close to one another (1.565 and 1.454 respectively). The values of A parameters are more diversified, with 201.727 for the summer half year and 134.841 for the winter half-year.

It should be emphasized that the equation parameters of $Z-R$ function for the summer half-year ($Z=201.727\cdot R^{1.565}$) are very similar to the calibration equation for POLRAD weather radars (i.e. $Z=200\cdot R^{1.6}$) (Moszkowicz and Tuszyńska, 2006). This conclusion

implies that there was no need to recalibrate radar products used in further analysis of the urban precipitation field.

The values of parameters in Z - R equations for the winter half-year ($Z=134.841 \cdot R^{1.454}$) are in the range of values, derived by Licznar and Krajewski (2016) for snow ($A=106.644$ and $b=1.436$) and for the mixture of rain and snow ($A=212.050$ and $b=1.534$) for the local Warsaw conditions. Moreover, the values of parameters are similar for those determined by Diem in 1966 for an area of Aexel Heiberg Land, where the dominant type of precipitation is snow ($A=137$ and $b= 1.36$) (Stout, Mueller, 1968). Z - R relationship parameters for the winter half-year are also in good agreement with the observed mixture type of precipitation over Warsaw with only partial components of solid, i.e. snow, precipitation.

5.4. Conclusions

The conclusions originating from the investigation of Z - R relationships for local conditions of Warsaw based on DSDs recorded by laser disdrometer are as follows:

1. Radar reflectivity Z values are strongly correlated with rain rate R values for all four analysed time resolutions (10-second, 1-minute, 5-minute, 10-minute);
2. The Z - R relationship may be described using the power-type function of which parameters should be estimated using logarithmic scale for Z and R values;
3. Estimates of A and b parameters of Z - R relationship obtained for local Warsaw conditions at the native disdrometer 10-second resolution ($A=163$ and $b=1.53$) are close to the known documented values for rainfall events, and are similar to the ones adopted in POLRAD ($A=200$ and $b=1.6$);
4. The time aggregation of Z and R values natively registered within 10-second resolution by the disdrometer strongly decreases the maximum values of both observational quantities and strongly influences on their power-type function parameters;
5. With the extension of the analysed time intervals, an increase in the value of A parameters and a decrease in the value of b parameters is observed. This can be explained by averaging Z and R values for increasing time intervals from 10 seconds to 10 minutes;

6. The Z - R relationships for the summer and winter half-years are different, which explains the occurrence of diverse precipitation types throughout the year;
7. The Z - R relationship for the summer half-year ($Z=201.727 \cdot R^{1.565}$) derived from local disdrometer records is nearly the same as the one implicitly adopted in POLRAD. Hence, there is no need to recalibrate estimates of rainfall accumulations originating from the POLRAD.

6. Comparison between rain gauge and radar data for Warsaw

6.1. Rain gauge vs. radar data for urban hydrology applications

Considering rain gauge vs. radar data application for urban hydrology needs, one should highlight the scale gap between measurements originating from rain gauges and C-band radars. Observation scales achievable with these two types of sensors differ with a ratio of approximately 10^7 (Gires et al., 2014). The rainfall data collected on the ground level is available for spatial resolution equal to the rain gauge orifice (approximately 200 cm^2), whereas a standard resolution for C-band radar (including radars from POLRAD) is 1 km^2 . Despite this fact, comparisons between rain gauge and radar measurements are widely undertaken. These studies are most often aimed at the radar calibration (see e.g. Wilson and Brandes, 1979).

In this particular research, a time series from rain gauge network and spatially corresponding radar cells for 25 locations in Warsaw were analysed in order to explore the existence of an expected time correlation of series, and to estimate the scale of potential discrepancies between rainfall estimates originating from these two different measuring techniques at a temporal scale of 10 min.

6.2. Metodology

The rainfall intensity series recorded by the electronic gauge network in Warsaw (as described in chapter 4.2.2), aggregated into 10-min resolution, are compared with coincident in the space and time radar rainfall intensity series (characterized in chapter 4.2.3). The comparison is conducted for the summer months: May to August in 2009. The period of analysis is limited due to data availability. Coincident in the time radar and gauge time series are available only for the years 2009 and 2010. However, due to incompleteness of radar scan series for 2010, it is excluded from the comparison. The location of 25 rain gauges displayed on the regular grid of $1 \text{ km} \times 1 \text{ km}$ radar products is shown in figure 6.1.

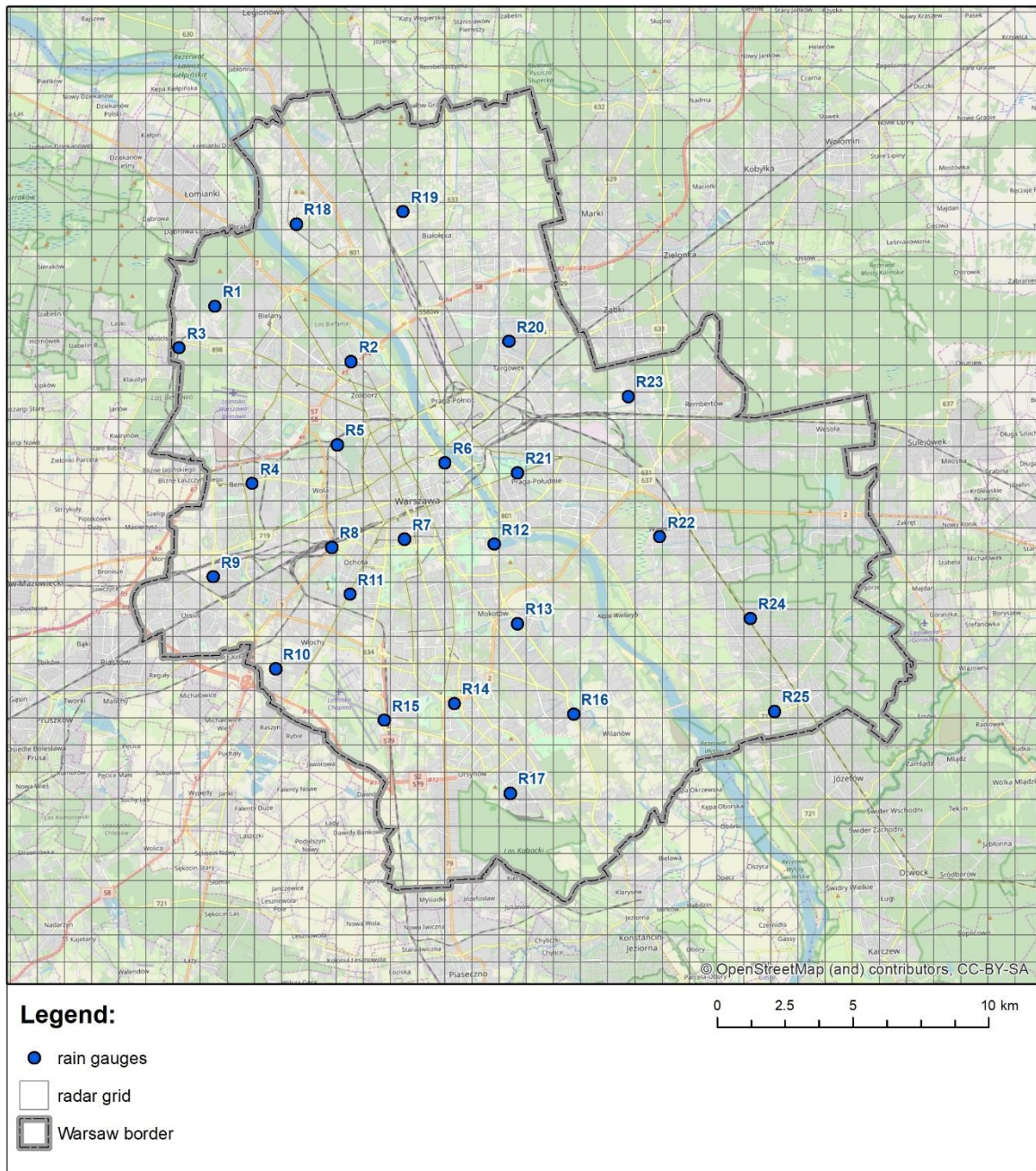


Figure 6.1 Rain gauges network in Warsaw, seen on a 1x1 km radar grid

6.3. Results and discussion

The entire set of figures comparing the rainfall time series, originating from both source– rain gauge (*G*) and radar (*R*), for each of the 25 localisations for the summer months (May - August) in of 2009 is provided in Appendix A. An example of such a comparison for the localisation of gauge R10 is presented in figure 6.2. The similarity of both rainfall time series is visible, however the rainfall temporal intensity values

recorded by gauge and radar are not the same. One may observe a good correlation in time for wet and dry periods, as well as an extreme intensity in 10-min intervals. However, in general, high temporal rainfall intensity values estimated based on radar scans are often higher than the ones recorded directly by gauge.

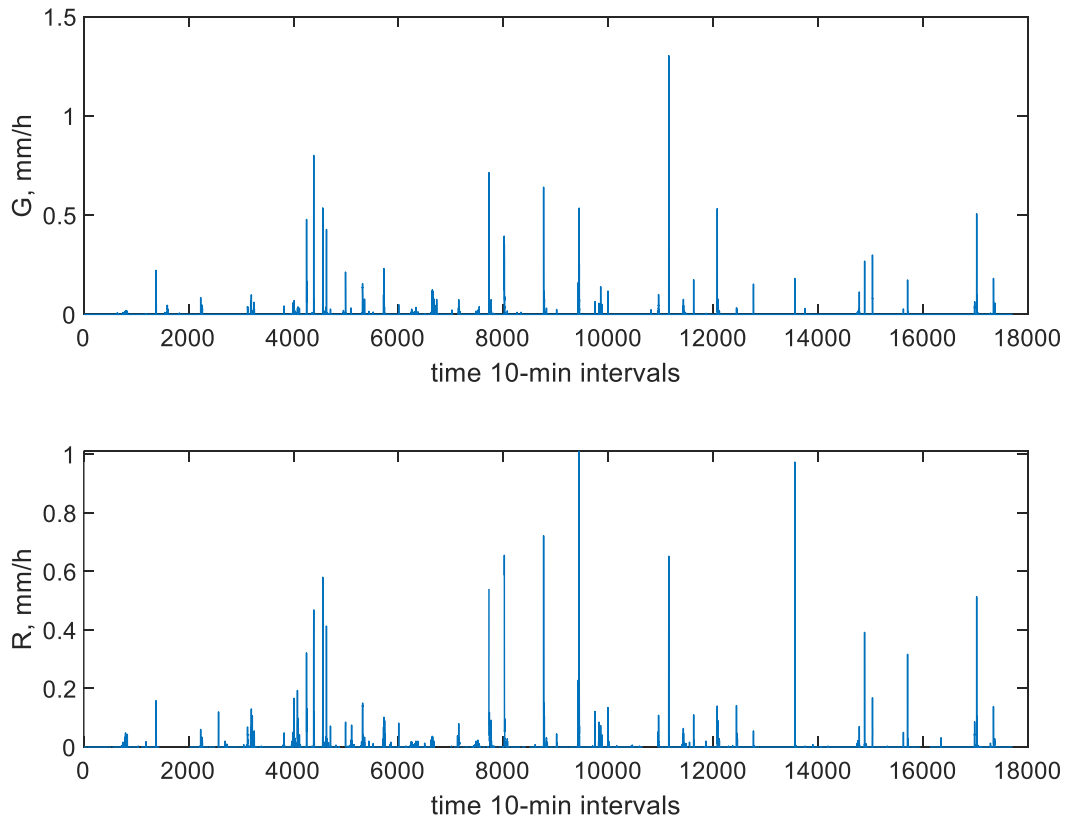


Figure 6.2 Rainfall intensity series recorded by gauge R10 (G) during summer months (May-August) 2009 (upper panel) and coincident in space radar rainfall intensity (R) series for the same period (lower panel). Both time series are in 10-min resolution

The above-mentioned visible coincidence in time of rain gauge and radar time series was investigated in more detail by means of both signals cross correlation diagrams. An exemplary time series cross correlation diagram for the location of gauge R10 is shown in figure 6.3, and a set for all 25 locations is presented in Appendix A. Prior to the development of cross correlation diagrams, the issue of differences in time stamps of radar and gauge data was analysed. Firstly, radar and gauge series were recorded in different operating times. The radar series were recorded in UTC, whereas the gauge series in CEST (UTC + 2h). Moreover, an additional time shift of 10 min was generated by rainfall data aggregation. The aggregation procedure of the original 1-min time series from gauges developed in MATLAB allows to assign a summed up, 1-minute registration from 00:00 to 00:10 to 00:00, time stamp. For the radar PAC product, the opposite was true. PAC products, as explained in chapter 3.2.6, are a result of radar

data interpolation between two following measurements. For example, scans made after 00:00 and after 00:10 are used to calculate PAC values with an assigned timestamp of 00:10. Eventually, a 1 h and 50 min timestamp delay of rainfall time series vs. radar series was assumed as a precondition in both series cross correlation.

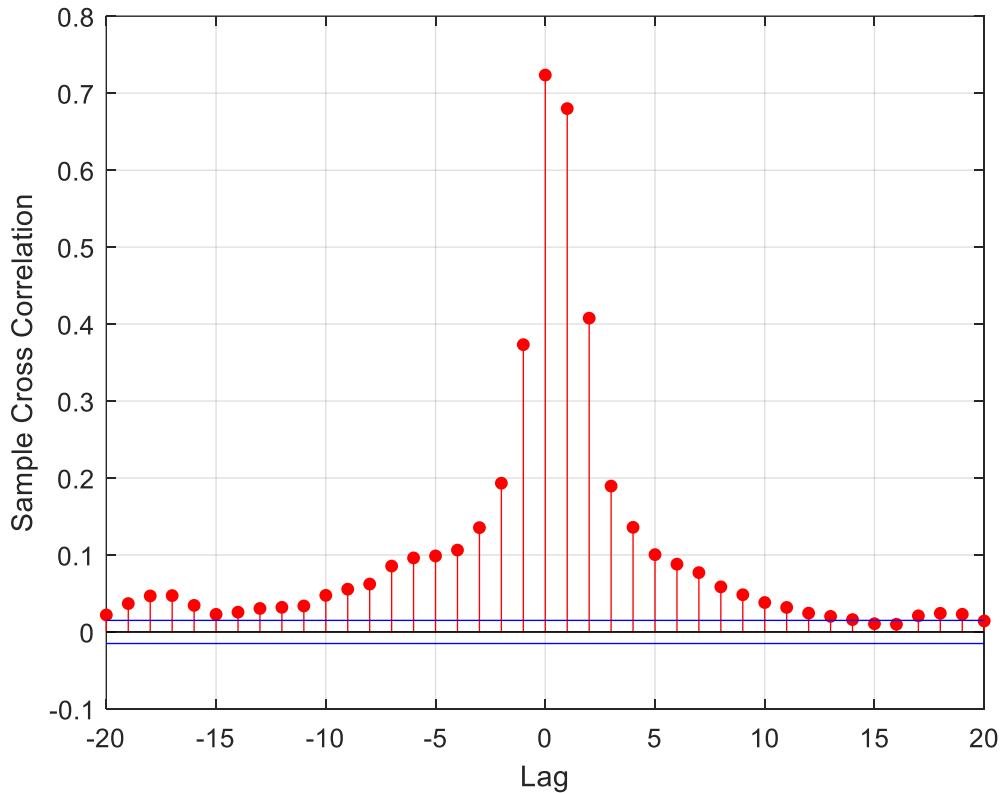


Figure 6.3 Cross-correlation of rainfall intensity time series registered by gauge (G) and radar (R) for gauge R10 location

A single unit in the cross-correlation diagrams, as shown in fig. 6.3, corresponds to a 10-minute lag. For most of the locations (sixteen out of twenty-five) the highest time correlation was observed for zero lag. This correlation value exceeded usually 0.7 and proved the very good correlation of rainfall time series from gauges and radar in a high temporal resolution of 10 min over Warsaw. For the rest of locations (nine out of twenty-five) the highest correlation value was observed for a 10 min lag. This phenomenon may be at least partly explained by the differences of measurement procedures. For rain gauges, measurements are conducted on ground level (rainfall is recorded after drops arrival into the gauge inner tank). In addition, the real rainfall intensities are subjected to some deformations and delays due to “step error” typical for electronic weighing type gauges. This topic was studied in detail by Licznar et al. (2015) for Warsaw gauges and the magnitude of step error was estimated to be equal to about 5 min. In the case of radar – rainfall is estimated based on aerial scans on different altitudes. PAC products

are developed for standard elevations of 1 km above the ground. It means, that the minimum time-shift, for the largest drops (with equivalent spherical diameter 4 mm and more) with terminal fall velocity above $8 \text{ m}\cdot\text{s}^{-1}$ (see: figure 6.4), is not less than 2 min. To conclude, one may assume that radar records in advance rainfall drops that ultimately fall into the gauges are recorded as a delayed temporal rainfall intensity series.

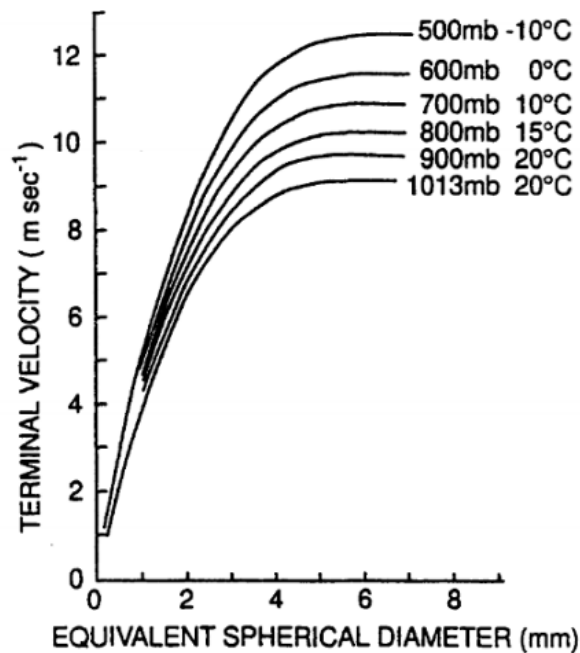


Figure 6.4 Variation with size of terminal fall velocity of water drops larger than $500 \mu\text{m}$ in air. Reproduced from Pruppacher and Klett, 2010

The relationship between non-zero radar rainfall intensity values versus non-zero intensity values registered by rain gauges is additionally investigated by means of linear regressions functions. These function parameters (a_1 and b_1) and coefficients of determination R^2 are estimated for each localisation and are reported in table 6.1. The coefficient values of determination R^2 range from 0.195 (for gauge R18) to 0.623 (for gauge R8). These values indicate, that the correlation between non-zero temporal rainfall intensity values recorded by both techniques occur, but were far from perfect. Values less than 1 of parameter a_1 in tab. 6.1 for most localizations suggest the overall tendency of underestimation of rainfall intensity values by radar with respect to gauge measurements.

The exemplary log-log plot of radar rainfall intensity R values versus rainfall intensity G values recorded by gauge R10 for the summer months in 2009, with a best-fitted linear function, is presented in figure 6.5. Only non-zero rainfall intensity values

exceeding $10^{-3} \text{ mm}\cdot\text{h}^{-1}$ are plotted. Also, a 95% confidence interval of best line fit is presented. The set for all 25 locations of similar log-log plots is presented in Appendix A.

Table 6.1 Parameters of linear relationships fits for non-zero rainfall intensity values derived from radar and rain gauges time series for 25 locations (R1-R25) in Warsaw in 2009

<i>Rain gauge location</i>	$R = a_1 \cdot G + b_1$		
	R^2	a_1	b_1
R1	0.252	0.649	0.016
R2	0.515	0.685	0.013
R3	0.486	0.715	0.013
R4	0.606	0.849	0.011
R5	0.330	0.714	0.017
R6	0.465	0.709	0.012
R7	0.620	0.904	0.008
R8	0.623	0.862	0.009
R9	0.496	1.025	0.007
R10	0.529	0.756	0.014
R11	0.474	0.692	0.016
R12	0.304	0.726	0.016
R13	0.326	0.510	0.024
R14	0.543	0.895	0.008
R15	0.451	0.882	0.012
R16	0.370	0.689	0.016
R17	0.459	0.747	0.010
R18	0.195	0.493	0.018
R19	0.419	0.557	0.014
R20	0.402	1.126	0.000
R21	0.347	0.683	0.013
R22	0.371	0.728	0.014
R23	0.527	1.165	-0.003
R24	0.539	0.601	0.016
R25	0.411	0.840	0.009

A comparison between rain gauges and radar data reveals also the discrepancies in measurement accuracy. It is visible on plots 6.5, which present the relation between on-ground and radar rainfall data. Discretization of radar derived rainfall intensities is clearly visible. It is especially noticeable, for the small rain rate values registered by gauges that correspond to a few discrete levels of radar estimated rainfall intensities. It is caused by the method of radar reflectivity recording in the original radar scans as discrete values i.e. integer numbers at the range from 0 to 255.

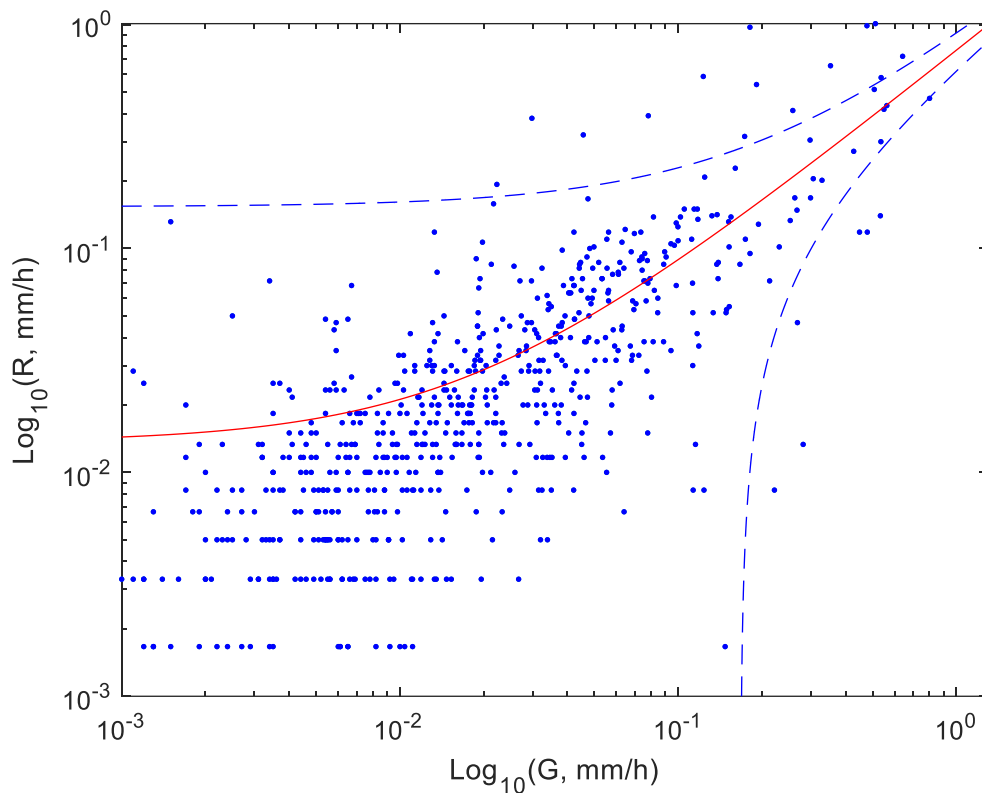


Figure 6.5 Log-log plot of 10-min non-zero radar rainfall intensity R values versus non-zero rainfall intensity G values from gauge R10 for summer months of 2009 with best fitted linear function with its 95% confidence intervals

6.4. Conclusions

The similarity of rain gauges and radar time series is detectable. However, usually the maximum rain rates obtained from rain gauges are higher than those registered by weather radar. Similar phenomena was noticed by Jakubiak et al. (2014) for Warsaw, and Siekanowicz-Grochowina et al. (2017) for Wrocław. Most probably it results from measurement scale differences. Single radar cell resolution is 1x1 km, whereas gauges

orifice is ca. 200 cm², so an averaging of the rain rate in space during radar measurement occurs.

The coefficient of determination R^2 values for non-zero radar and gauge temporal rainfall intensities range from 0.195 (for R18) to 0.623 (for R8). Thus, discrepancies between radar and gauge measurements of temporal rainfall intensities at high resolutions of 10 min are clearly noticeable. Regardless of the issue of spatial scale gaps between radar and gauges, these discrepancies could also result from the combination of sampling and instrument error of radar and errors associated with the Z - R relationship evaluation (Wilson and Brandes, 1979). Despite the fact that Z - R relationships (used in POLRAD) are confirmed by disdrometer data analysis, especially for summer half-year (chapters: 5.3 and 5.4), nevertheless for single, especially intensive rainfall events or for single rain rate peak values, standard Z - R parameters may not be adequate.

Clearly the radar rainfall time series should not be considered as a direct equivalent for gauge series at high resolution of 10 min. Some underestimations of maximum point rainfall intensities by radar should be expected. Simultaneously, good cross correlation of rainfall intensity series from gauges and radar confirms the credibility of PAC rainfall estimates as the source of information about precipitation distribution in space and time over the whole Warsaw city area.

7. Multifractal analysis and modelling of Warsaw precipitation field

Multifractal theory (Falconer, 1990; Feder, 1988) was first used to model velocity fluctuations in turbulent flows (Benzi et al., 1984), and since then has progressively developed, also in the field of precipitation process modelling. Multifractal formalism is applied because of its capability to control the statistical moments of a given distribution of measures (such as turbulent velocity gradients or precipitation data) in a wide range of space and time scales.

The majority of research involving multifractal analysis and simulation of rainfall focusses on modelling only one aspect of the precipitation variability - time or space.

The investigations on statistical behaviour of precipitation events in time are often conducted without considering the spatial variability of the precipitation field itself. The case studies of time series analysis of rainfalls and simulation of synthetic series with one-dimensional multifractal models preserving scaling laws observed in nature were undertaken, i.a. by Deidda et al. (1999a), Georgakakos et al. (1994); Hubert et al. (1993); Menabde et al. (1997b); Rodriguez-Iturbe et al. (1989); Svensson et al. (1996).

The subject of analysis and simulation of rainfall distribution in space with two-dimensional multifractal models was investigated by Deidda (1999b), Gupta and Waymire (1993), Kumar and Foufoula-Georgiou (1993 a, b), Lovejoy and Schertzer (1990); Olson and Niemczynowicz (1996); Over and Gupta (1994), Svensson et al. (1996), Tessier et al. (1993). In these studies, only spatial statistical properties of rainfall on a fixed time duration were analysed, and the precipitation field variability in time was not taken into account.

The multifractal analysis of rainfall time series for local conditions of the Warsaw precipitation field were conducted by Licznar et al. (2015) and Dzugaj (2017) based on data obtained from 25 rain gauge networks. The technique proposed by Licznar et al. (2015) used microcanonical cascade models to show local variability of short precipitation time series within an urban monitoring network. Dzugaj (2017) used continuous universal random cascade models based on universal parameters to generate a synthetic rainfall time series. Nevertheless, in both studies the aspect of spatial precipitation variability was not considered.

The variability in space of the Warsaw precipitation field was investigated by Rupp et al., (2016). The discrete multiplicative random cascade method was used to generate

realistic rainfall fields for the local conditions. The input data also was obtained from 25 rain gauge network. Spatial distribution of 15-minute rainfall rate was investigated. Using this model, 15-minute rainfall rate was downscaled from 20x20 km area to a scale of a single rain gauge of 15x15 cm.

However, the covariant properties that characterize real precipitation in both space and time domain was not preserved in any of the mentioned research.

Hence, this study focuses on both – spatial and temporal – aspects of precipitation variability and intermittency and aims to test the performance of the 3-D space-time multifractal cascade model by Deidda (2000) for the Warsaw local conditions. Deidda's STRAIN model (acronym for: Space-Time Rainfall), was design based on data from the Global Atmospheric Research Program (GARP) Atlantic Tropical Experiment (GATE) campaign (Kuettner, 1974), thus the adjustment for Warsaw conditions and its further performance evaluation are required.

As the first step to perform multifractal analysis of the precipitation field, the structure functions charactering its statistical properties should be defined. In the downscaling process the link between precipitation amounts over different areas and different accumulation times is important.

For the downscaling process, an instantaneous rainfall intensity $i(x, y, t)$ is introduced, which is continuous in space and time (Fabry, 1996). The definition of an integral measure P of rainfall over an area $\lambda_x \times \lambda_y$ and a cumulative time τ is then (eq. 7.1):

$$P_{\lambda_x, \lambda_y, \tau}(x, y, z) = \int_x^{x+\lambda_x} d\xi \int_y^{y+\lambda_y} d\theta \int_t^{t+\tau} d\sigma i(\xi, \theta, \sigma). \quad (7.1)$$

The downscaling process allows to determine the probability distribution of precipitation amounts - $P_{\lambda_0, \lambda_0, \tau_0}$ over spatial scales $\lambda_0 \times \lambda_0$ and accumulation times τ (fine enough for catchment modelling) based on an amount of rainfall $P_{L, L, T}$ over an area $L \times L$ and a time scale T (which corresponds to e.g. the resolution of a meteorological model and C-band data). The short formulation of downscaling process will be referred to as: $P_{L, L, T} : \rightarrow P_{\lambda_0, \lambda_0, \tau_0}$.

7.1. Space-Time Rainfall (STRAIN) model

The methodology of the conducted analysis and modelling of urban precipitation field is based on Deidda's STRAIN model (2000). The spectrum of STRAIN usage is a rainfall downscaling from large-scale meteorological models to rainfall-runoff processes.

The assumptions of the STRAIN model are as follows (Deidda, 2000):

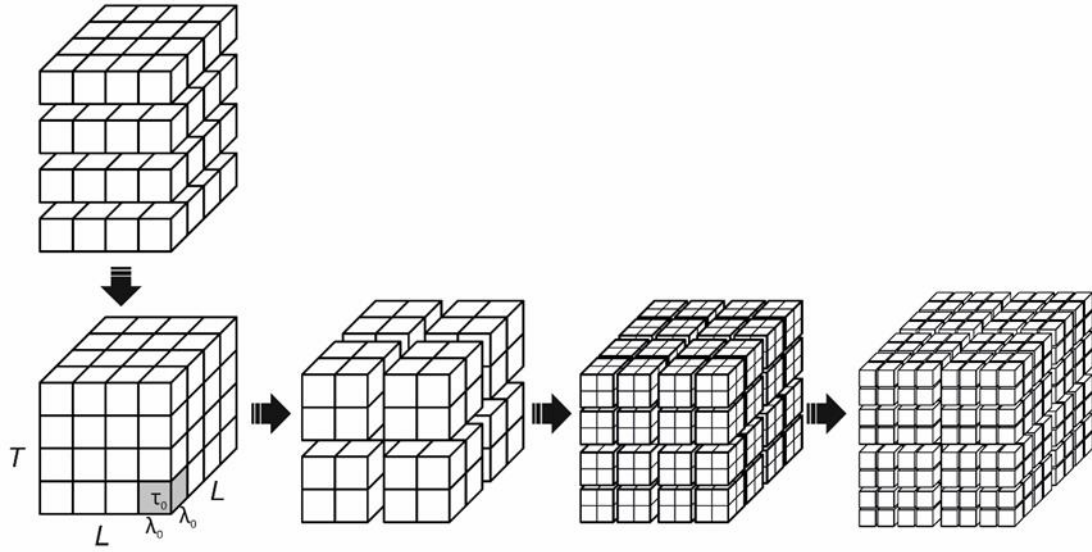
1. precipitation fields are isotropic and statistically homogeneous in space;
2. self-similarity occurs, so that rescaling time dimension is needed to perform by advection velocity U , rainfall event is a fully homogeneous and isotropic process in the space-time domain (Taylor hypothesis);
3. statistical properties of rainfall event are described by an "a priori" known multifractal behaviour, the space-time multifractal properties are estimated from observed precipitation fields.

A more detailed description of STRAIN model assumptions, i.e. the Taylor hypothesis and multifractal properties of precipitation field, mentioned in point 3 above, are discussed in more detail below.

STRAIN is a generalization of the multidimensional model developed by Deidda et al. (Deidda et al., 1999a) to generate a space-time rainfall cascade based on scale covariance using an infinitely divisible log-Poisson distribution (Dubrulle, 1994; She and Leveque, 1994; She and Waymire, 1995).

Figure 6.1 shows the approach to direct space-time rainfall downscaling based on the Taylor hypothesis. The three-dimensional (3-D) space-time cascade is constructed from a sequence of radar scans assuming that the anisotropy between space and time is only related to overall advection velocity (U).

With a direct "space-time modelling" of rainfall using 3-D multifractal models, the reproduction of the statistical properties of real rainfall for any intermediate scale λ ($\lambda_0 < \lambda < L$) and τ ($\tau_0 < \tau < T$) is expected.



$$P_{L,L,T} : \rightarrow P_{\lambda_0, \lambda_0, \tau_0}$$

Figure 7.1 Schematic diagram showing the approach to direct space-time rainfall downscaling based on Taylor hypothesis

The advection velocity is called a rescaling dimensional parameter that allows to eliminate temporal anisotropy and is assumed to be a constant for the analysed scale range. After rescaling the time dimension with U , rainfall fields must be isotropic in each of the three dimensions. The self-similarity of this structure is assumed. Then, the following structure function $S_q(\lambda)$ characterizes its statistical properties can be introduced (eq.7.2):

$$S_q(\lambda) = \langle [P_{\lambda, \lambda, \tau = \lambda/U}(x, y, t)]^q \rangle, \quad (7.2)$$

where $\langle \rangle$ is an ensemble average or an average operator over samples started in different points x , y , and t in the space-time domain.

When the advection velocity U is estimated as was earlier described, the structure function (eq. 7.1) can be written as:

$$S_q(\lambda) \sim \lambda^{\zeta(q)}. \quad (7.3)$$

Rainfall events can be considered as a 3-D self-similar multifractal process and the scaling law (eq. 7.3) holds with exponent $\zeta(q)$, which is a nonlinear function of the moment q and depends on neither the spatial nor time dimension.

According to Deidda et al. (1999) the structure function $S_q(\lambda)$ obeys the scaling law (eq. 7.3) with multifractal exponents $\zeta(q)$, that depends only on the moments of the generator η ensemble averages:

$$\zeta(q) = q(3 + \log_2 \bar{\eta}) - \log_2 \overline{\eta^q} \quad (7.4)$$

To describe the multifractal behaviour of precipitation fields, the random generator η uses an infinitely divisible log-Poisson distribution, as follows (eq. 7.5):

$$\eta = e^A \beta^y P(y = m) = \frac{c^m e^{-c}}{m!}. \quad (7.5)$$

Where A and β are constant parameters, and y is a Poisson distributed random variable with parameter c : $E[y]=c$. Thus, the q -order moment of the log-Poisson distribution is defined as $\overline{\eta^q} = \exp [qA + c(\beta^q - 1)]$.

Finally, the scaling of precipitations in space and time can be evaluated:

$$\zeta(q) = 3q + c \frac{q(\beta - 1) - (\beta^q - 1)}{\ln 2} \quad (7.6)$$

In equation 7.6 the multifractal exponent $\zeta(q)$ depends only on the parameters c and β , which are scale independent and can be estimated by solving the following minimization problem (eq. 6.7):

$$\min_{c, \beta} \sum_q \left[\frac{\hat{\zeta}(q) - \zeta(q)}{\sigma(q)} \right], \quad (7.7)$$

where $\hat{\zeta}(q)$ are the sample multifractal exponents, $\zeta(q)$ is the theoretical expectation (eq. 7.6), and $\sigma(q) = q - 1$ is the standard deviation of $\zeta(q)$.

Scaling law (eq. 7.3) can be alternatively redefined: exponent $\zeta(q)$ is substituted by moments of scaling exponent function $K(q)$. In the case of 3D domain of multifractal analysis, the relation between both functions of moments order q could be written as follows:

$$\zeta(q) = 3q - K(q). \quad (7.8)$$

7.2. Taylor hypothesis verification and advection velocity estimation

To conduct multifractal analysis and modelling of the precipitation field based on the self-similarity assumptions of STRAIN model (Deidda, 2000), the Taylor hypothesis of “frozen turbulence” (Taylor, 1938) must be verified for local conditions of Warsaw precipitation field.

The study conducted by Taylor in 1938 focused on the relation between the spectrum of turbulence measured at a fixed location and simultaneous velocity value measurements for two points. According to his research, the temporal variations at a fixed location might have been interpreted as spatial variations.

The temporal anisotropy was eliminated using rescaling parameter - the overall advection velocity of which the value is constant for each analysed scale λ . The time dimension is rescaled; thus, the precipitation field became isotropic in both spatial dimensions (X and Y) and in time (rescaled with advection velocity U).

Discrete resolution in time ($\tau = 10$ min) and space (λ_x and $\lambda_y = 1$ km) of the analysed original PAC radar datasets allowed for only some discrete velocities U values to be considered to perform a space-time multifractal analysis. The advection velocity U value was estimated by iteratively repeated calculations for the assumed levels of the 3-D cascade. The higher the assumed advection velocity, the more extended the spatial dimensions of the analysed precipitations field were. The aggregation of spatial dimensions of the precipitation field was conducted to ensure the precipitation field homogeneity in space and to investigate its correlation with rescaled time dimension T , which was aligned to the spatial range to obtain a 3-D cubic structure. In Appendix B the spatial range of analysed precipitation fields was presented for each of assumed advection velocities – respectively for: 12 km·h⁻¹, 18 km·h⁻¹, 24 km·h⁻¹, 30 km·h⁻¹, 36 km·h⁻¹, 42 km·h⁻¹, 48 km·h⁻¹, 54 km·h⁻¹ and 60 km·h⁻¹.

The calculations were conducted based on a collection of radar scans from May to September 2015.

A continuous collection of PAC radar scans was used to select a set of independent rainfall events, using a moving window algorithm (described in detail in chapter 7.3). The number of selected rainfall events for assumed advection velocity values varied from 21 to 31 due to changes of the analysed spatial ranges (see tab. 7.1). For each selected event, the autocorrelation functions for spatial X and Y dimensions and time T rescaled by assumed advection velocity U were calculated. Finally, the mean

autocorrelation functions of all events for each direction were derived for assumed advection velocity U values.

To identify the most suitable advection velocity value from the spectra of analysed values, the Pearson correlation coefficients were calculated for mean autocorrelation functions of spatial and temporal dimensions of cubic structures, using the following formulas (equations: 7.8, 7.9, 7.10):

$$\rho(X, Y) = \frac{1}{N-1} \sum_{i=1}^N \left(\frac{\overline{X_i - \mu_X}}{\sigma_X} \right) \left(\frac{Y_i - \mu_Y}{\sigma_Y} \right) \quad (7.9)$$

$$\rho(X, T) = \frac{1}{N-1} \sum_{i=1}^N \left(\frac{\overline{X_i - \mu_X}}{\sigma_X} \right) \left(\frac{T_i - \mu_T}{\sigma_T} \right) \quad (7.10)$$

$$\rho(Y, T) = \frac{1}{N-1} \sum_{i=1}^N \left(\frac{\overline{X_i - \mu_Y}}{\sigma_Y} \right) \left(\frac{T_i - \mu_T}{\sigma_T} \right) \quad (7.11)$$

where μ_X and σ_X are the mean and standard deviation of X -dimension of matrix respectively, μ_Y and σ_Y are the mean and standard deviation of Y -dimension of matrix and μ_T and σ_T are the mean and standard deviation of T -dimension of 3D rainfall matrix (cubic structure).

An example of autocorrelation functions of PAC values along X and Y directions and for the rescaled time direction T , for the assumed advection velocity $U=16 \text{ km}\cdot\text{h}^{-1}$, for a selected radar sequence started on 07.07.2015 at 22:30 is presented in fig. 7.2. It is an example of the result of inadequate assumption of the advection velocity U value. Whereas autocorrelation functions along X and Y directions follow, expected closely related pattern of systematic reduction of correlation values with extending distances between observations in space, the incompatibility of the autocorrelation function along rescaled time direction T is visible.

Plots of mean autocorrelation functions of all selected radar sequences along X and Y directions and rescaled time direction T for different advection velocity assumptions are presented in Appendix C. The values of correlation coefficients $\rho(X, Y)$, $\rho(X, T)$, $\rho(Y, T)$ for the assumed advection velocities are presented in table 7.1.

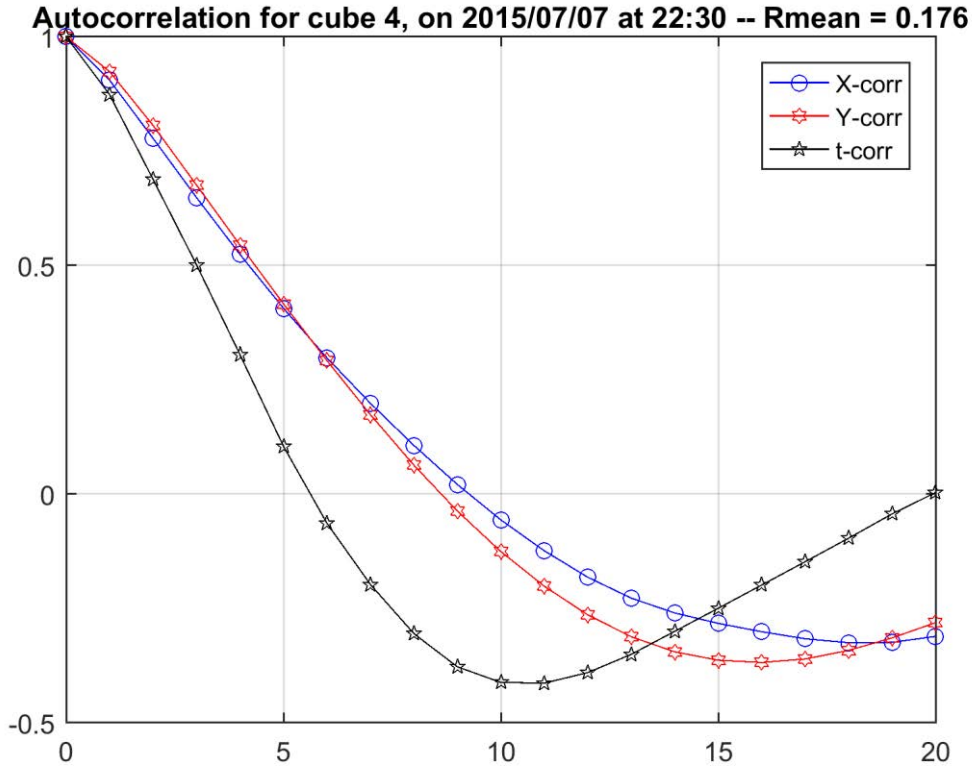


Figure 7.2 An exemplary autocorrelation functions along x (x-corr) and y (y-corr) directions and time (t-corr) for 320-min aggregated radar sequence selected from 2015 for advection velocity $U=16 \text{ km}\cdot\text{h}^{-1}$. The rainfall event started on 07.07.2015 at 22:30. The horizontal axis represents the shift in the radar grid aggregated to $4\times 4 \text{ km}$.

Table 7.1 Pearson correlation coefficients calculated for pairs of mean autocorrelation functions for spatial and temporal dimensions of cubic structures for a hierarchy of assumed advection velocities

Assumed advection velocity	Spatial range of analysed precipitation field	Size of aggregated radar grid	Number of selected rainfall events	$\rho(X, Y)$	$\rho(X, T)$	$\rho(Y, T)$
12 km h^{-1}	64 x 64 km	2 x 2 km	27	0.9995	0.9442	0.9395
18 km h^{-1}	96 x 96 km	3 x 3 km	31	0.9996	0.9737	0.9736
24 km h^{-1}	128 x 128 km	4 x 4 km	31	0.9994	0.9866	0.9885
30 km h^{-1}	160 x 160 km	5 x 5 km	29	0.9994	0.9925	0.9936
36 km h^{-1}	192 x 192 km	6 x 6 km	26	0.9993	0.9958	0.9961
42 km h^{-1}	224 x 224 km	7 x 7 km	27	0.9991	0.9979	0.9988
48 km h^{-1}	256 x 256 km	8 x 8 km	22	0.9996	0.9992	0.9997
54 km h^{-1}	288 x 288 km	9 x 9 km	22	0.9988	0.9995	0.9995
60 km h^{-1}	320 x 320 km	10 x 10 km	21	0.9984	0.999	0.9983

Based on data reported in tab. 7.1, the optimal advection velocity U value for Central Poland conditions is equal to $48 \text{ km}\cdot\text{h}^{-1}$. For this velocity, all three mean autocorrelation functions have a very close course (fig. 7.3) and Pearson correlation coefficients along all of 3 directions have close and high values exceeding 0.999 (tab. 7.1).

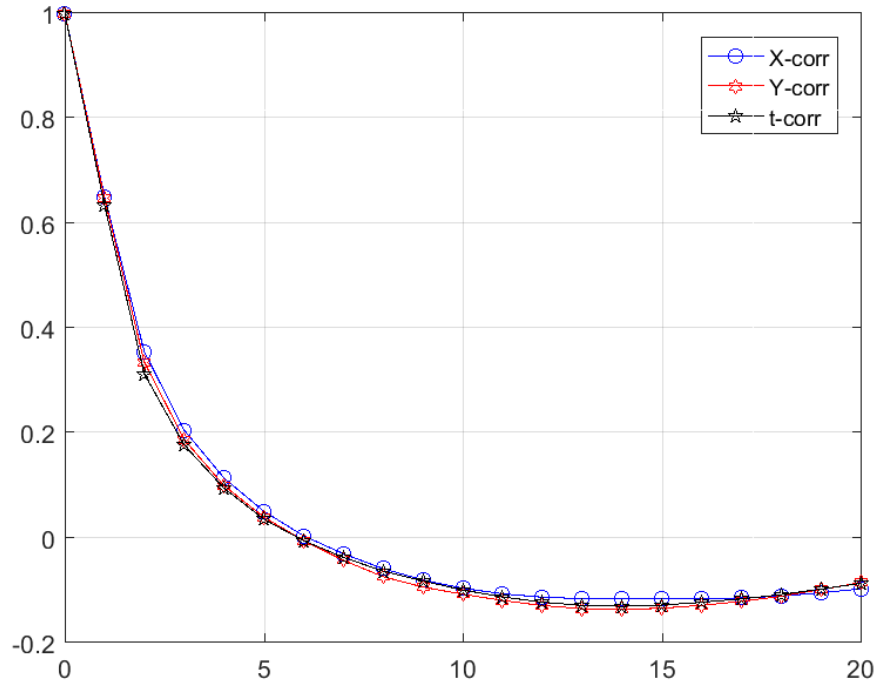


Figure 7.3 Mean autocorrelation functions along X (X-corr) and Y (Y-corr) directions and rescaled time (t-corr) direction for 320-min aggregated radar sequences selected from summer months of 2015 for advection velocity $U=48 \text{ km}\cdot\text{h}^{-1}$. The horizontal axis represents the shift in the radar grid aggregated to $8\times 8 \text{ km}$

The coincidence of autocorrelation functions along X (X-corr) and Y (Y-corr) directions and rescaled for advection velocity $U=48 \text{ km}\cdot\text{h}^{-1}$ time (t-corr) direction, for 320-min aggregated radar sequences, can be visually inspected for most of the 22 selected rainfall events from the summer months of 2015 on a series of individual plots collected in Appendix D. A good example of this is presented based on rainfall event started on 23.07.2015 at 1:20 AM in fig. 7.4. Overall advection velocity, derived for Central Poland in this study is 3 times higher than the value: $16 \text{ km}\cdot\text{h}^{-1}$ reported by Deidda (2000) in the first STRAIN model introduction. The sources of these differences for the overall advection velocity values remain unknown. It can be only speculated that this could be, at least partly, explained by climate differences between Central Europe and tropical regions of the Atlantic Ocean.

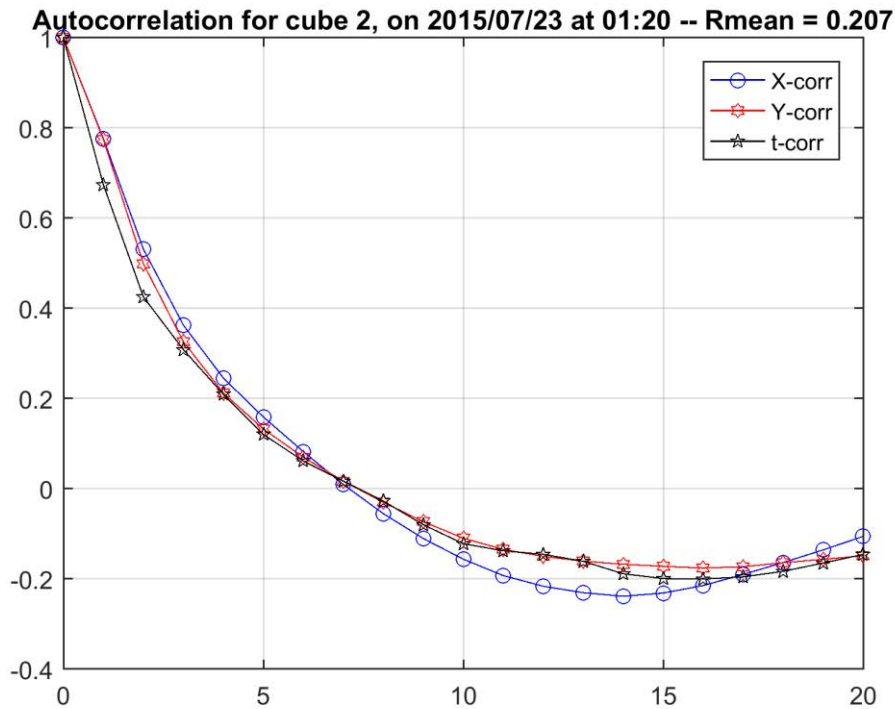


Figure 7.4 An exemplary autocorrelation functions along x (x-corr) and y (y-corr) directions and time (t-corr) for 320-min aggregated radar sequence selected from 2015 for advection velocity $U=48 \text{ km}\cdot\text{h}^{-1}$. The rainfall event started on 23.07.2015 at 1:20 AM. The horizontal axis represents the shift in the radar grid aggregated to 8x8 km.

The conducted research has proven the correctness of the Taylor hypothesis of “frozen turbulence” in the case of PAC radar sequences over Central Poland. Thus, the self-similarity assumption could be achieved by adapting the STRAIN model to Polish conditions by introducing the overall advection velocity of $U=48 \text{ km}\cdot\text{h}^{-1}$. For this velocity value, the construction of a 3-D cascade without deterioration of the original time resolution of 10 min, requires an aggregation of the original radar scans from 1x1km to 8x8 km in space. As a result, the domain size of the final 3-D cascade, which allows for rainfall disaggregation from 320 min to 10 min, is 256x256 km. This space domain is shown in fig. 7.5 and is centred over the Warsaw area and is mostly covered by the range of single C-band radar deployed in Legionowo.

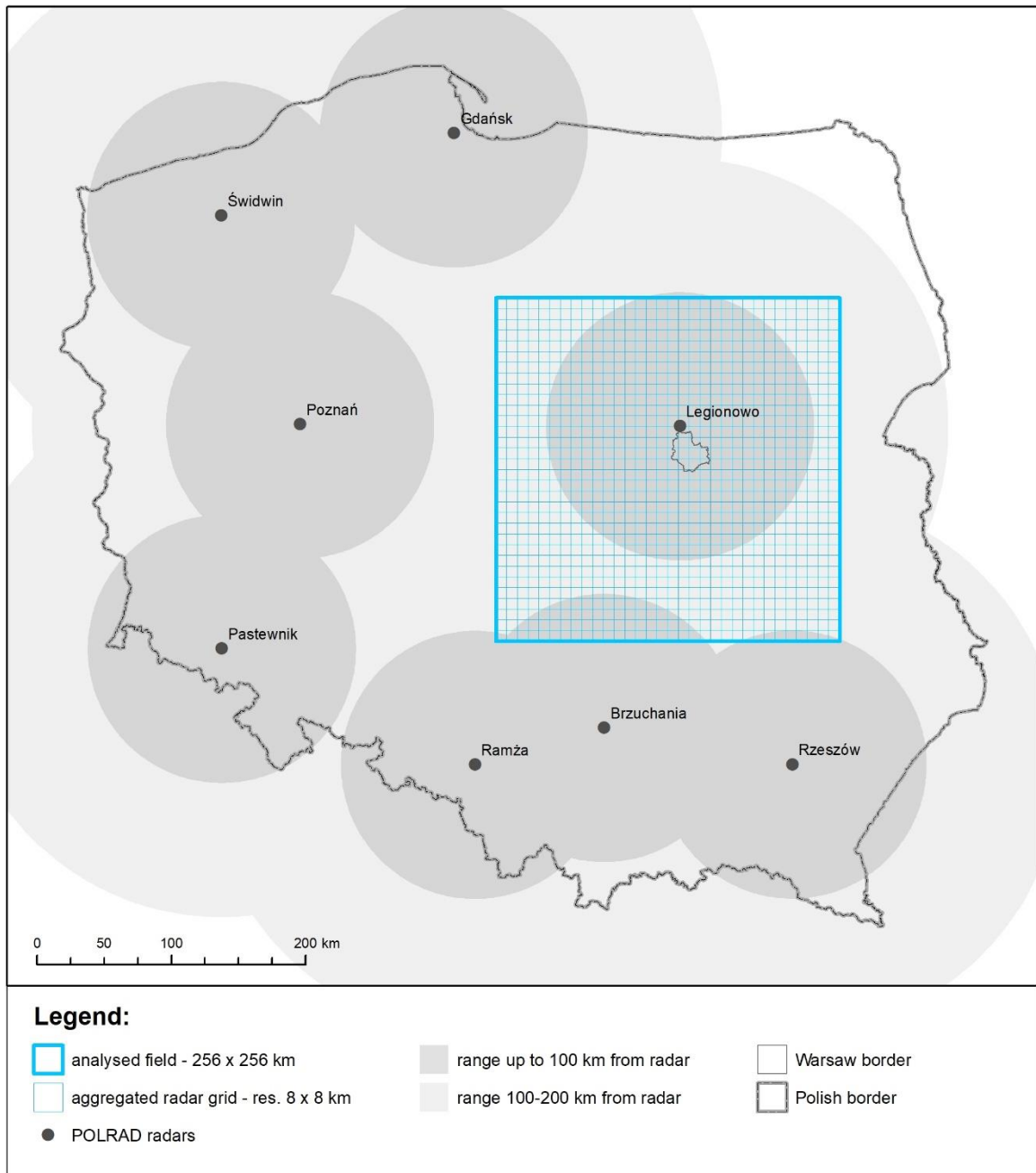


Figure 7.5 Spatial range of analysed precipitation field for assumed advection velocity $U = 48\text{km}\cdot\text{h}^{-1}$

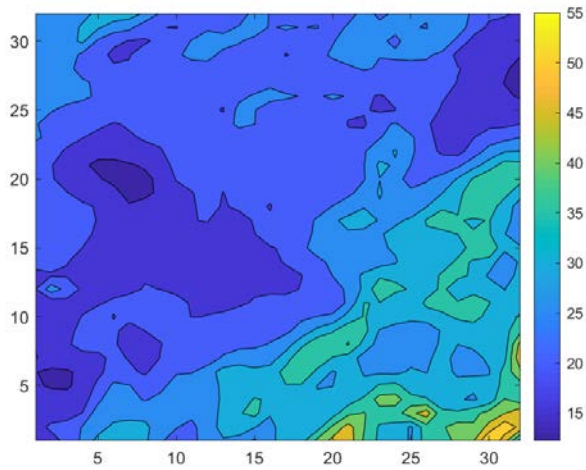
7.3. Moving window algorithm and rainfall events selection

To select rainfall events for further analysis a moving window algorithm was used. The selection threshold was set to 2 mm of mean depth precipitation on the whole area for a duration of 320 minutes (mean depth of single processed data frame covering analysed area above 0.0625 mm). The above-mentioned time window of 320 min was strictly connected with the formalism of conducted multifractal analysis and the number of 3-D cascade levels. The selection was carried out in a spatially aggregated and averaged data for each of the assumed advection velocity values. The cubic structure was supposed to be obtained, so every analysed precipitation field has had a spatial resolution of 32 x 32 aggregated cells and 320-minute duration (32 x 10 minutes per frame). The processed radar frames for each month were piled sequentially by time. The monthly rainfall depths derived from the aggregated and averaged PAC data from 2015 are shown in figure 7.6. Non-aggregated and non-averaged values of PAC are presented in figure 7.7. The spatial variability of monthly precipitation fields is apparent in both figures and no traces of systematic errors like for example radar beam blockage are visible. However, the spatial variability in fig. 7.6 is naturally smoothed by the process of radar scan spatial aggregation.

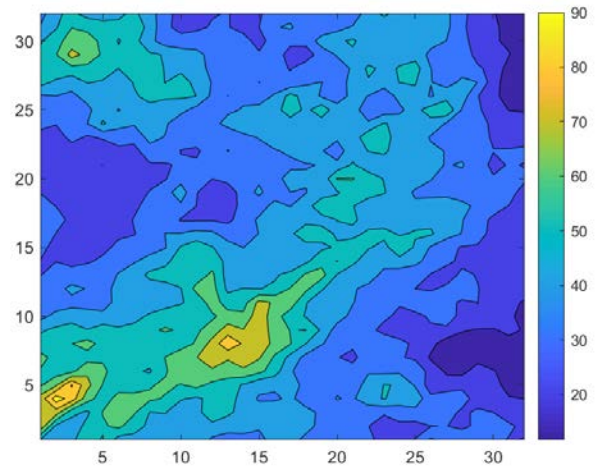
For each month, non-overlapping rainfalls were chosen, considering the given threshold. The numbers of rainfall events each year were separated using a moving window algorithm for assumed advection velocity $U=48 \text{ km}\cdot\text{h}^{-1}$ are listed in table 7.2.

Table 7.2 The number of rainfall events selected using moving window algorithm for each year

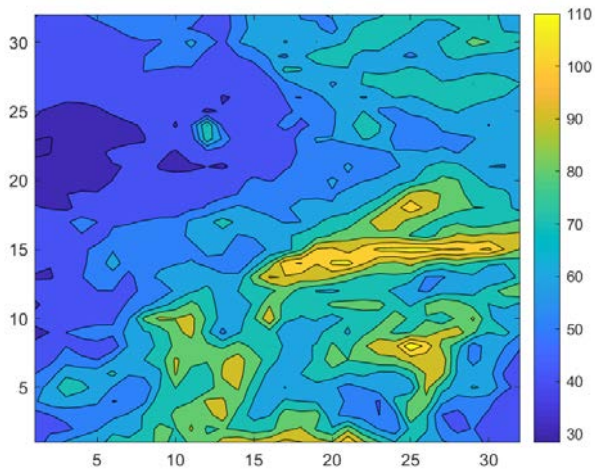
<i>Year</i>	<i>Number of separated rainfall events</i>
2009	28
2010	23
2013	29
2014	13
2015	22



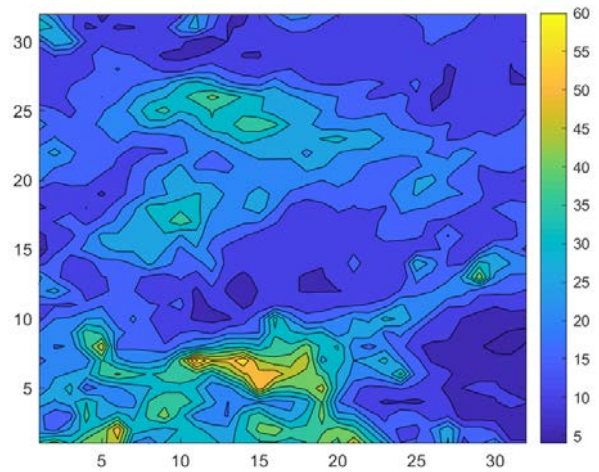
May 2015



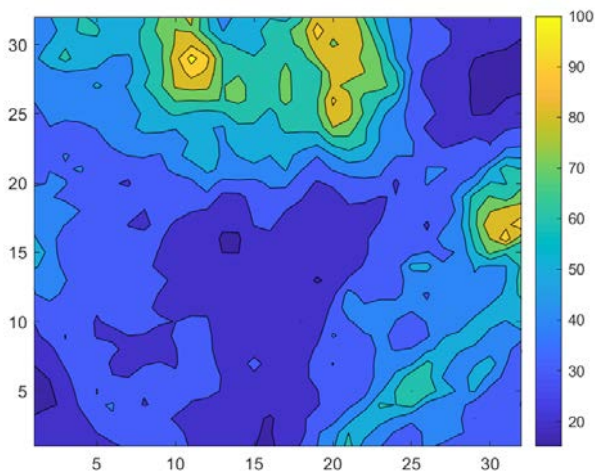
June 2015



July 2015

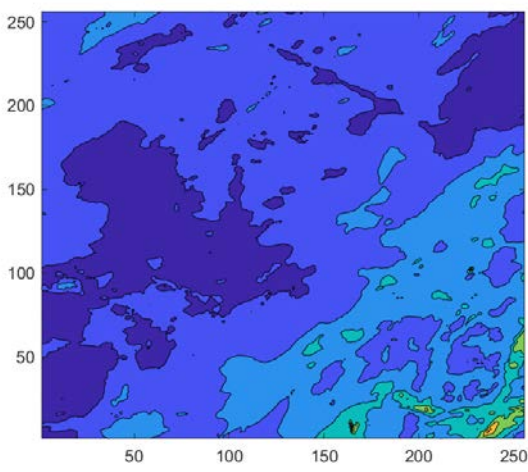


August 2015

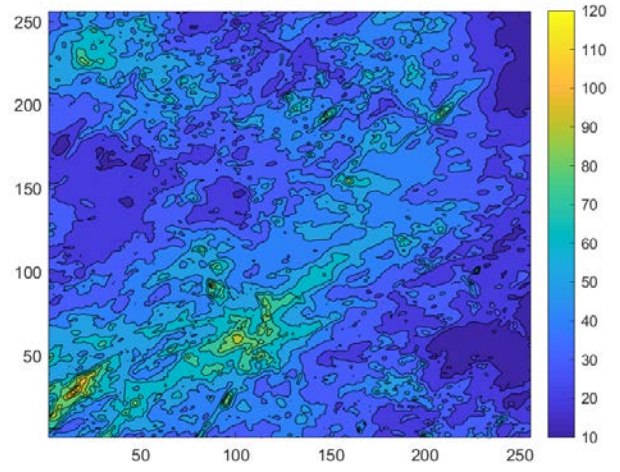


September 2015

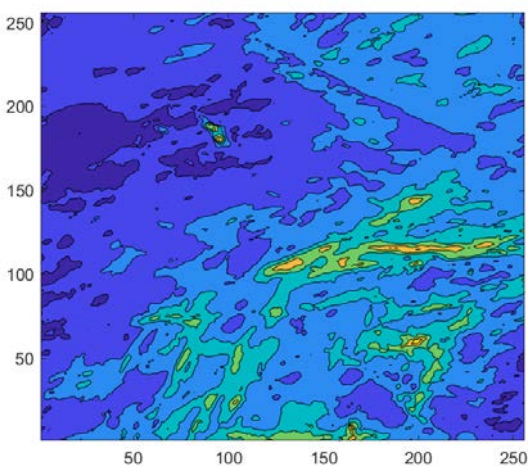
Figure 7.6 Monthly mean rainfall depths of precipitation field for analysed summer months of 2015. The spatial range of the field is 32 x 32 aggregated cells (each of 8x8 km)



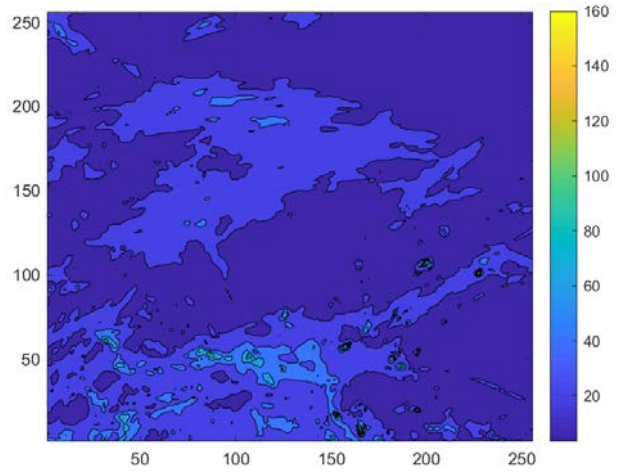
May 2015



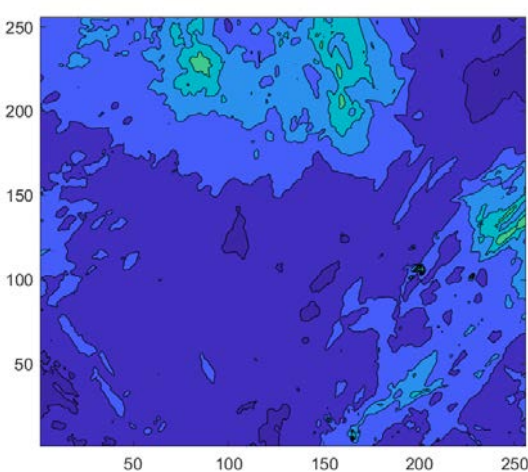
June 2015



July 2015



August 2015



September 2015

Figure 7.7 Monthly rainfall depths of precipitation field for analysed summer months of 2015. The spatial range of the field is 256 x 256 km

The total number of separated rainfall events used to further analysis is 115. The detailed list of selected rainfall events is listed in Appendix E. The mean depth for each 10-minute processed data frame is also included there. The events are listed descending by mean precipitation depth value and grouped by each year of observations. An exemplary 320-min precipitation structure of rainfall event started on 23.07.2015 at 1:20 AM is shown in figure 7.8. The mean rainfall rate calculated for the aggregated spatial resolution of 8x8 km (mm/10min) is presented in colour scale. All aggregated precipitation fields analysed for 2015 are visualised in Appendix F.

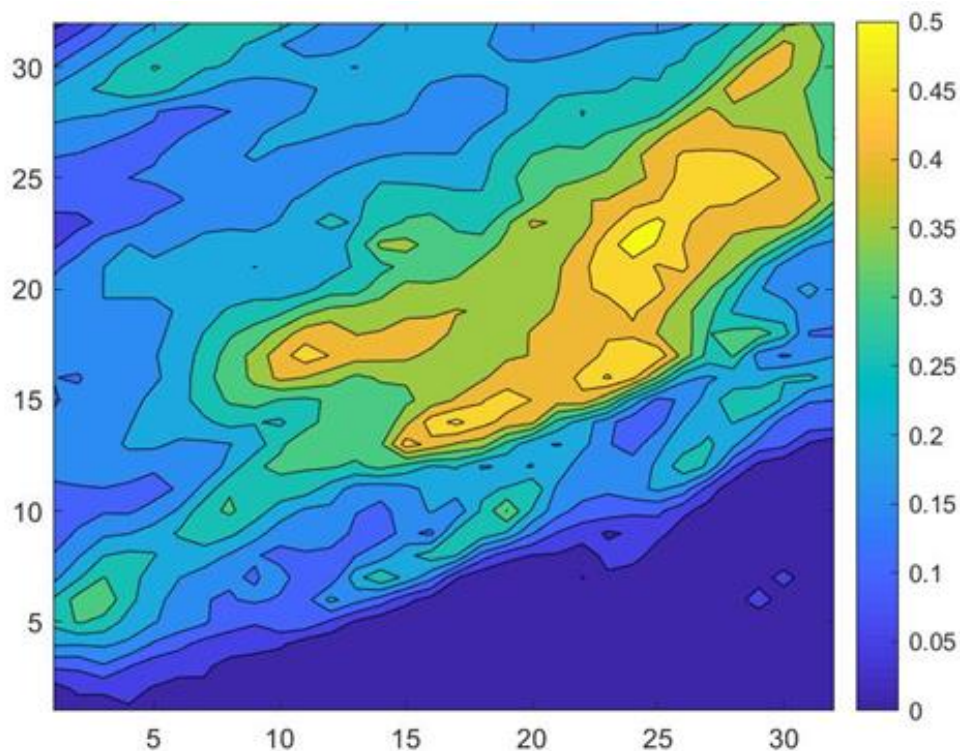


Figure 7.8 Mean rainfall rate (mm/10min) of an exemplary 320-min aggregated radar sequence. The rainfall event started on 23.07.2015 at 1:20 AM

7.4. Results and discussion

This chapter is divided into two parts. The first part is dedicated to the analysis of precipitation structures. This analysis is focused on properties of selected radar sequences – i.e. the distribution of rain rates for each selected rainfall event and their variability. Most of all, the multifractal theory, including 3-D random cascade is applied to investigate the statistical moments of the rainfall structures. For this purpose, the methodology originally proposed by Deidda (2000) described in chapter 7.1, is used. Finally, parameters of developed 3-D cascade models are derived and a rainfall disaggregation in time and space is performed.

Synthetic generated rainfall fields are analysed statistically and compared to similar statistics derived for original radar sequences for selected rainfall events in the second part of this chapter. On this basis, final conclusions concerning the STRAIN model performance are formulated.

7.4.1. Multifractal analysis of Warsaw precipitation field

Firstly, to enable the comparison of observed and synthetically generated precipitation structures, quantitative and spatial properties of the selected 115 rainfalls were investigated. Then, an analysis of selected precipitation fields was conducted using multifractal formalism proposed in STRAIN as described on chapter 7.1.

The analysis was performed on 115 structures selected with the moving window algorithm (chapter 7.3). The duration of each was 320 min (5 hours and 20 minutes). This specific rainfall phase duration originates from the regular cubic structure of cascade and temporal resolution of radar, but, on the other hand, disaggregation of rainfalls of longer durations is usually out of scope of urban hydrology. Stormwater outfall from building rooftops and paved city areas is fast, and its further transit in even the expanded underground network of conduits does not exceed a few hours.

An exemplary precipitation field of 320-min was shown in the previous chapter 7.3 (fig. 7.8). The aggregated fields were used to investigate the multifractal properties of 3-D rainfall structures, whereas non-aggregated ones were statistically analysed as a reference material for further comparison with statistic properties of synthetically generated rainfall events.

To explore the variability of rain rate values in analysed rainfall events, the complementary cumulative distribution function (cCDF) is calculated. The cCDF shows the distribution of probability of exceedance for increasing limiting values of r – rain rate (mm/10 min) in analysed radar sequences. The calculations are made for both – aggregated and non-aggregated radar sequences. An exemplary cCDF for the event on 23.07.2015 at 1:20 AM is presented in figure 7.9. All cCDFs for aggregated radar sequences selected from 2015 are listed in Appendix G. The cCDFs for non-aggregated radar sequences (256 x 256 km and 320-minute) for all 115 events are plotted in figure 7.10. It is clearly visible that in all 115 chosen sequences, 90 % of the r values are less than 1mm/10 min and 99 % are less than 5 mm/10 min. The major differences observed between all compared sequences comes from the incidence and the relative frequency of the highest rain rate values. The highest rainfall rate values are considered in theory

of multifractals as singularities, thus. their frequency of occurrence in limited observational sets is expected to be low. What is worth to emphasised, the visual inspection of all CDFs has revealed that plots are almost smooth and continuous on the whole range. Some departures, manifested by the loss of continuity are very rarely observed – of course not in every event, and only between the highest rain rate values for which occurrence probabilities are less than $10^{-4} \div 10^{-5}$ per cent.

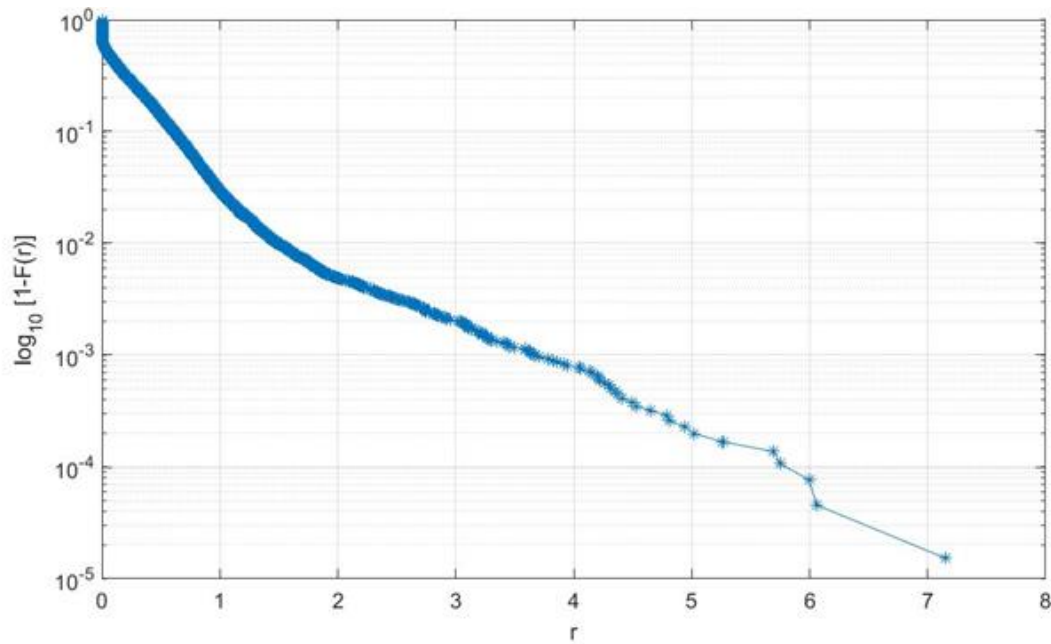


Figure 7.9 Complementary cumulative distribution function (cCDF) of rainfall rate (r in mm/10min) for 320-min aggregated radar sequence. The rainfall event started on 23.07.2015 at 1:20 AM

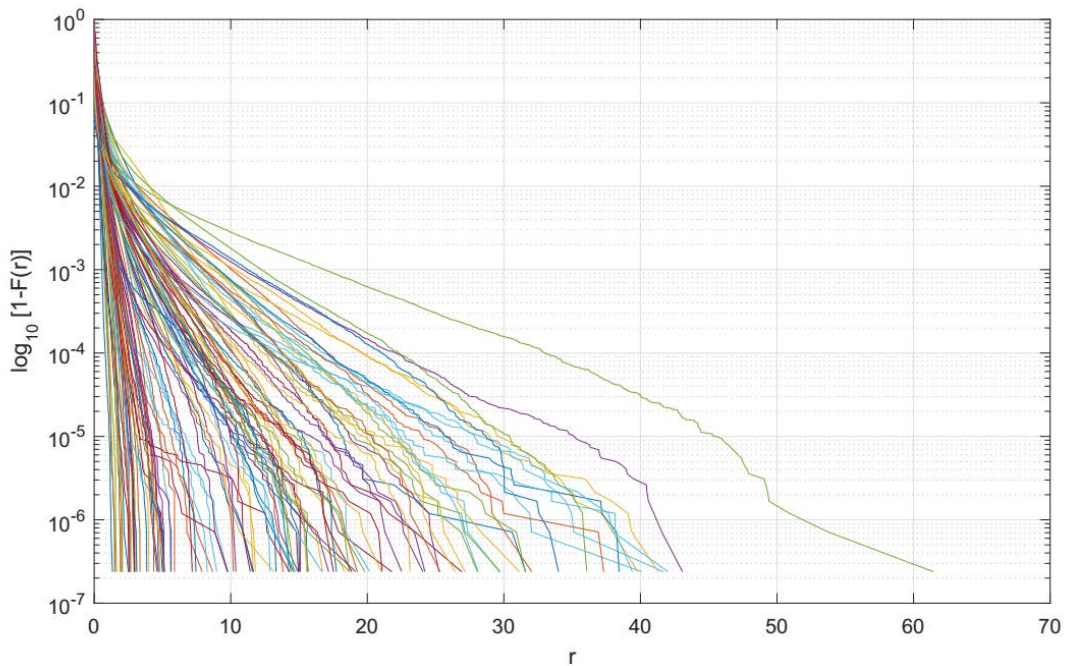


Figure 7.10 Complementary cumulative distribution functions (cCDFs) of rain rate r (in mm/10 min) for all 115 analysed 320-minute rainfall events distributed over the area of 256 x 256 km

The spatial variability of the observed precipitation fields was evaluated using the semivariogram function (eq. 7.12) (Venkatachalam and Kumar (2017)):

$$2\gamma(d) = \frac{1}{n(d)} \sum_{\text{distance}(i,j)=d} (z_i - z_j)^2 \quad (7.12)$$

where:

γ – semivariogram

z_i, z_j – observed values

d – distance between pairs of observations

n – the number of observations

Semivariograms analysis could be considered as an effective tool for diagnosis of spatial variability of rainfall over synthetically generated fields. The possibility of semivariograms implementation for this purpose over the urban Warsaw precipitation field was already demonstrated by Rupp et al. (2012).

The semivariograms were calculated in X and Y direction for each of the 115 selected precipitation fields in their original resolution (1 x 1 km). In figures 7.11 and 7.12, the semivariograms set for the analysed precipitation fields is presented respectively in X and Y. Moreover, the mean semivariograms in X-direction (upper panel) and in Y-direction (lower panel) are shown in figure 7.13. In these plots, not only the mean, but also the standard deviation values are presented. The occurrence of negative values for semivariograms for the plotted standard deviation ranges (from 0.5σ to σ) have no physical interpretation and results from the wide variability of semivariogram values of the 115 analysed rainfalls and, thus, the standard deviation values are high.

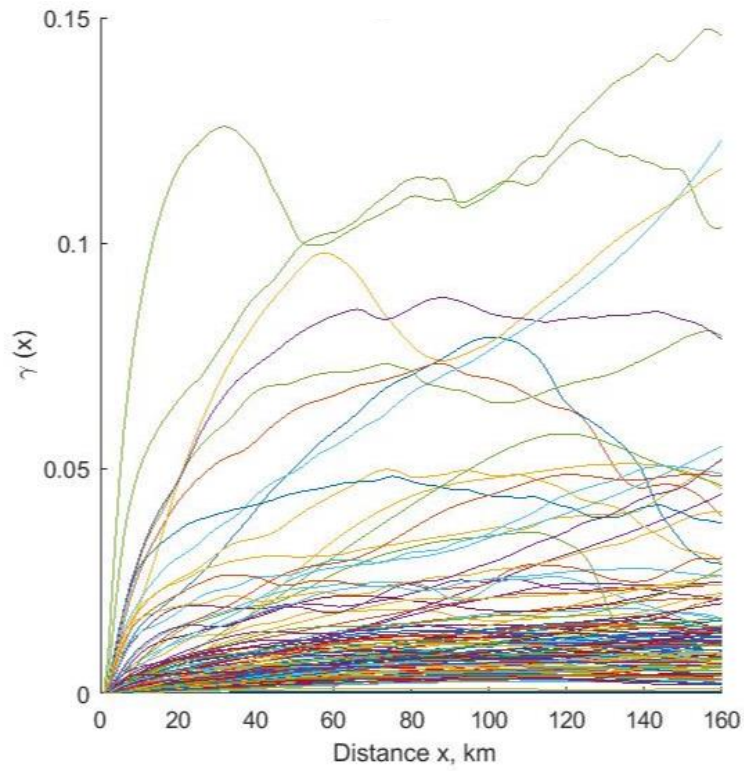


Figure 7.11 Set of semivariograms in X-direction for 115 analysed 320-minute rainfall events distributed over the area of 256 x 256 km

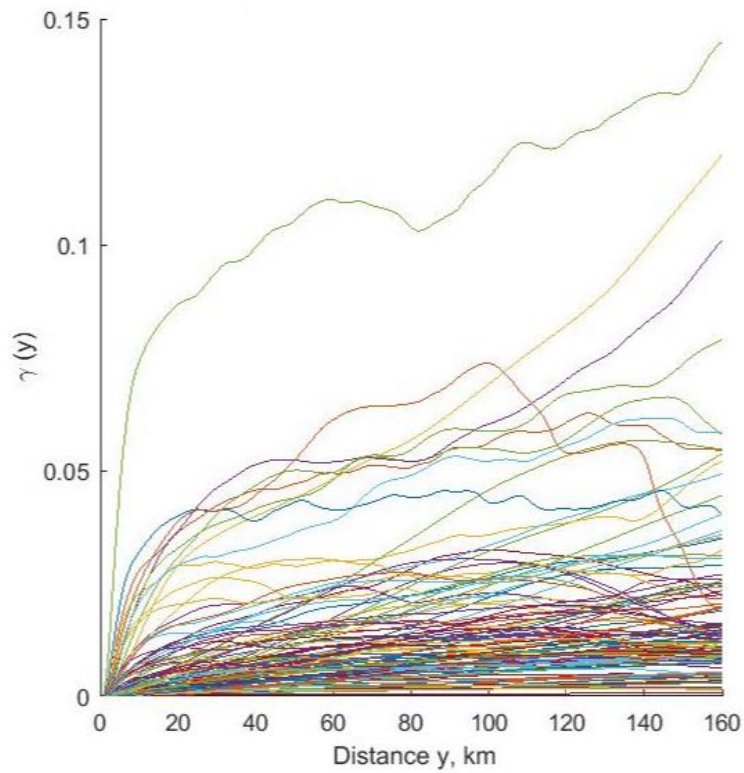


Figure 7.12 Set of semivariograms in Y-direction for 115 analysed 320-minute rainfall events distributed over the area of 256 x 256 km

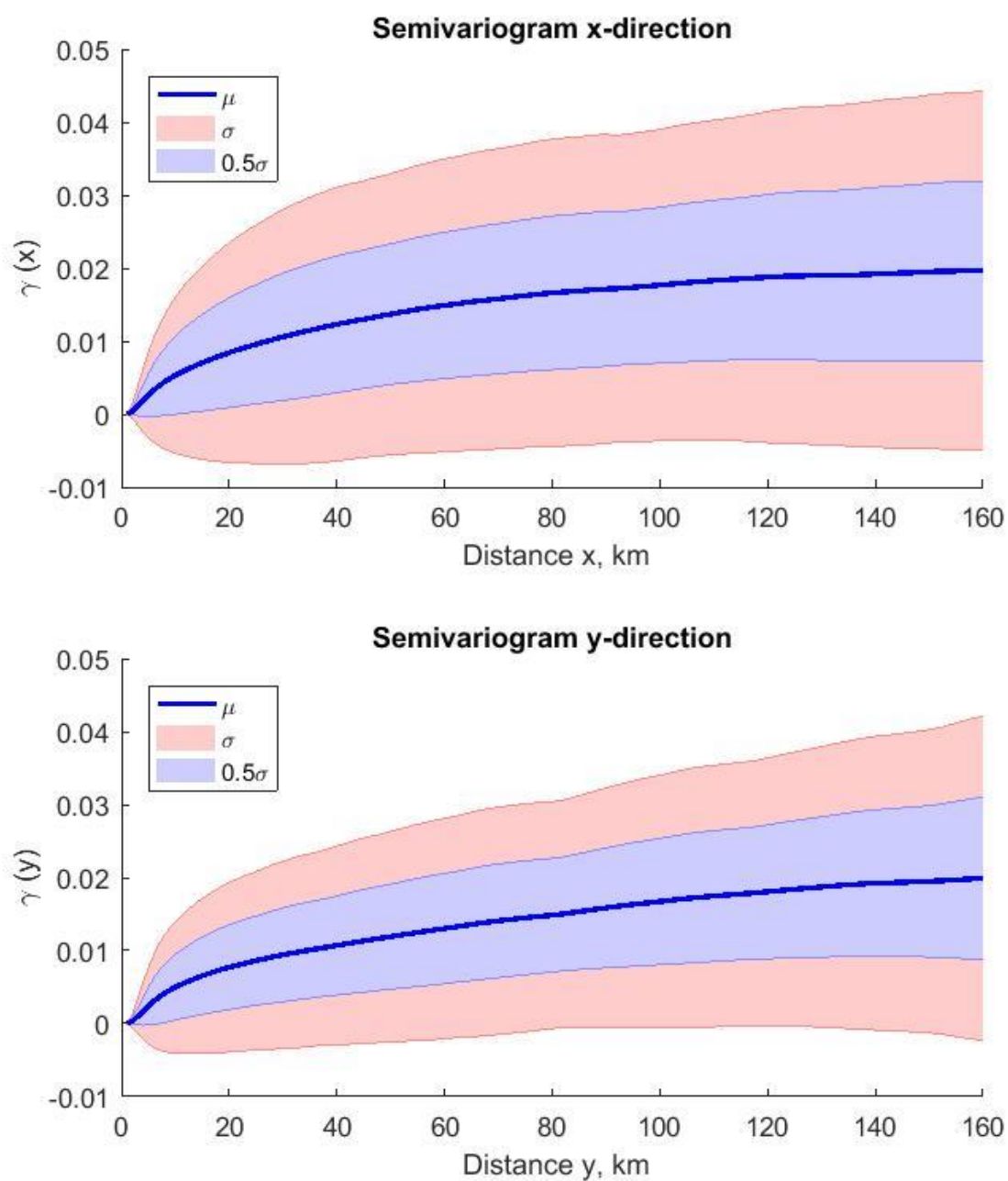


Figure 7.13 The averaged semivariograms (μ) in X-direction (upper panel) and Y-direction (lower panel) derived based on set of 115 semivariograms for selected rainfalls distributed over the area 256 x 256 km. The standard deviation ranges: from 0 to 0.5 σ (0.5σ) and from 0.5 σ to σ (σ) are additionally plotted

The multifractal analysis of the selected precipitation fields began with verification of the scaling law (eq. 7.3). Space-time structure functions $S_q(\lambda)$ were calculated for each selected and aggregated radar sequence for the hierarchy of scales ranging from $\lambda_0=8\text{km}$ to $L=256\text{km}$ and $\tau_0=10\text{ min}$ to $T=320\text{ min}$. $S_q(\lambda)$ was obtained for the assumed number of cascade levels (5) and for the statistical moments q ranging from 0 to 3 in increments of 0.25. The log-log plots of $S_q(\lambda)$ for all selected radar sequences from 2015 are provided in Appendix H. An exemplary plot of structure functions $S_q(\lambda)$ for the selected radar sequence from 2015 (rainfall event started on 23.07.2015 at 1:20 AM) is presented in figure 7.14.

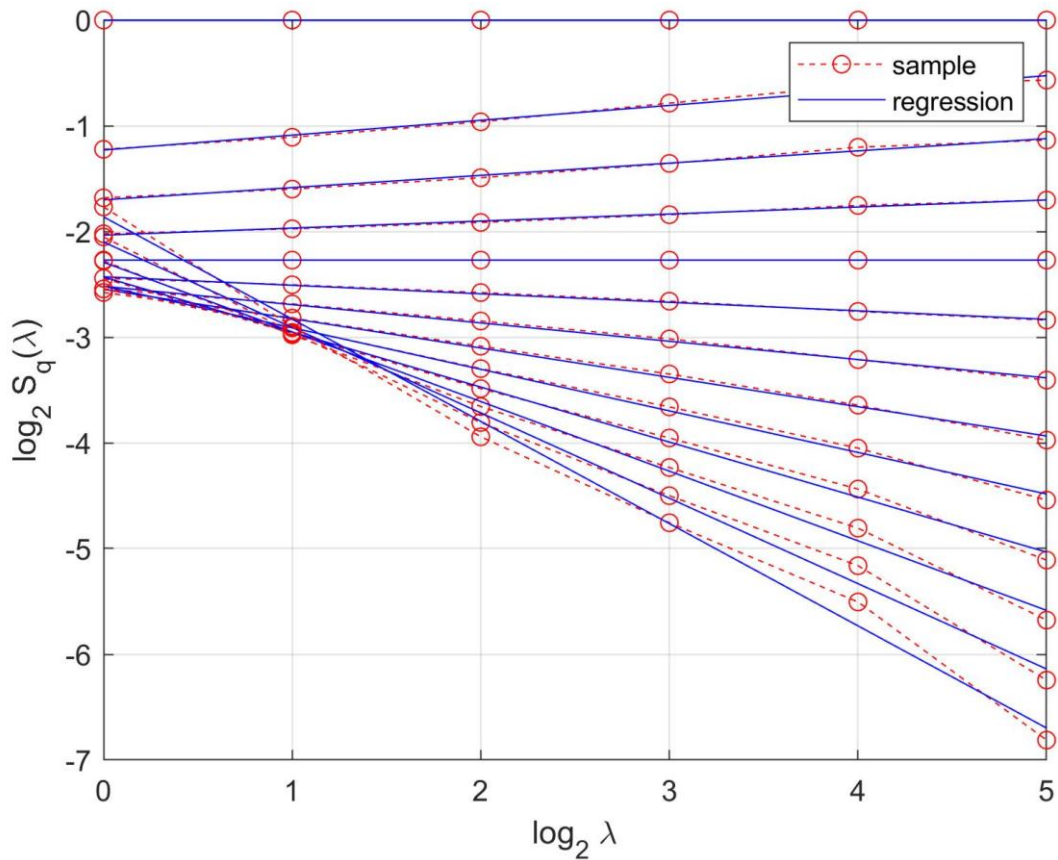


Figure 7.14 Log-log plot of the space-time structure function $S_q(\lambda)$ for 320-min aggregated radar sequence. The rainfall event started on 23.07.2015 at 1:20 AM

The obtained functions $S_q(\lambda)$, plotted in double logarithmic axes, follow the straight-line pattern. The slopes of $S_q(\lambda)$ provide the estimates of $K(q)$ (eq. 7.8) function values for the following orders q as shown in figure 7.15. Plots of derived $K(q)$ functions for all selected radar sequences from 2015 are given in Appendix I. The overall shape of $K(q)$ function for each of the analysed radar sequences follows very close a theoretical model of the multifractal moments scaling exponent function (Lovejoy and Schertzer, 2013). In each case, functions are convex and have two zero points: $K(0)=0$ and $K(1)=0$.

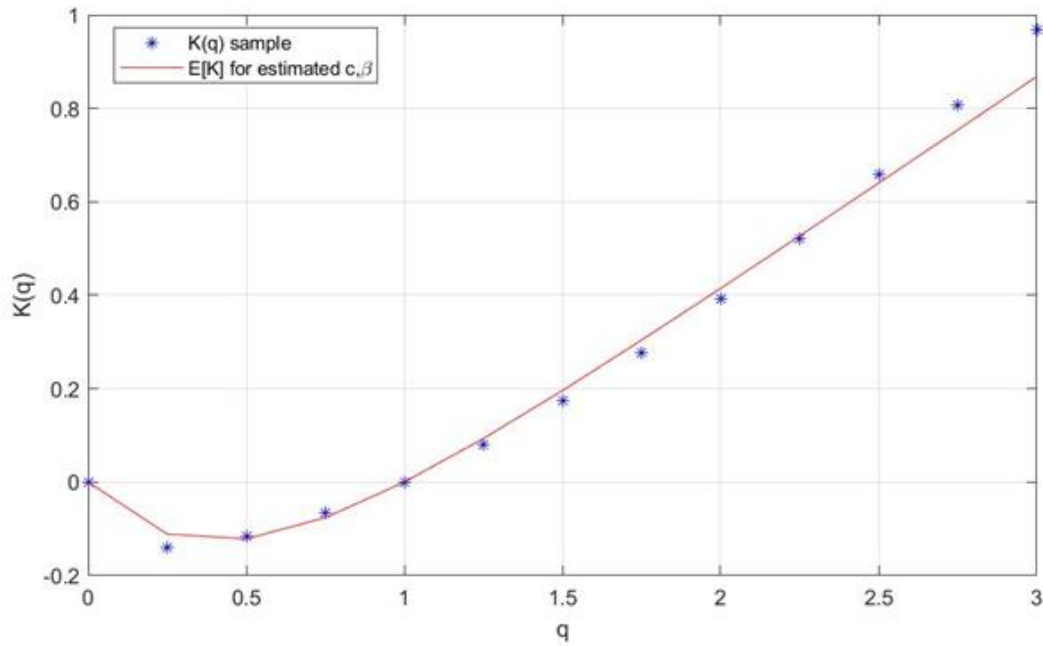


Figure 7.15 Empirical multifractal scaling function $K(q)$ for 320-min aggregated radar sequence together with fitted theoretical $K(q)$ function model for estimated c and β parameters. The rainfall event started on 23.07.2015 at 1:20 AM.

The above reported observations made for all 115 rainfall structures prove the hypothesis of the “universal” scaling law is applicable for Warsaw precipitation fields. Simultaneously, the possibility of practical space-time rainfall disaggregation at the range of analysed spatial and temporal scales, based on the phenomenology of 3-D random cascades is confirmed. Hence, the log-Poisson c and β parameters estimation (eq. 7.6) is justified. The estimated values of c and β , listed in Appendix J, are strongly variable and vary in range from 0.192 to 1.459 and from 0.007 to 0.498 respectively. In figure 7.16 and 7.17 the values of c and β parameters versus mean rainfall rate R in mm/10min over 256x256 km² for all selected radar sequences are plotted. In contrast to Deidda’s study (2000), the obtained values of log-Poisson parameters in the case of Warsaw precipitation field are more diversified and usually much smaller. The mean value of the β parameters is equal to $\beta=0.097$ and is much smaller in comparison to the averaged β obtained by Deidda (2000) of 0.35. For a constant β parameter equal to 0.097, the c parameter was once more estimated for all 115 radar scans. The new set of c values (marked as $c_{\beta=const}$) was less diversified and ranged from 0.175 to 0.973. The values $c_{\beta=const}$ for all selected radar sequences are also listed in Appendix J and illustrated in fig. 7.18 and 7.19. In the case of Deidda’s (2000) study, the assumption of constant and averaged β parameter resulted in smaller and less diversified $c_{\beta=const}$ parameter values.

The assumption of a constant $\beta=0.097$ value and estimation of only $c_{\beta=const}$ does not influence in a significant way the shape of fitted $K(q)$ functions. An exemplary $K(q)$ theoretical model for the estimated c parameter and fixed β parameter is presented in figure and 7.20 and is very similar to the plot of the $K(q)$ function for both c and β fitted parameters presented in figure 7.15. Empirical multifractal scaling functions $K(q)$ for 320-min aggregated radar sequences and fitted $K(q)$ theoretical models for estimated $c_{\beta=const}$ parameter and fixed β parameter for all selected radar sequences from 2015 are listed in Appendix K.

A visual inspection of plots for c and β parameters values vs. mean rain rate in figures 7.16 – 7.18 show that there is no relation of these parameters to the mean rain rate. In case of analysed rainfall events, it is impossible to account for so-called large scale forcing. The concept of large scale forcing was originally introduced into the precipitation cascade models by Over and Gupta (1994) and Over (1995). It assumes that large scale meteorological conditions influenced the dynamics of precipitation processes. Thus, precipitation cascade models should have different parameters depending on the type of precipitation (e.g. stratiform or convective).

When working with rainfall records and developing cascades models for rainfall disaggregation the information about precipitation types is often not available. Some general assumptions can be made and introduced into the cascade generators. In simple terms, convective precipitations are characterised usually by higher mean rain rates in comparison to stratiform ones. As a result, some relation between cascade parameters and mean rain rate can be expected. In the case of simple canonical cascades for disaggregation of rainfall time series, the relation between β and σ cascades parameters and mean rain rate at the timescale of 24 hours was established by Molnar and Burlano (2005) for Zurich, Switzerland. This similar analysis performed by Licznar (2009) for rainfall time series for Wrocław, Poland, revealed only large scale forcing relationship for β cascade parameter.

In the case of a 3-D cascade models, the relation of $c_{\beta=const}$ parameter and mean rain rate was reported by Deidda (2000) for the analysed precipitation radar sequences from the GATE experiment. However, Central Poland precipitation fields challenge such a relationship. The explanation of these results remains unknown. It can be speculated, that a 320-min average rain rate over the area of 256 x 256 km was most probably not the best suitable measure to describe the large scale meteorological conditions during precipitation events over the Central Poland area.

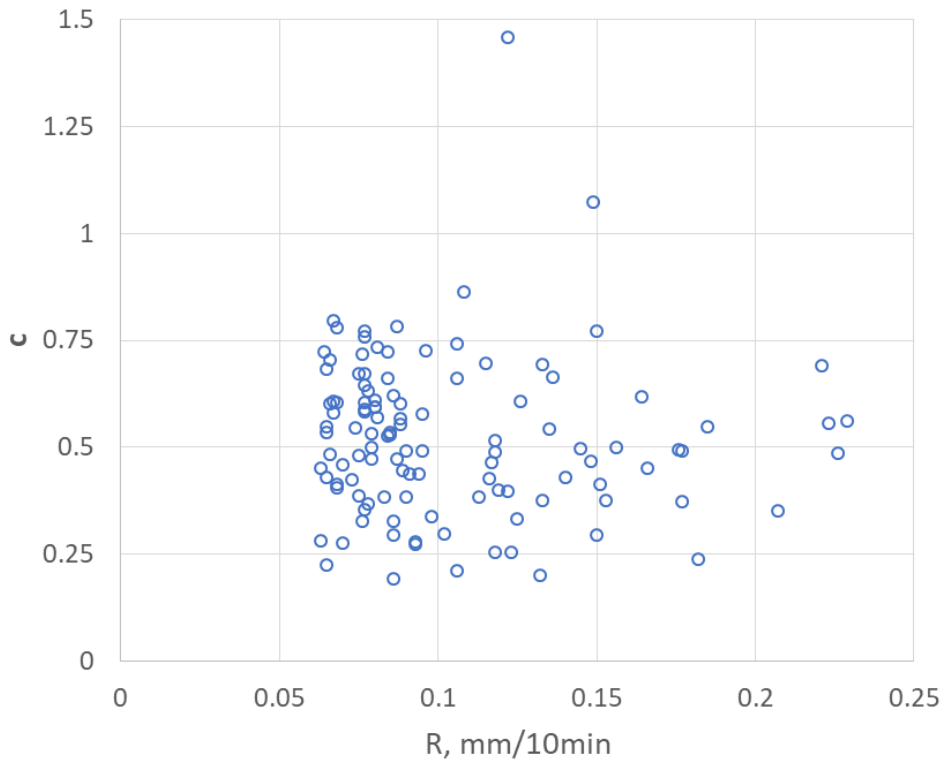


Figure 7.16 Plot of log-Poisson parameter c versus mean rainfall rate R over $256 \times 256 \text{ km}^2$ for all selected radar sequences.

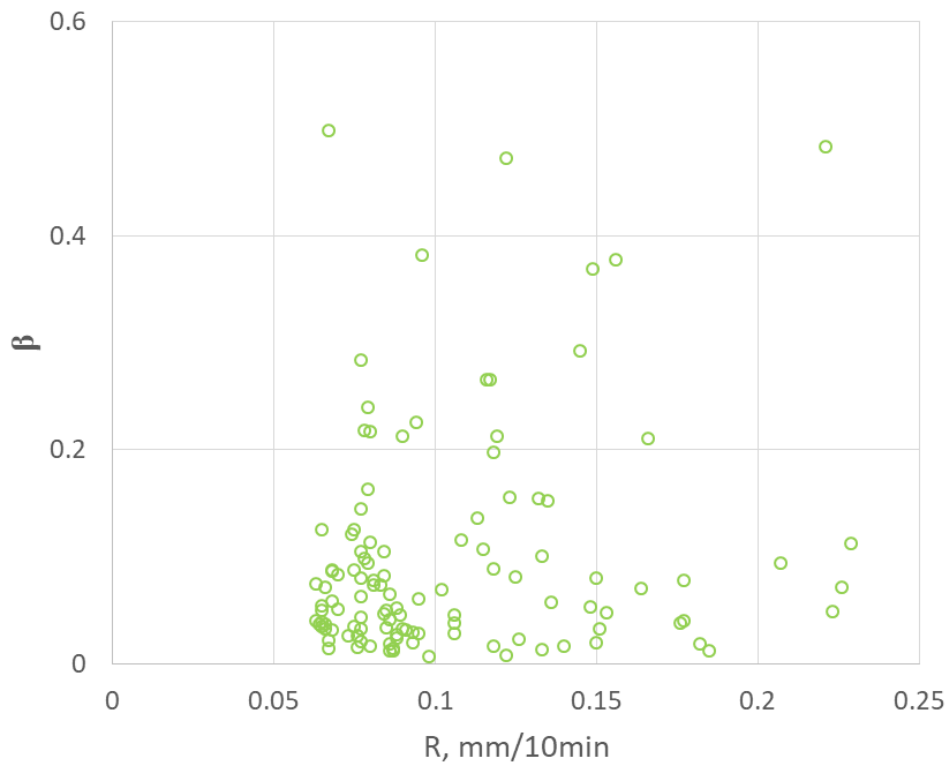


Figure 7.17 Plot of log-Poisson parameter β versus mean rainfall rate R over $256 \times 256 \text{ km}^2$ for all selected radar sequences.

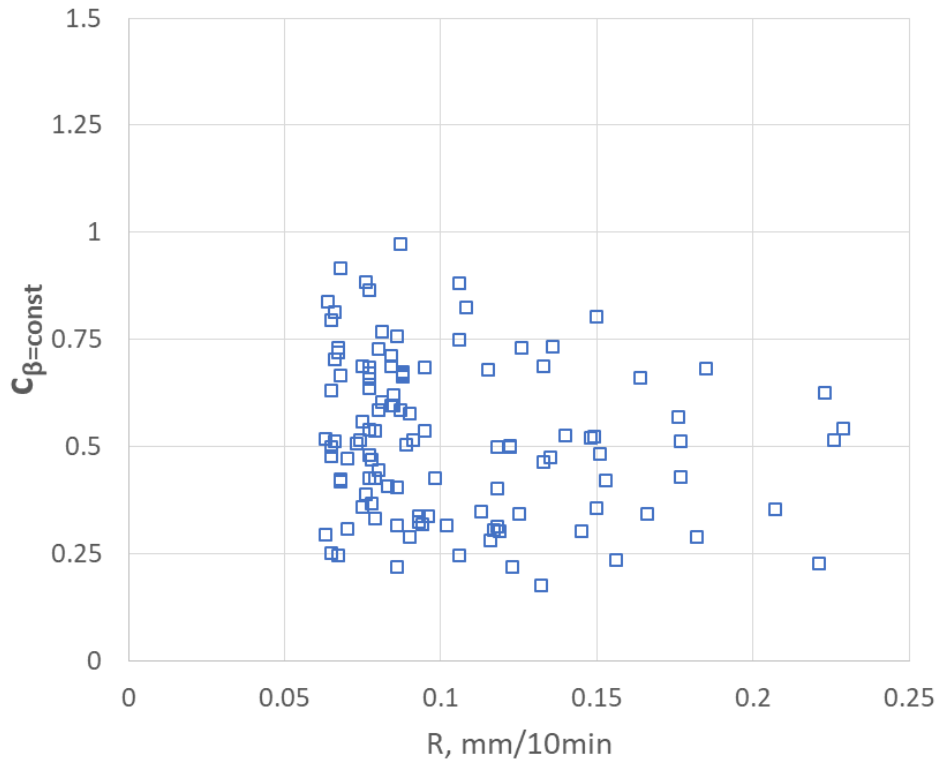


Figure 7.18 Plot of log-Poisson parameter $c_{\beta=const}$, keeping $\beta=0.01$ constant, versus mean rainfall rate R over $256 \times 256 \text{ km}^2$ for all selected radar sequences.

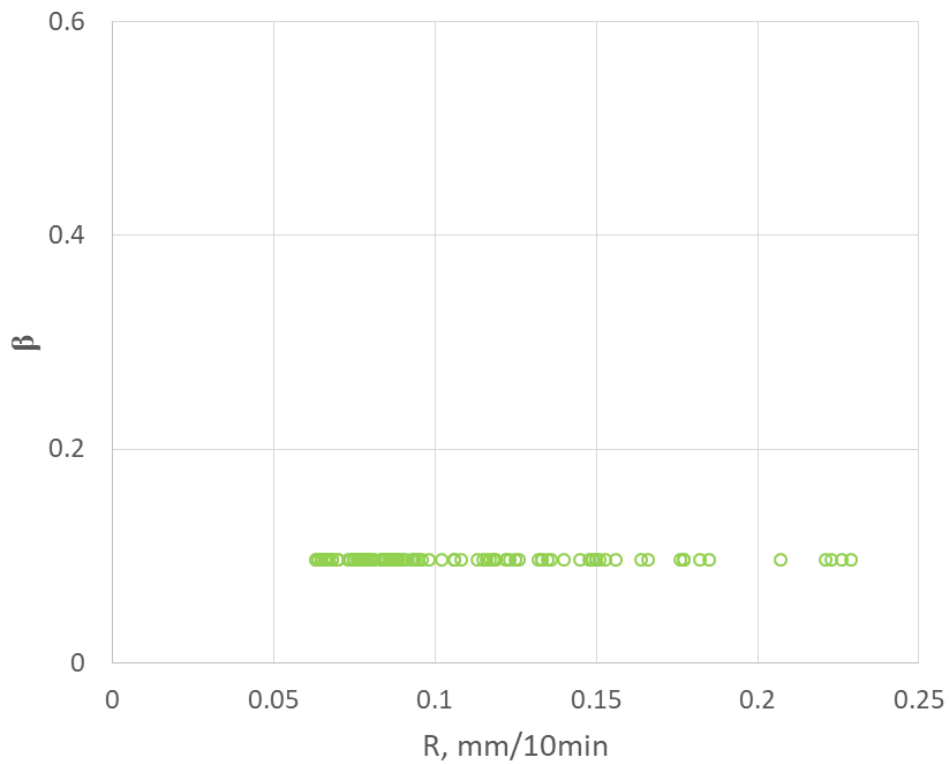


Figure 7.19 Plot of log-Poisson parameter $\beta = 0.01$ constant, versus mean rainfall rate R over $256 \times 256 \text{ km}^2$ for all selected radar sequences

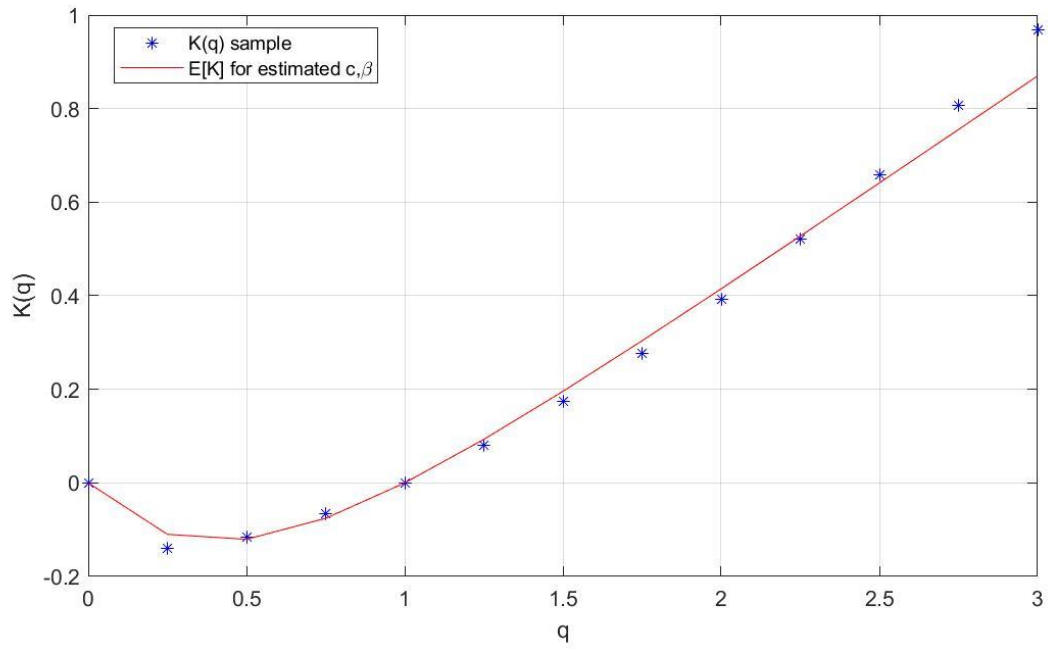


Figure 7.20 Empirical multifractal scaling function $K(q)$ for 320-min aggregated radar sequence together with fitted theoretical $K(q)$ function model for estimated c and fixed β parameter. The rainfall event started on 23.07.2015 at 1:20 AM.

7.4.2. Multifractal modelling of precipitation field

To generate the synthetic precipitation fields in space-time domain, STRAIN was applied. The time domain was rescaled using the constant advection velocity $U=48$ km·h⁻¹.

A set of 115 synthetic precipitation structures was generated using c and β parameters derived from observed rainfall events. The spatial and time dimensions of the synthetic rainfall structures were the same as those used in the previous analysis in chapter 7.4.1, i.e. 256 x 256 km and 320-min. The cascade generator based on log-Poisson distribution parameters was used to generate rain rates on the same field size and the same duration of time as for analysed radar sequences, based on the set of derived log-Poisson parameters. The number of the cascade levels was adjusted to obtain the native spatial resolution of radar scans – 1x1 km – to enable the comparison between the properties of the observed and synthetically generated rainfall structures. Also, the implementation of dressing process in the cascade realization was tested.

The idea of the dressing process is illustrated in figure 7.21. On the left side the construction of a “bare” cascade is shown, on the right side – the “dressed” one. The realisation on each level of dressed cascade is a result of spatial averaging of the cascade developed over the full range, i.e. $\lambda = 2^7$, which is presented in the bottom of the figure to the same scale as located on the left for “bare” realisation (Lovejoy and Schertzer, 2013). The differences between “bare” and “dressed” cascade process were described by Schertzer and Lovejoy (1991) – the first is a process with a cut-off of small-scale interactions, the second one restores them. For both studied cases, with and without dressing, the spatial and time resolutions obtained at each cascade level are presented in figure 7.22 and 7.23 respectively.

This research introduces only one more level (hidden layer) during the disaggregation with dressing due to a computing limitation for assumed time and space resolutions. The handling of the 3-dimensional matrix structures necessary for 3-D cascades models exceeding 9 levels was impossible in MATLAB due to RAM memory shortage on the accessible workstation.

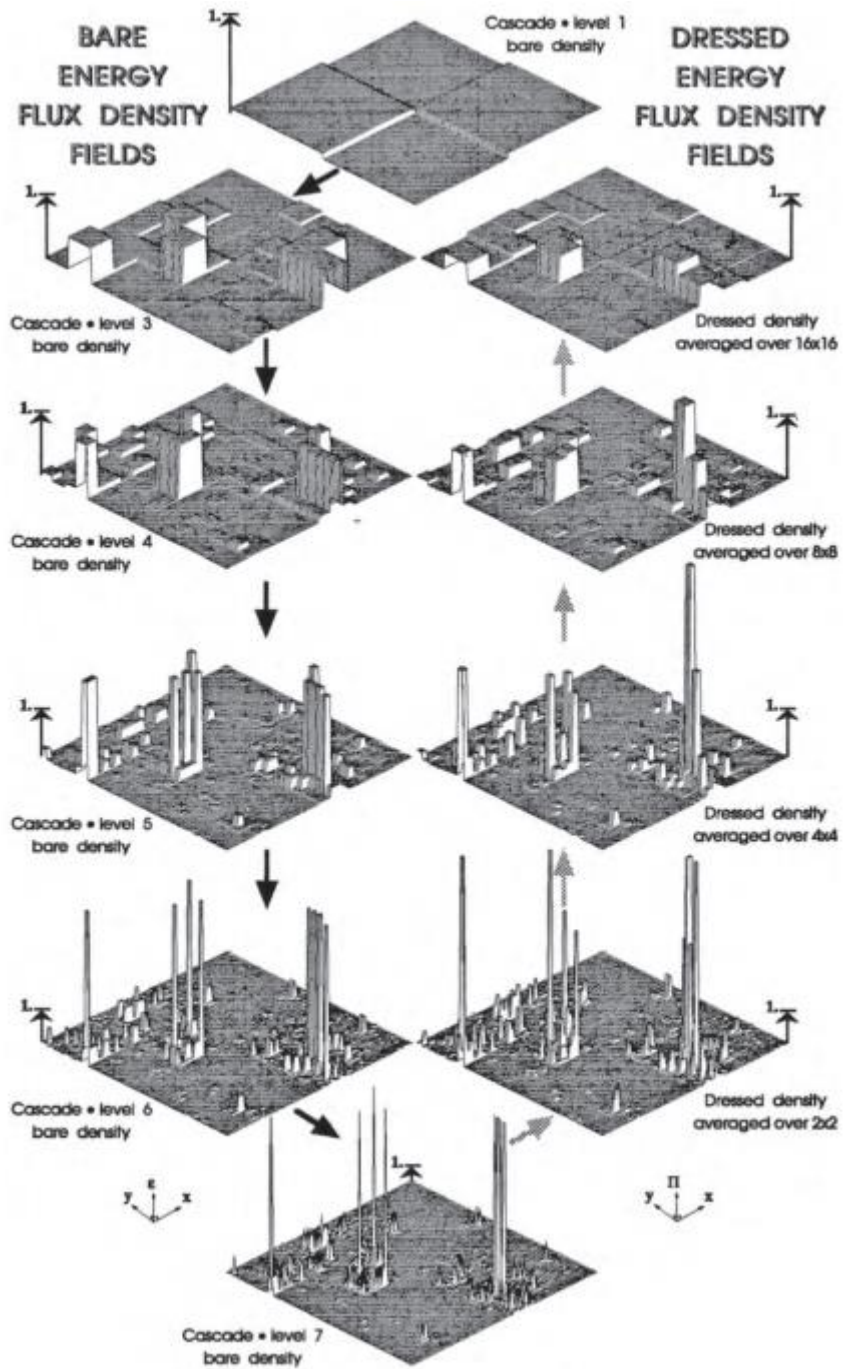
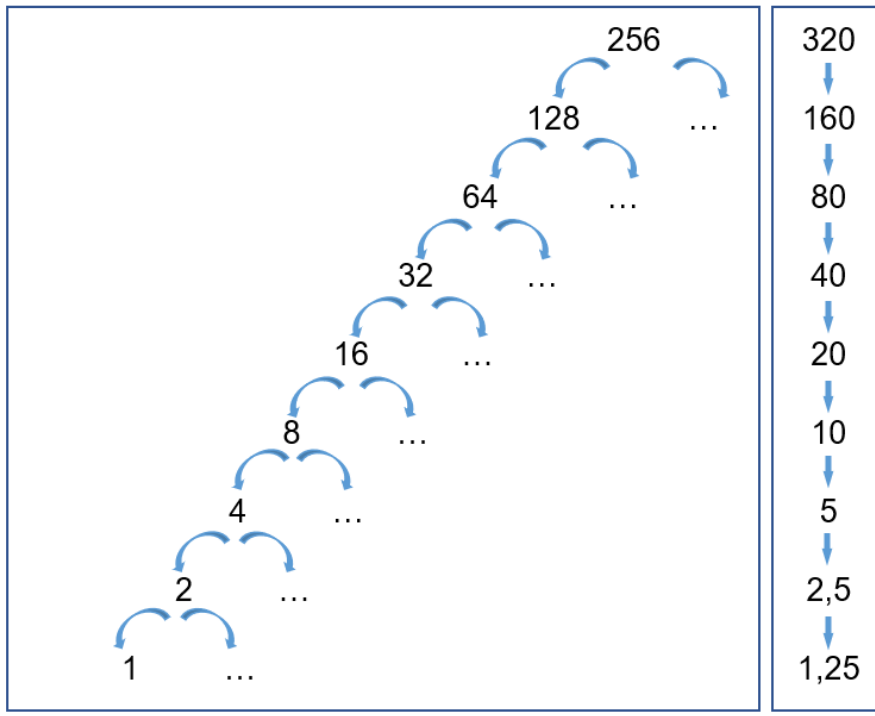


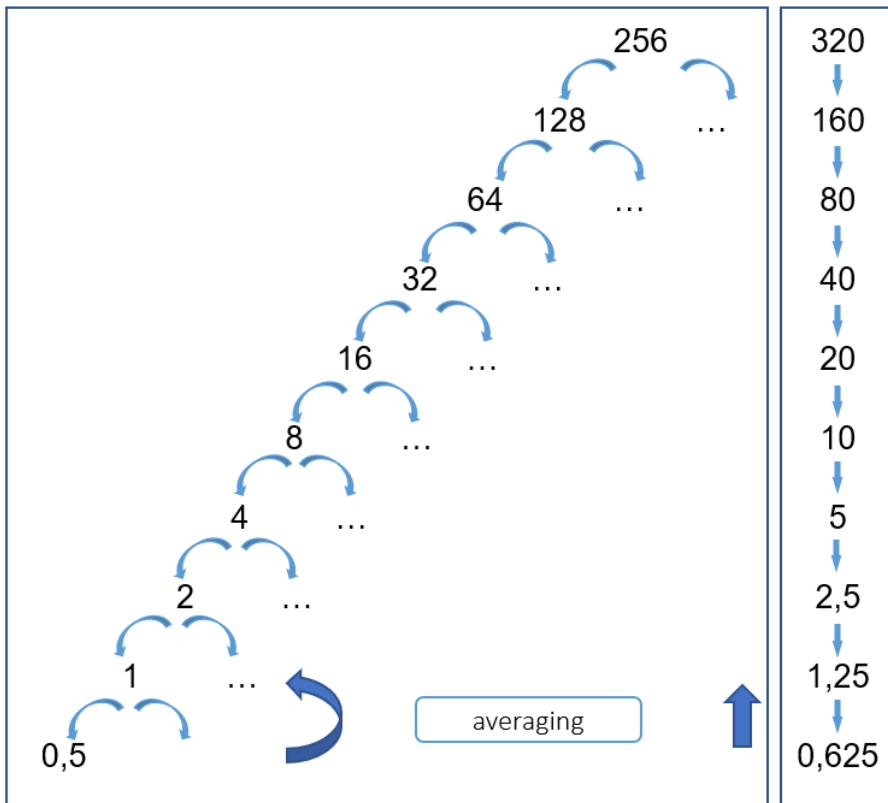
Figure 7.21. The concept of dressing process: on the left side – the step-by-step construction of a (“bare”), on the right side - “dressed” cascade. Reproduced from Lovejoy and Schertzer, 2013



Space scales λ , km

Time scales τ , min

Figure 7.22 Space and time scales of the random cascade without dressing process



Space scales λ , km

Time scales τ , min

Figure 7.23 Space and time scales of the random cascade with dressing process

This part of the chapter analyses the ability of random cascade to reproduce the properties of observed rainfall events. The comparison between realisations of random cascade without and with dressing process is also performed.

At first, the comparison of cCDFs and semivariograms obtained from the observed and synthetic rainfall structures is carried out.

In figure 7.24 and 7.25 cCDFs for 115 synthetically generated rainfall events using cascade without and with dressing process are presented respectively. The rain rate values for 115 synthetically generated rainfall events are close to those observed for selected radar sequences. However, the cCDF graduality is evidently visible in figure 7.24 – obtained for “bare” cascades realisations. The dressing process allows to preserve smoother characteristics of the cCDF – i.e. rain rate values are more diversified (fig. 7.25). The dressing process encloses the shapes of cCDFs to those characteristic for rainfall events observed in nature (figure 7.10). Dressing has also a pronounced effect on most extreme rain rates occurrences considered as singularities in multifractal theory. The rain rate threshold of 30 mm/10 min was exceeded by “cells” in 15 events in case of the set of observed rainfall structures, whereas in the set of those generated using bare cascade only in 1 event and in the set obtained from dressed cascade generator only 3 events.

It can only be speculated that the introduction of more than one hidden cascade layer might have resulted in smoother and more continuous cCDF shapes obtained from synthetically generated rainfall events and higher diversification of rain rate values because the variability, observed in smaller scales might have been preserved, despite averaging.

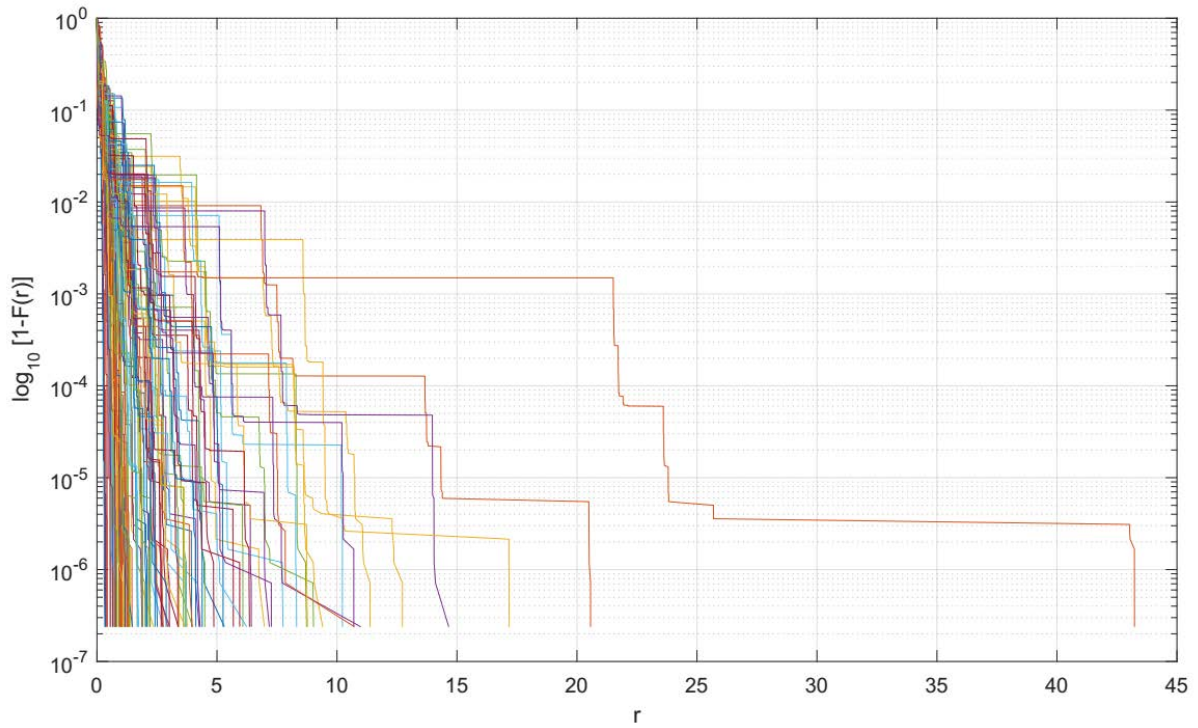


Figure 7.24 Complementary cumulative distribution function (cCDF) of rain rate r (in mm/10 min) for 115 synthetically generated 320-minute rainfall events on the area 256 x 256 km without dressing

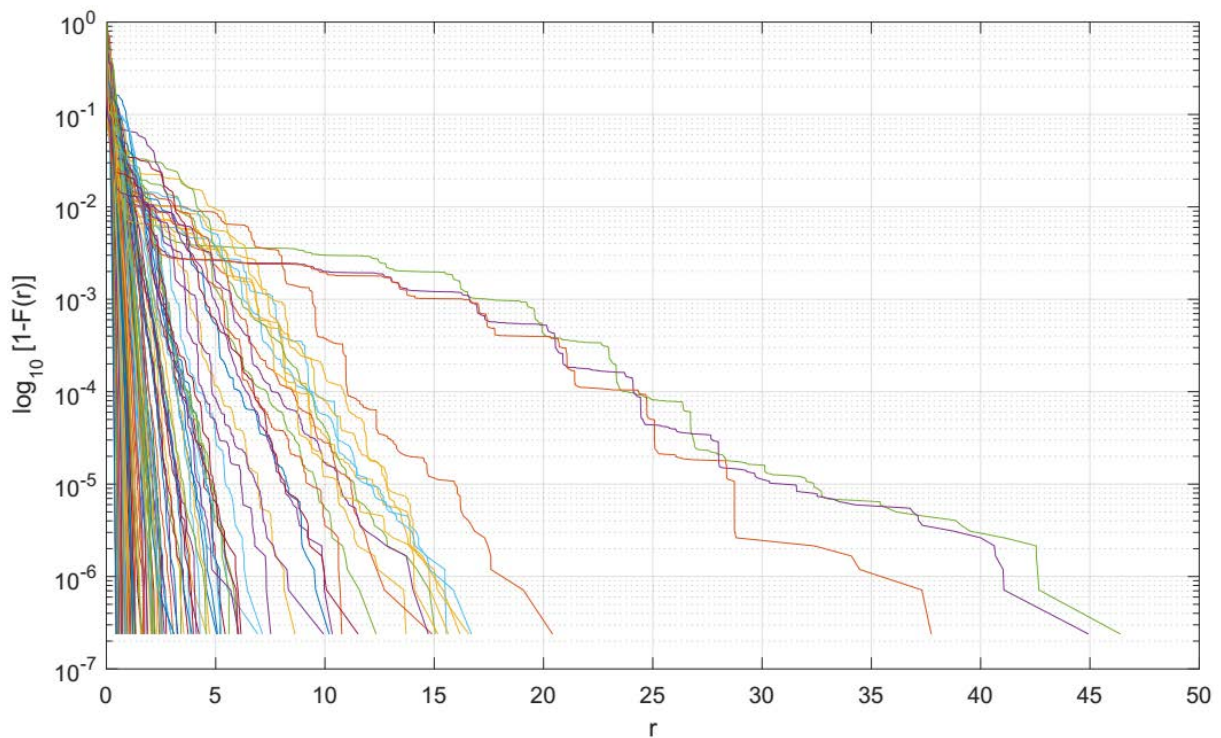


Figure 7.25 Complementary cumulative distribution function (cCDF) of rain rate r (in mm/10 min) for 115 synthetically generated 320-minute rainfall events on the area 256 x 256 km using cascade with dressing process

In 7.26 and 7.27 the sets of semivariograms in *X*-direction and *Y*-direction respectively are presented. The sets are derived for 115 synthetic rainfall events generated using cascades without dressing process, on the area 256 x 256 km and for a duration of 320 min. The next two figures (7.28 and 7.29) show the similar sets of semivariograms in *X*-direction and *Y*-direction, but for 115 synthetically rainfall events generated with use of 3-D cascade with dressing. The comparison of these four figures (7.26-7.29) with the sets of original semivariograms describing the spatial variability of precipitation fields observed in nature (figures 7.11 in *X*-direction and 7.12 in *Y*-direction) was carried out. The detailed shapes of semivariograms are not directly comparable, hence the averaged semivariograms were calculated. However, in general, the ensembles of semivariograms obtained from synthetic rainfall structures looks similar to ensembles obtained for observed precipitations.

The averaged semivariograms (μ) in *X*-direction and *Y*-direction derived for synthetically generated precipitation fields (256 x 256 km) using cascades without dressing process are presented in figure 7.30 and the average semivariograms for generated precipitation fields using cascades with dressing process in figure 7.31. They are compared with averaged semivariograms obtained for analysed radar sequences of the same spatial range (figure 7.13).

The averaged semivariograms of precipitation fields generated using dressed cascades are closer to those derived from observed values. Spatial variability in those structures, generated using bare cascade is higher than in empirical ones.

As a result of synthetic rainfall structure generation, the average semivariograms are not ideally smooth and their course at some characteristic distance points is distinctly changing in slope. This phenomenon is slightly less visible in the case of dressed cascades. The occurrence of characteristic distance points on semivariogram plots is related with spatial dimensions of the cascades presented in figures 7.22 and 7.23. Obviously, the averaged semivariograms derived for observed rainfall structures are smooth (fig. 7.13). Regardless of this, the values and shapes of mean semivariograms and their standard of deviation ranges for synthetic rainfall events, generated both by bare or dressed cascades, are close to those obtained for the selected radar sequences.

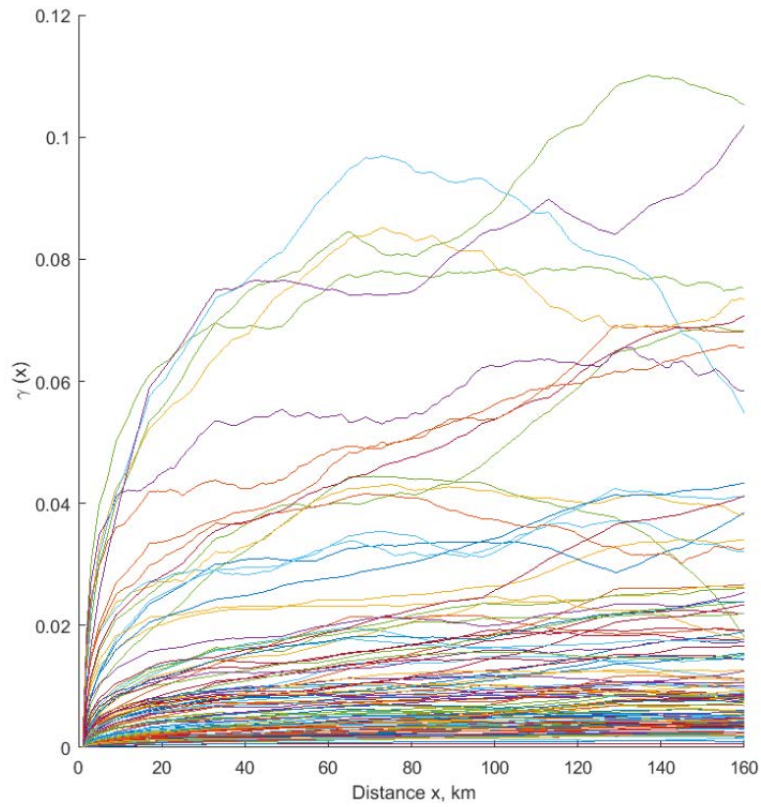


Figure 7.26 Set of semivariograms in X-direction for 115 synthetically generated using cascade without dressing process 320-minute rainfall events over the area 256 x 256 km

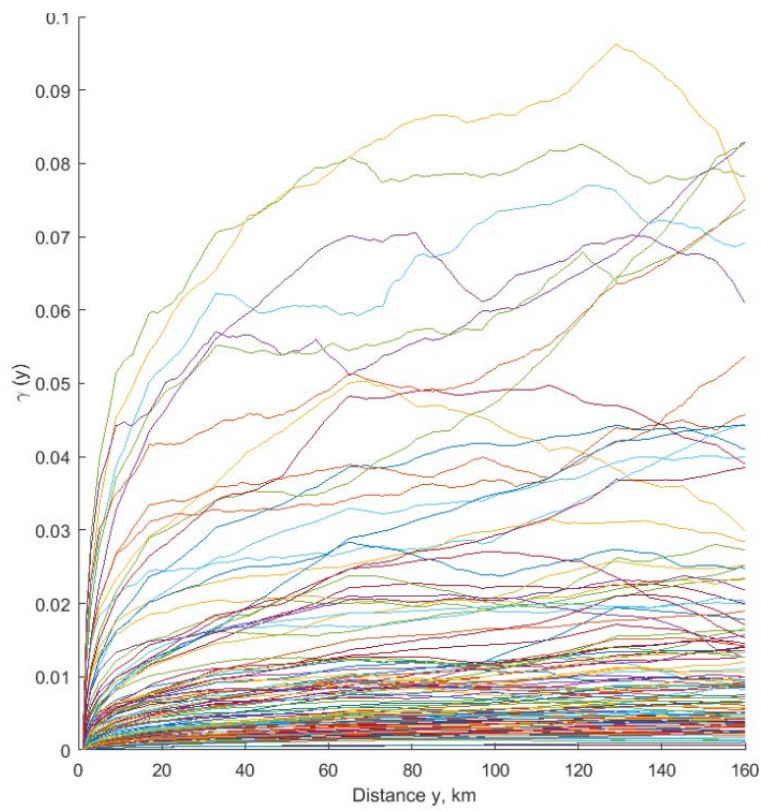


Figure 7.27 Set of semivariograms in Y-direction for 115 synthetically generated using cascade without dressing process 320-minute rainfall events over the area 256 x 256 km

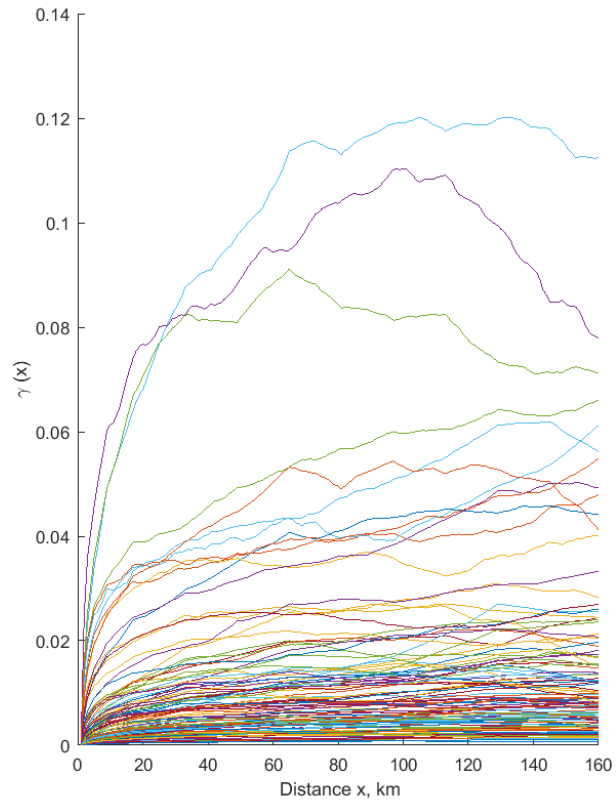


Figure 7.28 Set of semivariograms in X-direction for 115 synthetically generated using cascade with dressing process 320-minute rainfall events over the area 256 x 256 km

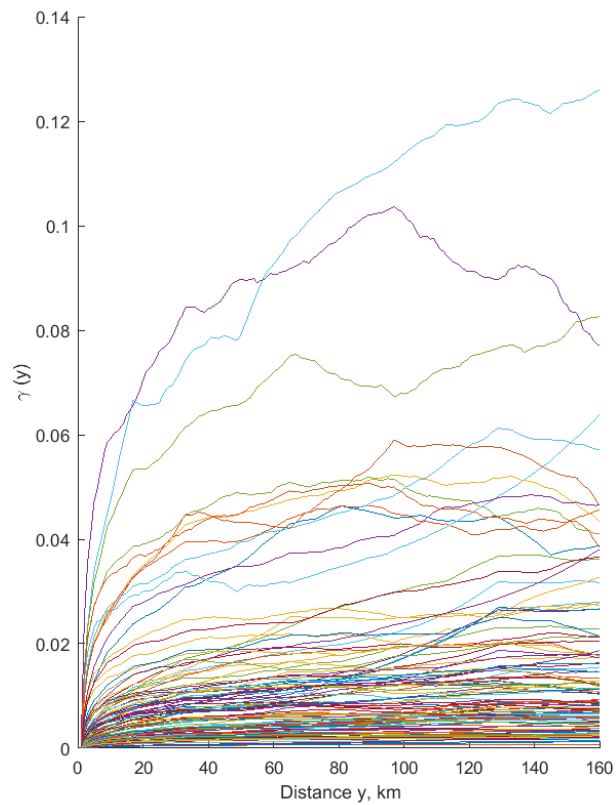


Figure 7.29 Set of semivariograms in Y-direction for 115 synthetically generated using cascade with dressing process 320-minute rainfall events over the area 256 x 256 km

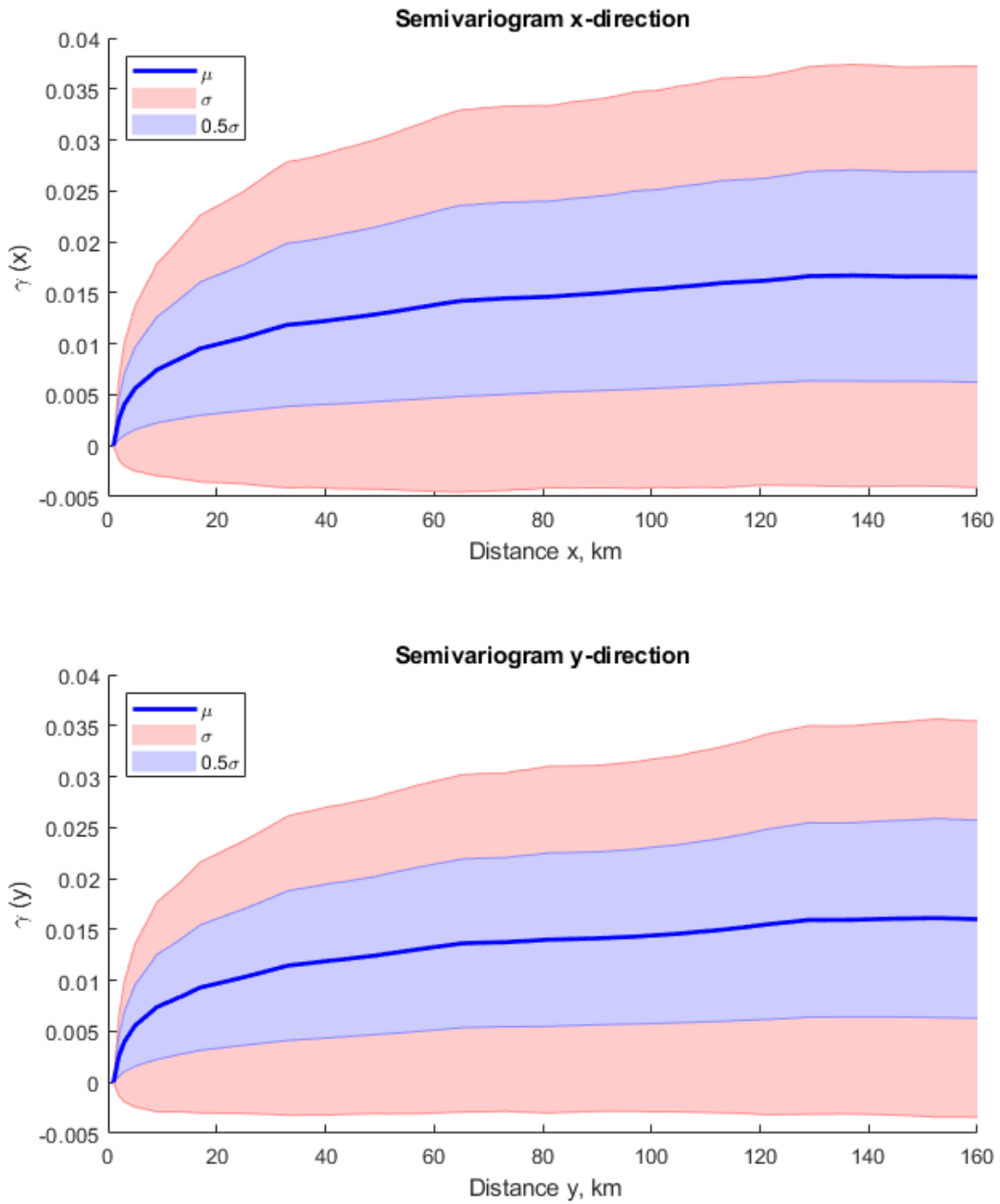


Figure 7.30 The averaged semivariograms (μ) in X-direction (upper panel) and Y-direction (lower panel) derived based on set of 115 semivariograms for synthetically generated rainfalls (using cascade with dressing process) distributed over the area 256 x 256 km. The standard deviation ranges: from 0 to 0.5 σ (0.5σ) and from 0.5 σ to σ (σ) are additionally plotted

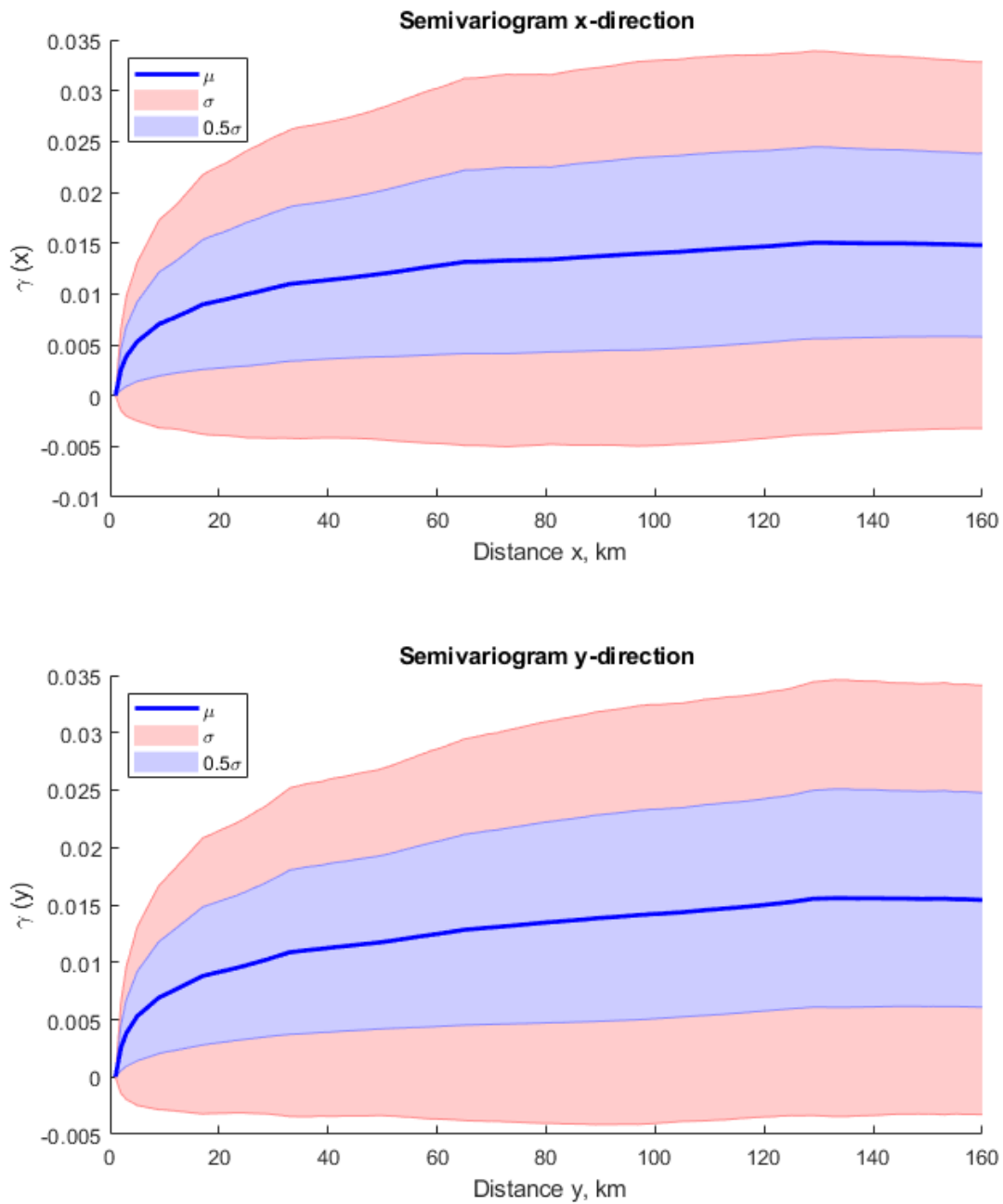


Figure 7.31 The averaged semivariograms (μ) in X-direction (upper panel) and Y-direction (lower panel) derived based on set of 115 semivariograms for synthetically generated rainfalls (using cascade with dressing process) distributed over the area 256 x 256 km. The standard deviation ranges: from 0 to 0.5 σ (0.5σ) and from 0.5 σ to σ (σ) are additionally plotted

7.5. Conclusions

The following conclusions from the parametrization of the SRTAIN model and its performance evaluation for precipitation field in Central Poland are as follows:

1. Overall advection velocity U , which introduction allows to bind the space and time dimension of analysed precipitation structures and to assume rainfall event as an isotropic process in the space-time domain is estimated to be equal to $U = 48 \text{ km} \cdot \text{h}^{-1}$.
2. Scaling law is held at the range of scales: from 8 km to 256 km in space and from 10 min to 320 min in time. Also, the overall shape of $K(q)$ function obtained for every analysed radar sequence is very close to a theoretical model of multifractal moments scaling exponent function.
3. The estimated values of log-Poisson distribution parameters: c and β are strongly variable and not related to the mean rain rate over the spatial domain of 256x256 km. Their values vary in range from 0.192 to 1.459 and from 0.007 to 0.498 respectively. The c and β values for Warsaw precipitation field are more diversified and usually much smaller than those, –reported by Deidda (2000) for eastern Atlantic coast of Africa. The averaging of β parameter ($\beta = 0.097$) and imposing it as constant influences negligible on the shape of theoretical multifractal scaling functions $K(q)$.
4. The Space-Time Rainfall (STRAIN) model's ability to generate rainfall events, which statistical properties are close to those observed for Warsaw precipitation field, is confirmed.
5. Three-dimensional random cascade based on log-Poisson distribution parameters is found as a proper tool to downscale precipitation structures.
6. The introduction of dressing process into the random cascade generator causes refinement of its ability to reproduce properties of the natural structure of precipitation. Studies on implementation of generators with more than one hidden layer are recommended in the future.
7. The main disadvantage of STRAIN model is that cascade generator for this discrete 3-D model implicates occurrence of step-like structures (visible on mean semivariograms) strictly connected with the dimension of each cascade level.

8. Summary and final conclusions

The weather radar data from the POLRAD network is used to conduct analysis and modelling of the urban precipitation field over Warsaw and its surrounding area in both the space and time dimension.

To verify POLRAD radar data applicability to space-time precipitation analysis and modelling over Warsaw area, preliminary studies were conducted. Primarily, the radar data calibration parameters were confirmed based on independent precipitation data sources. Sets of radar reflectivity values Z and rainfall rain rates R , derived from raindrop size distributions recorded with high temporal resolution of 10 s by laser disdrometer installed in Warsaw were used for fitting the Z - R function. The estimates of a and b parameters of Z - R relationships obtained based on disdrometer data, especially for the summer half-year, were close to values postulated by Marshall and Palmer (1948) for liquid rain precipitation and were similar to these applied in POLRAD ($a=200$ and $b=1.6$).

Secondly, the comparisons between local urban rain gauges network and weather radar measurements were conducted. Despite the differences in both rainfall measurement techniques, the similarity between the rainfall time series from gauges and coincidentally in space radar pixels was noticeable for each of the 25 analysed locations. However, the maximum rain rates derived from radar observations for pixels of 1x1km were lower than those recorded by gauges with the 200 cm² orifice.

The above observations confirmed the applicability of POLRAD radar data for further studies on precipitation field.

The analysis and modelling of the Warsaw precipitation field were conducted using the Space-Time Rainfall (STRAIN) model introduced by Deidda (2000). In this model, the multifractal formalism is applied to determine the statistical properties of precipitation structures and to generate synthetic rainfall events using three-dimensional random cascades based on parameters of log-Poisson distribution. To implement the STRAIN model, the Taylor hypothesis was verified for precipitation fields over Central Poland, and the overall advection velocity was estimated. The parameters of the log-Poisson distribution were derived and analysed for a total number of 115 selected rainfall events. Based on parametrization of 3-D cascade models, it was possible to disaggregate total rainfall depths accumulated for 320 min over the area of 256x256 km into the final resolution of 1x1 km in space and 1.25 min in time. The developed models were run in

two variants, with and without dressing. Finally, the statistical properties of original rainfall structures recorded by weather radar were compared to statistical properties of synthetically generated rainfall fields.

Based on above mentioned research, the following conclusions were formulated:

1. The hypothesis of space-time rainfall scaling is confirmed. Calculated empirical $K(q)$ functions closely follow the pattern of the theoretical $K(q)$ function model for an ideal multifractal process. Thus, space-time rainfall structures over Central Poland could be considered as multifractals, and their modelling using multiplicative cascade models is justified.
2. Synthetically generated rainfall events using the Space-Time Rainfall (STRAIN) model hold statistical properties close to those found in the original radar scans of the precipitation field. Hence, three-dimensional random cascade is an adequate tool for disaggregation of some assumed precipitation depths over 320 min above space domain of 256x256 km into space-time structures of final resolution of 1km in space and 1.25 min in time. Generated by the adopted to local conditions, STRAIN model rainfall scenarios can be used as precipitation inputs for urban hydrology models in Warsaw.
3. The STRAIN model can be adjusted by three-parameters: the overall advection velocity U and the log-Poisson parameters c and β .

Based on the analysis of the correlation of rainfall rates in space and time for the most severe rainfall events exceeding 2 mm of mean depth on the whole area for 320 minutes, the overall advection velocity U value for the Central Poland precipitation field centred over Warsaw is estimated to be equal to 48 km h⁻¹.

The values of parameters c and β obtained from the analysed set of 115 rainfall structures are strongly variable. The magnitude of c and β parameters in the set of 115 rainfall events from Poland is much smaller in comparison to the magnitude of similar parameters derived by Deidda (2000) for the eastern Atlantic coast of Africa. Most probably, these differences can be explained by the varying dynamics of precipitation processes over these remote areas.

The averaging of the β parameter and imposing its constant value during $K(q)$ functions fitting does not significantly affect the shape of multifractal scaling functions.

The values of log-Poisson parameters c and β derived for 115 selected rainfall events do not display a large-scale forcing relationship with mean rainfall rate. Additional research in this field is necessary. As a further step for STRAIN model tuning, the estimation of overall advection velocity U for each single rainfall event should be considered. Next, the advection velocity U should be assumed as a taxonomic parameter for rainfall events. For each subset of rainfall events of the same advection velocity, log-Poisson parameters should be recalculated and its relation to mean rain rate should be investigated.

4. The dressing process implemented into the STRAIN model random cascade generator allows to obtain a better reproduction of properties of natural structures of precipitation. Dressing process is doubly beneficial. Firstly, rainfall rates are dressed in singularities occurring in smaller space and time scale. Therefore, the probability of occurrence of maximum rainfall rates in synthetic structures generated with dressing increases. Secondly, dressed rainfall rates are more variable. It allows to, at least partly, mask the discrete character of STRAIN cascade model with regard to rain rates values probability occurrence in the whole set of generated values (smoother CDFs reproduction) and rain rate values distribution over the modelled space domain (smoother semivariograms reproduction). The further studies on generators with more than one hidden layer are suggested. It is expected that the introduction of additional hidden layers should improve the generator ability of reproduction of natural rainfalls properties.

References

- Allen, R.J. and DeGaetano, A.T. (2005) Considerations for the use of radar-derived precipitation estimates in determining return intervals for extreme areal precipitation amounts. *Journal of Hydrology* 315 (1–4), 203–219.
- Alves de Souza, B., da Silva Rocha Paz, I., Ichiba, A., Willinger, B., Gires, A., Amorim J. C. C., de Miranda Reis M., Tisserand B., Tchiguirinskaia I. and Schertzer D. (2018) Multi-hydro hydrological modelling of a complex peri-urban catchment with storage basins comparing C-band and X-band radar rainfall data. *Hydrological Sciences Journal* 63(11), 1619-1635.
- Battan, L. J. (1973) *Radar observation of the atmosphere*. University of Chicago Press.
- Benzi, R., Paladin, G., Parisi, G. and Vulpiani, A. (1984) On the multifractal nature of fully developed turbulence and chaotic systems. *Journal of Physics A Mathematical and General* 17, 3521-3531.
- Berne, A., Delrieu, G., Creutin, J.-B. and Obled, C. (2004) Temporal and spatial resolution of rainfall measurements required for urban hydrology. *Journal of Hydrology* 299, 166–179
- Berg P., Norin L. and Olsson, J. (2015) Creation of a high resolution precipitation data set by merging gridded gauge data and radar observations for Sweden. *Journal of Hydrology* 541, 6–13.
- Borup, M., Grum, M., Linde, J. J. and Mikkelsen, P. S. (2009) Application of high resolution X-band radar data for urban runoff modelling: constant vs. dynamic calibration. In: *8th International Workshop on Precipitation in Urban Areas Rainfall in the Urban Context: Forecasting, Risk and Climate Change*, St. Moritz, Switzerland, 10-13 December, 27-31.
- Brock, F. V. and Richardson, S. J. (2001) *Meteorological Measurement Systems*. Oxford University Press.
- Campisano, A., Cabot Ple, J., Muschalla, D., Pleau, M. and Vanrolleghem, P. A. (2013) Potential and limitations of modern equipment for real time control of urban wastewater systems. *Urban Water Journal* 10(5), 300-311.
- Ciach, G.J., Krajewski, W.F. and Villarini, G. (2007) Product-error-driven uncertainty model for probabilistic quantitative precipitation estimation with NEXRAD data. *Journal of Hydrometeorology* 8, 1325-1347.
- Cunha, L. K., Smith, J. A., Baeck, M., L., Krajewski, W. F. (2013) An early performance evaluation of the NEXRAD dual-Polarization radar rainfall estimates for urban flood applications. *Weather and Forecasting* 28, 1478-1479.
- Deidda, R., Benzi, R. and Siccardi, R. (1999a) Multifractal modeling of anomalous scaling laws in rainfall. *Water Resources Research* 35(6), 1853–1868.
- Deidda, R. (1999b) Multifractal analysis and simulation of rainfall fields in space. *Physics and Chemistry of the Earth* 24(1-2), 73-78,
- Deidda, R. (2000) Rainfall downscaling in a space-time multifractal framework. *Water Resources Research* 36(7), 1779– 1794.
- Deidda, R., Badas, M. G. and Piga, E. (2004) Space-time scaling in high-intensity Tropical Ocean Global Atmosphere Coupled Ocean-Atmosphere Response Experiment (TOGA-COARE) storms. *Water Resources Research* 40, W02506
- Dixon, M., Li, Z., Lean, H., Roberts, N. and Bolland, S. (2009) Impact of data assimilation on forecasting convection over the United Kingdom using a high-resolution version of the Met Office unified model. *Monthly Weather Review* 137, 1562–1584.

- Dmochowska, H. (editor) (2015) *Statistical Yearbook of the Republic of Poland*. Warsaw: Statistics in Poland.
- Douglas, R. H. (1990) The Stormy Weather Group (Canada). In: Atlas, D. (editor) *Radar in Meteorology*. Boston: American Meteorological Society. 61-68.
- Dotzek N. and Beheng, K. D. (2001) The influence of deep convective motions on the variability of Z–R relations. *Atmospheric Research* 59–60, 15–39.
- Dubrulle, B. (1994) Intermittency in fully developed turbulence: Log-Poisson statistics and generalized scale-covariance. *Physical Review Letters* 73, 959–962
- Dzugaj, D. (2017) *Intermittency, scales, and extremes in urban precipitation*. PhD Thesis. Wrocław University of Science and Technology <https://www.dbc.wroc.pl/dlibra/docmetadata?id=37077&from=pubindex&dirids=61&lp=70> Accessed 15 September 2018.
- Ebtehaj, M. and Foufoula-Georgiou, E. (2010) Orographic signature on multiscale statistics of extreme rainfall: A storm-scale study. *Journal of Geophysical Research Atmospheres* 115(23), D23112
- Einfalt, T., Krejci V. and Schilling, W. (1998) Rainfall Data in Urban Hydrology. In Marsalek, J., Maksimovic, C., Zeman, E. and Price, R. (editors) *Hydroinformatics Tools for Planning, Design, Operation and Rehabilitation of Sewer Systems. NATO ASI Series (Series 2: Environment), vol 44*. Dordrecht: Springer. 129-168.
- Einfalt T., Arnbjerg-Nielsen K., Golz C., Jensen N.-E., Quirnbach M., Vaes G. and Vieux B. (2004) Towards a roadmap for use of radar rainfall data in urban drainage. *Journal of Hydrology* 299, 186–202
- Einfalt, T., Szturc, J. and Ośródkka, K. (2010) The quality index for radar precipitation data: a tower of Babel?. *Atmospheric Science Letters* 11(2), 139-144
- Eaves, J. and Reedy, E. (1987) *Principles of Modern Radar*. Springer.
- Fabry, F., Bellon, A., Duncan, M. R. and Austin, G. L. (1994) High resolution rainfall measurements by radar for very small basins: the sampling problem reexamined. *Journal of Hydrology* 161, 415–428.
- Falconer K. J. (1990) *Fractal Geometry: Mathematical Foundations and Applications*. New York: Wiley.
- Feder J. (1988) *Fractals*. New York: Plenum Press.
- Ferraris, L., Gabellani, S., Rebora, N. and Provenzale, A. (2003) A comparison of stochastic models for spatial rainfall downscaling. *Water Resources Research* 39(12), SWC121-SWC1216.
- Fornasiero, A., Alberoni, P. P., Amorati, R., Ferraris, L. and Taramasso, A. C. (2005) Effects of propagation conditions on radar beam-ground interaction: impact on data quality. *Advances in Geoscience* 2, 201–208.
- French, M. M., Burgess, D .W., Mansell, E. R., and Wicker, L. J. (2015) Bulk hook echo raindrop sizes retrieved using mobile, polarimetric Doppler radar observations. *Journal of Applied Meteorology and Climatology* 54, 423–450.
- Fuchs, L. and Beeneken, T. (2005) Development and implementation of a real time control strategy for the sewer system of the city of Vienna. *Water Science & Technology* 52, 187–194.
- Georgakakos, K. P., Carsteanu, A. A., Sturdevant, P. L. and Cramer, J. A. (1994) Observation and analysis of Midwestern rain rates. *Journal of Applied Meteorology* 33(12), 1433-1444.
- Gires, A., Onof C., Maksimovic C., Schertzer D., Tehiguirinskaia I. and Simoes, N. (2012) Quantifying the impact of small scale unmeasured rainfall variability on urban hydrology through multifractal downscaling: a case study. *Journal of Hydrology* 442–443, 117–128.
- Gires, A., Tehiguirinskaia, I., Schertzer D. and Lovejoy, S. (2013) Multifractal analysis of a semi-distributed urban hydrological model. *Urban Water Journal* 10(3), 195-208

- Gires, A., Tchiguirinskaia, I., Schertzer D., Schellart, A., Berne, A. and Lovejoy, S. (2014) Influence of small scale rainfall variability on standard comparison tools between radar and rain gauge data. *Atmospheric Research* 138, 125-138.
- Gires, A., Giangola-Murzyn, A., Abbes, J., Tchiguirinskaia, I., Schertzer, D. and Lovejoy, S. (2015) Impacts of small scale rainfall variability in urban areas: a case study with 1D and 1D/2D hydrological models in a multifractal framework. *Urban Water Journal* 12(8), 607-617
- Goudenhoofdt, E. and Delobbe, L. (2009) Evaluation of radar-gauge merging methods for quantitative precipitation estimates. *Hydrology and Earth System Sciences* 13, 195–203.
- Gupta, V. K. and Waymire, E. C. (1993) A statistical analysis of mesoscale rainfall as a random cascade. *Journal of Applied Meteorology* 32(2), 251-267.
- Harris, D., Menabde, M., Seed, A. and Austin G. (1996) Multifractal characterization of rain fields with a strong orographic influence. *Journal of Geophysical Research* 101(D21), 26405-26414.
- Harrison, D. L. (2007) *Questionnaire report. OPERA III working document WP 1.2a* (on OPERA FTP server). Cited in: Einfalt, T., Szturc, J. and Ósródka, K. (2010) The quality index for radar precipitation data: a tower of Babel?. *Atmospheric Science Letters* 11(2): 140.
- Helmert, K., Hassler, B. and Seltmann, J. (2012) An operational tool to quality control 2D radar reflectivity data for assimilation in COSMO-DE. *International Journal of Remote Sensing* 33(11), 3456-3471.
- Heymsfield, G. M., Tian, L., Li, L., McLinden, M. and Cervantes J. (2013) Airborne radar observations of severe hailstorms Implications for future spaceborne radar. *Journal of Applied Meteorology and Climatology* 52, 1851–1867.
- Hubert, P., Tessier, Y., Lovejoy, S., Schertzer, D., Schmitt, F., Ladoy, P., Carbonnel, J. P., Violette, S. and Desuroisne I. (1993) Multifractals and extreme rainfall events. *Geophysical Research Letters* 20(10), 931-934.
- International Organization for Standardisation (2017) *ISO 19926 Meteorology – Ground-based remote sensing of precipitation weather radar*.
- Jakubiak B., Licznar P. and Malinowski Sz. (2014) Rainfall estimates from radar vs. raingauge measurements. Warsaw case study. *Environment Protection Engineering* 40(2), 162-170.
- Jessen, M., Einfalt, T., Stoffer, A. and Mehlig, B. (2005) Analysis of heavy rainfall events in North Rhine–Westphalia with radar and raingauge data. *Atmospheric Research* 77, 337–346.
- Kalesse, H., W. Szyrmer, S. Kneifel, P. Kollias, and Luke, E. (2016) Fingerprints of a riming event on cloud radar: Doppler spectra observations and modeling. *Atmospheric Chemistry and Physics* 16, 2997–3012.
- Kang, B. and Ramirez, J. A. (2010) A coupled stochastic space-time intermittent random cascade model for rainfall downscaling. *Water Resources Research* 46(10), W10534.
- Kendon, E., Roberts, N. and Fowler, H. (2014) Heavier summer downpours with climate change revealed by weather forecast resolution model. *Nature Climate Change* 4, 1–7.
- Kneifel, S., von Lerber A., Tiira J., Moisseev D., Kollias P. and Leinonen J. (2015) Observed relations between snowfall microphysics and triple-frequency radar measurements. *Journal of Geophysical Research-Atmospheres* 120, 6034–6055.
- Kozłowska, Z. (editor) (2014) *Statistical Yearbook of Warsaw*. Warsaw: Statistical Office in Warsaw.
- Kozłowska, Z. (editor) (2015) *Statistical Yearbook of Warsaw*. Warsaw: Statistical Office in Warsaw.
- Kozłowska, Z. (editor) (2018) *Statistical Yearbook of Warsaw*. Warsaw: Statistical Office in Warsaw.

- Krajewski, W. F., Ciach, G. J., Habib, E. (2003) An analysis of small-scale rainfall variability in different climatic regimes. *Hydrological Sciences Journal* 48(2), 151–162.
- Kuettner, J. P., (1974) General description and central program of GATE. *Bulletin of the American Meteorological Society*, 55, 712-719.
- Kumar, P. and Foufoula-Georgiou, E. (1993a) A multicomponent decomposition of spatial rainfall fields, 1, Segregation of large-and small scale features using wavelet transform. *Water Resources Research* 29(8), 2515-2532.
- Kumar, P. and Foufoula-Georgiou, E. (1993b) A multicomponent decomposition of spatial rainfall fields, 2, Self-similarity in fluctuations. *Water Resources Research* 29(8), 2533-2544.
- Kumjian, M. R. (2018) Weather Radars. In Andronache C. (editor) *Remote Sensing of Clouds and Precipitation, vol 44*. Cham: Springer. 15-63.
- Lee, L. and Zawadzki, I. (2005) Variability of Drop Size Distributions: Time-Scale Dependence of the Variability and Its Effects on Rain Estimation. *Journal of Applied Meteorology* 44, 241-255.
- Leijnse, H., Uijlenhoet, R., van de Beek, C. Z., Overeem, A., Otto, T., Unal, C.M., Dufournet, Y., Russchenberg, H.W., Figueras i Ventura, J., Klein Baltink, H. and Holleman, I. (2010) Precipitation Measurement at CESAR, the Netherlands. *Journal of Hydrometeorology* 11, 1322–1329.
- Licznar, P. (2009) *Generatory syntetycznych szeregów opadowych do modelowania sieci kanalizacji deszczowych i ogólnospławnych*. Wrocław: Wydawnictwo Uniwersytetu Przyrodniczego we Wrocławiu.
- Licznar, P., De Michele, C. and Adamowski, W. (2015) Precipitation variability within an urban monitoring network via microcanonical cascade generators. *Hydrology and Earth System Sciences* 19, 485-506.
- Licznar, P. and Siekanowicz-Grochowina, K. (2015) Wykorzystanie disdrometru laserowego do kalibracji obrazów pochodzących z radarów opadowych na przykładzie Warszawy [Application of laser disdrometer to weather radar image calibration in the example of Warsaw]. *Ochrona Środowiska*, 37(2), 11–16.
- Licznar, P., Krajewski, W. F. (2016) Precipitation type specific radar reflectivity-rain rate relationships for Warsaw, Poland. *Acta Geophysica* 64(5), 1840-1857.
- List, R. (1988) A linear radar reflectivity – rain rate relationship for steady tropical rain. *Journal of the Atmospheric Sciences* 45, 3564–3572.
- Lovejoy, S., Schertzer D. (1990) Multifractals, universality classes, and satellite and radar measurements of cloud and rain fields. *Journal of Geophysical Research: Atmospheres* 95(D3), 2021-2031.
- Lovejoy, S., Schertzer, D. (2013) *The Weather and Climate: Emergent Laws and Multifractal Cascades*. Cambridge University Press.
- Löffler-Mang, M. and Joss, J. (2000) An optical disdrometer for measuring size and velocity of hydrometeors. *Journal of Atmospheric and Oceanic Technology* 17, 130-139.
- Marshall, J. S., Langille, R. C. and Palmer, W. M. (1947) Measurement of rainfall by radar. *Journal of Meteorology* 4, 186–192.
- Marshall, J. S. and Palmer, W. M. (1948) The distribution of raindrops with size. *Journal of Atmospheric Sciences* 5, 165–166.
- Marra, F. and Morin, E. (2015) Use of radar QPE for the derivation of Intensity–Duration–Frequency curves in a range of climatic regimes. *Journal of Hydrology* 531, 427–440.
- Menabde, M., Seed, A., Harris, D. and Austin, G. (1997a) Self-similar random fields and rainfall simulations. *Journal of Geophysical Research: Atmospheres* 102(D12), 13509–13515.

- Menabde, M., Harris, D., Seed, A., Austin, G. and Stow, D. (1997b) Multiscaling properties of rainfall and bounded random cascades. *Water Resources Research* 33(12), 2823-2830.
- Michelson, D. (2006) The Swedish weather radar production chain. *Proceedings of ERAD 2006*, 382–385. <http://crahi.upc.edu/ERAD2006/proceedingsMask/00101.pdf> Accessed 10 September 2018.
- Mishra, K. V., Krajewski, W. F., Goska, R., Ceynar, D., Seo, B.-C., Kruger, A., Niemeier, J. J., Galvez, M. B., Thurai, M., Bringi, V. N., Tolstoy, L., Kucera, P. A., Petersen, W. A., Grazioli, J. and Pazmany, A. L. (2016) Deployment and Performance Analyses of High-Resolution Iowa XPOL Radar System during the NASA IFloodS Campaign. *Journal of Hydrometeorology* 17, 455–479.
- Molnar P. and Burlando P. (2005) Preservation of rainfall properties in stochastic disaggregation by a simple random cascade model. *Atmospheric Research* 77, 137 – 151.
- Moszkowicz, S. and Tuszyńska, I. (2006) *Meteorologia radarowa. Podręcznik użytkownika informacji radarowej IMGW*. Warszawa: Instytut Meteorologii i Gospodarki Wodnej.
- Nemeth, K. and Hahn, J.-M. *OTT Parsivel®- Enhanced precipitation identifier and new generation of present weather sensor by OTT Messtechnik, Germany* <https://www.ott.com/en-uk/products/download/ott-parsivel-white-paper/> Accessed 5 September 2018.
- Nielsen J. E., Thorndahl S. and Rasmussen M. R. (2014) A numerical method to generate high temporal resolution precipitation time series by combining weather radar measurements with a nowcast model. *Atmospheric Research* 138, 1–12.
- Ochoa-Rodriguez, S., Li-Pen Wang , Gires A., Pina, R. D. , Reinoso-Rondinel, R., Bruni, G., Ichiba, A., Gaitan, S., Cristiano, E., van Assel, J., Kroll, S., Murlà-Tuyls, D., Tisserand, B., Schertzer, D., Tchiguirinskaia, I., Onof, C., Willems, P. and ten Veldhuis, M.-C. (2015a) Impact of spatial and temporal resolution of rainfall inputs on urban hydrodynamic modelling outputs: A multi-catchment investigation. *Journal of Hydrology* 531, 389–407.
- Ochoa-Rodriguez, S., Sandford, C., Norman, K., Wang, L., Jewell, S., Akerboom, M., and Onof, C. (2015b) Evaluation of the Met Office super-resolution C-band radar rainfall product over London. In: *AMS 37th Conference on Radar Meteorology*. Norman, US, 14–18 September 2015. http://www.raingain.eu/sites/default/files/susana_superresolution_poster_ams_v2.pdf Accessed 17 September 2018.
- Oke, T. (2006a) *Initial guidance to obtain representative meteorological observations at urban sites, Instruments and Observing Methods*. World Meteorological Organization. WMO/TD- No. 1250; IOM Report- No. 81
- Oke, T. (2006b) Towards better scientific communication in urban climate. *Theoretical and Applied Climatology* 84, 179-190.
- Olson, J. and Niemczynowicz, J. (1996) Multifractal analysis of daily spatial rainfall distributions, *Journal of Hydrology* 187, 29-43.
- Operating instructions Present Weather Sensor OTT Parsivel²*. Document number 70.210.001.B.E 03-1218 OTT Hydromet GmbH <https://www.ott.com/download/operating-instructions-present-weather-sensor-ott-parsivel2-without-screen-heating/> Accessed 12 April 2015
- Ośródka K and Szturc J. (2015) Quality-based generation of weather radar Cartesian products, *Atmospheric Measurement Techniques* 8, 2173–2181.
- Over, T. M. and Gupta, V. K. (1994) Statistical analysis of mesoscale rainfall: Dependence of a random cascade generator on large-scale forcing. *Journal of Applied Meteorology* 33(12), 1526-1542.

- Over, T. M. (1995) *Modeling space-time rainfall at the mesoscale using random cascades* PhD Thesis. University of Colorado https://www.researchgate.net/publication/253120917_Modeling_Space-Time_Rainfall_at_the_Mesoscale_Using_Random_Cascades Accessed 16 September 2018.
- Overeem, A., Buishand, T. A. and Holleman, I. (2009a) Derivation of a 10-Year Radar-Based Climatology of Rainfall. *Journal of Applied Meteorology and Climatology* 48, 1448–1463.
- Overeem, A., Buishand, T. A. and Holleman, I. (2009b) Extreme rainfall analysis and estimation of depth-duration-frequency curves using weather radar. *Water Resources Research* 45, W10424.
- Overeem, A., Buishand, T. A., Holleman, I. and Uijlenhoet, R. (2010) Extreme value modeling of areal rainfall from weather radar, *Water Resources Research* 46, 1–10.
- Pawlak, J., Teisseyre – Sierpińska, M., Badałow, G., Pietrusiewicz, W., Cieszewska, A., Kaliszuk, E., Salwicka, J., Szablowska, K., Szulczewska, B., Wolski, P. and Zantonowicz, K. (2006) *Opracowanie ekofizjograficzne do studium uwarunkowań i kierunków zagospodarowania przestrzennego m. St. Warszawy*, Warszawa: Urząd Miasta Stołecznego Warszawy.
- Paixao, E., Mirza, M. M. Q., Shephard, M. W., Auld, H., Klaassen, J. and Smith, G. (2015) An integrated approach for identifying homogeneous regions of extreme rainfall events and estimating IDF curves in Southern Ontario, Canada: incorporating radar observations. *Journal of Hydrology* 528, 734–750.
- Pazmany, A. L., Mead, J. B., Bluestein H. B., Snyder J. C. and Houser J. B. (2013) A mobile, rapid-scanning X-band polarimetric (RaXPoL) Doppler radar system. *Journal of Atmospheric and Oceanic Technology* 30, 1398–1413.
- Peleg, N., Marra, F., Fatichi, S., Paschalis, A., Molnar, P. and Burlando, P. (2018) Spatial variability of extreme rainfall at radar subpixel scale. *Journal of Hydrology* 556, 922–933.
- Peura M., Koistinen J. and Hohti H. (2006) Quality information in processing weather radar data for varying user needs. *Proceedings of ERAD 2006*, 563–566. <http://crahi.upc.edu/ERAD2006/proceedingsMask/00152.pdf> Accessed 10 September 2018.
- Pleau, M., Fradet, O., Colas, H. and Marcoux, C. (2010) Giving the rivers back to the public. Ten years of Real Time Control in Quebec City. In: *Proceedings international conference on sustainable techniques and strategies in urban water management (Novatech2010)*, Lyon, France 27 June – 1 July 2010. <http://documents.irevues.inist.fr/bitstream/handle/2042/35732/31805-055PLE.pdf?sequence=1> Accessed 25 August 2018
- Pruppacher, H. and Klett, J. (2010) Hydrodynamics of single cloud and precipitation particles. In: Pruppacher, H. and Klett, J. (editors) *Microphysics of Clouds and Precipitation*. Atmospheric and Oceanographic Sciences Library, vol 18. Dordrecht: Springer, 361-446.
- Rodriguez-Iturbe, I., Febres de Power, B., Sharifi, M. B. and Georgakakos, K. P. (1989) Chaos in rainfall. *Water Resources Research* 25, 1667-1675.
- Rozkrut, D. (editor) (2016) *Statistical Yearbook of the Republic of Poland*. Warsaw: Statistics in Poland.
- Rozkrut, D. (editor) (2017) *Statistical Yearbook of the Republic of Poland*. Warsaw: Statistics in Poland.
- Rozkrut, D. (editor) (2018) *Statistical Yearbook of the Republic of Poland*. Warsaw: Statistics in Poland.
- Rupp, D. E., Licznar, P., Adamowski, W. and Leśniewski, M. (2012) Multiplicative cascade models for fine spatial downscaling of rainfall: parameterization with rain gauge data. *Hydrology and Earth System Sciences* 16, 671-684.
- Sassi, M. G., Leijnse, H. and Uijlenhoet, R. (2014) Sensitivity of power functions to aggregation: Bias and uncertainty in radar rainfall retrieval. *Water Resources Research* 50, 8050– 8065.

- Schertzer, D. and Lovejoy, S. (1991) Nonlinear geodynamical variability: Multiple singularities, universality and observables. In: Schertzer, D. and Lovejoy, S. (editors) *Non-linear variability in geophysics: scaling and fractals*, Kluwer Academic Publishers, 41–82.
- Schertzer D. and Lovejoy S. (2011) Multifractals, generalized scale invariance and complexity in geophysics. *International Journal of Bifurcation and Chaos* 21(12), 3417–3456.
- Schilling, W. (1991) Rainfall data for urban hydrology: what do we need?. *Atmospheric Research* 27, 5–21.
- Schütze, M., Campisano, A., Colas, H., Schilling, W. and Vanrolleghem, P. A. (2004) Real time control of urban wastewater systems – Where do we stand today?. *Journal of Hydrology* 299, 335–348.
- She, Z.-S. and Leveque, E. (1994) Universal scaling laws in fully developed turbulence. *Physical Review Letters* 72, 336–339.
- She, Z.-S. and Waymire, E. C. (1995) Quantized energy cascade and logPoisson statistics in fully developed turbulence. *Physical Review Letters* 74, 262–265.
- Siekanowicz-Grochowina, K., Licznar, P., Konieczny, T. and Zaleski J. (2017) Porównanie danych opadowych z sieci deszczomierzy i radaru meteorologicznego dla Wrocławia [Comparison of precipitation data from rain-gauge network and meteorological radar – Wrocław case study]. *Gaz, Woda i Technika Sanitarna* 91(7), 303-307.
- Smith, J. A., Baeck, M. L., Meierdiercks, K. L., Miller, A. J., and Krajewski, W. F. (2007) Radar rainfall estimation for flash flood forecasting in small urban watersheds. *Advances in Water Resources* 30, 2087–2097.
- Steiner, M., Smith, J. A. and Uijlenhoet, R. (2004) A microphysical interpretation of radar reflectivity–rain rate relationships. *Journal of the Atmospheric Sciences* 61, 1114–1131.
- Stephan, K., Klink, S. and Schraff, C. (2008) Assimilation of radar derived rain rates into the convective-scale model COSMODE at DWD. *Quarterly Journal of The Royal Meteorological Society* 134, 1315–1326.
- Stout, G.E. and E.A., Mueller (1968) Survey of relationships between rainfall rate and radar reflectivity in the measurement of precipitation. *Journal of Applied Meteorology* 7(3), 465–474.
- Svensson, C., Olson, J. and Berndtsson, R. (1996) Multifractal properties of daily rainfall in two different climates. *Water Resources Research* 32(8), 2463-2472.
- Szturc, J., Ośródką, K., Jurczyk, A. and Jelonek, L. (2008a) Concept of dealing with uncertainty in radar-based data for hydrological purpose. *Natural Hazards and Earth System Sciences* 8, 267–279.
- Szturc, J., Ośródką, K. and Jurczyk, A. (2008b) Parameterization of QI scheme for radar-based precipitation data. *Proceedings of ERAD 2008*. Cited in: Einfalt, T., Szturc, J. and Ośródką, K. (2010) The quality index for radar precipitation data: a tower of Babel?. *Atmospheric Science Letters* 11(2): 140.
- Szturc, J. (2018) Personal communication, 16 August.
- Taylor, G. I. (1938) The spectrum of turbulence. *Proceedings of the Royal Society A* 164(919), 476–490.
- Tabary, P., Desplats, J., Do Khac, K., Eidelman, F., Gueguen C. and Heinrich, J.-C. (2007) The new French operational radar rainfall product. Part II: validation. *Weather Forecasting* 22, 409–427.
- Tessier, Y., Lovejoy S. and Schertzer D. (1993) Universal multifractals: Theory and observations for rain and clouds. *Journal of Applied Meteorology* 32, 223-250.
- Thiessen, A. H. (1911) Precipitation for large areas. *Monthly Weather Review* 39, 1082–1084.

- Thorndahl, S., Smith, J. A., Baeck, M. L. and Krajewski, W. F. (2014) Analyses of the temporal and spatial structures of heavy rainfall from a catalog of high-resolution radar rainfall fields. *Atmospheric Research* 144, 111–125.
- Thorndahl, S., Einfalt, T., Willems, P., Nielsen, J. E., ten Veldhuis, M., Arnbjerg-Nielsen, K., Rasmussen, M. R. and Molnar, P. (2017) Weather radar rainfall data in urban hydrology. *Hydrology and Earth System Sciences* 21, 1359–1380.
- Tuszyńska I. (2011) *Charakterystyka produktów radarowych*. Warszawa: Instytut Meteorologii i Gospodarki Wodnej Państwowy Instytut Badawczy.
- Uijlenhoet, R. (2001) Raindrop size distributions and radar reflectivity–rain rate relationships for radar hydrology. *Hydrology and Earth System Sciences* 5, 615–628.
- United Nations (2018) *The speed of urbanization around the world. Populations Facts*. Department of Economic and Social Affairs, Population Division, United Nations. https://population.un.org/wup/Publications/Files/WUP2018-PopFacts_2018-1.pdf Accessed 30 December 2018.
- U.S. Environmental Protection Agency (2018) *Smart data infrastructure for wet weather control and decision support*, U.S. Environmental Protection Agency, Office of Wastewater Management.
- van de Beek, C. Z., Leijnse, H., Torfs, P. J. J. F. and Uijlenhoet, R. (2012) Seasonal semi-variance of Dutch rainfall at hourly to daily scales. *Advances in Water Resources* 45, 76–85.
- von Storch V., Zorita E. and Cubasch U. (1993) Downscaling of global climate change estimates to regional scales: an application to Iberian rainfall in wintertime. *Journal of Climate* 6, 1161–1171.
- VDI (2014) *VDI 3786 Part 20. Environmental meteorology – Ground-based remote sensing of precipitation – Weather radar*. Berlin: Beuth Verlag.
- Venkatachalam P. and Kumar M. (2017) Space-Time Variogram Modeling. In: Shekhar S., Xiong H., Zhou X. (editors) *Encyclopedia of GIS*. Cham: Springer.
- Villarini, G. and Krajewski, W. F. (2010) Review of the different sources of uncertainty in single polarization radar-based estimates of rainfall. *Surveys in Geophysics* 31(1), 107–129.
- World Meteorological Organization (2012) *Guide to Meteorological Instruments and Methods of Observation. No.8*. WMO.
- Wilson, J. W. and Brandes, E. A. (1979) Radar measurement of rainfall—a summary. *Bulletin of the American Meteorological Society* 60(9), 1048–1058.
- World Economic Forum (2018) *The Global Risks Report 2018. 13th Edition*. Geneva: World Economic Forum.
- Woś, A. (1993) *Regiony klimatyczne Polski w świetle częstości występowania różnych typów pogody*. Zeszyty Instytutu Geografii i Przestrzennego Zagospodarowania PAN No. 20. Polska Akademia Nauk, Instytut Geografii i Przestrzennego Zagospodarowania PAN.
- Wright, D. B., Smith, J. A., Villarini, G. and Baeck, M. L. (2014) Long-Term High-Resolution Radar Rainfall Fields for Urban Hydrology. *Journal of the American Water Resources Association* 50, 713–734.
- Wurman, J. M. and Kosiba K. A. (2013) Fine scale radar observations of tornado and mesocyclone structures. *Weather and Forecasting* 28, 1157–1174.
- Yang, L., Smith, J. A., Wright, D. B., Baeck, M. L., Villarini, G., Tian, F. and Hu, H. (2013) Urbanization and climate change: an examination of nonstationarities in urban flooding. *Journal of Hydrometeorology* 14, 1791–1809.

List of web pages

Urban Atlas [online access: 03.11.2018], available at: <https://land.copernicus.eu/local/urban-atlas>

Map of imperviousness density in 2012 in Europe [online access: 03.11.2018], available at: <https://www.eea.europa.eu/data-and-maps/figures/map-showing-based-on-a-1#tab-based-on-data>

Map of mean annual sum of precipitation for 1981-2014 in Warsaw [online access: 20.10.2018], available at: <http://adaptcity.pl/opady-roczne/>

Map of mean annual sum of precipitation for 2008-2014 [online access: 20.10.2018], available at: <http://mapa.um.warszawa.pl/mapaApp1/mapa>

List of appendices

Appendix A: Comparison of rain gauge and radar data	128
Appendix B: Spatial range of analysed precipitation fields for each of assumed advection velocity	172
Appendix C: Mean autocorrelation functions of selected radar sequences from 2015 along X and Y directions and time for different advection velocity assumptions	182
Appendix D: Autocorrelation functions of selected radar sequences from 2015 along X and Y directions and time	188
Appendix E: List of rainfall events selected using moving window algorithm	201
Appendix F: Mean rainfall depths for averaged radar sequences from 2015.....	205
Appendix G: Complementary cumulative distribution function (cCDF) for selected radar sequences from 2015	210
Appendix H: Space-time structure function $Sq(\lambda)$ for selected radar sequences from 2015.....	220
Appendix I: Multifractal scaling function $K(q)$ for selected radar sequences from 2015. $K(q)$ theoretical model for estimated c and β parameters	233
Appendix J: List of c , $c_{\beta=const}$ and β parameters of selected rainfall events	246
Appendix K: Multifractal scaling function $K(q)$ for selected radar sequences from 2015. $K(q)$ theoretical model for estimated $c_{\beta=const}$ and β parameters	250

List of figures and tables

Figures

Figure 1.1 The Global Risks Landscape 2018 (World Economic Forum, 2018)	11
Figure 3.1 Spatial scales of urban climate analysis schematic of climatic scales and vertical layers found in urban areas. Reprinted from World Meteorological Organization, 2012	18
Figure 3.2 Time and space scales involved in urban climate phenomena.....	20
Figure 3.3 Radar basic system elements (based on: Eaves, 1987).....	22
Figure 3.4 Example of radar reflectivity at four different Cartesian spatial resolutions over Aalborg, Denmark. Reproduced from Thorndahl et al., 2017	27
Figure 3.5 (a) The 69 power law Z–R relationships $Z = AR^b$ quoted by Battan (1973), including 5 deviating relationships (dashed lines): 4 which have prefactors A smaller than 100 and 1 of which has a high exponent b (2.87). The bold line indicates the linear relationship $Z = 742R$ (List, 1988). (b) the mean of Battan’s relationships, $Z = 238R^{1.50}$ (bold solid line), the reference relationship $Z = 200R^{1.6}$ (bold dashed line) and the envelope of 64 (the thin solid lines in (a)) of Battan’s 69 Z–R relationships (thin solid lines). Reproduced from Uijlenhoet, 2001.....	32
Figure 3.6 POLRAD radar network in Poland	38
Figure 3.7 Geometry of CAPPI and PCAPPI products (based on: Tuszyńska, 2011)	40
Figure 4.1 Changes in land cover - impervious surfaces paved between 2006-2012 in Warsaw (based on data from: Urban Atlas. Change 2006-2012, https://land.copernicus.eu/local/urban-atlas)	46
Figure 4.2 Impervious surfaces in Warsaw in 2012 (based on data from: Urban Atlas: https://land.copernicus.eu/local/urban-atlas)	47
Figure 4.3 Pervious surfaces in Warsaw in 2012 (based on data from: Urban Atlas: https://land.copernicus.eu/local/urban-atlas)	48
Figure 4.4 Imperviousness density in 2012 aggregated to 10 km grid (source: European Environment Agency https://www.eea.europa.eu/data-and-maps/figures/map-showing-based-on-a-1#tab-based-on-data)	49
Figure 4.5 Built-up and urbanized areas in Warsaw by types between 2012-2017 based on Statistical Yearbook of Warsaw (Kozłowska 2014, 2015, 2018).....	50
Figure 4.6 Mean annual sum of precipitation for (a) 1981-2014 (source: http://adaptcity.pl/opady-roczne/); (b) 2008-2014 (source: http://mapa.um.warszawa.pl/mapaApp1/mapa) in Warsaw	52
Figure 5.1 Time series of reflectivity Z (lower panel) and rain rate R (upper panel) registered by disdrometer OTT in Warsaw Parsivel ² for year 2013.....	54
Figure 5.2 Z-R functional relationships for Warsaw, developed based on laser disdrometer records in temporal resolution of 10 seconds.....	57
Figure 5.3 Z-R functional relationships for Warsaw, developed based on laser disdrometer records in temporal resolution of 1 minute	57
Figure 5.4 Z-R functional relationships for Warsaw, developed based on laser disdrometer records in temporal resolution of 5 minutes.....	58
Figure 5.5 Z-R functional relationships for Warsaw, developed based on laser disdrometer records in temporal resolution of 10 minutes.....	58

Figure 5.6 Z-R functional relationships for Warsaw for summertime period based on Parsivel ² records.	59
Figure 5.7 Z-R functional relationships for Warsaw for wintertime period based on Parsivel ² records.	60
Figure 6.1 Rain gauges network in Warsaw, seen on a 1x1 km radar grid	65
Figure 6.2 Rainfall intensity series recorded by gauge R10 (G) during summer months (May-August) 2009 (upper panel) and coincident in space radar rainfall intensity (R) series for the same period (lower panel). Both time series are in 10-min resolution	66
Figure 6.3 Cross-correlation of rainfall intensity time series registered by gauge (G) and radar (R) for gauge R10 location	67
Figure 6.4 Variation with size of terminal fall velocity of water drops larger than 500 μm in air. Reproduced from Pruppacher and Klett, 2010.	68
Figure 6.5 Log-log plot of 10-min non-zero radar rainfall intensity R values versus non-zero rainfall intensity G values from gauge R10 for summer months of 2009 with best fitted linear function with its 95% confidence intervals.	70
Figure 7.1 Schematic diagram showing the approach to direct space-time rainfall downscaling based on Taylor hypothesis	75
Figure 7.2 An exemplary autocorrelation functions along x (x-corr) and y (y-corr) directions and time (t-corr) for 320-min aggregated radar sequence selected from 2015 for advection velocity $U=16 \text{ km}\cdot\text{h}^{-1}$. The rainfall event started on 07.07.2015 at 22:30. The horizontal axis represents the shift in the radar grid aggregated to 4x4 km.	79
Figure 7.3 Mean autocorrelation functions along X (X-corr) and Y (Y-corr) directions and rescaled time (t-corr) direction for 320-min aggregated radar sequences selected from summer months of 2015 for advection velocity $U=48 \text{ km}\cdot\text{h}^{-1}$. The horizontal axis represents the shift in the radar grid aggregated to 8x8 km	80
Figure 7.4 An exemplary autocorrelation functions along x (x-corr) and y (y-corr) directions and time (t-corr) for 320-min aggregated radar sequence selected from 2015 for advection velocity $U=48 \text{ km}\cdot\text{h}^{-1}$. The rainfall event started on 23.07.2015 at 1:20 AM. The horizontal axis represents the shift in the radar grid aggregated to 8x8 km.	81
Figure 7.5 Spatial range of analysed precipitation field for assumed advection velocity $U = 48 \text{ km}\cdot\text{h}^{-1}$.	82
Figure 7.6 Monthly mean rainfall depths of precipitation field for analysed summer months of 2015. The spatial range of the field is 32 x 32 aggregated cells (each of 8x8 km)	84
Figure 7.7 Monthly rainfall depths of precipitation field for analysed summer months of 2015. The spatial range of the field is 256 x 256 km	85
Figure 7.8 Mean rainfall rate (mm/10min) of an exemplary 320-min aggregated radar sequence. The rainfall event started on 23.07.2015 at 1:20 AM	86
Figure 7.9 Complementary cumulative distribution function (cCDF) of rainfall rate (r in mm/10min) for 320-min aggregated radar sequence. The rainfall event started on 23.07.2015 at 1:20 AM	88
Figure 7.10 Complementary cumulative distribution functions (cCDFs) of rain rate r (in mm/10 min) for all 115 analysed 320-minute rainfall events distributed over the area of 256 x 256 km	88
Figure 7.11 Set of semivariograms in X-direction for 115 analysed 320-minute rainfall events distributed over the area of 256 x 256 km	90
Figure 7.12 Set of semivariograms in Y-direction for 115 analysed 320-minute rainfall events distributed over the area of 256 x 256 km	90

Figure 7.13 The averaged semivariograms (μ) in X-direction (upper panel) and Y-direction (lower panel) derived based on set of 115 semivariograms for selected rainfalls distributed over the area 256 x 256 km. The standard deviation ranges: from 0 to 0.5 σ (0.5 σ) and from 0.5 σ to σ (σ) are additionally plotted	91
Figure 7.14 Log-log plot of the space-time structure function $S_q(\lambda)$ for 320-min aggregated radar sequence. The rainfall event started on 23.07.2015 at 1:20 AM	92
Figure 7.15 Empirical multifractal scaling function $K(q)$ for 320-min aggregated radar sequence together with fitted theoretical $K(q)$ function model for estimated c and β parameters. The rainfall event started on 23.07.2015 at 1:20 AM.....	93
Figure 7.16 Plot of log-Poisson parameter c versus mean rainfall rate R over 256x256 km ² for all selected radar sequences.....	95
Figure 7.17 Plot of log-Poisson parameter β versus mean rainfall rate R over 256x256 km ² for all selected radar sequences.....	95
Figure 7.18 Plot of log-Poisson parameter $c_{\beta=\text{const}}$, keeping $\beta=0.01$ constant, versus mean rainfall rate R over 256x256 km ² for all selected radar sequences.....	96
Figure 7.19 Plot of log-Poisson parameter $\beta =0.01$ constant, versus mean rainfall rate R over 256x256 km ² for all selected radar sequences	96
Figure 7.20 Empirical multifractal scaling function $K(q)$ for 320-min aggregated radar sequence together with fitted theoretical $K(q)$ function model for estimated c and fixed β parameter. The rainfall event started on 23.07.2015 at 1:20 AM.....	97
Figure 7.21. The concept of dressing process: on the left side – the step-by-step construction of a (“bare”), on the right side - “dressed” cascade. Reproduced from Lovejoy and Schertzer, 2013.....	99
Figure 7.22 Space and time scales of the random cascade without dressing process	100
Figure 7.23 Space and time scales of the random cascade with dressing process	100
Figure 7.24 Complementary cumulative distribution function (cCDF) of rain rate r (in mm/10 min) for 115 synthetically generated 320-minute rainfall events on the area 256 x 256 km without dressing.....	102
Figure 7.25 Complementary cumulative distribution function (cCDF) of rain rate r (in mm/10 min) for 115 synthetically generated 320-minute rainfall events on the area 256 x 256 km using cascade with dressing process.....	102
Figure 7.26 Set of semivariograms in X-direction for 115 synthetically generated using cascade without dressing process 320-minute rainfall events over the area 256 x 256 km	104
Figure 7.27 Set of semivariograms in Y-direction for 115 synthetically generated using cascade without dressing process 320-minute rainfall events over the area 256 x 256 km	104
Figure 7.28 Set of semivariograms in X-direction for 115 synthetically generated using cascade with dressing process 320-minute rainfall events over the area 256 x 256 km	105
Figure 7.29 Set of semivariograms in Y-direction for 115 synthetically generated using cascade with dressing process 320-minute rainfall events over the area 256 x 256 km	105
Figure 7.30 The averaged semivariograms (μ) in X-direction (upper panel) and Y-direction (lower panel) derived based on set of 115 semivariograms for synthetically generated rainfalls (using cascade with dressing process) distributed over the area 256 x 256 km. The standard deviation ranges: from 0 to 0.5 σ (0.5 σ) and from 0.5 σ to σ (σ) are additionally plotted.....	106

Figure 7.31 The averaged semivariograms (μ) in X-direction (upper panel) and Y-direction (lower panel) derived based on set of 115 semivariograms for synthetically generated rainfalls (using cascade with dressing process) distributed over the area 256 x 256 km. The standard deviation ranges: from 0 to 0.5 σ (0.5 σ) and from 0.5 σ to σ (σ) are additionally plotted..... 107

Tables

Table 3.1 Characteristics of some important precipitation systems (Einfalt et al., 1998)	16
Table 3.2 The derivation of target data based on received and transmitted signals correlation (Eaves, 1987)	21
Table 3.3 Naming conventions for different frequency bands and wavelengths (Kumjian, 2018)	24
Table 3.4 An approximate probabilities of meteorological objects detection by radar (Moszkowicz and Tuszyńska, 2006).....	25
Table 3.5 Typical operating resolutions and maximum ranges for different types of weather radars used in hydrological applications (Thorndahl et al, 2017)	27
Table 3.6 Recommended spatial and temporal resolution for weather radar data for defined catchment sizes.....	28
Table 3.7 Radar reflectivity, rainfall rate relationship from direct measurement (Stout and Mueller, 1968)	30
Table 3.8 Radar reflectivity, rainfall rate relationship from drop size spectra (Stout and Mueller, 1968)	31
Table 3.9 Quality index schemes operationally used in European national meteorological services for surface precipitation fields (Einfalt et al., 2010)	34
Table 3.10 Magnitude, frequency and range of rain radar errors (Szturc et al., 2008a)	35
Table 3.11 List of POLRAD radars (Szturc, personal communication)	37
Table 3.12 Scan parameters used in the POLRAD weather radar network (Ośródką and Szturc, 2015) ..	38
Table 3.13 Application fields for radar rainfall in urban hydrology (Thorndhal et al., 2017).....	41
Table 4.1 Built-up and urbanized areas in Warsaw in 2012-2017 based on Statistical Yearbook of Warsaw (Kozłowska 2014, 2015, 2018).....	49
Table 4.2 Total annual precipitation in Warsaw, in mm (Dmochowska 2015; Rozkurt 2016, 2017, 2018)	51
Table 4.3 Monthly precipitation in Warsaw, in mm (Dmochowska 2015; Rozkurt 2016, 2017, 2018)	52
Table 5.1 Values characterizing disdrometer observational sets for analysed temporal resolutions	56
Table 5.2 Values characterizing fitted models and parameters of Z-R relations	56
Table 5.3 Values characterizing fitted models and parameters of Z-R relations for summer and winter half year	60
Table 6.1 Parameters of linear relationships fits for non-zero rainfall intensity values derived from radar and rain gauges time series for 25 locations (R1-R25) in Warsaw in 2009	69
Table 7.1 Pearson correlation coefficients calculated for pairs of mean autocorrelation functions for spatial and temporal dimensions of cubic structures for a hierarchy of assumed advection velocities	79
Table 7.2 The number of rainfall events selected using moving window algorithm for each year	83

List of symbols and abbreviations

List of symbols

A – parameter in Z - R relationship

b – parameter in Z - R relationship

β – log-Poisson distribution parameter

c – speed of light

c – log-Poisson distribution parameter

$c_{\beta=const}$ – log-Poisson distribution parameter for $\beta = const$

D - diameter of the particle

d – distance between pairs of observations

γ –semivariogram

$\zeta(q)$ - nonlinear function of the moment q

G - precipitation intensities registered by rain gauge

θ_1 – antenna beam width

$K(q)$ multifractal scaling function

$|K_w|^2$ – parameter associated with the complex index of refraction of the scatterer

$L \times L$ – spatial dimensions of precipitation structure before downscaling

$\lambda_x \times \lambda_y$ – intermediate spatial dimensions of precipitation structure in downscaling

$\lambda_0 \times \lambda_0$ – spatial dimensions of precipitation structure after downscaling

λ – wavelength

μ - averaged semivariogram

N - number of particles

n – the number of observations,

P - integral measure of rainfall over a given area $\lambda_x \times \lambda_y$ in a given cumulative time τ

P_r – received power

P_t – transmitted power

q - statistical moment

ρ – correlation coefficient

R – rain rate

r – range to target

R_{min} - minimal rainfall intensity

R_{max} - maximal rainfall intensity

R^2 - coefficients of determination

S – signal loss factor due to absorption along the path

$S_q(\lambda)$ - structure function

σ - standard deviation

T – time scale of precipitation structure before downscaling

τ – accumulation time of precipitation

τ_0 – time scale of precipitation structure after downscaling

U - overall advection velocity

V_t - drop terminal fall velocity

ω – pulse width

z_i, z_j – observed values

Z – radar reflectivity

[List of abbreviations](#)

cCDF – complementary cumulative distribution function

DDF – depth–duration–frequency

DSD – Drop Size Distribution

GARP – Global Atmospheric Research Program

GATE – GARP Atlantic Tropical Experiment

IDF – intensity–duration–frequency

IMGW – Instytut Meteorologii I Gospodarki Wodnej

IGiPZ PAN – Instytut Geografii i Przestrzennego Zagospodarowania Polskiej Akademii Nauk

MPWiK S A – Miejskie Przedsiębiorstwo Wodociągów i Kanalizacji SA

NEXRAD – (Next-Generation Radar) name of network of weather radars operated by the National Weather Service in the USA

PAC – precipitation accumulation, one of the radar products obtained from POLRAD

POLRAD – name of radar network in Poland managed by the Institute of Meteorology and Water Management – National Research Institute

QI – quality index

RAINBOW – computer processing system delivered as part of POLRAD

RMSE – root-mean-square error

RTC – real time control

SGGW – Szkoła Główna Gospodarstwa Wiejskiego w Warszawie

STRAIN – name of multifractal model (Space Time Rainfall)

WMO – World Meteorological Organization

APPENDIX A

Table of contents

<i>A-1 Rainfall intensity series recorded by gauge R1 (G) during summer months (May-August) 2009 (upper panel) and coincident in space radar rainfall intensity (R) series for the same period (lower panel). Both time series are in 10-min resolution</i>	<i>134</i>
<i>A-2 Rainfall intensity series recorded by gauge R2 (G) during summer months (May-August) 2009 (upper panel) and coincident in space radar rainfall intensity (R) series for the same period (lower panel). Both time series are in 10-min resolution</i>	<i>134</i>
<i>A-3 Rainfall intensity series recorded by gauge R3 (G) during summer months (May-August) 2009 (upper panel) and coincident in space radar rainfall intensity (R) series for the same period (lower panel). Both time series are in 10-min resolution</i>	<i>135</i>
<i>A-4 Rainfall intensity series recorded by gauge R4 (G) during summer months (May-August) 2009 (upper panel) and coincident in space radar rainfall intensity (R) series for the same period (lower panel). Both time series are in 10-min resolution</i>	<i>135</i>
<i>A-5 Rainfall intensity series recorded by gauge R3 (G) during summer months (May-August) 2009 (upper panel) and coincident in space radar rainfall intensity (R) series for the same period (lower panel). Both time series are in 10-min resolution</i>	<i>136</i>
<i>A-6 Rainfall intensity series recorded by gauge R6 (G) during summer months (May-August) 2009 (upper panel) and coincident in space radar rainfall intensity (R) series for the same period (lower panel). Both time series are in 10-min resolution</i>	<i>136</i>
<i>A-7 Rainfall intensity series recorded by gauge R7 (G) during summer months (May-August) 2009 (upper panel) and coincident in space radar rainfall intensity (R) series for the same period (lower panel). Both time series are in 10-min resolution</i>	<i>137</i>
<i>A-8 Rainfall intensity series recorded by gauge R8 (G) during summer months (May-August) 2009 (upper panel) and coincident in space radar rainfall intensity (R) series for the same period (lower panel). Both time series are in 10-min resolution</i>	<i>137</i>
<i>A-9 Rainfall intensity series recorded by gauge R9 (G) during summer months (May-August) 2009 (upper panel) and coincident in space radar rainfall intensity (R) series for the same period (lower panel). Both time series are in 10-min resolution</i>	<i>138</i>
<i>A-10 Rainfall intensity series recorded by gauge R10 (G) during summer months (May-August) 2009 (upper panel) and coincident in space radar rainfall intensity (R) series for the same period (lower panel). Both time series are in 10-min resolution</i>	<i>138</i>
<i>A-11 Rainfall intensity series recorded by gauge R11 (G) during summer months (May-August) 2009 (upper panel) and coincident in space radar rainfall intensity (R) series for the same period (lower panel). Both time series are in 10-min resolution</i>	<i>139</i>
<i>A-12 Rainfall intensity series recorded by gauge R12 (G) during summer months (May-August) 2009 (upper panel) and coincident in space radar rainfall intensity (R) series for the same period (lower panel). Both time series are in 10-min resolution</i>	<i>139</i>

APPENDIX A: COMPARISON OF RAIN GAUGE AND RADAR DATA

A-13 Rainfall intensity series recorded by gauge R13 (G) during summer months (May-August) 2009 (upper panel) and coincident in space radar rainfall intensity (R) series for the same period (lower panel). Both time series are in 10-min resolution 140

A-14 Rainfall intensity series recorded by gauge R14 (G) during summer months (May-August) 2009 (upper panel) and coincident in space radar rainfall intensity (R) series for the same period (lower panel). Both time series are in 10-min resolution 140

A-15 Rainfall intensity series recorded by gauge R15 (G) during summer months (May-August) 2009 (upper panel) and coincident in space radar rainfall intensity (R) series for the same period (lower panel). Both time series are in 10-min resolution 141

A-16 Rainfall intensity series recorded by gauge R16 (G) during summer months (May-August) 2009 (upper panel) and coincident in space radar rainfall intensity (R) series for the same period (lower panel). Both time series are in 10-min resolution 141

A-17 Rainfall intensity series recorded by gauge R17 (G) during summer months (May-August) 2009 (upper panel) and coincident in space radar rainfall intensity (R) series for the same period (lower panel). Both time series are in 10-min resolution 142

A-18 Rainfall intensity series recorded by gauge R18 (G) during summer months (May-August) 2009 (upper panel) and coincident in space radar rainfall intensity (R) series for the same period (lower panel). Both time series are in 10-min resolution 142

A-19 Rainfall intensity series recorded by gauge R19 (G) during summer months (May-August) 2009 (upper panel) and coincident in space radar rainfall intensity (R) series for the same period (lower panel). Both time series are in 10-min resolution 143

A-20 Rainfall intensity series recorded by gauge R20 (G) during summer months (May-August) 2009 (upper panel) and coincident in space radar rainfall intensity (R) series for the same period (lower panel). Both time series are in 10-min resolution 143

A-21 Rainfall intensity series recorded by gauge R21 (G) during summer months (May-August) 2009 (upper panel) and coincident in space radar rainfall intensity (R) series for the same period (lower panel). Both time series are in 10-min resolution 144

A-22 Rainfall intensity series recorded by gauge R22 (G) during summer months (May-August) 2009 (upper panel) and coincident in space radar rainfall intensity (R) series for the same period (lower panel). Both time series are in 10-min resolution 144

A-23 Rainfall intensity series recorded by gauge R23 (G) during summer months (May-August) 2009 (upper panel) and coincident in space radar rainfall intensity (R) series for the same period (lower panel). Both time series are in 10-min resolution 145

A-24 Rainfall intensity series recorded by gauge R24 (G) during summer months (May-August) 2009 (upper panel) and coincident in space radar rainfall intensity (R) series for the same period (lower panel). Both time series are in 10-min resolution 145

A-25 Rainfall intensity series recorded by gauge R25 (G) during summer months (May-August) 2009 (upper panel) and coincident in space radar rainfall intensity (R) series for the same period (lower panel). Both time series are in 10-min resolution 146

A-26 Cross correlation of rainfall intensity time series registered by gauge (G) and radar (R) for gauge R1 location 146

APPENDIX A: COMPARISON OF RAIN GAUGE AND RADAR DATA

A-27 Cross correlation of rainfall intensity time series registered by gauge (G) and radar (R) for gauge R2 location 147

A-28 Cross correlation of rainfall intensity time series registered by gauge (G) and radar (R) for gauge R3 location 147

A-29 Cross correlation of rainfall intensity time series registered by gauge (G) and radar (R) for gauge R4 location 148

A-30 Cross correlation of rainfall intensity time series registered by gauge (G) and radar (R) for gauge R5 location 148

A-31 Cross correlation of rainfall intensity time series registered by gauge (G) and radar (R) for gauge R6 location 149

A-32 Cross correlation of rainfall intensity time series registered by gauge (G) and radar (R) for gauge R7 location 149

A-33 Cross correlation of rainfall intensity time series registered by gauge (G) and radar (R) for gauge R8 location 150

A-34 Cross correlation of rainfall intensity time series registered by gauge (G) and radar (R) for gauge R9 location 150

A-35 Cross correlation of rainfall intensity time series registered by gauge (G) and radar (R) for gauge R10 location 151

A-36 Cross correlation of rainfall intensity time series registered by gauge (G) and radar (R) for gauge R11 location 151

A-37 Cross correlation of rainfall intensity time series registered by gauge (G) and radar (R) for gauge R12 location 152

A-38 Cross correlation of rainfall intensity time series registered by gauge (G) and radar (R) for gauge R13 location 152

A-39 Cross correlation of rainfall intensity time series registered by gauge (G) and radar (R) for gauge R14 location 153

A-40 Cross correlation of rainfall intensity time series registered by gauge (G) and radar (R) for gauge R15 location 153

A-41 Cross correlation of rainfall intensity time series registered by gauge (G) and radar (R) for gauge R16 location 154

A-42 Cross correlation of rainfall intensity time series registered by gauge (G) and radar (R) for gauge R17 location 154

A-43 Cross correlation of rainfall intensity time series registered by gauge (G) and radar (R) for gauge R18 location 155

A-44 Cross correlation of rainfall intensity time series registered by gauge (G) and radar (R) for gauge R19 location 155

APPENDIX A: COMPARISON OF RAIN GAUGE AND RADAR DATA

A-45 Cross correlation of rainfall intensity time series registered by gauge (G) and radar (R) for gauge R20 location 156

A-46 Cross correlation of rainfall intensity time series registered by gauge (G) and radar (R) for gauge R21 location 156

A-47 Cross correlation of rainfall intensity time series registered by gauge (G) and radar (R) for gauge R22 location 157

A-48 Cross correlation of rainfall intensity time series registered by gauge (G) and radar (R) for gauge R23 location 157

A-49 Cross correlation of rainfall intensity time series registered by gauge (G) and radar (R) for gauge R24 location 158

A-50 Cross correlation of rainfall intensity time series registered by gauge (G) and radar (R) for gauge R25 location 158

A-51 Log-log plot of 10-min non-zero radar rainfall intensity R values versus non-zero rainfall intensity G values from gauge R1 for summer months of 2009 with best fitted linear function with its 95% confidence intervals 159

A-52 Log-log plot of 10-min non-zero radar rainfall intensity R values versus non-zero rainfall intensity G values from gauge R2 for summer months of 2009 with best fitted linear function with its 95% confidence intervals 159

A-53 Log-log plot of 10-min non-zero radar rainfall intensity R values versus non-zero rainfall intensity G values from gauge R3 for summer months of 2009 with best fitted linear function with its 95% confidence intervals 160

A-54 Log-log plot of 10-min non-zero radar rainfall intensity R values versus non-zero rainfall intensity G values from gauge R4 for summer months of 2009 with best fitted linear function with its 95% confidence intervals 160

A-55 Log-log plot of 10-min non-zero radar rainfall intensity R values versus non-zero rainfall intensity G values from gauge R5 for summer months of 2009 with best fitted linear function with its 95% confidence intervals 161

A-56 Log-log plot of 10-min non-zero radar rainfall intensity R values versus non-zero rainfall intensity G values from gauge R6 for summer months of 2009 with best fitted linear function with its 95% confidence intervals 161

A-57 Log-log plot of 10-min non-zero radar rainfall intensity R values versus non-zero rainfall intensity G values from gauge R7 for summer months of 2009 with best fitted linear function with its 95% confidence intervals 162

A-58 Log-log plot of 10-min non-zero radar rainfall intensity R values versus non-zero rainfall intensity G values from gauge R8 for summer months of 2009 with best fitted linear function with its 95% confidence intervals 162

A-59 Log-log plot of 10-min non-zero radar rainfall intensity R values versus non-zero rainfall intensity G values from gauge R9 for summer months of 2009 with best fitted linear function with its 95% confidence intervals 163

A-60 Log-log plot of 10-min non-zero radar rainfall intensity R values versus non-zero rainfall intensity G values from gauge R10 for summer months of 2009 with best fitted linear function with its 95% confidence intervals 163

A-61 Log-log plot of 10-min non-zero radar rainfall intensity R values versus non-zero rainfall intensity G values from gauge R11 for summer months of 2009 with best fitted linear function with its 95% confidence intervals 164

APPENDIX A: COMPARISON OF RAIN GAUGE AND RADAR DATA

A-62 Log-log plot of 10-min non-zero radar rainfall intensity R values versus non-zero rainfall intensity G values from gauge R12 for summer months of 2009 with best fitted linear function with its 95% confidence intervals 164

A-63 Log-log plot of 10-min non-zero radar rainfall intensity R values versus non-zero rainfall intensity G values from gauge R13 for summer months of 2009 with best fitted linear function with its 95% confidence intervals 165

A-64 Log-log plot of 10-min non-zero radar rainfall intensity R values versus non-zero rainfall intensity G values from gauge R14 for summer months of 2009 with best fitted linear function with its 95% confidence intervals 165

A-65 Log-log plot of 10-min non-zero radar rainfall intensity R values versus non-zero rainfall intensity G values from gauge R15 for summer months of 2009 with best fitted linear function with its 95% confidence intervals 166

A-66 Log-log plot of 10-min non-zero radar rainfall intensity R values versus non-zero rainfall intensity G values from gauge R16 for summer months of 2009 with best fitted linear function with its 95% confidence intervals 166

A-67 Log-log plot of 10-min non-zero radar rainfall intensity R values versus non-zero rainfall intensity G values from gauge R17 for summer months of 2009 with best fitted linear function with its 95% confidence intervals 167

A-68 Log-log plot of 10-min non-zero radar rainfall intensity R values versus non-zero rainfall intensity G values from gauge R18 for summer months of 2009 with best fitted linear function with its 95% confidence intervals 167

A-69 Log-log plot of 10-min non-zero radar rainfall intensity R values versus non-zero rainfall intensity G values from gauge R19 for summer months of 2009 with best fitted linear function with its 95% confidence intervals 168

A-70 Log-log plot of 10-min non-zero radar rainfall intensity R values versus non-zero rainfall intensity G values from gauge R20 for summer months of 2009 with best fitted linear function with its 95% confidence intervals 168

A-71 Log-log plot of 10-min non-zero radar rainfall intensity R values versus non-zero rainfall intensity G values from gauge R21 for summer months of 2009 with best fitted linear function with its 95% confidence intervals 169

A-72 Log-log plot of 10-min non-zero radar rainfall intensity R values versus non-zero rainfall intensity G values from gauge R22 for summer months of 2009 with best fitted linear function with its 95% confidence intervals 169

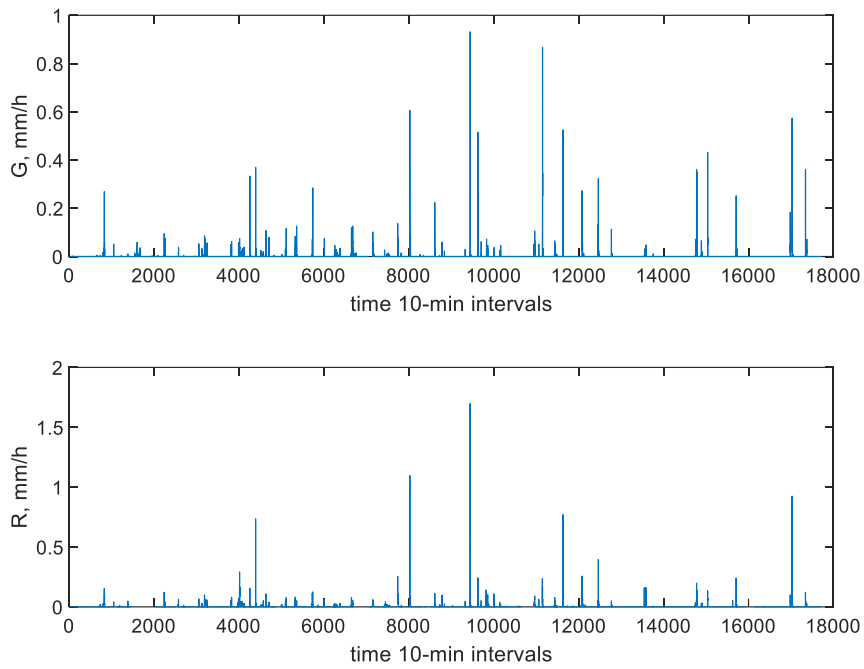
A-73 Log-log plot of 10-min non-zero radar rainfall intensity R values versus non-zero rainfall intensity G values from gauge R23 for summer months of 2009 with best fitted linear function with its 95% confidence intervals 170

A-74 Log-log plot of 10-min non-zero radar rainfall intensity R values versus non-zero rainfall intensity G values from gauge R24 for summer months of 2009 with best fitted linear function with its 95% confidence intervals 170

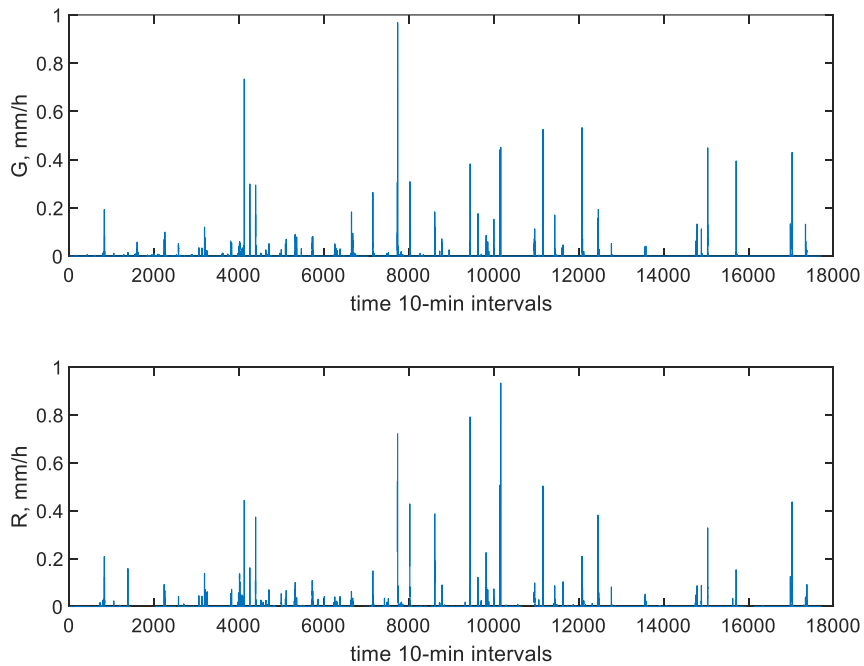
APPENDIX A: COMPARISON OF RAIN GAUGE AND RADAR DATA

A-75 Log-log plot of 10-min non-zero radar rainfall intensity R values versus non-zero rainfall intensity G values from gauge R25 for summer months of 2009 with best fitted linear function with its 95% confidence intervals
..... 171

APPENDIX A: COMPARISON OF RAIN GAUGE AND RADAR DATA

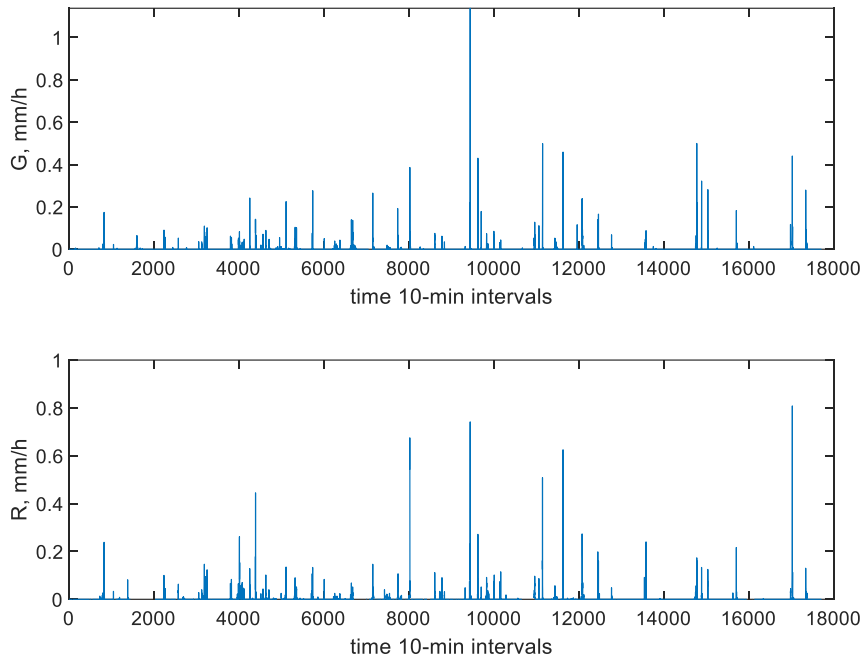


A-1 Rainfall intensity series recorded by gauge R1 (G) during summer months (May-August) 2009 (upper panel) and coincident in space radar rainfall intensity (R) series for the same period (lower panel). Both time series are in 10-min resolution

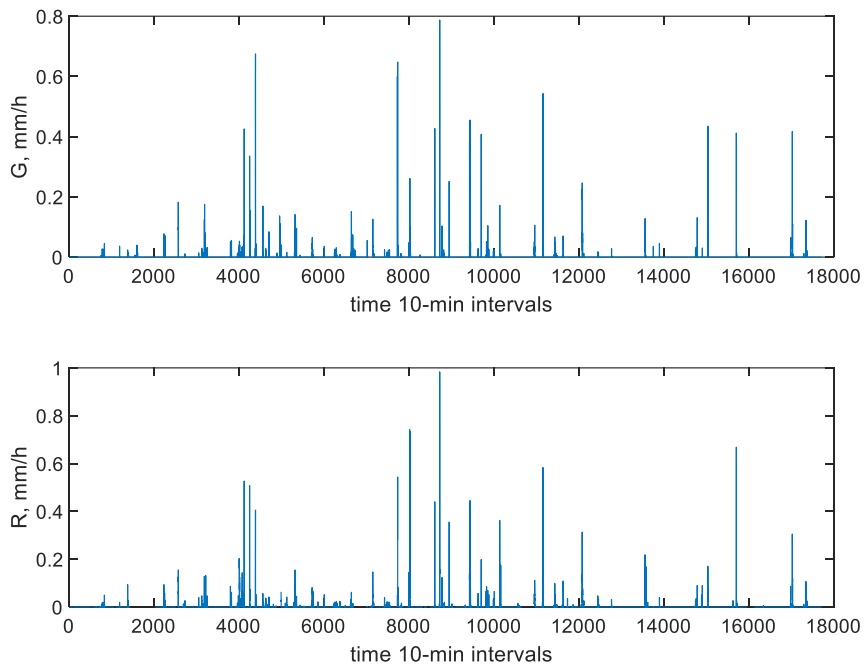


A-2 Rainfall intensity series recorded by gauge R2 (G) during summer months (May-August) 2009 (upper panel) and coincident in space radar rainfall intensity (R) series for the same period (lower panel). Both time series are in 10-min resolution

APPENDIX A: COMPARISON OF RAIN GAUGE AND RADAR DATA

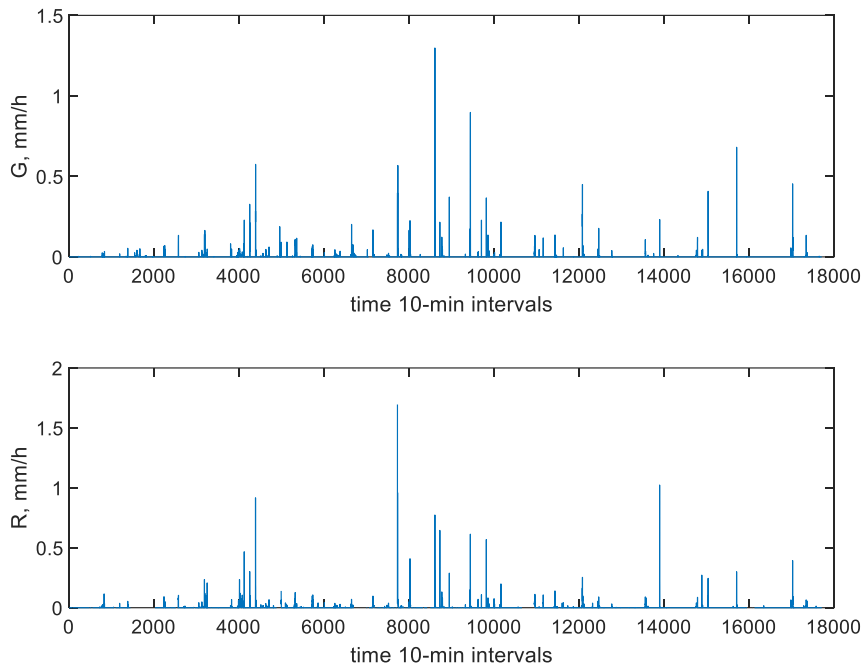


A-3 Rainfall intensity series recorded by gauge R3 (G) during summer months (May-August) 2009 (upper panel) and coincident in space radar rainfall intensity (R) series for the same period (lower panel). Both time series are in 10-min resolution

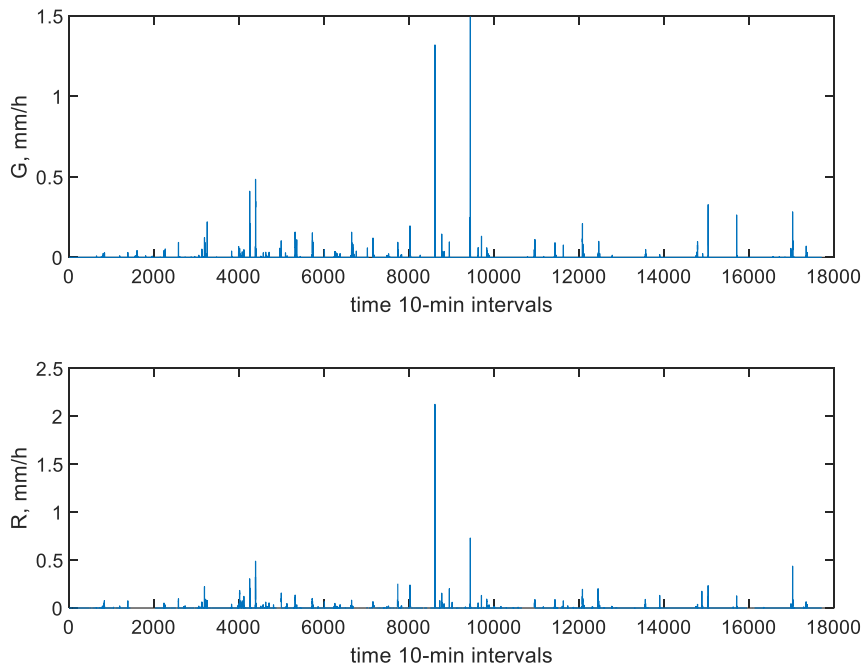


A-4 Rainfall intensity series recorded by gauge R4 (G) during summer months (May-August) 2009 (upper panel) and coincident in space radar rainfall intensity (R) series for the same period (lower panel). Both time series are in 10-min resolution

APPENDIX A: COMPARISON OF RAIN GAUGE AND RADAR DATA

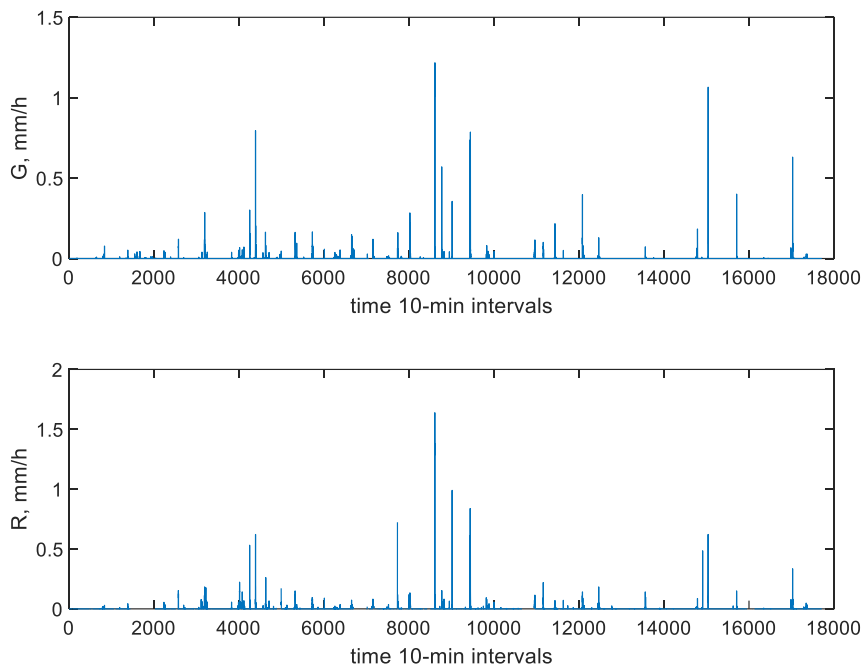


A-5 Rainfall intensity series recorded by gauge R3 (G) during summer months (May-August) 2009 (upper panel) and coincident in space radar rainfall intensity (R) series for the same period (lower panel). Both time series are in 10-min resolution

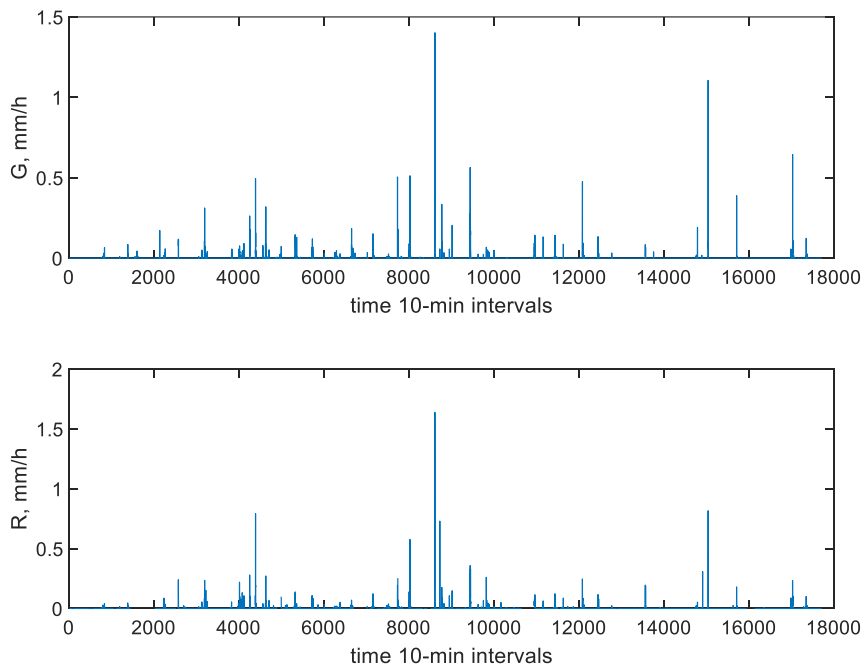


A-6 Rainfall intensity series recorded by gauge R6 (G) during summer months (May-August) 2009 (upper panel) and coincident in space radar rainfall intensity (R) series for the same period (lower panel). Both time series are in 10-min resolution

APPENDIX A: COMPARISON OF RAIN GAUGE AND RADAR DATA

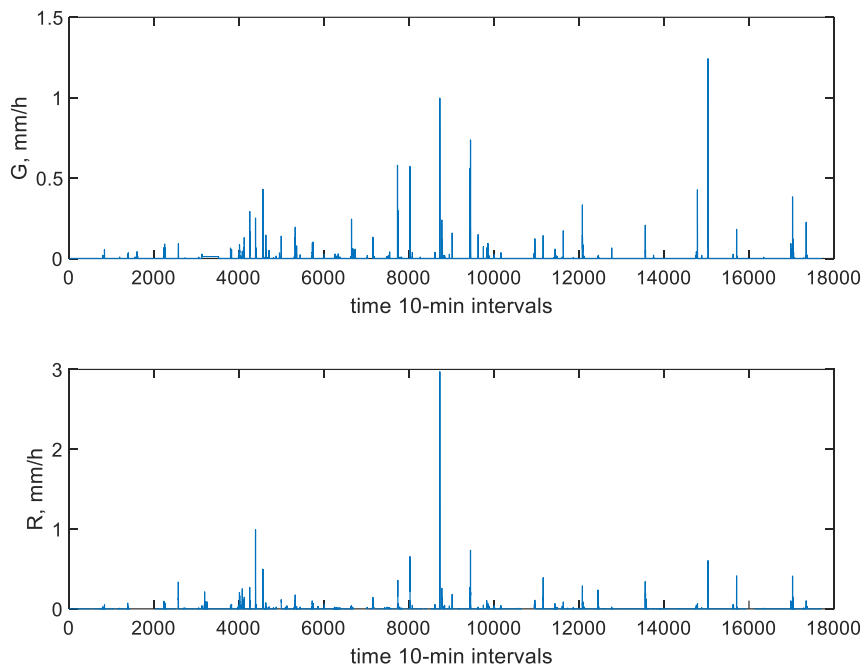


A-7 Rainfall intensity series recorded by gauge R7 (G) during summer months (May-August) 2009 (upper panel) and coincident in space radar rainfall intensity (R) series for the same period (lower panel). Both time series are in 10-min resolution

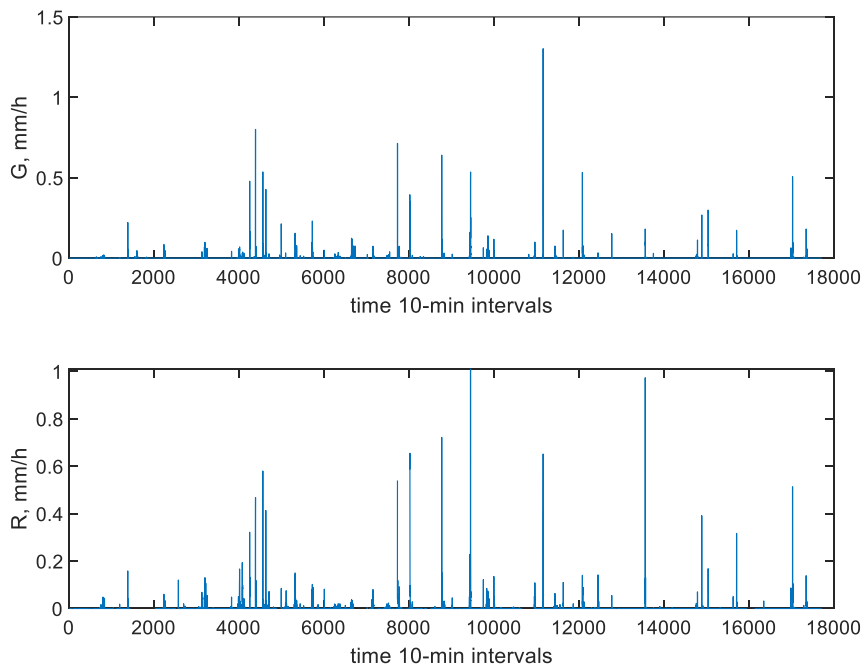


A-8 Rainfall intensity series recorded by gauge R8 (G) during summer months (May-August) 2009 (upper panel) and coincident in space radar rainfall intensity (R) series for the same period (lower panel). Both time series are in 10-min resolution

APPENDIX A: COMPARISON OF RAIN GAUGE AND RADAR DATA

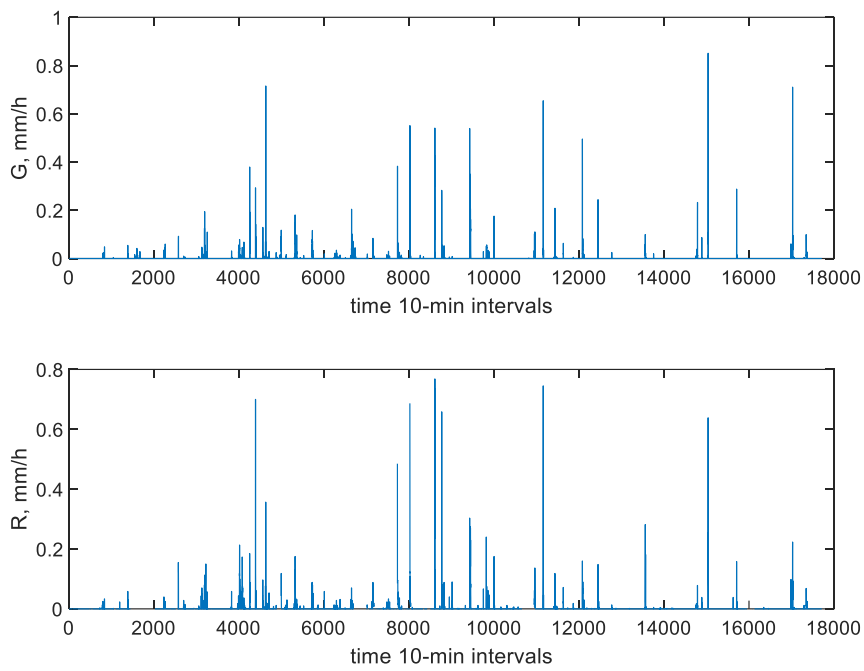


A-9 Rainfall intensity series recorded by gauge R9 (G) during summer months (May-August) 2009 (upper panel) and coincident in space radar rainfall intensity (R) series for the same period (lower panel). Both time series are in 10-min resolution

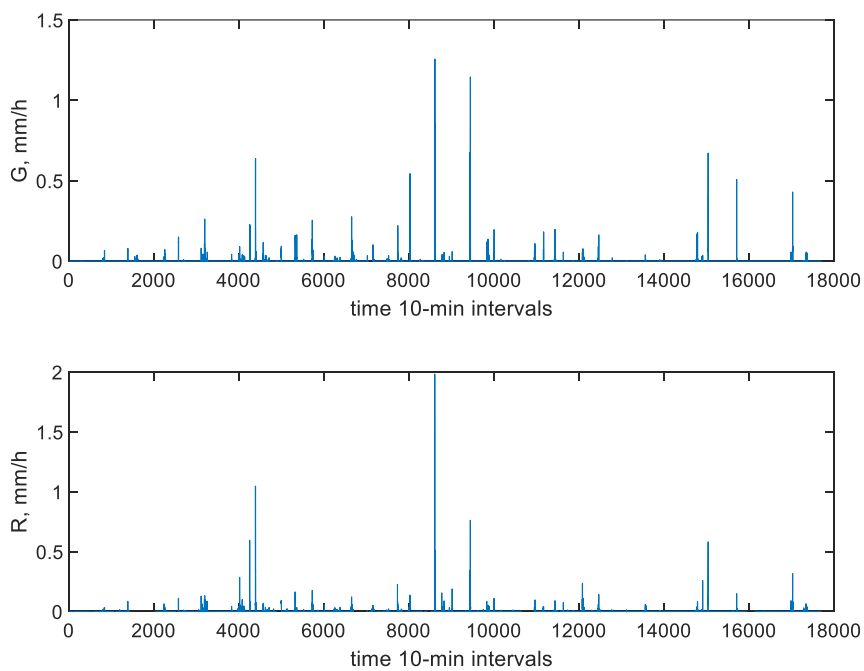


A-10 Rainfall intensity series recorded by gauge R10 (G) during summer months (May-August) 2009 (upper panel) and coincident in space radar rainfall intensity (R) series for the same period (lower panel). Both time series are in 10-min resolution

APPENDIX A: COMPARISON OF RAIN GAUGE AND RADAR DATA

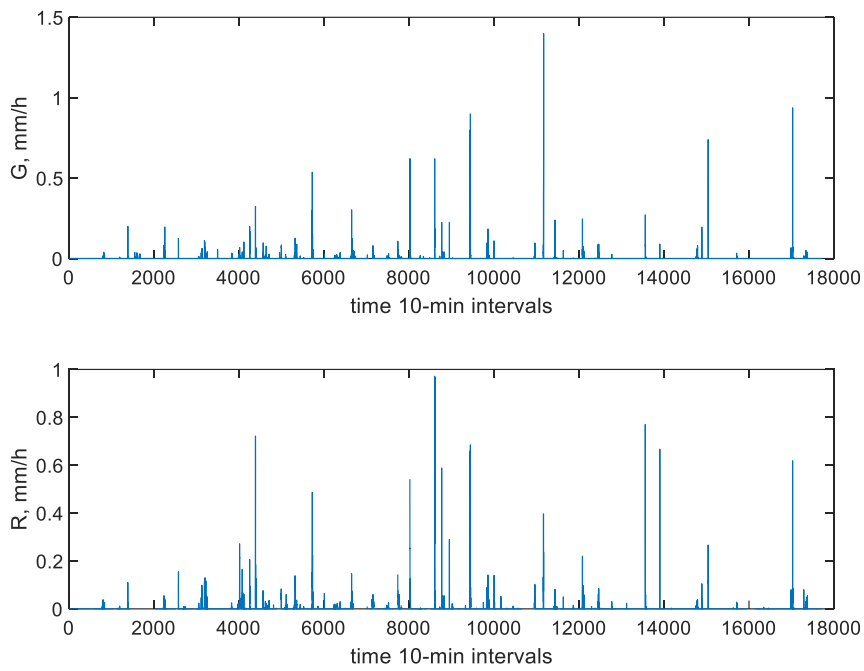


A-11 Rainfall intensity series recorded by gauge R11 (G) during summer months (May-August) 2009 (upper panel) and coincident in space radar rainfall intensity (R) series for the same period (lower panel). Both time series are in 10-min resolution

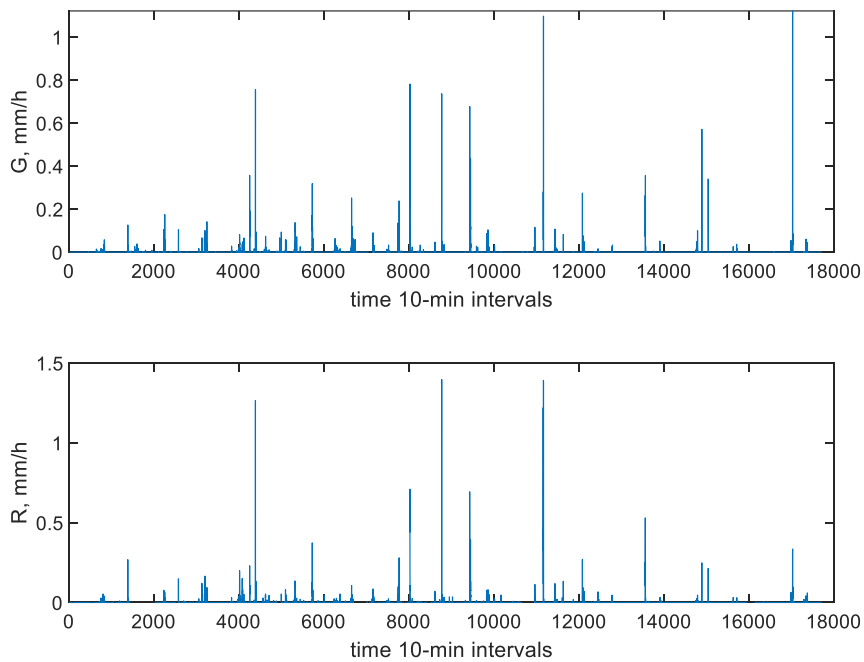


A-12 Rainfall intensity series recorded by gauge R12 (G) during summer months (May-August) 2009 (upper panel) and coincident in space radar rainfall intensity (R) series for the same period (lower panel). Both time series are in 10-min resolution

APPENDIX A: COMPARISON OF RAIN GAUGE AND RADAR DATA

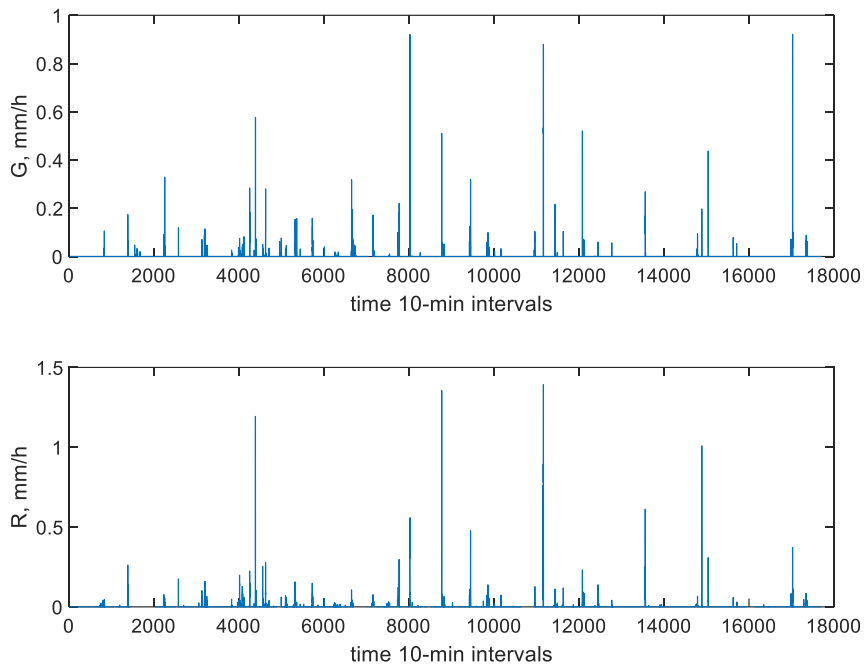


A-13 Rainfall intensity series recorded by gauge R13 (G) during summer months (May-August) 2009 (upper panel) and coincident in space radar rainfall intensity (R) series for the same period (lower panel). Both time series are in 10-min resolution

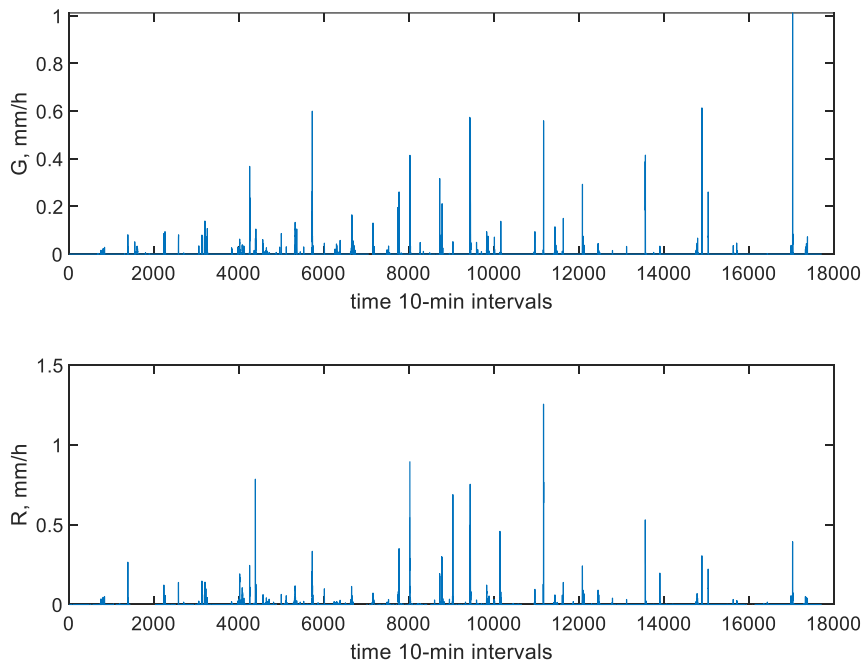


A-14 Rainfall intensity series recorded by gauge R14 (G) during summer months (May-August) 2009 (upper panel) and coincident in space radar rainfall intensity (R) series for the same period (lower panel). Both time series are in 10-min resolution

APPENDIX A: COMPARISON OF RAIN GAUGE AND RADAR DATA

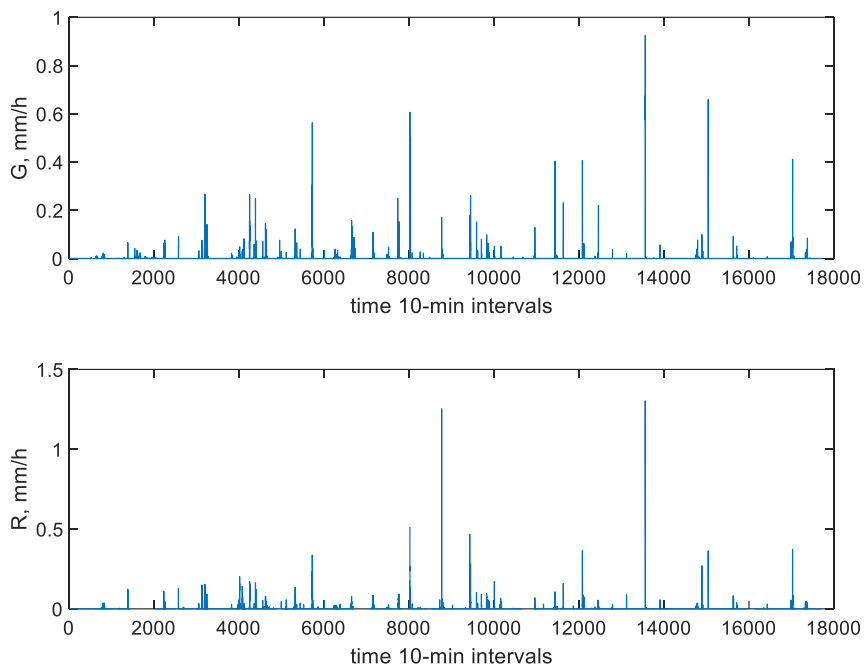


A-15 Rainfall intensity series recorded by gauge R15 (G) during summer months (May-August) 2009 (upper panel) and coincident in space radar rainfall intensity (R) series for the same period (lower panel). Both time series are in 10-min resolution

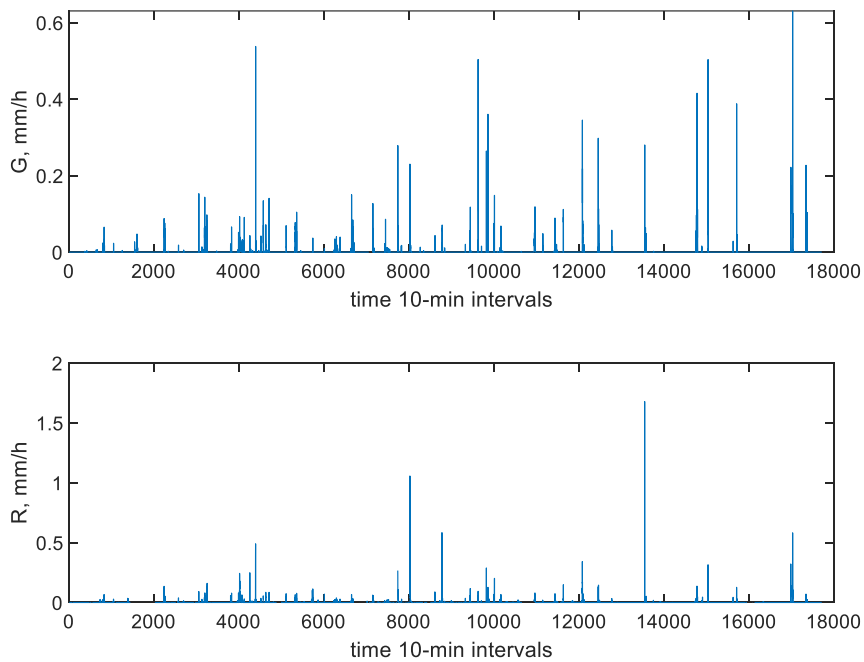


A-16 Rainfall intensity series recorded by gauge R16 (G) during summer months (May-August) 2009 (upper panel) and coincident in space radar rainfall intensity (R) series for the same period (lower panel). Both time series are in 10-min resolution

APPENDIX A: COMPARISON OF RAIN GAUGE AND RADAR DATA

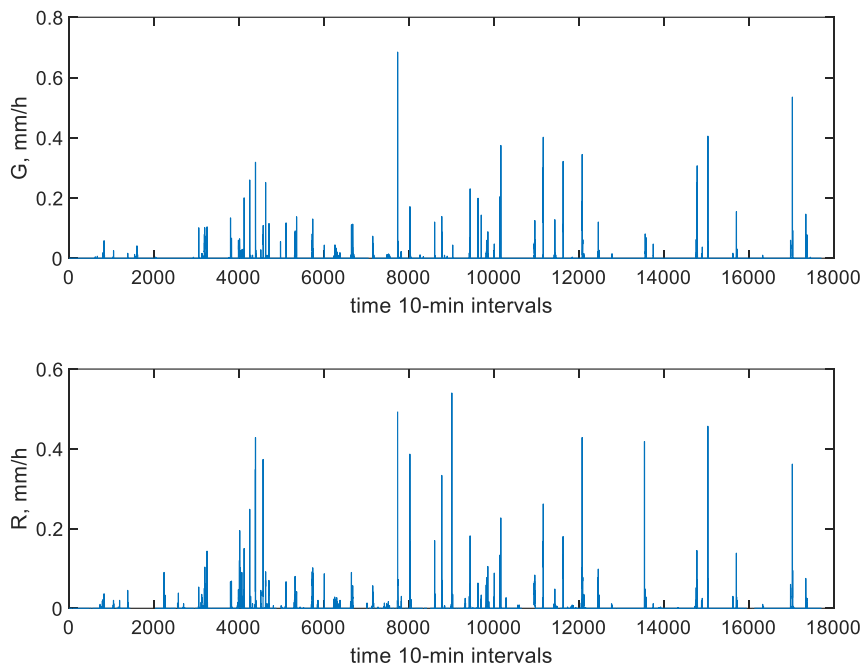


A-17 Rainfall intensity series recorded by gauge R17 (G) during summer months (May-August) 2009 (upper panel) and coincident in space radar rainfall intensity (R) series for the same period (lower panel). Both time series are in 10-min resolution

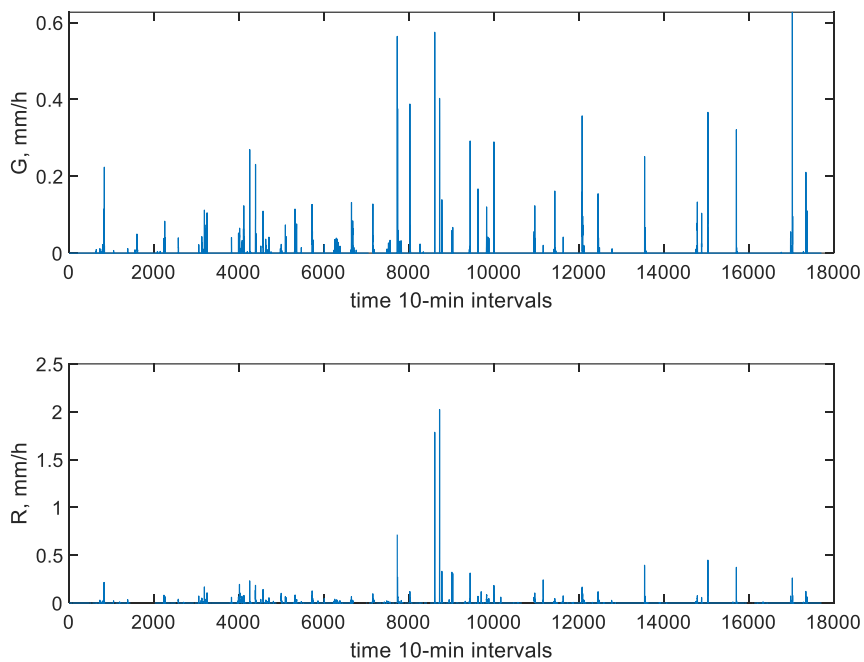


A-18 Rainfall intensity series recorded by gauge R18 (G) during summer months (May-August) 2009 (upper panel) and coincident in space radar rainfall intensity (R) series for the same period (lower panel). Both time series are in 10-min resolution

APPENDIX A: COMPARISON OF RAIN GAUGE AND RADAR DATA

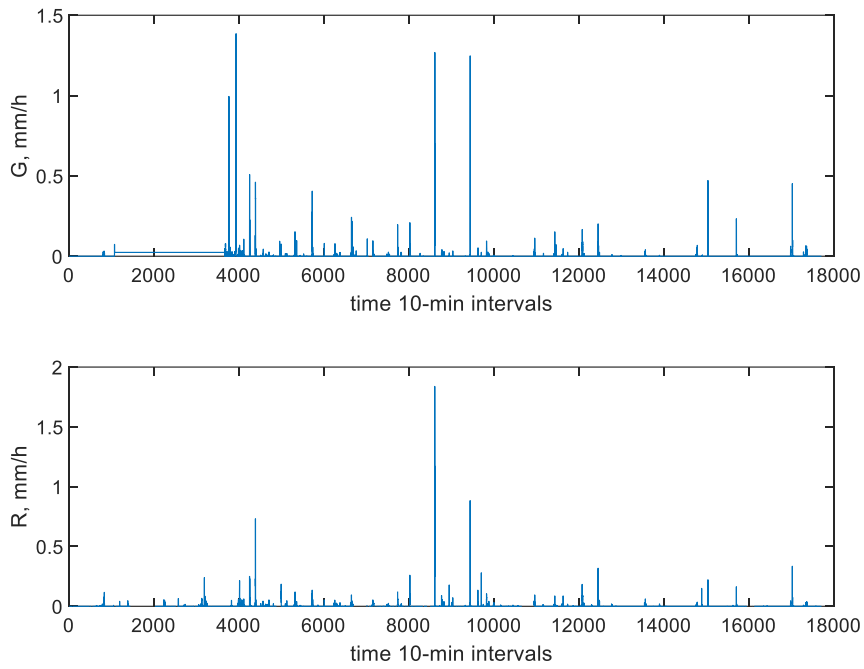


A-19 Rainfall intensity series recorded by gauge R19 (G) during summer months (May-August) 2009 (upper panel) and coincident in space radar rainfall intensity (R) series for the same period (lower panel). Both time series are in 10-min resolution

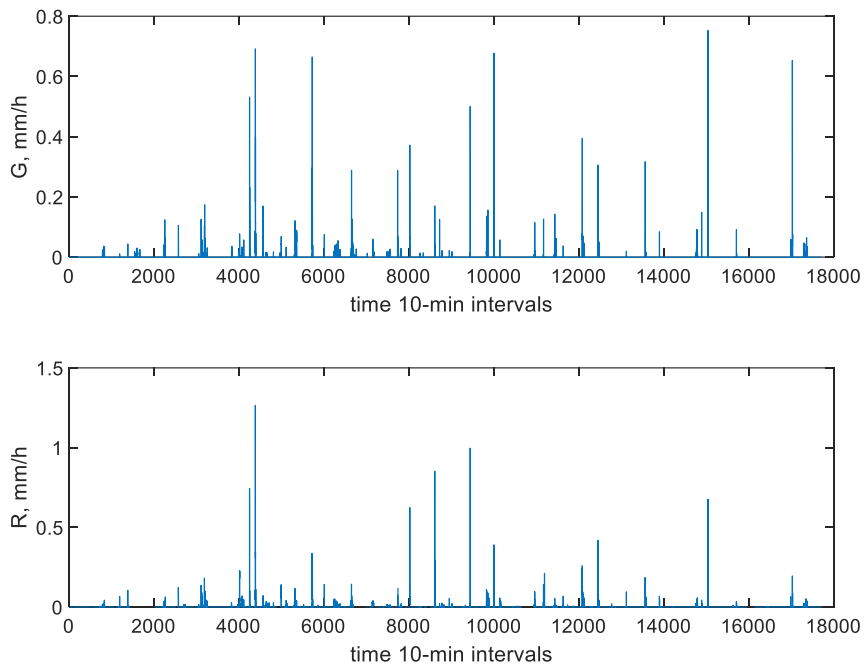


A-20 Rainfall intensity series recorded by gauge R20 (G) during summer months (May-August) 2009 (upper panel) and coincident in space radar rainfall intensity (R) series for the same period (lower panel). Both time series are in 10-min resolution

APPENDIX A: COMPARISON OF RAIN GAUGE AND RADAR DATA

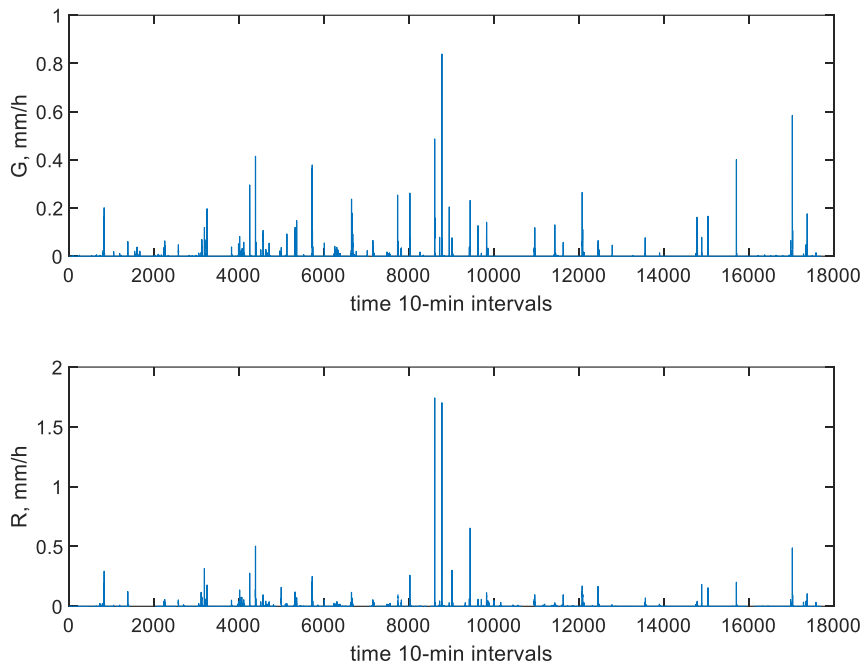


A-21 Rainfall intensity series recorded by gauge R21 (G) during summer months (May-August) 2009 (upper panel) and coincident in space radar rainfall intensity (R) series for the same period (lower panel). Both time series are in 10-min resolution

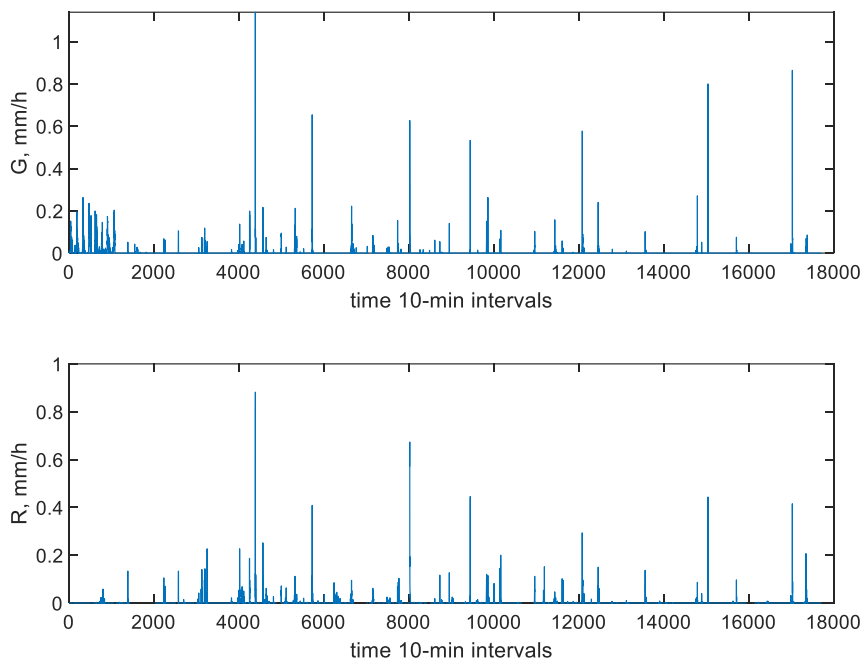


A-22 Rainfall intensity series recorded by gauge R22 (G) during summer months (May-August) 2009 (upper panel) and coincident in space radar rainfall intensity (R) series for the same period (lower panel). Both time series are in 10-min resolution

APPENDIX A: COMPARISON OF RAIN GAUGE AND RADAR DATA

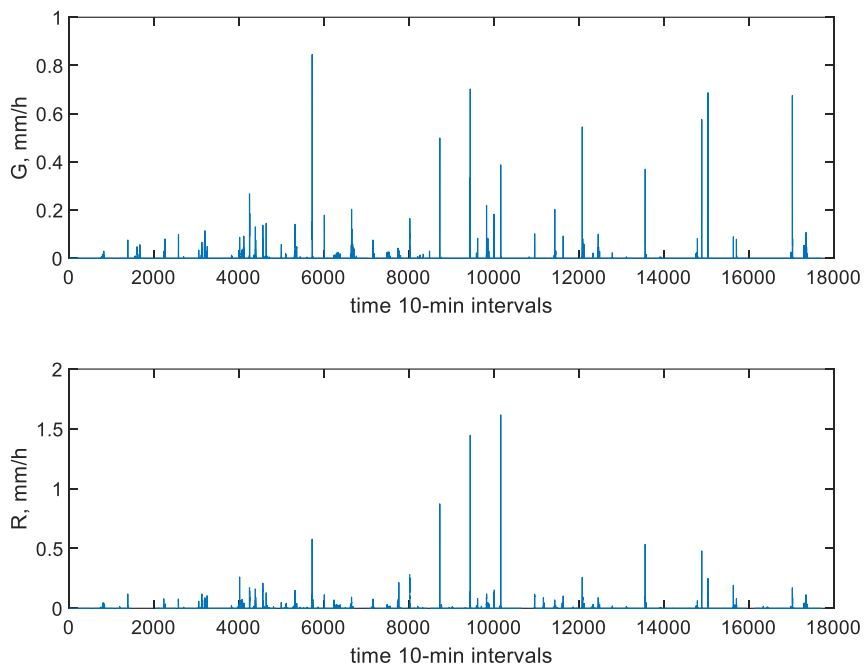


A-23 Rainfall intensity series recorded by gauge R23 (G) during summer months (May-August) 2009 (upper panel) and coincident in space radar rainfall intensity (R) series for the same period (lower panel). Both time series are in 10-min resolution

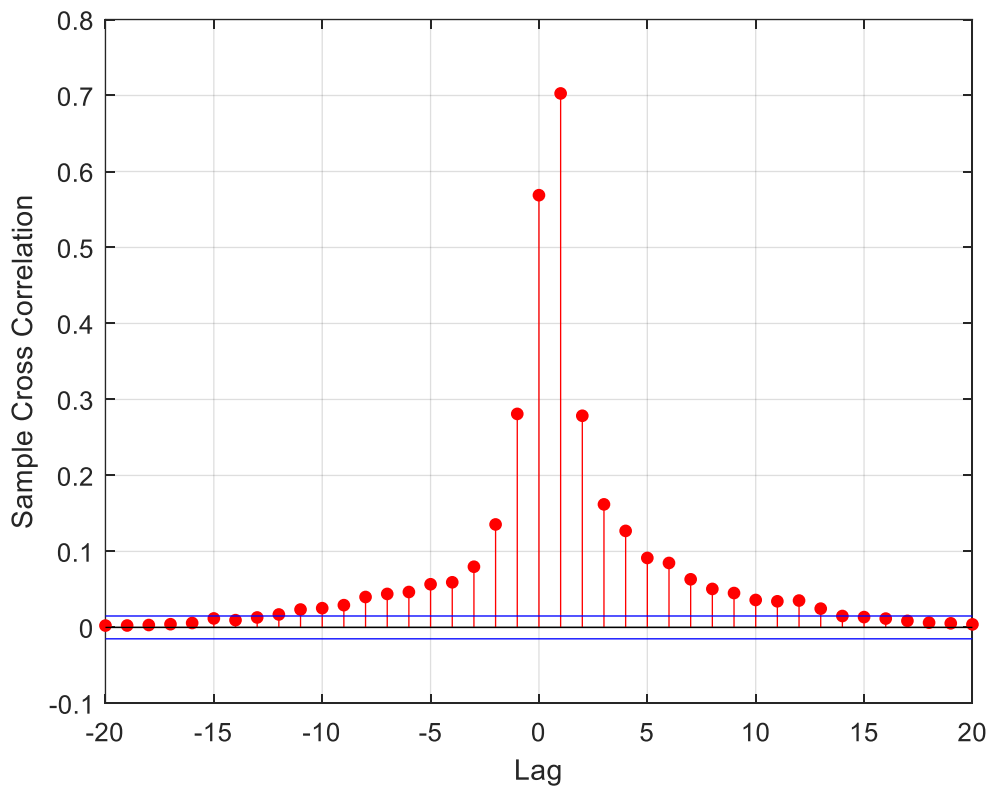


A-24 Rainfall intensity series recorded by gauge R24 (G) during summer months (May-August) 2009 (upper panel) and coincident in space radar rainfall intensity (R) series for the same period (lower panel). Both time series are in 10-min resolution

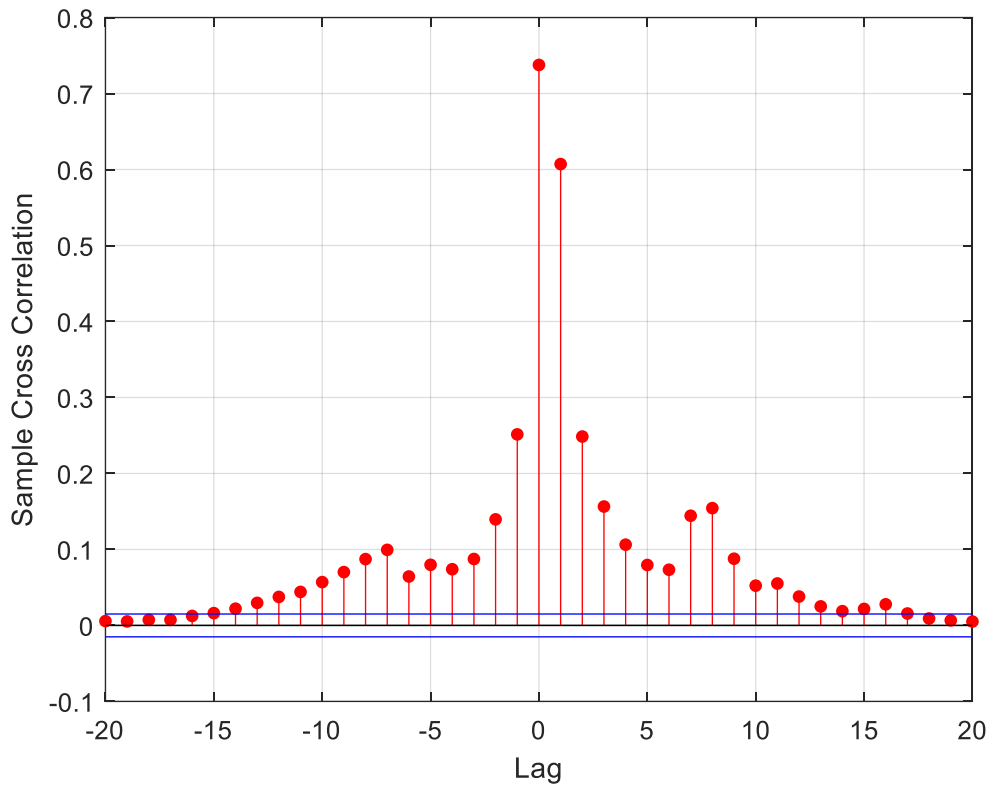
APPENDIX A: COMPARISON OF RAIN GAUGE AND RADAR DATA



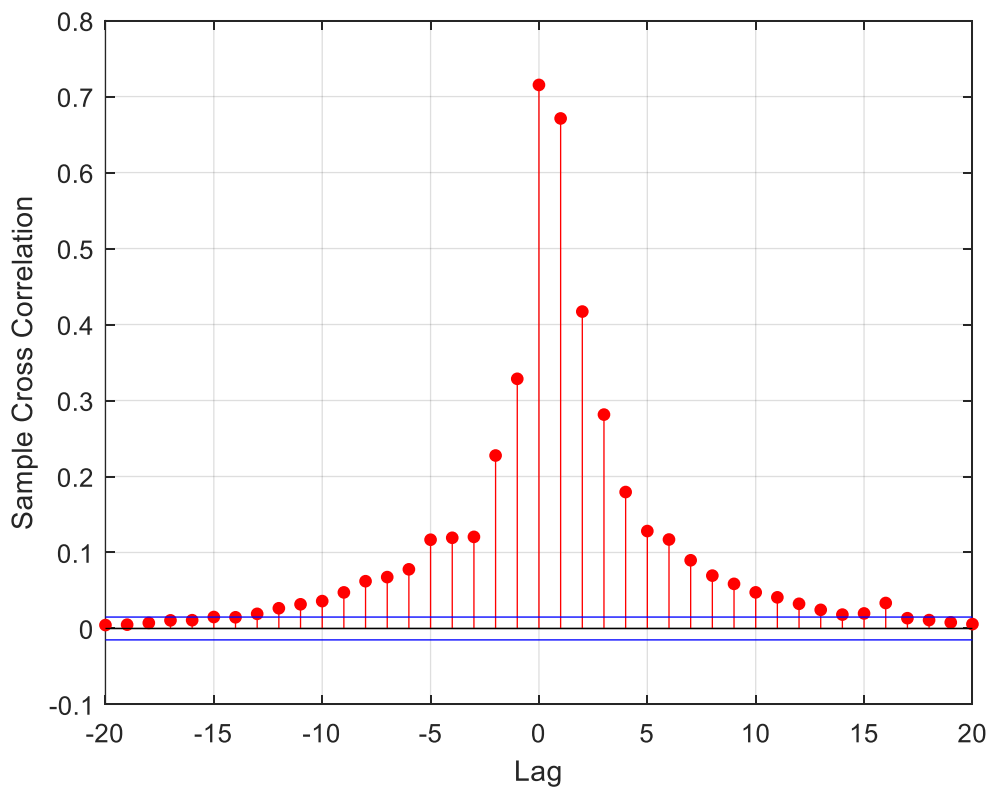
A-25 Rainfall intensity series recorded by gauge R25 (G) during summer months (May-August) 2009 (upper panel) and coincident in space radar rainfall intensity (R) series for the same period (lower panel). Both time series are in 10-min resolution



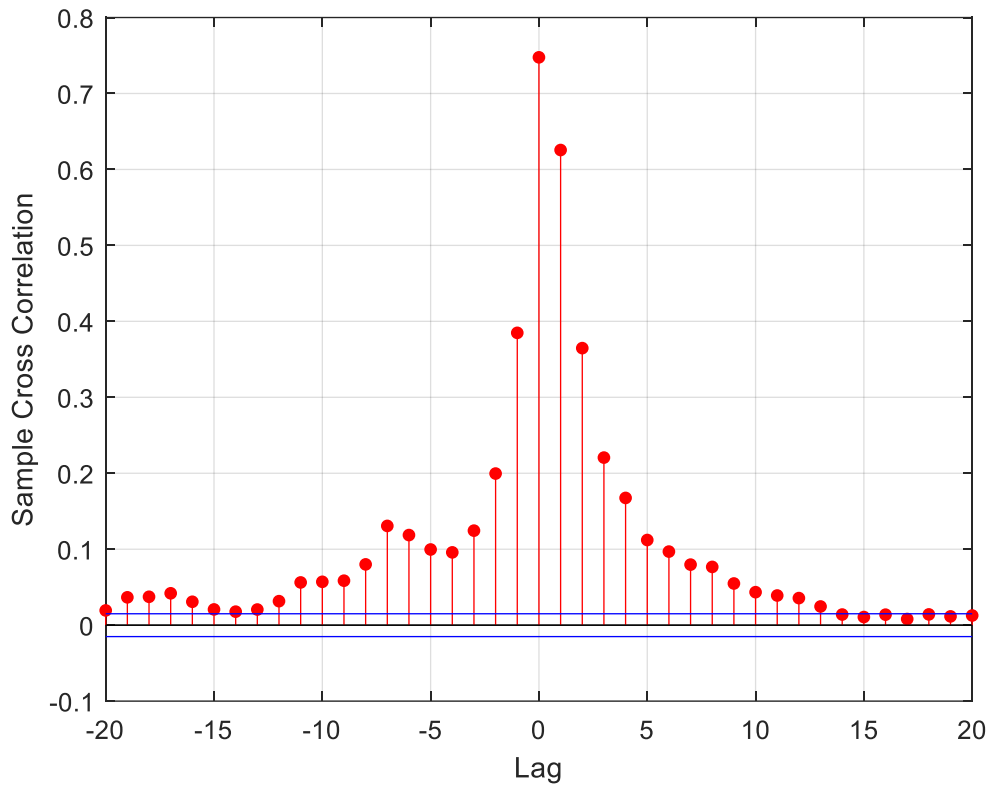
A-26 Cross correlation of rainfall intensity time series registered by gauge (G) and radar (R) for gauge R1 location



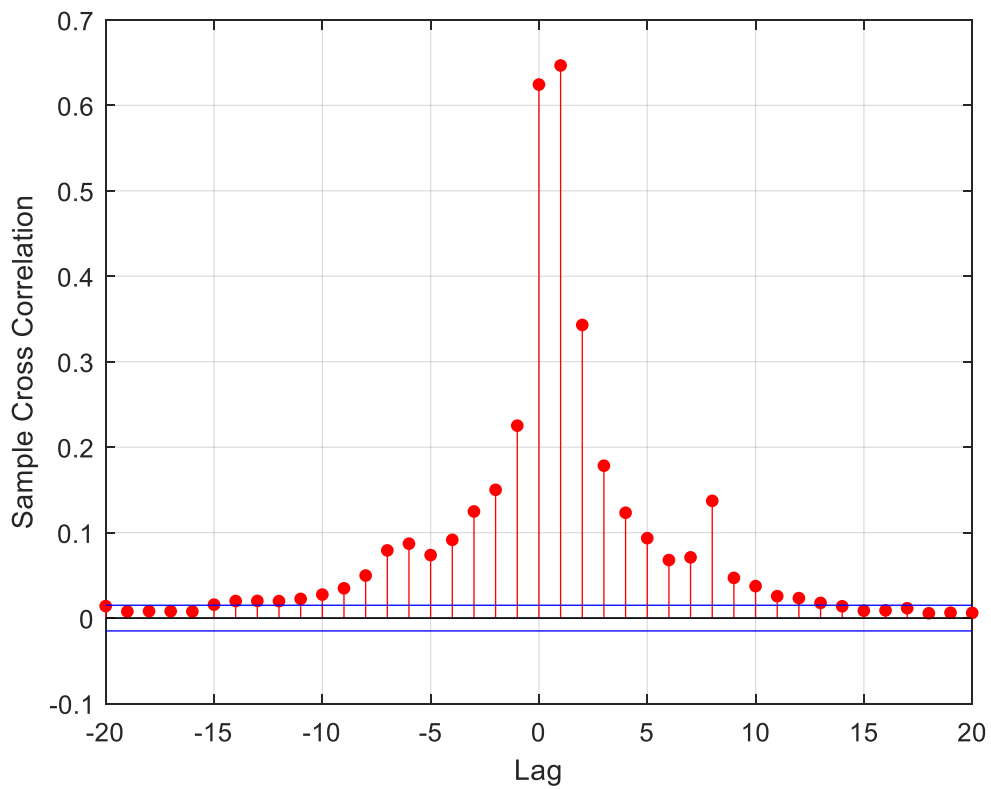
A-27 Cross correlation of rainfall intensity time series registered by gauge (G) and radar (R) for gauge R2 location



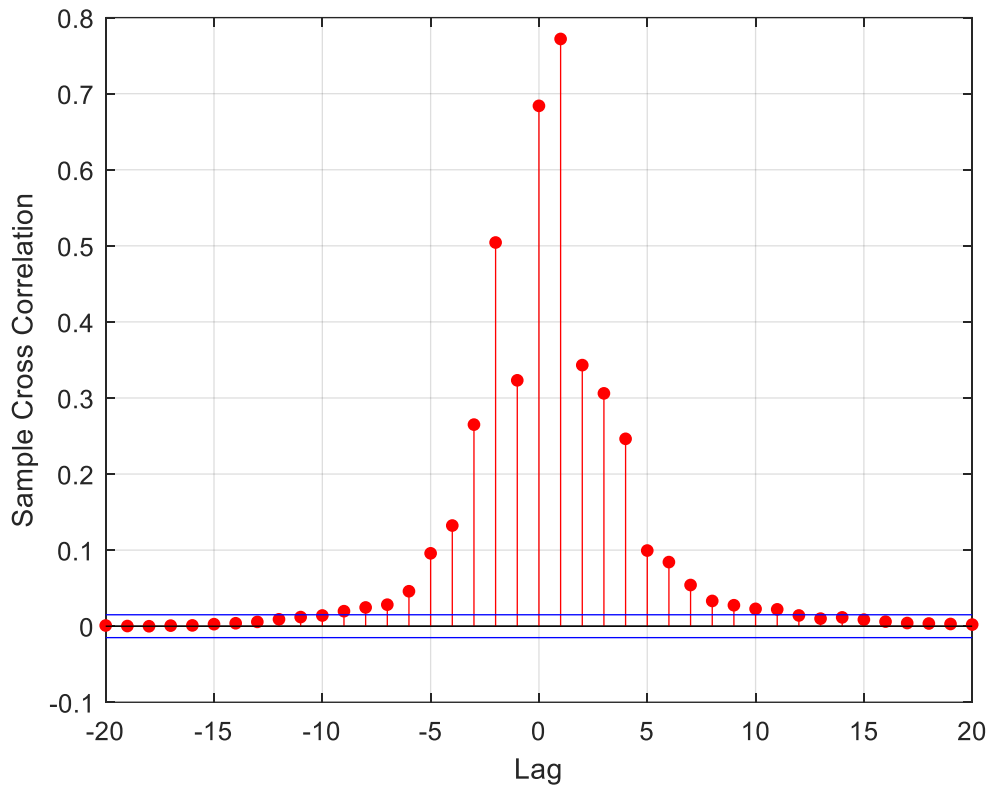
A-28 Cross correlation of rainfall intensity time series registered by gauge (G) and radar (R) for gauge R3 location



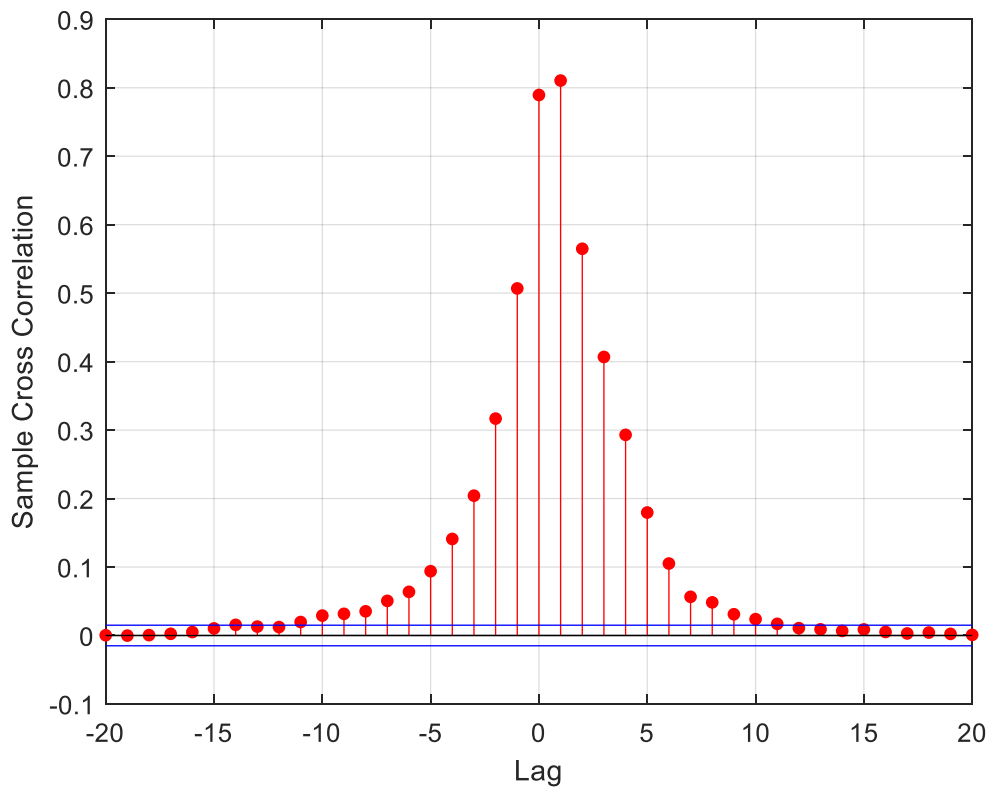
A-29 Cross correlation of rainfall intensity time series registered by gauge (G) and radar (R) for gauge R4 location



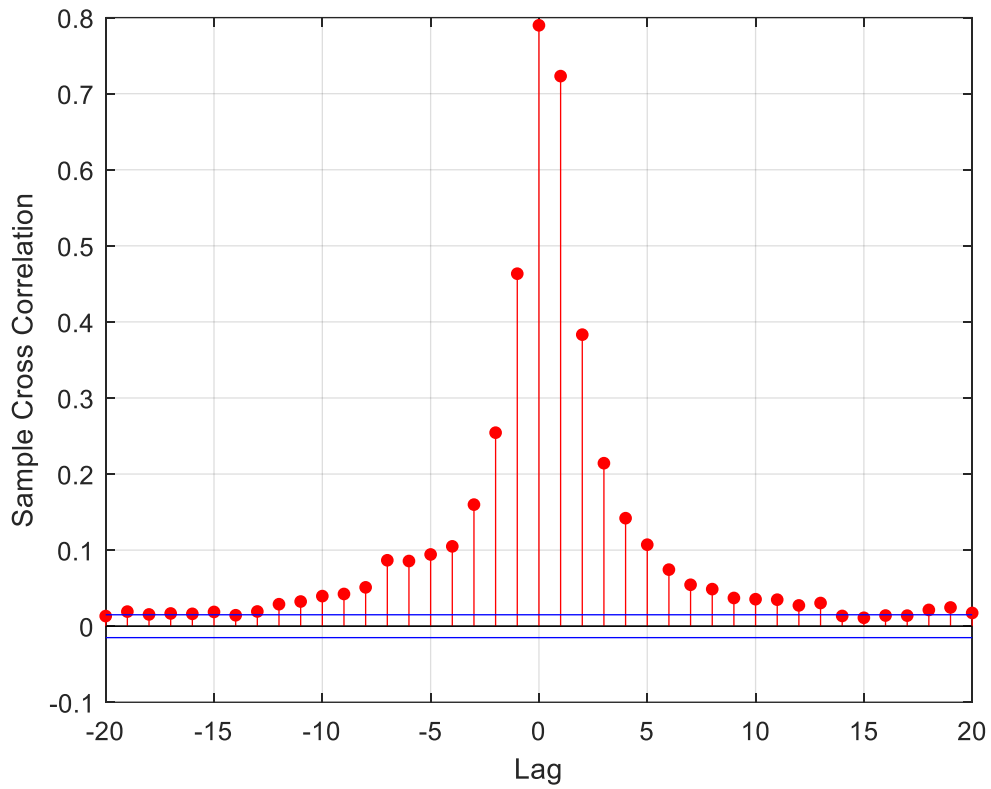
A-30 Cross correlation of rainfall intensity time series registered by gauge (G) and radar (R) for gauge R5 location



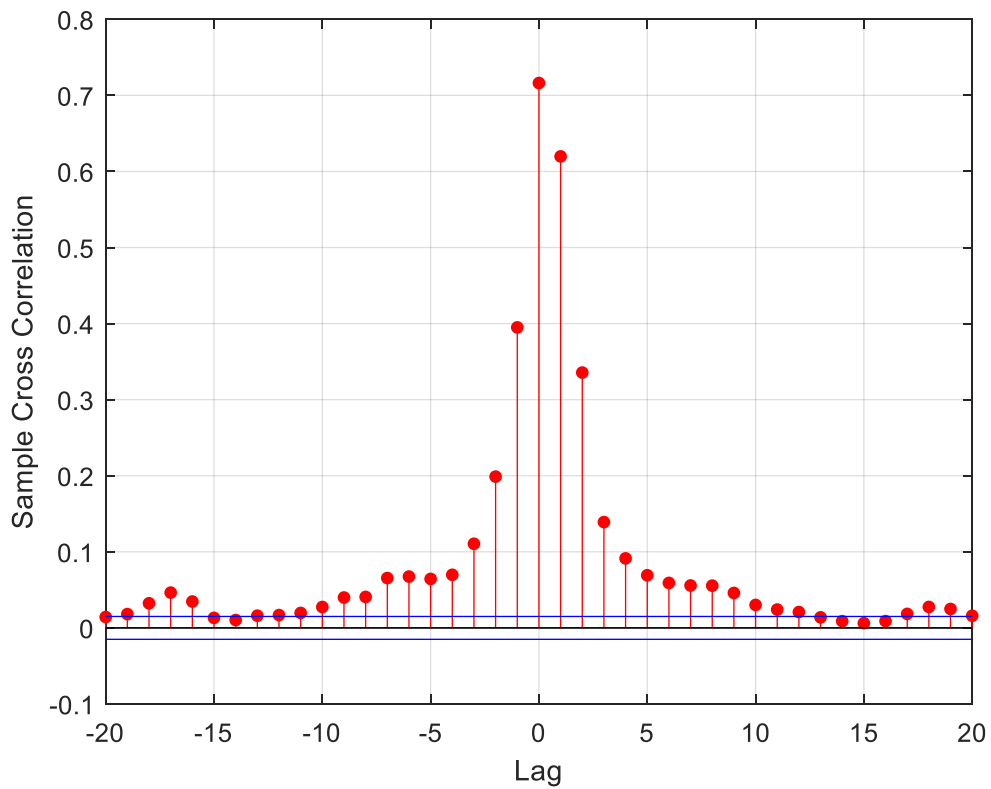
A-31 Cross correlation of rainfall intensity time series registered by gauge (G) and radar (R) for gauge R6 location



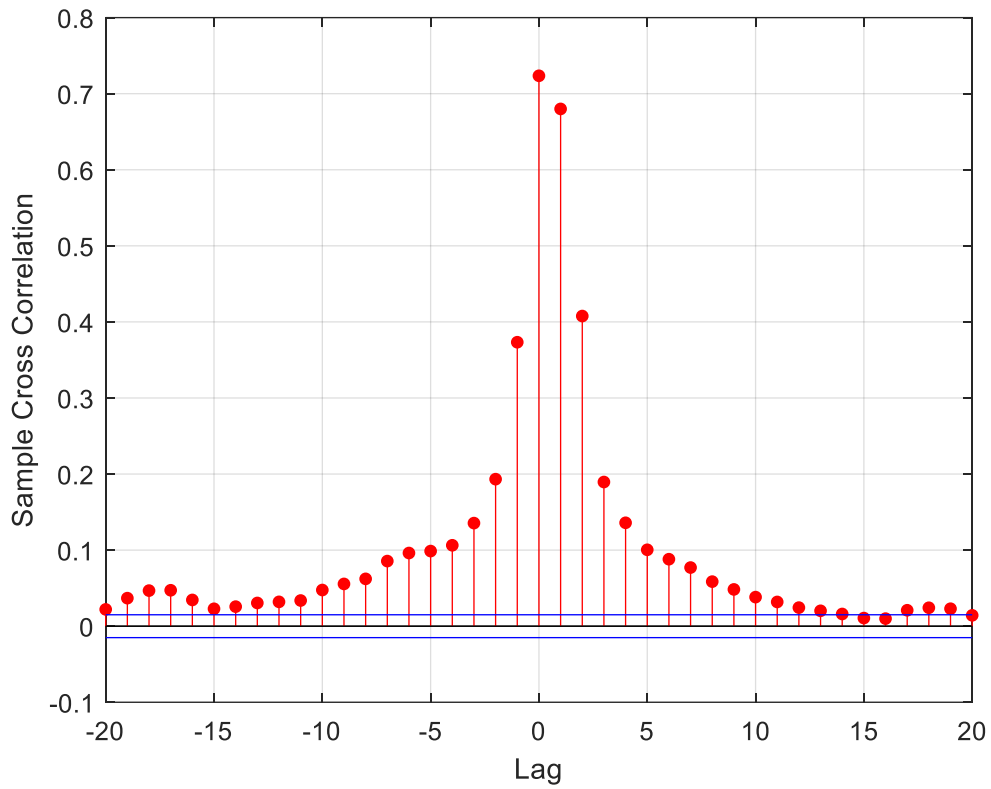
A-32 Cross correlation of rainfall intensity time series registered by gauge (G) and radar (R) for gauge R7 location



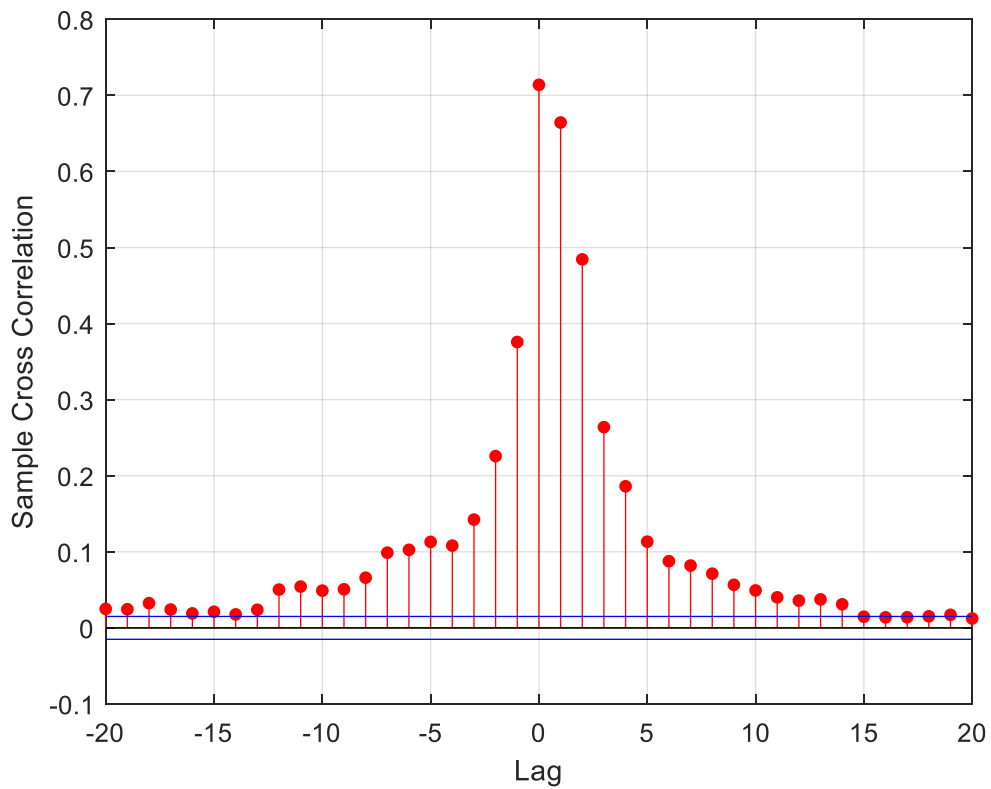
A-33 Cross correlation of rainfall intensity time series registered by gauge (G) and radar (R) for gauge R8 location



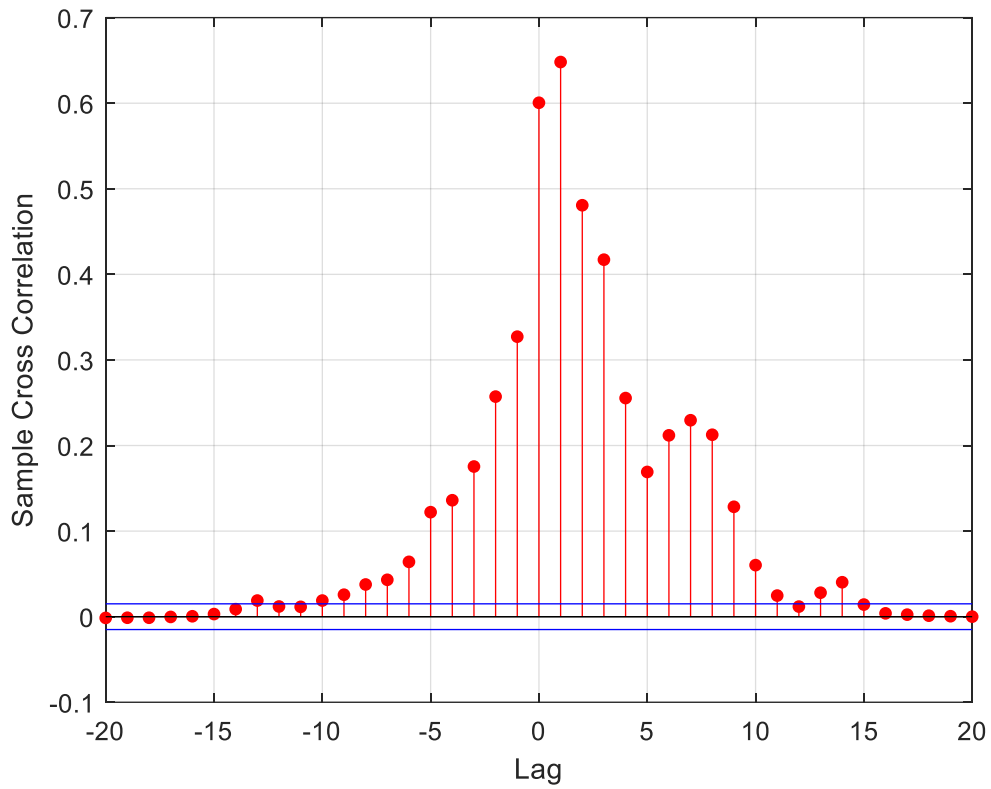
A-34 Cross correlation of rainfall intensity time series registered by gauge (G) and radar (R) for gauge R9 location



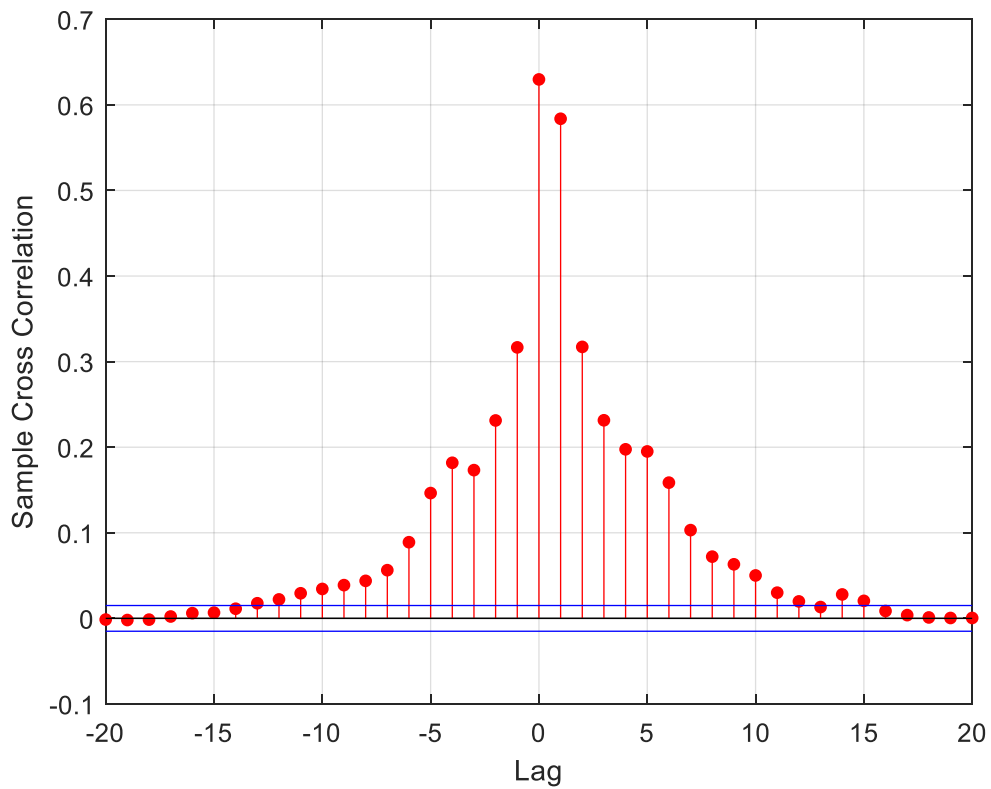
A-35 Cross correlation of rainfall intensity time series registered by gauge (G) and radar (R) for gauge R10 location



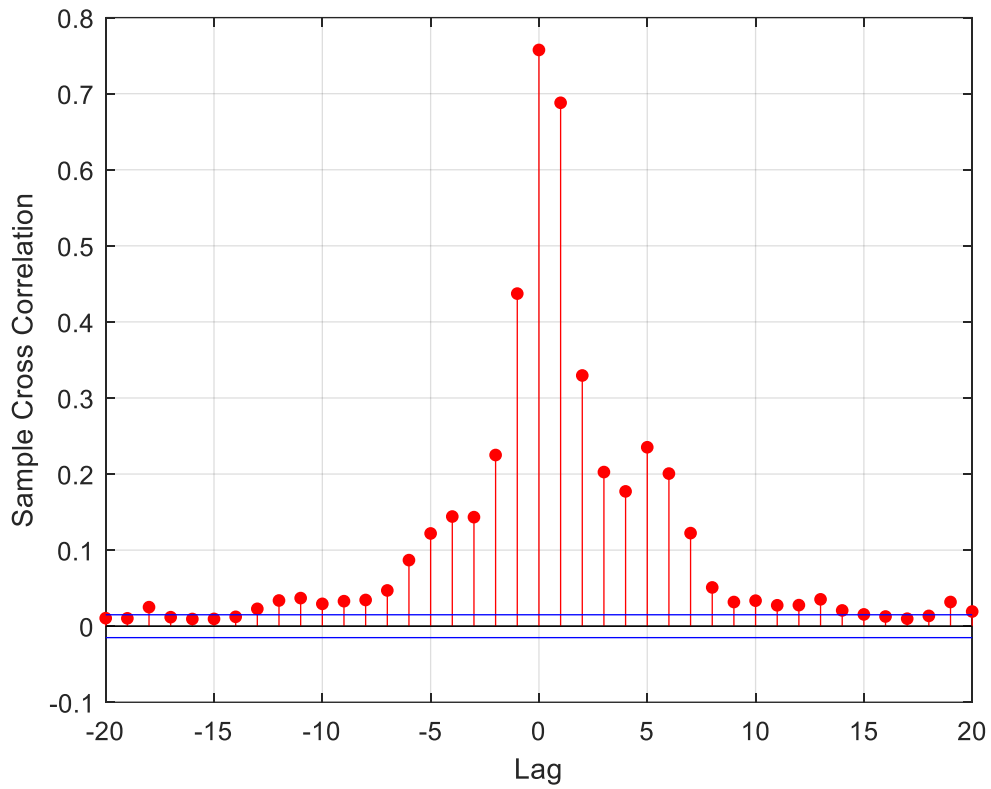
A-36 Cross correlation of rainfall intensity time series registered by gauge (G) and radar (R) for gauge R11 location



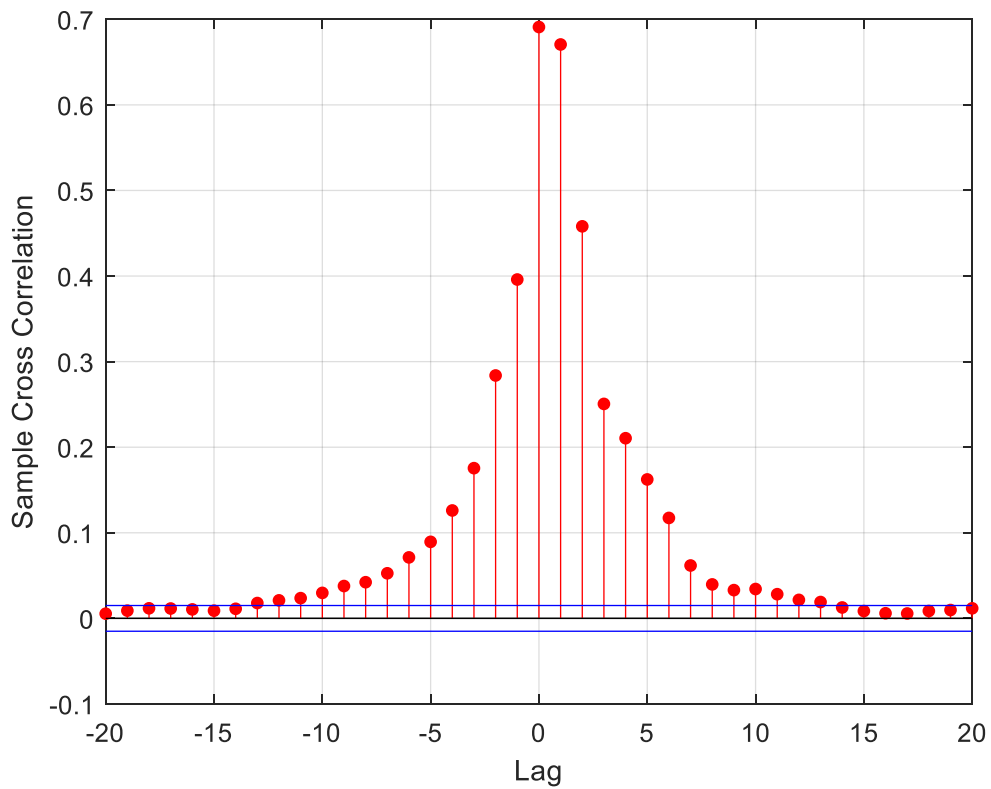
A-37 Cross correlation of rainfall intensity time series registered by gauge (G) and radar (R) for gauge R12 location



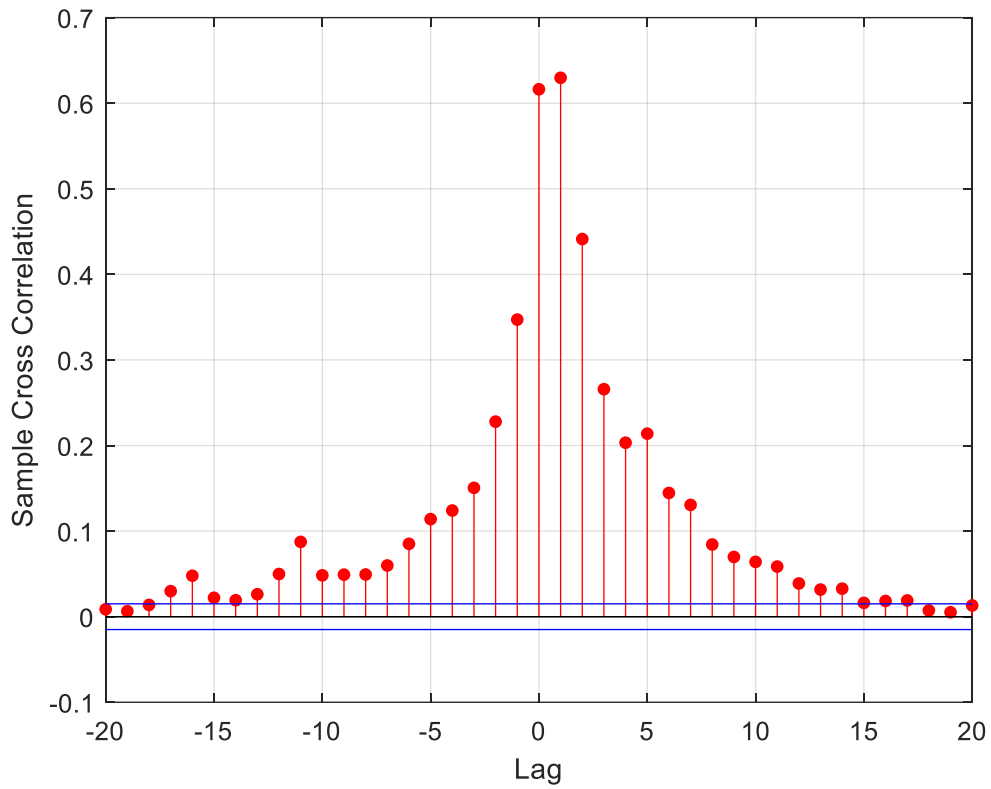
A-38 Cross correlation of rainfall intensity time series registered by gauge (G) and radar (R) for gauge R13 location



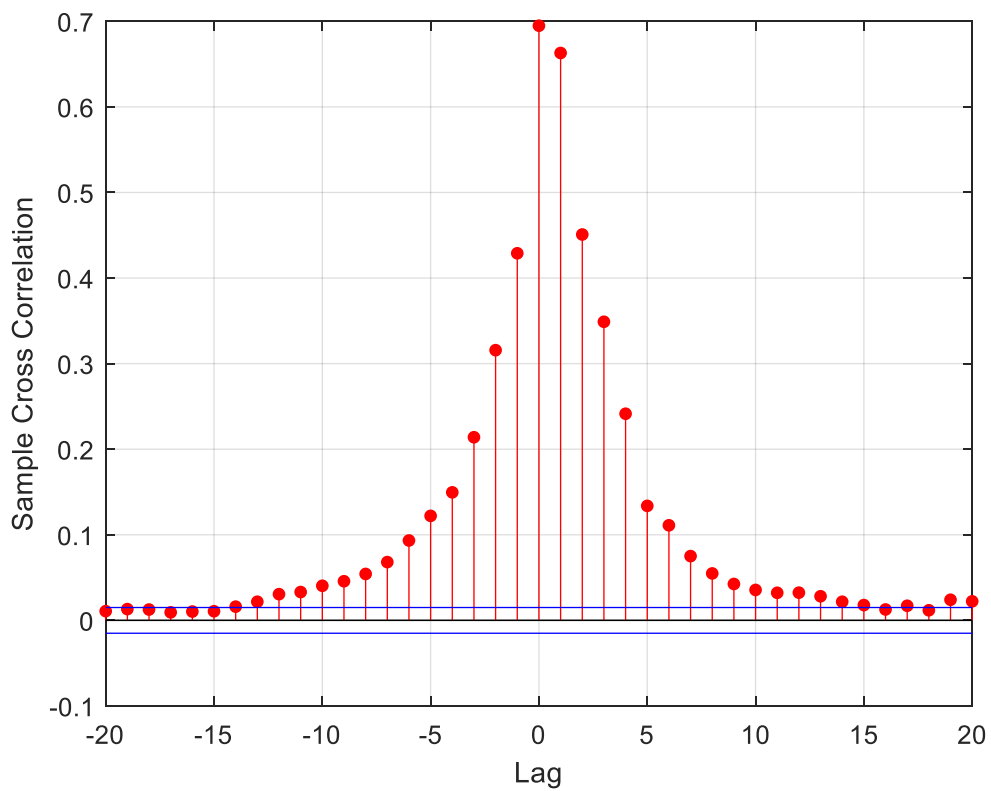
A-39 Cross correlation of rainfall intensity time series registered by gauge (G) and radar (R) for gauge R14 location



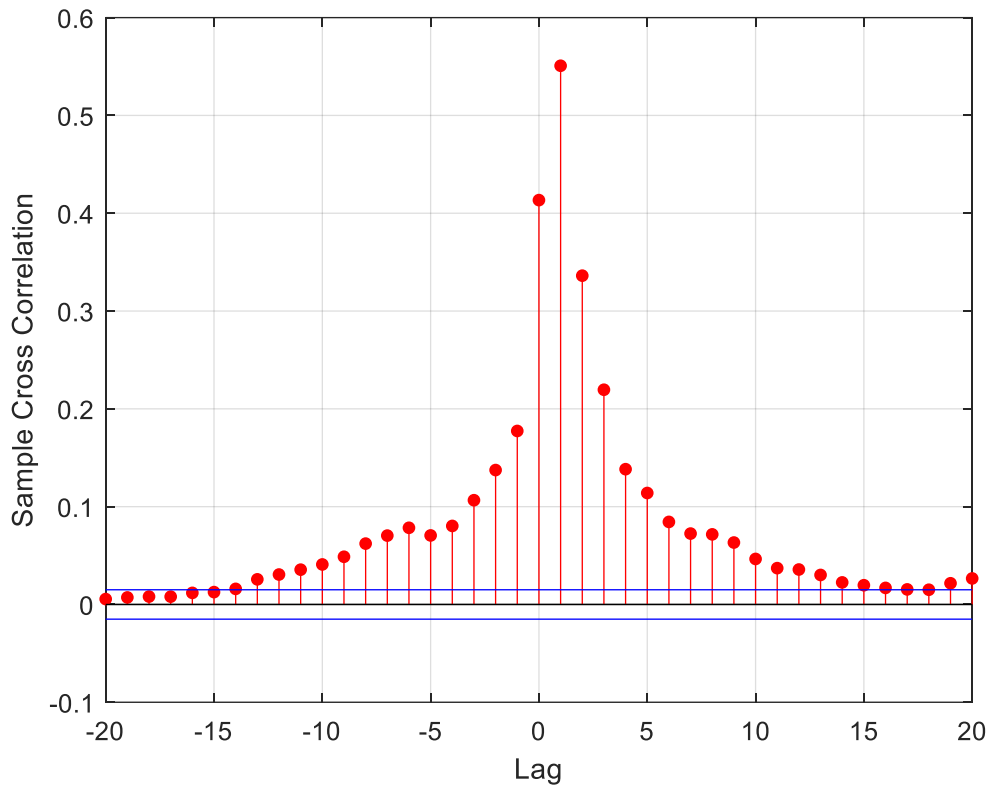
A-40 Cross correlation of rainfall intensity time series registered by gauge (G) and radar (R) for gauge R15 location



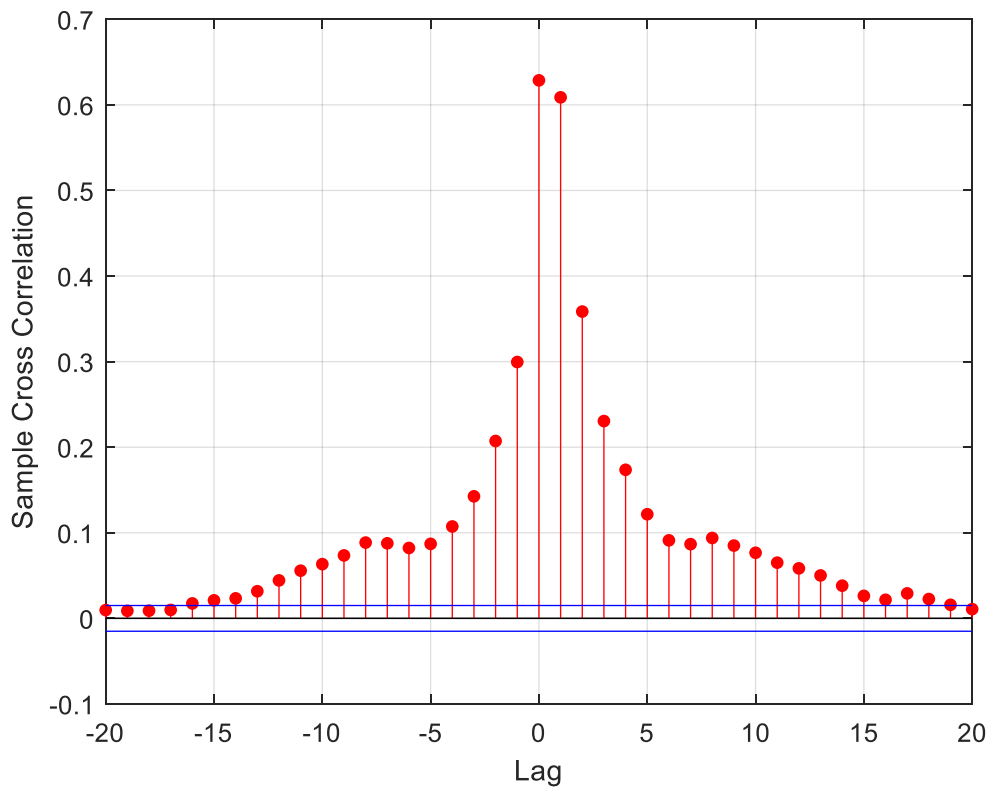
A-41 Cross correlation of rainfall intensity time series registered by gauge (G) and radar (R) for gauge R16 location



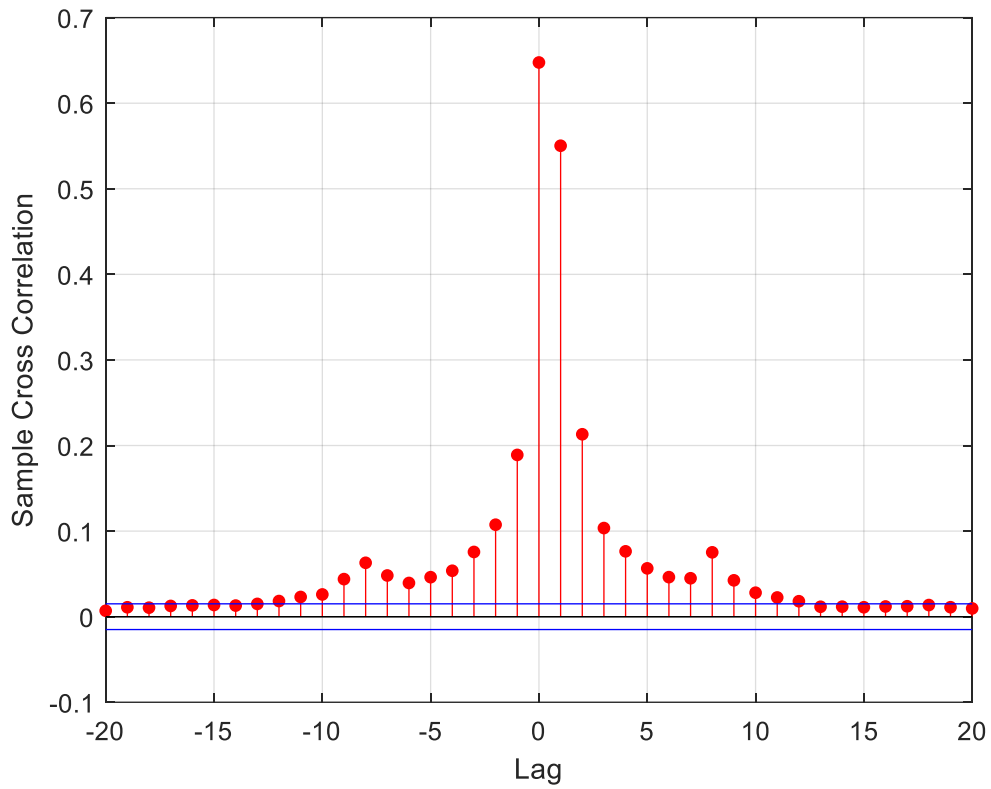
A-42 Cross correlation of rainfall intensity time series registered by gauge (G) and radar (R) for gauge R17 location



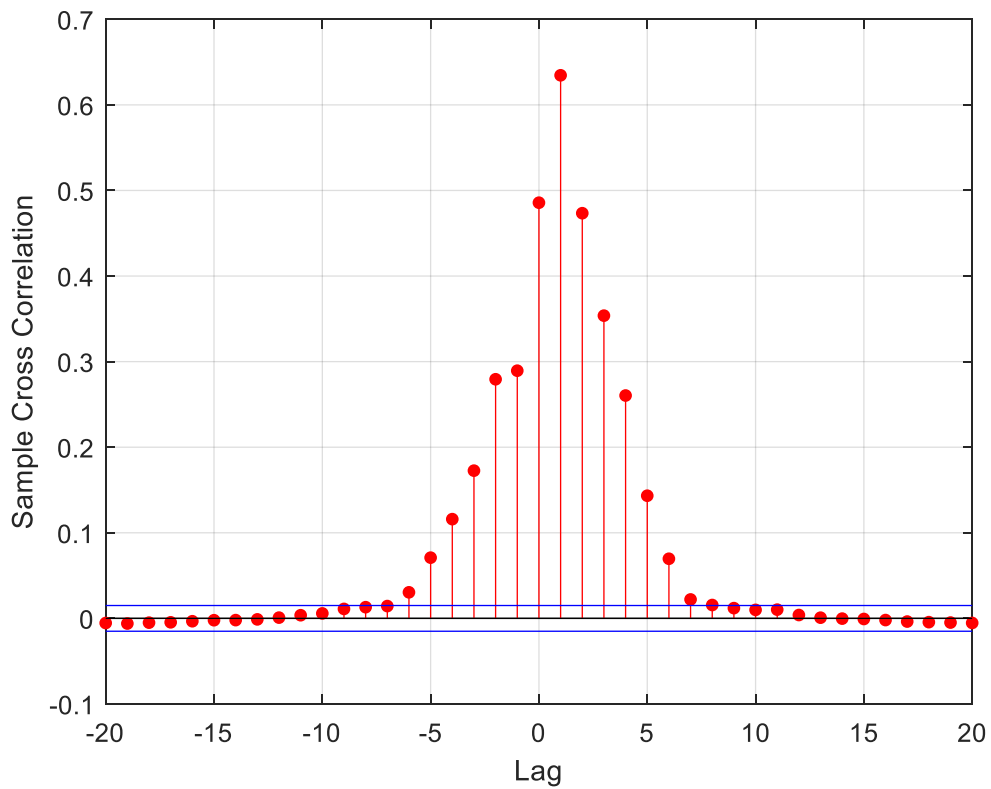
A-43 Cross correlation of rainfall intensity time series registered by gauge (G) and radar (R) for gauge R18 location



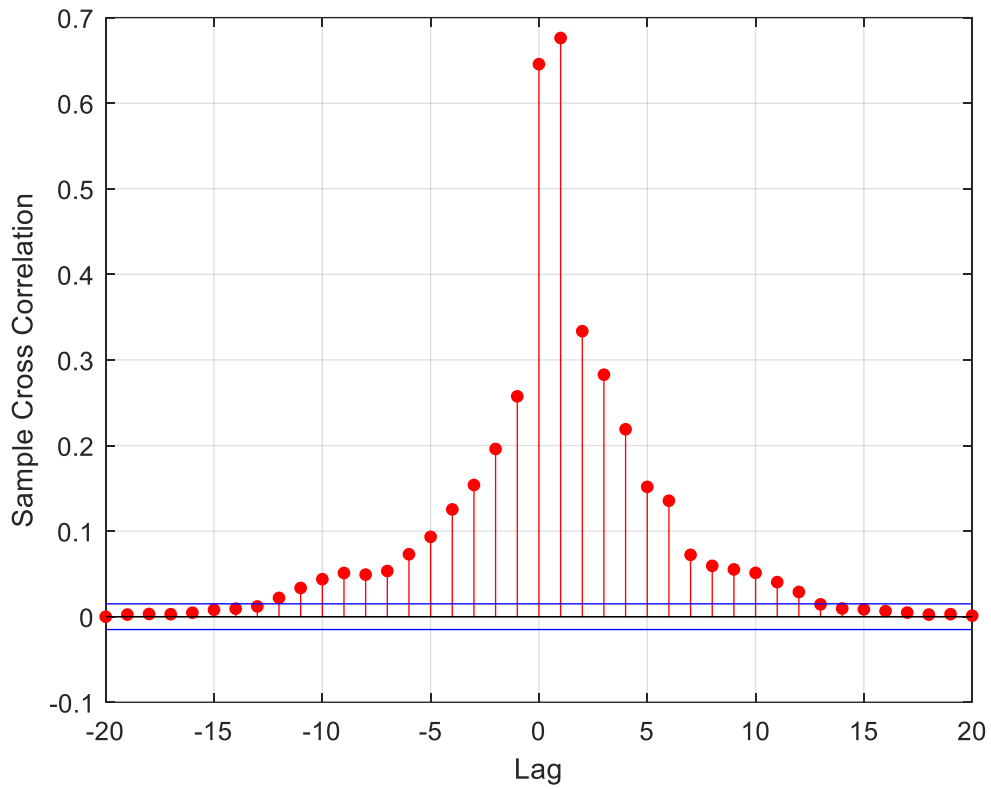
A-44 Cross correlation of rainfall intensity time series registered by gauge (G) and radar (R) for gauge R19 location



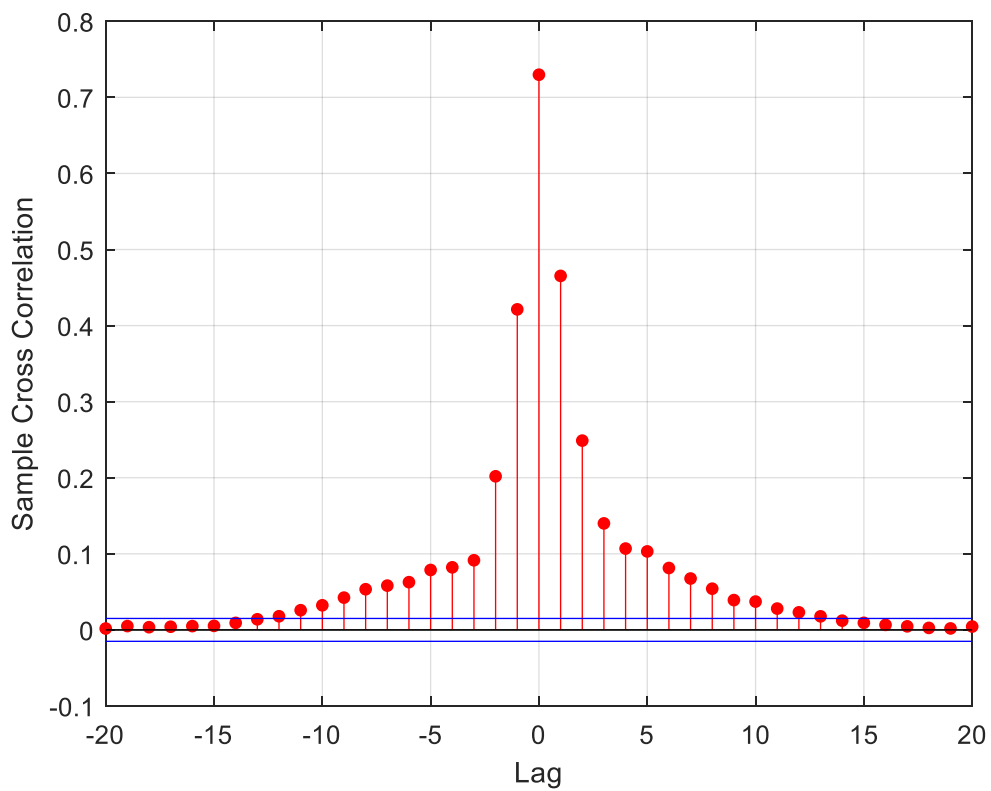
A-45 Cross correlation of rainfall intensity time series registered by gauge (G) and radar (R) for gauge R20 location



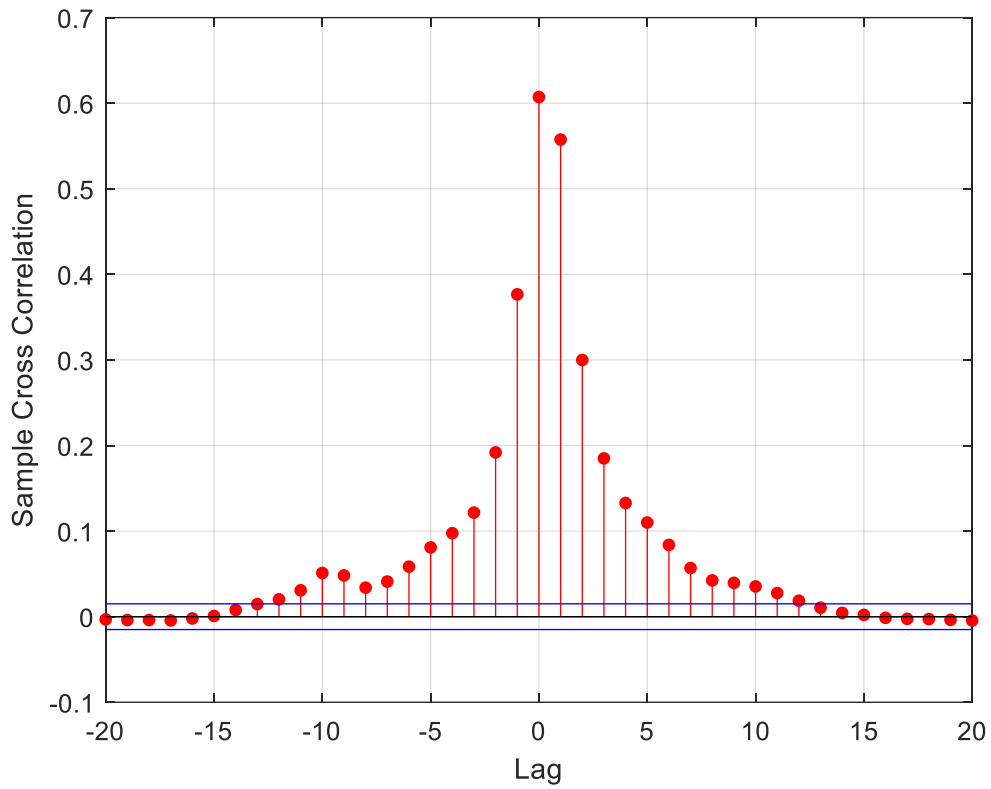
A-46 Cross correlation of rainfall intensity time series registered by gauge (G) and radar (R) for gauge R21 location



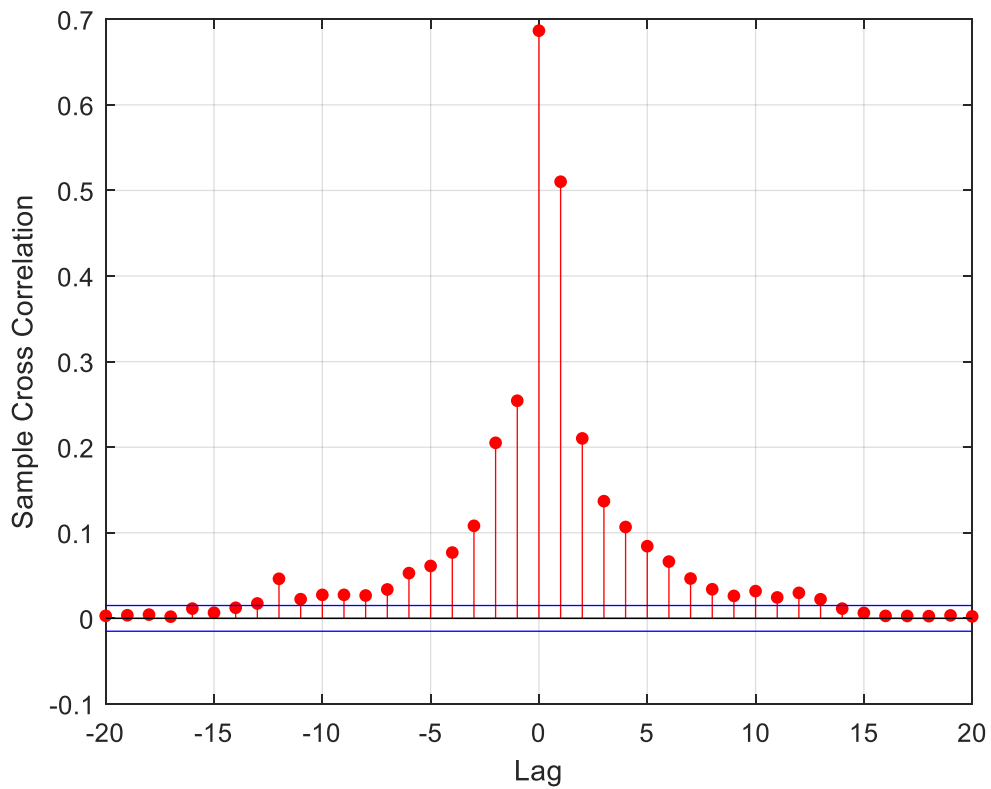
A-47 Cross correlation of rainfall intensity time series registered by gauge (G) and radar (R) for gauge R22 location



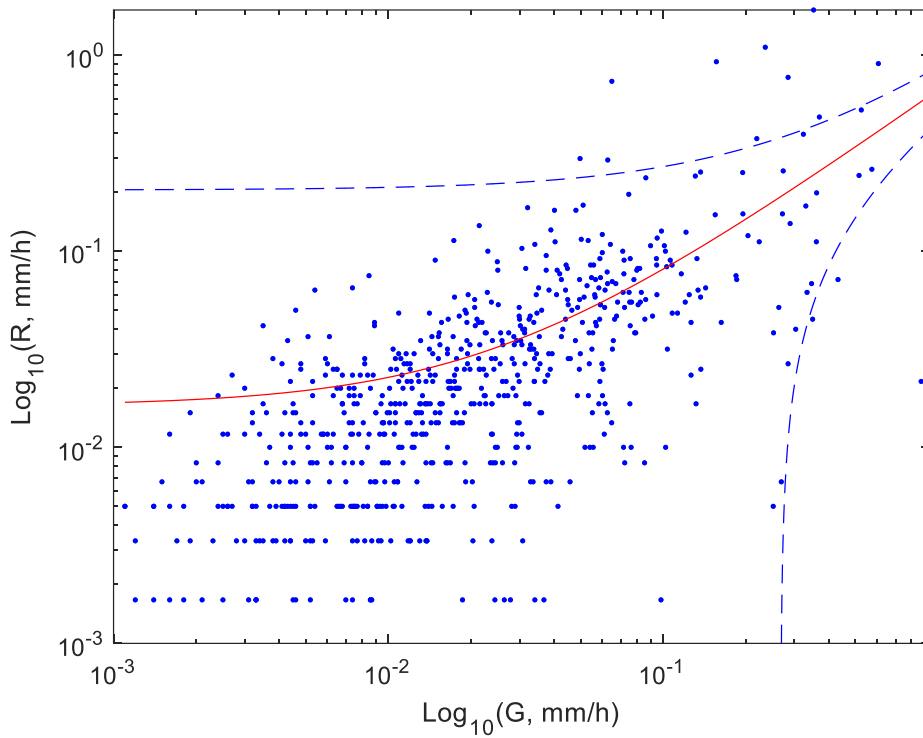
A-48 Cross correlation of rainfall intensity time series registered by gauge (G) and radar (R) for gauge R23 location



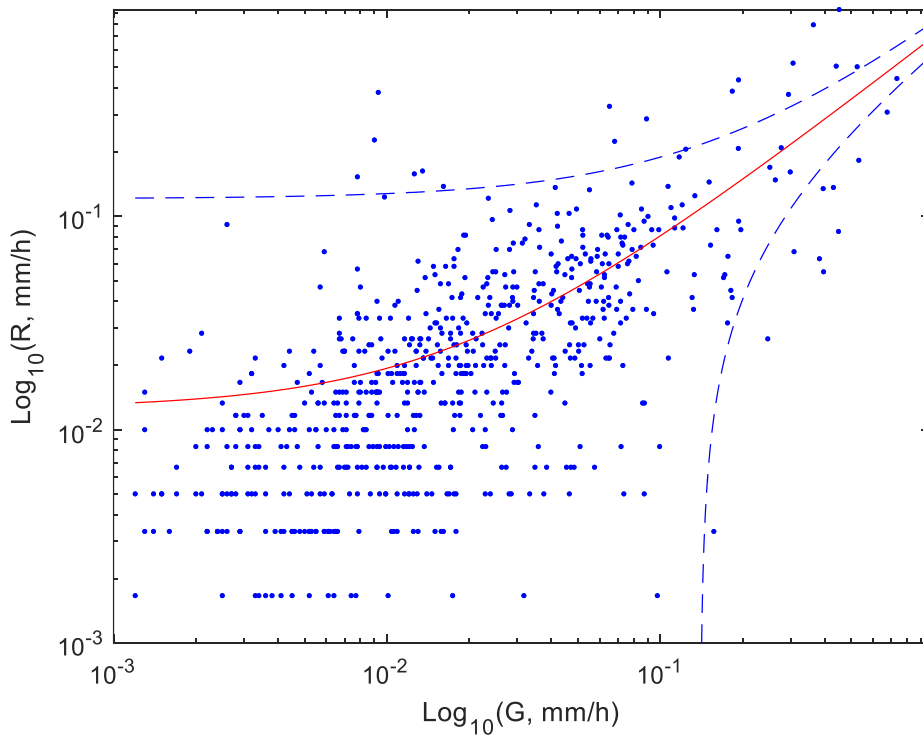
A-49 Cross correlation of rainfall intensity time series registered by gauge (G) and radar (R) for gauge R24 location



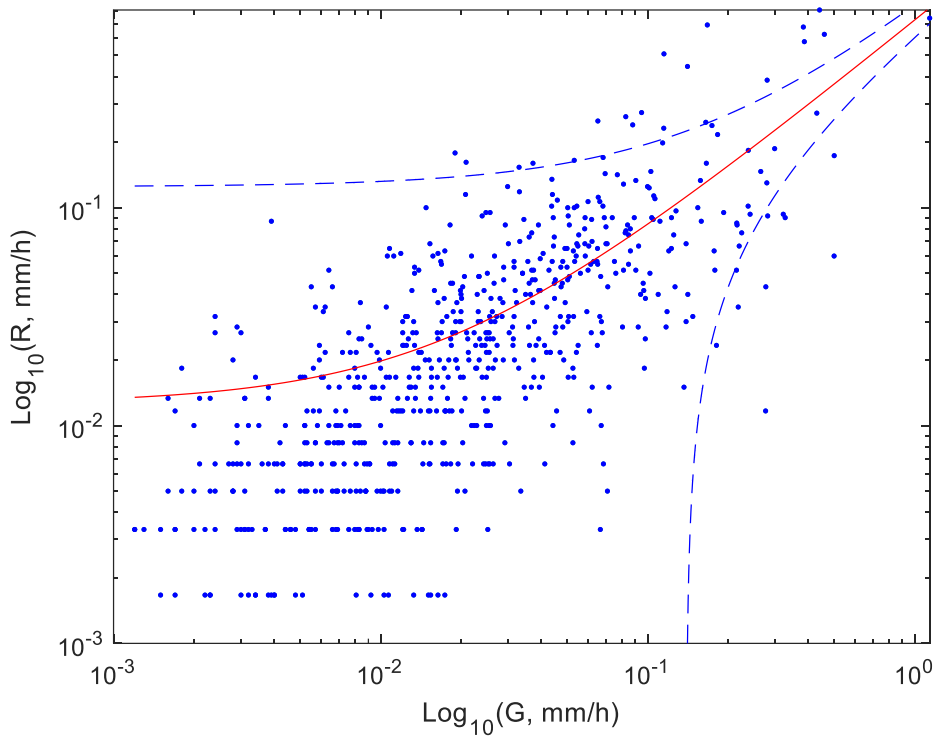
A-50 Cross correlation of rainfall intensity time series registered by gauge (G) and radar (R) for gauge R25 location



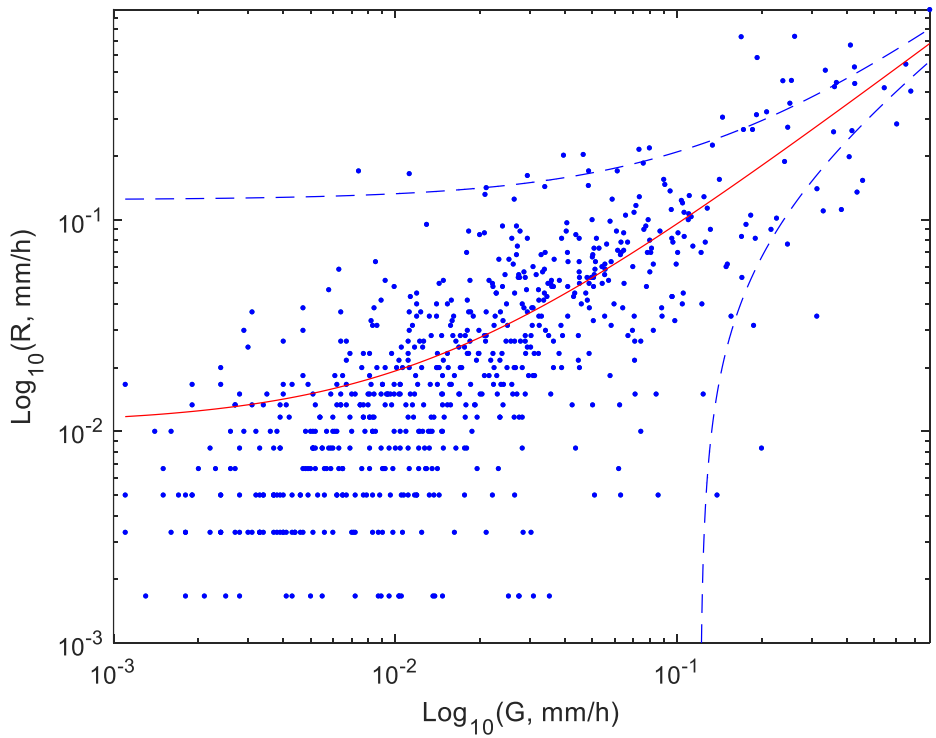
A-51 Log-log plot of 10-min non-zero radar rainfall intensity R values versus non-zero rainfall intensity G values from gauge R1 for summer months of 2009 with best fitted linear function with its 95% confidence intervals



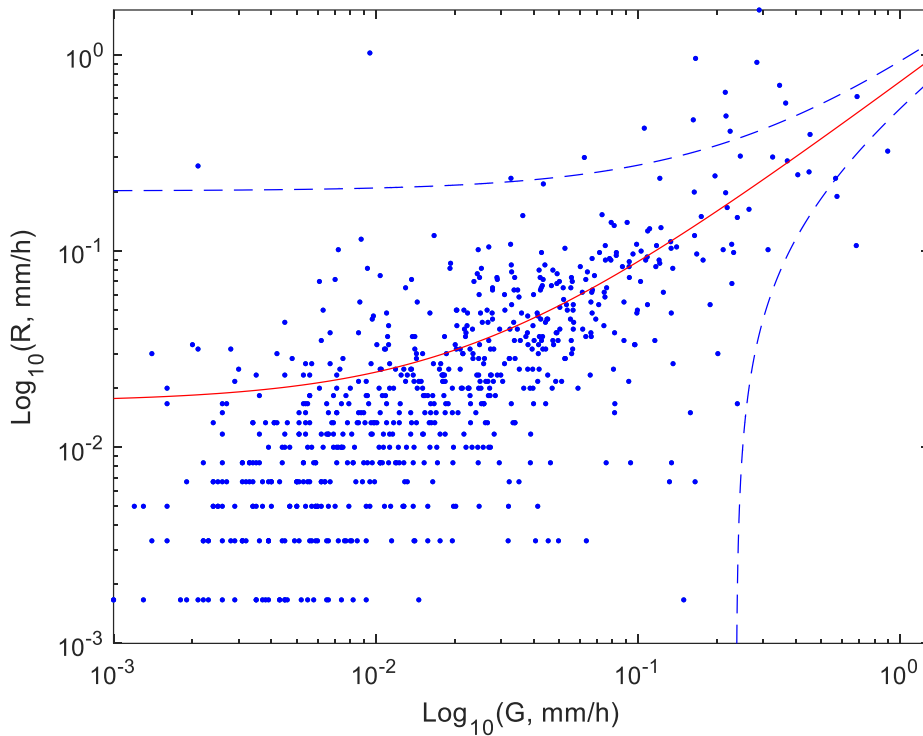
A-52 Log-log plot of 10-min non-zero radar rainfall intensity R values versus non-zero rainfall intensity G values from gauge R2 for summer months of 2009 with best fitted linear function with its 95% confidence intervals



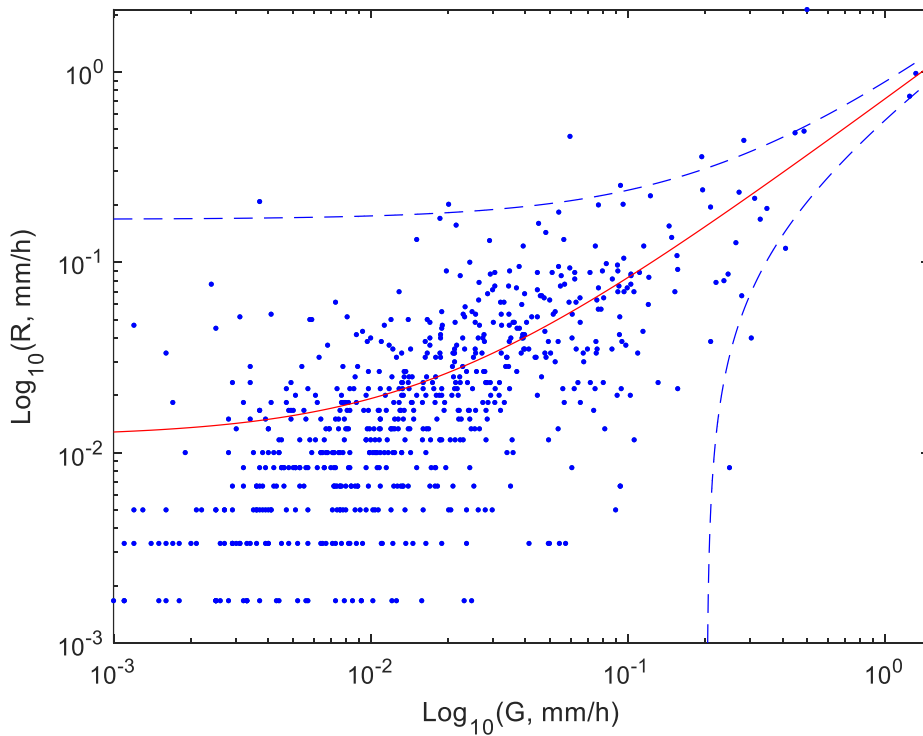
A-53 Log-log plot of 10-min non-zero radar rainfall intensity R values versus non-zero rainfall intensity G values from gauge R3 for summer months of 2009 with best fitted linear function with its 95% confidence intervals



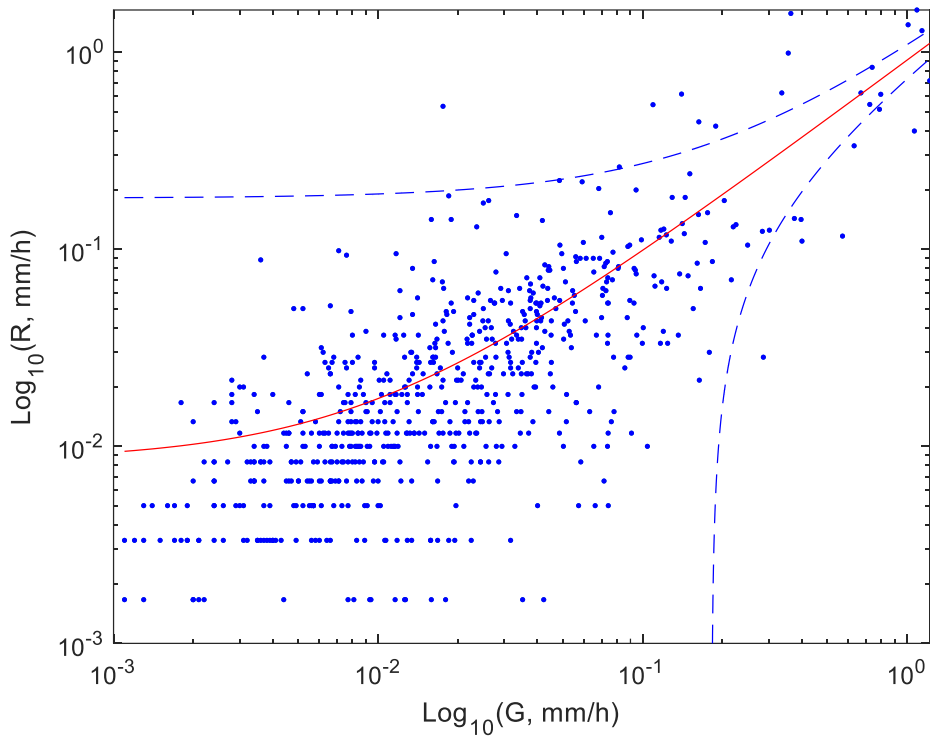
A-54 Log-log plot of 10-min non-zero radar rainfall intensity R values versus non-zero rainfall intensity G values from gauge R4 for summer months of 2009 with best fitted linear function with its 95% confidence intervals



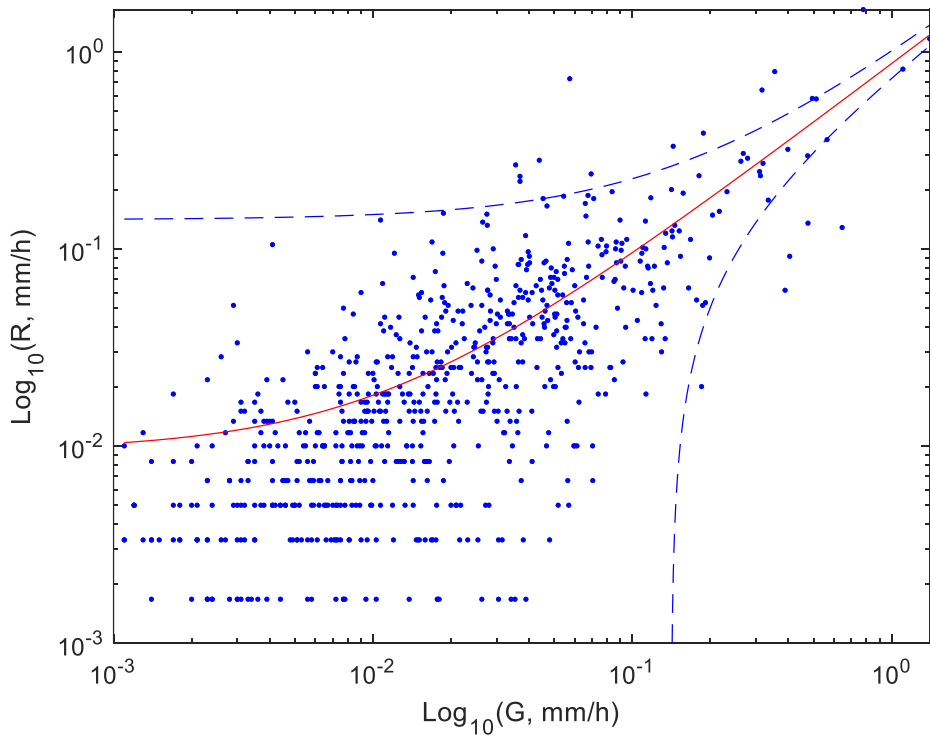
A-55 Log-log plot of 10-min non-zero radar rainfall intensity R values versus non-zero rainfall intensity G values from gauge R5 for summer months of 2009 with best fitted linear function with its 95% confidence intervals



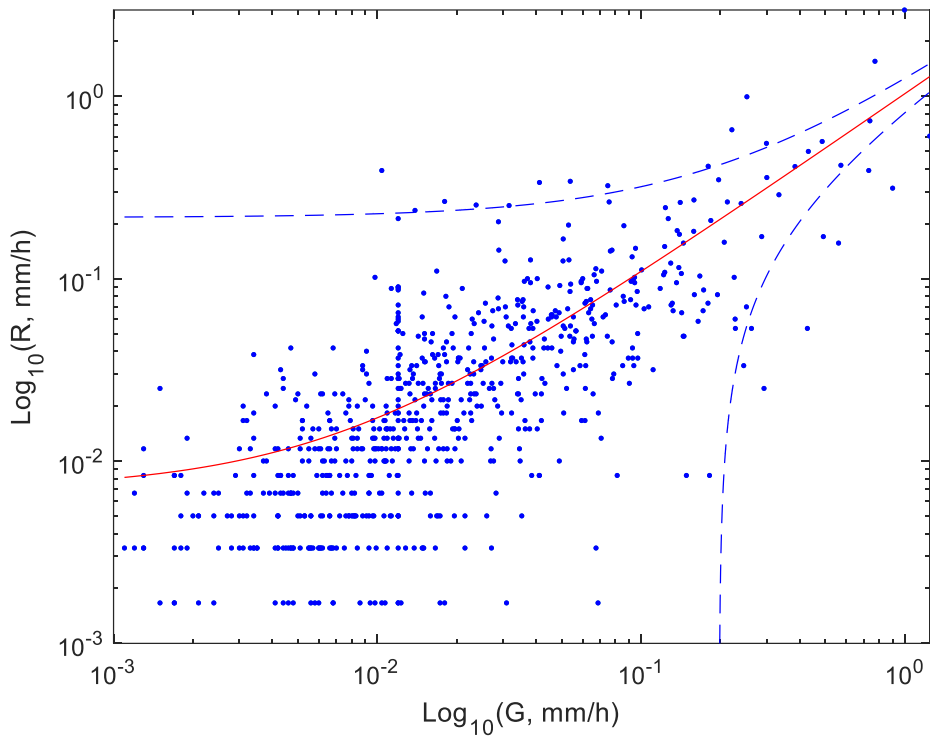
A-56 Log-log plot of 10-min non-zero radar rainfall intensity R values versus non-zero rainfall intensity G values from gauge R6 for summer months of 2009 with best fitted linear function with its 95% confidence intervals



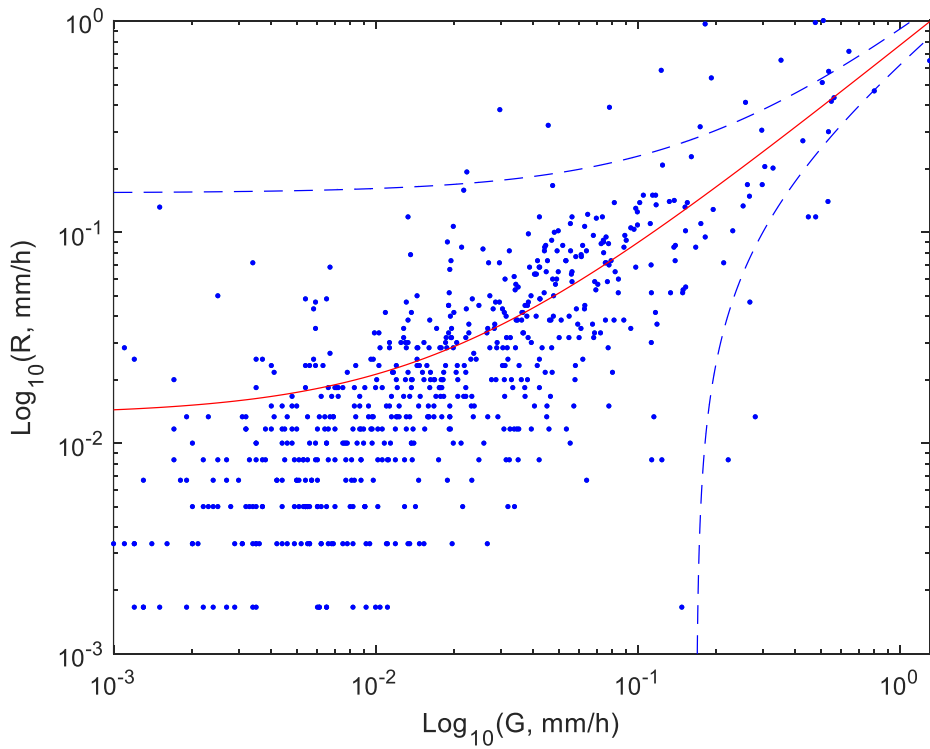
A-57 Log-log plot of 10-min non-zero radar rainfall intensity R values versus non-zero rainfall intensity G values from gauge R7 for summer months of 2009 with best fitted linear function with its 95% confidence intervals



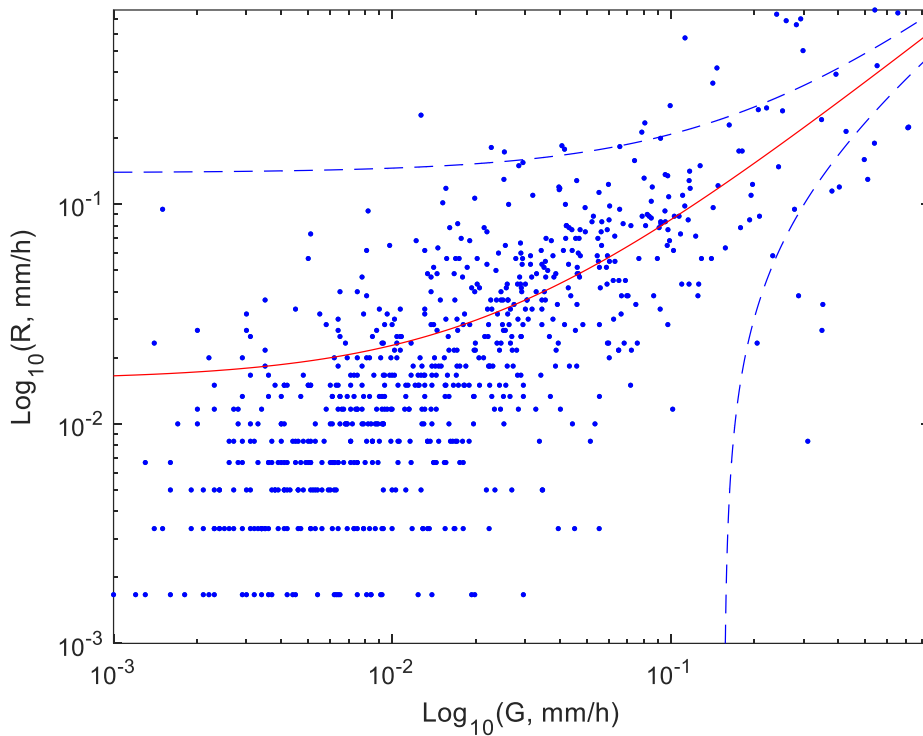
A-58 Log-log plot of 10-min non-zero radar rainfall intensity R values versus non-zero rainfall intensity G values from gauge R8 for summer months of 2009 with best fitted linear function with its 95% confidence intervals



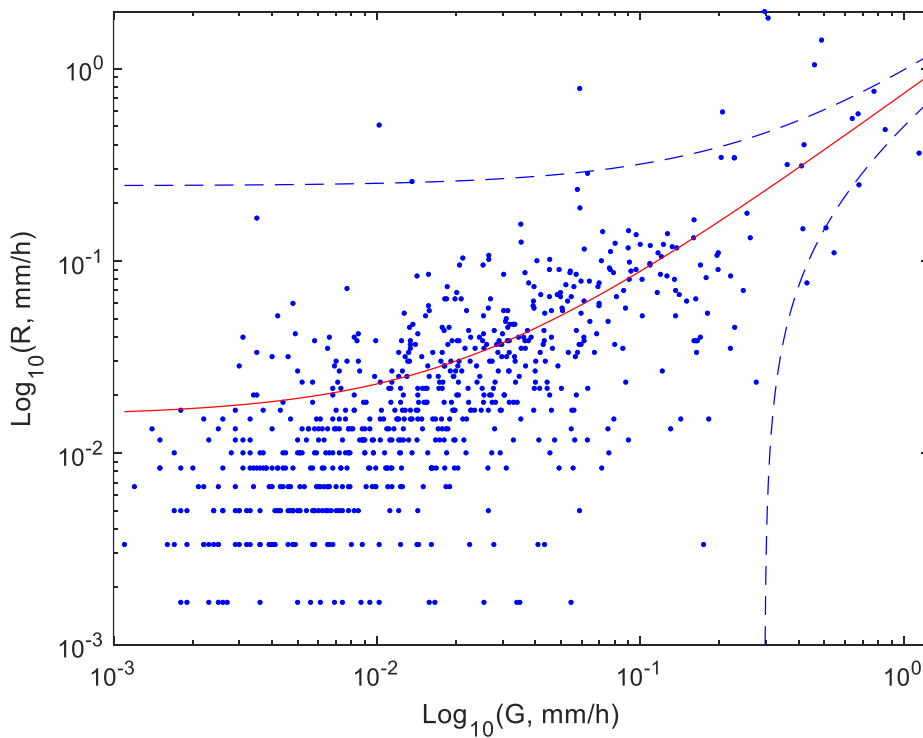
A-59 Log-log plot of 10-min non-zero radar rainfall intensity R values versus non-zero rainfall intensity G values from gauge R9 for summer months of 2009 with best fitted linear function with its 95% confidence intervals



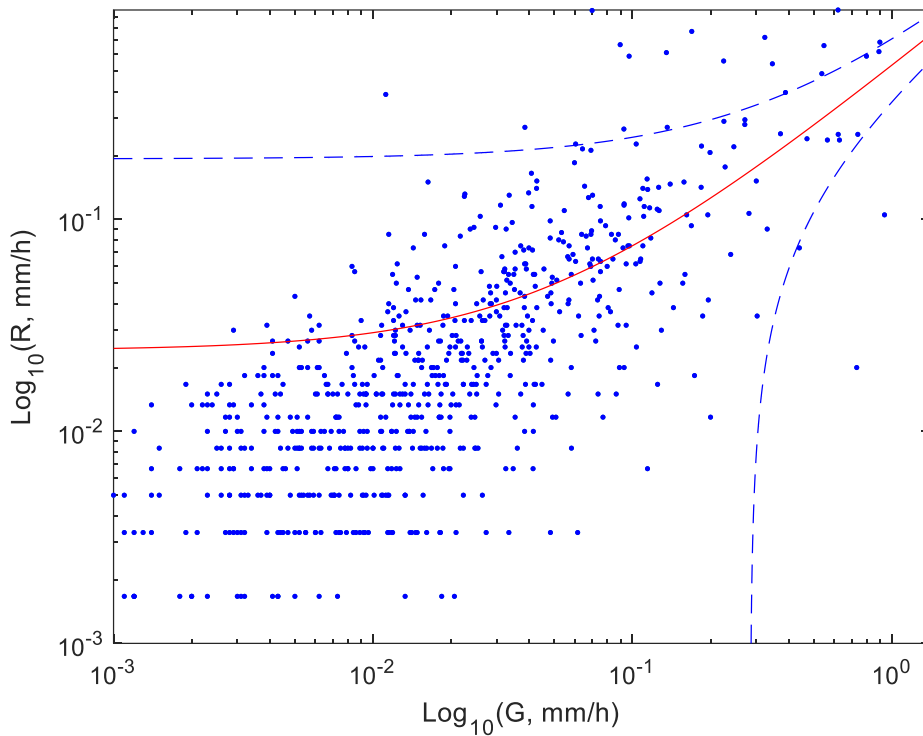
A-60 Log-log plot of 10-min non-zero radar rainfall intensity R values versus non-zero rainfall intensity G values from gauge R10 for summer months of 2009 with best fitted linear function with its 95% confidence intervals



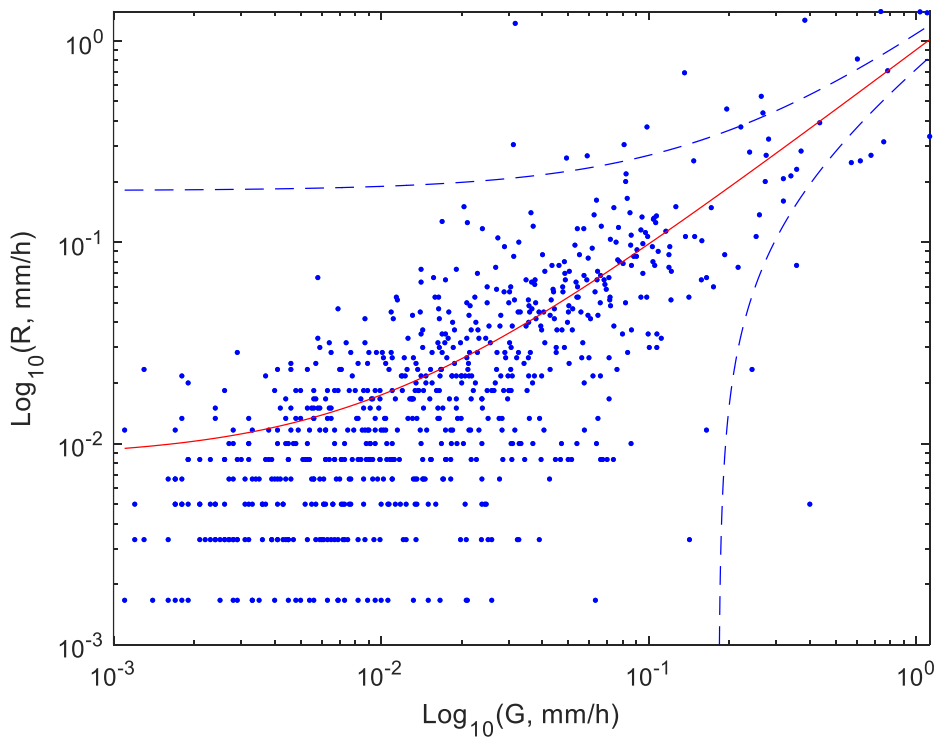
A-61 Log-log plot of 10-min non-zero radar rainfall intensity R values versus non-zero rainfall intensity G values from gauge R11 for summer months of 2009 with best fitted linear function with its 95% confidence intervals



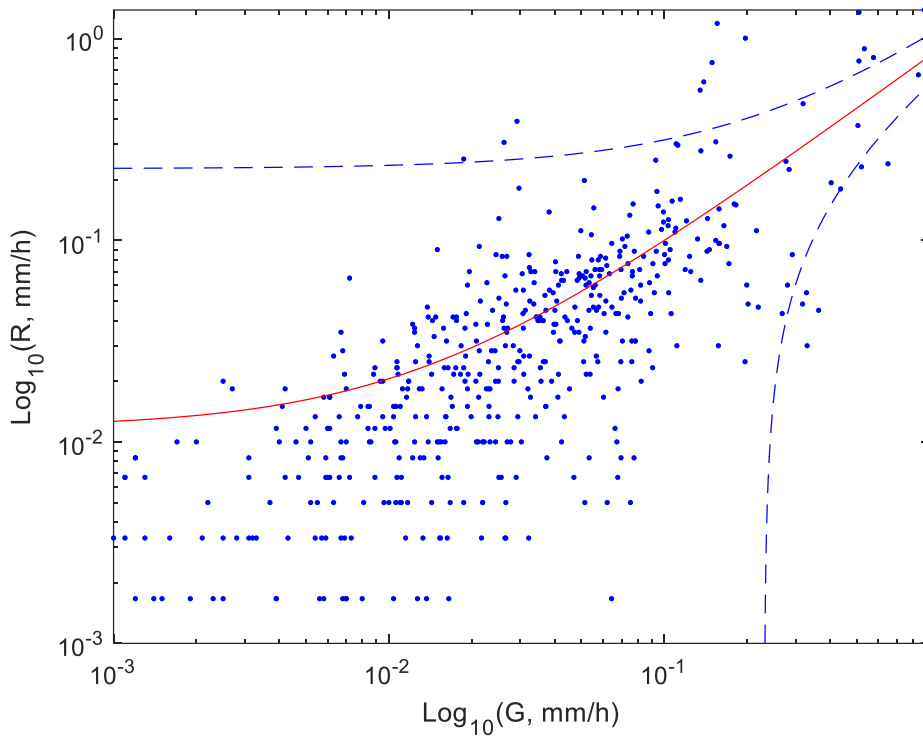
A-62 Log-log plot of 10-min non-zero radar rainfall intensity R values versus non-zero rainfall intensity G values from gauge R12 for summer months of 2009 with best fitted linear function with its 95% confidence intervals



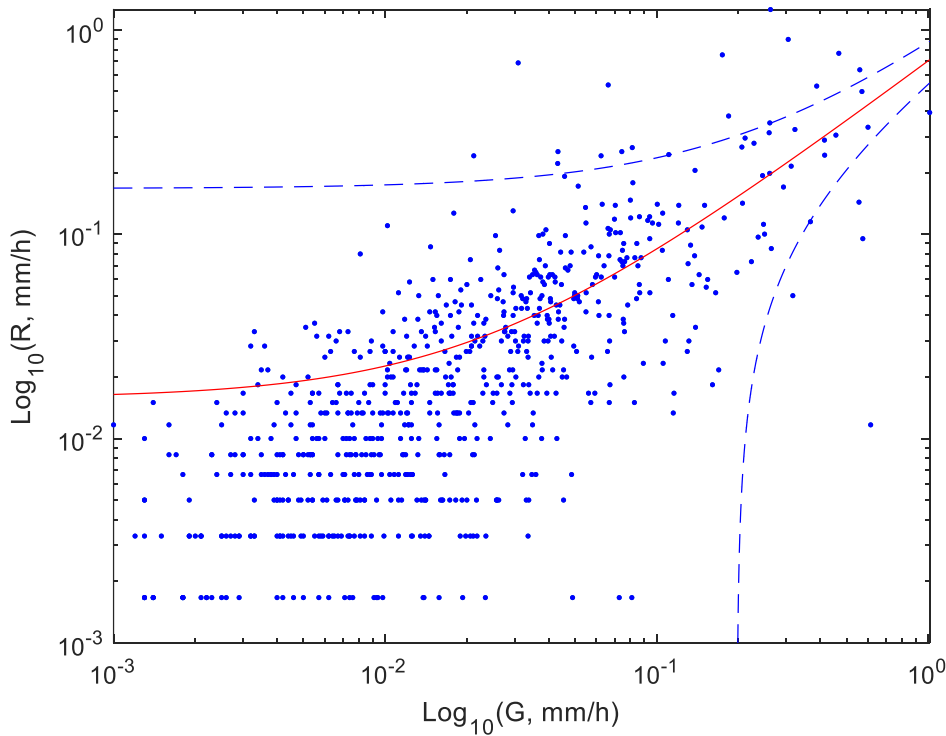
A-63 Log-log plot of 10-min non-zero radar rainfall intensity R values versus non-zero rainfall intensity G values from gauge R13 for summer months of 2009 with best fitted linear function with its 95% confidence intervals



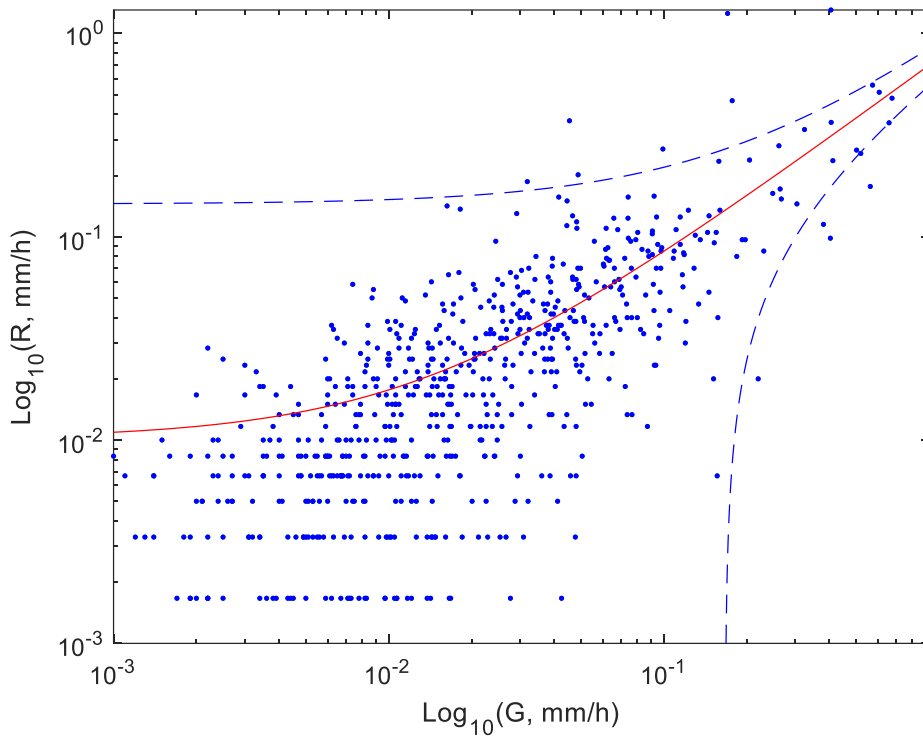
A-64 Log-log plot of 10-min non-zero radar rainfall intensity R values versus non-zero rainfall intensity G values from gauge R14 for summer months of 2009 with best fitted linear function with its 95% confidence intervals



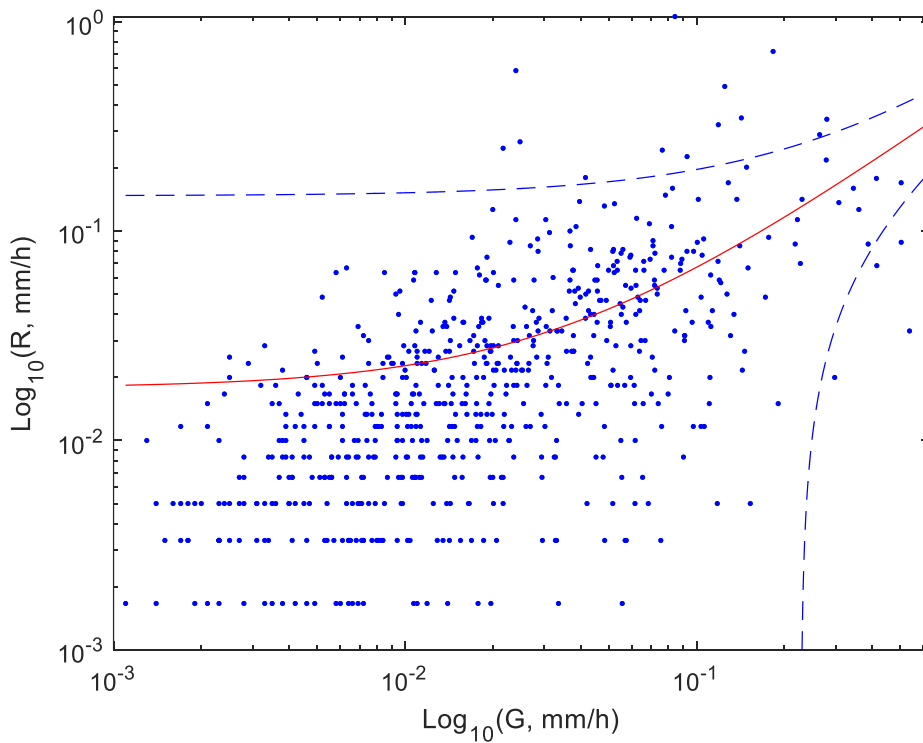
A-65 Log-log plot of 10-min non-zero radar rainfall intensity R values versus non-zero rainfall intensity G values from gauge R15 for summer months of 2009 with best fitted linear function with its 95% confidence intervals



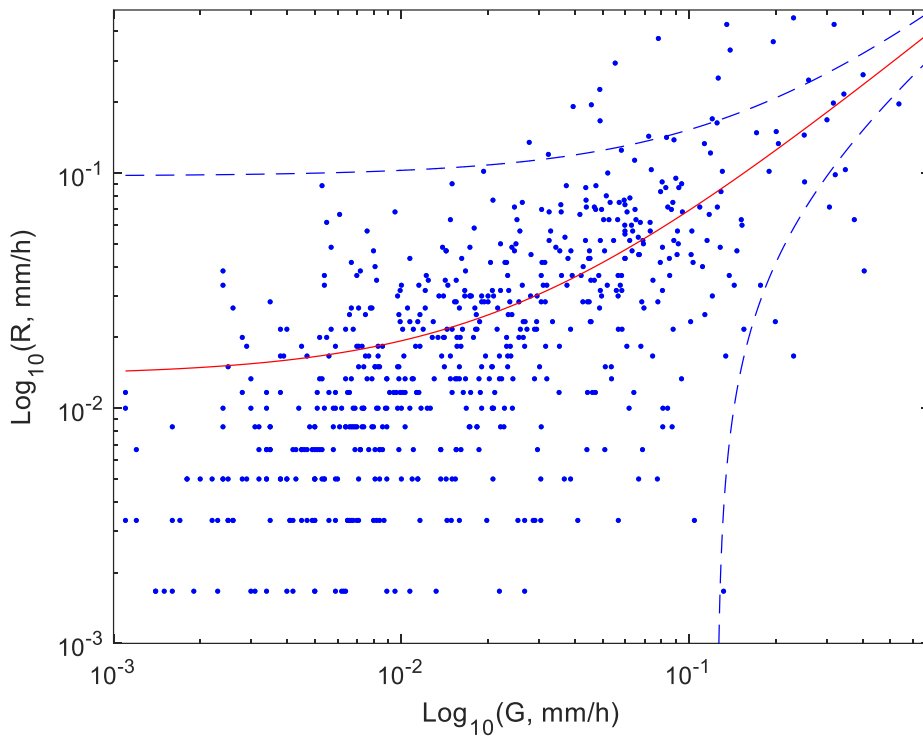
A-66 Log-log plot of 10-min non-zero radar rainfall intensity R values versus non-zero rainfall intensity G values from gauge R16 for summer months of 2009 with best fitted linear function with its 95% confidence intervals



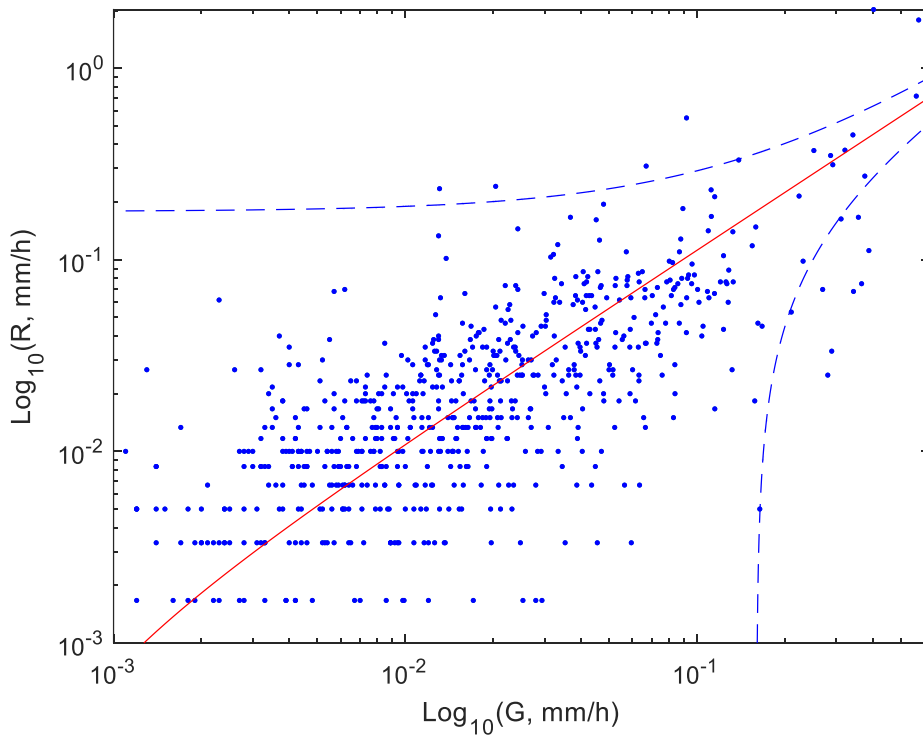
A-67 Log-log plot of 10-min non-zero radar rainfall intensity R values versus non-zero rainfall intensity G values from gauge R17 for summer months of 2009 with best fitted linear function with its 95% confidence intervals



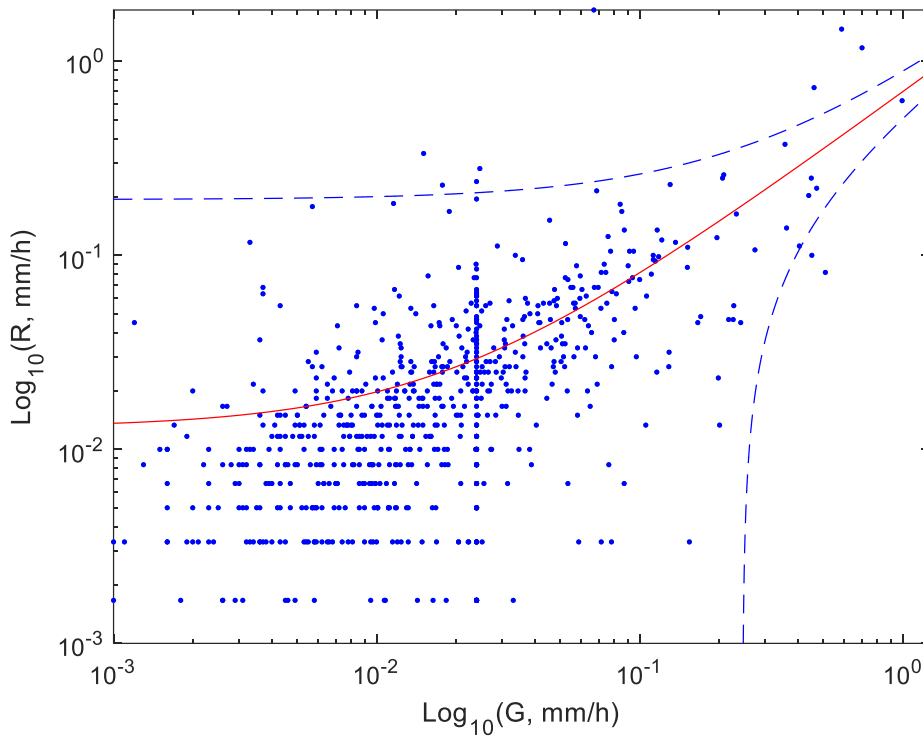
A-68 Log-log plot of 10-min non-zero radar rainfall intensity R values versus non-zero rainfall intensity G values from gauge R18 for summer months of 2009 with best fitted linear function with its 95% confidence intervals



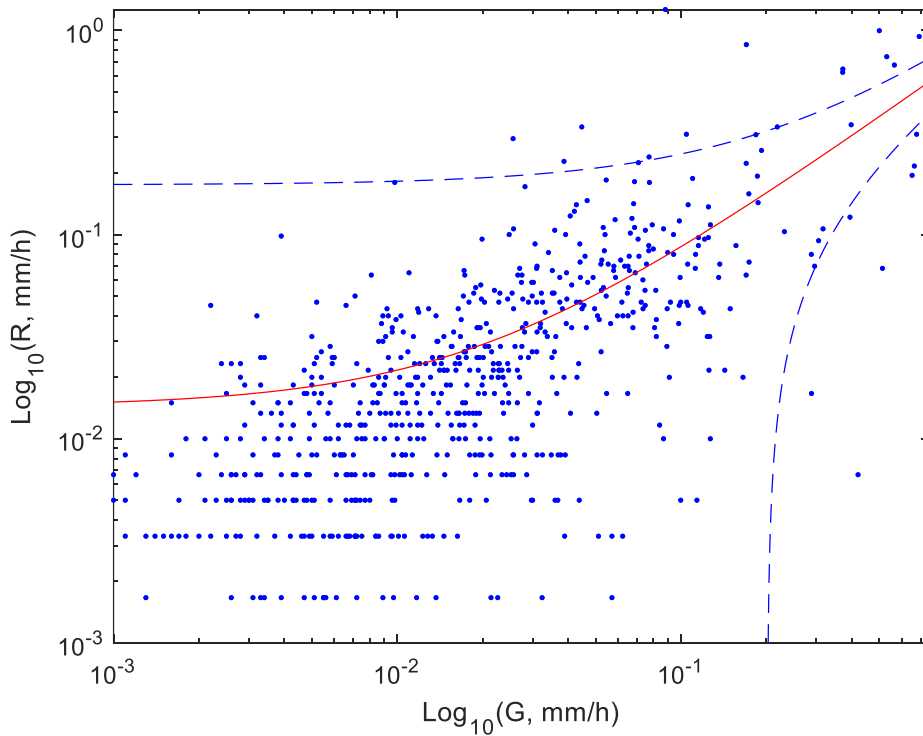
A-69 Log-log plot of 10-min non-zero radar rainfall intensity R values versus non-zero rainfall intensity G values from gauge R19 for summer months of 2009 with best fitted linear function with its 95% confidence intervals



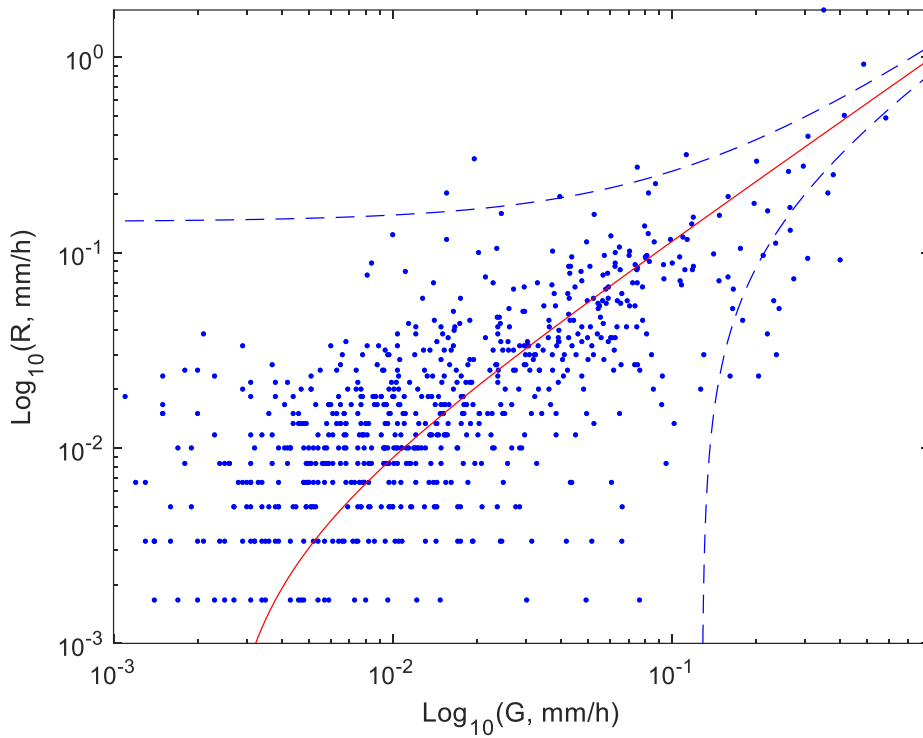
A-70 Log-log plot of 10-min non-zero radar rainfall intensity R values versus non-zero rainfall intensity G values from gauge R20 for summer months of 2009 with best fitted linear function with its 95% confidence intervals



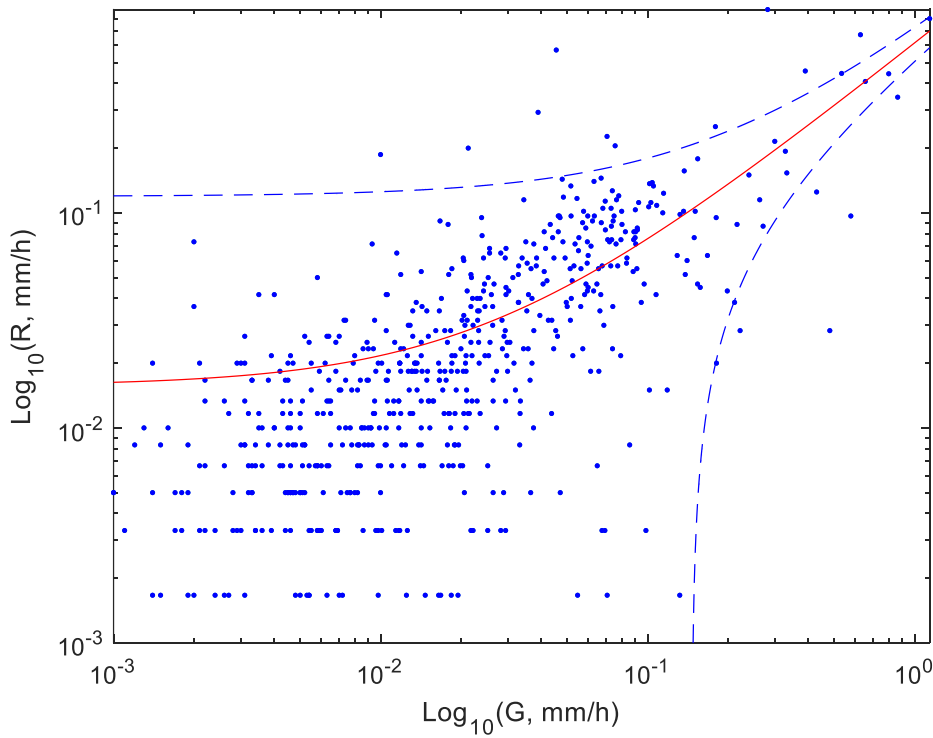
A-71 Log-log plot of 10-min non-zero radar rainfall intensity R values versus non-zero rainfall intensity G values from gauge R21 for summer months of 2009 with best fitted linear function with its 95% confidence intervals



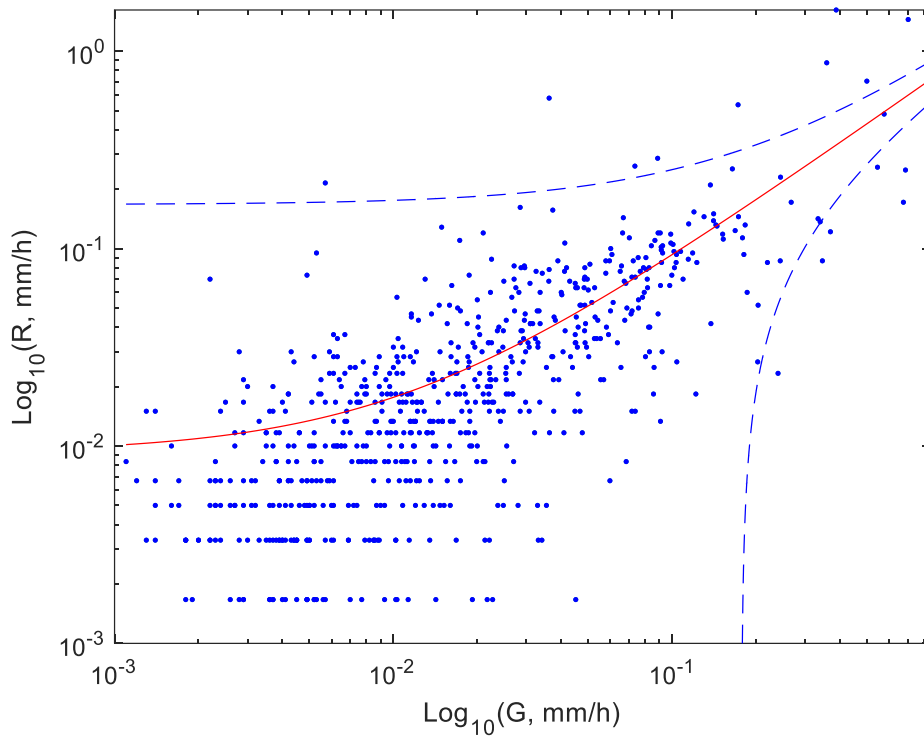
A-72 Log-log plot of 10-min non-zero radar rainfall intensity R values versus non-zero rainfall intensity G values from gauge R22 for summer months of 2009 with best fitted linear function with its 95% confidence intervals



A-73 Log-log plot of 10-min non-zero radar rainfall intensity R values versus non-zero rainfall intensity G values from gauge R23 for summer months of 2009 with best fitted linear function with its 95% confidence intervals



A-74 Log-log plot of 10-min non-zero radar rainfall intensity R values versus non-zero rainfall intensity G values from gauge R24 for summer months of 2009 with best fitted linear function with its 95% confidence intervals



A-75 Log-log plot of 10-min non-zero radar rainfall intensity R values versus non-zero rainfall intensity G values from gauge R25 for summer months of 2009 with best fitted linear function with its 95% confidence intervals

APPENDIX B

Table of contents

<i>Figure B-1 Spatial range of analysed precipitation field for assumed advection velocity $U = 12 \text{ km}\cdot\text{h}^{-1}$.....</i>	<i>173</i>
<i>Figure B-2 Spatial range of analysed precipitation field for assumed advection velocity $U = 18 \text{ km}\cdot\text{h}^{-1}$.....</i>	<i>174</i>
<i>Figure B-3 Spatial range of analysed precipitation field for assumed advection velocity $U = 24 \text{ km}\cdot\text{h}^{-1}$.....</i>	<i>175</i>
<i>Figure B-4 Spatial range of analysed precipitation field for assumed advection velocity $U = 30 \text{ km}\cdot\text{h}^{-1}$.....</i>	<i>176</i>
<i>Figure B-5 Spatial range of analysed precipitation field for assumed advection velocity $U = 36 \text{ km}\cdot\text{h}^{-1}$.....</i>	<i>177</i>
<i>Figure B-6 Spatial range of analysed precipitation field for assumed advection velocity $U = 42 \text{ km}\cdot\text{h}^{-1}$.....</i>	<i>178</i>
<i>Figure B-7 Spatial range of analysed precipitation field for assumed advection velocity $U = 48 \text{ km}\cdot\text{h}^{-1}$.....</i>	<i>179</i>
<i>Figure B-8 Spatial range of analysed precipitation field for assumed advection velocity $U = 54 \text{ km}\cdot\text{h}^{-1}$.....</i>	<i>180</i>
<i>Figure B-9 Spatial range of analysed precipitation field for assumed advection velocity $U = 60 \text{ km}\cdot\text{h}^{-1}$.....</i>	<i>181</i>

APPENDIX B: SPATIAL RANGE OF ANALYSED PRECIPITATION FIELD FOR ASSUMED ADVECTION VELOCITY

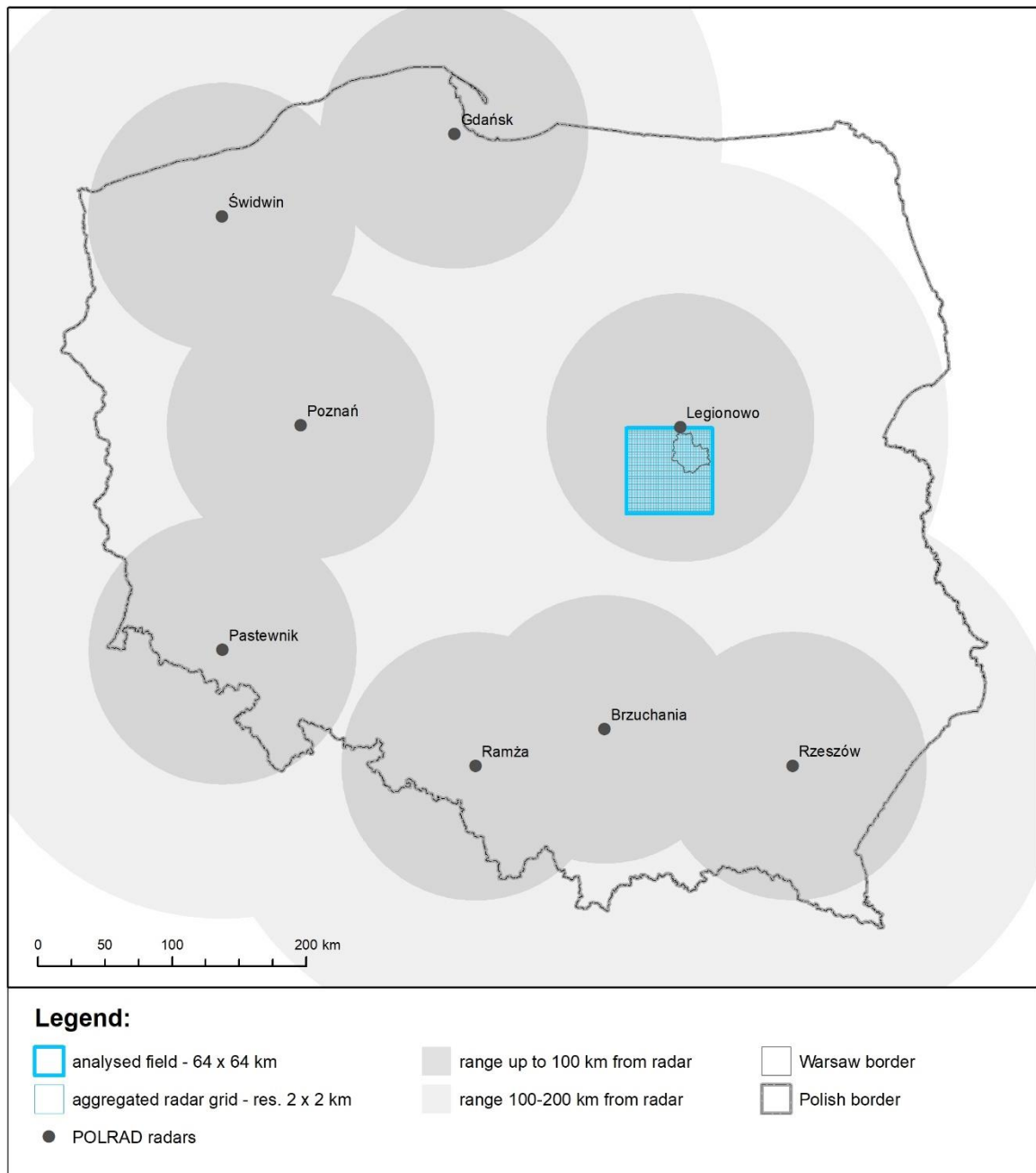


Figure B-1 Spatial range of analysed precipitation field for assumed advection velocity $U = 12 \text{ km}\cdot\text{h}^{-1}$

APPENDIX B: SPATIAL RANGE OF ANALYSED PRECIPITATION FIELD FOR ASSUMED ADVECTION VELOCITY

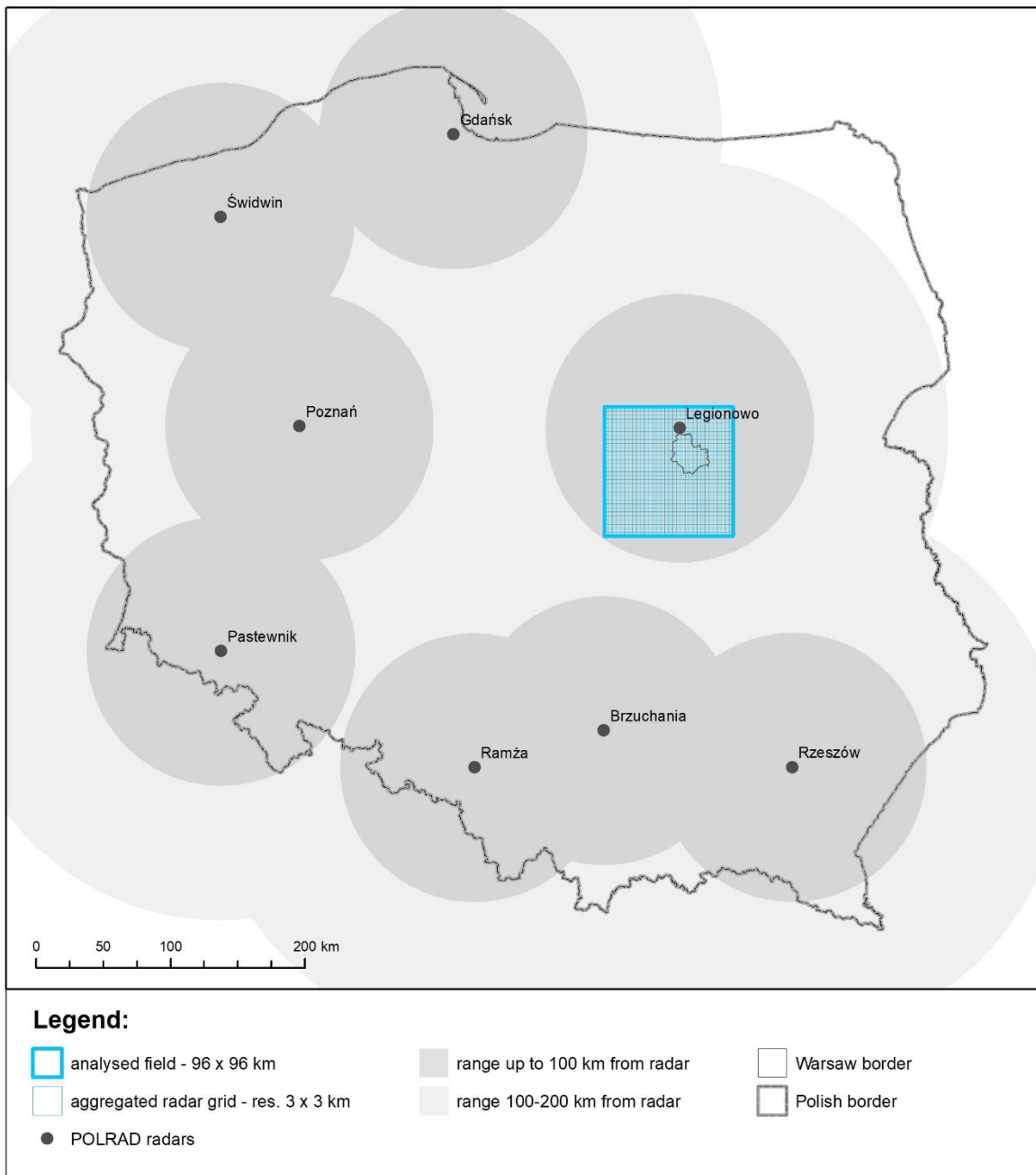


Figure B-2 Spatial range of analysed precipitation field for assumed advection velocity $U = 18 \text{ km}\cdot\text{h}^{-1}$

APPENDIX B: SPATIAL RANGE OF ANALYSED PRECIPITATION FIELD FOR ASSUMED ADVECTION VELOCITY

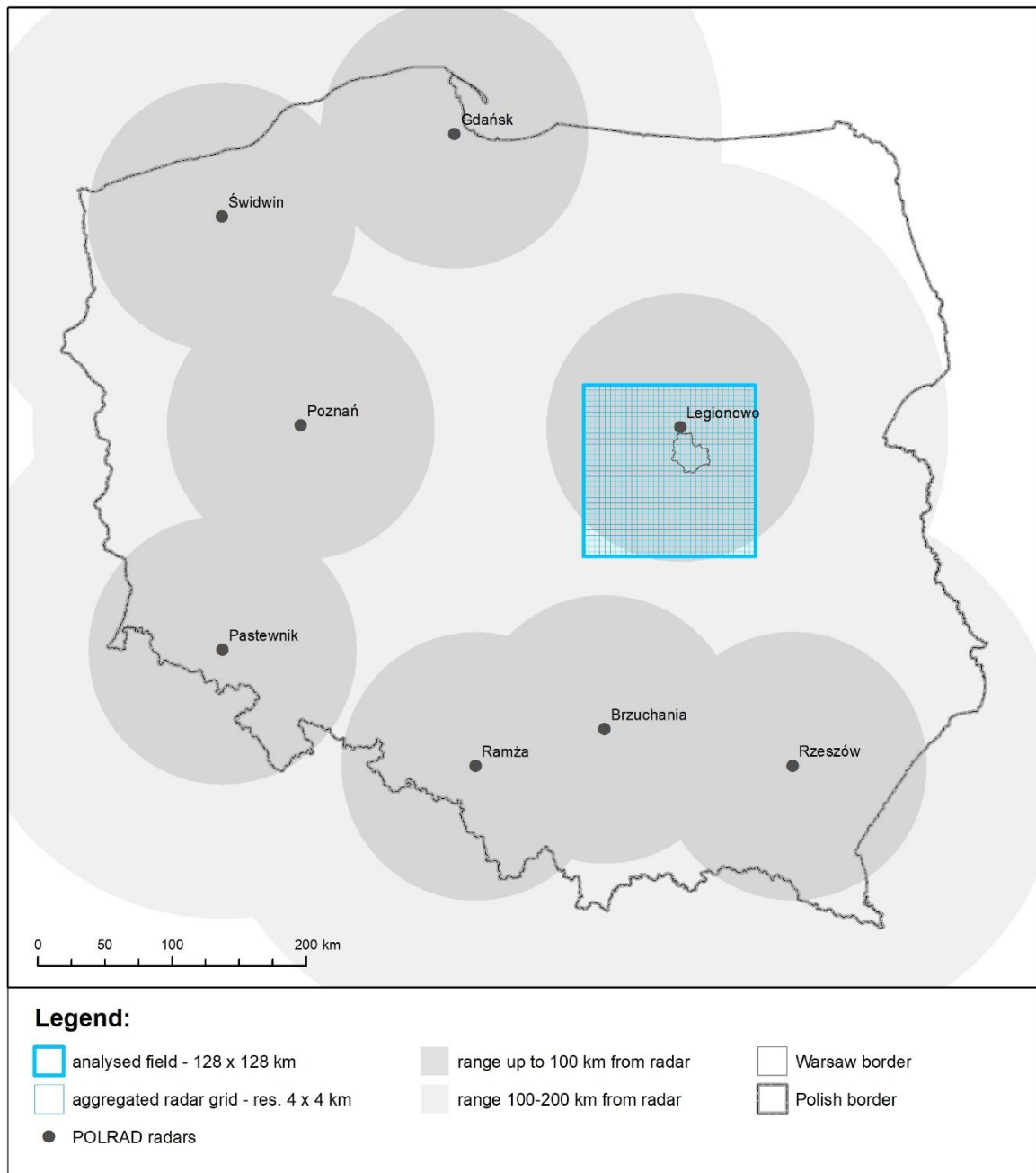


Figure B-3 Spatial range of analysed precipitation field for assumed advection velocity $U = 24 \text{ km}\cdot\text{h}^{-1}$

APPENDIX B: SPATIAL RANGE OF ANALYSED PRECIPITATION FIELD FOR ASSUMED ADVECTION VELOCITY

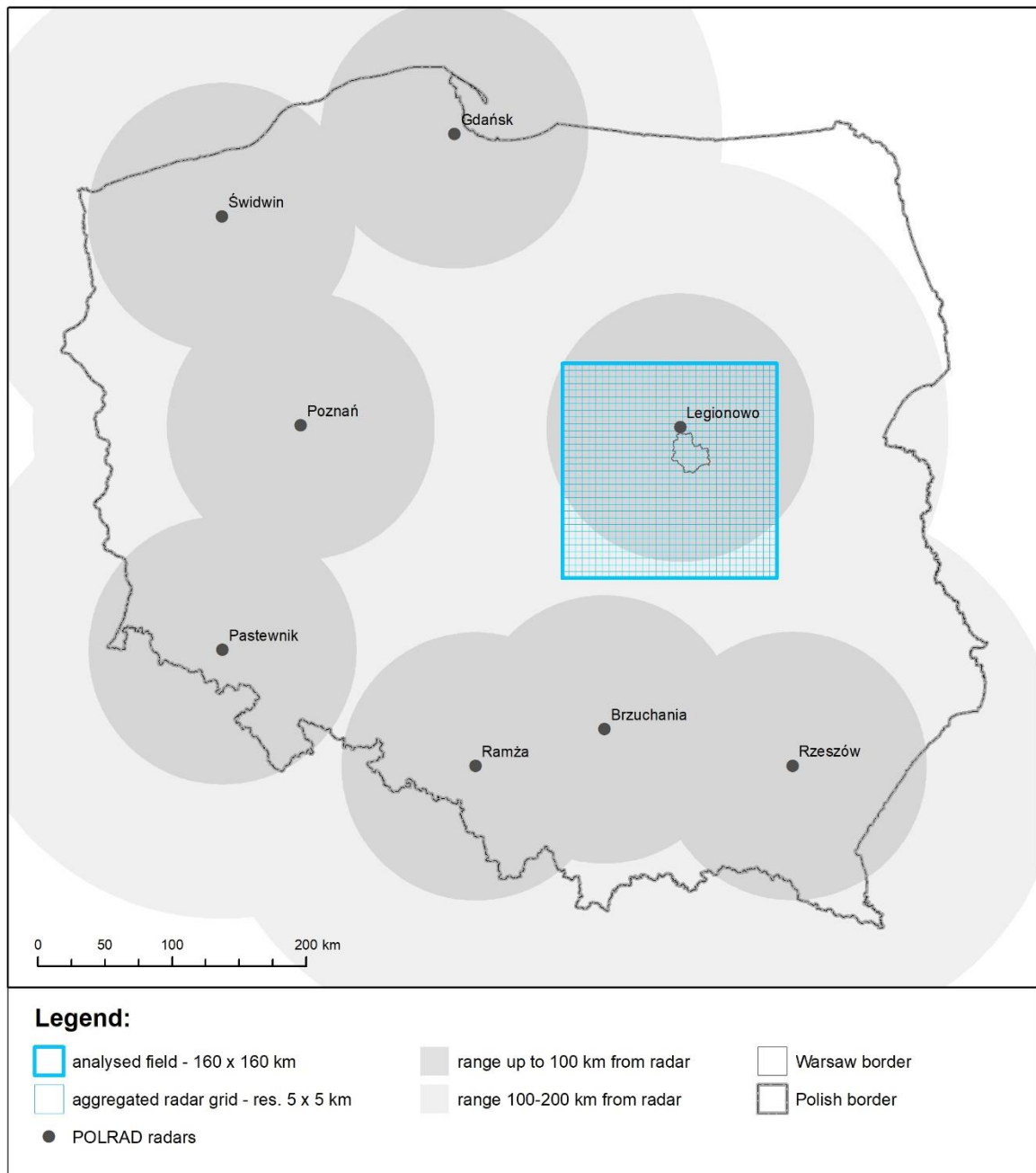


Figure B-4 Spatial range of analysed precipitation field for assumed advection velocity $U = 30 \text{ km}\cdot\text{h}^{-1}$

APPENDIX B: SPATIAL RANGE OF ANALYSED PRECIPITATION FIELD FOR ASSUMED ADVECTION VELOCITY

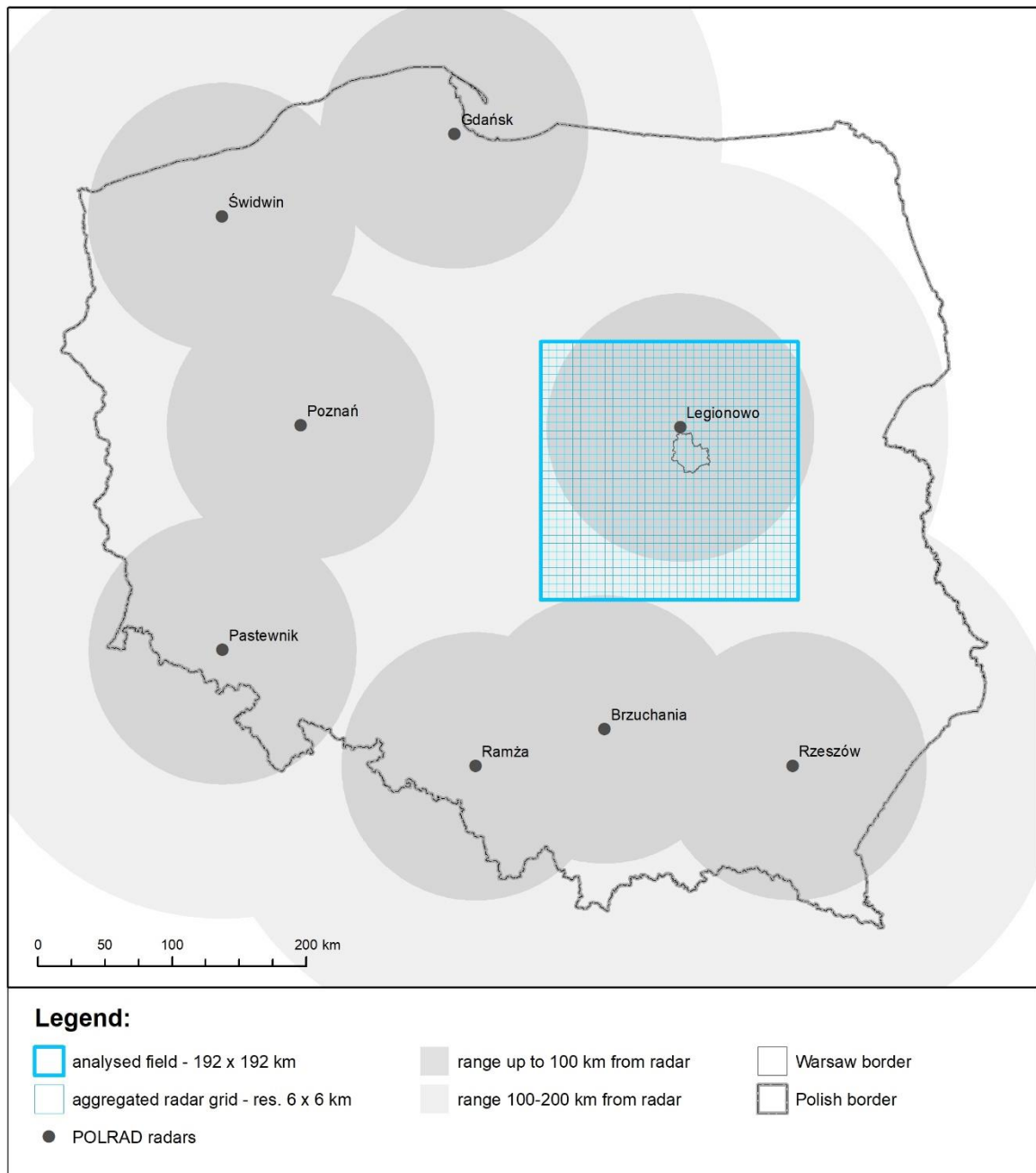


Figure B-5 Spatial range of analysed precipitation field for assumed advection velocity $U = 36 \text{ km}\cdot\text{h}^{-1}$

APPENDIX B: SPATIAL RANGE OF ANALYSED PRECIPITATION FIELD FOR ASSUMED ADVECTION VELOCITY

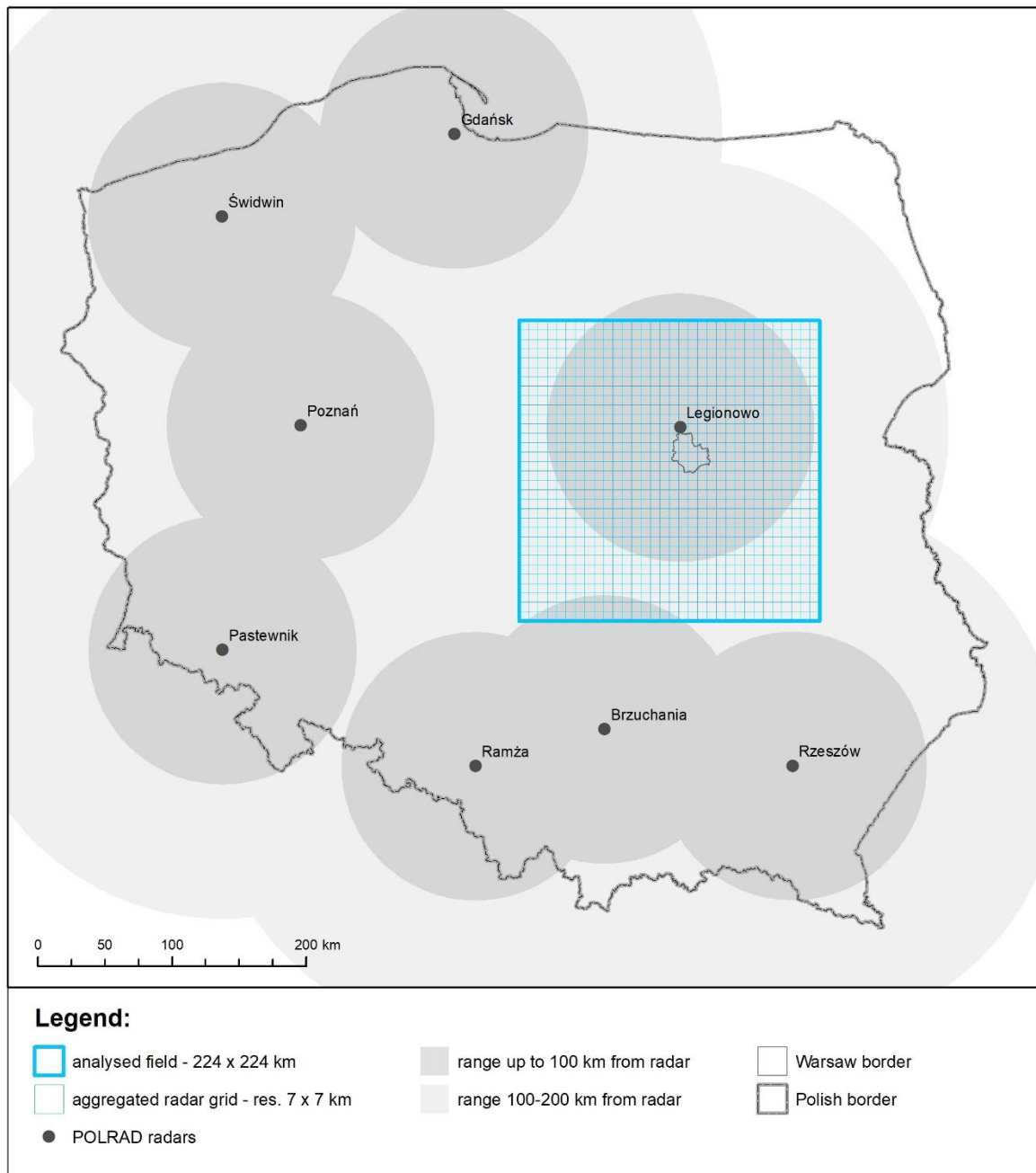


Figure B-6 Spatial range of analysed precipitation field for assumed advection velocity $U = 42 \text{ km}\cdot\text{h}^{-1}$

APPENDIX B: SPATIAL RANGE OF ANALYSED PRECIPITATION FIELD FOR ASSUMED ADVECTION VELOCITY

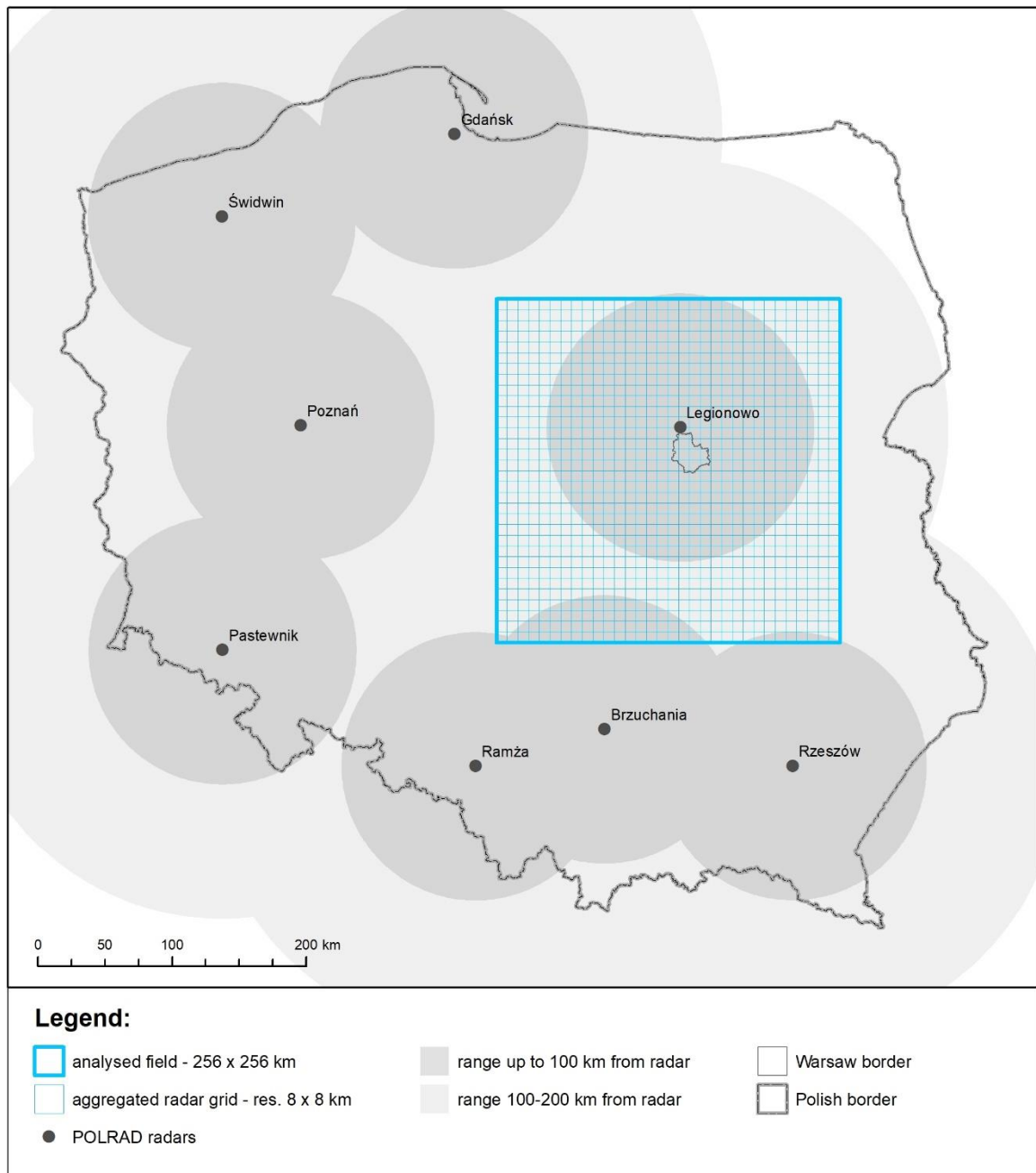


Figure B-7 Spatial range of analysed precipitation field for assumed advection velocity $U = 48 \text{ km}\cdot\text{h}^{-1}$

APPENDIX B: SPATIAL RANGE OF ANALYSED PRECIPITATION FIELD FOR ASSUMED ADVECTION VELOCITY

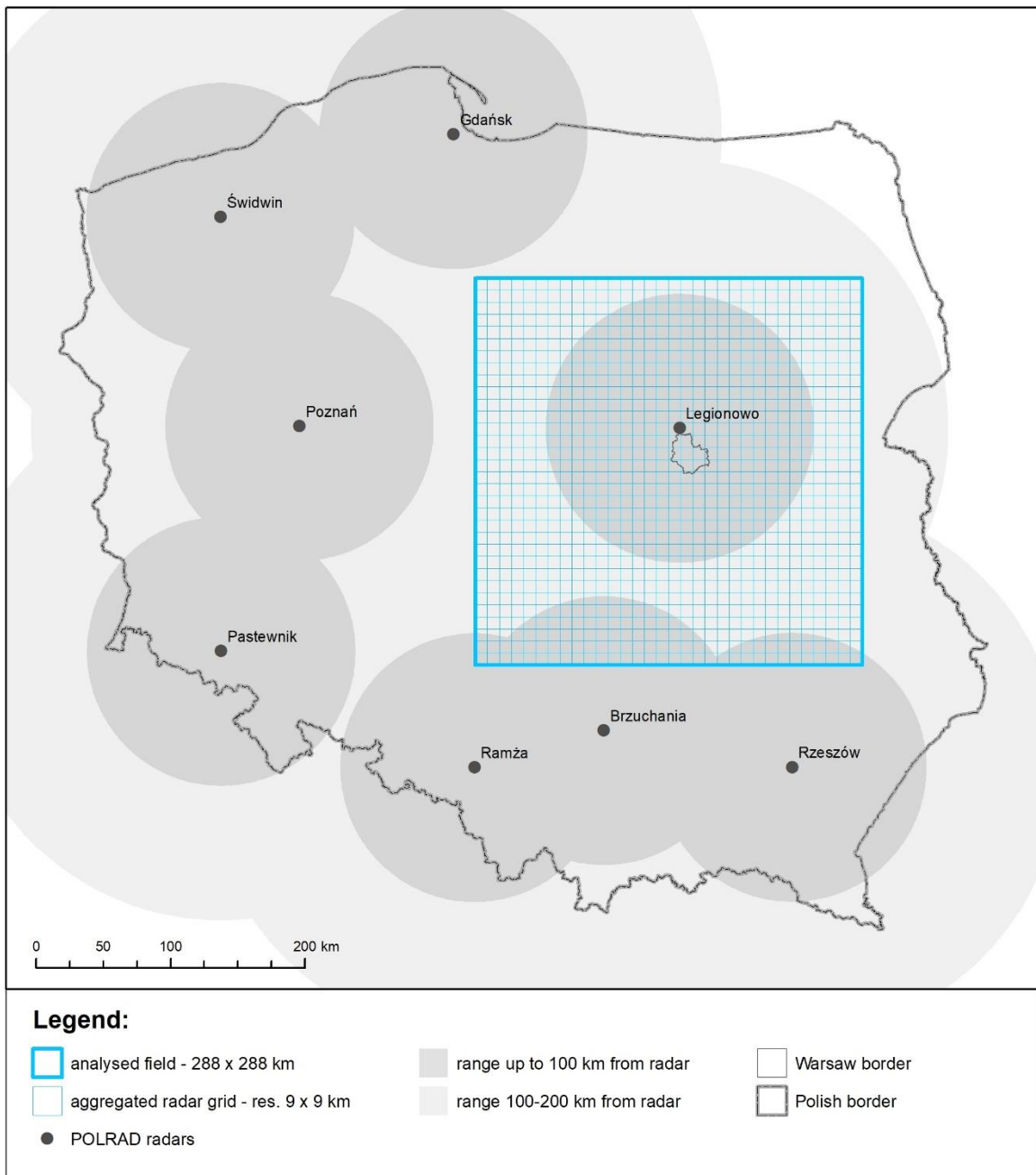


Figure B-8 Spatial range of analysed precipitation field for assumed advection velocity $U = 54 \text{ km}\cdot\text{h}^{-1}$

APPENDIX B: SPATIAL RANGE OF ANALYSED PRECIPITATION FIELD FOR ASSUMED ADVECTION VELOCITY

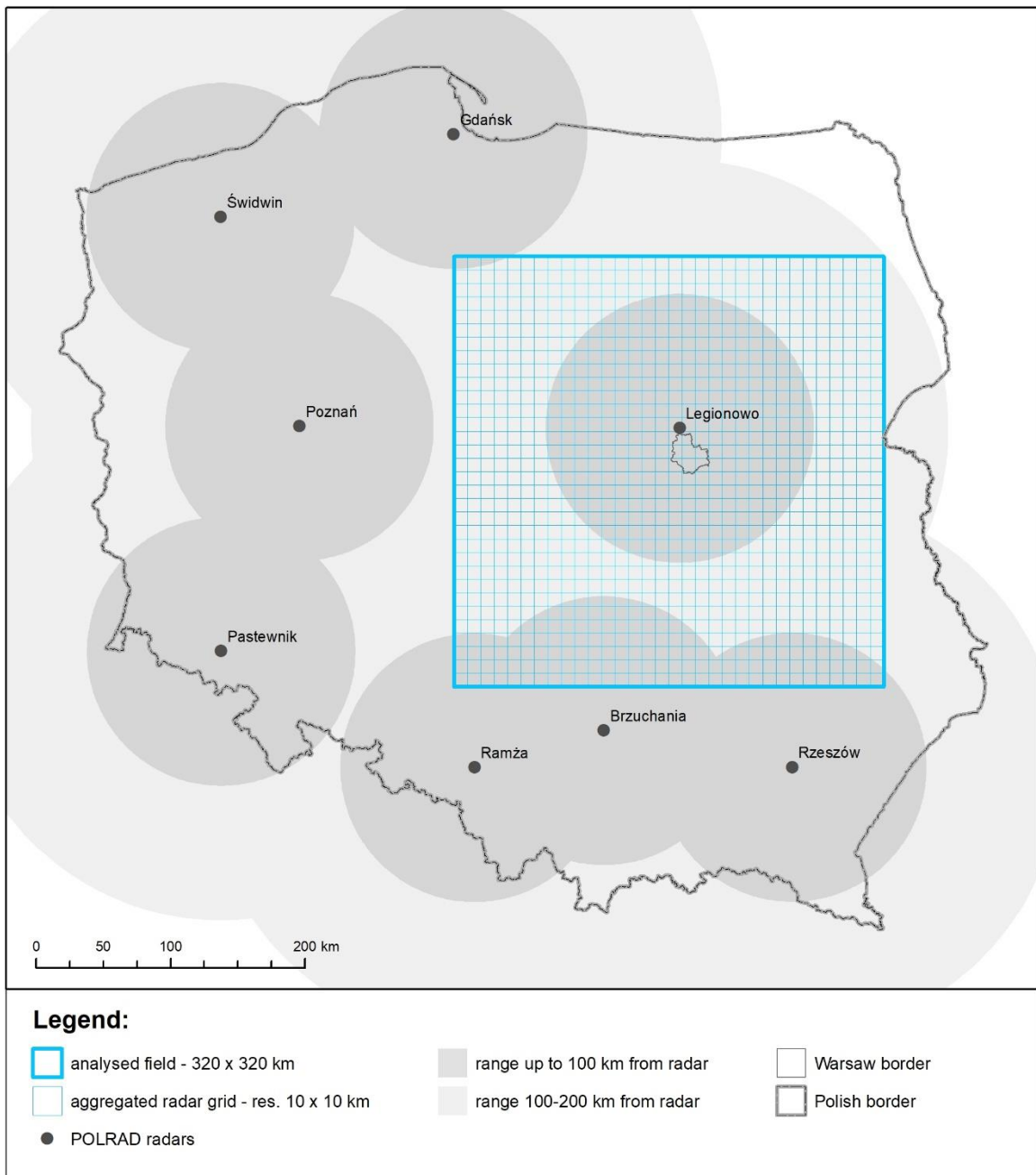


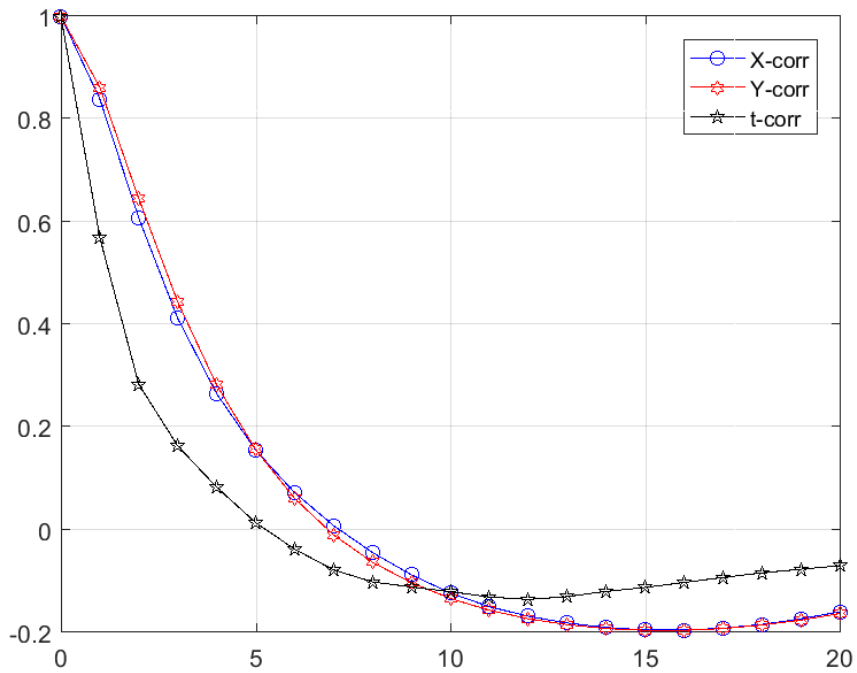
Figure B-9 Spatial range of analysed precipitation field for assumed advection velocity $U = 60 \text{ km}\cdot\text{h}^{-1}$

APPENDIX C

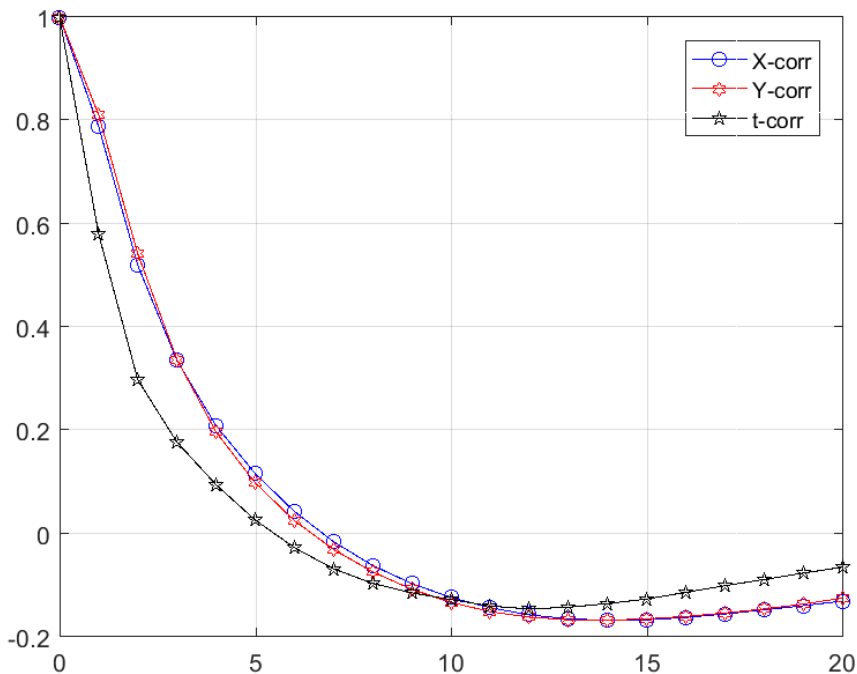
Table of contents

<i>C-1 Mean autocorrelation functions along X (X-corr) and Y (Y-corr) directions and rescaled time (t-corr) direction for 320-min aggregated radar sequences selected from summer months of 2015. Units on horizontal axis represent the shifts in radar grid aggregated to 2x2 km with respect to advection velocity of $U=12 \text{ km}\cdot\text{h}^{-1}$</i>	183
<i>C-2 Mean autocorrelation functions along X (X-corr) and Y (Y-corr) directions and rescaled time (t-corr) direction for 320-min aggregated radar sequences selected from summer months of 2015. Units on horizontal axis represent the shifts in radar grid aggregated to 3x3 km with respect to advection velocity of $U=18 \text{ km}\cdot\text{h}^{-1}$</i>	183
<i>C-3 Mean autocorrelation functions along X (X-corr) and Y (Y-corr) directions and rescaled time (t-corr) direction for 320-min aggregated radar sequences selected from summer months of 2015. Units on horizontal axis represent the shifts in radar grid aggregated to 4x4 km with respect to advection velocity of $U=24 \text{ km}\cdot\text{h}^{-1}$</i>	184
<i>C-4 Mean autocorrelation functions along X (X-corr) and Y (Y-corr) directions and rescaled time (t-corr) direction for 320-min aggregated radar sequences selected from summer months of 2015. Units on horizontal axis represent the shifts in radar grid aggregated to 5x5 km with respect to advection velocity of $U=30 \text{ km}\cdot\text{h}^{-1}$</i>	184
<i>C-5 Mean autocorrelation functions along X (X-corr) and Y (Y-corr) directions and rescaled time (t-corr) direction for 320-min aggregated radar sequences selected from summer months of 2015. Units on horizontal axis represent the shifts in radar grid aggregated to 6x6 km with respect to advection velocity of $U=36 \text{ km}\cdot\text{h}^{-1}$</i>	185
<i>C-6 Mean autocorrelation functions along X (X-corr) and Y (Y-corr) directions and rescaled time (t-corr) direction for 320-min aggregated radar sequences selected from summer months of 2015. Units on horizontal axis represent the shifts in radar grid aggregated to 7x7 km with respect to advection velocity of $U=42 \text{ km}\cdot\text{h}^{-1}$</i>	185
<i>C-7 Mean autocorrelation functions along X (X-corr) and Y (Y-corr) directions and rescaled time (t-corr) direction for 320-min aggregated radar sequences selected from summer months of 2015. Units on horizontal axis represent the shifts in radar grid aggregated to 8x8 km with respect to advection velocity of $U=48 \text{ km}\cdot\text{h}^{-1}$</i>	186
<i>C-8 Mean autocorrelation functions along X (X-corr) and Y (Y-corr) directions and rescaled time (t-corr) direction for 320-min aggregated radar sequences selected from summer months of 2015. Units on horizontal axis represent the shifts in radar grid aggregated to 9x9 km with respect to advection velocity of $U=54 \text{ km}\cdot\text{h}^{-1}$</i>	186
<i>C-9 Mean autocorrelation functions along X (X-corr) and Y (Y-corr) directions and rescaled time (t-corr) direction for 320-min aggregated radar sequences selected from summer months of 2015. Units on horizontal axis represent the shifts in radar grid aggregated to 10x10 km with respect to advection velocity of $U=60 \text{ km}\cdot\text{h}^{-1}$</i>	187

APPENDIX C: MEAN AUTOCORRELATION FUNCTIONS OF SELECTED RADAR SEQUENCES FROM 2015 ALONG X AND Y DIRECTIONS AND TIME FOR DIFFERENT ADVECTION VELOCITY ASSUMPTIONS

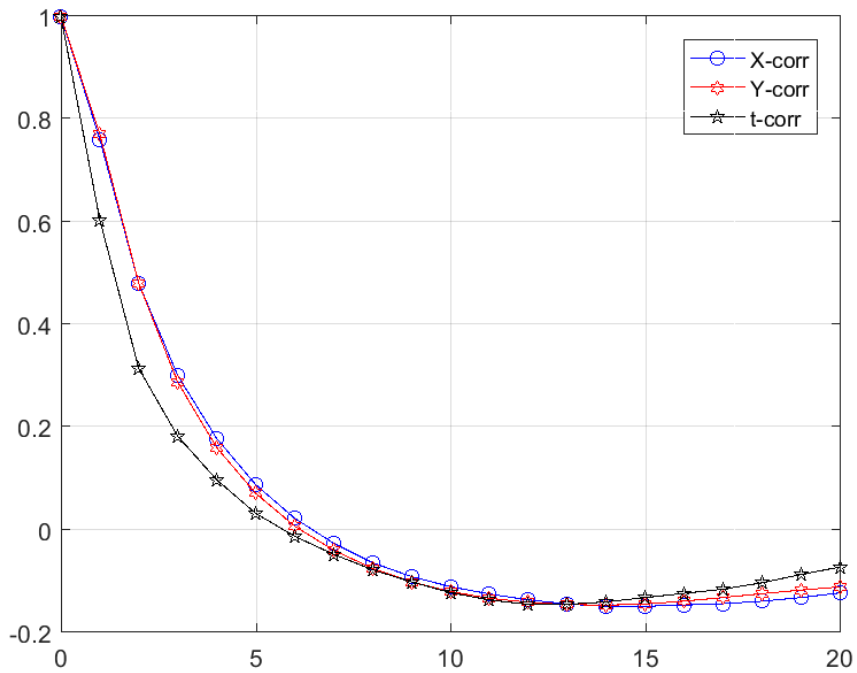


C-1 Mean autocorrelation functions along X (X-corr) and Y (Y-corr) directions and rescaled time (t-corr) direction for 320-min aggregated radar sequences selected from summer months of 2015. Units on horizontal axis represent the shifts in radar grid aggregated to 2x2 km with respect to advection velocity of $U=12 \text{ km}\cdot\text{h}^{-1}$

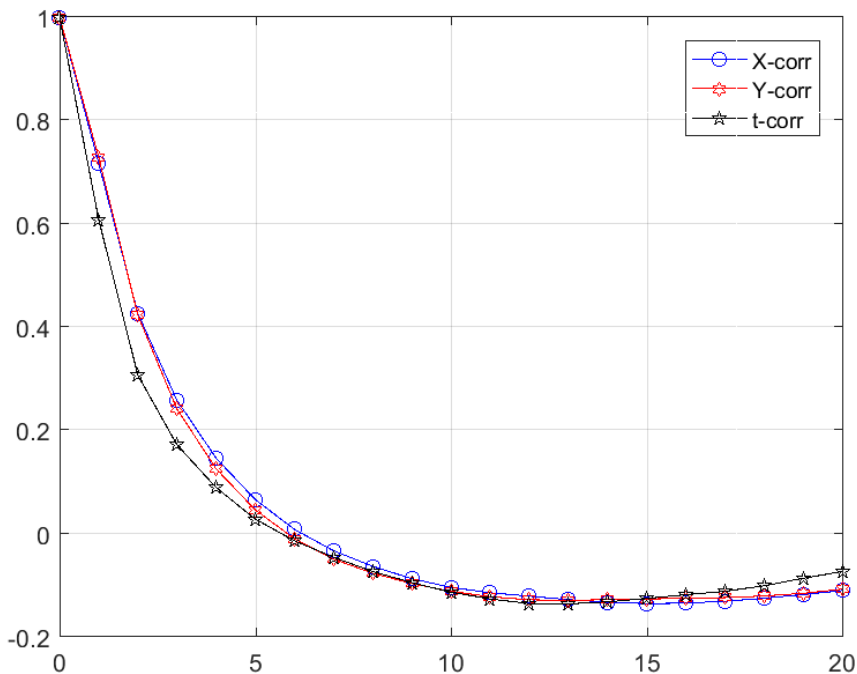


C-2 Mean autocorrelation functions along X (X-corr) and Y (Y-corr) directions and rescaled time (t-corr) direction for 320-min aggregated radar sequences selected from summer months of 2015. Units on horizontal axis represent the shifts in radar grid aggregated to 3x3 km with respect to advection velocity of $U=18 \text{ km}\cdot\text{h}^{-1}$

APPENDIX C: MEAN AUTOCORRELATION FUNCTIONS OF SELECTED RADAR SEQUENCES FROM 2015 ALONG X AND Y DIRECTIONS AND TIME FOR DIFFERENT ADVECTION VELOCITY ASSUMPTIONS

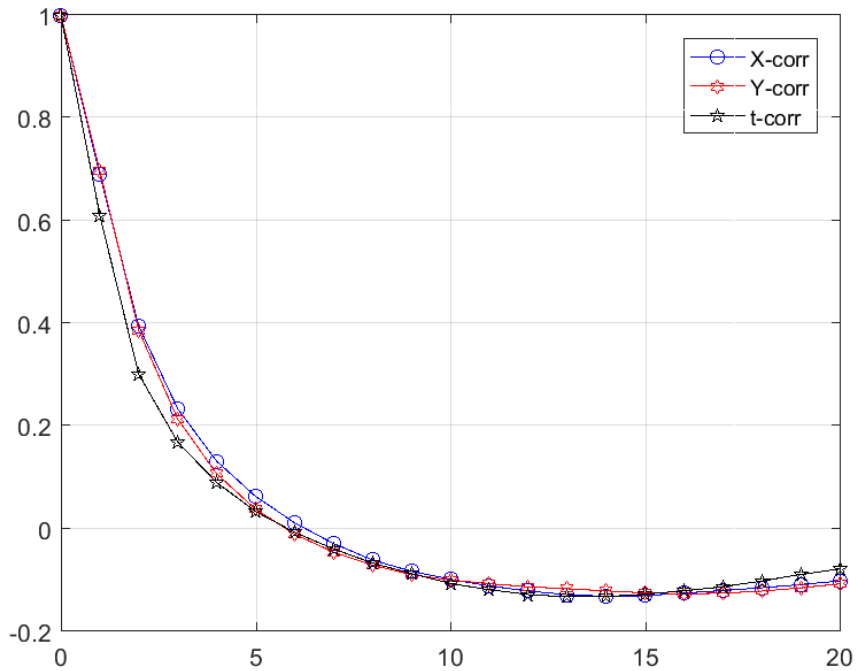


C-3 Mean autocorrelation functions along X (X-corr) and Y (Y-corr) directions and rescaled time (t-corr) direction for 320-min aggregated radar sequences selected from summer months of 2015. Units on horizontal axis represent the shifts in radar grid aggregated to $4\times 4 \text{ km}$ with respect to advection velocity of $U=24 \text{ km}\cdot\text{h}^{-1}$

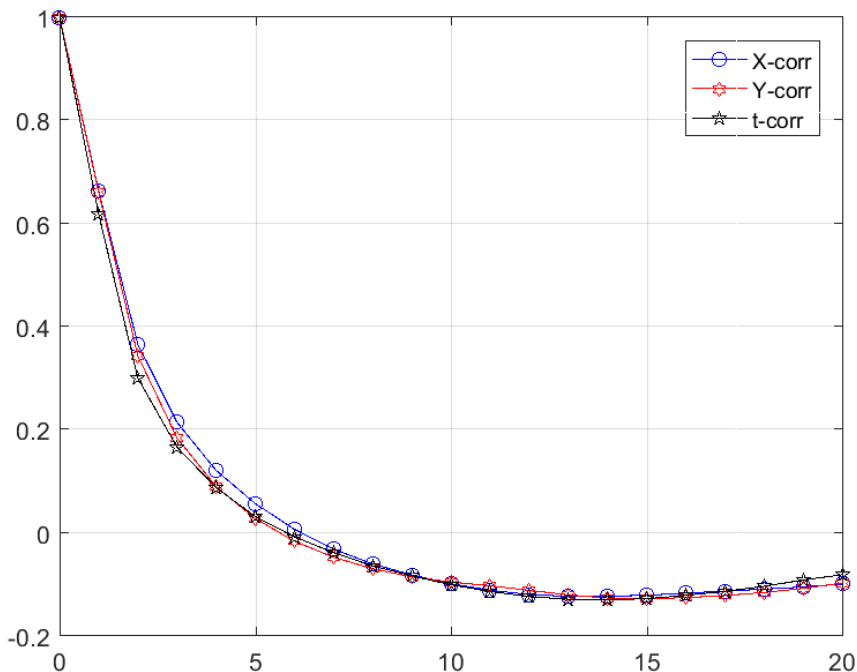


C-4 Mean autocorrelation functions along X (X-corr) and Y (Y-corr) directions and rescaled time (t-corr) direction for 320-min aggregated radar sequences selected from summer months of 2015. Units on horizontal axis represent the shifts in radar grid aggregated to $5\times 5 \text{ km}$ with respect to advection velocity of $U=30 \text{ km}\cdot\text{h}^{-1}$

APPENDIX C: MEAN AUTOCORRELATION FUNCTIONS OF SELECTED RADAR SEQUENCES FROM 2015 ALONG X AND Y DIRECTIONS AND TIME FOR DIFFERENT ADVECTION VELOCITY ASSUMPTIONS

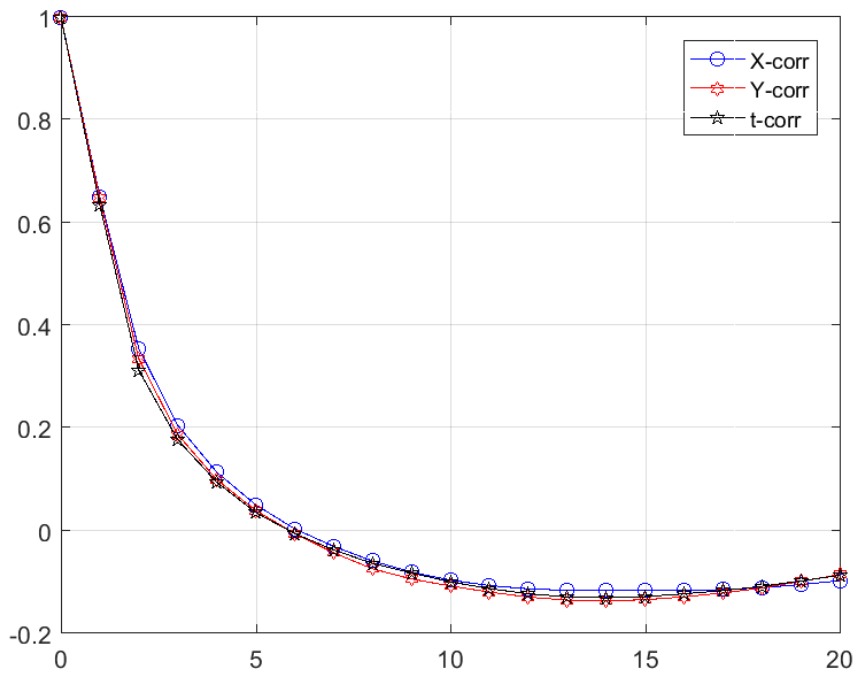


C-5 Mean autocorrelation functions along X (X-corr) and Y (Y-corr) directions and rescaled time (t-corr) direction for 320-min aggregated radar sequences selected from summer months of 2015. Units on horizontal axis represent the shifts in radar grid aggregated to 6x6 km with respect to advection velocity of $U=36 \text{ km}\cdot\text{h}^{-1}$

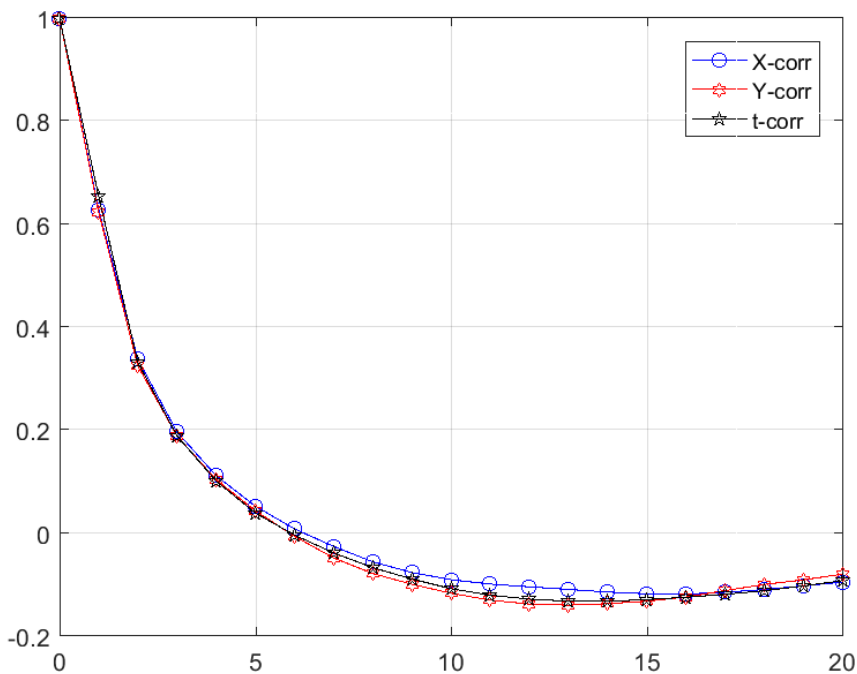


C-6 Mean autocorrelation functions along X (X-corr) and Y (Y-corr) directions and rescaled time (t-corr) direction for 320-min aggregated radar sequences selected from summer months of 2015. Units on horizontal axis represent the shifts in radar grid aggregated to 7x7 km with respect to advection velocity of $U=42 \text{ km}\cdot\text{h}^{-1}$

APPENDIX C: MEAN AUTOCORRELATION FUNCTIONS OF SELECTED RADAR SEQUENCES FROM 2015 ALONG X AND Y DIRECTIONS AND TIME FOR DIFFERENT ADVECTION VELOCITY ASSUMPTIONS

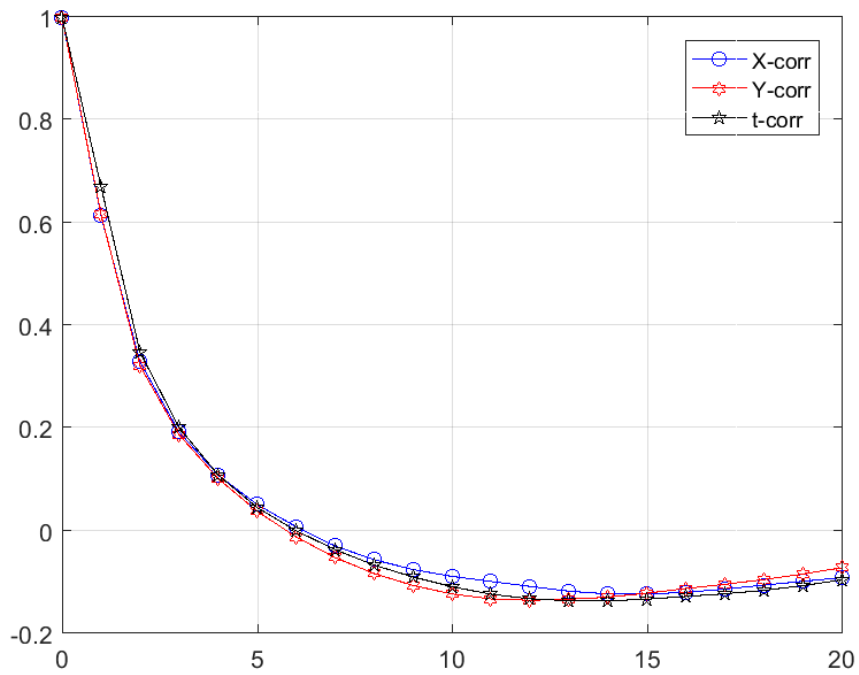


C-7 Mean autocorrelation functions along X (X-corr) and Y (Y-corr) directions and rescaled time (t-corr) direction for 320-min aggregated radar sequences selected from summer months of 2015. Units on horizontal axis represent the shifts in radar grid aggregated to $8\times 8 \text{ km}$ with respect to advection velocity of $U=48 \text{ km}\cdot\text{h}^{-1}$



C-8 Mean autocorrelation functions along X (X-corr) and Y (Y-corr) directions and rescaled time (t-corr) direction for 320-min aggregated radar sequences selected from summer months of 2015. Units on horizontal axis represent the shifts in radar grid aggregated to $9\times 9 \text{ km}$ with respect to advection velocity of $U=54 \text{ km}\cdot\text{h}^{-1}$

APPENDIX C: MEAN AUTOCORRELATION FUNCTIONS OF SELECTED RADAR SEQUENCES FROM 2015 ALONG X AND Y DIRECTIONS AND TIME FOR DIFFERENT ADVECTION VELOCITY ASSUMPTIONS



C-9 Mean autocorrelation functions along X (X-corr) and Y (Y-corr) directions and rescaled time (t-corr) direction for 320-min aggregated radar sequences selected from summer months of 2015. Units on horizontal axis represent the shifts in radar grid aggregated to 10x10 km with respect to advection velocity of $U=60 \text{ km}\cdot\text{h}^{-1}$

APPENDIX D

Table of contents

<i>D-1 Autocorrelation functions along x (x-corr) and y (y-corr) directions and time (t-corr) for 320-min aggregated radar 1st sequence selected from 2015 for advection velocity $U=48 \text{ km}\cdot\text{h}^{-1}$. The horizontal axis represents the shift in the radar grid aggregated to $8\times 8 \text{ km}$</i>	<i>190</i>
<i>D-2 Autocorrelation functions along x (x-corr) and y (y-corr) directions and time (t-corr) for 320-min aggregated radar 2nd sequence selected from 2015 for advection velocity $U=48 \text{ km}\cdot\text{h}^{-1}$. The horizontal axis represents the shift in the radar grid aggregated to $8\times 8 \text{ km}$</i>	<i>190</i>
<i>D-3 Autocorrelation functions along x (x-corr) and y (y-corr) directions and time (t-corr) for 320-min aggregated radar 3rd sequence selected from 2015 for advection velocity $U=48 \text{ km}\cdot\text{h}^{-1}$. The horizontal axis represents the shift in the radar grid aggregated to $8\times 8 \text{ km}$</i>	<i>191</i>
<i>D-4 Autocorrelation functions along x (x-corr) and y (y-corr) directions and time (t-corr) for 320-min aggregated radar 4th sequence selected from 2015 for advection velocity $U=48 \text{ km}\cdot\text{h}^{-1}$. The horizontal axis represents the shift in the radar grid aggregated to $8\times 8 \text{ km}$</i>	<i>191</i>
<i>D-5 Autocorrelation functions along x (x-corr) and y (y-corr) directions and time (t-corr) for 320-min aggregated radar 5th sequence selected from 2015 for advection velocity $U=48 \text{ km}\cdot\text{h}^{-1}$. The horizontal axis represents the shift in the radar grid aggregated to $8\times 8 \text{ km}$</i>	<i>192</i>
<i>D-6 Autocorrelation functions along x (x-corr) and y (y-corr) directions and time (t-corr) for 320-min aggregated radar 6th sequence selected from 2015 for advection velocity $U=48 \text{ km}\cdot\text{h}^{-1}$. The horizontal axis represents the shift in the radar grid aggregated to $8\times 8 \text{ km}$</i>	<i>192</i>
<i>D-7 Autocorrelation functions along x (x-corr) and y (y-corr) directions and time (t-corr) for 320-min aggregated radar 7th sequence selected from 2015 for advection velocity $U=48 \text{ km}\cdot\text{h}^{-1}$. The horizontal axis represents the shift in the radar grid aggregated to $8\times 8 \text{ km}$</i>	<i>193</i>
<i>D-8 Autocorrelation functions along x (x-corr) and y (y-corr) directions and time (t-corr) for 320-min aggregated radar 8th sequence selected from 2015 for advection velocity $U=48 \text{ km}\cdot\text{h}^{-1}$. The horizontal axis represents the shift in the radar grid aggregated to $8\times 8 \text{ km}$</i>	<i>193</i>
<i>D-9 Autocorrelation functions along x (x-corr) and y (y-corr) directions and time (t-corr) for 320-min aggregated radar 9th sequence selected from 2015 for advection velocity $U=48 \text{ km}\cdot\text{h}^{-1}$. The horizontal axis represents the shift in the radar grid aggregated to $8\times 8 \text{ km}$</i>	<i>194</i>
<i>D-10 Autocorrelation functions along x (x-corr) and y (y-corr) directions and time (t-corr) for 320-min aggregated radar 10th sequence selected from 2015 for advection velocity $U=48 \text{ km}\cdot\text{h}^{-1}$. The horizontal axis represents the shift in the radar grid aggregated to $8\times 8 \text{ km}$</i>	<i>194</i>
<i>D-11 Autocorrelation functions along x (x-corr) and y (y-corr) directions and time (t-corr) for 320-min aggregated radar 11th sequence selected from 2015 for advection velocity $U=48 \text{ km}\cdot\text{h}^{-1}$. The horizontal axis represents the shift in the radar grid aggregated to $8\times 8 \text{ km}$</i>	<i>195</i>
<i>D-12 Autocorrelation functions along x (x-corr) and y (y-corr) directions and time (t-corr) for 320-min aggregated radar 12th sequence selected from 2015 for advection velocity $U=48 \text{ km}\cdot\text{h}^{-1}$. The horizontal axis represents the shift in the radar grid aggregated to $8\times 8 \text{ km}$</i>	<i>195</i>

APPENDIX D: AUTOCORRELATION FUNCTIONS OF SELECTED RADAR SEQUENCES FROM 2015
ALONG X AND Y DIRECTIONS AND TIME

D-13 Autocorrelation functions along x (x-corr) and y (y-corr) directions and time (t-corr) for 320-min aggregated radar 13th sequence selected from 2015 for advection velocity $U=48 \text{ km}\cdot\text{h}^{-1}$. The horizontal axis represents the shift in the radar grid aggregated to $8\times 8 \text{ km}$ 196

D-14 Autocorrelation functions along x (x-corr) and y (y-corr) directions and time (t-corr) for 320-min aggregated radar 14th sequence selected from 2015 for advection velocity $U=48 \text{ km}\cdot\text{h}^{-1}$. The horizontal axis represents the shift in the radar grid aggregated to $8\times 8 \text{ km}$ 196

D-15 Autocorrelation functions along x (x-corr) and y (y-corr) directions and time (t-corr) for 320-min aggregated radar 15th sequence selected from 2015 for advection velocity $U=48 \text{ km}\cdot\text{h}^{-1}$. The horizontal axis represents the shift in the radar grid aggregated to $8\times 8 \text{ km}$ 197

D-16 Autocorrelation functions along x (x-corr) and y (y-corr) directions and time (t-corr) for 320-min aggregated radar 16th sequence selected from 2015 for advection velocity $U=48 \text{ km}\cdot\text{h}^{-1}$. The horizontal axis represents the shift in the radar grid aggregated to $8\times 8 \text{ km}$ 197

D-17 Autocorrelation functions along x (x-corr) and y (y-corr) directions and time (t-corr) for 320-min aggregated radar 17th sequence selected from 2015 for advection velocity $U=48 \text{ km}\cdot\text{h}^{-1}$. The horizontal axis represents the shift in the radar grid aggregated to $8\times 8 \text{ km}$ 198

D-18 Autocorrelation functions along x (x-corr) and y (y-corr) directions and time (t-corr) for 320-min aggregated radar 18th sequence selected from 2015 for advection velocity $U=48 \text{ km}\cdot\text{h}^{-1}$. The horizontal axis represents the shift in the radar grid aggregated to $8\times 8 \text{ km}$ 198

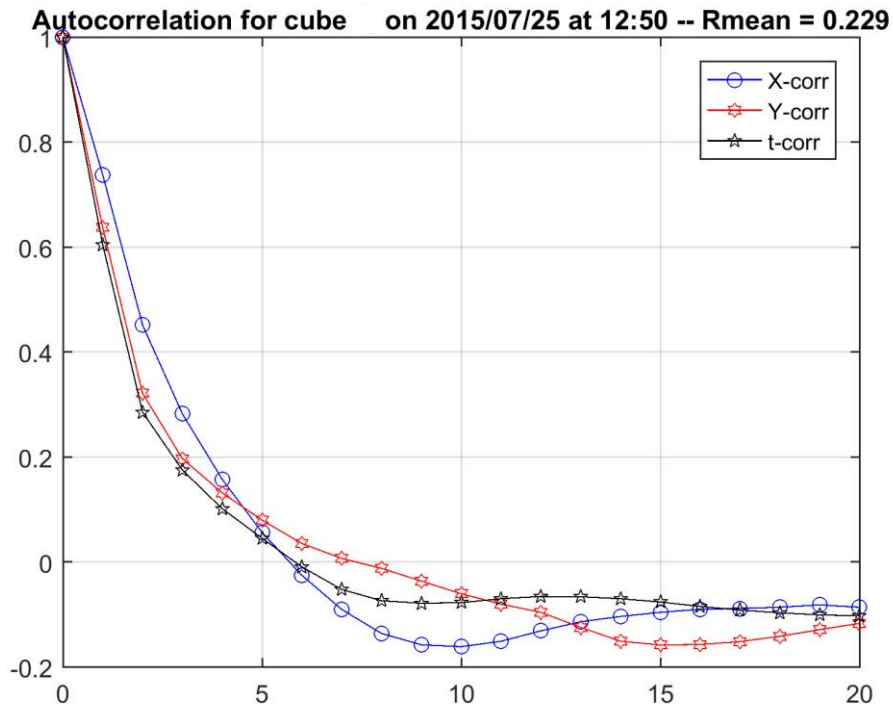
D-19 Autocorrelation functions along x (x-corr) and y (y-corr) directions and time (t-corr) for 320-min aggregated radar 19th sequence selected from 2015 for advection velocity $U=48 \text{ km}\cdot\text{h}^{-1}$. The horizontal axis represents the shift in the radar grid aggregated to $8\times 8 \text{ km}$ 199

D-20 Autocorrelation functions along x (x-corr) and y (y-corr) directions and time (t-corr) for 320-min aggregated radar 20th sequence selected from 2015 for advection velocity $U=48 \text{ km}\cdot\text{h}^{-1}$. The horizontal axis represents the shift in the radar grid aggregated to $8\times 8 \text{ km}$ 199

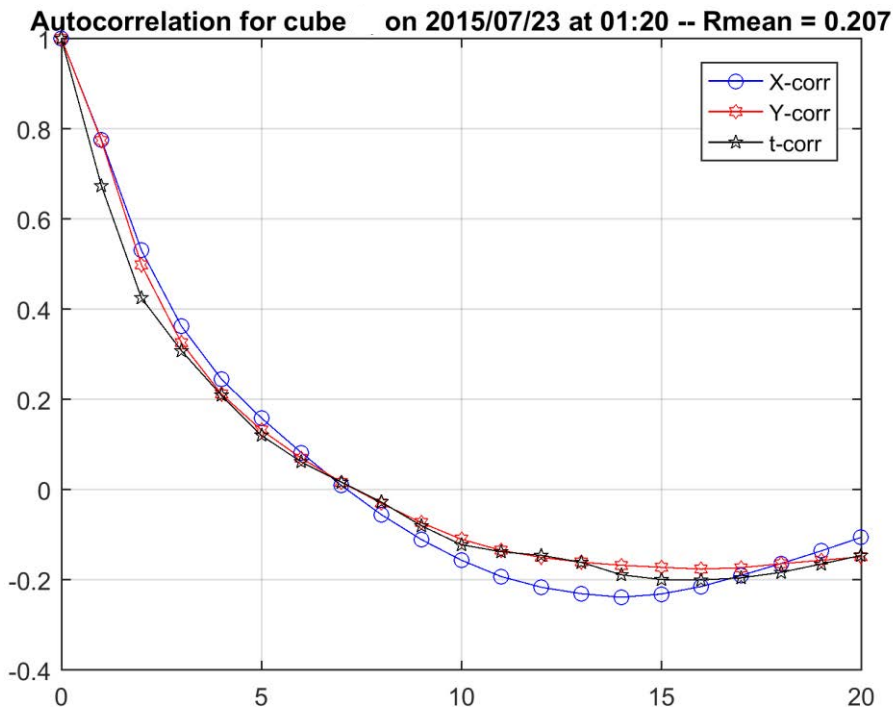
D-21 Autocorrelation functions along x (x-corr) and y (y-corr) directions and time (t-corr) for 320-min aggregated radar 21st sequence selected from 2015 for advection velocity $U=48 \text{ km}\cdot\text{h}^{-1}$. The horizontal axis represents the shift in the radar grid aggregated to $8\times 8 \text{ km}$ 200

D-22 Autocorrelation functions along x (x-corr) and y (y-corr) directions and time (t-corr) for 320-min aggregated radar 22nd sequence selected from 2015 for advection velocity $U=48 \text{ km}\cdot\text{h}^{-1}$. The horizontal axis represents the shift in the radar grid aggregated to $8\times 8 \text{ km}$ 200

APPENDIX D: AUTOCORRELATION FUNCTIONS OF SELECTED RADAR SEQUENCES FROM 2015
ALONG X AND Y DIRECTIONS AND TIME

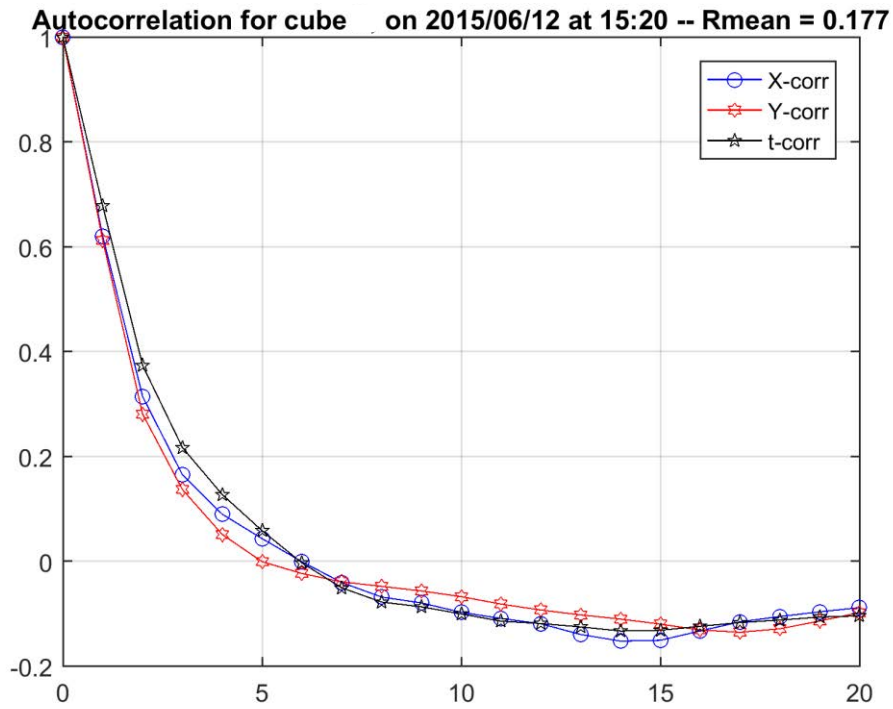


D-1 Autocorrelation functions along x (x-corr) and y (y-corr) directions and time (t-corr) for 320-min aggregated radar 1st sequence selected from 2015 for advection velocity $U=48 \text{ km}\cdot\text{h}^{-1}$. The horizontal axis represents the shift in the radar grid aggregated to $8\times 8 \text{ km}$

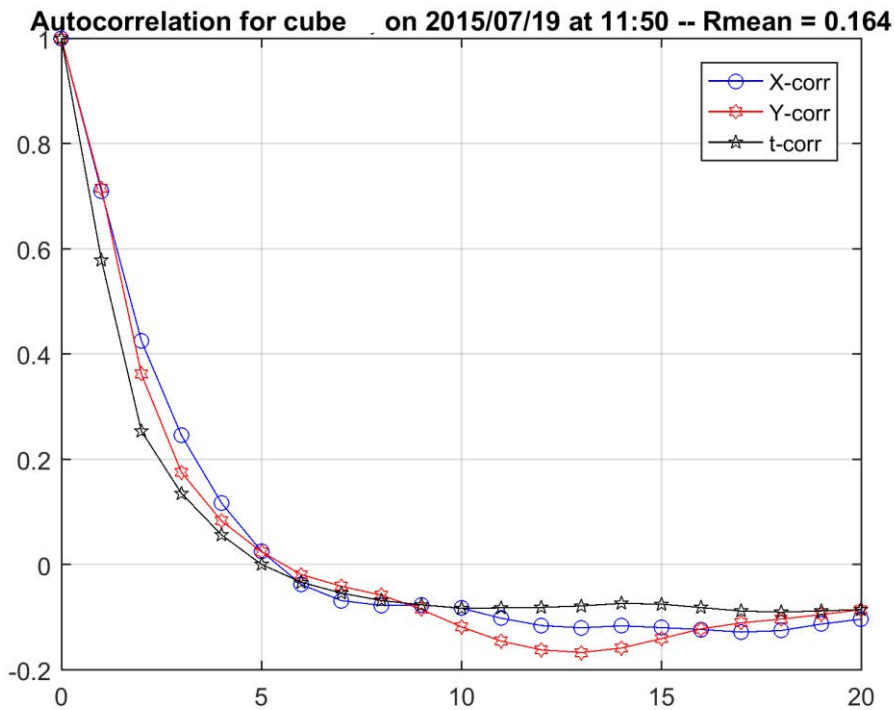


D-2 Autocorrelation functions along x (x-corr) and y (y-corr) directions and time (t-corr) for 320-min aggregated radar 2nd sequence selected from 2015 for advection velocity $U=48 \text{ km}\cdot\text{h}^{-1}$. The horizontal axis represents the shift in the radar grid aggregated to $8\times 8 \text{ km}$

APPENDIX D: AUTOCORRELATION FUNCTIONS OF SELECTED RADAR SEQUENCES FROM 2015
ALONG X AND Y DIRECTIONS AND TIME

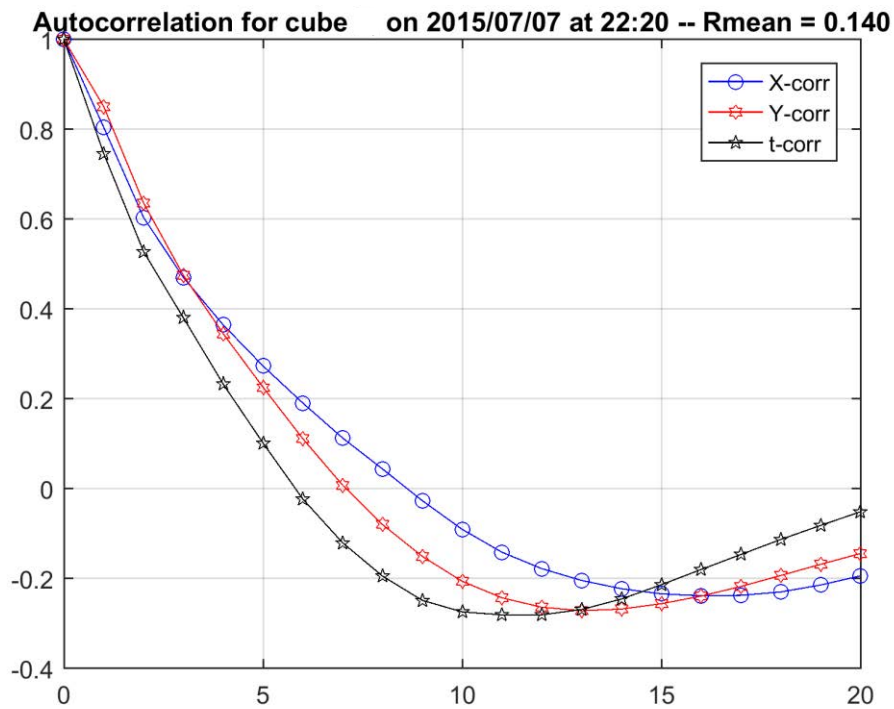


D-3 Autocorrelation functions along x (x-corr) and y (y-corr) directions and time (t-corr) for 320-min aggregated radar 3rd sequence selected from 2015 for advection velocity $U=48 \text{ km}\cdot\text{h}^{-1}$. The horizontal axis represents the shift in the radar grid aggregated to $8\times 8 \text{ km}$

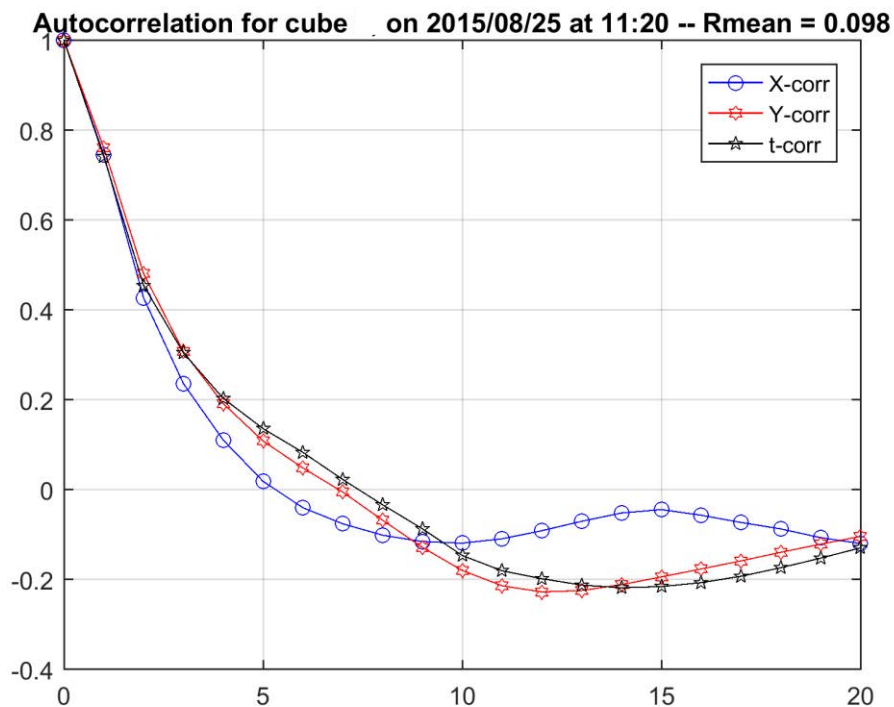


D-4 Autocorrelation functions along x (x-corr) and y (y-corr) directions and time (t-corr) for 320-min aggregated radar 4th sequence selected from 2015 for advection velocity $U=48 \text{ km}\cdot\text{h}^{-1}$. The horizontal axis represents the shift in the radar grid aggregated to $8\times 8 \text{ km}$

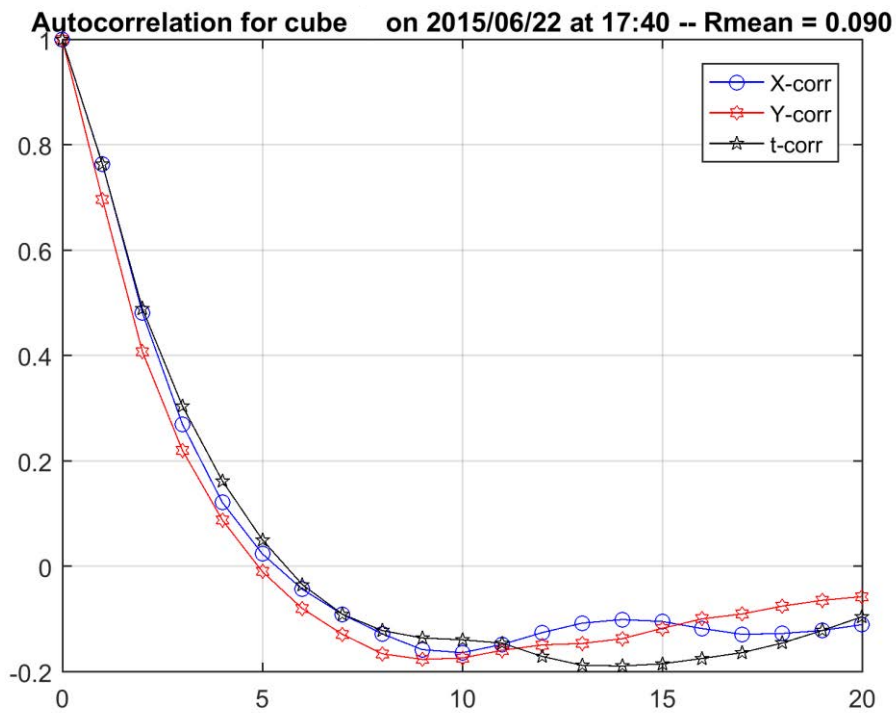
APPENDIX D: AUTOCORRELATION FUNCTIONS OF SELECTED RADAR SEQUENCES FROM 2015
ALONG X AND Y DIRECTIONS AND TIME



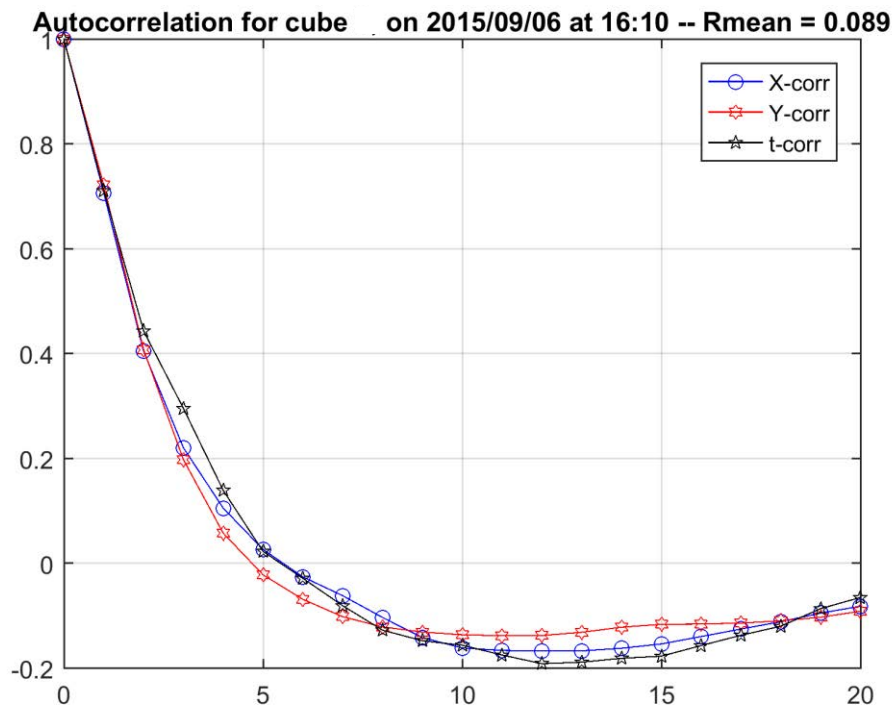
D-5 Autocorrelation functions along x (x-corr) and y (y-corr) directions and time (t-corr) for 320-min aggregated radar 5th sequence selected from 2015 for advection velocity $U=48 \text{ km}\cdot\text{h}^{-1}$. The horizontal axis represents the shift in the radar grid aggregated to $8\times 8 \text{ km}$



D-6 Autocorrelation functions along x (x-corr) and y (y-corr) directions and time (t-corr) for 320-min aggregated radar 6th sequence selected from 2015 for advection velocity $U=48 \text{ km}\cdot\text{h}^{-1}$. The horizontal axis represents the shift in the radar grid aggregated to $8\times 8 \text{ km}$

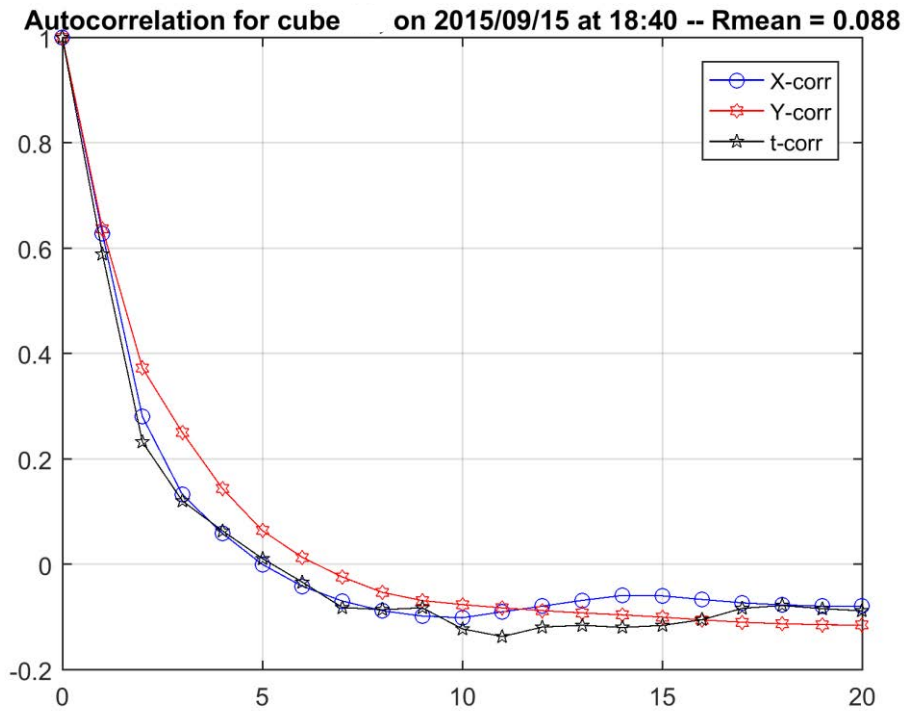


D-7 Autocorrelation functions along x (x-corr) and y (y-corr) directions and time (t-corr) for 320-min aggregated radar 7th sequence selected from 2015 for advection velocity $U=48 \text{ km}\cdot\text{h}^{-1}$. The horizontal axis represents the shift in the radar grid aggregated to $8\times 8 \text{ km}$

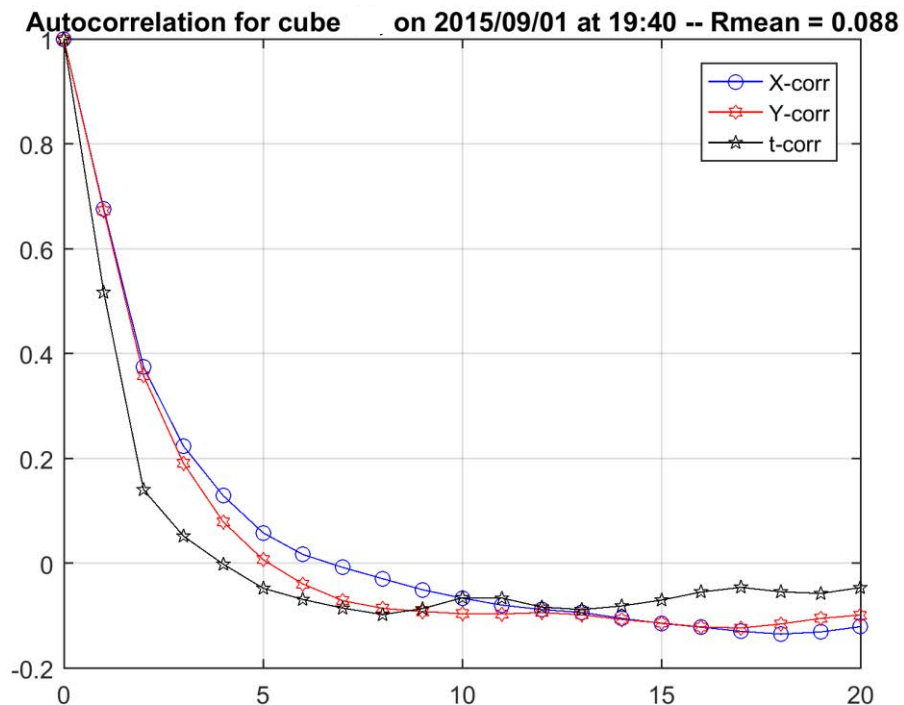


D-8 Autocorrelation functions along x (x-corr) and y (y-corr) directions and time (t-corr) for 320-min aggregated radar 8th sequence selected from 2015 for advection velocity $U=48 \text{ km}\cdot\text{h}^{-1}$. The horizontal axis represents the shift in the radar grid aggregated to $8\times 8 \text{ km}$

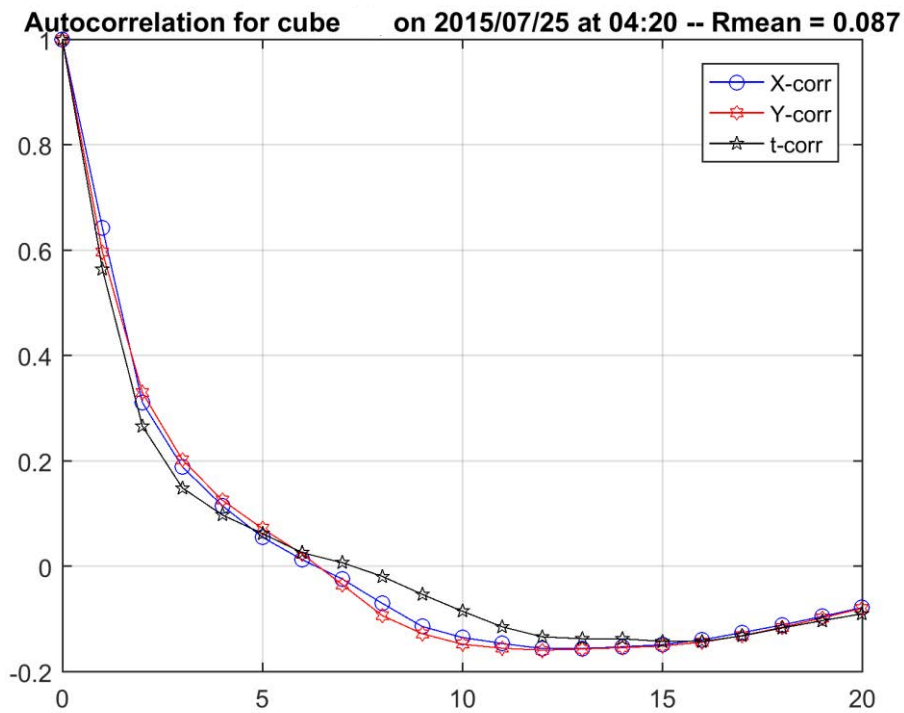
APPENDIX D: AUTOCORRELATION FUNCTIONS OF SELECTED RADAR SEQUENCES FROM 2015
ALONG X AND Y DIRECTIONS AND TIME



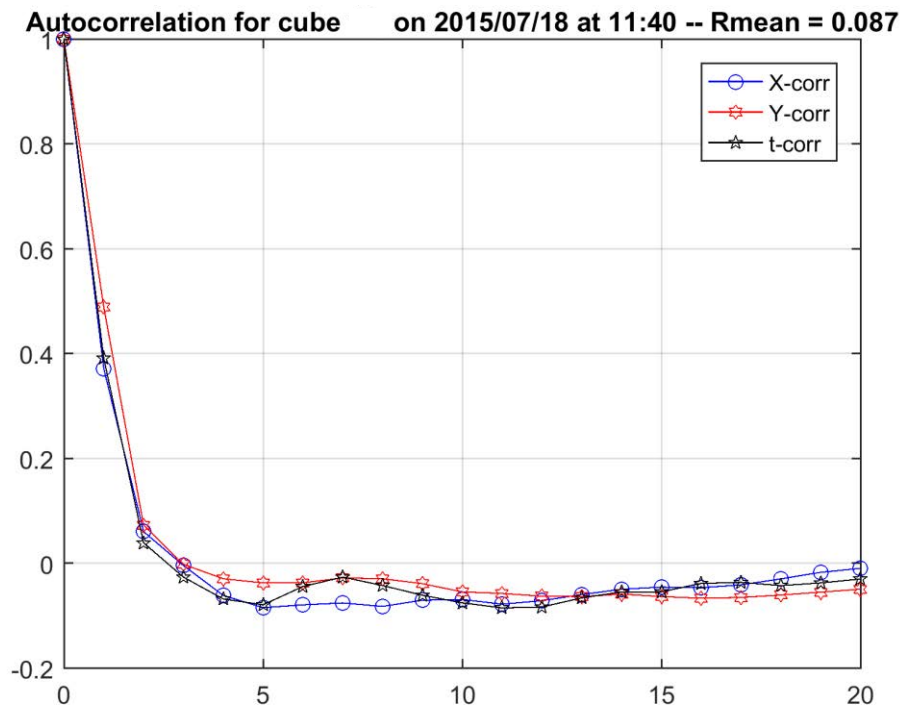
D-9 Autocorrelation functions along x (x-corr) and y (y-corr) directions and time (t-corr) for 320-min aggregated radar 9th sequence selected from 2015 for advection velocity $U=48 \text{ km}\cdot\text{h}^{-1}$. The horizontal axis represents the shift in the radar grid aggregated to $8\times 8 \text{ km}$



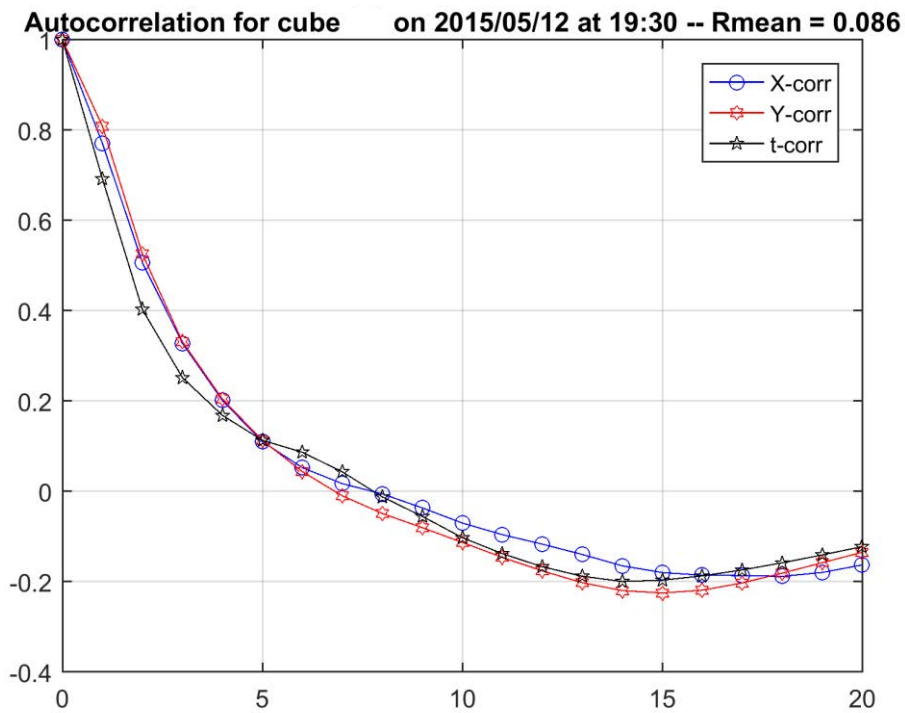
D-10 Autocorrelation functions along x (x-corr) and y (y-corr) directions and time (t-corr) for 320-min aggregated radar 10th sequence selected from 2015 for advection velocity $U=48 \text{ km}\cdot\text{h}^{-1}$. The horizontal axis represents the shift in the radar grid aggregated to $8\times 8 \text{ km}$



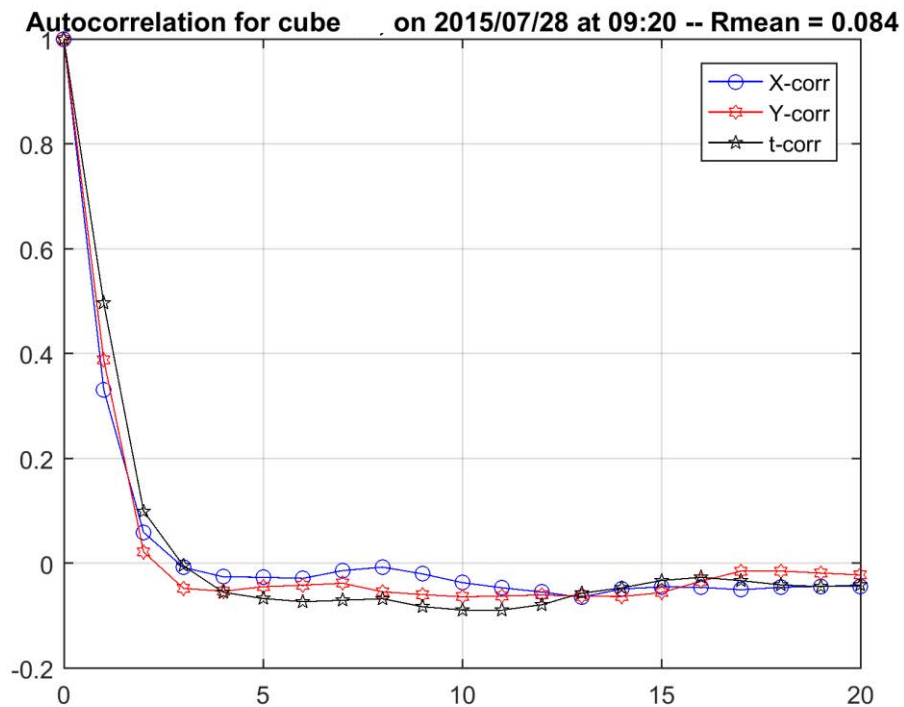
D-11 Autocorrelation functions along x (x-corr) and y (y-corr) directions and time (t-corr) for 320-min aggregated radar 11th sequence selected from 2015 for advection velocity $U=48 \text{ km}\cdot\text{h}^{-1}$. The horizontal axis represents the shift in the radar grid aggregated to $8\times 8 \text{ km}$



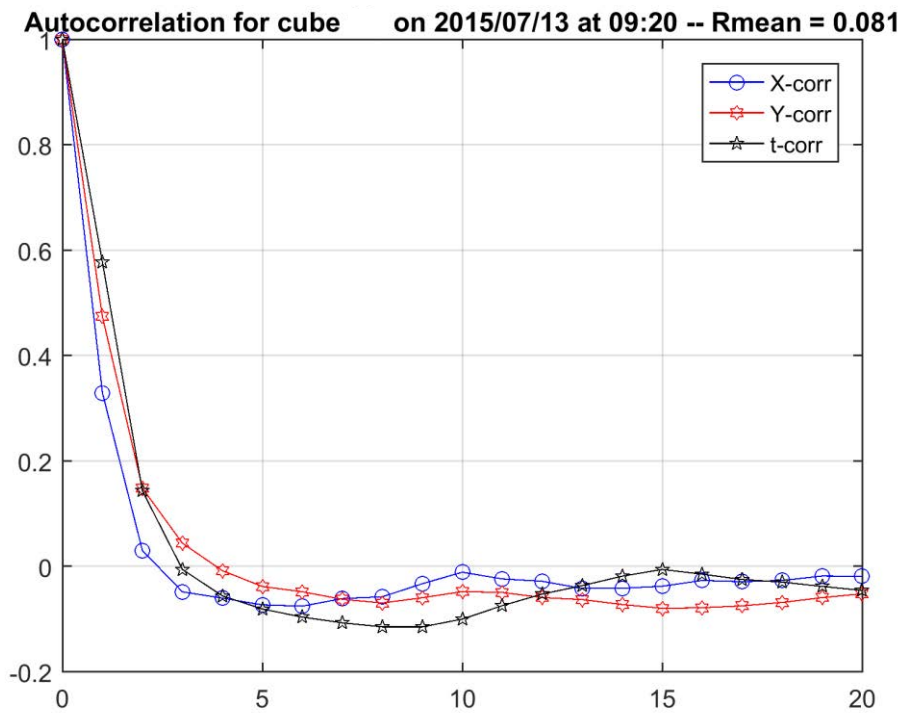
D-12 Autocorrelation functions along x (x-corr) and y (y-corr) directions and time (t-corr) for 320-min aggregated radar 12th sequence selected from 2015 for advection velocity $U=48 \text{ km}\cdot\text{h}^{-1}$. The horizontal axis represents the shift in the radar grid aggregated to $8\times 8 \text{ km}$



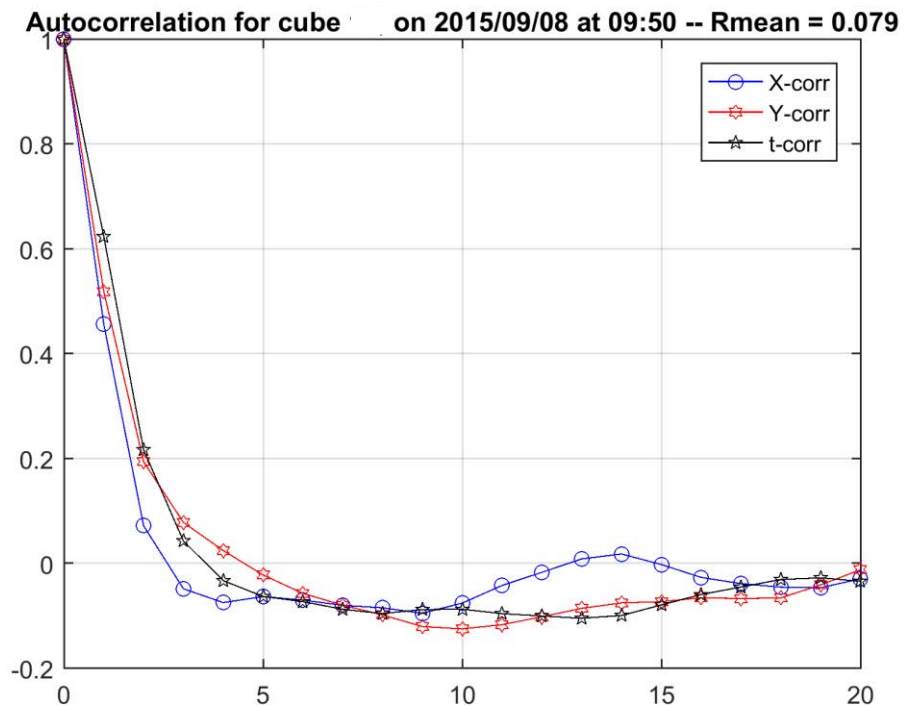
D-13 Autocorrelation functions along x (x-corr) and y (y-corr) directions and time (t-corr) for 320-min aggregated radar 13th sequence selected from 2015 for advection velocity $U=48 \text{ km}\cdot\text{h}^{-1}$. The horizontal axis represents the shift in the radar grid aggregated to $8\times 8 \text{ km}$



D-14 Autocorrelation functions along x (x-corr) and y (y-corr) directions and time (t-corr) for 320-min aggregated radar 14th sequence selected from 2015 for advection velocity $U=48 \text{ km}\cdot\text{h}^{-1}$. The horizontal axis represents the shift in the radar grid aggregated to $8\times 8 \text{ km}$

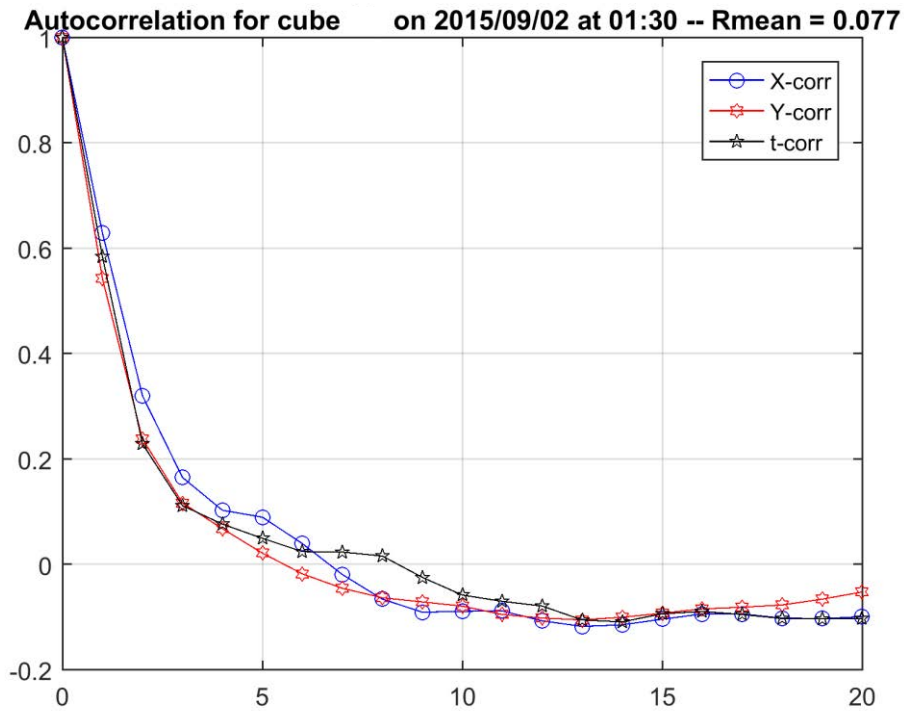


D-15 Autocorrelation functions along x (x-corr) and y (y-corr) directions and time (t-corr) for 320-min aggregated radar 15th sequence selected from 2015 for advection velocity $U=48 \text{ km}\cdot\text{h}^{-1}$. The horizontal axis represents the shift in the radar grid aggregated to $8\times 8 \text{ km}$

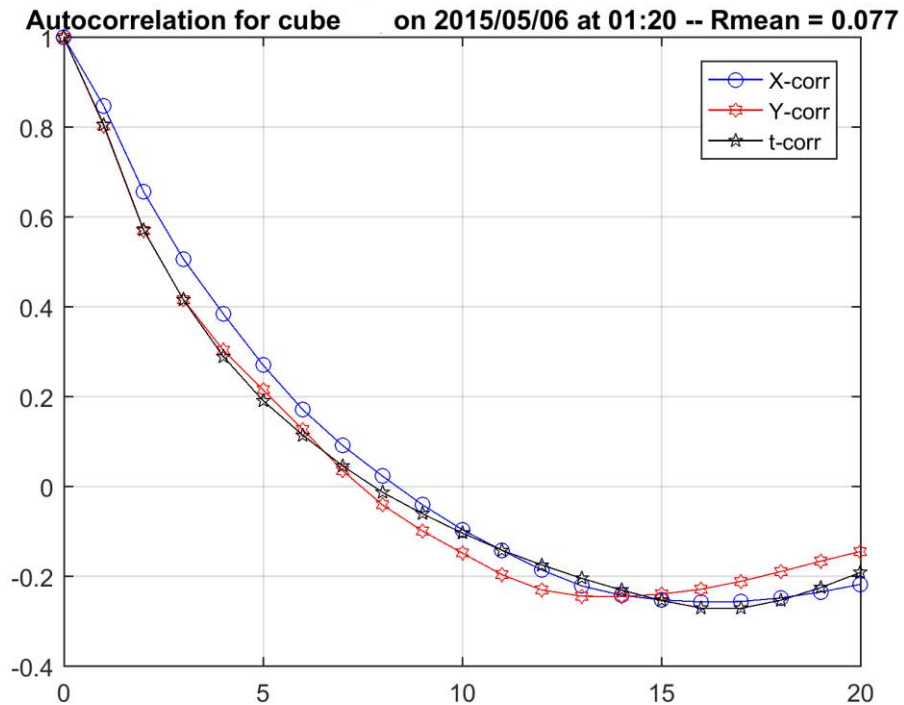


D-16 Autocorrelation functions along x (x-corr) and y (y-corr) directions and time (t-corr) for 320-min aggregated radar 16th sequence selected from 2015 for advection velocity $U=48 \text{ km}\cdot\text{h}^{-1}$. The horizontal axis represents the shift in the radar grid aggregated to $8\times 8 \text{ km}$

APPENDIX D: AUTOCORRELATION FUNCTIONS OF SELECTED RADAR SEQUENCES FROM 2015
ALONG X AND Y DIRECTIONS AND TIME

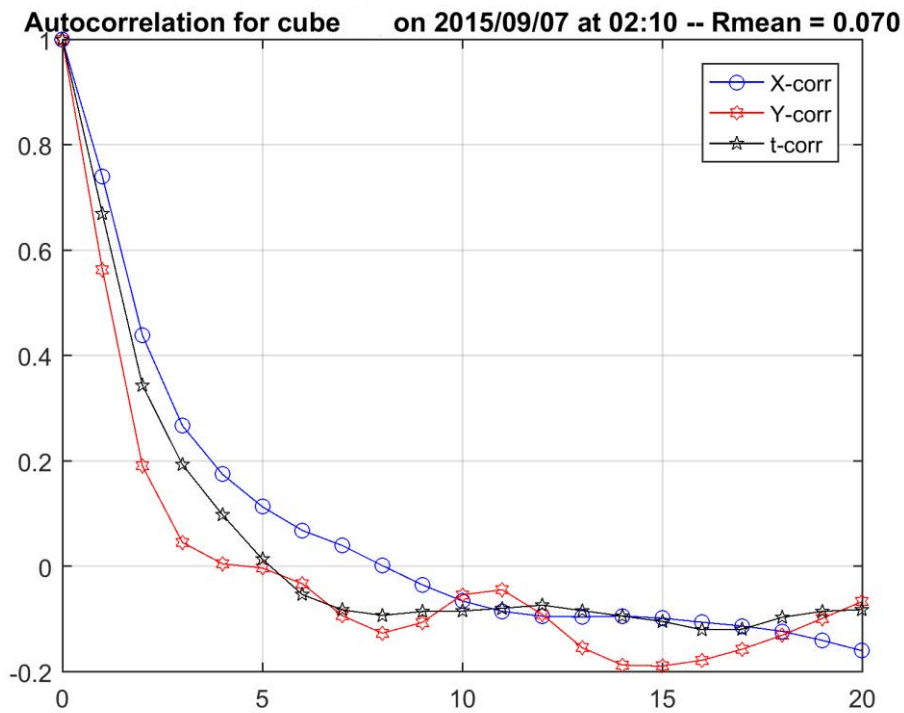


D-17 Autocorrelation functions along x (x-corr) and y (y-corr) directions and time (t-corr) for 320-min aggregated radar 17th sequence selected from 2015 for advection velocity $U=48 \text{ km}\cdot\text{h}^{-1}$. The horizontal axis represents the shift in the radar grid aggregated to $8\times 8 \text{ km}$

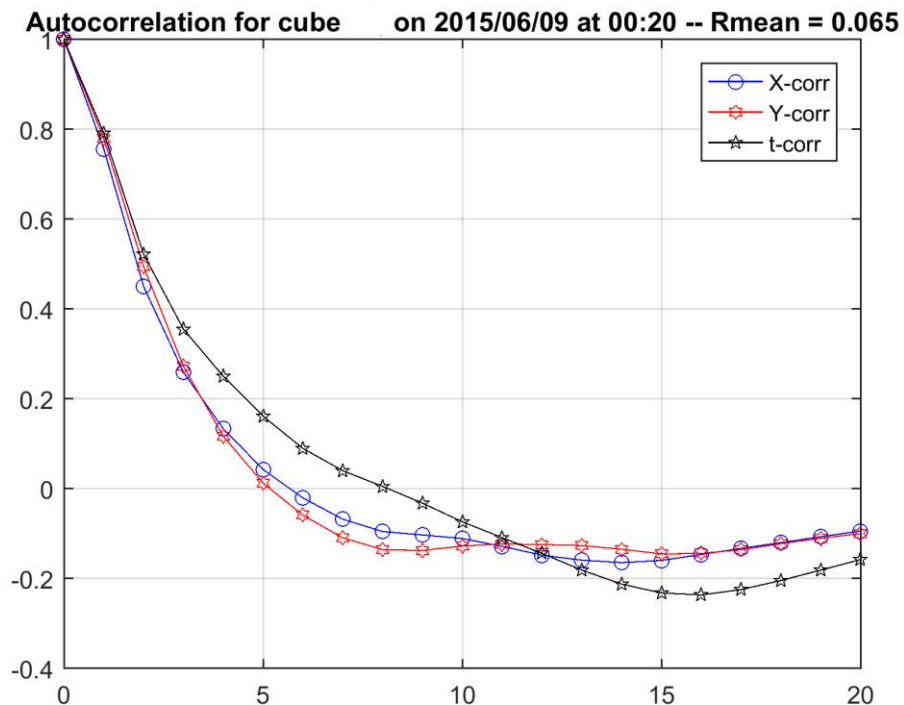


D-18 Autocorrelation functions along x (x-corr) and y (y-corr) directions and time (t-corr) for 320-min aggregated radar 18th sequence selected from 2015 for advection velocity $U=48 \text{ km}\cdot\text{h}^{-1}$. The horizontal axis represents the shift in the radar grid aggregated to $8\times 8 \text{ km}$

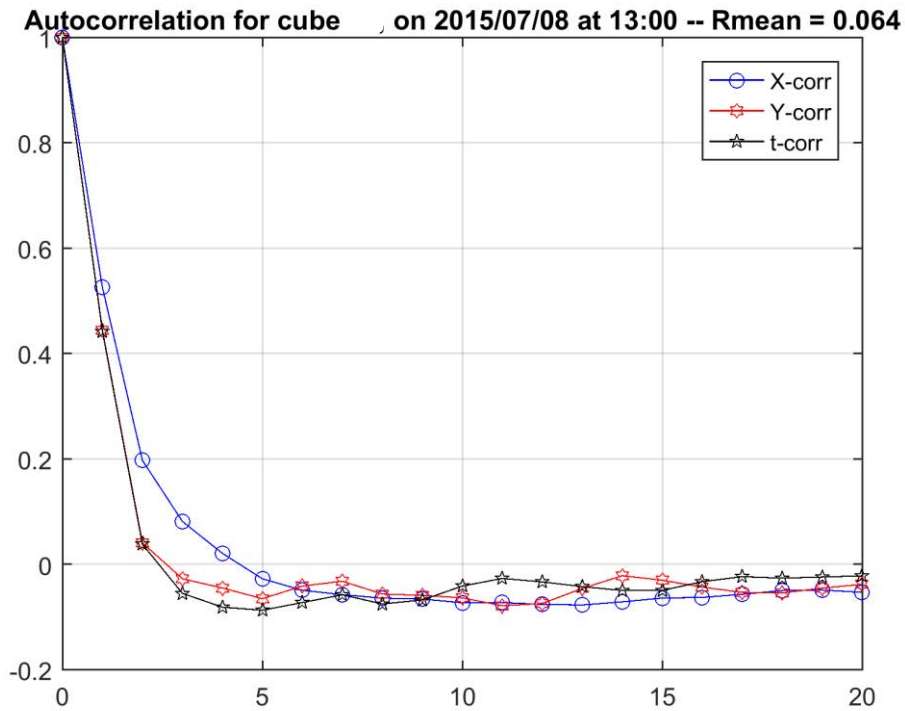
APPENDIX D: AUTOCORRELATION FUNCTIONS OF SELECTED RADAR SEQUENCES FROM 2015
ALONG X AND Y DIRECTIONS AND TIME



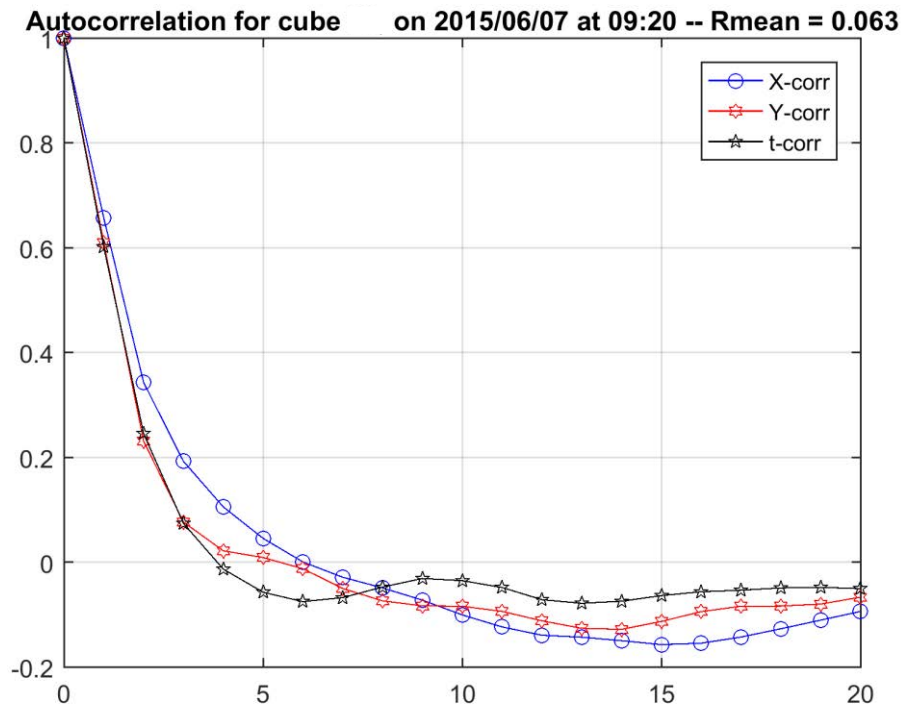
D-19 Autocorrelation functions along x (x-corr) and y (y-corr) directions and time (t-corr) for 320-min aggregated radar 19th sequence selected from 2015 for advection velocity $U=48 \text{ km}\cdot\text{h}^{-1}$. The horizontal axis represents the shift in the radar grid aggregated to $8\times 8 \text{ km}$



D-20 Autocorrelation functions along x (x-corr) and y (y-corr) directions and time (t-corr) for 320-min aggregated radar 20th sequence selected from 2015 for advection velocity $U=48 \text{ km}\cdot\text{h}^{-1}$. The horizontal axis represents the shift in the radar grid aggregated to $8\times 8 \text{ km}$



D-21 Autocorrelation functions along x (x-corr) and y (y-corr) directions and time (t-corr) for 320-min aggregated radar 21st sequence selected from 2015 for advection velocity $U=48 \text{ km}\cdot\text{h}^{-1}$. The horizontal axis represents the shift in the radar grid aggregated to $8\times 8 \text{ km}$



D-22 Autocorrelation functions along x (x-corr) and y (y-corr) directions and time (t-corr) for 320-min aggregated radar 22nd sequence selected from 2015 for advection velocity $U=48 \text{ km}\cdot\text{h}^{-1}$. The horizontal axis represents the shift in the radar grid aggregated to $8\times 8 \text{ km}$

APPENDIX E

Table of contents

<i>E-1 List of rainfall events selected using moving window algorithm</i>	<i>202</i>
---	------------

E-1 List of rainfall events selected using moving window algorithm

No.	No. of rainfall event in particular year	Start time					R, mm/10min
		Year	Month	Day	Hours	Minutes	
1	1	2009	7	18	16	30	0.226
2	2	2009	7	8	03	40	0.221
3	3	2009	6	9	15	00	0.166
4	4	2009	6	16	02	50	0.156
5	5	2009	6	30	14	10	0.150
6	6	2009	5	21	18	10	0.149
7	7	2009	5	31	12	10	0.148
8	8	2009	7	8	09	00	0.145
9	9	2009	6	29	10	20	0.136
10	10	2009	7	7	22	20	0.135
11	11	2009	5	16	13	00	0.123
12	12	2009	6	15	21	30	0.119
13	13	2009	6	6	23	00	0.118
14	14	2009	6	1	10	40	0.118
15	15	2009	5	28	10	30	0.117
16	16	2009	8	11	05	50	0.096
17	17	2009	5	30	12	30	0.095
18	18	2009	7	19	06	40	0.094
19	19	2009	8	3	02	50	0.088
20	20	2009	6	11	14	20	0.084
21	21	2009	5	27	05	00	0.083
22	22	2009	7	22	18	10	0.080
23	23	2009	5	6	10	10	0.077
24	24	2009	7	1	12	20	0.077
25	25	2009	7	5	08	00	0.077
26	26	2009	6	22	10	30	0.070
27	27	2009	6	10	13	30	0.068
28	28	2009	7	20	13	40	0.066
29	1	2010	7	24	05	40	0.153
30	2	2010	8	6	18	20	0.151
31	3	2010	7	28	01	10	0.150
32	4	2010	6	2	20	00	0.133
33	5	2010	7	23	11	30	0.133
34	6	2010	5	30	15	50	0.125
35	7	2010	7	28	10	50	0.122
36	8	2010	5	14	18	20	0.116
37	9	2010	8	3	04	10	0.090
38	10	2010	6	2	14	40	0.085

APPENDIX E: LIST OF RAINFALL EVENTS SELECTED USING MOVING WINDOW ALGORITHM

39	11	2010	7	24	11	0	0.085
40	12	2010	5	12	12	50	0.080
41	13	2010	5	31	08	40	0.079
42	14	2010	5	7	13	10	0.079
43	15	2010	8	7	07	10	0.077
44	16	2010	5	3	06	10	0.076
45	17	2010	7	28	23	20	0.075
46	18	2010	7	27	19	50	0.073
47	19	2010	5	30	21	10	0.066
48	20	2010	5	13	11	10	0.065
49	21	2010	5	7	07	50	0.065
50	22	2010	5	6	02	10	0.065
51	23	2010	5	17	02	50	0.063
52	1	2013	7	29	20	30	0.185
53	2	2013	6	25	03	30	0.182
54	3	2013	8	9	00	40	0.177
55	4	2013	5	9	14	00	0.176
56	5	2013	5	24	21	30	0.132
57	6	2013	9	13	18	00	0.118
58	7	2013	8	13	02	00	0.113
59	8	2013	5	20	09	50	0.108
60	9	2013	6	3	14	10	0.106
61	10	2013	5	25	02	50	0.106
62	11	2013	6	25	22	40	0.102
63	12	2013	6	2	18	20	0.095
64	13	2013	9	9	14	50	0.093
65	14	2013	5	25	08	10	0.093
66	15	2013	6	9	23	30	0.091
67	16	2013	5	30	14	50	0.086
68	17	2013	9	11	06	10	0.086
69	18	2013	8	10	06	30	0.086
70	19	2013	8	19	20	20	0.080
71	20	2013	9	2	13	00	0.078
72	21	2013	6	1	16	30	0.076
73	22	2013	5	22	12	30	0.075
74	23	2013	6	25	10	30	0.068
75	24	2013	5	27	15	10	0.068
76	25	2013	8	9	20	00	0.068
77	26	2013	5	24	16	10	0.067
78	27	2013	5	31	11	20	0.067
79	28	2013	7	29	02	40	0.067
80	29	2013	7	28	02	40	0.065
81	1	2014	5	24	13	00	0.223

APPENDIX E: LIST OF RAINFALL EVENTS SELECTED USING MOVING WINDOW ALGORITHM

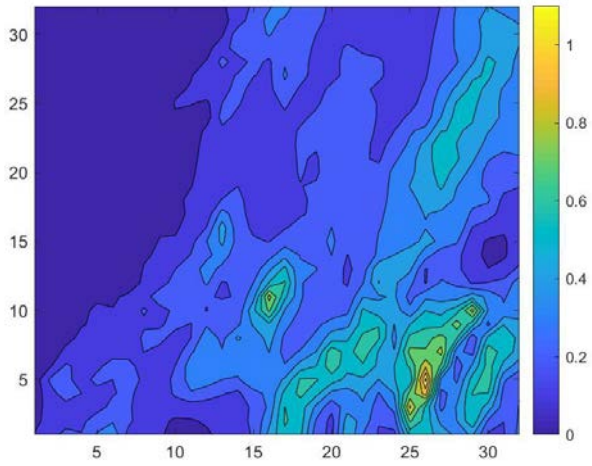
82	2	2014	7	7	17	10	0.126
83	3	2014	6	9	01	50	0.122
84	4	2014	7	6	11	10	0.115
85	5	2014	8	4	14	50	0.106
86	6	2014	5	17	19	20	0.084
87	7	2014	7	23	12	30	0.081
88	8	2014	5	11	01	20	0.078
89	9	2014	6	13	12	30	0.077
90	10	2014	8	15	13	20	0.077
91	11	2014	8	31	19	00	0.075
92	12	2014	8	24	10	00	0.074
93	13	2014	7	28	11	40	0.066
94	1	2015	7	25	12	50	0.229
95	2	2015	7	23	01	30	0.207
96	3	2015	6	12	15	20	0.177
97	4	2015	7	19	11	20	0.164
98	5	2015	7	7	22	40	0.140
99	6	2015	8	25	11	20	0.098
100	7	2015	6	22	17	50	0.090
101	8	2015	9	6	16	20	0.089
102	9	2015	9	15	18	50	0.088
103	10	2015	9	1	19	20	0.088
104	11	2015	7	25	4	20	0.087
105	12	2015	7	18	11	40	0.087
106	13	2015	5	12	19	20	0.086
107	14	2015	7	28	9	20	0.084
108	15	2015	7	13	9	0	0.081
109	16	2015	9	8	9	20	0.079
110	17	2015	9	2	1	10	0.077
111	18	2015	5	6	1	40	0.077
112	19	2015	9	7	2	40	0.070
113	20	2015	6	9	0	50	0.065
114	21	2015	7	8	13	30	0.064
115	22	2015	6	7	9	10	0.063

APPENDIX F

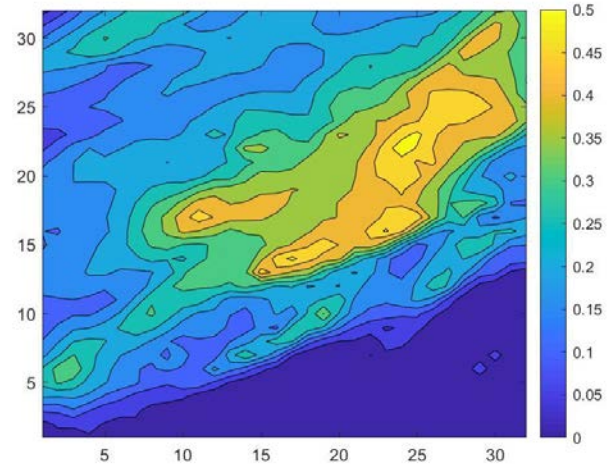
Table of contents

<i>F-1 Mean rainfall rate (mm/10min) of 320-min aggregated 1st radar sequence.....</i>	<i>206</i>
<i>F-2 Mean rainfall rate (mm/10min) of 320-min aggregated 2nd radar sequence.....</i>	<i>206</i>
<i>F-3 Mean rainfall rate (mm/10min) of 320-min aggregated 3th radar sequence</i>	<i>206</i>
<i>F-4 Mean rainfall rate (mm/10min) of 320-min aggregated 4th radar sequence</i>	<i>206</i>
<i>F-5 Mean rainfall rate (mm/10min) of 320-min aggregated 5th radar sequence</i>	<i>206</i>
<i>F-6 Mean rainfall rate (mm/10min) of 320-min aggregated 6th radar sequence</i>	<i>206</i>
<i>F-7 Mean rainfall rate (mm/10min) of 320-min aggregated 7th radar sequence</i>	<i>207</i>
<i>F-8 Mean rainfall rate (mm/10min) of 320-min aggregated 8th radar sequence</i>	<i>207</i>
<i>F-9 Mean rainfall rate (mm/10min) of 320-min aggregated 9th radar sequence</i>	<i>207</i>
<i>F-10 Mean rainfall rate (mm/10min) of 320-min aggregated 10th radar sequence</i>	<i>207</i>
<i>F-11 Mean rainfall rate (mm/10min) of 320-min aggregated 11th radar sequence</i>	<i>207</i>
<i>F-12 Mean rainfall rate (mm/10min) of 320-min aggregated 12th radar sequence</i>	<i>207</i>
<i>F-13 Mean rainfall rate (mm/10min) of 320-min aggregated 13th radar sequence</i>	<i>208</i>
<i>F-14 Mean rainfall rate (mm/10min) of 320-min aggregated 14th radar sequence</i>	<i>208</i>
<i>F-15 Mean rainfall rate (mm/10min) of 320-min aggregated 15th radar sequence</i>	<i>208</i>
<i>F-16 Mean rainfall rate (mm/10min) of 320-min aggregated 16th radar sequence</i>	<i>208</i>
<i>F-17 Mean rainfall rate (mm/10min) of 320-min aggregated 17th radar sequence</i>	<i>208</i>
<i>F-18 Mean rainfall rate (mm/10min) of 320-min aggregated 18th radar sequence</i>	<i>208</i>
<i>F-19 Mean rainfall rate (mm/10min) of 320-min aggregated 19th radar sequence</i>	<i>209</i>
<i>F-20 Mean rainfall rate (mm/10min) of 320-min aggregated 20th radar sequence</i>	<i>209</i>
<i>F-21 Mean rainfall rate (mm/10min) of 320-min aggregated 21st radar sequence.....</i>	<i>209</i>
<i>F-22 Mean rainfall rate (mm/10min) of 320-min aggregated 22nd radar sequence</i>	<i>209</i>

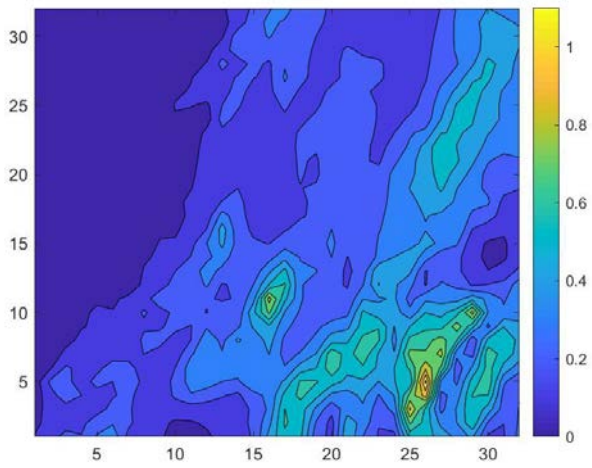
APPENDIX F: MEAN RAINFALL DEPTHS FOR AVERAGED RADAR SEQUENCES FROM 2015



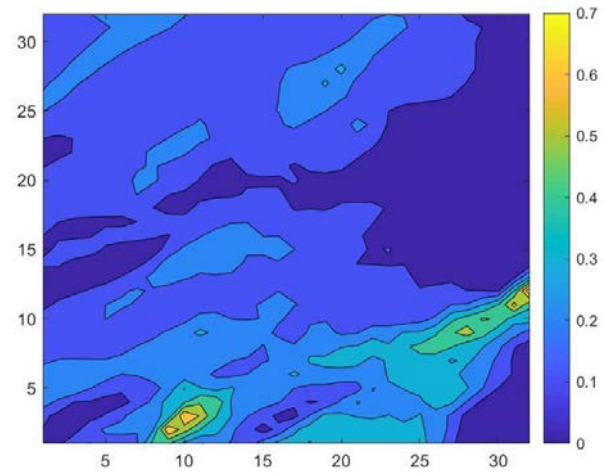
F-1 Mean rainfall rate (mm/10min) of 320-min aggregated 1st radar sequence



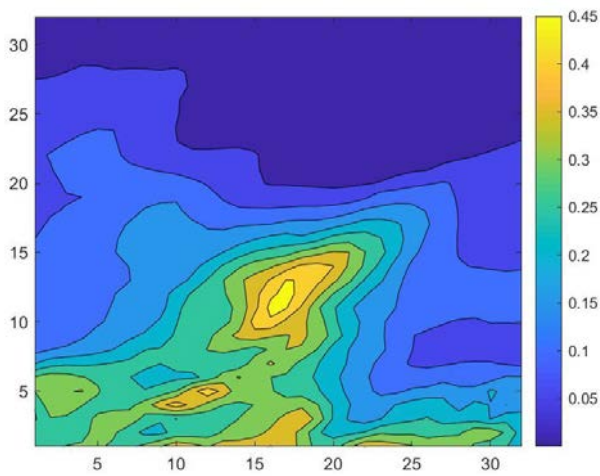
F-2 Mean rainfall rate (mm/10min) of 320-min aggregated 2nd radar sequence



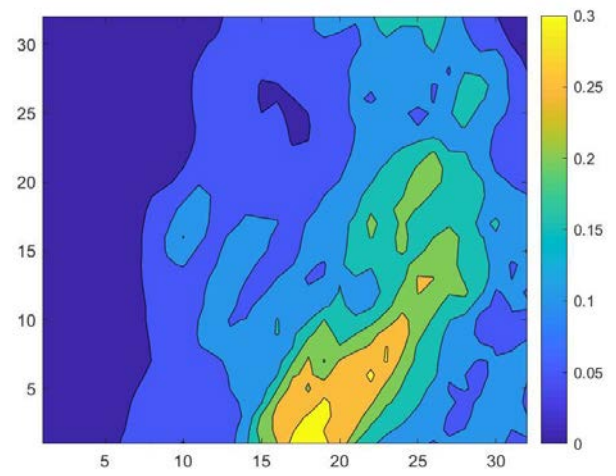
F-3 Mean rainfall rate (mm/10min) of 320-min aggregated 3rd radar sequence



F-4 Mean rainfall rate (mm/10min) of 320-min aggregated 4th radar sequence

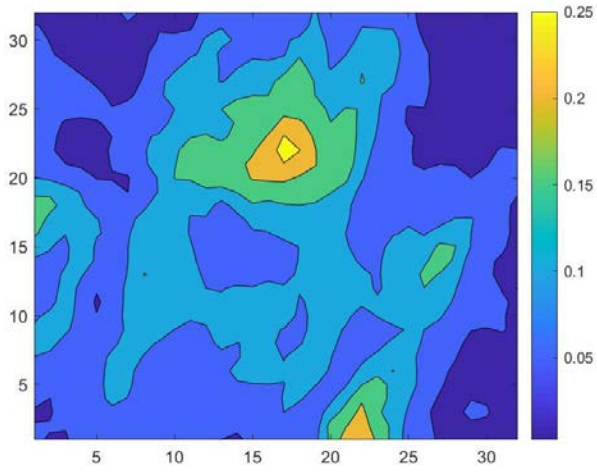


F-5 Mean rainfall rate (mm/10min) of 320-min aggregated 5th radar sequence

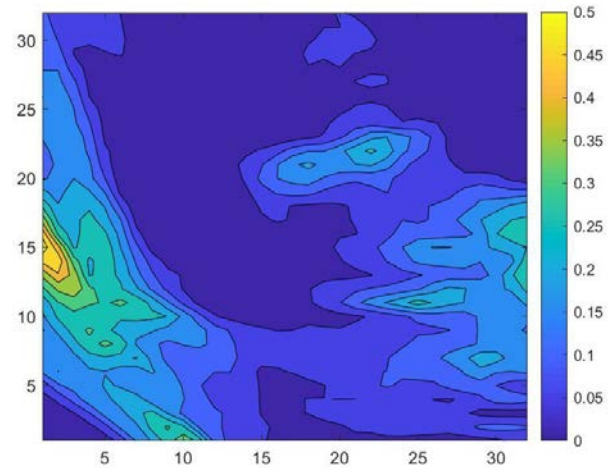


F-6 Mean rainfall rate (mm/10min) of 320-min aggregated 6th radar sequence

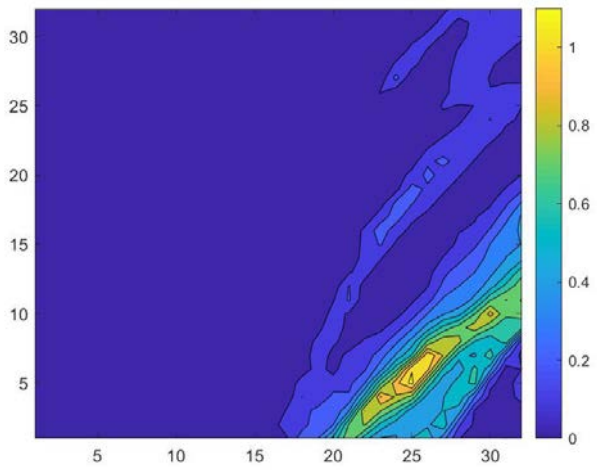
APPENDIX F: MEAN RAINFALL DEPTHS FOR AVERAGED RADAR SEQUENCES FROM 2015



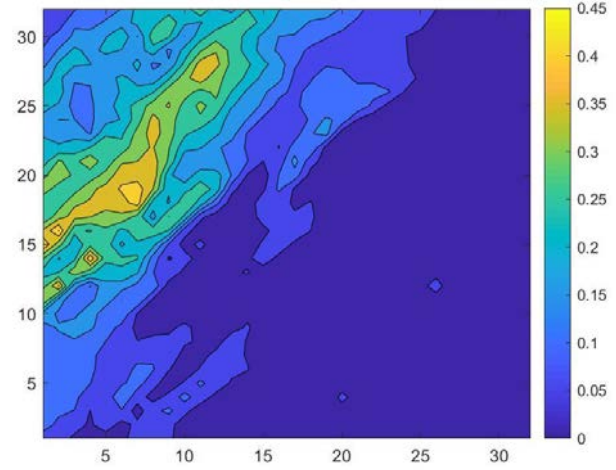
F-7 Mean rainfall rate (mm/10min) of 320-min aggregated 7th radar sequence



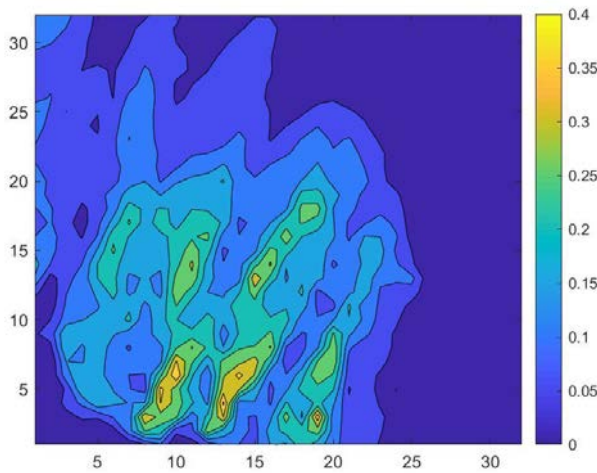
F-8 Mean rainfall rate (mm/10min) of 320-min aggregated 8th radar sequence



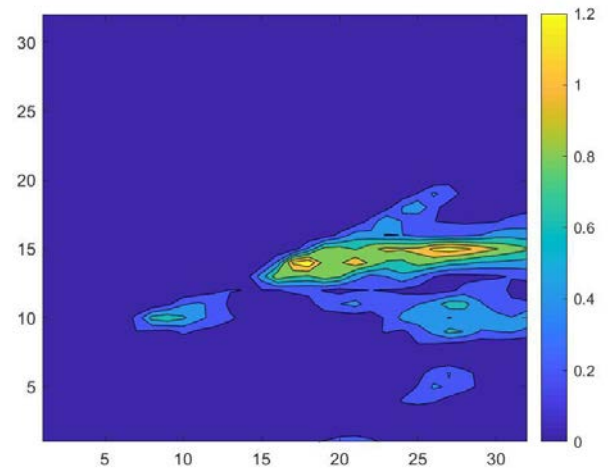
F-9 Mean rainfall rate (mm/10min) of 320-min aggregated 9th radar sequence



F-10 Mean rainfall rate (mm/10min) of 320-min aggregated 10th radar sequence

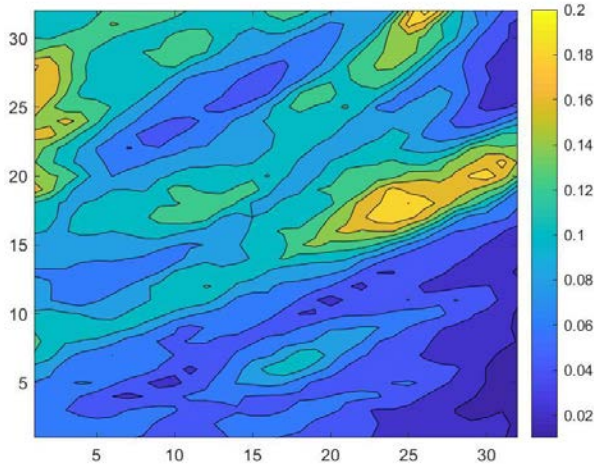


F-11 Mean rainfall rate (mm/10min) of 320-min aggregated 11th radar sequence

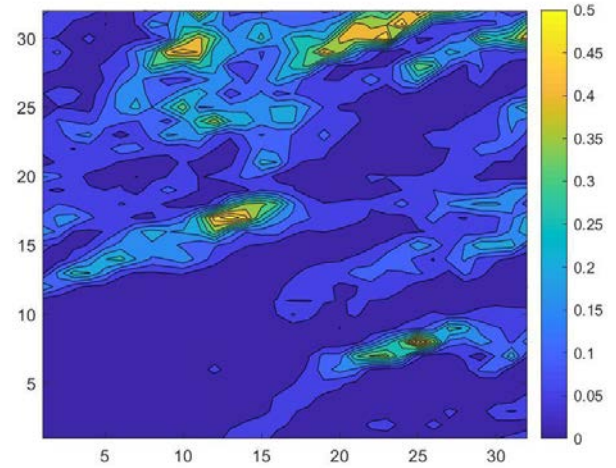


F-12 Mean rainfall rate (mm/10min) of 320-min aggregated 12th radar sequence

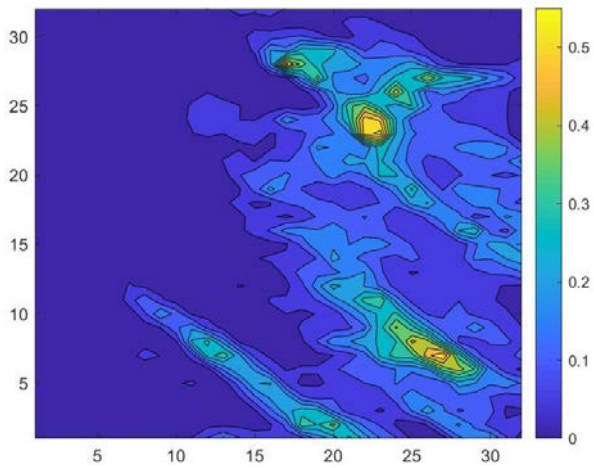
APPENDIX F: MEAN RAINFALL DEPTHS FOR AVERAGED RADAR SEQUENCES FROM 2015



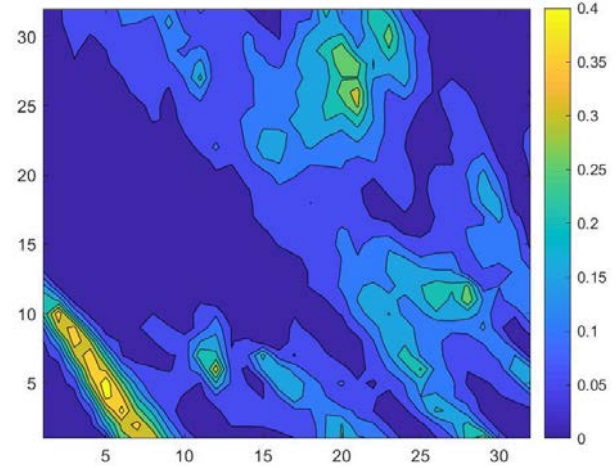
F-13 Mean rainfall rate (mm/10min) of 320-min aggregated 13th radar sequence



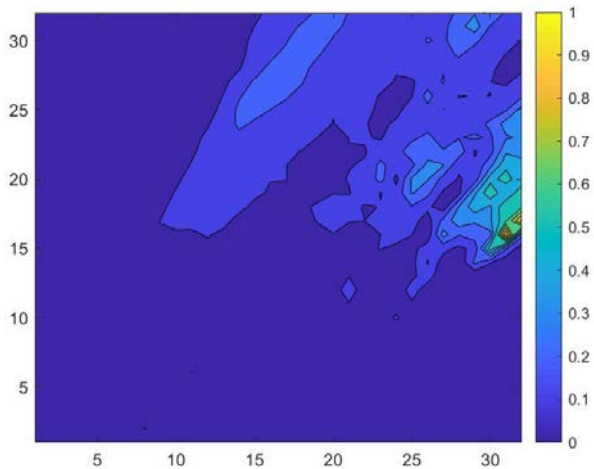
F-14 Mean rainfall rate (mm/10min) of 320-min aggregated 14th radar sequence



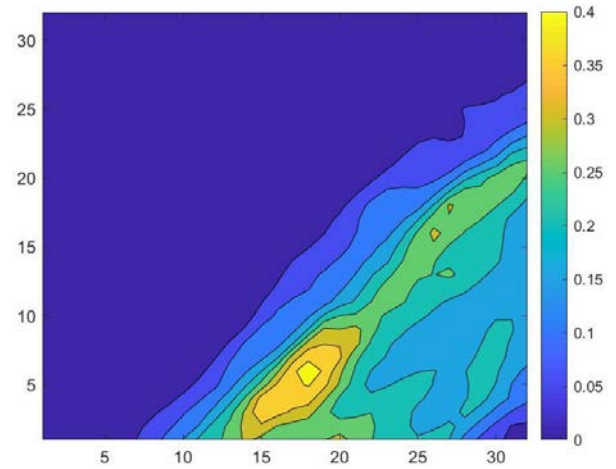
F-15 Mean rainfall rate (mm/10min) of 320-min aggregated 15th radar sequence



F-16 Mean rainfall rate (mm/10min) of 320-min aggregated 16th radar sequence

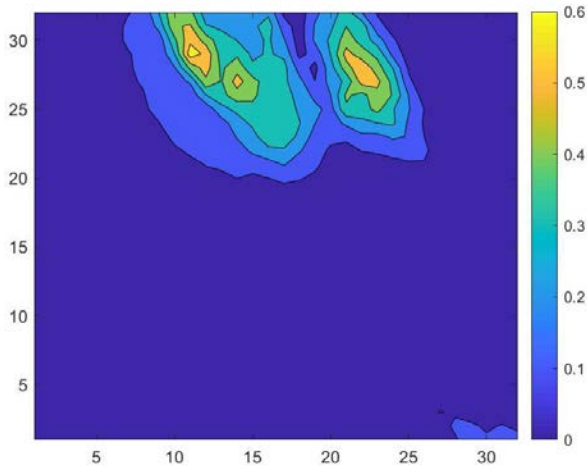


F-17 Mean rainfall rate (mm/10min) of 320-min aggregated 17th radar sequence

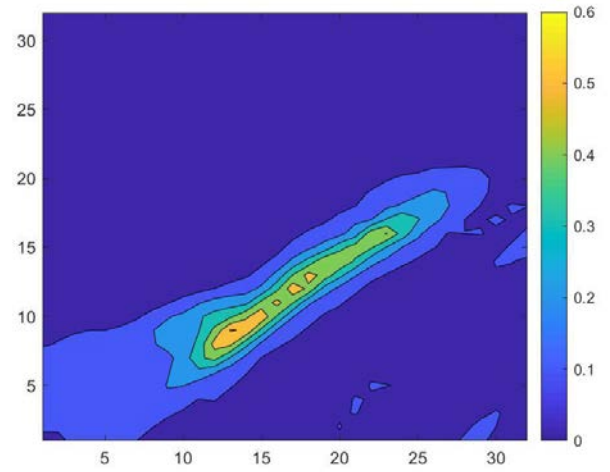


F-18 Mean rainfall rate (mm/10min) of 320-min aggregated 18th radar sequence

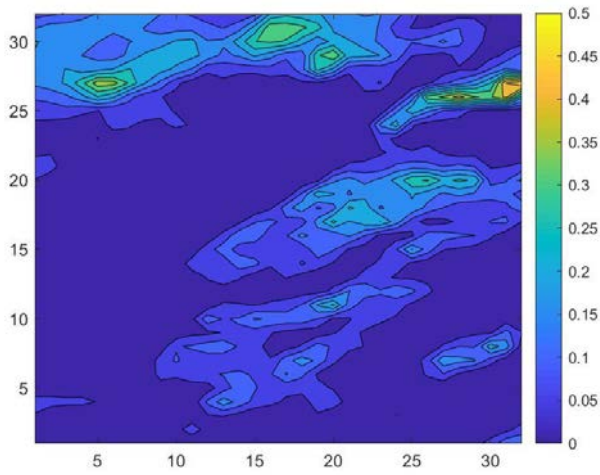
APPENDIX F: MEAN RAINFALL DEPTHS FOR AVERAGED RADAR SEQUENCES FROM 2015



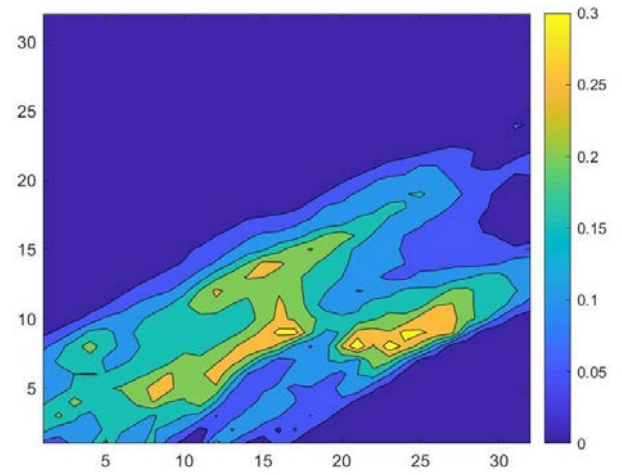
F-19 Mean rainfall rate (mm/10min) of 320-min aggregated 19th radar sequence



F-20 Mean rainfall rate (mm/10min) of 320-min aggregated 20th radar sequence



F-21 Mean rainfall rate (mm/10min) of 320-min aggregated 21st radar sequence



F-22 Mean rainfall rate (mm/10min) of 320-min aggregated 22nd radar sequence

APPENDIX G

Table of contents

<i>G-1 Complementary cumulative distribution function (cCDF) of rainfall rate (r in mm/10min) for 320-min aggregated radar 1st sequence selected from 2015.....</i>	<i>212</i>
<i>G-2 Complementary cumulative distribution function (cCDF) of rainfall rate (r in mm/10min) for 320-min aggregated radar 2nd sequence selected from 2015</i>	<i>212</i>
<i>G-3 Complementary cumulative distribution function (cCDF) of rainfall rate (r in mm/10min) for 320-min aggregated radar 3rd sequence selected from 2015</i>	<i>212</i>
<i>G-4 Complementary cumulative distribution function (cCDF) of rainfall rate (r in mm/10min) for 320-min aggregated radar 4th sequence selected from 2015</i>	<i>213</i>
<i>G-5 Complementary cumulative distribution function (cCDF) of rainfall rate (r in mm/10min) for 320-min aggregated radar 5th sequence selected from 2015</i>	<i>213</i>
<i>G-6 Complementary cumulative distribution function (cCDF) of rainfall rate (r in mm/10min) for 320-min aggregated radar 6th sequence selected from 2015</i>	<i>213</i>
<i>G-7 Complementary cumulative distribution function (cCDF) of rainfall rate (r in mm/10min) for 320-min aggregated radar 7th sequence selected from 2015</i>	<i>214</i>
<i>G-8 Complementary cumulative distribution function (cCDF) of rainfall rate (r in mm/10min) for 320-min aggregated radar 8th sequence selected from 2015</i>	<i>214</i>
<i>G-9 Complementary cumulative distribution function (cCDF) of rainfall rate (r in mm/10min) for 320-min aggregated radar 9th sequence selected from 2015</i>	<i>214</i>
<i>G-10 Complementary cumulative distribution function (cCDF) of rainfall rate (r in mm/10min) for 320-min aggregated radar 10th sequence selected from 2015</i>	<i>215</i>
<i>G-11 Complementary cumulative distribution function (cCDF) of rainfall rate (r in mm/10min) for 320-min aggregated radar 11th sequence selected from 2015</i>	<i>215</i>
<i>G-12 Complementary cumulative distribution function (cCDF) of rainfall rate (r in mm/10min) for 320-min aggregated radar 12th sequence selected from 2015</i>	<i>215</i>
<i>G-13 Complementary cumulative distribution function (cCDF) of rainfall rate (r in mm/10min) for 320-min aggregated radar 13th sequence selected from 2015</i>	<i>216</i>
<i>G-14 Complementary cumulative distribution function (cCDF) of rainfall rate (r in mm/10min) for 320-min aggregated radar 14th sequence selected from 2015</i>	<i>216</i>
<i>G-15 Complementary cumulative distribution function (cCDF) of rainfall rate (r in mm/10min) for 320-min aggregated radar 15th sequence selected from 2015</i>	<i>216</i>
<i>G-16 Complementary cumulative distribution function (cCDF) of rainfall rate (r in mm/10min) for 320-min aggregated radar 16th sequence selected from 2015</i>	<i>217</i>

APPENDIX G: COMPLEMENTARY CUMULATIVE DISTRIBUTION FUNCTION (cCDF) of rainfall rate (r in mm/10min) FOR SELECTED RADAR SEQUENCES FROM 2015

G-17 Complementary cumulative distribution function (cCDF) of rainfall rate (r in mm/10min) for 320-min aggregated radar 17th sequence selected from 2015 217

G-18 Complementary cumulative distribution function (cCDF) of rainfall rate (r in mm/10min) for 320-min aggregated radar 18th sequence selected from 2015 217

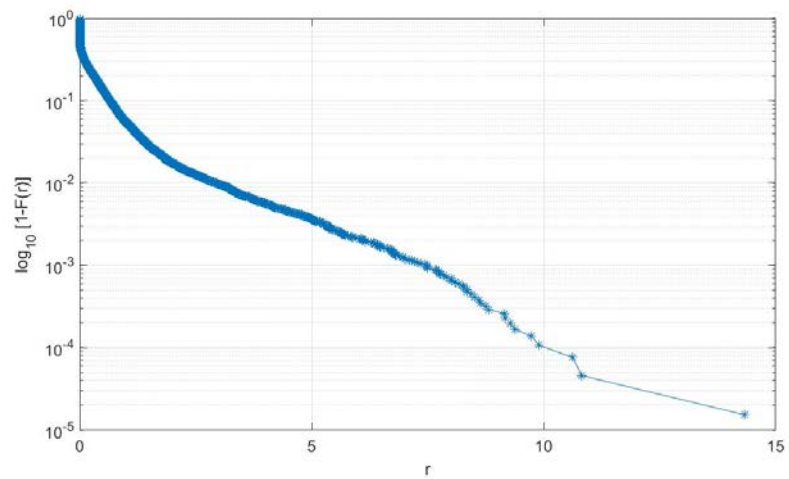
G-19 Complementary cumulative distribution function (cCDF) of rainfall rate (r in mm/10min) for 320-min aggregated radar 19th sequence selected from 2015 218

G-20 Complementary cumulative distribution function (cCDF) of rainfall rate (r in mm/10min) for 320-min aggregated radar 20th sequence selected from 2015 218

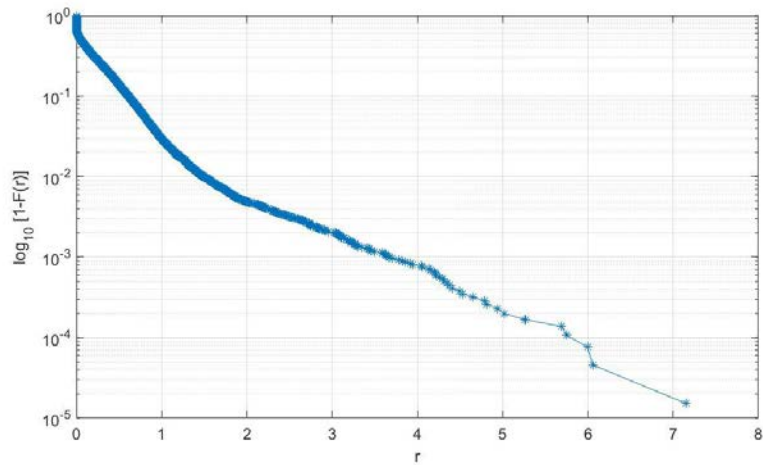
G-21 Complementary cumulative distribution function (cCDF) of rainfall rate (r in mm/10min) for 320-min aggregated radar 21st sequence selected from 2015..... 218

G-22 Complementary cumulative distribution function (cCDF) of rainfall rate (r in mm/10min) for 320-min aggregated radar 22nd sequence selected from 2015 219

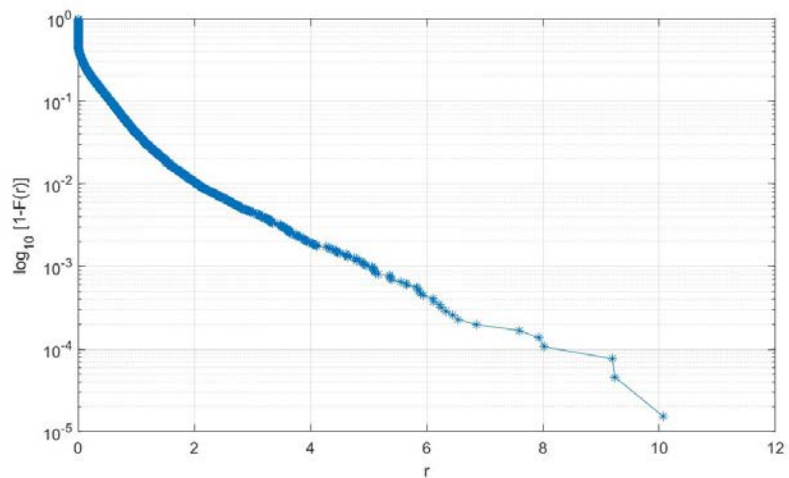
APPENDIX G: COMPLEMENTARY CUMULATIVE DISTRIBUTION FUNCTION (cCDF) of rainfall rate (r in mm/10min) FOR SELECTED RADAR SEQUENCES FROM 2015



G-1 Complementary cumulative distribution function (cCDF) of rainfall rate (r in mm/10min) for 320-min aggregated radar 1st sequence selected from 2015

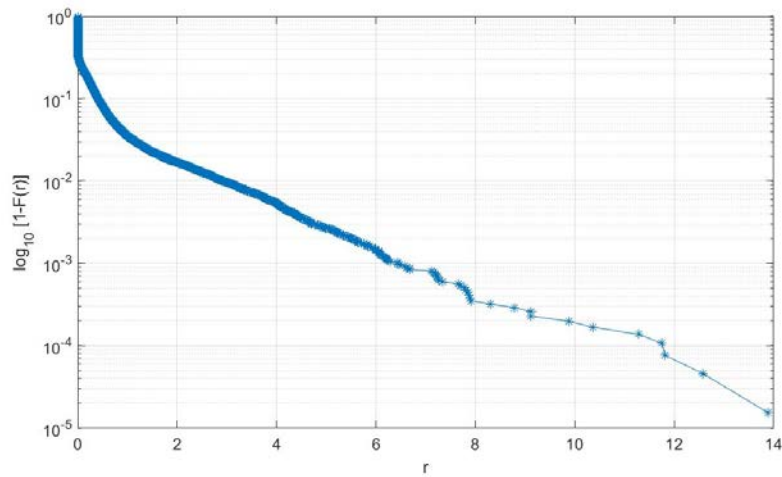


G-2 Complementary cumulative distribution function (cCDF) of rainfall rate (r in mm/10min) for 320-min aggregated radar 2nd sequence selected from 2015

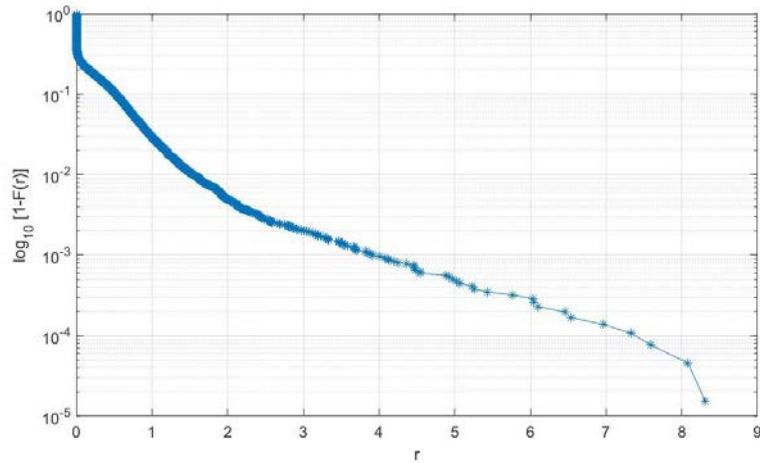


G-3 Complementary cumulative distribution function (cCDF) of rainfall rate (r in mm/10min) for 320-min aggregated radar 3rd sequence selected from 2015

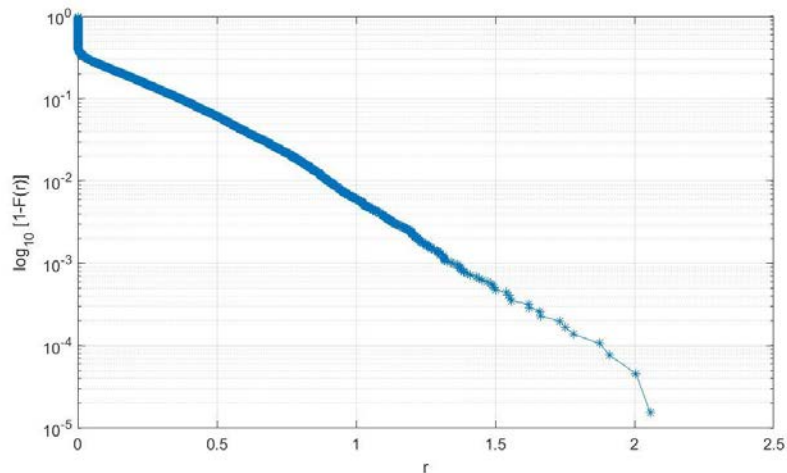
APPENDIX G: COMPLEMENTARY CUMULATIVE DISTRIBUTION FUNCTION (cCDF) of rainfall rate (r in mm/10min) FOR SELECTED RADAR SEQUENCES FROM 2015



G-4 Complementary cumulative distribution function (cCDF) of rainfall rate (r in mm/10min) for 320-min aggregated radar 4th sequence selected from 2015

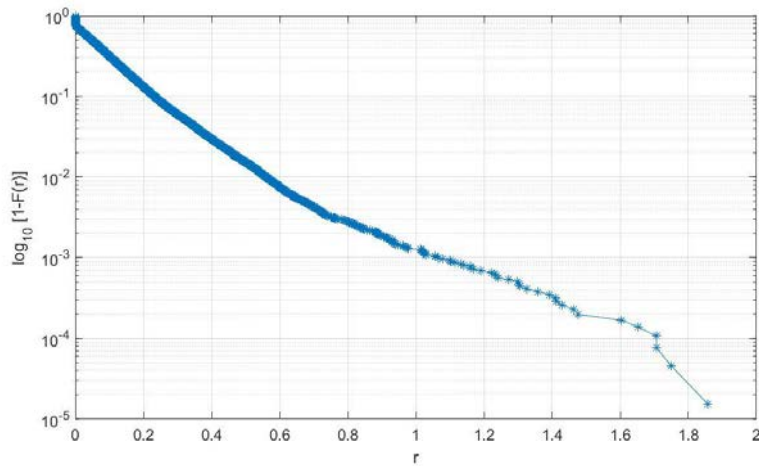


G-5 Complementary cumulative distribution function (cCDF) of rainfall rate (r in mm/10min) for 320-min aggregated radar 5th sequence selected from 2015

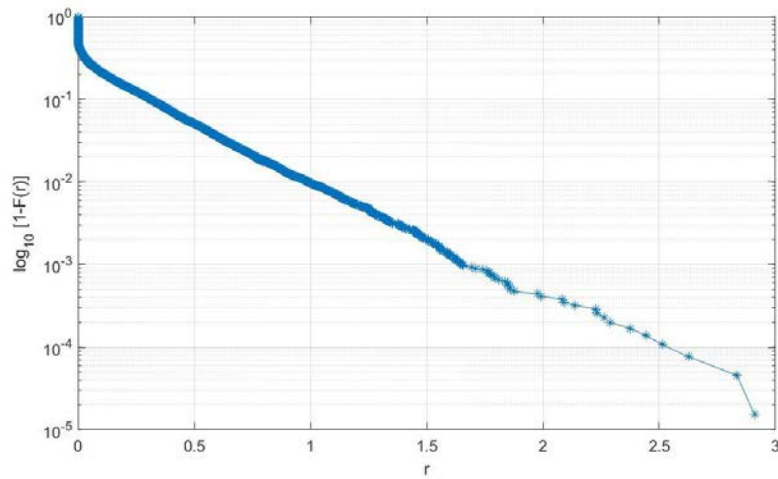


G-6 Complementary cumulative distribution function (cCDF) of rainfall rate (r in mm/10min) for 320-min aggregated radar 6th sequence selected from 2015

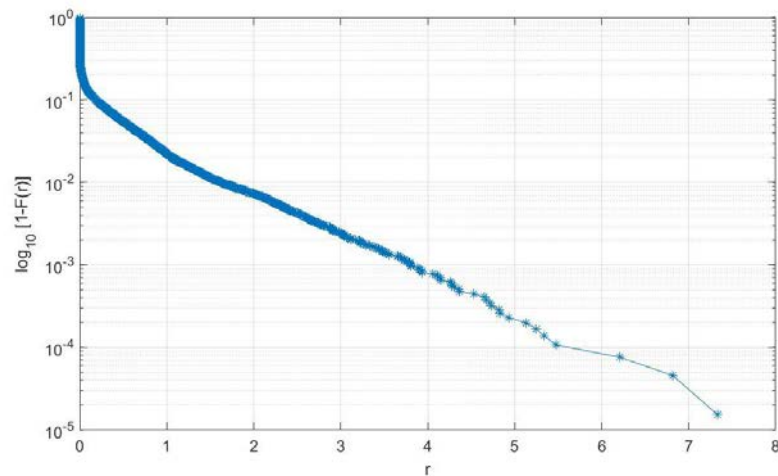
APPENDIX G: COMPLEMENTARY CUMULATIVE DISTRIBUTION FUNCTION (cCDF) of rainfall rate (r in mm/10min) FOR SELECTED RADAR SEQUENCES FROM 2015



G-7 Complementary cumulative distribution function (cCDF) of rainfall rate (r in mm/10min) for 320-min aggregated radar 7th sequence selected from 2015

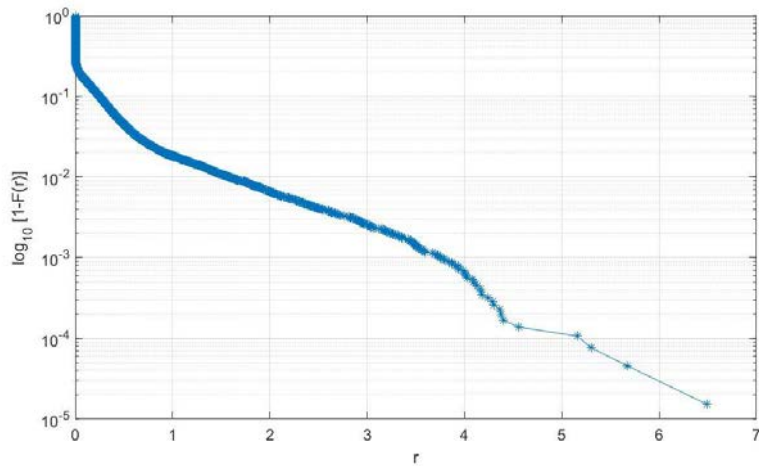


G-8 Complementary cumulative distribution function (cCDF) of rainfall rate (r in mm/10min) for 320-min aggregated radar 8th sequence selected from 2015

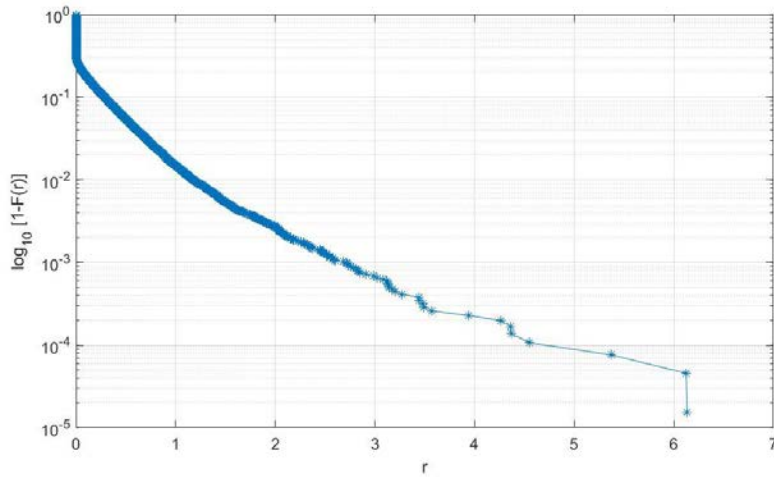


G-9 Complementary cumulative distribution function (cCDF) of rainfall rate (r in mm/10min) for 320-min aggregated radar 9th sequence selected from 2015

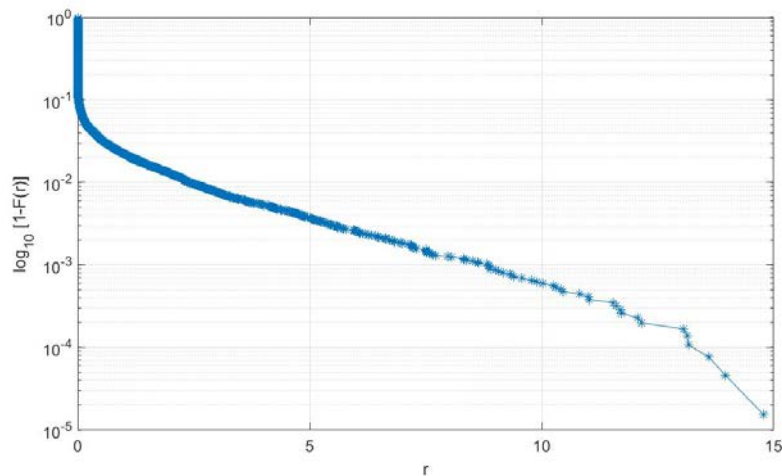
APPENDIX G: COMPLEMENTARY CUMULATIVE DISTRIBUTION FUNCTION (cCDF) of rainfall rate (r in mm/10min) FOR SELECTED RADAR SEQUENCES FROM 2015



G-10 Complementary cumulative distribution function (cCDF) of rainfall rate (r in mm/10min) for 320-min aggregated radar 10th sequence selected from 2015

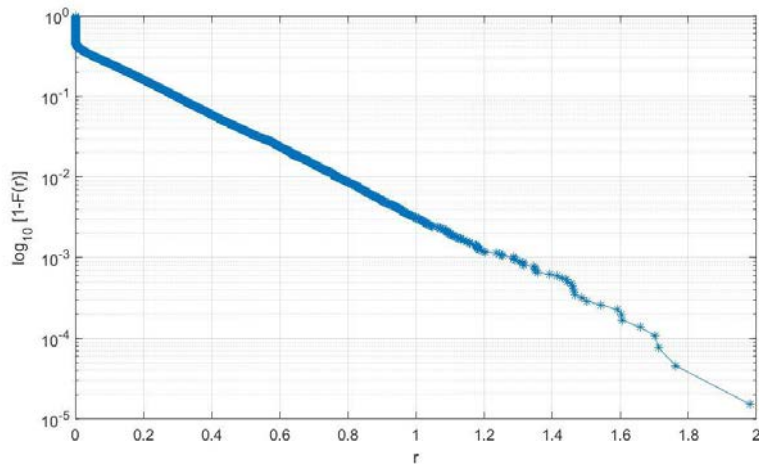


G-11 Complementary cumulative distribution function (cCDF) of rainfall rate (r in mm/10min) for 320-min aggregated radar 11th sequence selected from 2015

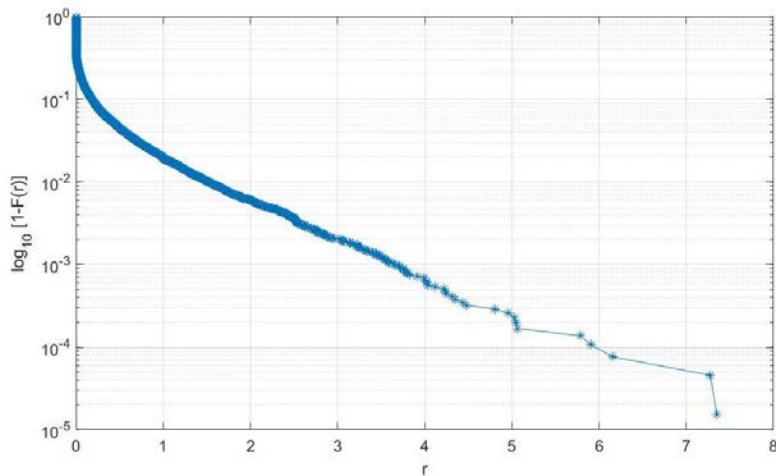


G-12 Complementary cumulative distribution function (cCDF) of rainfall rate (r in mm/10min) for 320-min aggregated radar 12th sequence selected from 2015

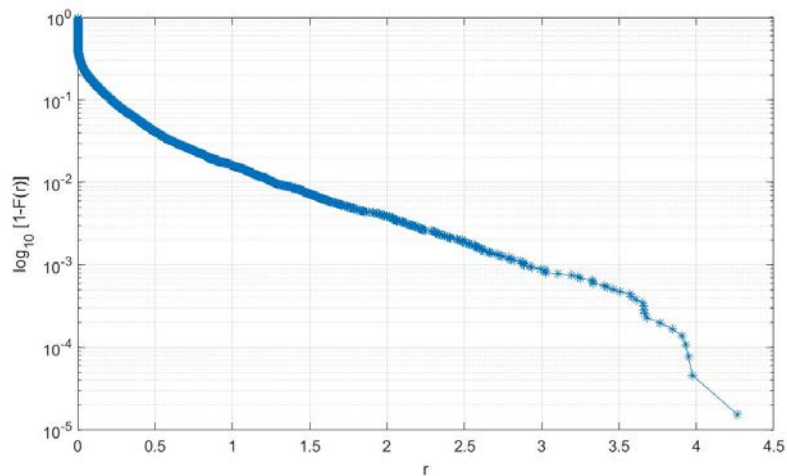
APPENDIX G: COMPLEMENTARY CUMULATIVE DISTRIBUTION FUNCTION (cCDF) of rainfall rate (r in mm/10min) FOR SELECTED RADAR SEQUENCES FROM 2015



G-13 Complementary cumulative distribution function (cCDF) of rainfall rate (r in mm/10min) for 320-min aggregated radar 13th sequence selected from 2015

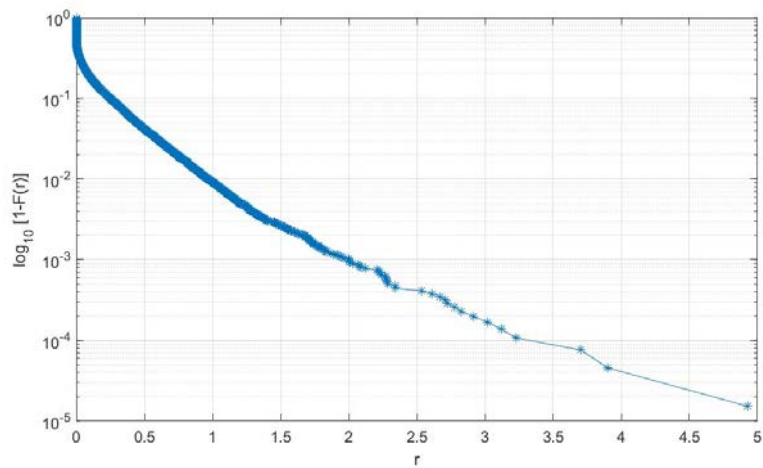


G-14 Complementary cumulative distribution function (cCDF) of rainfall rate (r in mm/10min) for 320-min aggregated radar 14th sequence selected from 2015

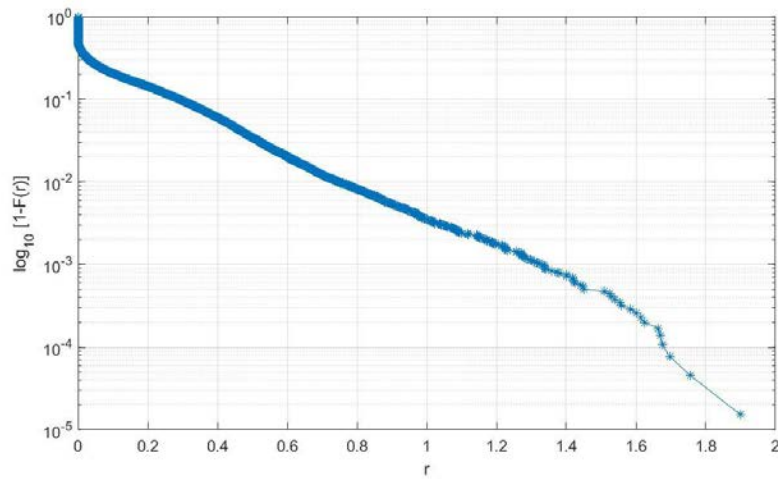


G-15 Complementary cumulative distribution function (cCDF) of rainfall rate (r in mm/10min) for 320-min aggregated radar 15th sequence selected from 2015

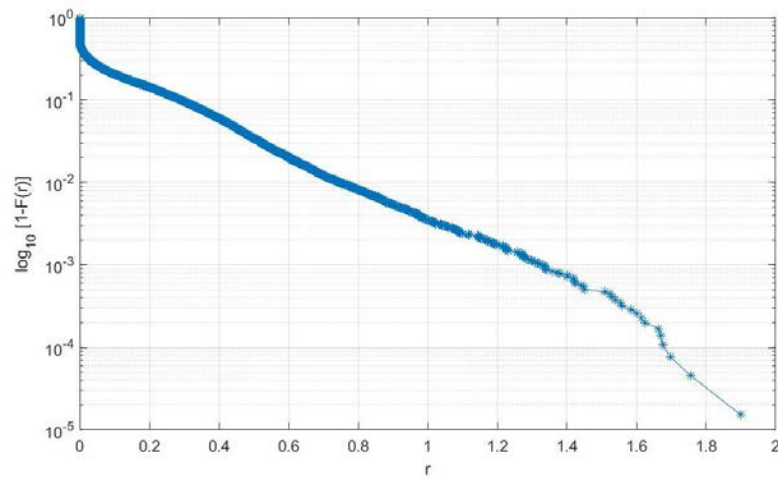
APPENDIX G: COMPLEMENTARY CUMULATIVE DISTRIBUTION FUNCTION (cCDF) of rainfall rate (r in mm/10min) FOR SELECTED RADAR SEQUENCES FROM 2015



G-16 Complementary cumulative distribution function (cCDF) of rainfall rate (r in mm/10min) for 320-min aggregated radar 16th sequence selected from 2015

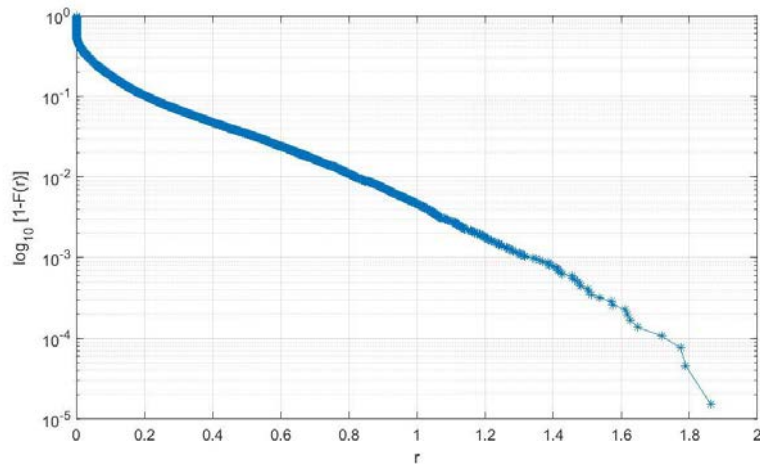


G-17 Complementary cumulative distribution function (cCDF) of rainfall rate (r in mm/10min) for 320-min aggregated radar 17th sequence selected from 2015

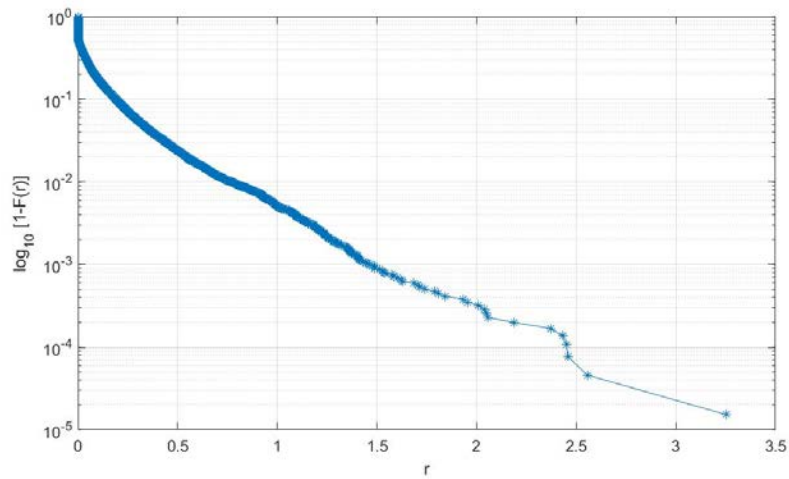


G-18 Complementary cumulative distribution function (cCDF) of rainfall rate (r in mm/10min) for 320-min aggregated radar 18th sequence selected from 2015

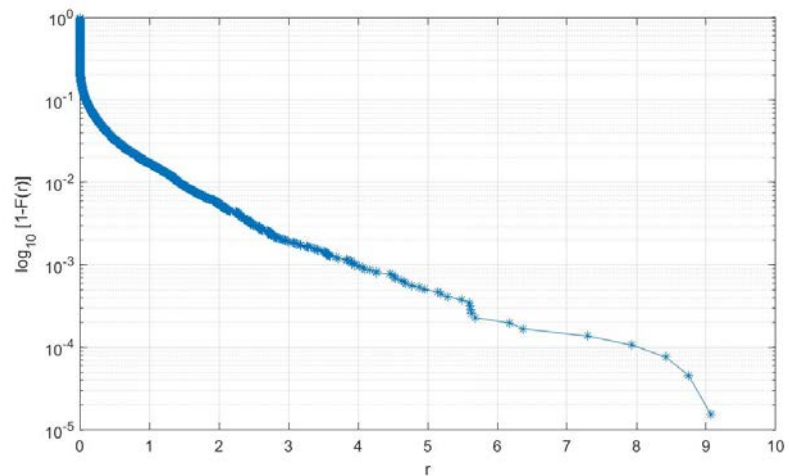
APPENDIX G: COMPLEMENTARY CUMULATIVE DISTRIBUTION FUNCTION (cCDF) of rainfall rate (r in mm/10min) FOR SELECTED RADAR SEQUENCES FROM 2015



G-19 Complementary cumulative distribution function (cCDF) of rainfall rate (r in mm/10min) for 320-min aggregated radar 19th sequence selected from 2015

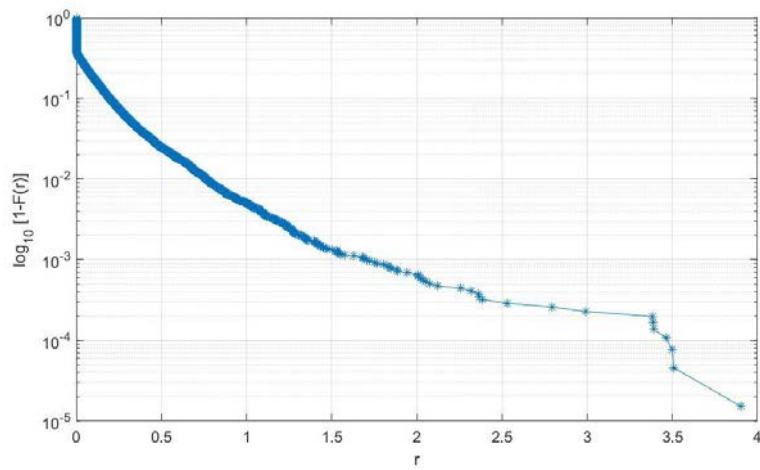


G-20 Complementary cumulative distribution function (cCDF) of rainfall rate (r in mm/10min) for 320-min aggregated radar 20th sequence selected from 2015



G-21 Complementary cumulative distribution function (cCDF) of rainfall rate (r in mm/10min) for 320-min aggregated radar 21st sequence selected from 2015

APPENDIX G: COMPLEMENTARY CUMULATIVE DISTRIBUTION FUNCTION (cCDF) of rainfall rate (r in mm/10min) FOR SELECTED RADAR SEQUENCES FROM 2015



G-22 Complementary cumulative distribution function (cCDF) of rainfall rate (r in mm/10min) for 320-min aggregated radar 22nd sequence selected from 2015

APPENDIX H

Table of contents

<i>H-1 Log-log plot of the space-time structure function $S_q(\lambda)$ for 320-min aggregated 1st radar sequence selected from 2015.....</i>	<i>222</i>
<i>H-2 Log-log plot of the space-time structure function $S_q(\lambda)$ for 320-min aggregated 2nd radar sequence selected from 2015.....</i>	<i>222</i>
<i>H-3 Log-log plot of the space-time structure function $S_q(\lambda)$ for 320-min aggregated 3rd radar sequence selected from 2015.....</i>	<i>223</i>
<i>H-4 Log-log plot of the space-time structure function $S_q(\lambda)$ for 320-min aggregated 4th radar sequence selected from 2015.....</i>	<i>223</i>
<i>H-5 Log-log plot of the space-time structure function $S_q(\lambda)$ for 320-min aggregated 5th radar sequence selected from 2015.....</i>	<i>224</i>
<i>H-6 Log-log plot of the space-time structure function $S_q(\lambda)$ for 320-min aggregated 6th radar sequence selected from 2015.....</i>	<i>224</i>
<i>H-7 Log-log plot of the space-time structure function $S_q(\lambda)$ for 320-min aggregated 7th radar sequence selected from 2015.....</i>	<i>225</i>
<i>H-8 Log-log plot of the space-time structure function $S_q(\lambda)$ for 320-min aggregated 8th radar sequence selected from 2015.....</i>	<i>225</i>
<i>H-9 Log-log plot of the space-time structure function $S_q(\lambda)$ for 320-min aggregated 9th radar sequence selected from 2015.....</i>	<i>226</i>
<i>H-10 Log-log plot of the space-time structure function $S_q(\lambda)$ for 320-min aggregated 10th radar sequence selected from 2015.....</i>	<i>226</i>
<i>H-11 Log-log plot of the space-time structure function $S_q(\lambda)$ for 320-min aggregated 11th radar sequence selected from 2015.....</i>	<i>227</i>
<i>H-12 Log-log plot of the space-time structure function $S_q(\lambda)$ for 320-min aggregated 12th radar sequence selected from 2015.....</i>	<i>227</i>
<i>H-13 Log-log plot of the space-time structure function $S_q(\lambda)$ for 320-min aggregated 13th radar sequence selected from 2015.....</i>	<i>228</i>
<i>H-14 Log-log plot of the space-time structure function $S_q(\lambda)$ for 320-min aggregated 14th radar sequence selected from 2015.....</i>	<i>228</i>
<i>H-15 Log-log plot of the space-time structure function $S_q(\lambda)$ for 320-min aggregated 15th radar sequence selected from 2015.....</i>	<i>229</i>
<i>H-16 Log-log plot of the space-time structure function $S_q(\lambda)$ for 320-min aggregated 16th radar sequence selected from 2015.....</i>	<i>229</i>

APPENDIX H: SPACE-TIME STRUCTURE FUNCTION $S_q(\lambda)$ FOR SELECTED RADAR SEQUENCES FROM 2015

H-17 Log-log plot of the space-time structure function $S_q(\lambda)$ for 320-min aggregated 17th radar sequence selected from 2015..... 230

H-18 Log-log plot of the space-time structure function $S_q(\lambda)$ for 320-min aggregated 18th radar sequence selected from 2015..... 230

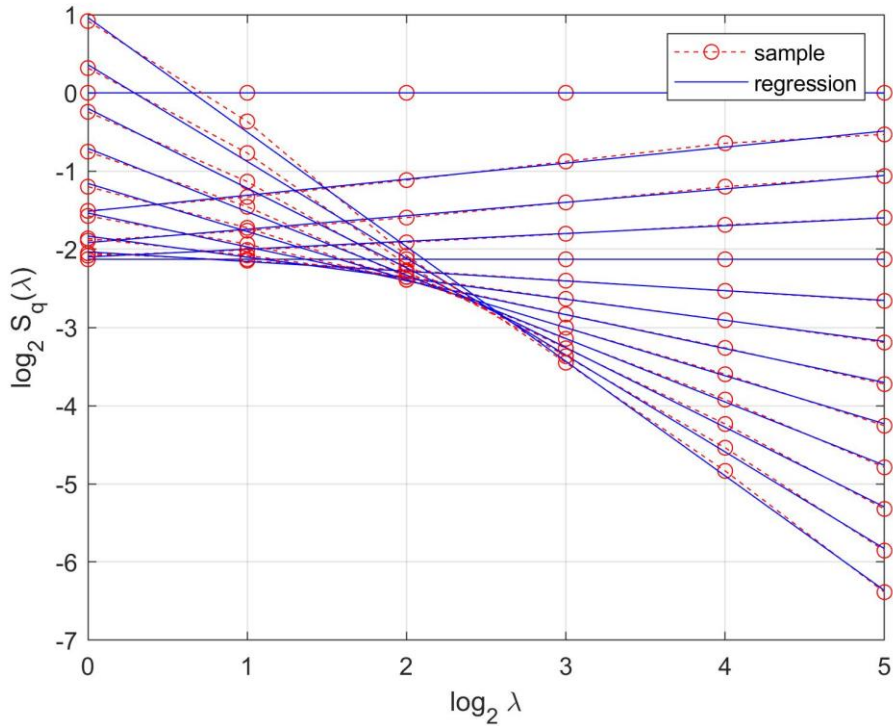
H-19 Log-log plot of the space-time structure function $S_q(\lambda)$ for 320-min aggregated 19th radar sequence selected from 2015..... 231

H-20 Log-log plot of the space-time structure function $S_q(\lambda)$ for 320-min aggregated 20th radar sequence selected from 2015..... 231

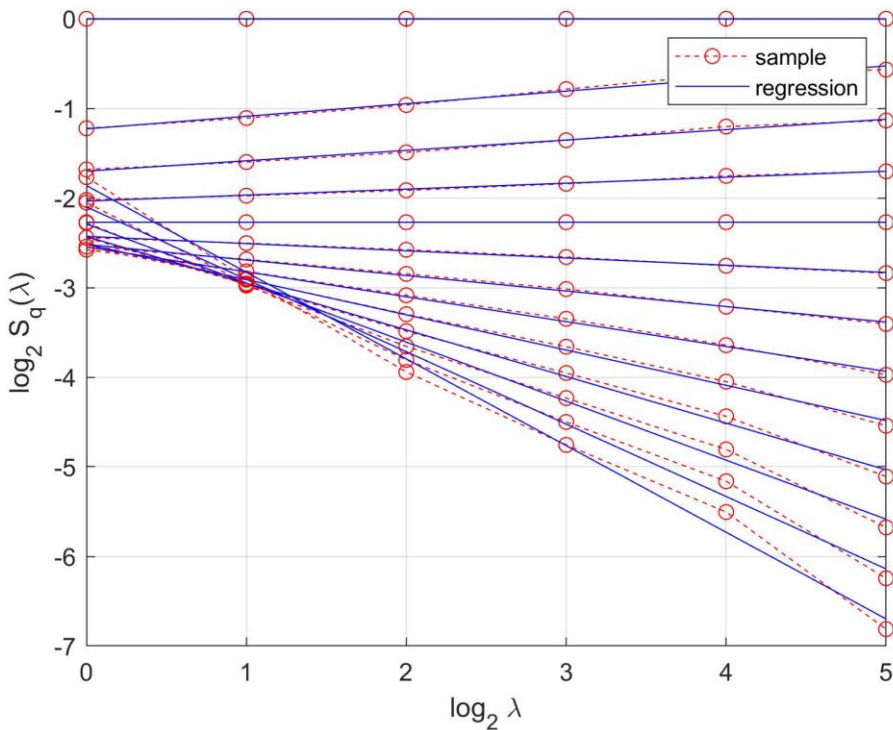
H-21 Log-log plot of the space-time structure function $S_q(\lambda)$ for 320-min aggregated 21st radar sequence selected from 2015..... 232

H-22 Log-log plot of the space-time structure function $S_q(\lambda)$ for 320-min aggregated 22nd radar sequence selected from 2015..... 232

APPENDIX H: SPACE-TIME STRUCTURE FUNCTION $S_q(\lambda)$ FOR SELECTED RADAR SEQUENCES FROM 2015

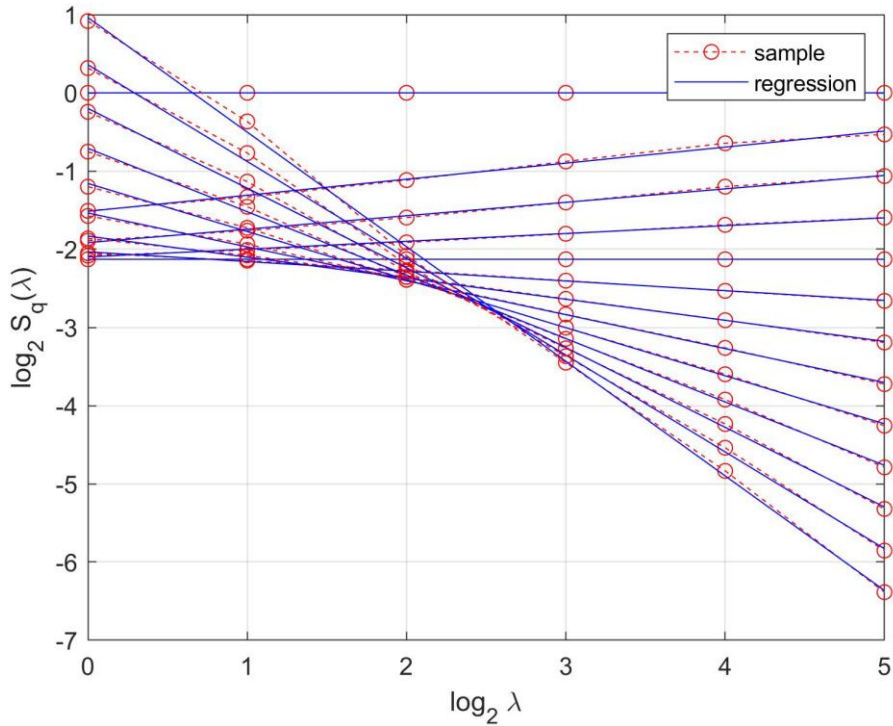


H-1 Log-log plot of the space-time structure function $S_q(\lambda)$ for 320-min aggregated 1st radar sequence selected from 2015

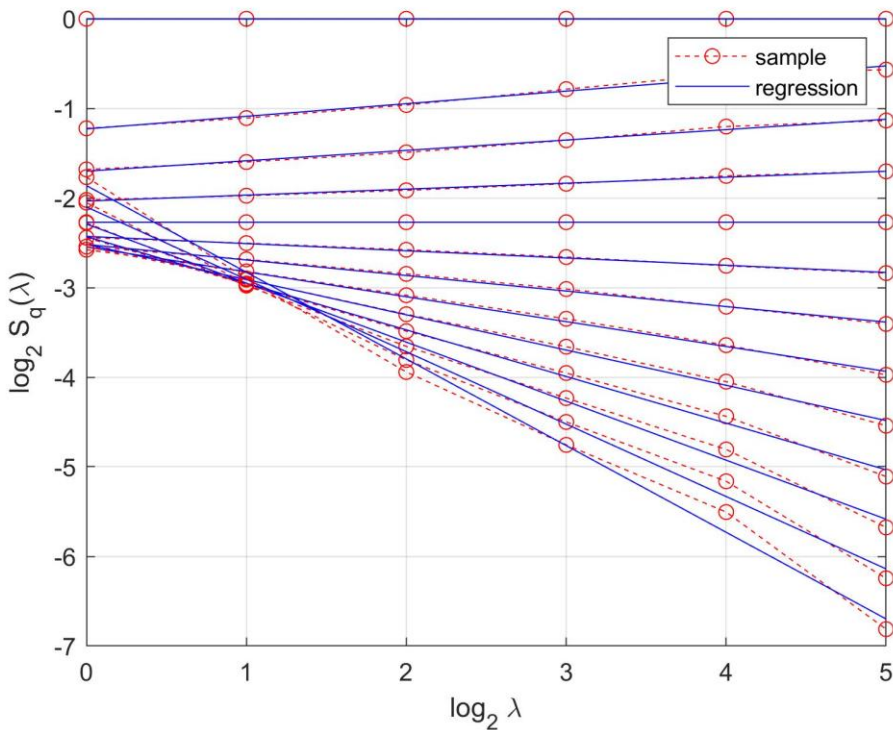


H-2 Log-log plot of the space-time structure function $S_q(\lambda)$ for 320-min aggregated 2nd radar sequence selected from 2015

APPENDIX H: SPACE-TIME STRUCTURE FUNCTION $S_q(\lambda)$ FOR SELECTED RADAR SEQUENCES FROM 2015

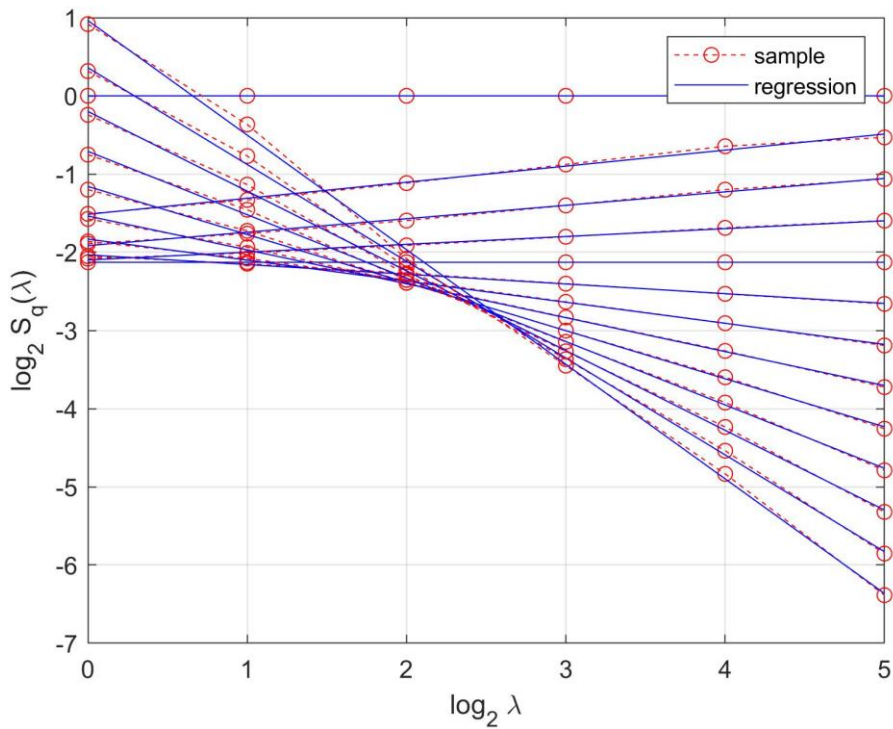


H-3 Log-log plot of the space-time structure function $S_q(\lambda)$ for 320-min aggregated 3rd radar sequence selected from 2015

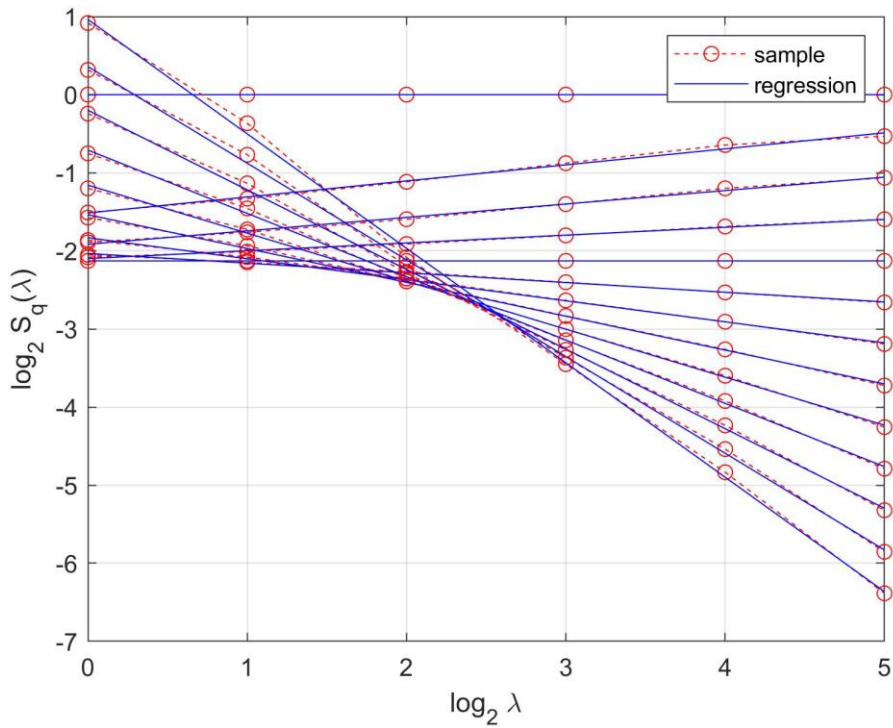


H-4 Log-log plot of the space-time structure function $S_q(\lambda)$ for 320-min aggregated 4th radar sequence selected from 2015

APPENDIX H: SPACE-TIME STRUCTURE FUNCTION $S_q(\lambda)$ FOR SELECTED RADAR SEQUENCES FROM 2015

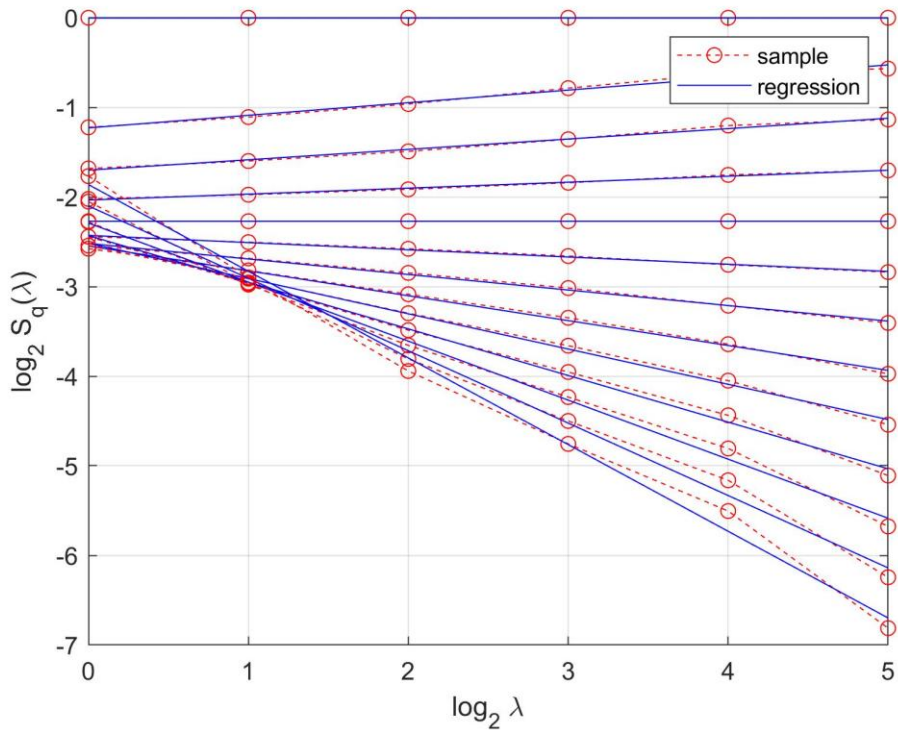


H-5 Log-log plot of the space-time structure function $S_q(\lambda)$ for 320-min aggregated 5th radar sequence selected from 2015

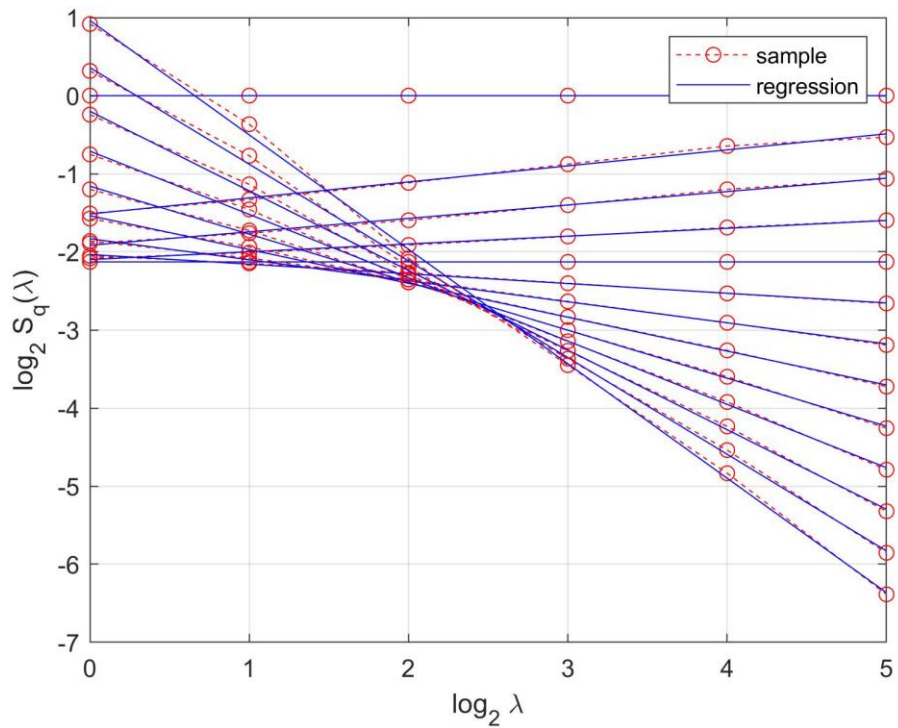


H-6 Log-log plot of the space-time structure function $S_q(\lambda)$ for 320-min aggregated 6th radar sequence selected from 2015

APPENDIX H: SPACE-TIME STRUCTURE FUNCTION $S_q(\lambda)$ FOR SELECTED RADAR SEQUENCES FROM 2015

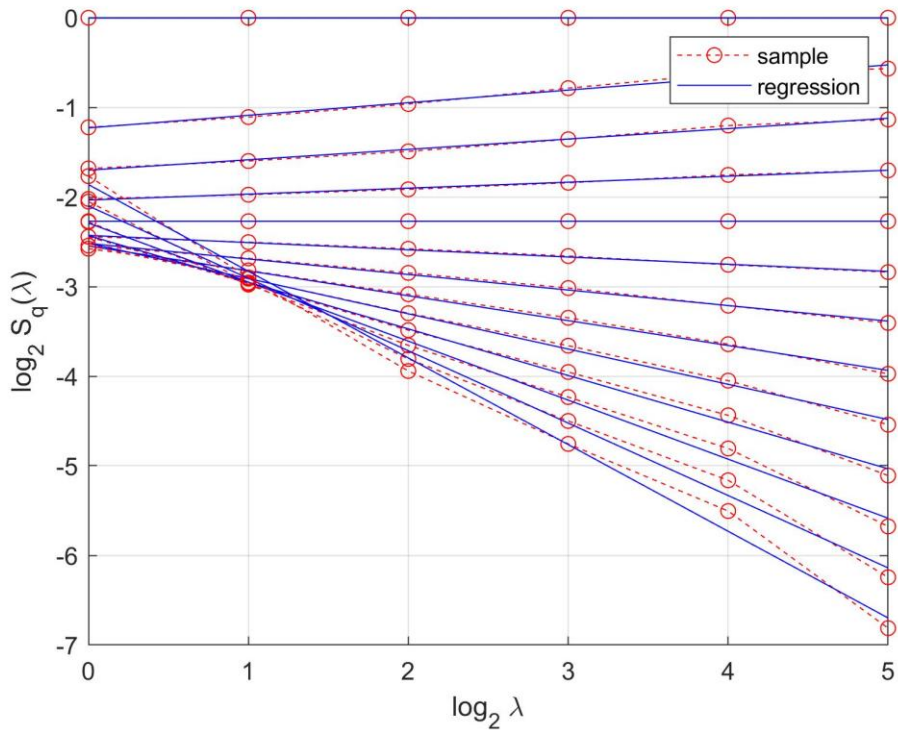


H-7 Log-log plot of the space-time structure function $S_q(\lambda)$ for 320-min aggregated 7th radar sequence selected from 2015

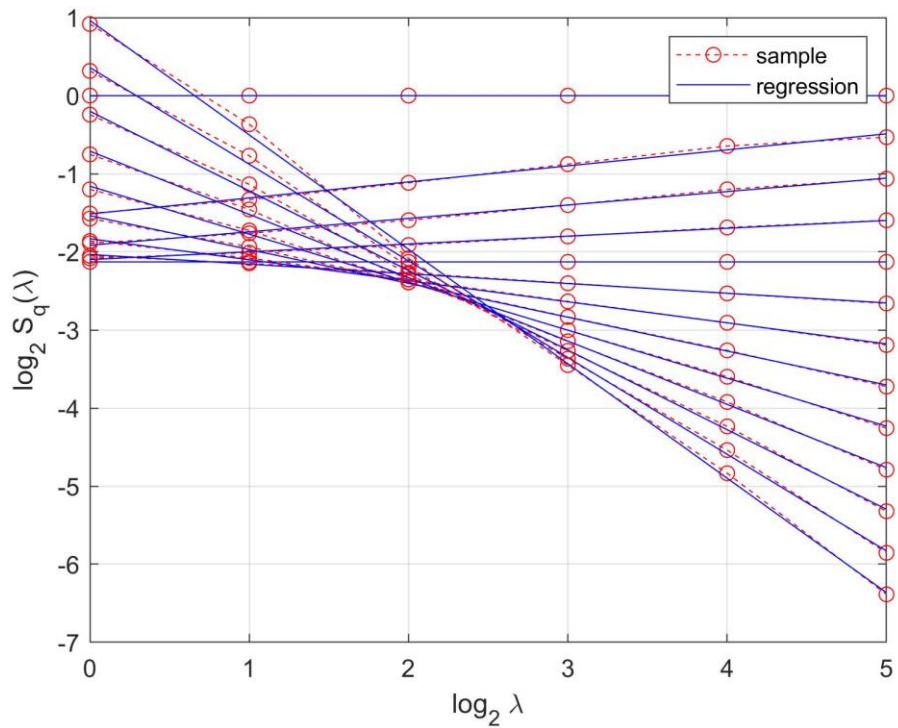


H-8 Log-log plot of the space-time structure function $S_q(\lambda)$ for 320-min aggregated 8th radar sequence selected from 2015

APPENDIX H: SPACE-TIME STRUCTURE FUNCTION $S_q(\lambda)$ FOR SELECTED RADAR SEQUENCES FROM 2015

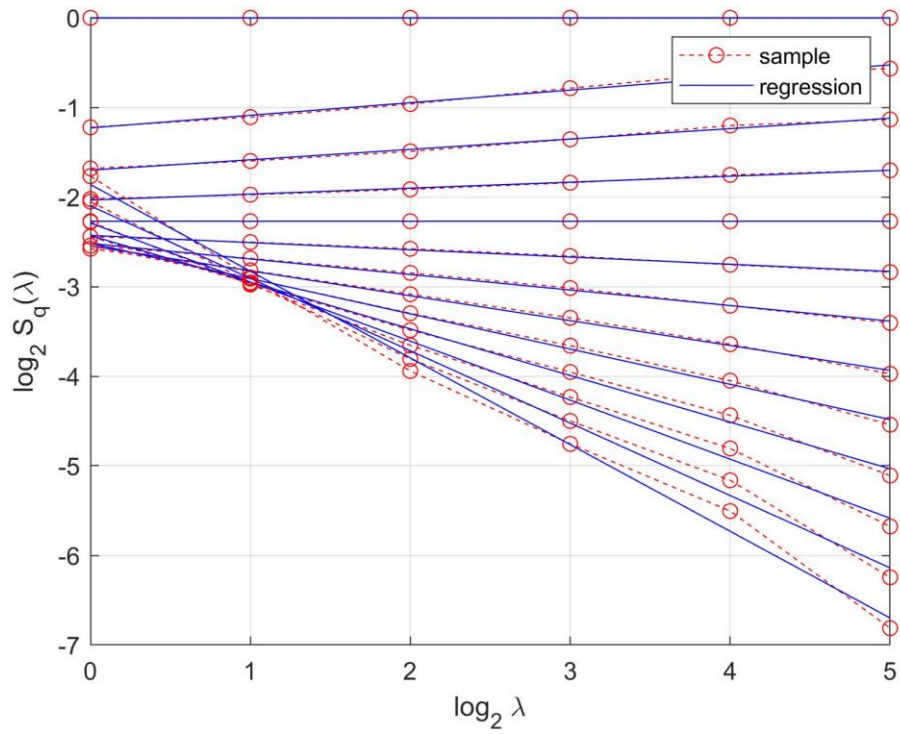


H-9 Log-log plot of the space-time structure function $S_q(\lambda)$ for 320-min aggregated 9th radar sequence selected from 2015

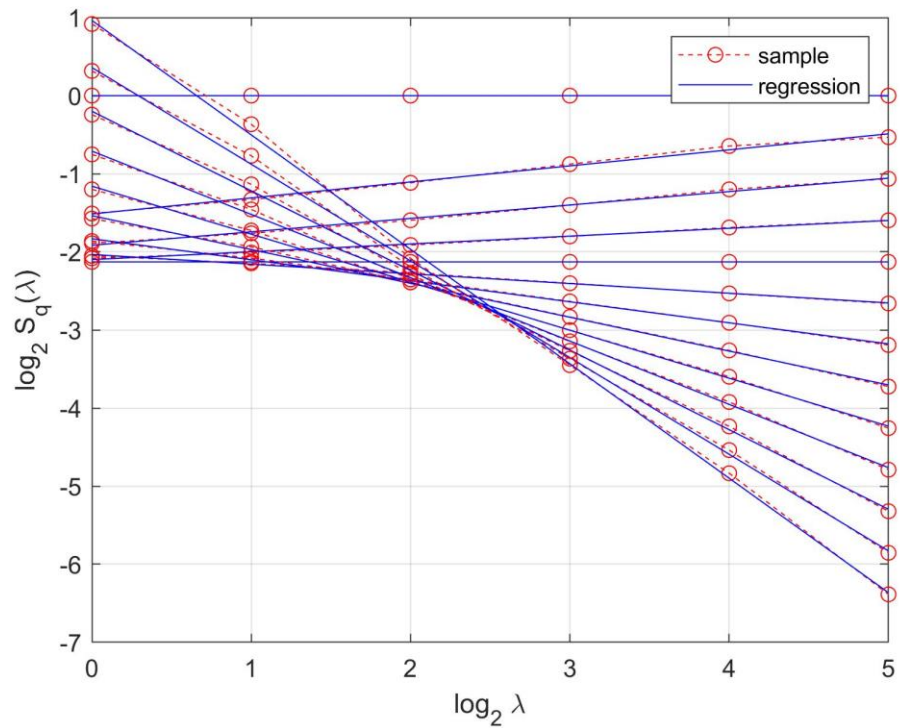


H-10 Log-log plot of the space-time structure function $S_q(\lambda)$ for 320-min aggregated 10th radar sequence selected from 2015

APPENDIX H: SPACE-TIME STRUCTURE FUNCTION $S_q(\lambda)$ FOR SELECTED RADAR SEQUENCES FROM 2015

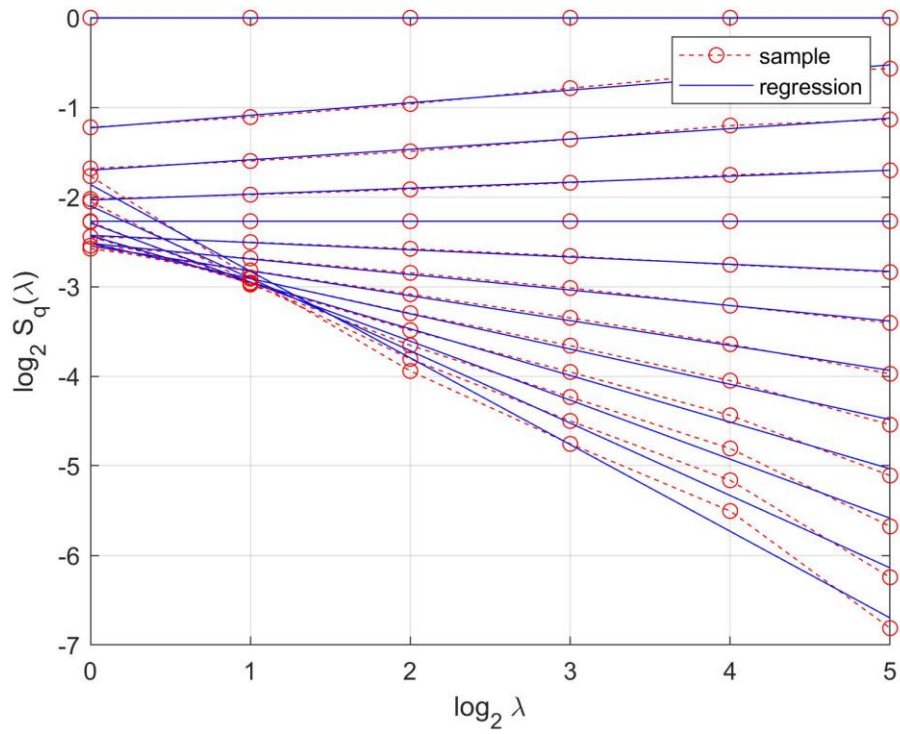


H-11 Log-log plot of the space-time structure function $S_q(\lambda)$ for 320-min aggregated 11th radar sequence selected from 2015

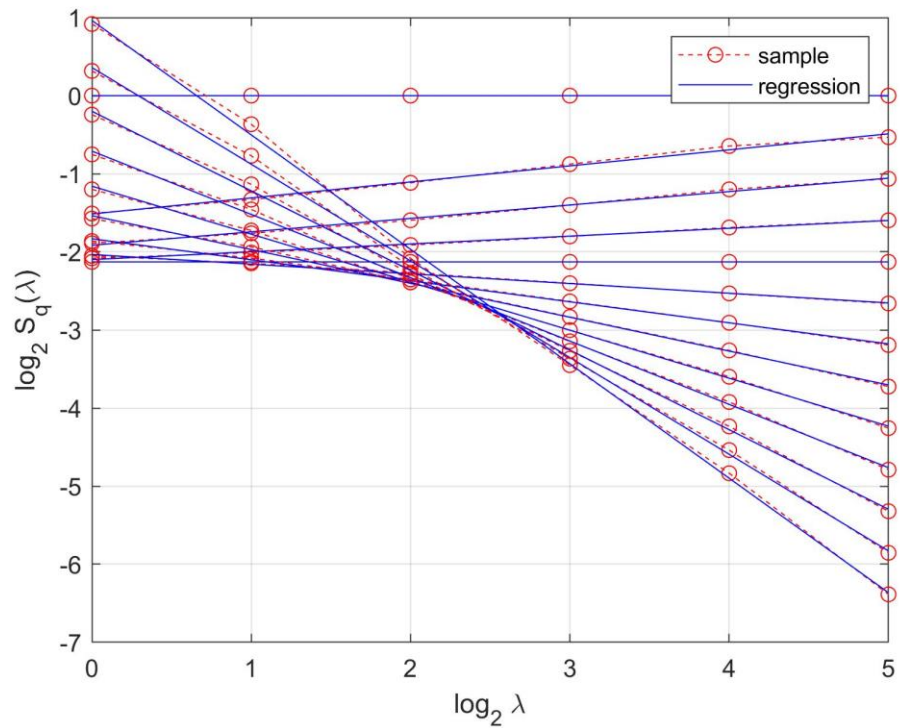


H-12 Log-log plot of the space-time structure function $S_q(\lambda)$ for 320-min aggregated 12th radar sequence selected from 2015

APPENDIX H: SPACE-TIME STRUCTURE FUNCTION $S_q(\lambda)$ FOR SELECTED RADAR SEQUENCES FROM 2015

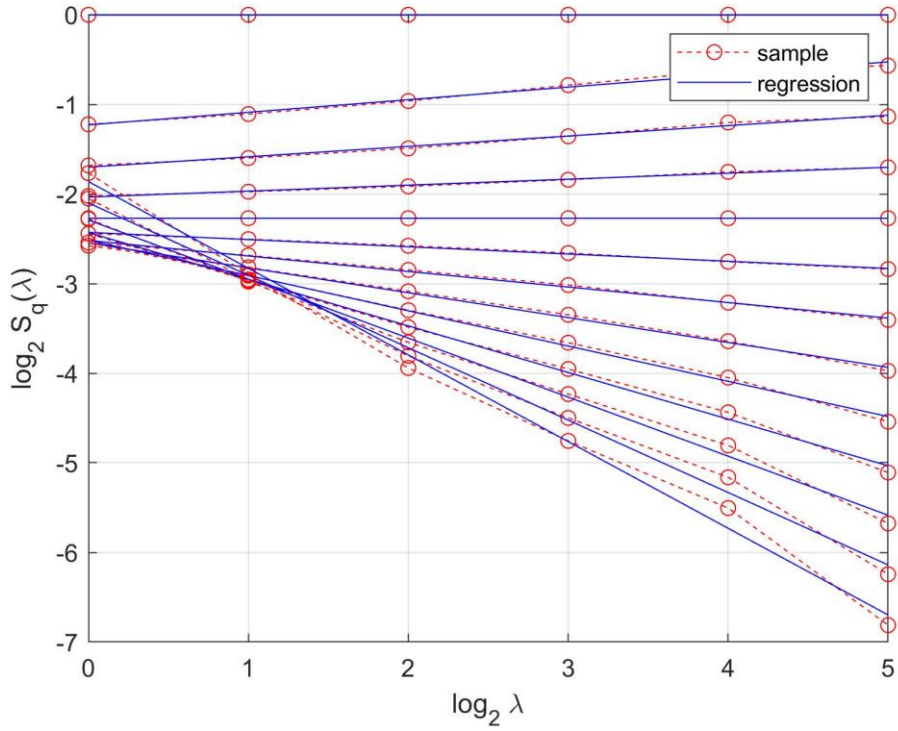


H-13 Log-log plot of the space-time structure function $S_q(\lambda)$ for 320-min aggregated 13th radar sequence selected from 2015

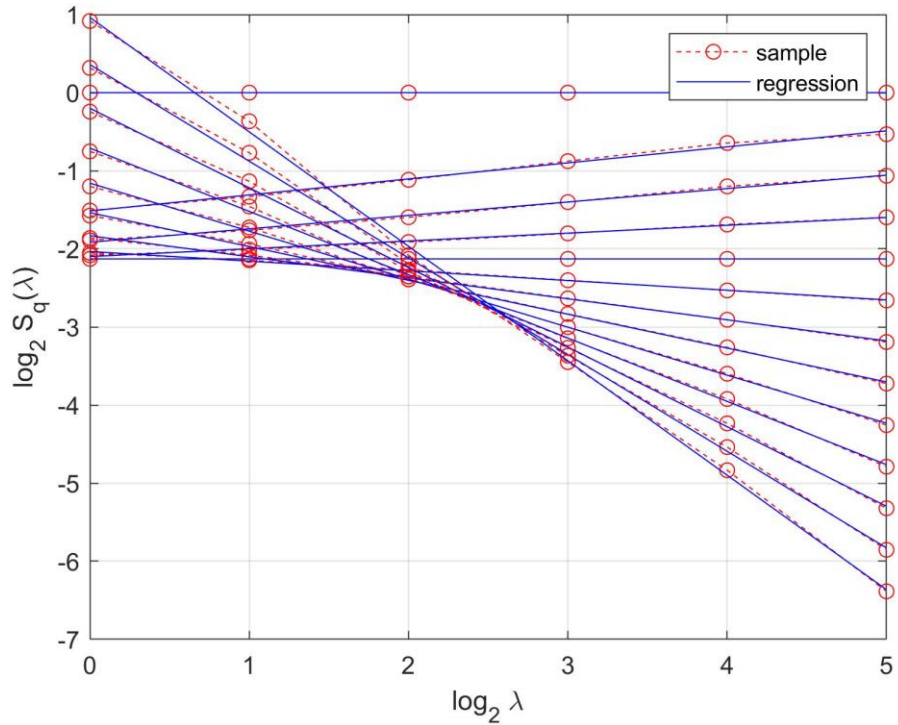


H-14 Log-log plot of the space-time structure function $S_q(\lambda)$ for 320-min aggregated 14th radar sequence selected from 2015

APPENDIX H: SPACE-TIME STRUCTURE FUNCTION $S_q(\lambda)$ FOR SELECTED RADAR SEQUENCES FROM 2015

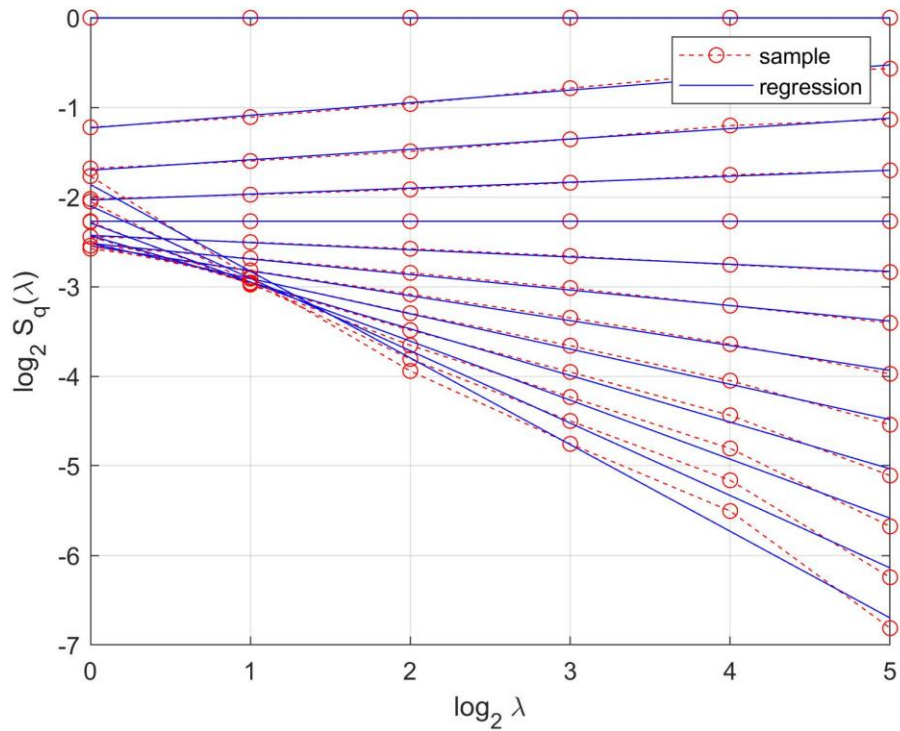


H-15 Log-log plot of the space-time structure function $S_q(\lambda)$ for 320-min aggregated 15th radar sequence selected from 2015

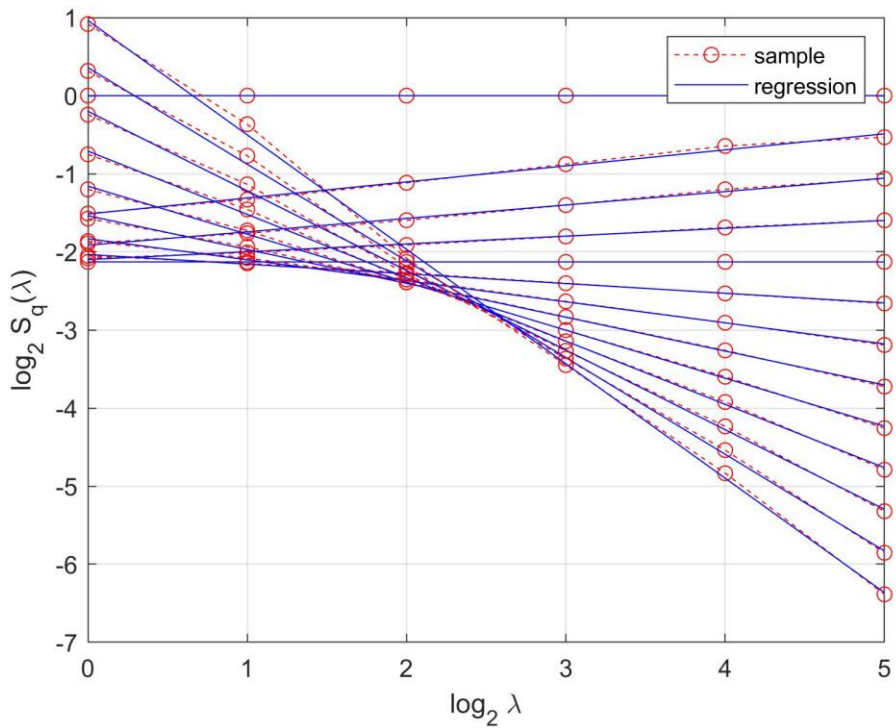


H-16 Log-log plot of the space-time structure function $S_q(\lambda)$ for 320-min aggregated 16th radar sequence selected from 2015

APPENDIX H: SPACE-TIME STRUCTURE FUNCTION $S_q(\lambda)$ FOR SELECTED RADAR SEQUENCES FROM 2015

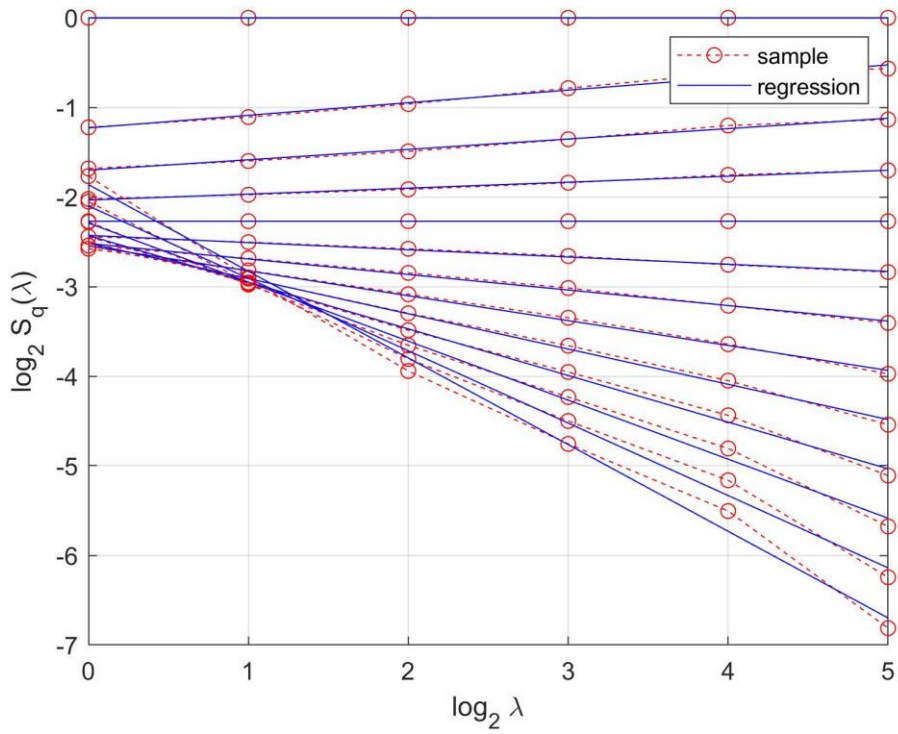


H-17 Log-log plot of the space-time structure function $S_q(\lambda)$ for 320-min aggregated 17th radar sequence selected from 2015

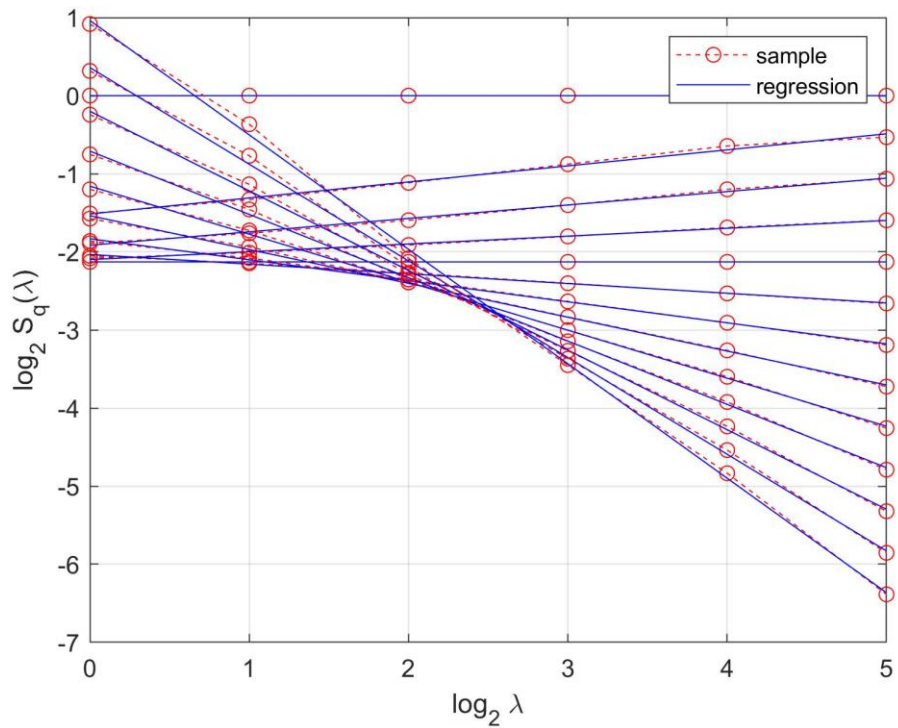


H-18 Log-log plot of the space-time structure function $S_q(\lambda)$ for 320-min aggregated 18th radar sequence selected from 2015

APPENDIX H: SPACE-TIME STRUCTURE FUNCTION $S_q(\lambda)$ FOR SELECTED RADAR SEQUENCES FROM 2015

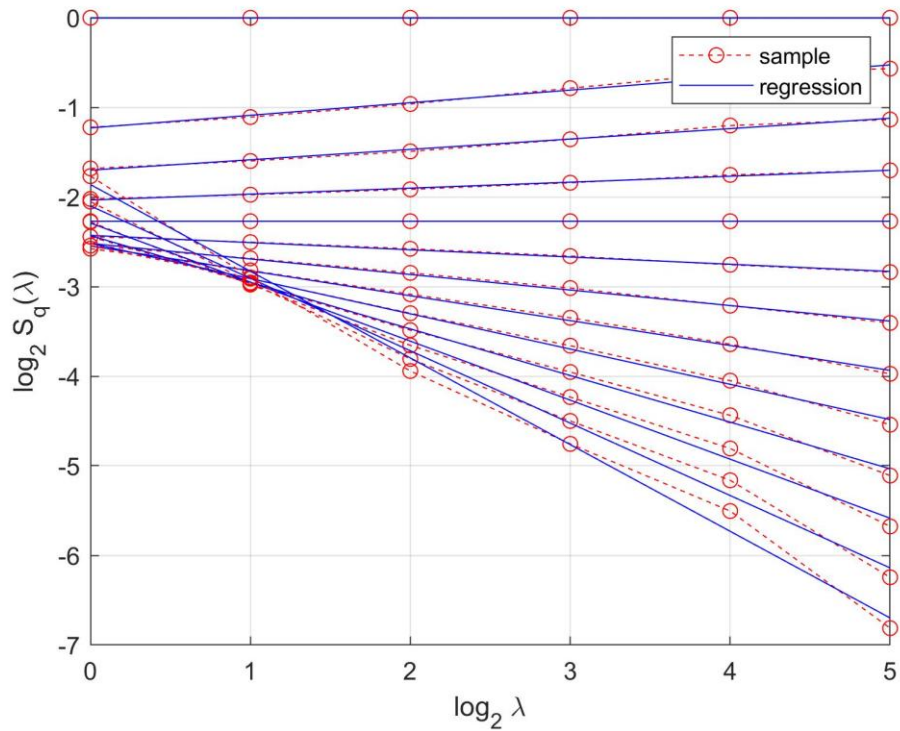


H-19 Log-log plot of the space-time structure function $S_q(\lambda)$ for 320-min aggregated 19th radar sequence selected from 2015

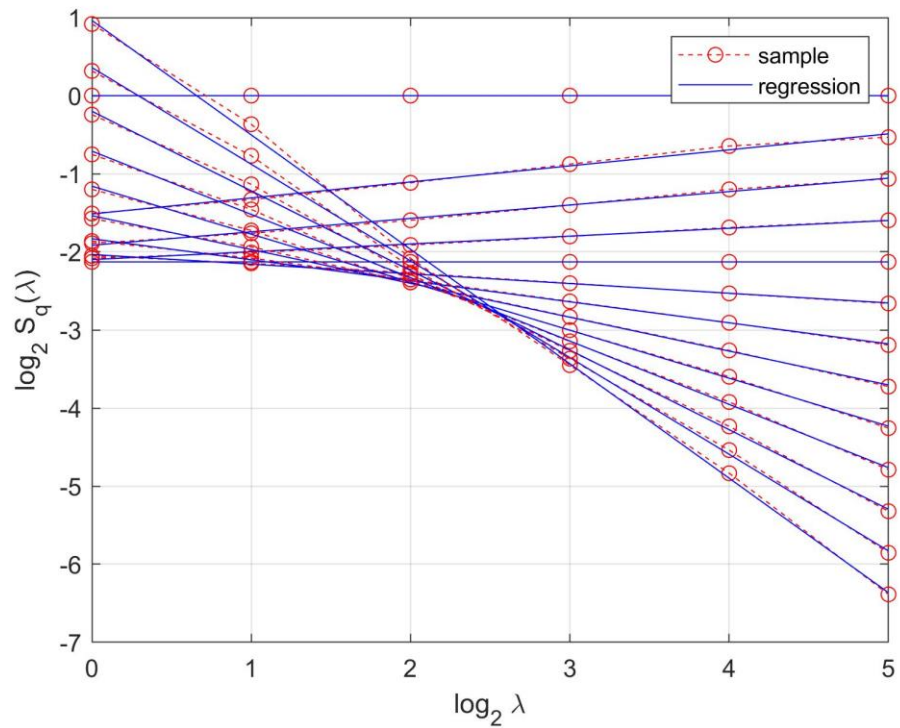


H-20 Log-log plot of the space-time structure function $S_q(\lambda)$ for 320-min aggregated 20th radar sequence selected from 2015

APPENDIX H: SPACE-TIME STRUCTURE FUNCTION $S_q(\lambda)$ FOR SELECTED RADAR SEQUENCES FROM 2015



H-21 Log-log plot of the space-time structure function $S_q(\lambda)$ for 320-min aggregated 21st radar sequence selected from 2015



H-22 Log-log plot of the space-time structure function $S_q(\lambda)$ for 320-min aggregated 22nd radar sequence selected from 2015

APPENDIX I

Table of contents

<i>I-1 Empirical multifractal scaling function $K(q)$ for 320-min aggregated 1st radar sequence selected from 2015 together with fitted theoretical $K(q)$ function model for estimated c and β parameters</i>	<i>235</i>
<i>I-2 Empirical multifractal scaling function $K(q)$ for 320-min aggregated 2nd radar sequence selected from 2015 together with fitted theoretical $K(q)$ function model for estimated c and β parameters</i>	<i>235</i>
<i>I-3 Empirical multifractal scaling function $K(q)$ for 320-min aggregated 3rd radar sequence selected from 2015 together with fitted theoretical $K(q)$ function model for estimated c and β parameters</i>	<i>236</i>
<i>I-4 Empirical multifractal scaling function $K(q)$ for 320-min aggregated 1st radar sequence selected from 2015 together with fitted theoretical $K(q)$ function model for estimated c and β parameters</i>	<i>236</i>
<i>I-5 Empirical multifractal scaling function $K(q)$ for 320-min aggregated 5th radar sequence selected from 2015 together with fitted theoretical $K(q)$ function model for estimated c and β parameters</i>	<i>237</i>
<i>I-6 Empirical multifractal scaling function $K(q)$ for 320-min aggregated 6th radar sequence selected from 2015 together with fitted theoretical $K(q)$ function model for estimated c and β parameters</i>	<i>237</i>
<i>I-7 Empirical multifractal scaling function $K(q)$ for 320-min aggregated 7th radar sequence selected from 2015 together with fitted theoretical $K(q)$ function model for estimated c and β parameters</i>	<i>238</i>
<i>I-8 Empirical multifractal scaling function $K(q)$ for 320-min aggregated 8th radar sequence selected from 2015 together with fitted theoretical $K(q)$ function model for estimated c and β parameters</i>	<i>238</i>
<i>I-9 Empirical multifractal scaling function $K(q)$ for 320-min aggregated 9th radar sequence selected from 2015 together with fitted theoretical $K(q)$ function model for estimated c and β parameters</i>	<i>239</i>
<i>I-10 Empirical multifractal scaling function $K(q)$ for 320-min aggregated 10th radar sequence selected from 2015 together with fitted theoretical $K(q)$ function model for estimated c and β parameters.....</i>	<i>239</i>
<i>I-11 Empirical multifractal scaling function $K(q)$ for 320-min aggregated 11th radar sequence selected from 2015 together with fitted theoretical $K(q)$ function model for estimated c and β parameters.....</i>	<i>240</i>
<i>I-12 Empirical multifractal scaling function $K(q)$ for 320-min aggregated 12th radar sequence selected from 2015 together with fitted theoretical $K(q)$ function model for estimated c and β parameters.....</i>	<i>240</i>
<i>I-13 Empirical multifractal scaling function $K(q)$ for 320-min aggregated 13th radar sequence selected from 2015 together with fitted theoretical $K(q)$ function model for estimated c and β parameters.....</i>	<i>241</i>
<i>I-14 Empirical multifractal scaling function $K(q)$ for 320-min aggregated 14th radar sequence selected from 2015 together with fitted theoretical $K(q)$ function model for estimated c and β parameters.....</i>	<i>241</i>
<i>I-15 Empirical multifractal scaling function $K(q)$ for 320-min aggregated 15th radar sequence selected from 2015 together with fitted theoretical $K(q)$ function model for estimated c and β parameters.....</i>	<i>242</i>

APPENDIX I: MULTIFRACTAL SCALING FUNCTION $K(q)$ FOR SELECTED RADAR SEQUENCE
RADAR SEQUENCES FROM 2015. $K(q)$ THEORETICAL MODEL FOR ESTIMATED c
AND β PARAMETERS

I-16 Empirical multifractal scaling function $K(q)$ for 320-min aggregated 16th radar sequence selected from 2015 together with fitted theoretical $K(q)$ function model for estimated c and β parameters..... 242

I-17 Empirical multifractal scaling function $K(q)$ for 320-min aggregated 17th radar sequence selected from 2015 together with fitted theoretical $K(q)$ function model for estimated c and β parameters..... 243

I-18 Empirical multifractal scaling function $K(q)$ for 320-min aggregated 18th radar sequence selected from 2015 together with fitted theoretical $K(q)$ function model for estimated c and β parameters..... 244

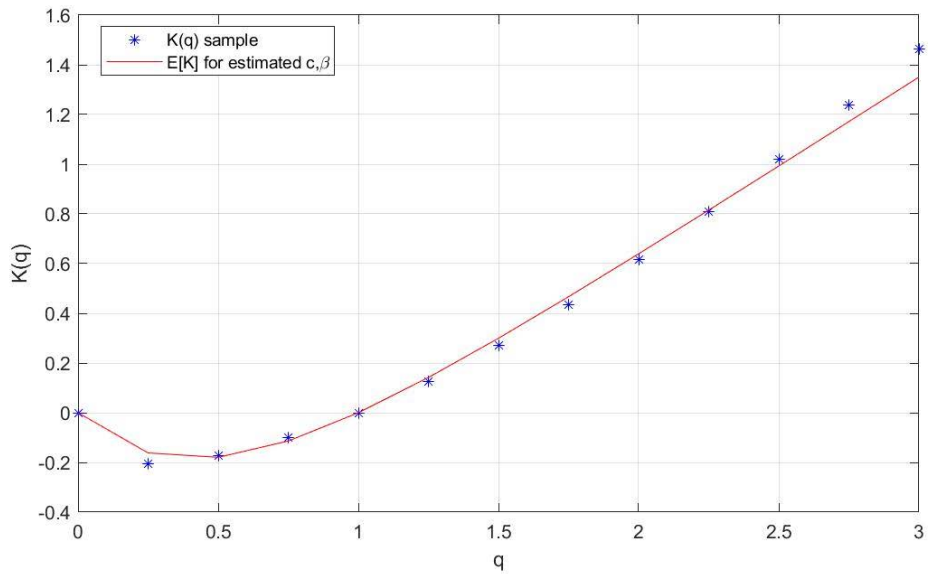
I-19 Empirical multifractal scaling function $K(q)$ for 320-min aggregated 19th radar sequence selected from 2015 together with fitted theoretical $K(q)$ function model for estimated c and β parameters..... 244

I-20 Empirical multifractal scaling function $K(q)$ for 320-min aggregated 20th radar sequence selected from 2015 together with fitted theoretical $K(q)$ function model for estimated c and β parameters..... 244

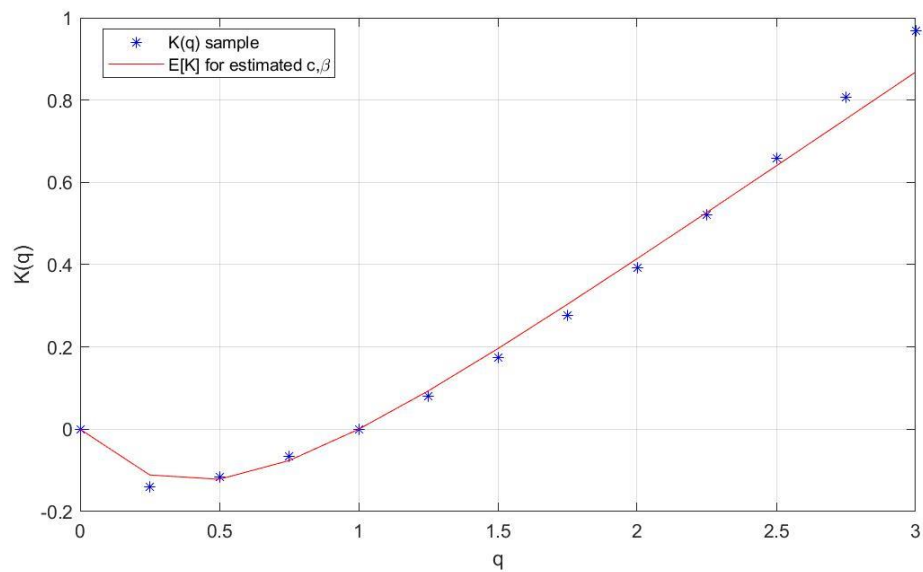
I-21 Empirical multifractal scaling function $K(q)$ for 320-min aggregated 21st radar sequence selected from 2015 together with fitted theoretical $K(q)$ function model for estimated c and β parameters..... 245

I-22 Empirical multifractal scaling function $K(q)$ for 320-min aggregated 22nd radar sequence selected from 2015 together with fitted theoretical $K(q)$ function model for estimated c and β parameters..... 245

APPENDIX I: MULTIFRACTAL SCALING FUNCTION $K(q)$ FOR SELECTED RADAR SEQUENCE
 RADAR SEQUENCES FROM 2015. $K(q)$ THEORETICAL MODEL FOR ESTIMATED c
 AND β PARAMETERS

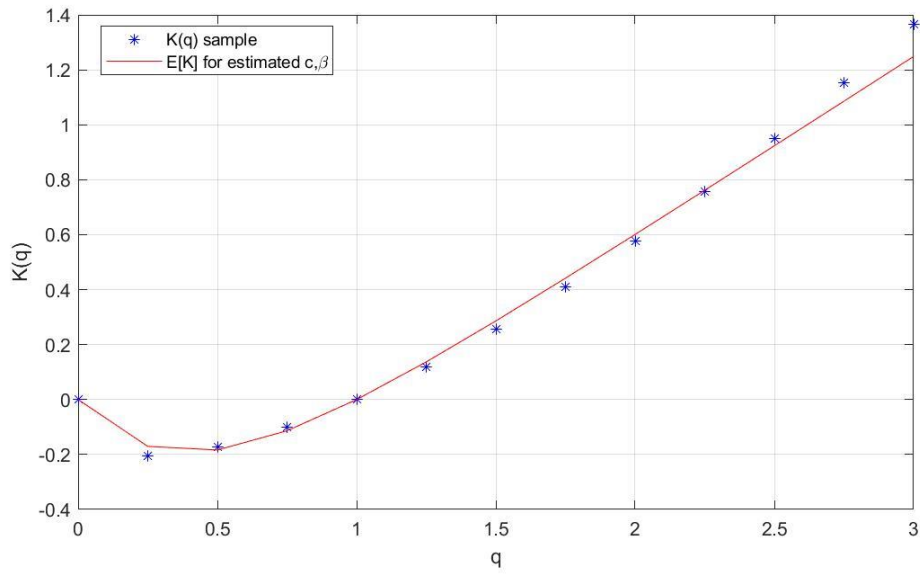


I-1 Empirical multifractal scaling function $K(q)$ for 320-min aggregated 1st radar sequence selected from 2015 together with fitted theoretical $K(q)$ function model for estimated c and β parameters

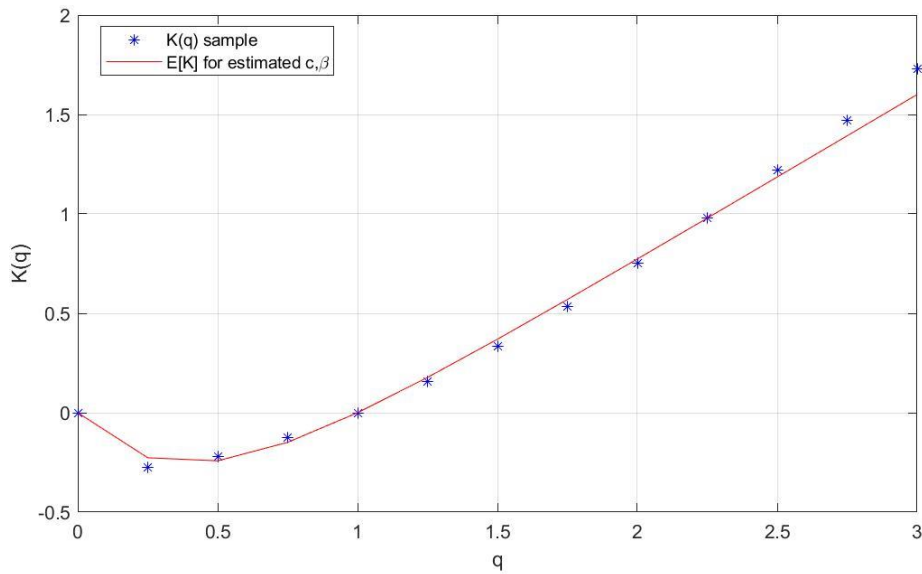


I-2 Empirical multifractal scaling function $K(q)$ for 320-min aggregated 2nd radar sequence selected from 2015 together with fitted theoretical $K(q)$ function model for estimated c and β parameters

APPENDIX I: MULTIFRACTAL SCALING FUNCTION $K(q)$ FOR SELECTED RADAR SEQUENCE
 RADAR SEQUENCES FROM 2015. $K(q)$ THEORETICAL MODEL FOR ESTIMATED c
 AND β PARAMETERS

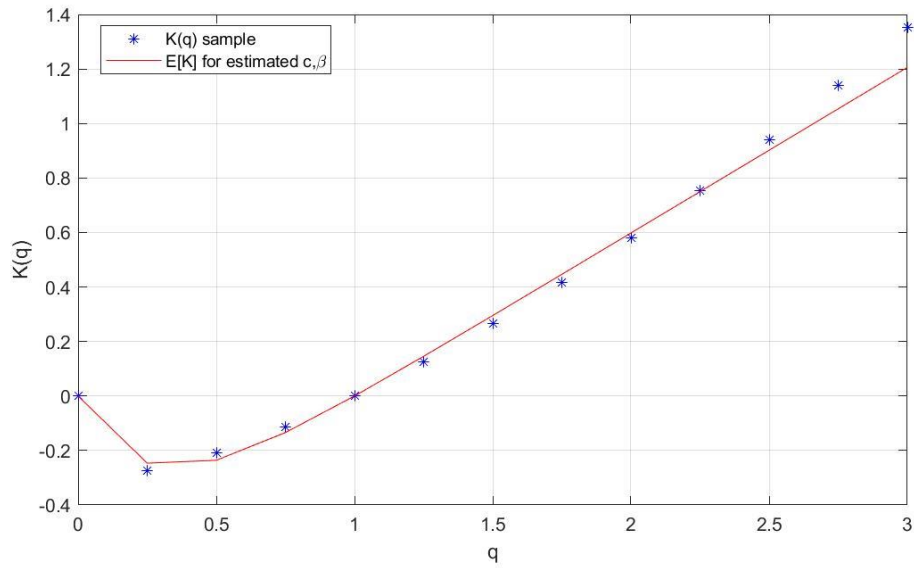


I-3 Empirical multifractal scaling function $K(q)$ for 320-min aggregated 3rd radar sequence selected from 2015 together with fitted theoretical $K(q)$ function model for estimated c and β parameters

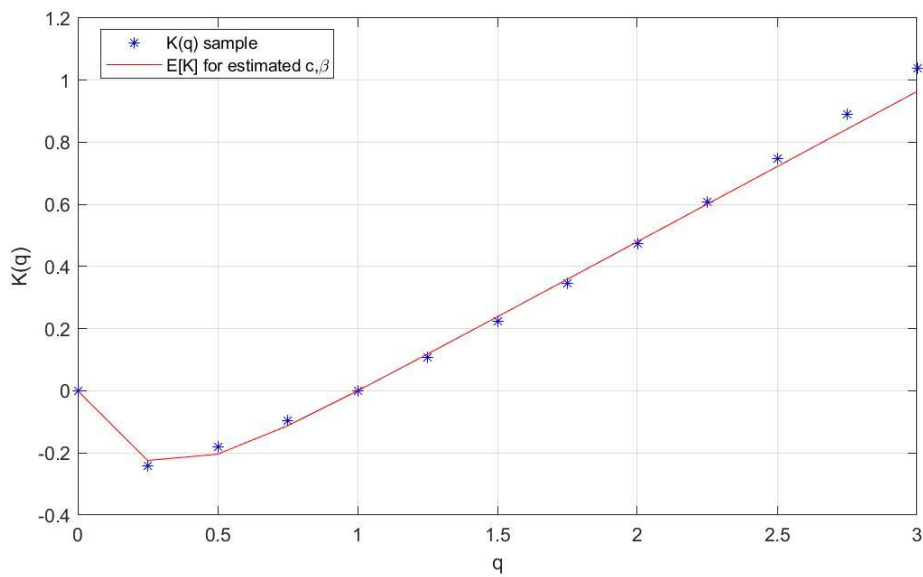


I-4 Empirical multifractal scaling function $K(q)$ for 320-min aggregated 1st radar sequence selected from 2015 together with fitted theoretical $K(q)$ function model for estimated c and β parameters

APPENDIX I: MULTIFRACTAL SCALING FUNCTION $K(q)$ FOR SELECTED RADAR SEQUENCE
 RADAR SEQUENCES FROM 2015. $K(q)$ THEORETICAL MODEL FOR ESTIMATED c
 AND β PARAMETERS

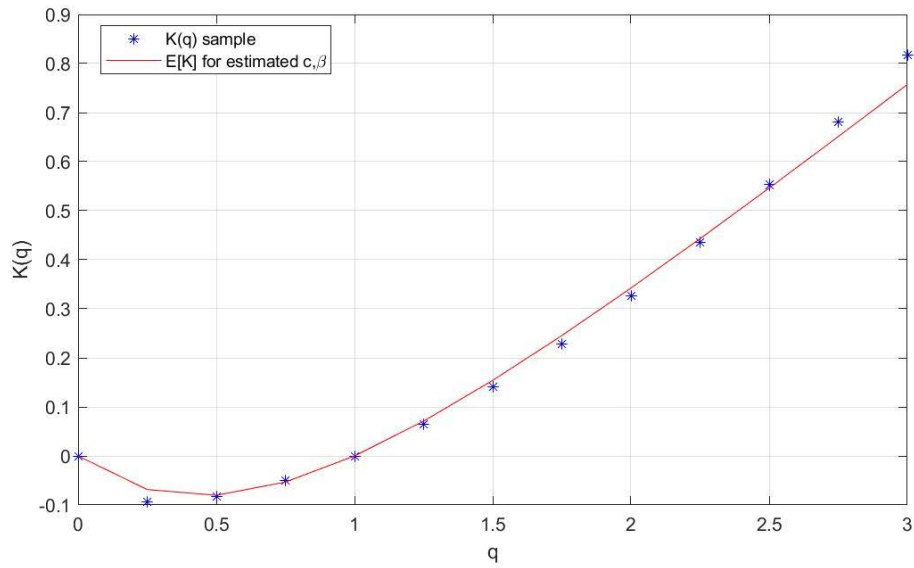


I-5 Empirical multifractal scaling function $K(q)$ for 320-min aggregated 5th radar sequence selected from 2015 together with fitted theoretical $K(q)$ function model for estimated c and β parameters

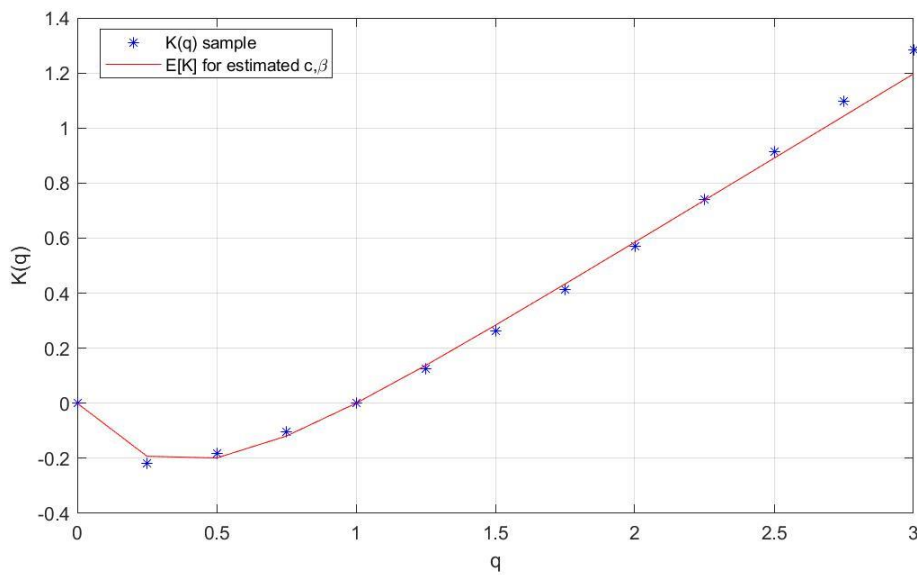


I-6 Empirical multifractal scaling function $K(q)$ for 320-min aggregated 6th radar sequence selected from 2015 together with fitted theoretical $K(q)$ function model for estimated c and β parameters

APPENDIX I: MULTIFRACTAL SCALING FUNCTION $K(q)$ FOR SELECTED RADAR SEQUENCE
 RADAR SEQUENCES FROM 2015. $K(q)$ THEORETICAL MODEL FOR ESTIMATED c
 AND β PARAMETERS

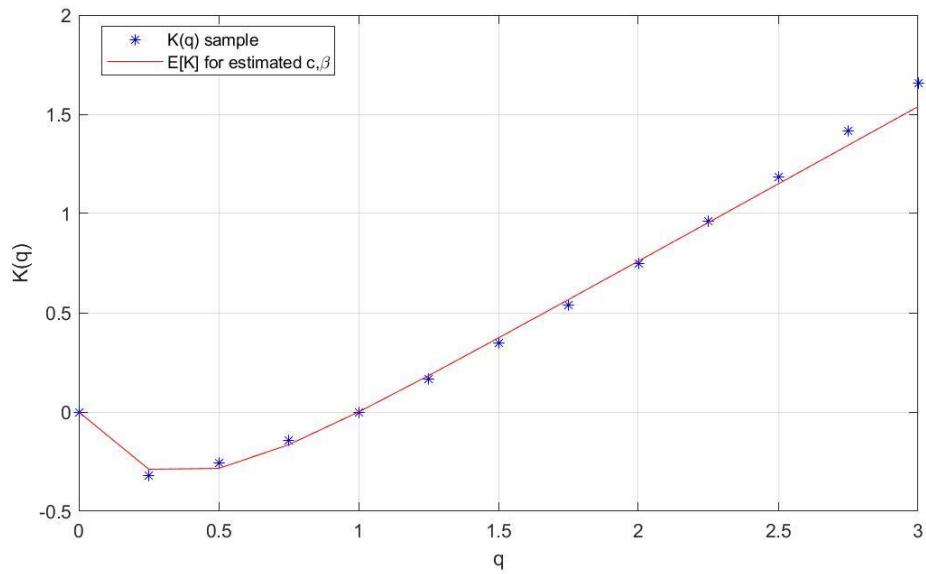


I-7 Empirical multifractal scaling function $K(q)$ for 320-min aggregated 7th radar sequence selected from 2015 together with fitted theoretical $K(q)$ function model for estimated c and β parameters

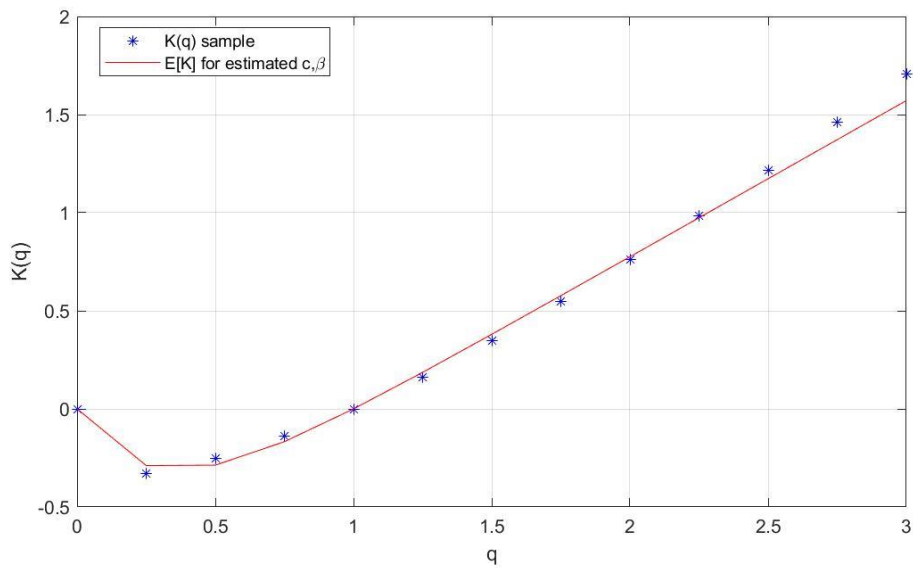


I-8 Empirical multifractal scaling function $K(q)$ for 320-min aggregated 8th radar sequence selected from 2015 together with fitted theoretical $K(q)$ function model for estimated c and β parameters

APPENDIX I: MULTIFRACTAL SCALING FUNCTION $K(q)$ FOR SELECTED RADAR SEQUENCE
 RADAR SEQUENCES FROM 2015. $K(q)$ THEORETICAL MODEL FOR ESTIMATED c
 AND β PARAMETERS

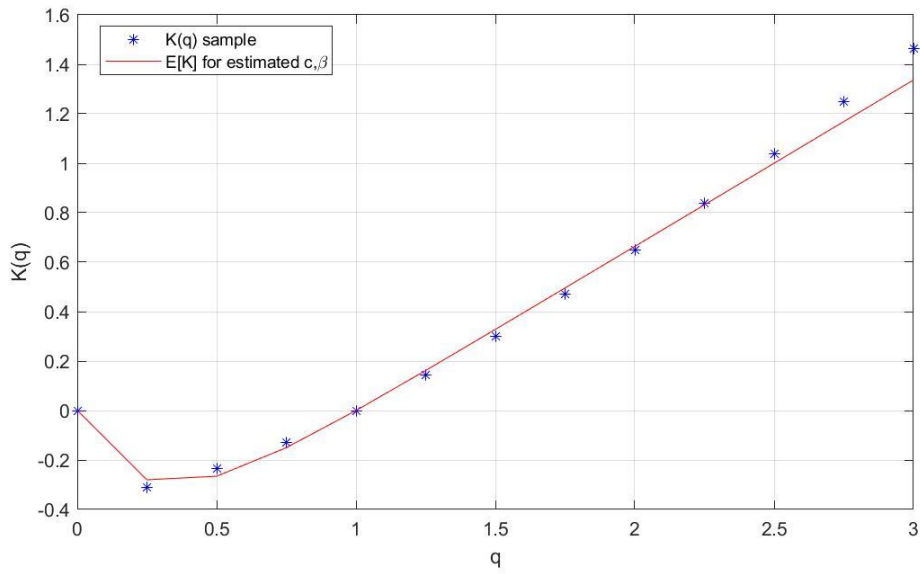


I-9 Empirical multifractal scaling function $K(q)$ for 320-min aggregated 9th radar sequence selected from 2015 together with fitted theoretical $K(q)$ function model for estimated c and β parameters

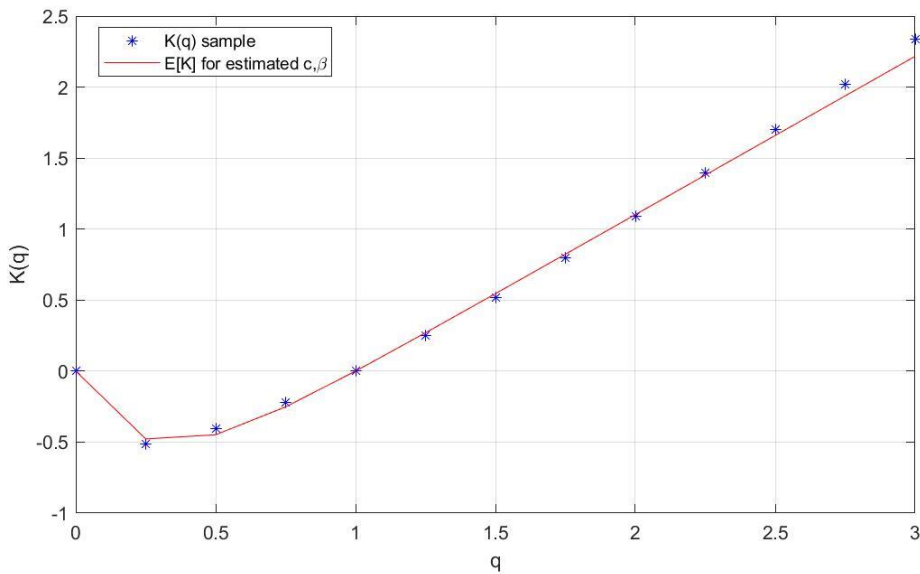


I-10 Empirical multifractal scaling function $K(q)$ for 320-min aggregated 10th radar sequence selected from 2015 together with fitted theoretical $K(q)$ function model for estimated c and β parameters

APPENDIX I: MULTIFRACTAL SCALING FUNCTION $K(q)$ FOR SELECTED RADAR SEQUENCE
 RADAR SEQUENCES FROM 2015. $K(q)$ THEORETICAL MODEL FOR ESTIMATED c
 AND β PARAMETERS

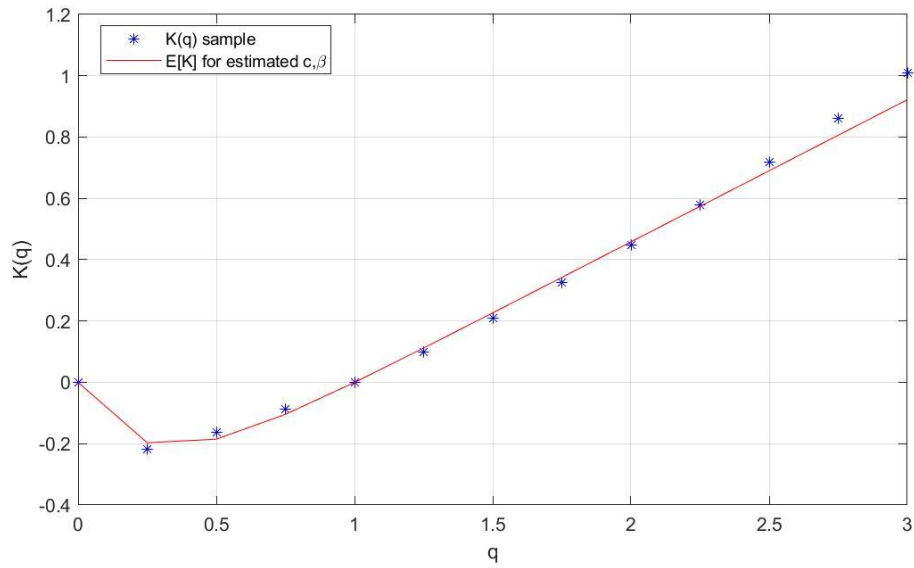


I-11 Empirical multifractal scaling function $K(q)$ for 320-min aggregated 11th radar sequence selected from 2015 together with fitted theoretical $K(q)$ function model for estimated c and β parameters

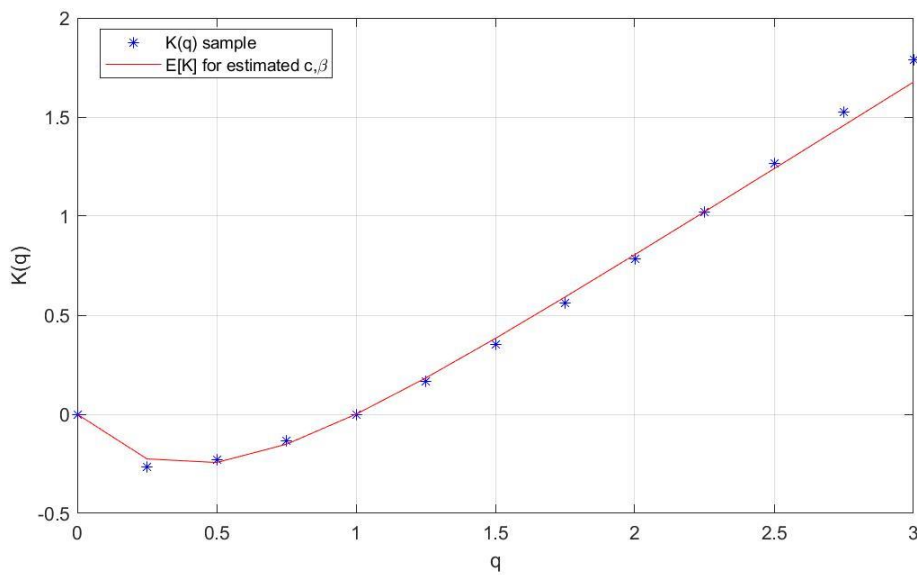


I-12 Empirical multifractal scaling function $K(q)$ for 320-min aggregated 12th radar sequence selected from 2015 together with fitted theoretical $K(q)$ function model for estimated c and β parameters

APPENDIX I: MULTIFRACTAL SCALING FUNCTION $K(q)$ FOR SELECTED RADAR SEQUENCE
 RADAR SEQUENCES FROM 2015. $K(q)$ THEORETICAL MODEL FOR ESTIMATED c
 AND β PARAMETERS

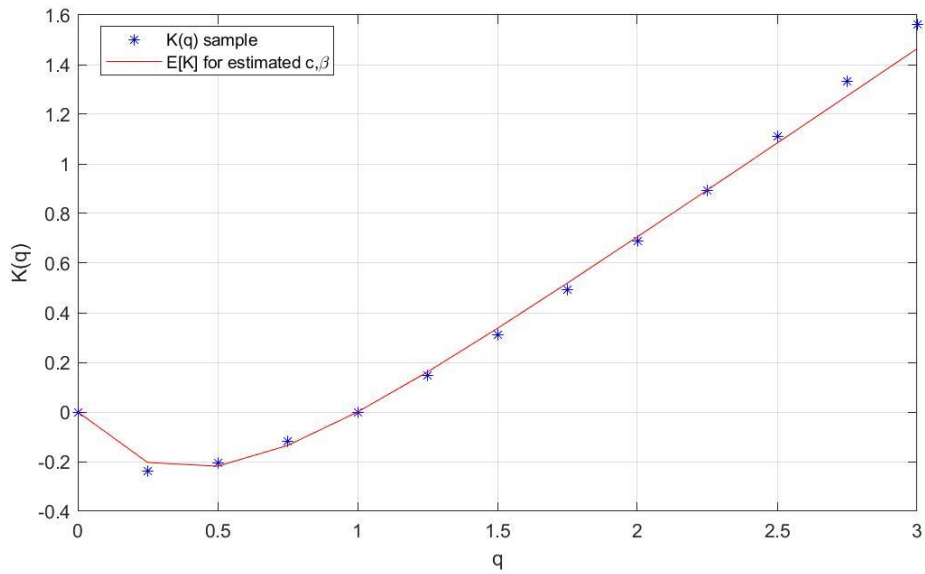


I-13 Empirical multifractal scaling function $K(q)$ for 320-min aggregated 13th radar sequence selected from 2015 together with fitted theoretical $K(q)$ function model for estimated c and β parameters

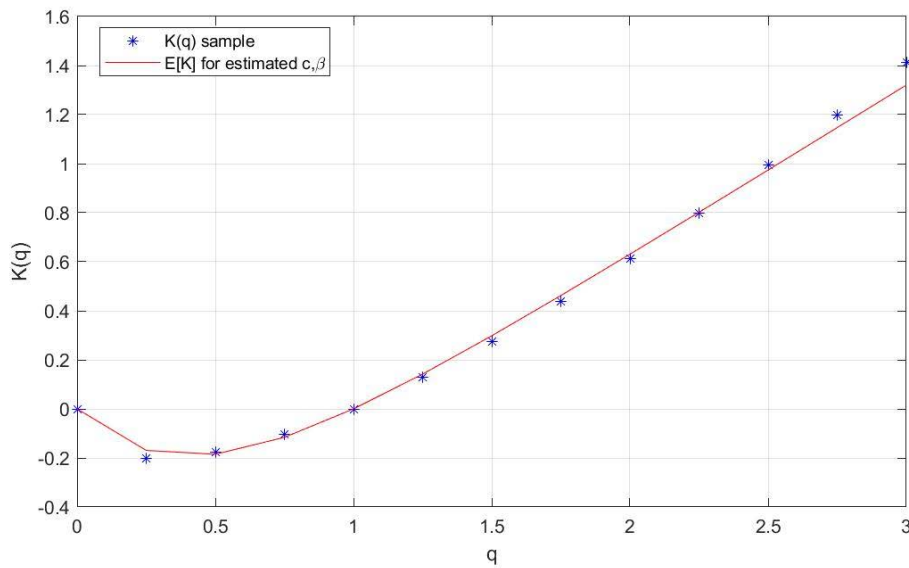


I-14 Empirical multifractal scaling function $K(q)$ for 320-min aggregated 14th radar sequence selected from 2015 together with fitted theoretical $K(q)$ function model for estimated c and β parameters

APPENDIX I: MULTIFRACTAL SCALING FUNCTION $K(q)$ FOR SELECTED RADAR SEQUENCE
 RADAR SEQUENCES FROM 2015. $K(q)$ THEORETICAL MODEL FOR ESTIMATED c
 AND β PARAMETERS

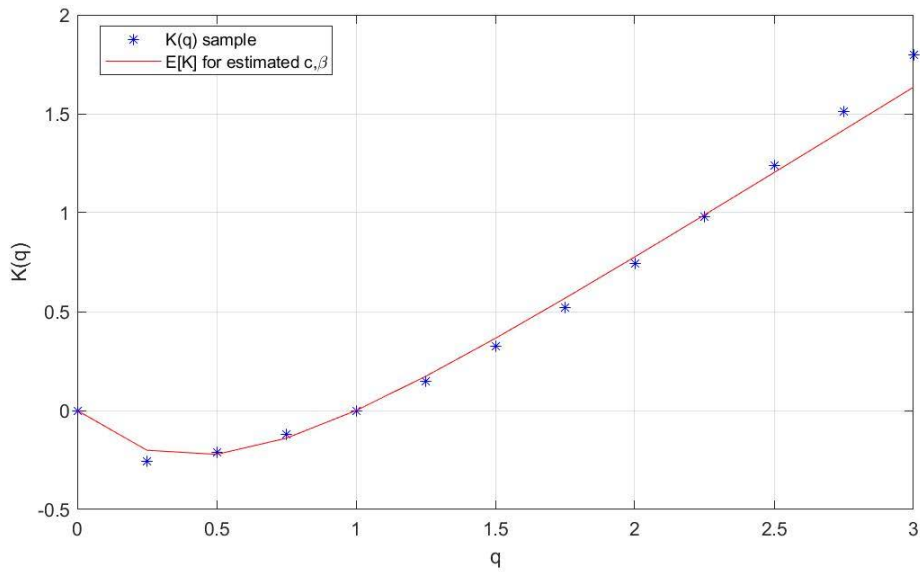


I-15 Empirical multifractal scaling function $K(q)$ for 320-min aggregated 15th radar sequence selected from 2015 together with fitted theoretical $K(q)$ function model for estimated c and β parameters

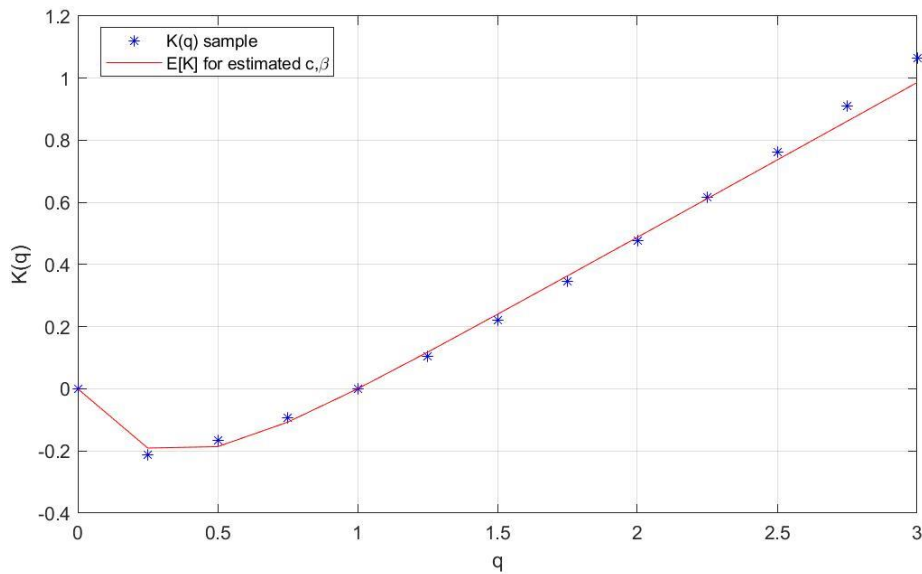


I-16 Empirical multifractal scaling function $K(q)$ for 320-min aggregated 16th radar sequence selected from 2015 together with fitted theoretical $K(q)$ function model for estimated c and β parameters

APPENDIX I: MULTIFRACTAL SCALING FUNCTION $K(q)$ FOR SELECTED RADAR SEQUENCE
 RADAR SEQUENCES FROM 2015. $K(q)$ THEORETICAL MODEL FOR ESTIMATED c
 AND β PARAMETERS

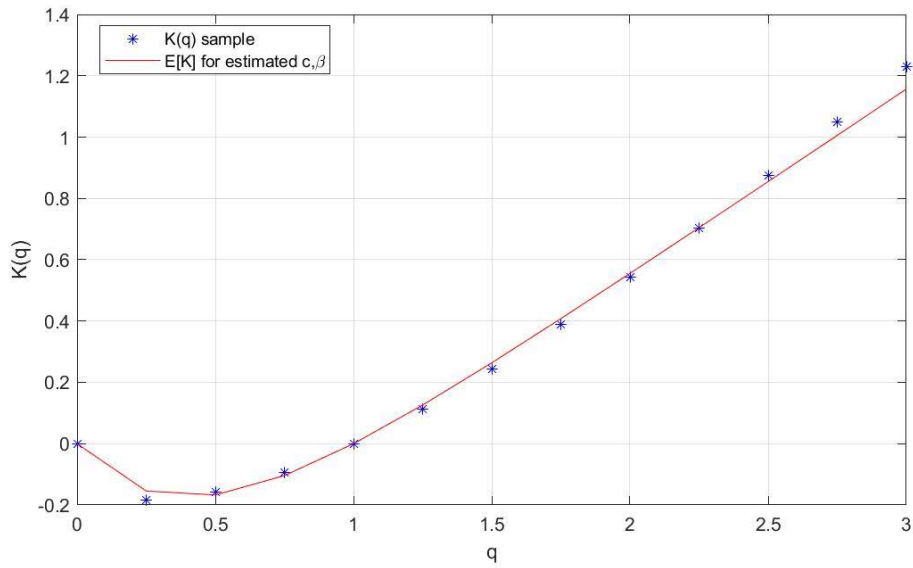


I-17 Empirical multifractal scaling function $K(q)$ for 320-min aggregated 17th radar sequence selected from 2015 together with fitted theoretical $K(q)$ function model for estimated c and β parameters

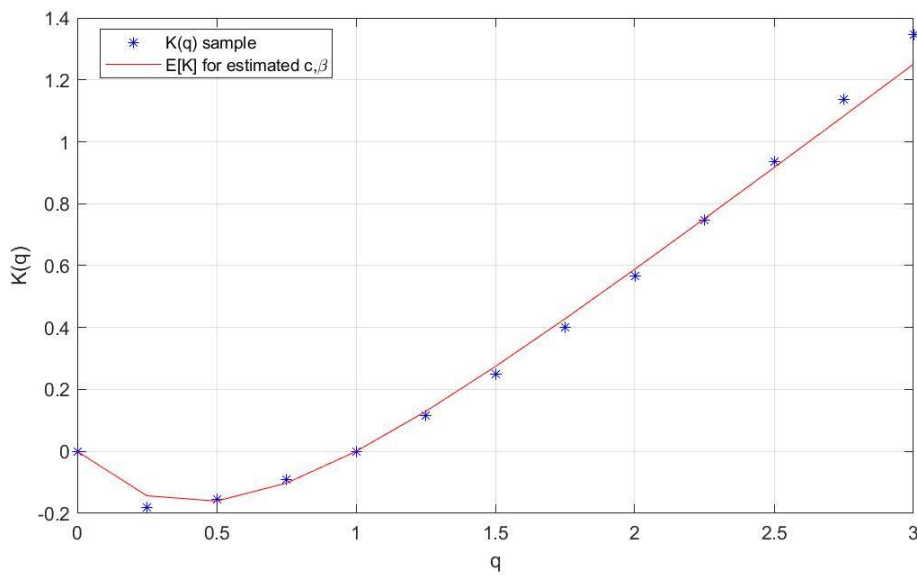


I-18 Empirical multifractal scaling function $K(q)$ for 320-min aggregated 18th radar sequence selected from 2015 together with fitted theoretical $K(q)$ function model for estimated c and β parameters

APPENDIX I: MULTIFRACTAL SCALING FUNCTION $K(q)$ FOR SELECTED RADAR SEQUENCE
 RADAR SEQUENCES FROM 2015. $K(q)$ THEORETICAL MODEL FOR ESTIMATED c
 AND β PARAMETERS

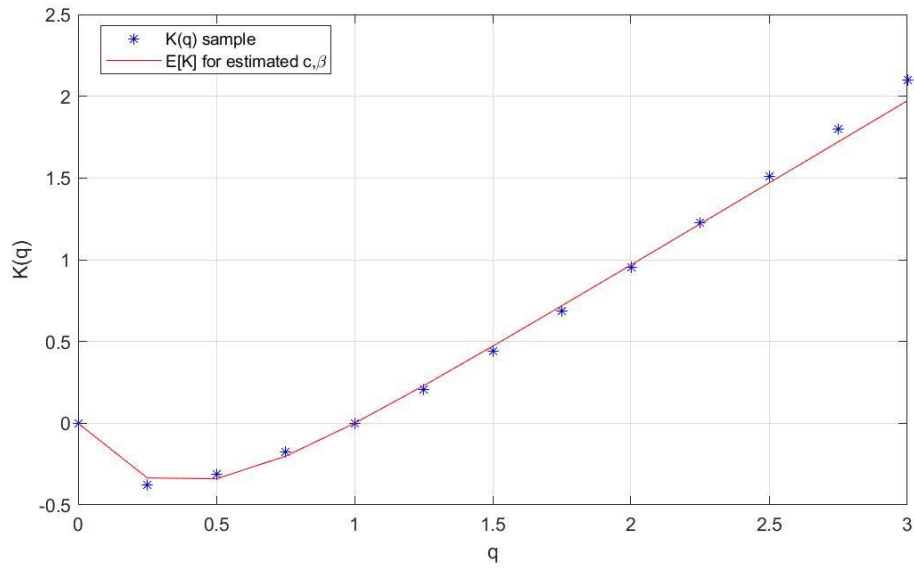


I-19 Empirical multifractal scaling function $K(q)$ for 320-min aggregated 19th radar sequence selected from 2015 together with fitted theoretical $K(q)$ function model for estimated c and β parameters

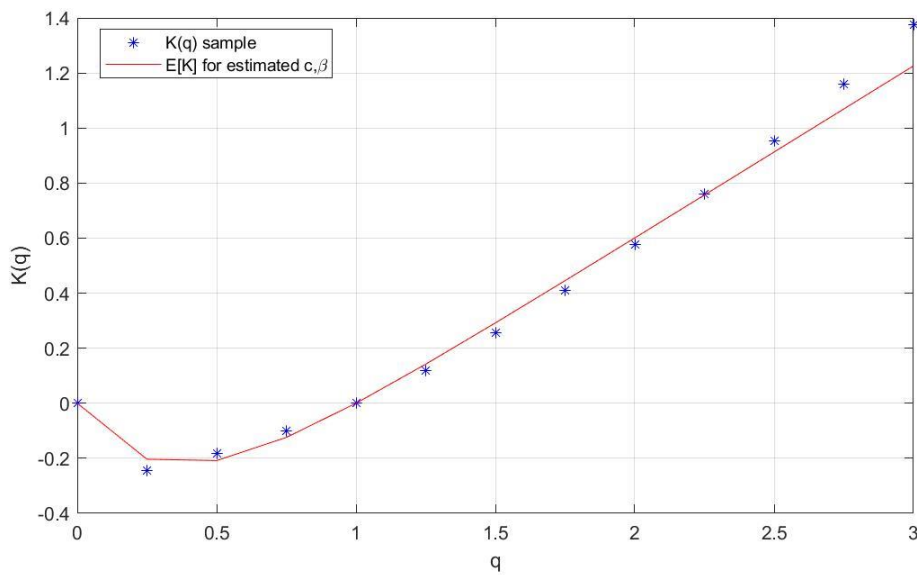


I-20 Empirical multifractal scaling function $K(q)$ for 320-min aggregated 20th radar sequence selected from 2015 together with fitted theoretical $K(q)$ function model for estimated c and β parameters

APPENDIX I: MULTIFRACTAL SCALING FUNCTION $K(q)$ FOR SELECTED RADAR SEQUENCE
 RADAR SEQUENCES FROM 2015. $K(q)$ THEORETICAL MODEL FOR ESTIMATED C
 AND β PARAMETERS



I-21 Empirical multifractal scaling function $K(q)$ for 320-min aggregated 21st radar sequence selected from 2015 together with fitted theoretical $K(q)$ function model for estimated c and β parameters



I-22 Empirical multifractal scaling function $K(q)$ for 320-min aggregated 22nd radar sequence selected from 2015 together with fitted theoretical $K(q)$ function model for estimated c and β parameters

APPENDIX J: LIST OF LOG-POISSON c , β AND $c_{\beta=CONST}$ PARAMETERS FOR THE SELECTED RAINFALL EVENTS

APPENDIX J

Table of contents

J-1 List of log-Poisson c , β and $c_{\beta=const}$ parameters for the selected rainfall events 247

APPENDIX J: LIST OF LOG-POISSON c , β AND $C_{\beta=CONST}$ PARAMETERS FOR THE SELECTED RAINFALL EVENTS

J-1 List of log-Poisson c , β and $c_{\beta=const}$ parameters for the selected rainfall events

No.	Year	No. of rainfall event in particular year	R, mm/10min	β	c	$C_{\beta=const}$
1	2009	1	0.226	0.071	0.485	0.515
2	2009	2	0.221	0.483	0.690	0.227
3	2009	3	0.166	0.210	0.450	0.342
4	2009	4	0.156	0.378	0.500	0.236
5	2009	5	0.150	0.080	0.772	0.803
6	2009	6	0.149	0.369	1.075	0.524
7	2009	7	0.148	0.053	0.468	0.521
8	2009	8	0.145	0.292	0.496	0.303
9	2009	9	0.136	0.057	0.665	0.732
10	2009	10	0.135	0.152	0.542	0.475
11	2009	11	0.123	0.155	0.253	0.220
12	2009	12	0.119	0.213	0.400	0.301
13	2009	13	0.118	0.198	0.515	0.403
14	2009	14	0.118	0.089	0.488	0.498
15	2009	15	0.117	0.265	0.465	0.305
16	2009	16	0.096	0.382	0.725	0.338
17	2009	17	0.095	0.028	0.578	0.685
18	2009	18	0.094	0.226	0.436	0.318
19	2009	19	0.088	0.052	0.601	0.669
20	2009	20	0.084	0.105	0.724	0.711
21	2009	21	0.083	0.073	0.384	0.407
22	2009	22	0.080	0.016	0.593	0.728
23	2009	23	0.077	0.284	0.772	0.481
24	2009	24	0.077	0.043	0.758	0.864
25	2009	25	0.077	0.032	0.584	0.685
26	2009	26	0.070	0.051	0.275	0.307
27	2009	27	0.068	0.031	0.780	0.916
28	2009	28	0.066	0.033	0.603	0.704
29	2010	1	0.153	0.048	0.374	0.420
30	2010	2	0.151	0.033	0.414	0.484
31	2010	3	0.150	0.020	0.294	0.356
32	2010	4	0.133	0.013	0.374	0.463
33	2010	5	0.133	0.100	0.693	0.688
34	2010	6	0.125	0.081	0.331	0.344
35	2010	7	0.122	0.473	1.459	0.499
36	2010	8	0.116	0.266	0.426	0.280
37	2010	9	0.090	0.033	0.492	0.576

APPENDIX J: LIST OF LOG-POISSON C , β AND $C_{\beta=CONST}$ PARAMETERS FOR THE SELECTED RAINFALL EVENTS

38	2010	10	0.085	0.034	0.530	0.619
39	2010	11	0.085	0.050	0.533	0.597
40	2010	12	0.080	0.113	0.609	0.585
41	2010	13	0.079	0.240	0.473	0.333
42	2010	14	0.079	0.163	0.499	0.427
43	2010	15	0.077	0.080	0.645	0.671
44	2010	16	0.076	0.026	0.326	0.388
45	2010	17	0.075	0.125	0.386	0.360
46	2010	18	0.073	0.026	0.424	0.506
47	2010	19	0.066	0.071	0.482	0.512
48	2010	20	0.065	0.039	0.549	0.632
49	2010	21	0.065	0.054	0.430	0.477
50	2010	22	0.065	0.050	0.223	0.250
51	2010	23	0.063	0.075	0.280	0.294
52	2013	1	0.185	0.012	0.547	0.681
53	2013	2	0.182	0.019	0.238	0.290
54	2013	3	0.177	0.040	0.373	0.429
55	2013	4	0.176	0.038	0.493	0.570
56	2013	5	0.132	0.154	0.200	0.175
57	2013	6	0.118	0.016	0.254	0.312
58	2013	7	0.113	0.136	0.384	0.349
59	2013	8	0.108	0.116	0.863	0.825
60	2013	9	0.106	0.028	0.743	0.882
61	2013	10	0.106	0.038	0.212	0.245
62	2013	11	0.102	0.069	0.296	0.317
63	2013	12	0.095	0.061	0.492	0.536
64	2013	13	0.093	0.029	0.272	0.323
65	2013	14	0.093	0.020	0.277	0.336
66	2013	15	0.091	0.031	0.437	0.514
67	2013	16	0.086	0.018	0.620	0.758
68	2013	17	0.086	0.065	0.294	0.317
69	2013	18	0.086	0.041	0.192	0.220
70	2013	19	0.080	0.217	0.595	0.444
71	2013	20	0.078	0.218	0.632	0.470
72	2013	21	0.076	0.015	0.717	0.884
73	2013	22	0.075	0.088	0.673	0.688
74	2013	23	0.068	0.058	0.605	0.665
75	2013	24	0.068	0.086	0.406	0.417
76	2013	25	0.068	0.088	0.414	0.423
77	2013	26	0.067	0.498	0.795	0.247
78	2013	27	0.067	0.022	0.606	0.731
79	2013	28	0.067	0.014	0.581	0.719

APPENDIX J: LIST OF LOG-POISSON C , β AND $C_{\beta=CONST}$ PARAMETERS FOR THE SELECTED RAINFALL EVENTS

80	2013	29	0.065	0.035	0.682	0.795
81	2014	1	0.223	0.049	0.556	0.625
82	2014	2	0.126	0.023	0.608	0.731
83	2014	3	0.122	0.008	0.398	0.502
84	2014	4	0.115	0.107	0.696	0.680
85	2014	5	0.106	0.045	0.661	0.750
86	2014	6	0.084	0.046	0.527	0.596
87	2014	7	0.081	0.078	0.735	0.768
88	2014	8	0.078	0.098	0.367	0.367
89	2014	9	0.077	0.145	0.604	0.539
90	2014	10	0.077	0.063	0.587	0.637
91	2014	11	0.075	0.035	0.480	0.558
92	2014	12	0.074	0.121	0.544	0.514
93	2014	13	0.066	0.037	0.703	0.813
94	2015	1	0.229	0.112	0.562	0.542
95	2015	2	0.207	0.094	0.350	0.353
96	2015	3	0.177	0.078	0.490	0.513
97	2015	4	0.164	0.070	0.619	0.661
98	2015	5	0.140	0.016	0.428	0.526
99	2015	6	0.098	0.007	0.338	0.427
100	2015	7	0.090	0.213	0.383	0.289
101	2015	8	0.089	0.045	0.445	0.504
102	2015	9	0.088	0.024	0.553	0.663
103	2015	10	0.088	0.027	0.567	0.675
104	2015	11	0.087	0.014	0.473	0.585
105	2015	12	0.087	0.012	0.782	0.973
106	2015	13	0.086	0.012	0.326	0.405
107	2015	14	0.084	0.082	0.662	0.687
108	2015	15	0.081	0.074	0.570	0.603
109	2015	16	0.079	0.094	0.532	0.536
110	2015	17	0.077	0.105	0.672	0.659
111	2015	18	0.077	0.021	0.353	0.427
112	2015	19	0.070	0.083	0.458	0.473
113	2015	20	0.065	0.125	0.533	0.498
114	2015	21	0.064	0.037	0.724	0.838
115	2015	22	0.063	0.040	0.452	0.519

APPENDIX K

Table of contents

<i>K-1 Empirical multifractal scaling function $K(q)$ for 320-min aggregated 1st radar sequence selected from 2015 together with fitted theoretical $K(q)$ function model for estimated c and fixed β parameter</i>	<i>253</i>
<i>K-2 Empirical multifractal scaling function $K(q)$ for 320-min aggregated 2nd radar sequence selected from 2015 together with fitted theoretical $K(q)$ function model for estimated c and fixed β parameter</i>	<i>252</i>
<i>K-3 Empirical multifractal scaling function $K(q)$ for 320-min aggregated 3rd radar sequence selected from 2015 together with fitted theoretical $K(q)$ function model for estimated c and fixed β parameter</i>	<i>253</i>
<i>K-4 Empirical multifractal scaling function $K(q)$ for 320-min aggregated 4th radar sequence selected from 2015 together with fitted theoretical $K(q)$ function model for estimated c and fixed β parameter</i>	<i>253</i>
<i>K-5 Empirical multifractal scaling function $K(q)$ for 320-min aggregated 5th radar sequence selected from 2015 together with fitted theoretical $K(q)$ function model for estimated c and fixed β parameter</i>	<i>254</i>
<i>K-6 Empirical multifractal scaling function $K(q)$ for 320-min aggregated 6th radar sequence selected from 2015 together with fitted theoretical $K(q)$ function model for estimated c and fixed β parameter</i>	<i>254</i>
<i>K-7 Empirical multifractal scaling function $K(q)$ for 320-min aggregated 7th radar sequence selected from 2015 together with fitted theoretical $K(q)$ function model for estimated c and fixed β parameter</i>	<i>255</i>
<i>K-8 Empirical multifractal scaling function $K(q)$ for 320-min aggregated 8th radar sequence selected from 2015 together with fitted theoretical $K(q)$ function model for estimated c and fixed β parameter</i>	<i>255</i>
<i>K-9 Empirical multifractal scaling function $K(q)$ for 320-min aggregated 9th radar sequence selected from 2015 together with fitted theoretical $K(q)$ function model for estimated c and fixed β parameter</i>	<i>256</i>
<i>K-10 Empirical multifractal scaling function $K(q)$ for 320-min aggregated 10th radar sequence selected from 2015 together with fitted theoretical $K(q)$ function model for estimated c and fixed β parameter</i>	<i>256</i>
<i>K-11 Empirical multifractal scaling function $K(q)$ for 320-min aggregated 11th radar sequence selected from 2015 together with fitted theoretical $K(q)$ function model for estimated c and fixed β parameter</i>	<i>257</i>
<i>K-12 Empirical multifractal scaling function $K(q)$ for 320-min aggregated 12th radar sequence selected from 2015 together with fitted theoretical $K(q)$ function model for estimated c and fixed β parameter</i>	<i>257</i>
<i>K-13 Empirical multifractal scaling function $K(q)$ for 320-min aggregated 13th radar sequence selected from 2015 together with fitted theoretical $K(q)$ function model for estimated c and fixed β parameter</i>	<i>258</i>
<i>K-14 Empirical multifractal scaling function $K(q)$ for 320-min aggregated 14th radar sequence selected from 2015 together with fitted theoretical $K(q)$ function model for estimated c and fixed β parameter</i>	<i>258</i>
<i>K-15 Empirical multifractal scaling function $K(q)$ for 320-min aggregated 15th radar sequence selected from 2015 together with fitted theoretical $K(q)$ function model for estimated c and fixed β parameter</i>	<i>259</i>

APPENDIX K: MULTIFRACTAL SCALING FUNCTION $K(q)$ FOR SELECTED RADAR SEQUENCES FROM 2015. $K(q)$ THEORETICAL MODEL FOR ESTIMATED c PARAMETER AND FIXED β PARAMETER

K-16 Empirical multifractal scaling function $K(q)$ for 320-min aggregated 16th radar sequence selected from 2015 together with fitted theoretical $K(q)$ function model for estimated c and fixed β parameter 259

K-17 Empirical multifractal scaling function $K(q)$ for 320-min aggregated 17th radar sequence selected from 2015 together with fitted theoretical $K(q)$ function model for estimated c and fixed β parameter 260

K-18 Empirical multifractal scaling function $K(q)$ for 320-min aggregated 18th radar sequence selected from 2015 together with fitted theoretical $K(q)$ function model for estimated c and fixed β parameter 260

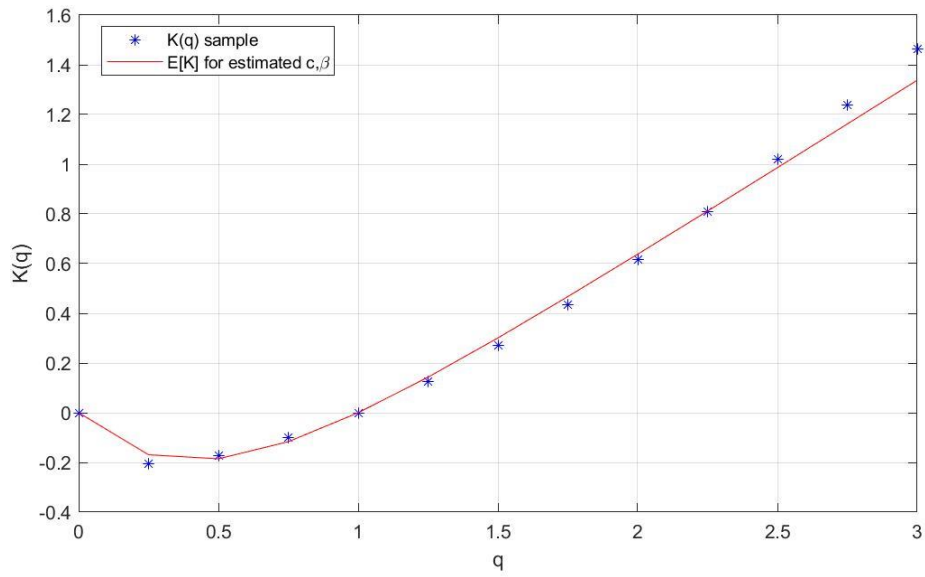
K-19 Empirical multifractal scaling function $K(q)$ for 320-min aggregated 19th radar sequence selected from 2015 together with fitted theoretical $K(q)$ function model for estimated c and fixed β parameter 261

K-20 Empirical multifractal scaling function $K(q)$ for 320-min aggregated 20th radar sequence selected from 2015 together with fitted theoretical $K(q)$ function model for estimated c and fixed β parameter 261

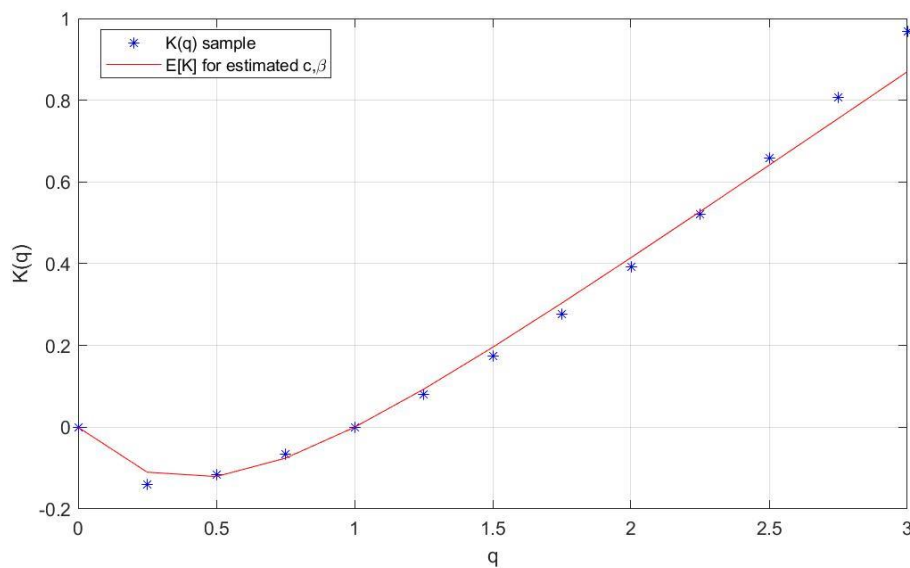
K-21 Empirical multifractal scaling function $K(q)$ for 320-min aggregated 21st radar sequence selected from 2015 together with fitted theoretical $K(q)$ function model for estimated c and fixed β parameter 262

K-22 Empirical multifractal scaling function $K(q)$ for 320-min aggregated 22nd radar sequence selected from 2015 together with fitted theoretical $K(q)$ function model for estimated c and fixed β parameter 262

APPENDIX K: MULTIFRACTAL SCALING FUNCTION $K(q)$ FOR SELECTED RADAR SEQUENCES FROM 2015. $K(q)$ THEORETICAL MODEL FOR ESTIMATED c PARAMETER AND FIXED β PARAMETER

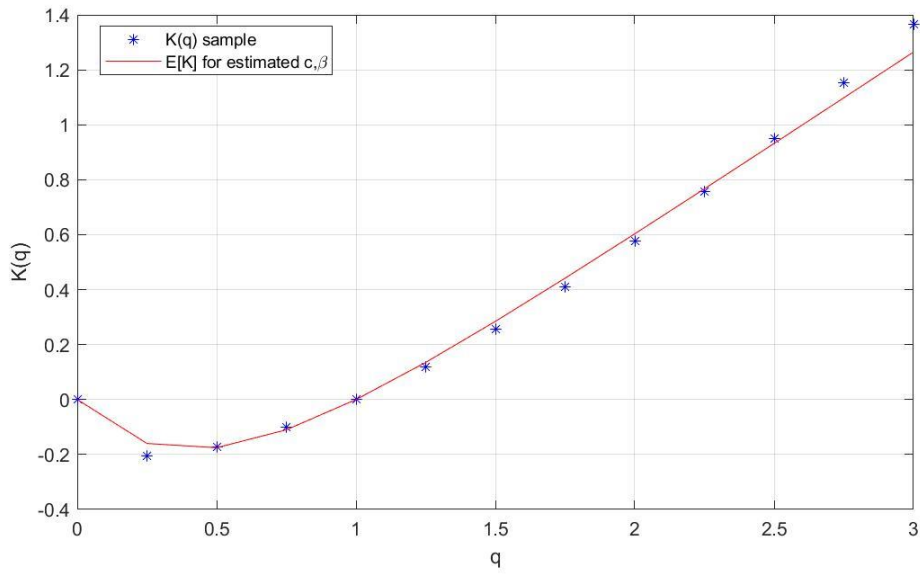


K-1 Empirical multifractal scaling function $K(q)$ for 320-min aggregated 1st radar sequence selected from 2015 together with fitted theoretical $K(q)$ function model for estimated c and fixed β parameter

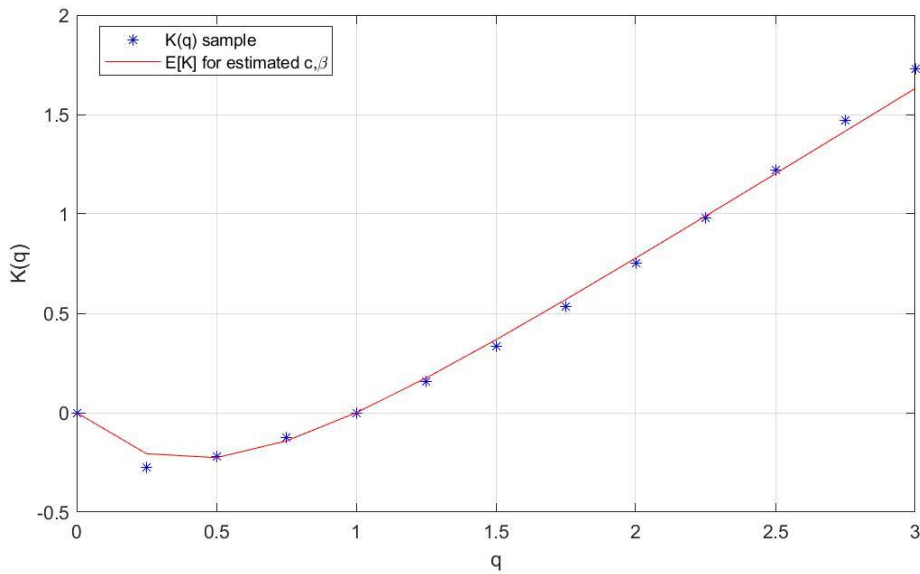


K-2 Empirical multifractal scaling function $K(q)$ for 320-min aggregated 2nd radar sequence selected from 2015 together with fitted theoretical $K(q)$ function model for estimated c and fixed β parameter

APPENDIX K: MULTIFRACTAL SCALING FUNCTION $K(q)$ FOR SELECTED RADAR SEQUENCES FROM 2015. $K(q)$ THEORETICAL MODEL FOR ESTIMATED c PARAMETER AND FIXED β PARAMETER

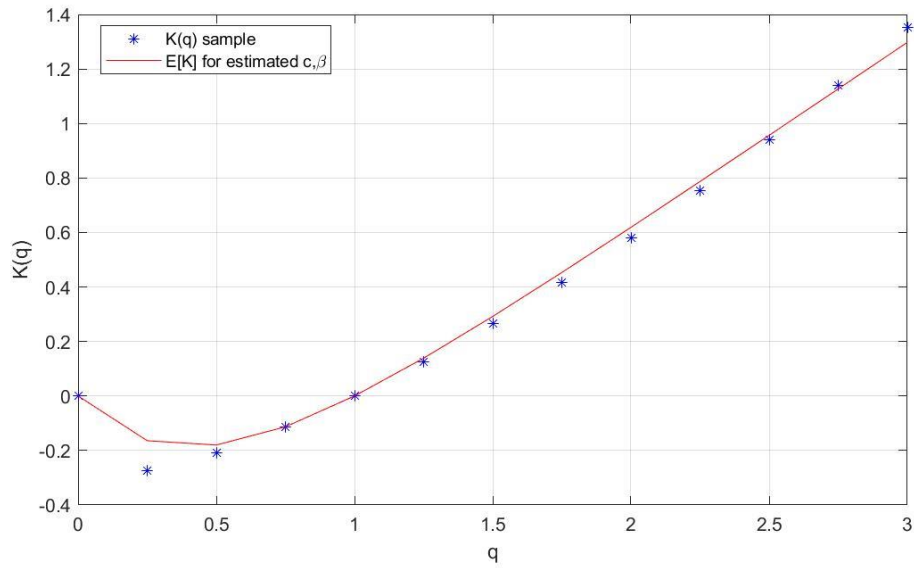


K-3 Empirical multifractal scaling function $K(q)$ for 320-min aggregated 3rd radar sequence selected from 2015 together with fitted theoretical $K(q)$ function model for estimated c and fixed β parameter

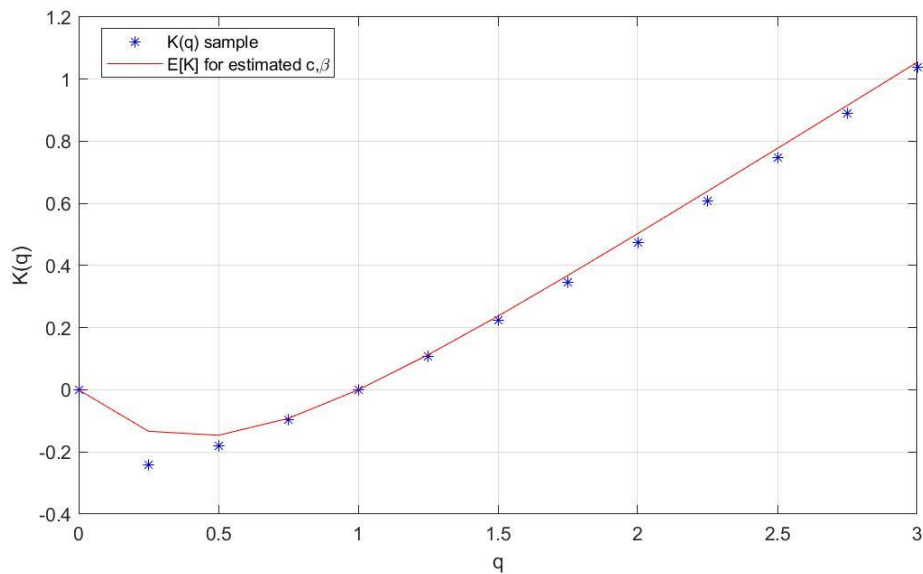


K-4 Empirical multifractal scaling function $K(q)$ for 320-min aggregated 4th radar sequence selected from 2015 together with fitted theoretical $K(q)$ function model for estimated c and fixed β parameter

APPENDIX K: MULTIFRACTAL SCALING FUNCTION $K(q)$ FOR SELECTED RADAR SEQUENCES FROM 2015. $K(q)$ THEORETICAL MODEL FOR ESTIMATED c PARAMETER AND FIXED β PARAMETER

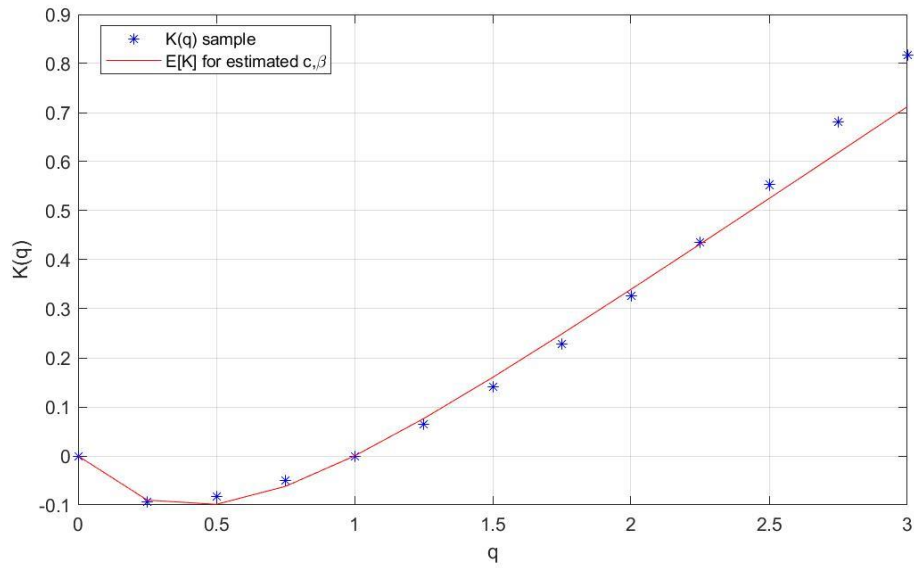


K-5 Empirical multifractal scaling function $K(q)$ for 320-min aggregated 5th radar sequence selected from 2015 together with fitted theoretical $K(q)$ function model for estimated c and fixed β parameter

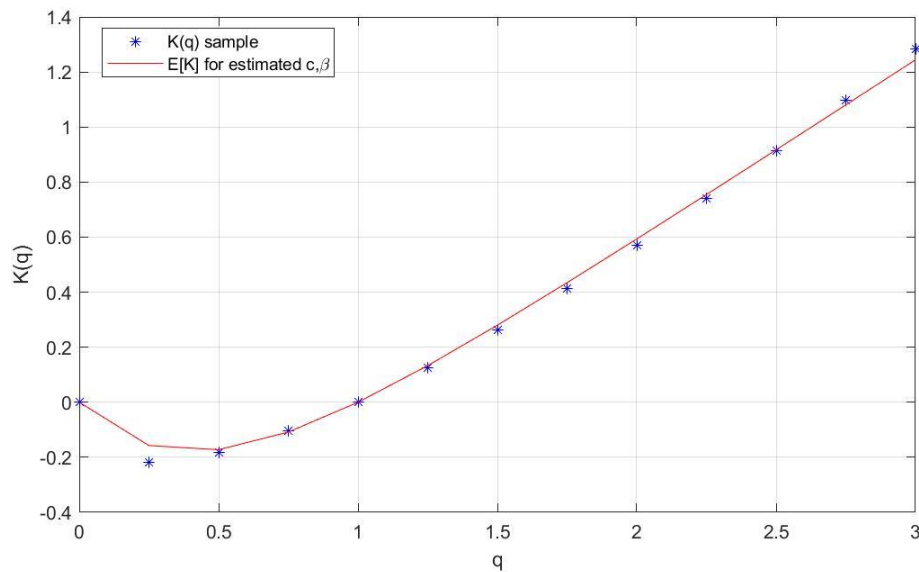


K-6 Empirical multifractal scaling function $K(q)$ for 320-min aggregated 6th radar sequence selected from 2015 together with fitted theoretical $K(q)$ function model for estimated c and fixed β parameter

APPENDIX K: MULTIFRACTAL SCALING FUNCTION $K(q)$ FOR SELECTED RADAR SEQUENCES FROM 2015. $K(q)$ THEORETICAL MODEL FOR ESTIMATED c PARAMETER AND FIXED β PARAMETER

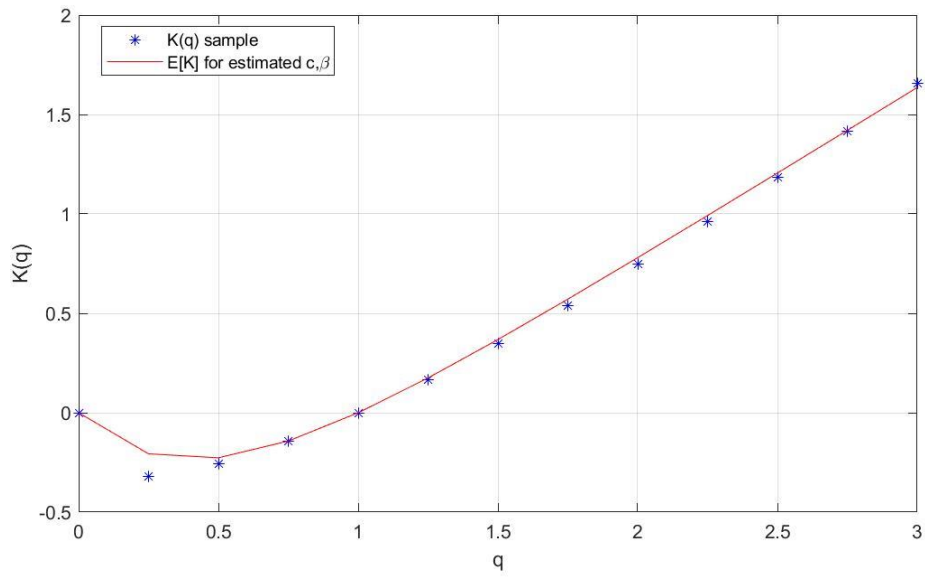


K-7 Empirical multifractal scaling function $K(q)$ for 320-min aggregated 7th radar sequence selected from 2015 together with fitted theoretical $K(q)$ function model for estimated c and fixed β parameter

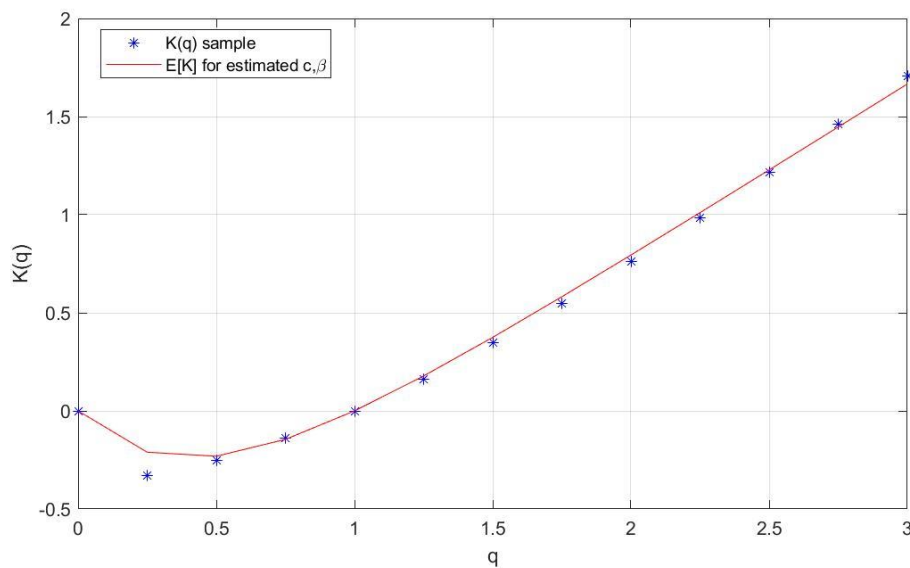


K-8 Empirical multifractal scaling function $K(q)$ for 320-min aggregated 8th radar sequence selected from 2015 together with fitted theoretical $K(q)$ function model for estimated c and fixed β parameter

APPENDIX K: MULTIFRACTAL SCALING FUNCTION $K(q)$ FOR SELECTED RADAR SEQUENCES FROM 2015. $K(q)$ THEORETICAL MODEL FOR ESTIMATED c PARAMETER AND FIXED β PARAMETER

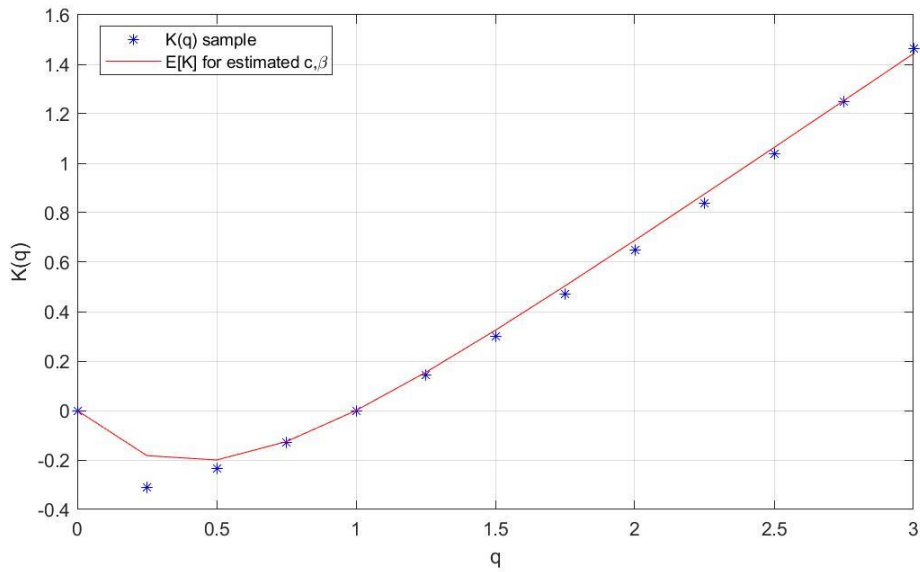


K-9 Empirical multifractal scaling function $K(q)$ for 320-min aggregated 9th radar sequence selected from 2015 together with fitted theoretical $K(q)$ function model for estimated c and fixed β parameter

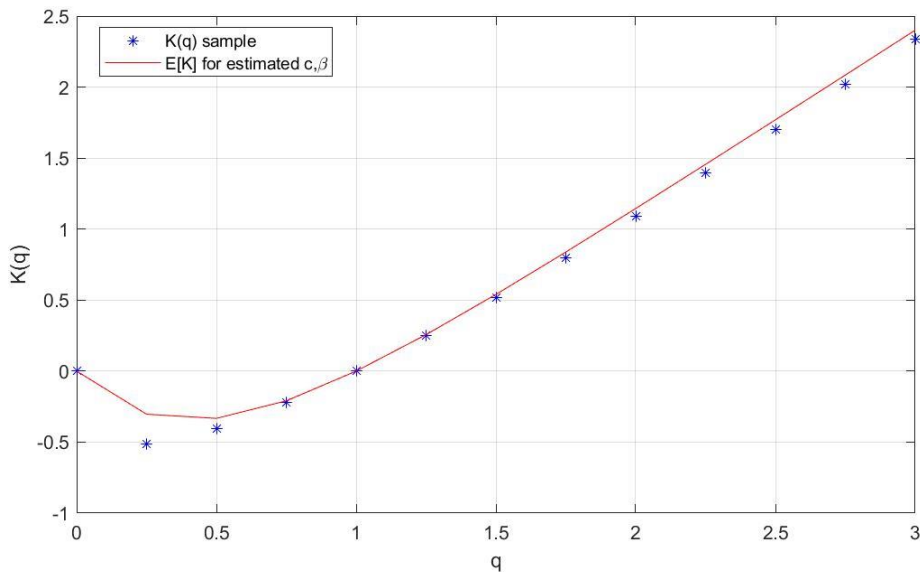


K-10 Empirical multifractal scaling function $K(q)$ for 320-min aggregated 10th radar sequence selected from 2015 together with fitted theoretical $K(q)$ function model for estimated c and fixed β parameter

APPENDIX K: MULTIFRACTAL SCALING FUNCTION $K(q)$ FOR SELECTED RADAR SEQUENCES FROM 2015. $K(q)$ THEORETICAL MODEL FOR ESTIMATED c PARAMETER AND FIXED β PARAMETER

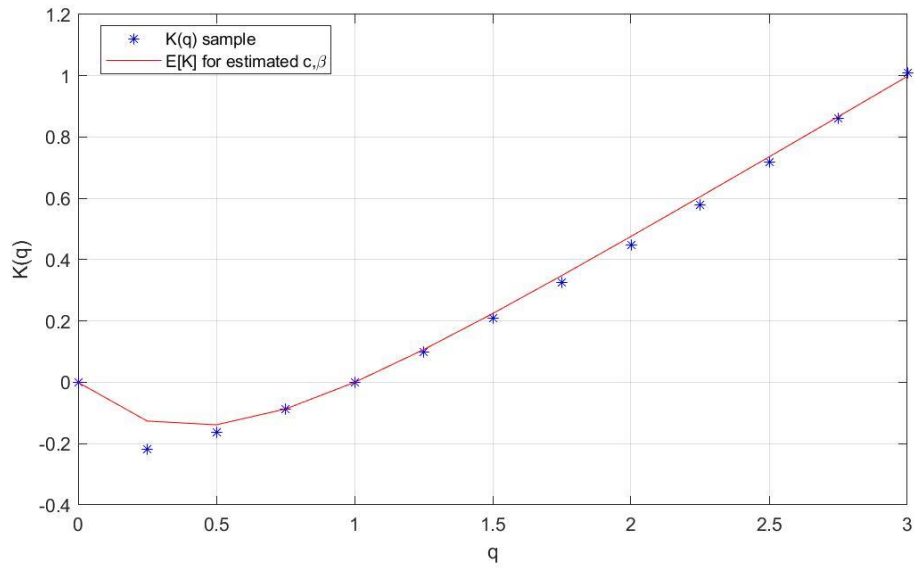


K-11 Empirical multifractal scaling function $K(q)$ for 320-min aggregated 11th radar sequence selected from 2015 together with fitted theoretical $K(q)$ function model for estimated c and fixed β parameter

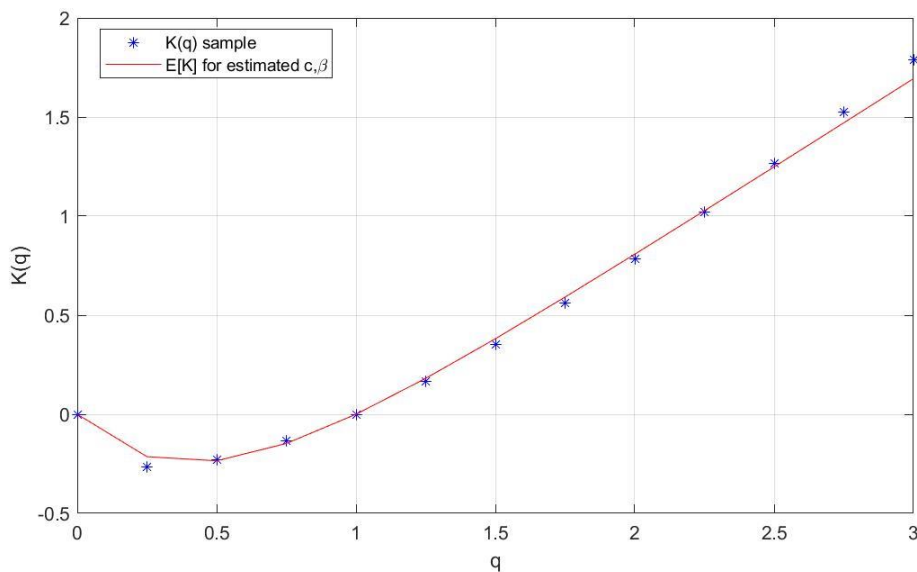


K-12 Empirical multifractal scaling function $K(q)$ for 320-min aggregated 12th radar sequence selected from 2015 together with fitted theoretical $K(q)$ function model for estimated c and fixed β parameter

APPENDIX K: MULTIFRACTAL SCALING FUNCTION $K(q)$ FOR SELECTED RADAR SEQUENCES FROM 2015. $K(q)$ THEORETICAL MODEL FOR ESTIMATED c PARAMETER AND FIXED β PARAMETER

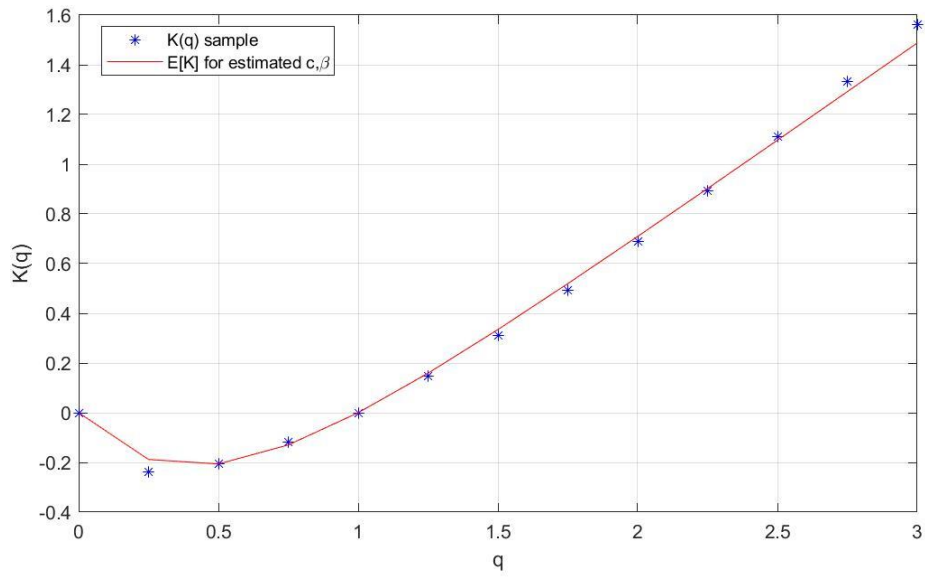


K-13 Empirical multifractal scaling function $K(q)$ for 320-min aggregated 13th radar sequence selected from 2015 together with fitted theoretical $K(q)$ function model for estimated c and fixed β parameter

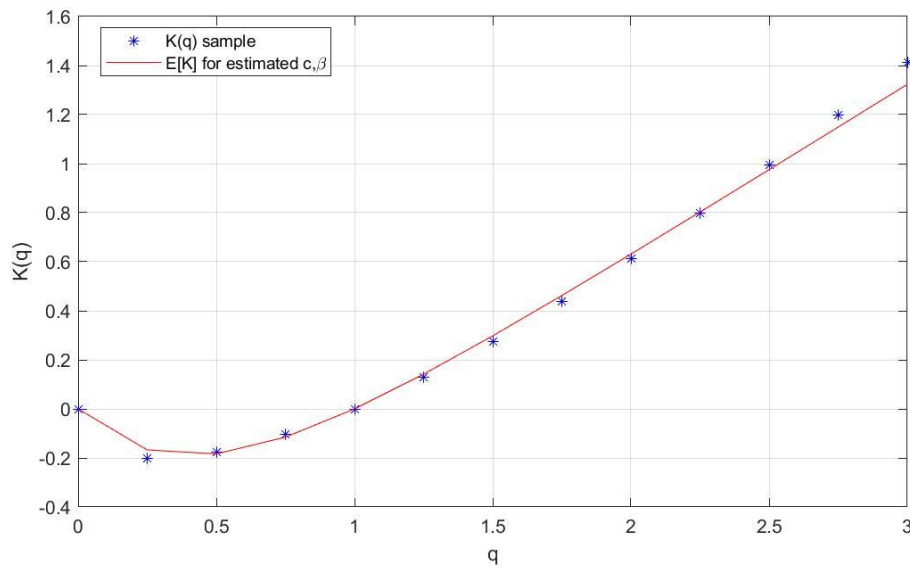


K-14 Empirical multifractal scaling function $K(q)$ for 320-min aggregated 14th radar sequence selected from 2015 together with fitted theoretical $K(q)$ function model for estimated c and fixed β parameter

APPENDIX K: MULTIFRACTAL SCALING FUNCTION $K(q)$ FOR SELECTED RADAR SEQUENCES FROM 2015. $K(q)$ THEORETICAL MODEL FOR ESTIMATED c PARAMETER AND FIXED β PARAMETER

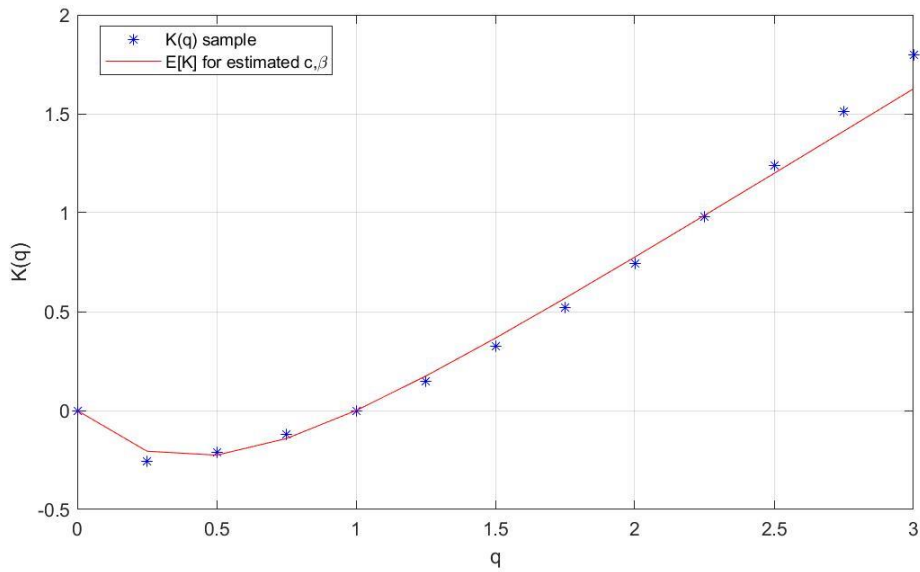


K-15 Empirical multifractal scaling function $K(q)$ for 320-min aggregated 15th radar sequence selected from 2015 together with fitted theoretical $K(q)$ function model for estimated c and fixed β parameter

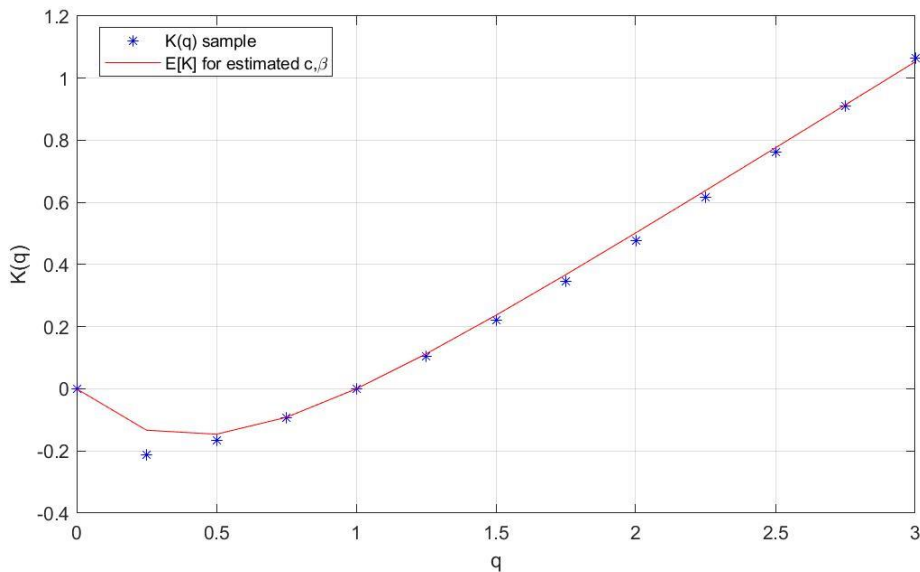


K-16 Empirical multifractal scaling function $K(q)$ for 320-min aggregated 16th radar sequence selected from 2015 together with fitted theoretical $K(q)$ function model for estimated c and fixed β parameter

APPENDIX K: MULTIFRACTAL SCALING FUNCTION $K(q)$ FOR SELECTED RADAR SEQUENCES FROM 2015. $K(q)$ THEORETICAL MODEL FOR ESTIMATED c PARAMETER AND FIXED β PARAMETER

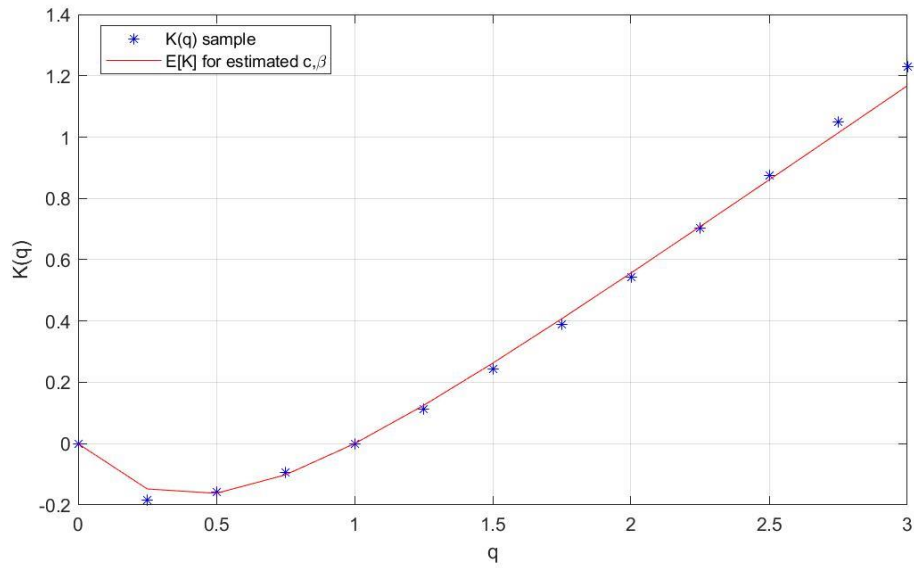


K-17 Empirical multifractal scaling function $K(q)$ for 320-min aggregated 17th radar sequence selected from 2015 together with fitted theoretical $K(q)$ function model for estimated c and fixed β parameter

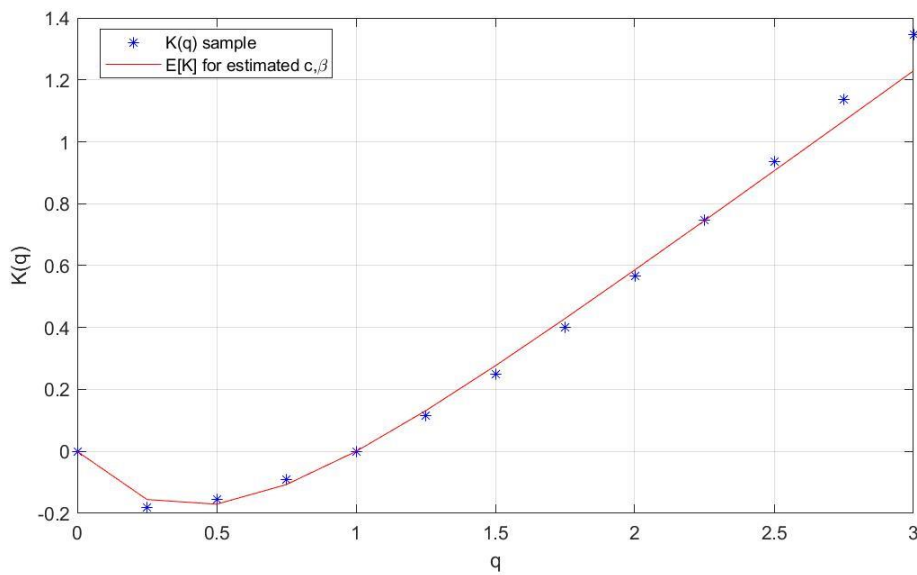


K-18 Empirical multifractal scaling function $K(q)$ for 320-min aggregated 18th radar sequence selected from 2015 together with fitted theoretical $K(q)$ function model for estimated c and fixed β parameter

APPENDIX K: MULTIFRACTAL SCALING FUNCTION $K(q)$ FOR SELECTED RADAR SEQUENCES FROM 2015. $K(q)$ THEORETICAL MODEL FOR ESTIMATED c PARAMETER AND FIXED β PARAMETER

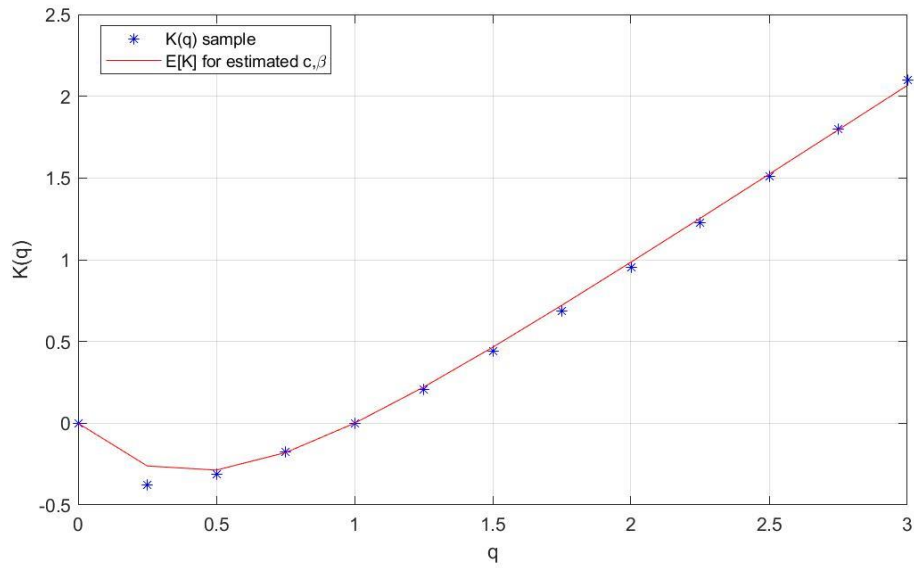


K-19 Empirical multifractal scaling function $K(q)$ for 320-min aggregated 19th radar sequence selected from 2015 together with fitted theoretical $K(q)$ function model for estimated c and fixed β parameter

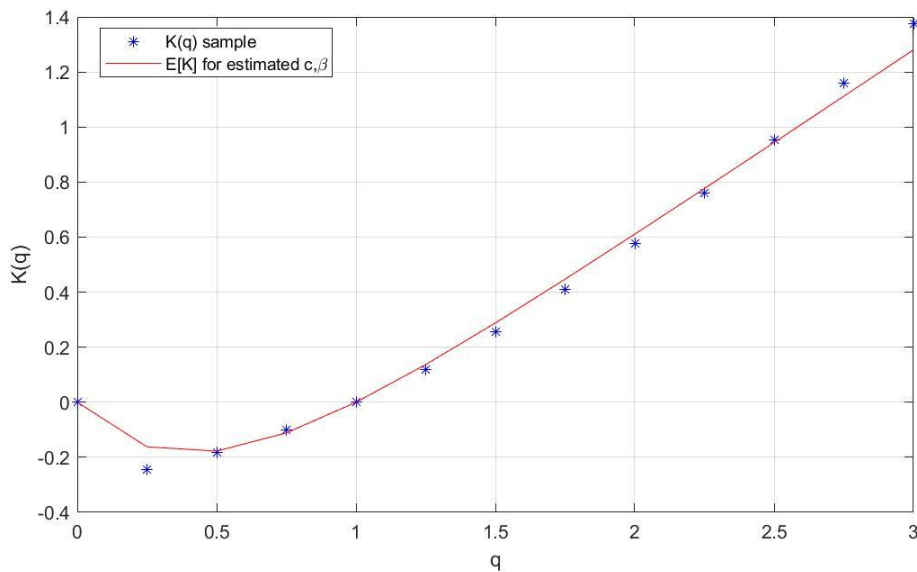


K-20 Empirical multifractal scaling function $K(q)$ for 320-min aggregated 20th radar sequence selected from 2015 together with fitted theoretical $K(q)$ function model for estimated c and fixed β parameter

APPENDIX K: MULTIFRACTAL SCALING FUNCTION $K(q)$ FOR SELECTED RADAR SEQUENCES FROM 2015. $K(q)$ THEORETICAL MODEL FOR ESTIMATED c PARAMETER AND FIXED β PARAMETER



K-21 Empirical multifractal scaling function $K(q)$ for 320-min aggregated 21st radar sequence selected from 2015 together with fitted theoretical $K(q)$ function model for estimated c and fixed β parameter



K-22 Empirical multifractal scaling function $K(q)$ for 320-min aggregated 22nd radar sequence selected from 2015 together with fitted theoretical $K(q)$ function model for estimated c and fixed β parameter